Development and Evaluation of Selective Matrix Metalloproteinase-13 PET Radiotracers for Imaging Atherosclerosis

Ariel Buchler

Thesis submitted to the University of Ottawa
in partial fulfillment of the requirements for the
Doctorate in Philosophy degree in Chemistry

Department of Chemistry and Biomolecular Sciences
Faculty of Science
University of Ottawa

© Ariel Buchler, Ottawa, Canada, 2024

ABSTRACT

Atherosclerosis is a chronic inflammatory disease characterized by the buildup of lipid-rich plaques within the coronary arteries and a leading cause of death worldwide. Given that plaque rupture occurs due to molecular changes in plaque composition and is considered the primary cause of heart attack and stroke, molecular imaging by positron emission tomography (PET) provides the opportunity to assess disease severity and may assist in the prevention of severe cardiovascular events and associated fatal outcomes.

Matrix metalloproteinases (MMPs) represent a class of zinc-chelating enzymes with diverse functions in extracellular matrix (ECM) remodeling during normal physiological processes and inflammatory diseases. As MMPs possess distinct substrate specificity and differential roles in disease progression, selective targeting of individual MMPs should be prioritized for diagnosis and therapy. Upregulated MMP-13 activity has been extensively implicated with atherosclerotic plaque destabilization due to uncontrolled ECM degradation and formation of thin-capped and collagen-poor plaques that are most susceptible to rupture. As such, MMP-13 represents a compelling molecular biomarker of unstable atherosclerosis for selective PET radiotracer development. This thesis outlines the synthesis, optimization, and evaluation of MMP-13 selective PET radiotracers for imaging atherosclerosis. Chapter I introduces atherosclerosis, provides an overview of MMPs as therapeutics and diagnostics, and describes available strategies for MMP-13 selective radiotracer development.

Chapter II outlines a head-to-head comparison of MMP-13 selective and broad-spectrum MMP imaging with existing fluorine-18 labeled PET radiotracers. In this study, the first *in vivo* evaluation of [^{18}F]FMBP and [^{18}F]BR-351, as MMP-13 selective and non-selective MMP-targeted radiotracers based on the pyrimidine-dicarboxamide and non-peptidic aryl sulfonamide inhibitor

classes, was performed in a mouse model of atherosclerosis. Determination of radiotracer pharmacokinetics, target specificity, and sensitivity to atherosclerotic tissue validated the feasibility of using an MMP-13 selective PET radiotracer to detect ECM remodeling in atherosclerotic plaques and demonstrated several advantages to this strategic imaging approach.

Chapter III describes the development and evaluation of novel MMP-13 selective PET radiotracers based on the most potent and selective quinazoline-2-carboxamide inhibitor class for imaging atherosclerosis. Structure-activity relationship (SAR) studies were performed with a particular focus on modifications that would facilitate late-stage radiolabeling with carbon-11 or fluorine-18 and pharmacokinetic characterization in atherosclerotic mice. The first biological evaluation of three candidate radiotracers [^{11}C]5b, [^{11}C]5f, and [^{18}F]5j was conducted and elucidated the structural determinants required to obtain *in vivo* functional activity, MMP-13 specificity/selectivity, and desirable pharmacokinetics for vascular imaging. This study further highlighted the superiority of the quinazoline-2-carboxamide scaffold for selective MMP-13 PET radiotracer development and identified [^{18}F]5j as a promising lead for *ex vivo* atherosclerotic plaque imaging.

Chapter IV focuses on the synthesis and design of highly functionalized second-generation MMP-13 selective PET radiotracers based on the quinazoline-2-carboxamide scaffold with greater contrast for non-invasive atherosclerotic plaque imaging. Structural modifications focused on restoring critical binding interactions, incorporating a new site for fluorine-18 or carbon-11 radiolabeling, and reducing lipophilicity. SAR uncovered the optimized inhibitor 29f as a promising lead radiotracer candidate with remarkably enhanced MMP-13 potency and off-target selectivity. *In vivo* evaluations of [^{11}C]29f in atherosclerotic mice demonstrated its favorable pharmacokinetic properties and assessed its potential utility for atherosclerosis.

ACKNOWLEDGMENTS

To my supervisor, Benjamin Rotstein, I am extremely lucky that you initially took a chance on me as an undergraduate student and entrusted me as the first member of your lab. Your kindness, unwavering support, and passion for radiochemistry were evident from the beginning, making my decision to pursue graduate studies under your guidance an easy choice. I feel incredibly fortunate to have had the opportunity to learn from you over the past 7 years and am immensely grateful for the diverse training you provided, your belief in my abilities, and your genuine commitment to my growth and success. I am especially appreciative of your mentorship and the relationship we've established on both a professional and personal level and hope to maintain this moving forward.

To my lab members, who have both greatly assisted with this work and built a positive and welcoming work environment. First, to Uzair Ismailani, I learned a lot from your critical thinking and innovative ideas during our late-night imaging studies and could not have done this without your support. To Maxime Munch, thank you for building my technical skills in chemistry and your patience with my countless questions. To Braeden Mair, it's not often that you get to complete your PhD alongside your best friend and I'm forever grateful that we got to share this experience and grow together. To Myriam Adi, your attention to detail and productivity was greatly motivating and accelerated the completion of this work. To Faduma Abdirahman, Jadde Tso, Christina Bi, Abhishek Patel, and Hala Almeneim I appreciated your assistance and kindness throughout my time in the lab. To all of you, the memories and friendships we've built over the years will always be remembered.

To my parents, thank you for your unconditional love, understanding, and encouragement throughout my academic journey. Thank you for instilling a strong work ethic in me, for putting me in a position to succeed, and for everything you do to help me excel. I know I can always count on you. To my brothers Matan, Noam, and Lior, thank you for your support and interest with my lab experiments, your ability to cheer me up and make me laugh, and for always giving honest reviews of my food and drinks.

TABLE OF CONTENTS

List of Figures, Tables and Schemes

List of Abbreviations

AAA	Abdominal aortic aneurysm
ADAM	A disintegrin and metalloproteinase
ApoB	Apolipoprotein B
$ApoE^{-/-}$	Apolipoprotein E knockout
BS	Bone scintigraphy
Bq	Becquerel
^{11}C	Carbon -11
$[^{11}C]CH_3I$	[^{11}C]methyl iodide
$[^{11}C]CH_3OTf$	[^{11}C]methyl triflate
$[^{11}C]CO_2$	[^{11}C]carbon dioxide
^{64}Cu	Copper-64
CAC	Coronary artery calcium
CAD	Coronary artery disease
CCTA	Coronary computed tomography angiography
CMA	Coronary microcalcification activity
CMR	Cardiac magnetic resonance
Cpv	Counts per voxel
CT	Computed tomography
DOTA	Dodecane tetraacetic acid
ECG	Electrocardiogram
ECM	Extracellular matrix
eV	Electron volt

^{18}F	Fluorine-18
[^{18}F]FDG	[^{18}F]2-deoxy-2-fluoro-D-glucose
[^{18}F]FDG-6P	[^{18}F]2-deoxy-2-fluoro-D-glucose-6-phosphate
Fbn1	Fibrillin 1
GLUT1	Glucose transporter 1
HA	Hydroxamic acid
HFD	High fat diet
HK2	Hexokinase 2
HYNIC	Hydrazinonicotinamide
%ID	Percentage injected dose
^{111}In	Indium-111
ICA	Invasive coronary angiography
ICAM-1	Intracellular adhesion molecule 1
IL-1/6	Interleukin 1/6
LDL	Low density lipoprotein
LDLR	Low density lipoprotein receptor
$LDLR^{-/-}$	Low density lipoprotein receptor knockout
MCP-1	Monocyte chemoattractant protein 1
MIA	Monoiodoacetate
MMP	Matrix metalloproteinase
MMPI	Matrix metalloproteinase inhibitor
MPI	Myocardial perfusion imaging
MRI	Magnetic resonance imaging

mRNA	Messenger ribonucleic acid
MSS	Musculoskeletal syndrome
Mac-2	Type 2 macrophage
^{14}N	Nitrogen-14
[^{18}F]NaF	[^{18}F]sodium fluoride
^{18}O	Oxygen-18
OA	Osteoarthritis
OAT	Organic anion transporter
ORO	Oil red O
Ox-LDL	Oxidized low density lipoprotein
PDGF	Platelet derived growth factor
PET	Positron emission tomography
p.i.	Post injection
SAR	Structure activity relationship
SMC	Smooth muscle cell
SN2	Nucleophilic substitution
SNAr	Nucleophilic aromatic substitution
SUV	Standardized uptake value
SPECT	Single photon emission computed tomography
^{99m}Tc	Technetium-99m
TIMP	Tissue inhibitor of metalloproteinase
TNFα	Tumor necrosis factor alpha
VCAM-1	Vascular cell adhesion protein 1

VEGF	Vascular endothelial growth factor
VLDL	Very low density lipoprotein
ZBG	Zinc binding group

1.0 INTRODUCTION

1.1 Positron Emission Tomography

Positron emission tomography (PET) is a molecular imaging modality used in nuclear medicine that harnesses injectable radiolabeled substances, known as radiotracers, to visualize and quantify *in vivo* biochemical processes.[1] PET imaging has become an integral part of routine clinical practice to diagnose and monitor pathophysiological conditions and continues to have a profound impact in cardiology, oncology, and neurology.[2–4] PET radiotracers integrate radionuclides into small molecules, peptides or antibodies which typically target a protein of interest and provide information on its distribution within the body and concentration over time.[1] PET radionuclides are commonly produced using a medical cyclotron which applies an oscillating electric field to rapidly accelerate a charged particle (proton) and irradiate a target material.[5,6] Upon bombardment, the resulting radionuclides are incorporated into biomolecules using various radiochemical transformations and purified, yielding the desired radiotracers for subsequent intravenous administration. Following radiotracer delivery, the radioactive signal is externally tracked using a PET camera containing a full-ring array of detectors surrounding the imaging subject (Figure 1.0 A).[1] As radioactive decay occurs, commonly through β+ decay, a proton is converted to a neutron while releasing a positron.[7] The emitted positron annihilates with an electron generating two antiparallel (180°) gamma photons of 511 keV energy that are simultaneously detected in coincidence (Figure 1.0 A).[1,7] Following application of iterative reconstruction algorithms to correct for scattering, random coincidence events, and signal attenuation, three-dimensional images are assembled, providing fully quantitative and dynamic information about the spatial distribution of radioactivity in different organs[1,7]. To further improve

the spatial resolution, multimodal imaging with computed tomography (CT) or magnetic resonance imaging (MRI) is routinely performed for anatomical orientation and enables accurate quantification of small structures (<1 mm).[8]

A

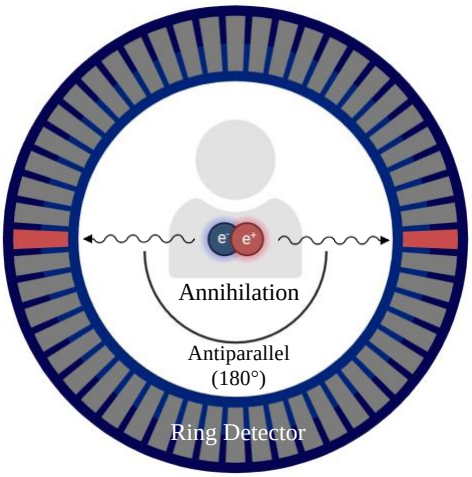

B

Radionuclide	Common Forms	Half-life (t ½ min)	Typical Reactivity
Fluorine-18	[^{18}F]Fluoride	109.7	Polar Nucleophilic
Carbon-11	[^{11}C]CO_2 [^{11}C]CH_3I [^{11}C]CH_3OTf	20.4	Polar Electrophilic

Figure 1.0 Positron emission tomography imaging and radionuclides. (A) PET scanner and detection method. (B) Reactivity of fluorine-18 and carbon-11.

1.2 Fluorine-18 Properties and Radiochemistry

Fluorine-18 represents the most widely utilized positron-emitting radionuclide for diagnostic imaging. This radionuclide is readily produced using a cyclotron by proton bombardment of oxygen-18 enriched water via the $^{18}O(p,n)^{18}F$ nuclear reaction.[1] The broad utility of fluorine-18 stems from its excellent nuclear properties including a short physical half-life of 109.8 min which permits centralized production with local radiotracer distribution. Furthermore, its intrinsic low energy positron emission (E_{max} = 0.63 MeV), short positron range (R_{max} = 2.4 mm), and high positron branching ratio (96.9%) confer excellent spatial resolution and sensitivity.[7] Due to the increasing prevalence of fluorinated small molecule pharmaceuticals and its applicability in medicinal chemistry research, efficient strategies for incorporation of fluorine-18

have become vital to drug discovery and PET radiotracer development.[9] Synthetic radiofluorination methods largely rely on aliphatic nucleophilic substitution (S_N2) or nucleophilic aromatic substitution (S_NAr) of electron-withdrawing precursors possessing a good leaving group with [^{18}F]fluoride (Figure 1.0 B).[1,10] Nevertheless, such strict electronic requirements along with the highly basic conditions and high reaction temperatures (>100 °C) necessary for radiofluorination can pose challenges for synthetic accessibility.[1,10]

1.3 Carbon-11 Properties and Radiochemistry

Considering the abundance of carbon in all organic molecules, carbon-11 represents a convenient alternative to access isotopically labeled radiopharmaceuticals.[11] Carbon-11 is typically generated as [^{11}C]carbon dioxide ([^{11}C]CO_2) using a cyclotron by proton bombardment of nitrogen-14 gas in the presence of trace oxygen (0.1-2%) via the $^{14}N(p,\alpha)^{11}C$ nuclear reaction.[1] Direct utilization of [^{11}C]CO_2 as radiolabeling synthon is an active area of method development to access a diverse array of functional groups bearing C-11 labeled carbonyls including carboxylic acids, amides, ureas, and carbamates.[12] Nonetheless, in clinical radiotracer production, conversion of [^{11}C]CO_2 to [^{11}C]methyl iodide ([^{11}C]CH_3I) or the more reactive [^{11}C]methyl triflate ([^{11}C]CH_3OTf) for ^{11}C-methylation is favored and generally offers greater operational simplicity.[12] Despite its short half-life of 20.4 min necessitating an on-site cyclotron for radiotracer production, carbon-11 PET minimizes patient radiation burden, and retains excellent imaging quality as a pure positron emitter (99.8%) with relatively low energy (E_{max} = 0.96 MeV) and short range (R_{max} = 4.2 mm).[7] Moreover, methylated heteroatoms are prevalent components of biomolecules and synthesis of radiolabeling precursors for ^{11}C-methylation is uncomplicated and efficiently yields radiotracers in high molar activity.[12] This strategy is particularly useful for accelerating preclinical screenings of radiotracer performance in rodents recapitulating human pathologies and identifying

lead candidates for clinical translation. Subsequent development of radiofluorinated analogues can be advantageous due to the incompatibility of carbon-11 with commercial distribution and delayed imaging timepoints required to achieve significant contrast for cancer and cardiovascular imaging.[13,14]

1.4 Atherosclerosis

1.4.1 Prevalence

Cardiovascular diseases, including heart failure and atherosclerosis, represent the second leading cause of death in Canada with 5-year survival of only 50% and over 60,000 deaths each year.[15,16] Atherosclerosis is a chronic inflammatory disease of the coronary arteries and is considered the primary cause of myocardial infarction, stroke, and sudden cardiac death.[17,18] As such, identification of the key molecular targets that contribute to atherosclerotic progression is of significant clinical interest to facilitate discovery of novel diagnostic or therapeutic agents that can detect early-stage disease and prevent life-threatening outcomes.

1.4.2 Risk Factors and Plaque Initiation

Atherosclerosis is a progressive inflammatory disease characterized by the accumulation of lipids and fibrous elements within the coronary arteries and aorta (Figure 1.1).[19–21] This process is initiated within the endothelium, which constitutes the innermost cellular lining of the vasculature, and plays a pivotal role in regulating vascular homeostasis, tone, and integrity.[22,23] Chronic exposure to cardiovascular risk factors including hypertension and hypercholesterolemia induces endothelial dysfunction, marked by vasoconstriction, increased permeability, and inflammation.[24] Loss of hemodynamic control causes endothelial damage as high blood pressure and disturbed flow applies shear stress on the vessel wall and enables accumulation of circulating

cholesterol packaged into low-density lipoprotein (LDL) particles (Figure 1.1 A).[19–21] Activated endothelial cells elicit production of adhesion molecules such as vascular cell adhesion molecule 1 (VCAM-1), intercellular adhesion molecule 1 (ICAM-1), and monocyte chemoattractant protein 1 (MCP-1) that augment monocyte attachment and infiltration (Figure 1.1 A).[19–22] Entry and retention of LDL particles is mediated by oxidation of LDL and surface-bound apolipoprotein-B (ApoB) preventing recognition and clearance by LDL receptors.[19–21]

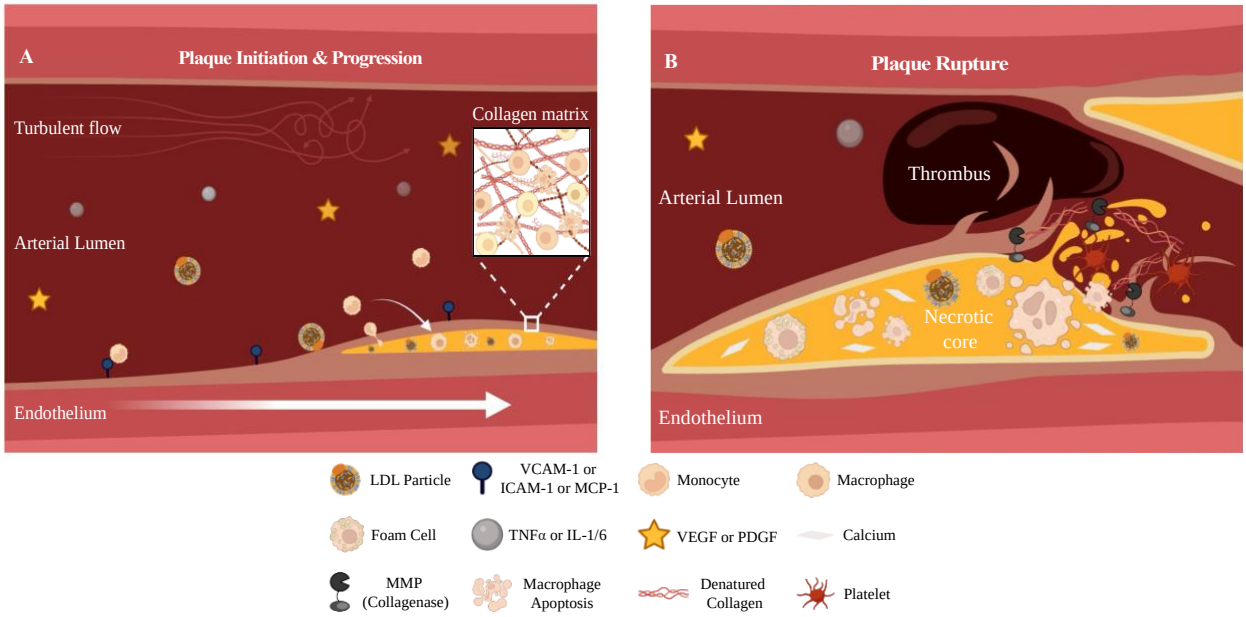

Figure 1.1 Mechanisms of atherosclerosis. (A) Initiation of atherosclerosis and plaque progression. (B) Plaque rupture and thrombosis. Turbulent blood flow applies shear stress on the vessel wall, resulting in endothelial damage and entry of circulating LDL. Recruited monocytes differentiate into macrophages and engulf LDL particles, leading to progressive plaque formation with a collagen-rich fibrous cap. Persistent inflammation activates MMPs that degrade collagen within the fibrous cap, weakening its structural integrity, and leading to plaque rupture. Thrombus formation blocks the coronary arteries and limits the supply of blood to the heart or brain, causing a heart attack or stroke.

1.4.3 Plaque Progression

Following differentiation of monocytes into macrophages, surface-expressed scavenger receptors bind and internalize ox-LDL forming foam cells and visible fatty steaks (Figure 1.1 A).[19–21,25,26] These foam cells perpetuate the inflammatory response through secretion of cytokines such as tumor necrosis factor alpha (TNFα) and interleukin-1/6 (IL-1/6) along with growth factors such as vascular endothelial growth factor (VEGF) and platelet-derived growth factor (PDGF) that stimulate smooth muscle cell (SMC) proliferation, calcification, and matrix metalloproteinase (MMP) activation (Figure 1.1 B).[19–21,27,28] Macrophage lipid overload triggers apoptosis while impaired efferocytosis contributes to an inflammatory acellular necrotic core (Figure 1.1 B). In response to inflammation and oxidative stress, SMCs differentiate into osteoblast-like cells that promote deposition of calcification and matrix mineralization (Figure 1.1 B).[19–21,29]

1.4.4 Plaque Rupture and Thrombosis

MMPs facilitate the release of SMC from the basement membrane and allow migration to the intima where they proliferate and synthesize a collagen-rich fibrous cap that encapsulates the necrotic core.[30–32] Elevated MMP activity significantly destabilizes atherosclerotic plaques by degradation of ECM components within the fibrous cap, resulting in thinning and weakening of its structural integrity (Figure 1.1 B).[27,31–33] While large plaques are responsible for myocardial ischemia and often accompanied by stable angina, rupture of vulnerable atherosclerotic plaques, characterized by thin and collagen-poor fibrous caps overlaying a large lipid-rich necrotic core are the primary cause of life-threatening cardiovascular events.[17,18,32,34–36] Following erosion of the fibrous cap and plaque rupture, circulating platelets adhere to exposed collagen and necrotic core

material and aggregate within the arterial lumen, initiating the coagulation cascade (Figure 1.1 B).[37,38] Formation of occlusive thrombin-mediated fibrin-based blood clots within the coronary and branching carotid arteries that supply oxygen-rich blood to the myocardium and brain are ultimately responsible for myocardial infarction, stroke, and associated fatal outcomes (Figure 1.1 B).[31,32,34,35] As such, early identification of vulnerable atherosclerotic plaques prior to rupture is critical for stratifying patients at risk of developing major adverse cardiovascular events.

1.5 Clinical Diagnosis of Atherosclerosis and Coronary Artery Disease

1.5.1 Functional Imaging

Symptomatic patients presenting with intermittent chest pain and suspected coronary artery disease (CAD) are first referred for an electrocardiogram (ECG). Concurrently, an initial assessment of pre-test probability is conducted to determine the likelihood that a patient has CAD based on their age, sex, medical history, and the presence of additional risk factors including hypertension, hyperlipidemia, diabetes, and smoking.[39] An ECG is used to assess cardiac function and identify electrical abnormalities indicative of underlying CAD.[40] By comparison of baseline and stress ECGs performed under exercise or pharmacological conditions, the capacity of the heart to respond to stress can delineate myocardial ischemia.[40] Similarly, rest-stress nuclear myocardial perfusion imaging (MPI) can assist in diagnosing CAD by identifying defects with reduced blood flow due to coronary artery stenosis or occlusion caused by atherosclerosis.[41] Absolute quantification of myocardial blood flow and myocardial flow reserve have proven to be important diagnostic measures of obstructive CAD with practical clinical utility in selecting patients for revascularization surgery.[41] Despite this, MPI cannot directly assess atherosclerotic plaque burden or non-obstructive disease and instead relies on indirect detection of myocardial ischemia as a functional consequence of coronary artery obstruction and may underestimate the prevalence of

CAD.[42] As with MPI, cardiovascular magnetic resonance imaging (CMR) with late gadolinium enhancement can be used to assess myocardial perfusion or viability and provides excellent soft tissue contrast. Nevertheless, CMR is not a part of routine clinical practice for CAD due to the lack of additional diagnostic benefit, limited accessibility, and high cost.[43]

1.5.2 Anatomical Imaging

While functional imaging tests are insufficient in predicting atherosclerosis alone, they are indispensable in screening patients with suspected CAD and complementary to anatomical imaging.[44] Invasive coronary angiography (ICA) was considered the gold standard for clinical diagnosis of CAD and involves direct catheterization and contrast-aided imaging of the coronary arteries to determine the location and severity of stenosis.[45] While ICA possesses high diagnostic accuracy, coronary computed tomography angiography (CCTA) has been adopted as a non-invasive alternative with comparable sensitivity and specificity for the detection of CAD and demonstrated improved patient outcomes in addition to standard patient care.[44–49] Rather than the degree of stenosis, CT can also be used for coronary artery calcium scoring (CAC) to quantify the extent and density of calcification and provide a score that reflects total atherosclerotic plaque burden.[50,51] Higher CAC scores are associated with increased risk of future cardiovascular events, however, the absence of coronary calcium does not exclude the presence of obstructive CAD and should not be used as a standalone diagnostic test.[50,52] Moreover, CAC does not provide incremental prognostic value to CCTA, but it can be used to guide clinical decisions regarding the initiation of statin therapy.[52,53]

1.5.3 Molecular Imaging

Conventional functional and anatomical assessments of coronary artery stenosis and atherosclerotic plaque burden have proven unreliable in the prediction of life-threatening

cardiovascular events.[54] While CAD risk is most closely related to atherosclerotic plaque stability, current diagnostic methods focus nearly exclusively on plaque appearance and size. Considering that atherosclerotic plaque rupture is the major cause of heart attack and stroke, early non-invasive detection of vulnerable atherosclerotic plaques susceptible to rupture is of critical importance for risk stratification and to prevent fatal outcomes.[17,18,34,35] Given that molecular changes in atherosclerotic plaque composition underlie instability, PET radiotracers targeting specific molecular processes associated with plaque vulnerability provide the potential to accurately characterize atherosclerosis and predict risk of rupture.[55] Beyond nuclear MPI agents, [^{18}F]2-deoxy-2-fluoro-D-glucose ([^{18}F]FDG) and [^{18}F]sodium fluoride ([^{18}F]NaF) represent the most commonly utilized clinical PET radiotracers for atherosclerotic plaque imaging (Figure 1.2).

A

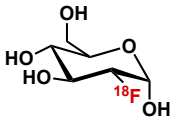

[^{18}F]2-Deoxy-2-fluoro-D-glucose ([^{18}F]FDG)

$Na^{+18}F^{-}$

Sodium [^{18}F]Fluoride ([^{18}F]NaF)

B

Radiotracer	Physiological Process	Anatomical Imaging Location	Cardiovascular Application
[^{18}F]FDG	Glucose metabolism	• Myocardium • Aorta	• Myocardial viability • Atherosclerosis inflammation
[^{18}F]NaF	Microcalcification activity	• Coronary arteries • Aorta	• CAD

Figure 1.2 Clinical PET radiotracers for atherosclerosis. (A) Chemical structures and (B) utility of [^{18}F]FDG and [^{18}F]NaF.

1.5.3.1 [^{18}F]2-Deoxy-2-fluoro-D-glucose ([^{18}F]FDG)

[^{18}F]FDG (Figure 1.2 A) is a radiofluorinated glucose analogue used to evaluate cellular metabolism with widespread clinical applicability for staging cancer, assessing myocardial viability, and detecting inflammatory cardiovascular diseases such as atherosclerosis and sarcoidosis (Figure 1.2 B).[56–59] Similar to glucose, cellular uptake of [^{18}F]FDG uptake is mediated by glucose transporter type 1 (GLUT1) but trapped intracellularly as [^{18}F]FDG-6P following

phosphorylation by hexokinase-2 (HK2).[60] As a deoxyglucose, [^{18}F]FDG is resistant to glycolysis and particularly useful for measuring the functional activity of metabolically active tissues such as the brain and heart or localizing tumors with elevated glucose utilization (Figure 1.2 B).[60] [^{18}F]FDG is routinely employed in combination with MPI among patients with ventricular dysfunction and suspected CAD to distinguish viable from nonviable myocardium (Figure 1.2 B). The presence of myocardial segments with decreased perfusion but preserved glucose metabolism, referred to as mismatch defects, are deemed ischemic but viable and predictive of functional recovery following coronary revascularization surgery.[61] Importantly, adherence to [^{18}F]FDG-PET guided management recommendations significantly reduced adverse cardiac events compared with standard care.[62]

[^{18}F]FDG can also be used to non-invasively assess arterial inflammation due to elevated macrophage expression of GLUT1 and HK2 activity in atherosclerotic plaques (Figure 1.2 B).[58,63,64] Although [^{18}F]FDG uptake has been shown to strongly correlate with the severity of inflammation, the association between radiotracer uptake and risk of plaque rupture has yet to be demonstrated.[58,64] Moreover, [^{18}F]FDG was unable to discern between culprit and non-culprit plaques among patients presenting with acute myocardial infarction.[65,66] Considering that [^{18}F]FDG is not a specific marker of inflammation and uptake is observed in all metabolically active cells, significant challenges exist in distinguishing coronary plaque uptake from physiologic radiotracer uptake in the myocardium.[67,68] Due to myocardial interference, localization of [^{18}F]FDG uptake is largely restricted to the carotid arteries and aorta and further impeded by the small anatomical size of coronary artery plaques and coronary motion (Figure 1.2 B).[66,69] While fusion of PET images with CT or angiography for anatomical referencing has improved the spatial resolution and to some extent the feasibility of coronary artery imaging, myocardial suppression

is still required.[66,69] High-fat low-carbohydrate diets may be used to reduce physiologic myocardial uptake by shifting metabolism toward preferential use of fatty acids, but the need for prolonged dietary preparation to obtain interpretable scans is unreliable and rather inconvenient for patients, limiting its practical utility.[69,70]

1.5.3.2 [^{18}F]Sodium Fluoride ([^{18}F]NaF)

[^{18}F]NaF (Figure 1.2 A) was originally developed as a PET alternative to ^{99m}Tc-labeled radiotracers for whole-body planar bone scintigraphy (BS) and single photon emission computed tomography (SPECT) imaging.[71] Alongside the inherent technological advantages regarding the spatial resolution of PET, [^{18}F]NaF exhibits superior diagnostic accuracy than BS or SPECT for the detection of metastatic bone lesions due to higher uptake and greater bone-to-soft tissue contrast.[72–74] [^{18}F]NaF is efficiently extracted from the plasma into the bone extracellular fluid where it is deposited as [^{18}F]fluoroapatite following ion exchange with hydroxyl groups of hydroxyapatite, a calcium-phosphate mineral that supports bone formation and turnover.[75] The major application of [^{18}F]NaF remains in detecting metastatic bone disease, but there is growing interest in its diagnostic utility for measuring vascular calcification in CAD (Figure 1.2 B).

Although calcification represents a universal marker of the atherosclerotic plaque, the size and pattern of calcium deposition has distinct implications on plaque stability.[76] Early-stage, small (<60 μm) spotty calcium deposits embedded within the fibrous cap, known as microcalcification, increase mechanical stress on the plaque surface and contribute to plaque instability.[55,76] In contrast, end-stage large macroscopic sheets of calcium within the necrotic core are associated with plaque stability and inflammation resolution.[76] Nevertheless, conventional CAC scoring is only capable of detecting macrocalcification due to limited spatial resolution and thus reports on

plaque burden but not plaque stability.[77] Meanwhile, [^{18}F]NaF preferentially accumulates in powdery regions of greatest hydroxyapatite surface area, reflecting active microcalcification, as hydroxyapatite crystal is largely inaccessible in the center of the macroscopic deposit (Figure 1.2 B).[75,78]

Owing to its favourable pharmacokinetics including low myocardial uptake and fast clearance from the blood pool, clear visualization of coronary artery [^{18}F]NaF uptake is feasible and offers the potential for early identification of vulnerable atherosclerotic plaques prone to rupture (Figure 1.2 B).[65,79] Clinical trials demonstrated that [^{18}F]NaF coronary microcalcification activity (CMA) represents a powerful predictor of disease progression and future myocardial infarction and outperforms both CAC scores and severity of coronary artery obstruction for risk stratification.[78,80,81] Moreover, among patients with myocardial infarction, [^{18}F]NaF was found to localize at the site of rupture with the highest uptake observed in culprit plaques, whereas [^{18}F]FDG was non-discriminatory and commonly obscured by myocardial uptake despite stringent dietary protocols.[65] Taken together, these finding suggests that molecular characterization of plaque composition by PET is a strategic approach toward differentiating vulnerable plaques and predicting risk of rupture.

1.6 Matrix Metalloproteinases (MMPs)

1.6.1 MMP Structure and Function

Matrix metalloproteinases (MMPs) represent a family of calcium-dependent, zinc-containing endopeptidases that are collectively capable of degrading all components of the extracellular matrix (ECM) with diverse physiological roles in tissue remodelling, embryonic morphogenesis, bone development, and wound repair.[82–84] MMPs belong to a larger metzincin

superfamily featuring a strictly conserved consensus sequence containing three histidine residues which coordinate the catalytic Zn^{2+} ion, and an essential methionine residue beneath the active site that forms a "Met-turn" and creates a structural base for the catalytic center (Figure 1.3 A).[83,85] MMPs are secreted to the extracellular environment and synthesized as inactive zymogens due to an intramolecular complex between a critical cysteine residue within the pro-peptide domain and the catalytic Zn^{2+} ion that blocks the active site (Figure 1.3 B).[82–86] Enzyme activation follows a "cysteine-switch" mechanism whereby the Cys-Zn interaction is disrupted through conformational changes and the pro-peptide domain is subsequently cleaved (Figure 1.3 B).[82,83,86,87] Once activated, the catalytic domain is accessible and works cooperatively with the hemopexin domain, connected via a short flexible hinge region, to degrade ECM proteins such as collagen, gelatin, elastin, and various proteoglycans.[82,83,85] The hinge region correctly orients the hemopexin domain to enable initial substrate recognition and unwinding prior to cleavage within the catalytic domain.[82,83,85,88] The structure of the catalytic domain and surrounding sub-pockets confer substrate specificity through distinct binding interactions within and adjacent to the active site.[82,84,85]

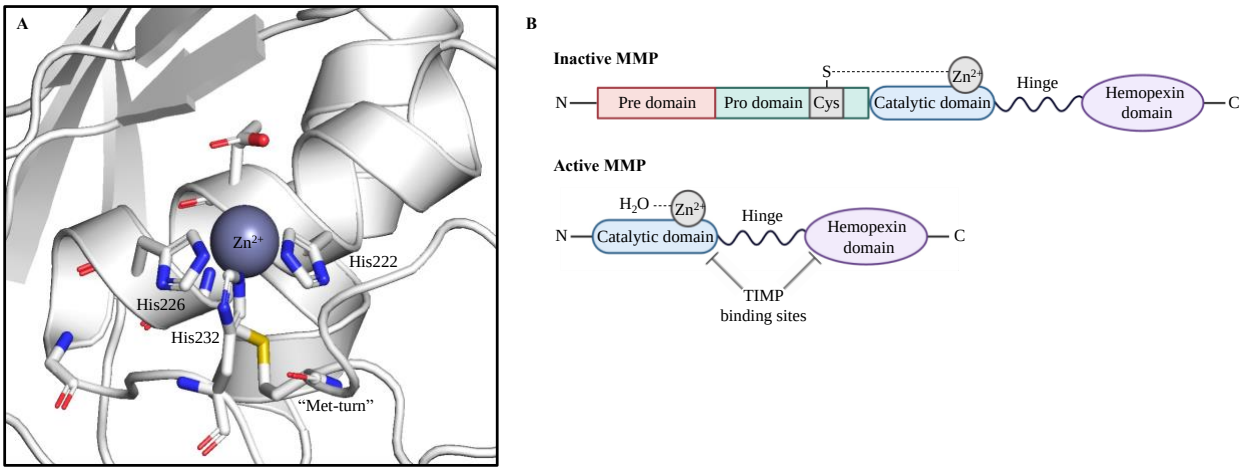

Figure 1.3 MMP structure and activation. (A) MMP-13 catalytic site (adapted from pdb: 1XUD). (B) Basic MMP structure and activation.

1.6.2 MMP Regulation

While there is considerable overlap, MMPs are classified according to their substrate specificity and functional activity into subgroups including the collagenases (MMP-1,-8,-13), gelatinases (MMP-2, -9), metalloelastases (MMP-12), and stromelysins (MMP-3,-10,-11), among others (Table 1.0).[84,87,89] Under quiescent conditions, MMP expression remains low and is tightly regulated by endogenous tissue inhibitors of matrix metalloproteinases (TIMPs) that interact with the hemopexin domain to maintain enzyme latency (Figure 1.3 B).[83,85,89,90] TIMPs also directly bind the active site and inhibit proteolytic activity through formation of 1:1 stoichiometric complexes (Figure 1.3 B).[83,85,90] TIMP expression is highly dependent on the tissue type and location and play a critical role in maintaining tissue homeostasis.[90]

Table 1.0 MMP classification and substrate specificity. [91,92]

Subfamily	MMP	Distinction	Primary Vascular Cell Sources	Primary Substrates
Collagenase	MMP-1	Collagenase 1	Fibroblasts, macrophages	Fibrillar (III > I > II), and non-fibrillar collagen
	MMP-8	Collagenase 2	Neutrophils, macrophages	Fibrillar (I > II > III) and non-fibrillar collagen
	MMP-13	Collagenase 3	Macrophages, SMCs	Fibrillar (II > III > I) and non-fibrillar collagen
Gelatinase	MMP-2	Gelatinase A	SMCs, macrophages	Gelatin, non-fibrillar collagen
	MMP-9	Gelatinase B	Leukocytes, macrophages	Gelatin, non-fibrillar collagen
Stromelysin	MMP-3	Stromelysin 1	Macrophages, SMCs	Proteoglycans, non-fibrillar collagen
	MMP-10	Stromelysin 2	Macrophages, SMCs	Proteoglycans, non-fibrillar collagen
	MMP-11	Stromelysin 3	Macrophages, leukocytes	Serine protease inhibitors (Serpins)
Elastase	MMP-12	Metalloelastase	Macrophages	Elastin, non-fibrillar collagen

1.7 Broad-Spectrum Matrix Metalloproteinase Inhibitors (MMPIs)

1.7.1 Peptidomimetic MMPIs

Given their broad implication in pathophysiological processes, MMP inhibitors (MMPIs) hold tremendous therapeutic potential to regulate destructive ECM remodelling and inflammation.[93] Initial drug discovery efforts were prompted by the potential of MMPIs as cancer therapeutics due to their pivotal role in remodeling of the tumor microenvironment and promotion of invasion, metastasis, and angiogenesis.[94] First generation MMPIs were based on peptidomimetics that resemble the native substrate and contain a zinc binding group (ZBG) which coordinates the catalytic Zn^{2+} ion to block enzymatic activity.[93,95,96] Among ZBGs, the hydroxamic acid (HA) is most frequently incorporated into MMPIs due to its relatively high binding affinity as compared with carboxylic acids, thiols, and phosphonates.[93,97] The HA moiety serves as bidentate ligand for the catalytic Zn^{2+} ion by forming tight binding interactions with its two oxygen

atoms in a distorted trigonal pyramidal geometry (Figure 1.4).[93,95,96] The hydroxamate oxyanion and NH groups are also optimally oriented and contribute two hydrogen bonds with Glu221 and Ala186 conserved within the catalytic site (Figure 1.4).[93,96] Additional binding interactions are established between the peptidomimetic scaffold and nearby amino acid residues which occupy adjacent subsites.[93,95,96] This binding mode blocks substrate access and renders the enzyme incapable of catalyzing peptide hydrolysis, accounting for the low nanomolar potency observed for HA-based MMPIs.

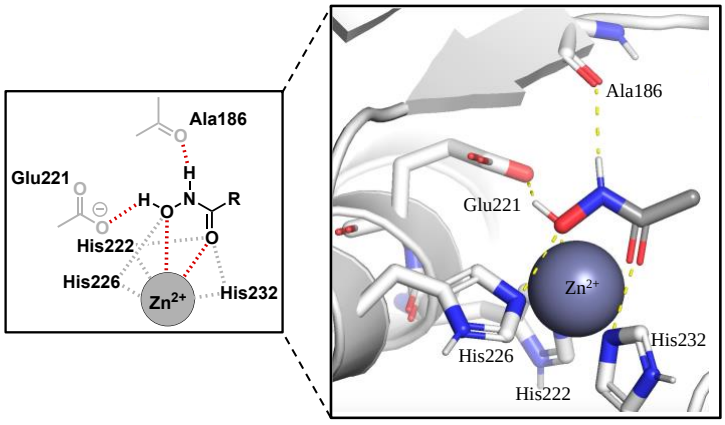

Figure 1.4 Representative binding mode of an HA-containing MMPI in the catalytic site of MMP-13. Adapted from pdb: 830C.

1.7.1.1 Batimastat

Several MMPIs have been designed based on this approach and evaluated for their anti-tumor activity in experimental mouse models (Figure 1.5).[93,95,96] Early preclinical assessments of batimastat (Figure 1.5 A) as a potent broad-spectrum MMP inhibitor for breast, ovarian, and colorectal cancer successfully demonstrated a decrease in tumor growth, a reduction in local invasion, the prevention of distant metastases, and prolonged overall survival.[98–102] Such promising results prompted phase I human studies among patients with advanced cancer, representing the first MMPI to enter clinical trials (Figure 1.5 A).[103] Batimastat was generally well

tolerated with no systemic toxicity and prolonged plasma circulation. Despite this, batimastat exhibits poor oral bioavailability due to limited aqueous solubility and requires intraperitoneal drug administration (Figure 1.5 A). As a result, substantial dose-related local peritoneal irritation and abdominal pain was observed, limiting its clinical utility.[103]

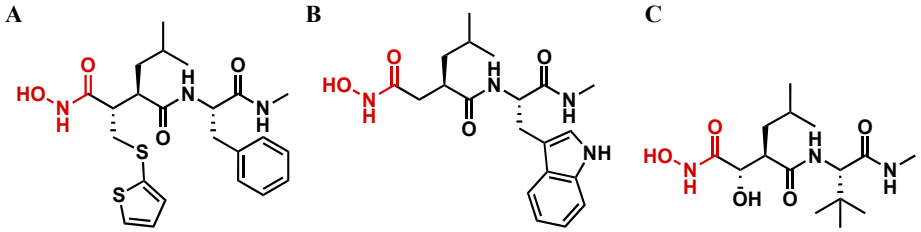

Figure 1.5 Chemical structures of broad spectrum peptidomimetic MMPIs. (A) Batimastat (B) Ilomastat (C) Marimastat. The ZBG is highlighted in red.

1.7.1.2 Ilomastat

Similarly, the related synthetic peptidyl hydroxamate MMPI, ilomastat (Figure 1.5 B), was investigated as a potential therapeutic for cancer metastasis, post-operative ocular scarring, and myocardial reperfusion injury.[104–107] *In vitro*, ilomastat reduced collagen degradation and dose dependently inhibited MMP activity, confirmed by gelatin zymography and western blot analysis.[108,109] In a mouse model of breast cancer, ilomastat treatment reduced tumor growth and formation and extended symptom-free survival.[110] The drug was further proven to modulate wound healing and improve surgical outcomes by significantly decreasing scar tissue formation following

glaucoma filtration surgery in rabbits.[105,106] Cardioprotection was also conferred by reducing infarct size before the onset of ischemia or reperfusion in rats.[107] A limited number of human clinical trials have been initiated, but akin to batimastat, progress was restricted due to poor water solubility and oral bioavailability necessitating intraperitoneal or topical drug administration (Figure 1.5 B).[111]

1.7.1.3 Marimastat

These studies cumulatively highlighted the need for MMPIs with improved pharmacokinetic properties to facilitate clinical translation. Marimastat was developed as an orally bioavailable structural analogue of batimastat that possesses a comparable inhibitory profile (Figure 1.5 C).[95,98,112] Preliminary evaluations in rodents were restricted due high first-pass metabolism and challenges associated with sustaining pharmacologically active plasma concentrations.[98] Nevertheless, initial phase I clinical trials in healthy volunteers demonstrated that plasma concentrations were linearly proportional to dose, the elimination half-life was prolonged, and tolerability was good.[113] Oral doses achieved plasma levels exceeding the inhibitory concentration of the target MMPs, validating this route of administration and supporting twice daily dosing for subsequent evaluations (Figure 1.5 C). Marimastat has been subject to numerous phase I/II/III clinical trials in patients with various metastatic malignancies of the breast, colon, lung, pancreas, prostate, ovary, skin, and stomach.[114–122] These studies revealed that repeated oral dosing resulted in significant dose-dependent musculoskeletal toxicity often requiring discontinuation of treatment.[95,98,123] Dose modification was performed to control the frequency and severity of these side effects, but lower doses failed to demonstrate additional therapeutic benefit as a standalone or combination cancer therapy and proved ineffective in prolonging progression free survival.[121,122] Ultimately, failure in clinical trials has been attributed to inadequate *in vivo*

efficacy, along with the frequent onset of musculoskeletal syndrome (MSS) characterized by joint pain and inflammation.[95,98,123,124]

1.7.2 Non-peptidomimetic MMPIs

1.7.2.1 CGS-27023A

Second generation MMPIs were developed based on non-peptidomimetic scaffolds in anticipation of improving oral bioavailability and metabolic stability (Figure 1.6). It was proposed that peptidic and carboxamide containing MMPIs largely occupy the catalytic site and shallower S2′ and S3′ pockets due to their restrictive planar geometry.[125,126] In comparison, it was postulated that sulfonamides would confer greater metabolic stability, enhance hydrogen bonding capabilities, and offer the conformational flexibility required to orient the associated aryl group deep into the hydrophobic S1' pocket to confer additional selectivity. [42,143] Early structure-activity relationship (SAR) studies identified the aryl sulfonamide CGS 27023A as an orally active, water soluble, low nanomolar affinity and moderately selective gelatinase (MMP-2/-9) and stromelysin (MMP-3) inhibitor (Figure 1.6 A).[127,128] This inhibitor was initially developed as a potential therapeutic for chronic joint diseases. In a rabbit model of osteoarthritis, CGS 27023A preserved cartilage-producing chondrocytes and inhibited the release of proteoglycan matrix into synovial fluid following intra-articular injection.[129] Not surprisingly, phase I dose escalation and pharmacokinetics studies revealed frequent dose-limiting side effects including rashes and MSS.[130,131]

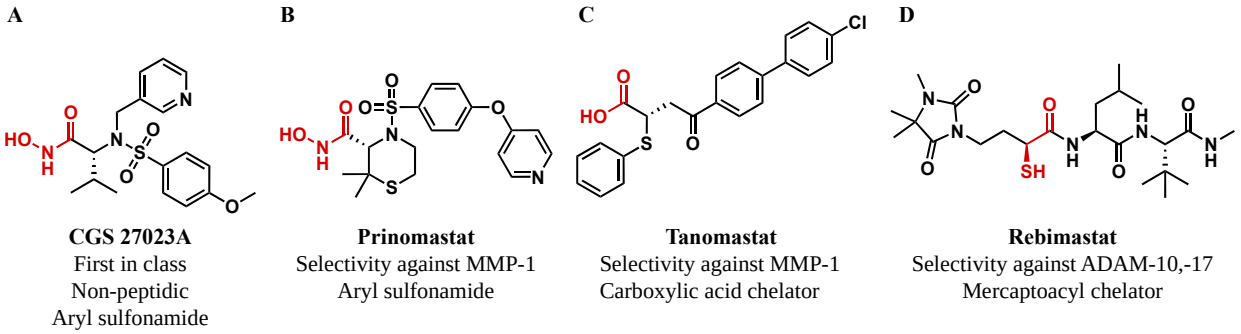

Figure 1.6 Chemical structures of non-peptidomimetic broad spectrum MMPIs. (A) CGS 27023A (B) Prinomastat (C) Tanomastat (D) Rebimastat. The ZBG is highlighted in red.

1.7.2.2 Prinomastat

MSS related toxicity was suspected to be caused by broad-spectrum inhibition of related metalloenzymes and anti-target MMPs.[95,112,124,132] Due to concerns surrounding the involvement of the interstitial collagenase MMP-1 in the occurrence of MSS, prinomastat (Figure 1.6 B) and tanomastat (Figure 1.6 C) were developed sparing this enzyme.[95,112,124,132] Several preclinical rodent studies of prinomastat demonstrated potent antitumor and antiangiogenic activities including cessation of primary tumor growth, prevention of metastasis formation, and improved survival.[133–137] Yet again, dose-related MSS toxicity was observed in human dose escalation studies and clinical trials among patients with small-cell lung cancer and esophageal adenocarcinoma.[138–140]

1.7.2.3 Tanomastat

Considering the detrimental effect of the HA moiety on inhibitor selectivity and its *in vivo* lability, this prompted the development of new MMPIs with alternative ZBGs to reduce side effects and avoid metabolic susceptibility.[96] Tanomastat contains a carboxylic acid for weaker catalytic zinc chelation but compensates by extending deeper into the adjacent S1’ side pocket to gain

additional binding interactions (Figure 1.6 C).[95,112] While such an approach reduced overall MMP affinity, it proved effective in enhancing selectivity against MMP-1 and retaining anti-angiogenic activity *in vitro* and in experimental models of colon and breast cancer.[141,142] Phase I clinical trials demonstrated that tanomastat was generally well tolerated with serum concentrations several orders of magnitude greater than its MMP affinity following oral administration and saturable absorption at elevated doses.[143–145] However, phase III studies among patients with small cell lung cancer, pancreatic metastatic adenocarcinoma, and advanced ovarian carcinoma were closed as recommended by the Data Safety Monitoring Board of the National Cancer Institute of Canada on the basis of inferior efficacy and progression free survival relative to current therapy or placebo controls.[146–148] Although it the cause of MSS remains unclear, the cumulative studies of prinomastat and tanomastat do not strongly comply with the belief that MMP-1 is responsible for such toxicity and may actually be required for therapeutic efficacy in cancer.

1.7.2.4 Rebimastat

It was further hypothesized that inhibition of specific members of a disintegrin and metalloproteinase (ADAM) family involved in the shedding of cell-associated inflammatory cytokines including TNFα and IL-1/6 could contribute to MSS.[95,124,132,149] To this end, rebimastat was designed as a marcaptoacyl containing MMPI with selectivity against ADAM-10 and ADAM-17 (Figure 1.6 D). Rebimastat was found to dose-dependently inhibit tumor growth and reduce the number metastases in an experimental mouse model of lung cancer and prevent endothelial cell migration in a matrigel plug angiogenesis model.[150] Pharmacokinetic profiles in mice further revealed that efficacious plasma concentrations were achieved following a single oral administration with no clinical signs of toxicity. Despite this, phase I/II clinical trials among patients with Kaposi sarcoma, prostate cancer, or breast cancer were discontinued due to a lack of

tumor response or frequent joint stiffness consistent with MSS.[151–154] Likewise, phase II/III studies using rebimastat in combination with carboplatin or paclitaxel in advanced non-small cell lung cancer were stopped as no survival advantage was provided and increased toxicity was observed.[155,156] Together these studies disproved that MMP-mediated shedding events were linked to MSS related toxicity.

1.7.3 Consensus on Broad Spectrum MMPIs

Despite the continuous effort to optimize broad-spectrum MMPIs, to date, none have been clinically approved for human use.[95,124] While significant improvements in inhibitor pharmacokinetics, alterations in catalytic site binding, and specific enzyme-sparing strategies have demonstrated promising preclinical results, human trials have consistently reported a lack of therapeutic efficacy and dose-limiting musculoskeletal toxicity.[95,96,124] These studies have strongly suggested that MSS does not appear to be caused by off-target inhibition of a single MMP or related metalloproteinase but rather collective inhibition of several MMPs.[124] Moreover, considering that MMPs are classified based on their unique substrate specificity and individual MMPs can have distinct and potentially opposing roles in disease progression, the development of selective MMP inhibitors should be prioritized.[124]

1.8 Selective MMPIs

1.8.1 Collagenase Selective MMPIs

1.8.1.1 Cipemastat

Cipemastat is a rationally designed and orally active collagenase-selective inhibitor with potent inhibitory activity against MMP-1,-8,-13 and relatively low activity against stromelysin 1

and the gelatinases (Figure 1.7).[157] As collagen represents the major structural component of cartilage and irreversible cleavage by collagenases may lead to loss of join integrity and mobility, cipemastat was first evaluated as anti-arthritic agent. Preclinical studies revealed that cipemastat possesses dose-dependent anti-inflammatory activity in vitro and prevents articular cartilage degradation in rodent models of arthritis *in vivo*.[157,158] Preliminary pharmacokinetic evaluations among patients with rheumatoid arthritis revealed that once daily dosing was sufficient to maintain effective plasma concentrations.[159] Meanwhile, cipemastat was well tolerated with only mild side effects occurring at similar frequency to placebo controls and no apparent dose-dependence.[159] While subsequent trials aimed at evaluating treatment efficacy did not prevent the progression of joint damage, no musculoskeletal side effects were reported (Figure 1.7).[159,160] This suggests that collagenase inhibition is not responsible for the onset of MSS toxicity observed among previously developed broad spectrum MMPIs and selective inhibition may prove useful for other collagenase-related disorders.

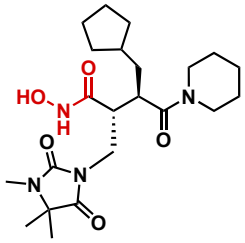

Cipemastat
Collagenase selective
No MSS

Figure 1.7 Chemical structure of collagenase selective MMPI Cipemastat. The ZBG is highlighted in red.

1.9 MMP-13 Selective MMPIs

MMP-13 (collagenase 3), most efficiently cleaves type II fibrillar collagen, representing the major structural component of joint cartilage, and has been identified as the primary MMP

involved in the progression of osteoarthritis (OA).[161–165] As such, tremendous efforts have been made toward the discovery of selective MMP-13 inhibitors that can prevent cartilage destruction within osteoarthritic joints and alleviate inflammation. To confer selectivity and avoid broad-spectrum inhibition of MMPs containing a catalytic Zn^{2+} ion, novel inhibitors were designed to be non-chelating and instead occupy the unique S1' and protruding S1" pockets adjacent the active site (Figure 1.8).

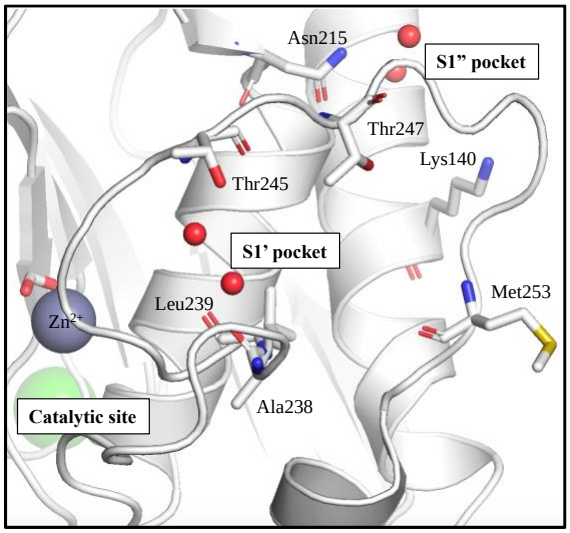

Figure 1.8 MMP-13 binding pockets and key residues. Adapted from pdb: 1XUD.

1.9.1 Symmetric S1' and S1" binding MMP-13 selective inhibitors

Early efforts identified a few moderately potent and selective MMP-13 inhibitors based on benzofuran carboxamide (Figure 1.9 A) and pyrimidinetrione (barbiturate) cores.[166–168] These lead structures proved critical in uncovering the key binding interactions required to enhance MMP-13 affinity and elucidating the structural features for the design of subsequent MMP-13 selective inhibitors.

1.9.1.1 Pyrimidine-dicarboxamide Scaffold

The first major class of MMP-13 selective inhibitors was reported by Aventis and comprised a set of pyrimidine dicarboxamides exhibiting nanomolar activity and exclusive inhibition of MMP-13 with no detectable inhibition of related MMPs below 100 μM (Figure 1.9 B).[169] Based on x-ray crystallography, the central pyrimidine-dicarboxamide scaffold forms several hydrogen-bonding interactions with Thr245, Thr247, Ala238, and Leu239 in the specificity loop of the S1' pocket and exhibits a bent conformation enabling the S1" pocket to deeply accommodate the distal that arm of the inhibitor (Figure 1.9 B).[169] Importantly, the proximal arm pointing toward the entrance of the S1' pocket does not sufficiently approach the catalytic zinc for binding (Figure 1.9 B). These unoptimized inhibitors possessing identical proximal and distal arms demonstrated that MMP-13 selectivity can be obtained by exploiting the S1' specificity loop and S1" side pocket not described for other MMPs, rather than the highly conserved catalytic site.

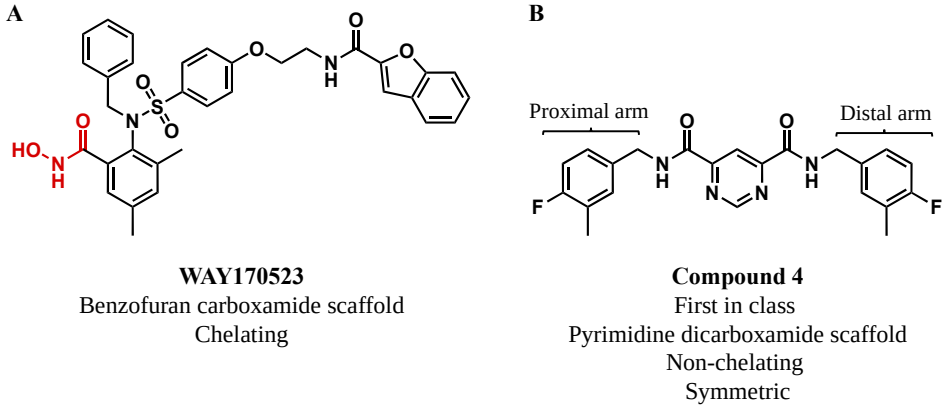

Figure 1.9 Chemical structures of earliest reported MMP-13 selective inhibitors. WAY170523 (B) Compound 4. The ZBG is highlighted in red.

1.9.2 Asymmetric S1' and S1" Binding Inhibitors

1.9.2.1 Pyrimidine-dicarboxamide Scaffold

Subsequent optimization of this inhibitor class by Amgen and Alantos focused on making asymmetrical derivatives with different proximal and distal arms to maximize binding interactions within the distinct S1' and S1" subsites (Figure 1.10).[170–173] SAR revealed a strong preference for a benzoic acid moiety on the distal arm with the potential to form an energetically favourable ionic interaction with Lys140 at the back of the S1" pocket. Several pyrimidine-based inhibitors possessing this terminal carboxylic acid have been shown to exhibit sub-nanomolar MMP-13 potencies while maintaining excellent off-target selectivity against other MMPs and zinc metalloproteinases below 20 μM (Figure 1.10).[170,171] Among the most well characterized, ALS 1-0365 (Figure 1.10 A) dose dependently inhibited bovine and human articular cartilage degradation with similar efficacy to broad-spectrum inhibitors, suggesting that MMP-13 inhibition alone is sufficient to block collagen degradation.[170,174] *In vivo*, ALS 1-0365 demonstrated a superior pharmacokinetic profile than previously reported broad-spectrum inhibitors with by greater oral bioavailability and cartilage penetration.[170] In various rat models of OA, selective inhibition of MMP-13 significantly reduced cartilage degeneration, joint pain, and provided chondroprotection. Importantly, no signs of MSS toxicity were detected following administration of ALS 1-0365 at 200-fold higher concentrations than marimastat, providing a large therapeutic window to achieve treatment efficacy (Figure 1.10 A).

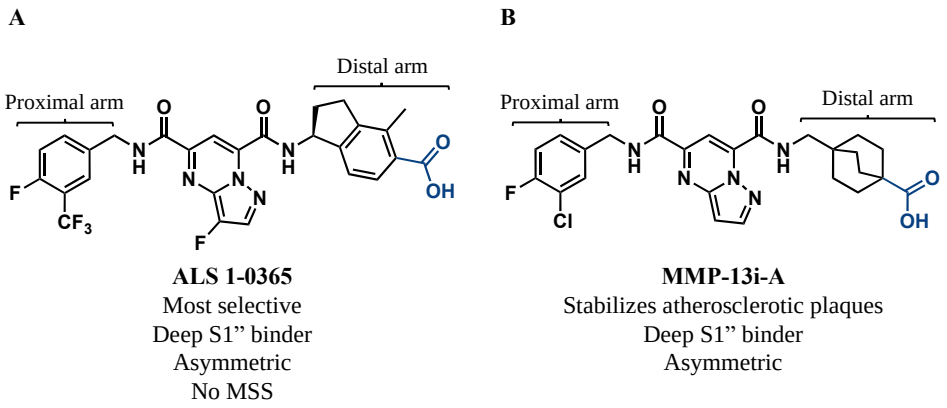

Figure 1.10 Chemical structures of asymmetric pyrimidine-dicarboxamide MMP-13 inhibitors. (A) ALS 1-0365 (B) MMP-13i-A. The deep S1" binding moiety highlighted in blue.

A structural analogue developed by Amgen, referred to as MMP-13i-A, was also evaluated as a therapeutic in atherosclerotic mice with evolving or established plaques (Figure 1.10 B).[173] *In vitro* characterization of MMP-13i-A revealed low nanomolar MMP-13 potency, no observable off-target inhibition below 20 μM, and the ability to block MMP-13 secreted by activated inflammatory macrophages. Twice daily oral treatment with MMP-13i-A did not alter plaque size, macrophage content, or SMC accumulation, but significantly decreased MMP-13 activity and substantially increased interstitial collagen content within the fibrous cap of atherosclerotic plaques. Selective inhibition of MMP-13 also afforded larger and thicker fibrous caps, a feature consistent with a stable phenotype observed in human atherosclerotic plaques (Figure 1.10 B). This study identifies MMP-13 as a major collagenase in atherosclerotic plaques and establishes that selective inhibition of MMP-13 in mice reinforces the collagen content of the fibrous cap and may confer resistance to rupture.

1.9.2.2 Fused-Pyrimidine and Quinazoline-2-Carboxamide Scaffolds

Extensive high-throughput screenings from Pfizer and Takeda discovered low nanomolar potent and remarkably selective (> 100 μM) compounds based on fused-pyrimidine (Figure 1.11 A) and quinazoline (quinazolinone) (Figure 1.11 B) pharmacophores that represented highly promising leads for computer-aided drug design and SAR studies.[175–178] As with the pyrimidine class, co-crystallization with MMP-13 showed that these inhibitors occupy the unique S1' and S1" subsites without binding the catalytic Zn^{2+} ion. These optimized core scaffolds gain hydrogen bonding interactions with the backbone and sidechains of Thr245 and Thr247 within the S1' specificity pocket. SAR of the proximal inhibitor arm revealed a preference for (hetero)aryl rings due to participation in co-planar stacking with His222 and tolerance toward small substituents at the 3-position which have a minor but beneficial effect on inhibitor potency (Figure 1.11).[175,178] A 3-methoxybenzylamine fragment attached via an amide linker was most optimal due to hydrogen bonding with Ala238 and Leu239 flanking the catalytic site and accordingly maintained during subsequent SAR.[175,177] Molecular modelling indicated that the S1" pocket is largely hydrophobic and of sufficient size to accommodate a phenyl ring connected to the quinazoline or fused-pyrimidine system by a three-atom linker at the 5-position (Figure 1.11).[176,177] Owing to an additional hydrogen bond with Thr247, ether-based benzyloxymethyl (Figure 1.11 A) or phenethyloxy linkers (Figure 1.11 B) are most desirable and afforded a significant improvement in MMP-13 potency.[176,177] Unique to the quinazoline-2-carboxamide class, introduction of fluorine at the 6-position provided a weak interaction with the backbone of Met253 located in the deeper region of the S1' pocket and afforded a slight increase in MMP-13 inhibitory activity (Figure 1.11 B).[177] Structural studies also revealed that additional interactions can be exploited at the bottom of the S1" pocket by incorporating appropriate hydrogen bond donor or acceptors at the 4-position of

the terminal phenyl ring (Figure 1.11).[175–177] Inhibitor derivatives bearing strong hydrogen bond acceptors proved to be most potent with a close association to functional group acidity.[175] Carboxylate-containing analogues gain hydrogen bonding and ionic interactions with Asn215 and Lys140 critical for driving target affinity down to the sub-nanomolar level and conferring best-in-class selectivity.[175–177] Simultaneously, addition of the carboxylate enhanced physicochemical properties such as oral bioavailability and aqueous solubility, largely addressing a previous limitation of these inhibitors. Pharmacokinetic profiles favourably displayed good oral absorption, moderate clearance, and high metabolic stability across various species.[175–177] Importantly, preliminary safety assessments revealed no musculoskeletal side effects following repeated oral administration at elevated doses in rats.[175] Meanwhile, treatment effectively prevented cartilage degradation in rabbit or rat models of OA, suggesting the potential for MMP-13 selective inhibitors as therapeutics.[175–177]

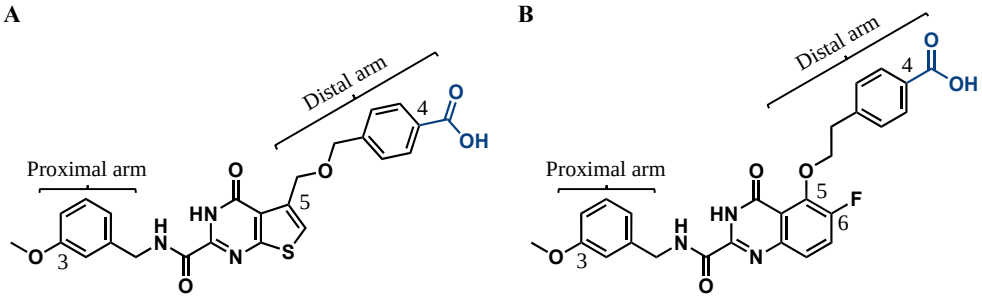

Figure 1.11 Chemical structures of fused-pyrimidine and quinazoline-2-carboxamide MMP-13 inhibitors. (A) Compound 26c (B) Compound 21k. The deep S1" binding moiety is highlighted in blue.

1.9.2.3 Susceptibility for the Organic Anion Transporter (OAT)

Translational studies on a number of these carboxylic acid-containing MMP-13 selective inhibitors in cynomolgus monkeys consistently revealed nephrotoxicity.[179] As organic anions at physiological pH, it was determined that the carboxylate functional group rendered these molecules a substrate of the organic anion transporter (OAT) and presented the risk of generating reactive acyl glucuronide metabolites that accumulate in proximal tubular cells.[179] Although the carboxylic acid has been shown to greatly improve MMP-13 potency and selectivity, alternative non-carboxylate containing inhibitors based on a central pyrimidine scaffold were developed to mitigate the potential risk of OAT mediated accumulation.[172] While removal of the carboxylate significantly reduced target affinity, systematic replacement with neutral functional groups including alcohols and amides that could similarly engage with lysine in the S1" pocket adequately recovered this loss of affinity.[172] Concurrently, incorporation of these stable functional groups would suppress concerns of metabolic liability. Indeed, these modifications retained biological efficacy in models of OA and toxicology studies in cynomolgus monkeys revealed excellent tolerability with no nephrotoxicity detected at exposures exceeding previously reported levels for such complications.[172,180]

1.9.3 S1' and S1 Binding Inhibitors

1.9.3.1 Fused-pyrimidine Scaffold

As an alternative strategy to circumvent the potential *in vivo* liability of carboxylate-containing MMP-13 selective inhibitors without sacrificing target affinity, several novel inhibitors which simultaneously occupy the S1' specificity pocket and S1 site near the catalytic Zn^{2+} ion have been designed (Figure 1.12).[181] Although zinc-chelation has generally been associated with poor selectivity and deemed responsible for inducing MSS related toxicity, these inhibitors display

excellent MMP potency in the single digit nanomolar range.[181] As such, it was hypothesized that inhibitor potency and selectivity could be maintained by combining interactions in these regions.

Traditionally, optimization of the proximal inhibitor arm which occupies the opening of the S1' pocket has been a less common approach as only hydrophobic contacts or pi-stacking interactions are observed and binding to conserved residues near catalytic Zn^{2+} ion is undesirable.[182] Nevertheless, a set of fused-pyrimidine inhibitors were designed to extend toward the catalytic Zn^{2+} ion with a biaryl ring system and incorporate an amide-based spacer for attachment of different non-chelating polar residues that bridge over the Zn^{2+} binding site and reach into a solvent accessible area (Figure 1.12 A).[181,183–185] These moieties respectively provided hydrophobic contacts with Leu184 and Pro242 and several new hydrogen bonding interactions with the backbone of Leu185 and Ala186 that significantly contribute to the single digit nanomolar MMP-13 affinity and excellent MMP selectivity (> 5 μM) of these inhibitors.[181,183–185] Moreover, many of these optimized compounds dose-dependently inhibited *in vitro* collagenolysis, displayed enhanced aqueous solubility, and possessed favourable membrane permeability.[181,184,185] *In vivo* pharmacokinetic studies also revealed cartilage penetration as detected in synovial fluid.[181]

Exceptionally, a number of structurally related compounds were found to exhibit adequate MMP-13 potency in the low nanomolar range and to a lesser extent retain selectivity (>100-fold) against closely related MMPs, despite the presence of an oxetane (Figure 1.12 B) or triazole ring (Figure 1.12 C) which weakly chelates the catalytic Zn^{2+} ion.[181,185–187] To further improve inhibitor selectivity, a series of MMPIs were designed to incorporate a linker at the 5-position of the fused-pyrimidine system and span the S1 to S1" pockets (Figure 1.12 C).[186,187] However, introduction of a small aryl group was not well tolerated as the core scaffold adopted a slightly shifted binding conformation when coupled to the rigid biaryl linker and ZBG.[187] Replacement with a flexible

ethylenedioxy linker restored the capability to accommodate an S1" occupying arene and remarkably afforded sub-nanomolar potency and 1500-fold selectivity (Figure 1.12 C).[186] Taken together, these studies demonstrate that it is possible to design highly potent and selective MMP-13 inhibitors by simultaneously exploiting interactions within the S1, S1', and S1" pockets and catalytic site. In rare cases, chelating yet selective inhibitors can similarly be designed via a combinatorial effect of interactions.

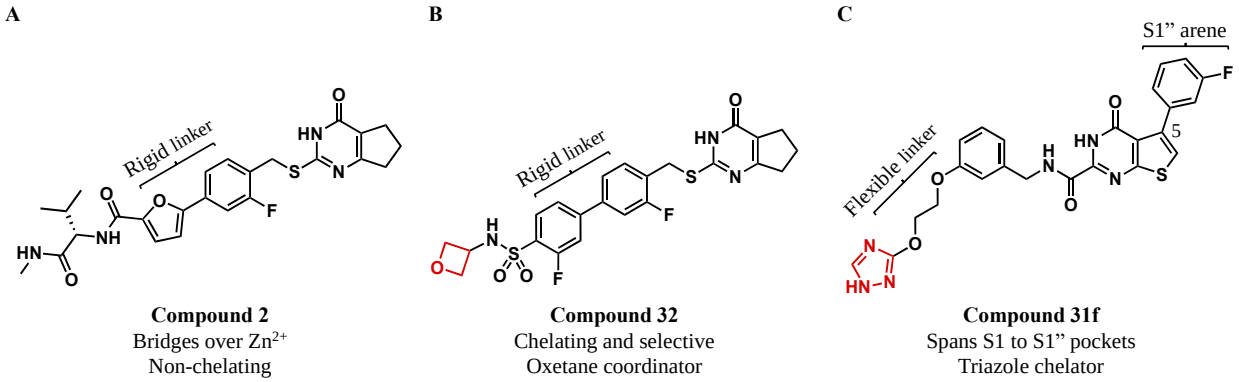

Figure 1.12 Chemical structures of S1 binding MMP-13 inhibitors. (A) Compound 2 (B) Compound 32 (C) Compound 31f. The ZBG is highlighted in red.

1.11 Broad-spectrum MMP radiotracers

Although broad-spectrum MMPIs have consistently suffered from MSS-related toxicity and failed to demonstrate therapeutic efficacy during clinical translation, such concerns are largely mitigated at sub-pharmacological radiotracer doses. Radiotracers based on broad-spectrum MMPIs would facilitate detailed pharmacokinetic evaluations that would critically improve our understanding of the biological distribution of MMPs, their (patho)physiological role, and may

identify *in vivo* liabilities. Importantly, the development of MMP-targeted radiotracers also offers the potential to non-invasively measure *in vivo* MMP activity and characterize disease severity.[188]

1.11.1 [^{11}C]CGS 25966

Accordingly, several PET and SPECT imaging agents have been designed based on the broad spectrum MMPIs CGS 27023A and its close analogue CGS 25966, derived from the non-peptidic aryl sulfonamide class (Figure 1.13).[189–191] These lead structures were selected as radiotracer targets due to a combination of their low nanomolar potency across several MMP subtypes, favourable pharmacokinetic profiles, and amenability to carbon-11 radiolabeling. Original radiosyntheses focused on labeling the hydroxamic acid by ^{11}C-O-methylation with [^{11}C]CH_3OTf to prepare several methylated CGS 27023A analogs.[189,190] This strategy proved to be highly efficient, but alteration of the ZBG is less desirable as it can disrupt the inhibitory activity or selectivity profile of the inhibitor. As such, subsequent radiosyntheses of [^{11}C]CGS 25966 (Figure 1.13 A) switched to labeling of the methoxy group on the terminal arene by ^{11}C-methylation of the corresponding phenol precursor with [^{11}C]CH_3OTf to provide the direct isotopologue.[191] The first *in vivo* evaluations of [^{11}C]CGS 25966 (cLogD = 3.80, pH 7.4) in breast cancer xenograft mouse models showed little tumor uptake (0.42 – 1.53 %ID·g^{-1}), and inadequate tumor/blood or tumor/muscles contrast ratios (0.84 – 1.95 and 1.09-1.27) for non-invasive tumor visualization by PET imaging.[192]

A

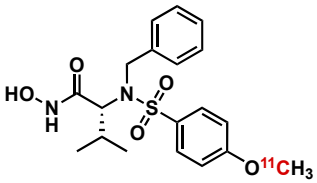

[^{11}C]CGS25966

B

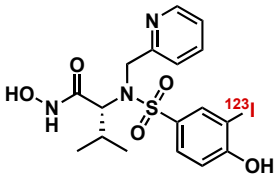

[^{123}I]HO-CGS 27023A

C

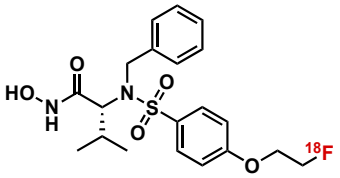

[^{18}F]BR351

Figure 1.13 Chemical structures of small molecule broad-spectrum MMP radiotracers. (A) [^{11}C]CGS 25966 (B) [^{123}I]HO-CGS 27023A (C) [^{18}F]BR351.

1.11.2 [^{123}I]HO-CGS 27023A

Nevertheless, numerous analogues of CGS 27023A and CGS 25966 continued to be developed with improved pharmacokinetics and radiolabeled with fluorine-18, carbon-11, or iodine-123 for PET and SPECT imaging.[193–200] Among the most well-characterized candidates, [^{123}I]HO-CGS 27023A (Figure 1.13 B) displayed nanomolar MMP affinities similar to that of the parent compound and moderate lipophilicity (clogD = 1.60, pH 7.4).[195] Evaluations in healthy mice uncovered rapid blood clearance and minimal tissue-specific accumulation, supporting the potential suitability of this radioligand *in vivo* imaging of MMP activity in disease models.[195]

Additional studies were conducted in atherosclerotic mice with carotid artery ligation as a model of arterial remodeling and MMP-expressing vascular lesions.[201] By planar scintigraphic imaging, [^{123}I]HO-CGS 27023A was found to steadily accumulate in the carotid lesion up to ~0.35 %ID over 2 hours. *In vivo* biodistribution studies favourably revealed rapid washout from the blood, mixed hepatobiliary and renal clearance, and no appreciable signal in the thoracic cavity. These features provide increased target-to-background contrast ratios and offer the potential for imaging of MMP activity in the coronary arteries and aorta with little signal interference from the myocardium. Critically, pre-administration of excess unlabeled CGS 27023A completely abolished carotid lesion radioligand uptake down to levels indistinguishable from wild-type or sham-operated controls (~0.25 %ID), indicative of MMP-specific binding. Comparative *ex vivo* gamma counting of the ligated and control carotid artery, demonstrated approximately 3-fold higher uptake in the ligated carotid artery that was significantly blocked by 87%, further

confirming that lesional uptake is specific. *Ex vivo* autoradiography and immunostaining of ligated carotid artery sections displayed intense focal radioligand uptake in regions expressing MMP-9 and rich in inflammatory macrophages. This provides evidence to support that the measured radioligand uptake within these lesions corresponds to the distribution of active MMPs and for the first time demonstrates the feasibility of using radiolabeled MMPIs for *in vivo* imaging MMP activity in atherosclerosis.

1.11.3 [^{18}F]BR351

Based on these promising results, focus was placed on making derivatives of CGS 27023A and CGS 25966 with superior potency which could be radiolabeled with fluorine-18 for PET imaging to take advantage of the superior spatial resolution and sensitivity.[196] SAR revealed that the methoxy group on the terminal arene could be conveniently replaced with a 2-fluoroethoxy unit while maintaining inhibitory activity in the low nanomolar range. Accordingly, radiolabeling was carried out by aliphatic nucleophilic substitution (S_N2) of the corresponding tosylate precursor with [^{18}F]fluoride. Comparative biodistribution studies in wild-type mice revealed that the CGS 25966 fluorinated analogue, later referred to as [^{18}F]BR351 (Figure 1.13 C), exhibited low background uptake with no quantifiable differences upon blocking, indicating a lack of specific accumulation in healthy tissues. Accordingly, [^{18}F]BR351 was investigated for imaging MMPs in disease models including glioma, colorectal cancer, and stroke.[202–204]

Most relevantly, ischemic strokes are primarily caused by progressive atherosclerosis in which rupture of vulnerable plaques and thrombus formation occludes the cerebral arteries. Activation of MMPs contribute to the worsening of post-ischemic stroke outcomes by disrupting blood brain barrier integrity, sustaining a pro-inflammatory response, and inducing neuronal damage through excessive ECM remodeling.[205] Translational studies with [^{18}F]BR351 in a mouse

model of transient middle cerebral artery occlusion were conducted to track the spatio-temporal distribution of active MMPs in the brain and its association with neuroinflammation.[204] *In vivo* PET imaging showed an increase in [^{18}F]BR351 uptake in the infarct core (0.9-1.6 % ID/cc) that was most pronounced within the first 7 days post-stroke (~1.4-1.5-fold contrast) and peak neuroinflammation persisting thereafter. Regions of elevated [^{18}F]BR351 uptake were confirmed positive for MMP-9 and overlapping with areas of neuroinflammation identified by PET and immunostaining. These results establish the utility of [^{18}F]BR351 for *in vivo* imaging of active MMPs following cerebrovascular events.

1.11.4 [^{111}In]RP782 and [^{99m}Tc]RP805

To confer greater metabolic stability, macrocyclic hydroxamate-containing MMPIs (Figure 1.14 A) originally designed by Bristol Meyers Squibb have also been radiolabeled with indium-111 and technetium-99m for vascular SPECT imaging of MMP activity.[206–213] Early characterization of [^{111}In]RP782 (Figure 1.14 B) and [^{99m}Tc]RP805 (Figure 1.14 C) demonstrated broad-spectrum activity with low nanomolar MMP affinities and validated specificity for MMP-2 in radioligand binding competition assays.[207] Favourable biodistributions and clearance kinetics for *in vivo* cardiovascular imaging were observed with little uptake in the liver, and excretion primarily through the kidneys. Both radiotracers were subsequently evaluated in mouse models of post-infarction myocardial remodeling.[207] *Ex vivo* autoradiographic imaging and quantification of myocardial tissue sections displayed increased focal retention in the infarct region (~3 %ID·g^{-1}) with good contrast over the remote non-infarcted region or healthy controls (~1 %ID·g^{-1}). Immunofluorescent staining of MMP-2 and -9 and *in situ* zymography further confirmed gelatinase activity and colocalized with the radiotracer distribution observed by autoradiography within the infarct zone. *In vivo* static μSPECT/CT imaging of [^{99m}Tc]RP805 90 min post injection

(p.i.) displayed focal radiotracer uptake in the infarcted myocardium, identified as a perfusion defect with ^{201}Tl. This study demonstrates the feasibility of employing [^{99m}Tc]RP805 for mapping changes in MMP activation and ECM remodelling after myocardial infarction.

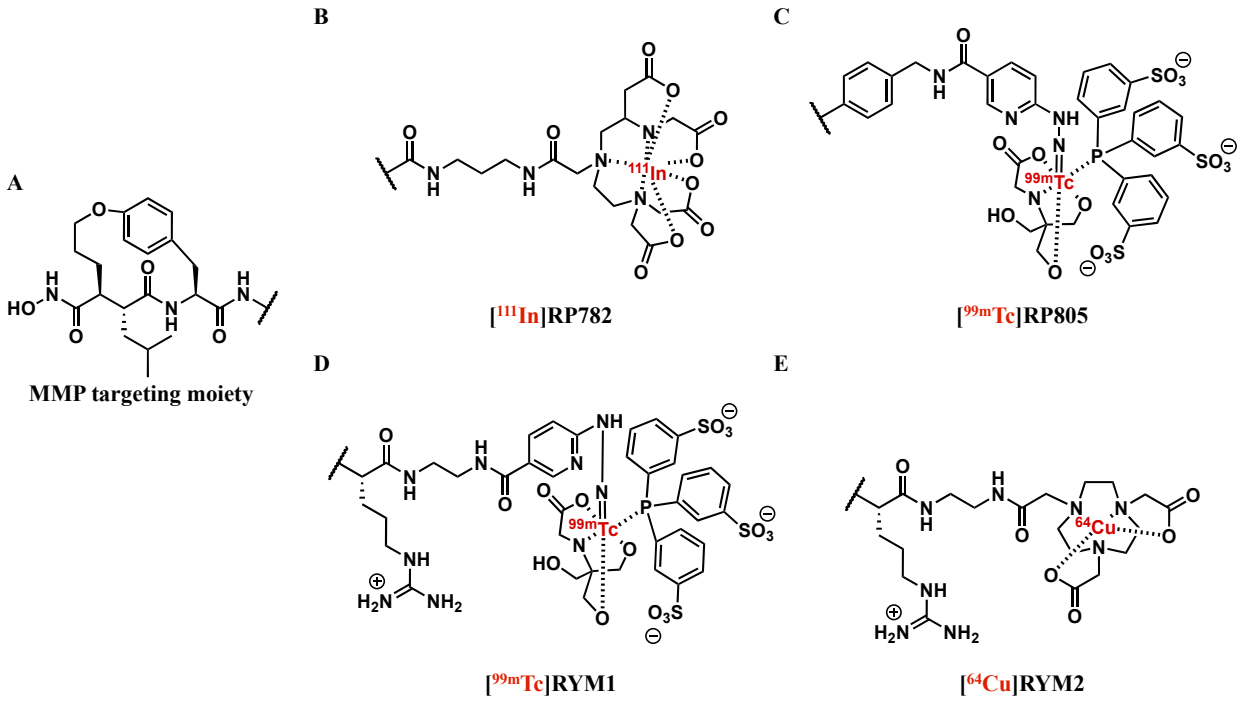

Figure 1.14 Chemical structures of radiometalated MMP radiotracers. (A) Macrocyclic MMPI (B) [^{111}In]RP782 (C) [^{99m}Tc]RP805 (D) [^{99m}Tc]RYM1 (E) [^{64}Cu]RYM2.

Alternatively, [^{111}In]RP782 and [^{99m}Tc]RP805 have been evaluated in models of carotid artery ligation, calcific aortic valve disease, atherosclerosis, and abdominal aortic aneurysm and demonstrated utility for molecular imaging of activated MMPs during vascular remodeling.[208–213] Of particular interest, [^{111}In]RP782 was used to track MMP activity during the progression of atherosclerosis in mice.[210] *In vivo* SPECT imaging and anatomical referencing by CT angiography showed increased aortic [^{111}In]RP782 uptake (~0.4 cpv·MBq^{-1}) with ~4-fold contrast over the inferior vena cava (~0.1 cpv·MBq^{-1}), serving as a control. Segmental quantification of the aorta

showed a heterogenous pattern of radiotracer uptake (~0.1-0.8 cpv·MBq^{-1}) that was highest in the proximal aorta and consistent with the distribution of plaque development identified by Oil Red O lipid staining. *Ex vivo* aortic autoradiography and quantification further confirmed the pattern of uptake and strongly correlated to *in vivo* measurements of [^{111}In]RP782 uptake. To investigate the temporal pattern of MMP activation during atherosclerotic plaque development, atherosclerotic mice fed a high fat diet between 1-3 months underwent SPECT/CT imaging and displayed a gradual increase in aortic [^{111}In]RP782 uptake from ~0.1 to ~0.2 and ~0.4 cpv·MBq^{-1}. Pre-administration of unlabeled RP782 revealed a significant reduction in aortic arch uptake by 75%, confirming radiotracer specificity. In a subset of animals which were withdrawn from high-fat diet and placed on normal chow, [^{111}In]RP782 uptake was reduced by 60%, as compared to animals maintained on diet. Concordantly, dietary intervention led to a significant reduction in MMP mRNA expression and correlated to *in vivo* [^{111}In]RP782 uptake. These results demonstrate that [^{111}In]RP782 can detect the heterogenous pattern of MMP activation in atherosclerotic plaques and appears sensitive to changes in plaque composition.

Analogous studies employing [^{99m}Tc]RP805, as a close structural analogue of [^{111}In]RP782, were conducted in a rabbit model of atherosclerosis induced by balloon de-endothelization of the abdominal aorta for *in vivo* molecular imaging of MMP activity in atherosclerotic plaques.[211] SPECT/CT imaging in atherosclerotic rabbits revealed that aortic plaques were most optimally visualized 3 to 4 hours after intravenous administration of [^{99m}Tc]RP805 as delayed imaging is required to provide sufficient time for radiotracer clearance from the blood pool and enhances target tissue contrast. Age-matched atherosclerotic rabbits receiving cholesterol lowering treatment with fluvastatin or withdrawn from their hypercholesterolemic diet displayed a marked reduction in [^{99m}Tc]RP805 uptake. *Ex vivo* imaging

of excised aortas showed intense focal uptake in the abdominal aorta of atherosclerotic animals and significantly lower uptake in the diet withdrawal and statin therapy groups, recapitulating *in vivo* observations. *Ex vivo* quantification of aortic segments confirmed elevated abdominal aortic radiotracer uptake (~0.1% ID/g) among those on an uninterrupted diet that was ~6-fold greater than control animals. Moreover, uptake decreased by 45% and 55% to ~0.04-0.06% ID/g in the statin and diet withdrawal intervention groups, respectively. Pre-administration of increasing doses of unlabeled RP805 dose-dependently decreased [^{99m}Tc]RP805 uptake from 35-86%, approaching levels observed in control animals and revealing *in vivo* specificity. Histological analysis of aortic segments showed significantly greater MMP-2 and MMP-9 positives areas (~5-8%) in the uninterrupted diet group as compared to the statin or and diet withdrawal groups (~1-3%) which correlated with [^{99m}Tc]RP805 uptake. Similarly, *in situ* gelatin zymography demonstrated that MMP-2 and -9 activity was elevated in experimental animals and significantly decreased in either treatment group. This data shows that the *in vivo* [^{99m}Tc]RP805 aortic uptake reflects the expression level and activity of MMPs in atherosclerotic plaques and that it can utilized to monitor response to therapy.

1.11.5 [^{99m}Tc]RYM1

It was however recognized that [^{99m}Tc]RP805 inconveniently requires delayed imaging, owing to its relatively prolonged blood circulation and possesses poor water solubility which has impeded *in vivo* blocking studies at suitable concentrations.[214] Therefore, macrocyclic hydroxamate-containing MMP-targeted radiotracers with improved physicochemical properties were developed to facilitate future clinical translation. To overcome such limitations, a structural analogue of [^{99m}Tc]RP805, [^{99m}Tc]RYM1, was designed by maintaining the MMP-targeting moiety and incorporating an arginine residue on the linker and a modulatory

hydrazinonicotinamide (HYNIC) chelator for radiolabeling to enhance water solubility and hydrophilicity (Figure 1.14 D). *In vitro* characterization of RYM-1 revealed target affinities in the low nanomolar range with 6-20-fold selectivity for MMP-12 over MMP-2,-9, and -13. These modifications greatly lowered radiotracer lipophilicity as indicated by a logD (octanol/water, pH 7.4) measurement of -4.0, representing a >10-fold reduction as compared to RP805 with a logD of -2.8.

[^{99m}Tc]RYM1 was subsequently evaluated in mouse models of carotid and abdominal aortic aneurysm (AAA).[215] AAA is most often caused by advanced atherosclerosis and characterized by expansive arterial remodeling as an adaptive response to regulate luminal stenosis and sheer stress on the vessel wall.[216] MMP-12 is extensively implicated in its pathogenesis through destructive remodeling of elastin, an integral protein that maintains the structural integrity and elasticity of the aortic vessel wall.[217] Preliminary assessments of [^{99m}Tc]RYM1in healthy mice revealed significantly faster clearance from the blood pool (~1 %ID·mL^{-1}) as compared with [^{99m}Tc]RP805 (~2.5 %ID·mL^{-1}) at 1 h p.i. Despite lower blood radioactivity, peripheral organ [^{99m}Tc]RYM1uptake was relatively higher, with little accumulation in the bile (<1% ID·g^{-1}), and highest uptake in the kidneys (~100 %ID·g^{-1}) and urine (~30%ID·g^{-1}), reflecting exclusive renal clearance. Aortic autoradiographic imaging and quantification conducted 2 h after IV administration of [^{99m}Tc]RYM1 in atherosclerotic mice with $CaCl_2$-induced left carotid aneurysm revealed elevated uptake at the site of aneurysm (~0.3% ID·cm^{-2}). Pre-injection of excess RYM1 led to a ~5-fold decrease in carotid aneurysm radiotracer uptake (~0.06% ID·cm^{-2}), confirming MMP-specific binding. Blocking also resulted in a 2-fold reduction in aortic vessel wall uptake and several peripheral organs, indicating an extent of systemic MMP expression. *In vivo* SPECT/CT imaging conducted in atherosclerotic mice with AAA induced by angiotensin II

infusion showed a range of detectable [^{99m}Tc]RYM1 uptake in the suprarenal abdominal aorta in accordance with the severity of AAA. Categorization by external aortic diameter into low remodelling and AAA groups reconciled the observed heterogeneity and uncovered a significant difference in [^{99m}Tc]RYM1 uptake (~0.7 vs ~0.4 cpv·MBq^{-1}) that correlated with MMP-12 activity detected by zymography. This data validates the utility of [^{99m}Tc]RYM1 for the *in vivo* detection and characterization of MMP-12 activity during aneurysm and possesses superior pharmacokinetics that facilitates imaging as early as 1 h p.i.

1.11.6 [^{64}Cu]RYM2

Based on the success of [^{99m}Tc]RYM1 for SPECT imaging of AAA, [^{64}Cu]RYM2 was designed for PET imaging by incorporation of a NOTA chelator for efficient ^{64}Cu radiolabeling and maintains a low nanomolar inhibitory profile with preference for MMP-12 (Figure 1.14 E).[218] [^{64}Cu]RYM2 PET offers fully quantitative capabilities, higher sensitivity, and better spatial resolution that are critical for imaging small vasculature structures and facilitating eventual clinical translation. Evaluations in healthy mice proved that [^{64}Cu]RYM2 behaved similarly to [^{99m}Tc]RYM1 with low residual blood activity and rapid renal clearance at 1 h p.i. Radio-metabolite analysis conducted at this timepoint indicated that the intact parent radiotracer corresponded to 84 and 94% of blood and urine radioactivity, respectively. By PET/CT imaging of ang-II infused AAA mice 50-60 min p.i, focal uptake of [^{64}Cu]RYM2 could be detected at the site of aneurysm (SUVmax: ~1.8) that was ~2- and 3- fold greater than the low remodeling (SUVmax: 0.8) or control groups (SUVmax: 0.6), respectively. To establish *in vivo* specificity, blocking studies were conducted in mouse models of AAA and carotid aneurysm by pre-administration of excess non-radioactive Cu-RYM2, revealing a significant reduction in [^{64}Cu]RYM2 uptake by 60% and 90%, respectively, along with several other organs. *Ex vivo*

zymographic evaluations of aneurysmal tissue showed greater activity of MMP-2,-12, and -13 in the AAA group than the low remodelling or control groups and correlated with the *in vivo* [^{64}Cu]RYM2 PET/CT aortic signal. To demonstrate the clinical applicability, specific binding to human AAA and non-aneurysmal tissue homogenates and aortic sections was quantified by gamma counting and autoradiography. When normalized to protein content, [^{64}Cu]RYM2 binding was ~1.5-fold higher than controls and significantly reduced in the presence of excess ilomastat. Zymography on this same tissue revealed MMP activity in accordance with the observe radiotracer uptake. Future clinical studies are warranted to establish the diagnostic benefit of [^{64}Cu]RYM2 PET and determine its capability to provide a risk assessment for AAA.

1.11.7 Limitations of Broad Spectrum MMP Radiotracers

1.11.7.1 Imaging Contrast

Based on the collective results from [^{11}C]CGS 25966, [^{18}F]BR351, [^{123}I]HO-CGS 27023A, [^{111}In]RP782/ [^{99m}Tc]RP805, [^{99m}Tc]RYM1, and [^{64}Cu]RYM2 it is well established that PET and SPECT radiotracers derived from MMPIs can be utilized for cardiovascular imaging applications. While the potential for risk stratification and prediction of rupture remains to be demonstrated, these radiotracers strongly correlate with the pathophysiological expression and measured *in vivo/ex vivo* MMP activity in mice. In pursuit of designing successful MMP-targeted radiotracers for non-invasive vascular imaging, optimization of physicochemical and pharmacokinetics properties is of critical importance. During these preclinical investigations, it has become evident that the ideal MMP-targeted radioligand should have low nanomolar affinity with minimal off-target binding and adequate *in vivo* metabolic stability to enable accumulation in target tissue.[215,218] Moreover, sufficient hydrophilicity is needed to confer a favourable biodistribution with rapid washout of radioactivity from the blood pool and preferential renal clearance such that target-to-

background contrast is maximized and uptake in nearby metabolic or peripheral organs does not interfere with aortic quantification.[215,218]

1.11.7.2 Indiscriminate Signal

While some of these parameters have been achieved with previously developed MMP-targeted radiotracers, these agents are largely based on broad-spectrum MMPIs and are inherently limited by the indiscriminate nature of their signal and suboptimal target tissue contrast.[215,219] Despite the collective role of the MMP family in ECM remodelling, MMPs possess distinct substrate specificity and exhibit diverse and potentially opposing pathophysiological functions with variable basal expression in healthy tissues.[220,221] *In vivo* uptake of these broad-spectrum MMP-targeted radiotracers may therefore not precisely correlate with cardiovascular risk due to engagement with multiple MMPs that are concomitantly up- and down-regulated and not related to rupture.[215,218,219] As such, selective PET imaging of individual MMPs with limited physiological expression that are specifically upregulated during atherosclerosis and directly associated with plaque vulnerability is advantageous. This strategic approach offers the potential for greater *in vivo* contrast to facilitate non-invasive detection of small atherosclerotic plaques, superior sensitivity for stratification of disease severity, and is expected to more accurately reflect destructive ECM remodelling for prediction of rupture.

1.11.7.3 Divergent Role of MMPs in Atherosclerosis

Although current MMP-targeted imaging agents are non-selective, MMP-2 represents a principal target of these radiotracers, leading preclinical investigations to focus on measuring *in vivo* gelatinase activity. Several studies in mice have determined that the activity of this gelatinase is indeed upregulated in atherosclerotic plaques, however few have addressed its functional role in modulating plaque stability. Comparative histology of aortic plaques from MMP-2 expressing

or deficient atherosclerotic mice clearly demonstrate that MMP-2 contributes to plaque formation but was accompanied by a thicker fibrous cap with increased SMC- and collagen- positive areas, characteristic of plaque stability (Table 1.1).[220] Analogous studies following knockout of MMP-3, -9, and -12 in atherosclerotic mice, which also comprise major targets of broad-spectrum MMPIs, sought to define their pro- or anti-atherogenic functions.[221] Genetic deletion of MMP-3 or MMP-9 resulted in a ~4- or 2-fold increase in atherosclerotic plaque area, an ~8- or 2-fold increase in the number of buried fibrous layers, and a ~2-fold reduction in SMC content, respectively (Table 1.1). Such changes in plaque composition confer stability and indicate protective roles for these enzymes, although other studies have reported variable results for MMP-9.[222] In contrast, genetic deletion of MMP-12 provided a ~2-fold decrease in atherosclerotic plaque area, the number of buried fibrous caps, and macrophage content confirming a role in plaque destabilization (Table 1.1). This demonstrates that specific MMPs can have divergent effects on cellular plaque composition and that the contributions of each enzyme to atherosclerotic plaque stability must be considered when interpreting radiotracer uptake.

Table 1.1 Summary of divergent roles of MMPs on atherosclerotic plaque composition and stability.

Subfamily	MMP	Effect of MMP Knockout on Plaque Composition[a]				Phenotype
		Area	Collagen	SMC	Macrophage	
Collagenase	MMP-8	-	-	-	-	-
	MMP-13	-	↑	↓	-	unstable
Gelatinase	MMP-2	↓	-	↓	-	stable
	MMP-9	↑↓	↓	↑↓	↑-	variable
Stromelysin	MMP-3	↑	↑	↓	-	stable
Matrilysin	MMP-7	-	-	↑	-	-
Elastase	MMP-12	↓	↑	↑	↓	unstable

[a]Up and down arrows indicate increases or decreases while dashes indicate no change in accumulation.

1.12 Validation of MMP-13 in Atherosclerosis

1.12.1 Characterization of Unstable Human Atherosclerotic Plaques

MMP-1, -8, and -13 form a subfamily of collagenases which are frequently targeted by broad-spectrum MMPIs and imaging agents. These enzymes are extensively involved in cardiovascular remodeling and catalyze the initial rate-limiting step in collagen breakdown.[223] Human carotid atherosclerotic plaques were categorized into fibrous (stable) and atheromatous (unstable) phenotypes according to morphological features including their fibrous cap thickness, SMC and macrophage positive areas, and lipid content.[224] Immunohistochemical analysis revealed that MMP-1 and MMP-13 colocalized and exhibited ~3- and ~5-fold greater uptake in atheromatous as compared to fibrous plaques, respectively. *In situ* hybridization and western

blotting additionally confirmed that MMP-13 mRNA and protein expression were predominantly elevated in atheromatous tissue, but not normal arteries. To provide evidence of collagenolytic activity, immunostaining of collagen fibrils was conducted and revealed an increase in cleaved collagen within atheromatous plaques that colocalized with MMP-1 and MMP-13. Quantification by western blotting showed ~2- and 5-fold more cleaved collagen in atheromatous plaques compared with fibrous plaques or healthy tissue and a reciprocal decrease of intact collagen, respectively. Proinflammatory cytokines such as IL-1 and TNFα which activate collagenases were also uniquely expressed in atheromatous plaques. This data demonstrates that MMP-1 and MMP-13 are primarily upregulated in inflammatory human atheromatous plaques and their collagenolytic activity may increase susceptibility to rupture.

1.12.2 MMP-13 Selective Knockout

Additional investigations in MMP-13 knockout mice were performed to evaluate the role of this collagenase on the development and structure of atherosclerotic plaques.[225] MMP-13 deficiency did not alter total plaque burden nor the accumulation of macrophages (Table 1.1). However, after 10 weeks of atherogenic diet, staining revealed a ~2-fold increase in collagen content in terms of both absolute and percent area (Table 1.1). Using circularly polarized light, collagen fiber morphology could be examined and showed that MMP-13 significantly decreased collagen fiber thickness, orientation, and organization by ~1.5-2-fold within the fibrous cap (Table 1.1). These results identify MMP-13 as a major *in vivo* regulator of destructive arterial collagen remodelling and suggest that MMP-13 mediated alterations in collagen content and structure may reduce atherosclerotic plaque stability.

Considering the lack of a functional rodent ortholog of MMP-1, a separate study sought to determine the relative contribution of the collagenase activity of MMP-8 and MMP-13 on atherosclerotic plaque composition.[226] In line with previous literature, single or double knockout of MMP-8 and MMP-13 in atherosclerotic mice did not alter plaque size in the aorta or brachiocephalic artery as determined by Oil red O lipid staining (Table 1.1). However, staining and analysis of collagen content revealed that a deficiency of MMP-13, but not MMP-8, significantly increased collagen accumulation by ~70% as compared to atherosclerotic controls with early or established plaques (Table 1.1). No additional increase was observed upon double knockout of both MMP-8 and MMP-13. Moreover, collagen fiber thickness visualized under polarized light, was solely increased in MMP-13 deficient mice and not further enriched by double knockout. *In situ* zymography was used to estimate the relative collagenolytic activity of MMP-8 and MMP-13. Deletion of MMP-13 alone was sufficient to completely inhibit collagen degradation in established plaques to levels indistinguishable from ilomastat blocking. As major sources of collagen production and MMPs, staining for SMCs and macrophages was also conducted. In established plaques with MMP-13 or combined MMP-8/13 deficiencies, there was a ~1.5-fold reduction in SMC content and a ~1.5-2-fold increase in the ratio of collagen/SMCs (Table 1.1). While neither deletion of MMP-13 nor MMP-8 altered macrophage accumulation, there was a trend towards decreased necrotic core size. Together this study provides strong evidence that MMP-13 predominates over MMP-8 as an interstitial collagenase in atherosclerotic mouse plaques and provides the rationale for selective targeting of MMP-13 for therapeutic and diagnostic applications.

1.12.3 MMP-13 Selective Inhibition

Accordingly, selective inhibition of MMP-13 was evaluated as therapeutic strategy to prevent collagen degradation and stabilize atherosclerotic plaques in mice.[173] *In vitro* incubation of murine or human activated macrophages with MMP-13i-A dose-dependently reduced MMP-13 activity by ~75% and ~50%, respectively. According to *in situ* zymography, treatment with MMP-13i-A blocked collagenolytic activity comparably to broad-spectrum inhibition with ilomastat. To assess the effects of MMP-13 inhibition on cellular plaque composition, atherosclerotic mice with evolving or established plaques orally received MMP-13i-A for 10 weeks. *Ex vivo* fluorescent resonance imaging of aortic plaques with a fluorescent activatable probe and nanoparticles demonstrated that MMP-13i-A reduced MMP-13 activity by approximately 35%, without affecting macrophage accumulation. In contrast, staining revealed that MMP-13i-A significantly increased collagen accumulation by ~1.5-fold in both evolving and established plaques. Differentiation of collagen fibril morphology under polarized light further indicated that treatment resulted in thicker and larger collagen fibrils. Moreover, the increase in plaque collagen content was largely observed within the fibrous cap and contributed to increased fibrous cap area and thickness, features consistent with stable atherosclerotic plaques. These results demonstrate that selective inhibition of MMP-13 can alter atherosclerotic plaque composition by reinforcing fibrous cap collagen content and appears to be a suitable molecular marker and therapeutic target of plaque stability.

1.13 MMP-13 Selective Radiotracers

Despite the abundance of MMP-13 selective inhibitors and considerable interest in this collagenase as a major molecular biomarker for osteoarthritis, breast cancer, and atherosclerosis, very few MMP-13 selective radiotracers have been developed for in vivo PET imaging.[227,228] Nevertheless, MMP-13 targeted radiotracers hold significant potential for early diagnosis of

MMP-13 related disorders and monitoring disease progression. Additionally, this approach could accelerate the discovery of MMP-13 selective inhibitors as therapeutic agents and assessing treatment efficacy.

1.13.1 Hydroxyproline Scaffold

To this end, a set of fluorinated small molecule inhibitors were developed based on the (hydroxy)proline-rich triple helical structure of collagen to mimic the native substrate of MMP-13 and radiolabeled for *in vivo* PET imaging in healthy mice.[227] The HA-containing (2*S*,4*S*)-configured 4-hydroxyproline scaffold (Figure 1.15 A) was identified as a lead structure which tightly coordinates the catalytic Zn^{2+} ion and forms key hydrogen bonds with surrounding active site residues. Accordingly, this core fragment was maintained during subsequent structural optimization. To obtain the desired selectivity profile, emphasis was placed on alterations of the N-terminus by attachment of a diphenylacetylene moiety elongated with lipophilic side chain at the 4-position of the distal phenyl ring that is oriented toward the S1' pocket and capable of reaching the unique S1" side pocket. Addition of a 5-fluoropentoxy chain afforded sub-nanomolar MMP-13 potency and >170-fold selectivity, representing a strong candidate for ^{18}F PET radiotracer development. As such, labeling of [^{18}F]4 (Figure 1.15 A) was conveniently performed by aliphatic nucleophilic substitution (S_N2) of the corresponding tosylate precursor with [^{18}F]fluoride.

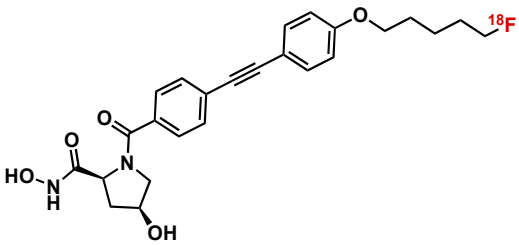

[^{18}F]4

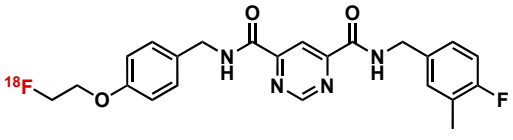

[^{18}F]2a ([^{18}F]FMBP)

Figure 1.15 Chemical structures of MMP-13 selective PET radiotracers. (A) [^{18}F]4 (B) [^{18}F]2a ([^{18}F]FMBP).

In vitro metabolic stability tests in human and mouse serum remarkably revealed only the parent compound with no observable radio-metabolites or decomposition present up to 90 min. In vivo dynamic PET imaging (0-90 min) in healthy mice showed rapid washout of radioactivity from the blood that stabilized at ~2.5% ID/mL. Most significantly, radioactivity in the liver peaked at ~45% ID/mL with prolonged washout to ~25% ID/mL and concomitant accumulation into the intestines over time from ~5-30 % ID/mL. Uptake into the kidneys was largely retained at ~10% ID/mL with minimal clearance into the urinary bladder. This data collectively reflects a hepatobiliary excretion mechanism and excludes a renal elimination pathway. After initial perfusion, analysis of peripheral organs revealed no region of interest with relatively increased radiotracer accumulation above 5% ID/mL. Altogether, this study exemplifies that MMP-13 selective inhibitors can be designed for radiolabeling and marks the first reported example of a selective MMP-13 targeted PET radiotracer. Importantly, the feasibility of this approach has been demonstrated and prompts further translation of non-chelating and highly selective MMP-13 inhibitors as radiotracers for *in vivo* imaging applications.

1.13.2 Pyrimidine-dicarboxamide Scaffold

Shortly thereafter, a series of radiolabeled MMP-13 selective inhibitors derived from the pyrimidine-dicarboxamide class (Figure 1.15 B) were designed and evaluated in healthy mice to characterize radiotracer pharmacokinetics and assess the potential to non-invasively measure MMP-13 activity *in vivo*.[228] The originally identified pyrimidine-dicarboxamide inhibitor

containing symmetrical proximal and distal arms consisting of 4-fluoro-3-methylbenzyl amides was selected as a highly potent and selective lead compound for radiotracer design. As the central pyrimidine-dicarboxamide core represents the anchoring point of molecule that occupies the S1' specificity loop and forms key binding interactions critical for achieving target affinity, this moiety remained invariant. Similarly, as the distal arm extending toward the adjacent S1" pocket is known to significantly drive MMP-13 selectivity, this arene was maintained on one side of the molecule. Structural modifications instead focus on the arene of the proximal arm as it is particularly tolerant toward substitutions at the 4-position and optimally positioned to incorporate reliable handles for late-stage radiolabeling with fluorine-18, carbon-11, or gallium-68 without disrupting inhibitor potency.

Among those synthesized, introduction of fluoroethoxy or methoxy groups on the proximal arm afforded inhibitors in the low nanomolar range which exhibit 1700 and 3800-fold selectivity and represent excellent candidates for fluorine-18 and carbon-11 radiolabeling, respectively. Incorporation of a DOTA chelator which was designed to protrude into the solvent accessible space via a short linker provided a candidate for gallium-68 labeling but was poorly tolerated and accompanied by a loss of MMP-13 selectivity. Radiofluorination of [^{18}F]2a ([^{18}F]FMBP, Figure 1.15 B) was accomplished via nucleophilic substitution (S_N2) of the corresponding tosylate precursor with [^{18}F]fluoride Meanwhile, labeling with carbon-11 was achieved by ^{11}C-methylation of the corresponding phenol precursor with [^{11}C]CH_3I.

Preliminary evaluations were conducted in healthy mice to characterize pharmacokinetics and assess radiotracer performance. *In vivo* dynamic PET imaging (0-60 min) revealed that the ^{18}F and ^{11}C labeled radioligands behave similarly with fast washout at ~1-2% ID/mL remaining in the blood, predominant retention of radioactivity in the liver and gall bladder between ~10-20%

ID/mL, and clearance into the intestines over time from ~5-15% ID/mL, suggestive of a hepatobiliary excretion route. Multi-timepoint *ex vivo* biodistributions of the ^{11}C derivative 5, 15, 30, and 60 min after intravenous administration demonstrated that the radiotracer does not appreciably accumulate in non-excretory organs above 2% ID/g, normally indicating non-specific binding, and recapitulated *in vivo* findings. Plasma radio-metabolite analysis showed moderate metabolic stability with 89 ± 1% and 38 ± 1% remaining intact at 15 and 45 min, respectively. These findings suggest that MMP-13 selective radiotracers based on the pyrimidine-dicarboxamide inhibitor class have significant potential for diagnostic PET imaging and warrants further evaluations in disease models overexpressing MMP-13.

1.14 Hypotheses and Research Aims

Project 1: Selective Imaging of Matrix Metalloproteinase-13 to Detect Extracellular Matrix Remodeling in Atherosclerotic Lesions (Chapter II)

Hypotheses:

1. MMP-13 is a suitable molecular target for PET imaging of atherosclerosis in mice
2. [^{18}F]FMBP can be used to selectively detect MMP-13 in atherosclerotic mouse plaques
3. [^{18}F]BR-351 can be used to broadly detect MMPs in atherosclerotic mouse plaques
4. Selective MMP-13 imaging is superior to broad-spectrum MMP imaging

Research Aims:

1. Validate the *in vitro* uptake and specificity of [^{18}F]FMBP and [^{18}F]BR-351 in atherosclerotic plaques by aortic autoradiography and dose-dependent homologous blocking
2. Characterize the *in vivo* pharmacokinetics of [^{18}F]FMBP and [^{18}F]BR-351 in healthy C57Bl/6 mice and atherosclerotic *ApoE*$^{-/-}$ mice by PET imaging, biodistribution, and plasma radio-metabolism
3. Compare the *in vivo* uptake, target specificity, and disease sensitivity of [^{18}F]FMBP and [^{18}F]BR-351 in atherosclerotic plaques by aortic autoradiography, homologous blocking, and Oil Red O staining
4. Determine the expression of Mac-2, MMP-2, MMP-9, and MMP-13 in atherosclerotic plaques detected with [^{18}F]FMBP and [^{18}F]BR-351 by immunofluorescent staining

Project 2: Quinazoline-2-Carboxamides as Selective PET Radiotracers for Matrix Metalloproteinase-13 Imaging in Atherosclerosis (Chapter III)

Hypotheses:

1. MMP-13 selective PET radiotracers derived from the quinazoline-2-carboxamide scaffold may offer superior pharmacokinetics for cardiovascular imaging
2. The 'best in class' MMP-13 selective inhibitor **21k** represents a promising lead candidate for PET radiotracer development
3. Selective PET radiotracer derived from the quinazoline-2-carboxamide scaffold can be used to detect MMP-13 in atherosclerotic mouse plaques

Research Aims:

1. Explore the structure-activity relationships of the quinazoline-2-carboxamide inhibitor class by synthesizing derivatives with reliable handles for fluorine-18 or carbon-11 radiolabeling
2. Characterize MMP-13 potency and selectivity with an *in vitro* enzyme inhibition assay
3. Develop radiosyntheses for **[^{11}C]21k** and 2 other lead candidates by ^{11}C-methylation or nucleophilic ^{18}F-fluorination
4. Evaluate *in vivo* radiotracer pharmacokinetics in *ApoE*$^{-/-}$ mice by PET imaging, biodistribution, and plasma radio-metabolism
5. Determine *in vivo* radiotracer uptake and target specificity in atherosclerotic mouse plaques by aortic autoradiography, homologous/heterologous blocking, and Oil Red O staining

Project 3: Neutral 5-Functionalized Quinazoline-2-Carboxamides as Matrix Metalloproteinase-13 Selective PET Radiotracers (IV)

Hypotheses:

1. Optimized second-generation MMP-13 selective PET radiotracers derived from the quinazoline-2-carboxamide scaffold have the potential for improved imaging contrast and *in vivo* MMP-13 specificity in atherosclerotic mouse plaques
2. Introducing additional heteroatoms and polar functional groups will reduce radiotracer lipophilicity and accelerate blood clearance
3. Incorporating strong hydrogen bond acceptors that are neutral at physiological pH will restore S1" binding interactions to improve MMP-13 potency and selectivity without rendering the molecule a substrate for the organic anion transporter

Research Aims:

1. Explore the structure-activity relationships of the S1' pocket (proximal inhibitor arm) by synthesizing intermediates containing 2-fluoropyridine regioisomers
2. Explore the structure-activity relationships of the S1" pocket (distal inhibitor arm) by synthesizing functionalized inhibitors containing 5-substituted phenethyl alcohols
3. Characterize MMP-13 potency and selectivity with an *in vitro* enzyme inhibition assay
4. Establish an automated radiosynthesis for the identified lead candidate
5. Evaluate *in vivo* radiotracer pharmacokinetics in *ApoE*$^{-/-}$ mice by PET/CT imaging, biodistribution, and plasma radio-metabolism

6. Determine *in vivo* radiotracer uptake and target specificity in atherosclerotic mouse plaques by aortic autoradiography, homologous/heterologous blocking, and Oil Red O staining

1.15 References

(1) Rong, J.; Haider, A.; Jeppesen, T. E.; Josephson, L.; Liang, S. H. Radiochemistry for Positron Emission Tomography. *Nat. Commun.* **2023**, *14* (1), 3257. https://doi.org/10.1038/s41467-023-36377-4.

(2) Stendahl, J. C.; Kwan, J. M.; Pucar, D.; Sadeghi, M. M. Radiotracers to Address Unmet Clinical Needs in Cardiovascular Imaging, Part 2: Inflammation, Fibrosis, Thrombosis, Calcification, and Amyloidosis Imaging. *J. Nucl. Med.* **2022**, *63* (7), 986–994. https://doi.org/10.2967/jnumed.121.263507.

(3) Bodei, L.; Herrmann, K.; Schöder, H.; Scott, A. M.; Lewis, J. S. Radiotheranostics in Oncology: Current Challenges and Emerging Opportunities. *Nat. Rev. Clin. Oncol.* **2022**, *19* (8), 534–550. https://doi.org/10.1038/s41571-022-00652-y.

(4) Jain, P.; Chaney, A.; Carlson, M. L.; Jackson, I. M.; Rao, A.; James, M. L. Neuroinflammation PET Imaging: Current Opinion and Future Directions. *J. Nucl. Med.* **2020**. https://doi.org/10.2967/jnumed.119.229443.

(5) Schmor, P. Review of Cyclotrons for the Production of Radioactive Isotopes for Medical and Industrial Applications. *Rev. Accel. Sci. Technol.* **2011**, *04* (01), 103–116. https://doi.org/10.1142/S1793626811000574.

(6) Synowiecki, M. A.; Perk, L. R.; Nijsen, J. F. W. Production of Novel Diagnostic Radionuclides in Small Medical Cyclotrons. *EJNMMI Radiopharm. Chem.* **2018**, *3* (1), 3. https://doi.org/10.1186/s41181-018-0038-z.

(7) Conti, M.; Eriksson, L. Physics of Pure and Non-Pure Positron Emitters for PET: A Review and a Discussion. *EJNMMI Phys.* **2016**, *3* (1), 8. https://doi.org/10.1186/s40658-016-0144-5.

(8) Vermeulen, I.; Isin, E. M.; Barton, P.; Cillero-Pastor, B.; Heeren, R. M. A. Multimodal Molecular Imaging in Drug Discovery and Development. *Drug Discov. Today* **2022**, *27* (8), 2086–2099. https://doi.org/10.1016/j.drudis.2022.04.009.

(9) Shah, P.; Westwell, A. D. The Role of Fluorine in Medicinal Chemistry. *J. Enzyme Inhib. Med. Chem.* **2007**, *22* (5), 527–540. https://doi.org/10.1080/14756360701425014.

(10) Jacobson, O.; Kiesewetter, D. O.; Chen, X. Fluorine-18 Radiochemistry, Labeling Strategies and Synthetic Routes. *Bioconjug. Chem.* **2015**, *26* (1), 1–18. https://doi.org/10.1021/bc500475e.

(11) Dollé, F. Carbon-11 and Fluorine-18 Chemistry Devoted to Molecular Probes for Imaging the Brain with Positron Emission Tomography. *J. Label. Compd. Radiopharm.* **2013**, *56* (3–4), 65–67. https://doi.org/10.1002/jlcr.3037.

(12) Pees, A.; Chassé, M.; Lindberg, A.; Vasdev, N. Recent Developments in Carbon-11 Chemistry and Applications for First-In-Human PET Studies. *Molecules* **2023**, *28* (3), 931. https://doi.org/10.3390/molecules28030931.

(13) Kubota, K.; Itoh, M.; Ozaki, K.; Ono, S.; Tashiro, M.; Yamaguchi, K.; Akaizawa, T.; Yamada, K.; Fukuda, H. Advantage of Delayed Whole-Body FDG-PET Imaging for Tumour Detection. *Eur. J. Nucl. Med.* **2001**, *28* (6), 696–703. https://doi.org/10.1007/s002590100537.

(14) Slart, R. H. J. A.; Glaudemans, A. W. J. M.; Gheysens, O.; Lubberink, M.; Kero, T.; Dweck, M. R.; Habib, G.; Gaemperli, O.; Saraste, A.; Gimelli, A.; Georgoulias, P.;

Verberne, H. J.; Bucerius, J.; Rischpler, C.; Hyafil, F.; Erba, P. A. Procedural Recommendations of Cardiac PET/CT Imaging: Standardization in Inflammatory-, Infective-, Infiltrative-, and Innervation- (4Is) Related Cardiovascular Diseases: A Joint Collaboration of the EACVI and the EANM: Summary. *Eur. Heart J. Cardiovasc. Imaging* **2020**, *21* (12), 1320–1330. https://doi.org/10.1093/ehjci/jeaa299.

(15) Government of Canada, S. C. *Leading causes of death, total population, by age group*. https://www150.statcan.gc.ca/t1/tbl1/en/tv.action?pid=1310039401 (accessed 2024-09-05).

(16) *Heart failure in Canada complex incurable and on the rise*. Heart and Stroke Foundation of Canada. https://www.heartandstroke.ca/en/what-we-do/media-centre/news-releases/heart-failure-in-canada-complex-incurable-and-on-the-rise/ (accessed 2024-09-05).

(17) Bentzon, J. F.; Otsuka, F.; Virmani, R.; Falk, E. Mechanisms of Plaque Formation and Rupture. *Circ. Res.* **2014**, *114* (12), 1852–1866. https://doi.org/10.1161/CIRCRESAHA.114.302721.

(18) Virmani, R.; Kolodgie, F. D.; Burke, A. P.; Farb, A.; Schwartz, S. M. Lessons from Sudden Coronary Death: A Comprehensive Morphological Classification Scheme for Atherosclerotic Lesions. *Arterioscler. Thromb. Vasc. Biol.* **2000**, *20* (5), 1262–1275. https://doi.org/10.1161/01.atv.20.5.1262.

(19) Lusis, A. J. Atherosclerosis. *Nature* **2000**, *407* (6801), 233–241. https://doi.org/10.1038/35025203.

(20) Libby, P.; Buring, J. E.; Badimon, L.; Hansson, G. K.; Deanfield, J.; Bittencourt, M. S.; Tokgözoğlu, L.; Lewis, E. F. Atherosclerosis. *Nat. Rev. Dis. Primer* **2019**, *5* (1), 1–18. https://doi.org/10.1038/s41572-019-0106-z.

(21) Jebari-Benslaiman, S.; Galicia-García, U.; Larrea-Sebal, A.; Olaetxea, J. R.; Alloza, I.; Vandenbroeck, K.; Benito-Vicente, A.; Martín, C. Pathophysiology of Atherosclerosis. *Int. J. Mol. Sci.* **2022**, *23* (6), 3346. https://doi.org/10.3390/ijms23063346.

(22) Rajendran, P.; Rengarajan, T.; Thangavel, J.; Nishigaki, Y.; Sakthisekaran, D.; Sethi, G.; Nishigaki, I. The Vascular Endothelium and Human Diseases. *Int. J. Biol. Sci.* **2013**, *9* (10), 1057–1069. https://doi.org/10.7150/ijbs.7502.

(23) Deanfield, J. E.; Halcox, J. P.; Rabelink, T. J. Endothelial Function and Dysfunction: Testing and Clinical Relevance. *Circulation* **2007**, *115* (10), 1285–1295. https://doi.org/10.1161/CIRCULATIONAHA.106.652859.

(24) Hadi, H. A.; Carr, C. S.; Al Suwaidi, J. Endothelial Dysfunction: Cardiovascular Risk Factors, Therapy, and Outcome. *Vasc. Health Risk Manag.* **2005**, *1* (3), 183–198.

(25) Khatana, C.; Saini, N. K.; Chakrabarti, S.; Saini, V.; Sharma, A.; Saini, R. V.; Saini, A. K. Mechanistic Insights into the Oxidized Low-Density Lipoprotein-Induced Atherosclerosis. *Oxid. Med. Cell. Longev.* **2020**, *2020*, 5245308. https://doi.org/10.1155/2020/5245308.

(26) Maiolino, G.; Rossitto, G.; Caielli, P.; Bisogni, V.; Rossi, G. P.; Calò, L. A. The Role of Oxidized Low-Density Lipoproteins in Atherosclerosis: The Myths and the Facts. *Mediators Inflamm.* **2013**, *2013*, 714653. https://doi.org/10.1155/2013/714653.

(27) Libby, P. Inflammation in Atherosclerosis. *Arterioscler. Thromb. Vasc. Biol.* **2012**, *32* (9), 2045–2051. https://doi.org/10.1161/ATVBAHA.108.179705.

(28) Rafieian-Kopaei, M.; Setorki, M.; Doudi, M.; Baradaran, A.; Nasri, H. Atherosclerosis: Process, Indicators, Risk Factors and New Hopes. *Int. J. Prev. Med.* **2014**, *5* (8), 927–946.

(29) Akers, E. J.; Nicholls, S. J.; Di Bartolo, B. A. Plaque Calcification. *Arterioscler. Thromb. Vasc. Biol.* **2019**, *39* (10), 1902–1910. https://doi.org/10.1161/ATVBAHA.119.311574.

(30) Wang, X.; Khalil, R. A. Matrix Metalloproteinases, Vascular Remodeling, and Vascular Disease. *Adv. Pharmacol. San Diego Calif* **2018**, *81*, 241–330. https://doi.org/10.1016/bs.apha.2017.08.002.

(31) Johnson, J. L. Matrix Metalloproteinases: Influence on Smooth Muscle Cells and Atherosclerotic Plaque Stability. *Expert Rev. Cardiovasc. Ther.* **2007**, *5* (2), 265–282. https://doi.org/10.1586/14779072.5.2.265.

(32) Newby, A. C. Dual Role of Matrix Metalloproteinases (Matrixins) in Intimal Thickening and Atherosclerotic Plaque Rupture. *Physiol. Rev.* **2005**, *85* (1), 1–31. https://doi.org/10.1152/physrev.00048.2003.

(33) Newby, A. C. Metalloproteinases and Vulnerable Atherosclerotic Plaques. *Trends Cardiovasc. Med.* **2007**, *17* (8), 253–258. https://doi.org/10.1016/j.tcm.2007.09.001.

(34) Finn, A. V.; Nakano, M.; Narula, J.; Kolodgie, F. D.; Virmani, R. Concept of Vulnerable/Unstable Plaque. *Arterioscler. Thromb. Vasc. Biol.* **2010**, *30* (7), 1282–1292. https://doi.org/10.1161/ATVBAHA.108.179739.

(35) Virmani, R.; Burke, A. P.; Farb, A.; Kolodgie, F. D. Pathology of the Vulnerable Plaque. *J. Am. Coll. Cardiol.* **2006**, *47* (8 Suppl), C13-18. https://doi.org/10.1016/j.jacc.2005.10.065.

(36) Newby, A. C. Metalloproteinases Promote Plaque Rupture and Myocardial Infarction: A Persuasive Concept Waiting for Clinical Translation. *Matrix Biol.* **2015**, *44–46*, 157–166. https://doi.org/10.1016/j.matbio.2015.01.015.

(37) Badimon, L.; Padró, T.; Vilahur, G. Atherosclerosis, Platelets and Thrombosis in Acute Ischaemic Heart Disease. *Eur. Heart J. Acute Cardiovasc. Care* **2012**, *1* (1), 60–74. https://doi.org/10.1177/2048872612441582.

(38) Olie, R. H.; van der Meijden, P. E. J.; ten Cate, H. The Coagulation System in Atherothrombosis: Implications for New Therapeutic Strategies. *Res. Pract. Thromb. Haemost.* **2018**, *2* (2), 188–198. https://doi.org/10.1002/rth2.12080.

(39) Winther, S.; Schmidt, S. E.; Rasmussen, L. D.; Juárez Orozco, L. E.; Steffensen, F. H.; Bøtker, H. E.; Knuuti, J.; Bøttcher, M.; on behalf of The Western Denmark Cardiac CT Study Group. Validation of the European Society of Cardiology Pre-Test Probability Model for Obstructive Coronary Artery Disease. *Eur. Heart J.* **2021**, *42* (14), 1401–1411. https://doi.org/10.1093/eurheartj/ehaa755.

(40) Sicari, R.; Cortigiani, L. The Clinical Use of Stress Echocardiography in Ischemic Heart Disease. *Cardiovasc. Ultrasound* **2017**, *15*, 7. https://doi.org/10.1186/s12947-017-0099-2.

(41) Klein, R.; Celiker-Guler, E.; Rotstein, B. H.; deKemp, R. A. PET and SPECT Tracers for Myocardial Perfusion Imaging. *Semin. Nucl. Med.* **2020**, *50* (3), 208–218. https://doi.org/10.1053/j.semnuclmed.2020.02.016.

(42) Stuijfzand, W. J.; van Rosendael, A. R.; Lin, F. Y.; Chang, H.-J.; van den Hoogen, I. J.; Gianni, U.; Choi, J. H.; Doh, J.-H.; Her, A.-Y.; Koo, B.-K.; Nam, C.-W.; Park, H.-B.; Shin, S.-H.; Cole, J.; Gimelli, A.; Khan, M. A.; Lu, B.; Gao, Y.; Nabi, F.; Nakazato, R.; Schoepf, U. J.; Driessen, R. S.; Bom, M. J.; Thompson, R.; Jang, J. J.; Ridner, M.; Rowan,

C.; Avelar, E.; Généreux, P.; Knaapen, P.; de Waard, G. A.; Pontone, G.; Andreini, D.; Al-Mallah, M. H.; Lu, Y.; Berman, D. S.; Narula, J.; Min, J. K.; Bax, J. J.; Shaw, L. J.; CREDENCE Investigators. Stress Myocardial Perfusion Imaging vs Coronary Computed Tomographic Angiography for Diagnosis of Invasive Vessel-Specific Coronary Physiology: Predictive Modeling Results From the Computed Tomographic Evaluation of Atherosclerotic Determinants of Myocardial Ischemia (CREDENCE) Trial. *JAMA Cardiol.* **2020**, *5* (12), 1338–1348. https://doi.org/10.1001/jamacardio.2020.3409.

(43) Foley, J. R. J.; Plein, S.; Greenwood, J. P. Assessment of Stable Coronary Artery Disease by Cardiovascular Magnetic Resonance Imaging: Current and Emerging Techniques. *World J. Cardiol.* **2017**, *9* (2), 92–108. https://doi.org/10.4330/wjc.v9.i2.92.

(44) Douglas, P. S.; Hoffmann, U.; Patel, M. R.; Mark, D. B.; Al-Khalidi, H. R.; Cavanaugh, B.; Cole, J.; Dolor, R. J.; Fordyce, C. B.; Huang, M.; Khan, M. A.; Kosinski, A. S.; Krucoff, M. W.; Malhotra, V.; Picard, M. H.; Udelson, J. E.; Velazquez, E. J.; Yow, E.; Cooper, L. S.; Lee, K. L. Outcomes of Anatomical versus Functional Testing for Coronary Artery Disease. *N. Engl. J. Med.* **2015**, *372* (14), 1291–1300. https://doi.org/10.1056/NEJMoa1415516.

(45) null, null. CT or Invasive Coronary Angiography in Stable Chest Pain. *N. Engl. J. Med.* **2022**, *386* (17), 1591–1602. https://doi.org/10.1056/NEJMoa2200963.

(46) Machado, M. F.; Felix, N.; Melo, P. H. C.; Gauza, M. M.; Calomeni, P.; Generoso, G.; Khatri, S.; Altmayer, S.; Blankstein, R.; Bittencourt, M. S.; Cardoso, R. Coronary Computed Tomography Angiography Versus Invasive Coronary Angiography in Stable Chest Pain: A Meta-Analysis of Randomized Controlled Trials. *Circ. Cardiovasc. Imaging* **2023**, *16* (11), e015800. https://doi.org/10.1161/CIRCIMAGING.123.015800.

(47) Hoffmann, U.; Ferencik, M.; Udelson, J. E.; Picard, M. H.; Truong, Q. A.; Patel, M. R.; Huang, M.; Pencina, M.; Mark, D. B.; Heitner, J. F.; Fordyce, C. B.; Pellikka, P. A.; Tardif, J.-C.; Budoff, M.; Nahhas, G.; Chow, B.; Kosinski, A. S.; Lee, K. L.; Douglas, P. S.; PROMISE Investigators. Prognostic Value of Noninvasive Cardiovascular Testing in Patients With Stable Chest Pain: Insights From the PROMISE Trial (Prospective Multicenter Imaging Study for Evaluation of Chest Pain). *Circulation* **2017**, *135* (24), 2320–2332. https://doi.org/10.1161/CIRCULATIONAHA.116.024360.

(48) Williams, M. C.; Kwiecinski, J.; Doris, M.; McElhinney, P.; D'Souza, M. S.; Cadet, S.; Adamson, P. D.; Moss, A. J.; Alam, S.; Hunter, A.; Shah, A. S. V.; Mills, N. L.; Pawade, T.; Wang, C.; Weir McCall, J.; Bonnici-Mallia, M.; Murrills, C.; Roditi, G.; van Beek, E. J. R.; Shaw, L. J.; Nicol, E. D.; Berman, D. S.; Slomka, P. J.; Newby, D. E.; Dweck, M. R.; Dey, D. Low-Attenuation Noncalcified Plaque on Coronary Computed Tomography Angiography Predicts Myocardial Infarction: Results From the Multicenter SCOT-HEART Trial (Scottish Computed Tomography of the HEART). *Circulation* **2020**, *141* (18), 1452–1462. https://doi.org/10.1161/CIRCULATIONAHA.119.044720.

(49) null, null. Coronary CT Angiography and 5-Year Risk of Myocardial Infarction. *N. Engl. J. Med.* **2018**, *379* (10), 924–933. https://doi.org/10.1056/NEJMoa1805971.

(50) Budoff, M. J.; Young, R.; Burke, G.; Jeffrey Carr, J.; Detrano, R. C.; Folsom, A. R.; Kronmal, R.; Lima, J. A. C.; Liu, K. J.; McClelland, R. L.; Michos, E.; Post, W. S.; Shea, S.; Watson, K. E.; Wong, N. D. Ten-Year Association of Coronary Artery Calcium with Atherosclerotic Cardiovascular Disease (ASCVD) Events: The Multi-Ethnic Study of Atherosclerosis (MESA). *Eur. Heart J.* **2018**, *39* (25), 2401–2408. https://doi.org/10.1093/eurheartj/ehy217.

(51) Greenland, P.; LaBree, L.; Azen, S. P.; Doherty, T. M.; Detrano, R. C. Coronary Artery Calcium Score Combined with Framingham Score for Risk Prediction in Asymptomatic Individuals. *JAMA* **2004**, *291* (2), 210–215. https://doi.org/10.1001/jama.291.2.210.

(52) Villines, T. C.; Hulten, E. A.; Shaw, L. J.; Goyal, M.; Dunning, A.; Achenbach, S.; Al-Mallah, M.; Berman, D. S.; Budoff, M. J.; Cademartiri, F.; Callister, T. Q.; Chang, H.-J.; Cheng, V. Y.; Chinnaiyan, K.; Chow, B. J. W.; Delago, A.; Hadamitzky, M.; Hausleiter, J.; Kaufmann, P.; Lin, F. Y.; Maffei, E.; Raff, G. L.; Min, J. K.; CONFIRM Registry Investigators. Prevalence and Severity of Coronary Artery Disease and Adverse Events among Symptomatic Patients with Coronary Artery Calcification Scores of Zero Undergoing Coronary Computed Tomography Angiography: Results from the CONFIRM (Coronary CT Angiography Evaluation for Clinical Outcomes: An International Multicenter) Registry. *J. Am. Coll. Cardiol.* **2011**, *58* (24), 2533–2540. https://doi.org/10.1016/j.jacc.2011.10.851.

(53) Grundy, S. M.; Stone, N. J.; Bailey, A. L.; Beam, C.; Birtcher, K. K.; Blumenthal, R. S.; Braun, L. T.; de Ferranti, S.; Faiella-Tommasino, J.; Forman, D. E.; Goldberg, R.; Heidenreich, P. A.; Hlatky, M. A.; Jones, D. W.; Lloyd-Jones, D.; Lopez-Pajares, N.; Ndumele, C. E.; Orringer, C. E.; Peralta, C. A.; Saseen, J. J.; Smith, S. C.; Sperling, L.; Virani, S. S.; Yeboah, J. 2018 AHA/ACC/AACVPR/AAPA/ABC/ACPM/ADA/AGS/ APhA/ASPC/NLA/PCNA Guideline on the Management of Blood Cholesterol: Executive Summary. *Circulation* **2019**, *139* (25), e1082–e1143. https://doi.org/10.1161/CIR.0000000000000625.

(54) Meijboom, W. B.; Van Mieghem, C. A. G.; van Pelt, N.; Weustink, A.; Pugliese, F.; Mollet, N. R.; Boersma, E.; Regar, E.; van Geuns, R. J.; de Jaegere, P. J.; Serruys, P. W.;

Krestin, G. P.; de Feyter, P. J. Comprehensive Assessment of Coronary Artery Stenoses: Computed Tomography Coronary Angiography Versus Conventional Coronary Angiography and Correlation With Fractional Flow Reserve in Patients With Stable Angina. *J. Am. Coll. Cardiol.* **2008**, *52* (8), 636–643. https://doi.org/10.1016/j.jacc.2008.05.024.

(55) Dweck, M. R.; Aikawa, E.; Newby, D. E.; Tarkin, J. M.; Rudd, J. H. F.; Narula, J.; Fayad, Z. A. Noninvasive Molecular Imaging of Disease Activity in Atherosclerosis. *Circ. Res.* **2016**, *119* (2), 330–340. https://doi.org/10.1161/CIRCRESAHA.116.307971.

(56) Fletcher, J. W.; Djulbegovic, B.; Soares, H. P.; Siegel, B. A.; Lowe, V. J.; Lyman, G. H.; Coleman, R. E.; Wahl, R.; Paschold, J. C.; Avril, N.; Einhorn, L. H.; Suh, W. W.; Samson, D.; Delbeke, D.; Gorman, M.; Shields, A. F. Recommendations on the Use of 18F-FDG PET in Oncology. *J. Nucl. Med.* **2008**, *49* (3), 480–508. https://doi.org/10.2967/jnumed.107.047787.

(57) Celiker-Guler, E.; Ruddy, T. D.; Wells, R. G. Acquisition, Processing, and Interpretation of PET 18F-FDG Viability and Inflammation Studies. *Curr. Cardiol. Rep.* **2021**, *23* (9), 124. https://doi.org/10.1007/s11886-021-01555-7.

(58) Tawakol, A.; Migrino, R. Q.; Bashian, G. G.; Bedri, S.; Vermylen, D.; Cury, R. C.; Yates, D.; LaMuraglia, G. M.; Furie, K.; Houser, S.; Gewirtz, H.; Muller, J. E.; Brady, T. J.; Fischman, A. J. In Vivo 18F-Fluorodeoxyglucose Positron Emission Tomography Imaging Provides a Noninvasive Measure of Carotid Plaque Inflammation in Patients. *J. Am. Coll. Cardiol.* **2006**, *48* (9), 1818–1824. https://doi.org/10.1016/j.jacc.2006.05.076.

(59) Okumura, W.; Iwasaki, T.; Toyama, T.; Iso, T.; Arai, M.; Oriuchi, N.; Endo, K.; Yokoyama, T.; Suzuki, T.; Kurabayashi, M. Usefulness of Fasting 18F-FDG PET in

Identification of Cardiac Sarcoidosis. *J. Nucl. Med. Off. Publ. Soc. Nucl. Med.* **2004**, *45* (12), 1989–1998.

(60) Barrio, J. R.; Huang, S.-C.; Satyamurthy, N.; Scafoglio, C. S.; Yu, A. S.; Alavi, A.; Krohn, K. A. Does 2-FDG PET Accurately Reflect Quantitative In Vivo Glucose Utilization? *J. Nucl. Med.* **2020**, *61* (6), 931–937. https://doi.org/10.2967/jnumed.119.237446.

(61) Beanlands, R. S. B.; Ruddy, T. D.; deKemp, R. A.; Iwanochko, R. M.; Coates, G.; Freeman, M.; Nahmias, C.; Hendry, P.; Burns, R. J.; Lamy, A.; Mickleborough, L.; Kostuk, W.; Fallen, E.; Nichol, G. Positron Emission Tomography and Recovery Following Revascularization (PARR-1): The Importance of Scar and the Development of a Prediction Rule for the Degree of Recovery of Left Ventricular Function. *J. Am. Coll. Cardiol.* **2002**, *40* (10), 1735–1743. https://doi.org/10.1016/S0735-1097(02)02489-0.

(62) Mc Ardle, B.; Shukla, T.; Nichol, G.; deKemp, R. A.; Bernick, J.; Guo, A.; Lim, S. P.; Davies, R. A.; Haddad, H.; Duchesne, L.; Hendry, P.; Masters, R.; Ross, H.; Freeman, M.; Gulenchyn, K.; Racine, N.; Humen, D.; Benard, F.; Ruddy, T. D.; Chow, B. J.; Mielniczuk, L.; DaSilva, J. N.; Garrard, L.; Wells, G. A.; Beanlands, R. S. B.; PARR-2 Investigators. Long-Term Follow-Up of Outcomes With F-18-Fluorodeoxyglucose Positron Emission Tomography Imaging-Assisted Management of Patients With Severe Left Ventricular Dysfunction Secondary to Coronary Disease. *Circ. Cardiovasc. Imaging* **2016**, *9* (9), e004331. https://doi.org/10.1161/CIRCIMAGING.115.004331.

(63) Figueroa, A. L.; Subramanian, S. S.; Cury, R. C.; Truong, Q. A.; Gardecki, J. A.; Tearney, G. J.; Hoffmann, U.; Brady, T. J.; Tawakol, A. Distribution of Inflammation within Carotid Atherosclerotic Plaques with High-Risk Morphological Features: A Comparison between Positron Emission Tomography Activity, Plaque Morphology, and

Histopathology. *Circ. Cardiovasc. Imaging* **2012**, *5* (1), 69–77. https://doi.org/10.1161/CIRCIMAGING.110.959478.

(64) Rudd, J. H. F.; Warburton, E. A.; Fryer, T. D.; Jones, H. A.; Clark, J. C.; Antoun, N.; Johnström, P.; Davenport, A. P.; Kirkpatrick, P. J.; Arch, B. N.; Pickard, J. D.; Weissberg, P. L. Imaging Atherosclerotic Plaque Inflammation with [18F]-Fluorodeoxyglucose Positron Emission Tomography. *Circulation* **2002**, *105* (23), 2708–2711. https://doi.org/10.1161/01.cir.0000020548.60110.76.

(65) Joshi, N. V.; Vesey, A. T.; Williams, M. C.; Shah, A. S. V.; Calvert, P. A.; Craighead, F. H. M.; Yeoh, S. E.; Wallace, W.; Salter, D.; Fletcher, A. M.; van Beek, E. J. R.; Flapan, A. D.; Uren, N. G.; Behan, M. W. H.; Cruden, N. L. M.; Mills, N. L.; Fox, K. A. A.; Rudd, J. H. F.; Dweck, M. R.; Newby, D. E. 18F-Fluoride Positron Emission Tomography for Identification of Ruptured and High-Risk Coronary Atherosclerotic Plaques: A Prospective Clinical Trial. *The Lancet* **2014**, *383* (9918), 705–713. https://doi.org/10.1016/S0140-6736(13)61754-7.

(66) Cheng, V. Y.; Slomka, P. J.; Le Meunier, L.; Tamarappoo, B. K.; Nakazato, R.; Dey, D.; Berman, D. S. Coronary Arterial 18F-FDG Uptake by Fusion of PET and Coronary CT Angiography at Sites of Percutaneous Stenting for Acute Myocardial Infarction and Stable Coronary Artery Disease. *J. Nucl. Med. Off. Publ. Soc. Nucl. Med.* **2012**, *53* (4), 575–583. https://doi.org/10.2967/jnumed.111.097550.

(67) Pijl, J. P.; Nienhuis, P. H.; Kwee, T. C.; Glaudemans, A. W. J. M.; Slart, R. H. J. A.; Gormsen, L. C. Limitations and Pitfalls of FDG-PET/CT in Infection and Inflammation. *Semin. Nucl. Med.* **2021**, *51* (6), 633–645. https://doi.org/10.1053/j.semnuclmed.2021.06.008.

(68) Rogers, I. S.; Nasir, K.; Figueroa, A. L.; Cury, R. C.; Hoffmann, U.; Vermylen, D. A.; Brady, T. J.; Tawakol, A. Feasibility of FDG Imaging of the Coronary Arteries: Comparison between Acute Coronary Syndrome and Stable Angina. *JACC Cardiovasc. Imaging* **2010**, *3* (4), 388–397. https://doi.org/10.1016/j.jcmg.2010.01.004.

(69) Wykrzykowska, J.; Lehman, S.; Williams, G.; Parker, J. A.; Palmer, M. R.; Varkey, S.; Kolodny, G.; Laham, R. Imaging of Inflamed and Vulnerable Plaque in Coronary Arteries with 18F-FDG PET/CT in Patients with Suppression of Myocardial Uptake Using a Low-Carbohydrate, High-Fat Preparation. *J. Nucl. Med. Off. Publ. Soc. Nucl. Med.* **2009**, *50* (4), 563–568. https://doi.org/10.2967/jnumed.108.055616.

(70) Williams, G.; Kolodny, G. M. Suppression of Myocardial 18F-FDG Uptake by Preparing Patients with a High-Fat, Low-Carbohydrate Diet. *AJR Am. J. Roentgenol.* **2008**, *190* (2), W151-156. https://doi.org/10.2214/AJR.07.2409.

(71) Araz, M.; Aras, G.; Küçük, Ö. N. The Role of 18F–NaF PET/CT in Metastatic Bone Disease. *J. Bone Oncol.* **2015**, *4* (3), 92–97. https://doi.org/10.1016/j.jbo.2015.08.002.

(72) Even-Sapir, E.; Mishani, E.; Flusser, G.; Metser, U. 18F-Fluoride Positron Emission Tomography and Positron Emission Tomography/Computed Tomography. *Semin. Nucl. Med.* **2007**, *37* (6), 462–469. https://doi.org/10.1053/j.semnuclmed.2007.07.002.

(73) Iagaru, A.; Young, P.; Mittra, E.; Dick, D. W.; Herfkens, R.; Gambhir, S. S. Pilot Prospective Evaluation of 99mTc-MDP Scintigraphy, 18F NaF PET/CT, 18F FDG PET/CT and Whole-Body MRI for Detection of Skeletal Metastases. *Clin. Nucl. Med.* **2013**, *38* (7), e290-296. https://doi.org/10.1097/RLU.0b013e3182815f64.

(74) Jambor, I.; Kuisma, A.; Ramadan, S.; Huovinen, R.; Sandell, M.; Kajander, S.; Kemppainen, J.; Kauppila, E.; Auren, J.; Merisaari, H.; Saunavaara, J.; Noponen, T.;

Minn, H.; Aronen, H. J.; Seppänen, M. Prospective Evaluation of Planar Bone Scintigraphy, SPECT, SPECT/CT, 18F-NaF PET/CT and Whole Body 1.5T MRI, Including DWI, for the Detection of Bone Metastases in High Risk Breast and Prostate Cancer Patients: SKELETA Clinical Trial. *Acta Oncol. Stockh. Swed.* **2016**, *55* (1), 59–67. https://doi.org/10.3109/0284186X.2015.1027411.

(75) Tzolos, E.; Dweck, M. R. 18F-Sodium Fluoride (18F-NaF) for Imaging Microcalcification Activity in the Cardiovascular System. *Arterioscler. Thromb. Vasc. Biol.* **2020**, *40* (7), 1620–1626. https://doi.org/10.1161/ATVBAHA.120.313785.

(76) Montanaro, M.; Scimeca, M.; Anemona, L.; Servadei, F.; Giacobbi, E.; Bonfiglio, R.; Bonanno, E.; Urbano, N.; Ippoliti, A.; Santeusanio, G.; Schillaci, O.; Mauriello, A. The Paradox Effect of Calcification in Carotid Atherosclerosis: Microcalcification Is Correlated with Plaque Instability. *Int. J. Mol. Sci.* **2021**, *22* (1), 395. https://doi.org/10.3390/ijms22010395.

(77) Vancheri, F.; Longo, G.; Vancheri, S.; Danial, J. S. H.; Henein, M. Y. Coronary Artery Microcalcification: Imaging and Clinical Implications. *Diagn. Basel Switz.* **2019**, *9* (4), 125. https://doi.org/10.3390/diagnostics9040125.

(78) Dweck, M. R.; Jenkins, W. S. A.; Vesey, A. T.; Pringle, M. A. H.; Chin, C. W. L.; Malley, T. S.; Cowie, W. J. A.; Tsampasian, V.; Richardson, H.; Fletcher, A.; Wallace, W. A.; Pessotto, R.; van Beek, E. J. R.; Boon, N. A.; Rudd, J. H. F.; Newby, D. E. 18F-Sodium Fluoride Uptake Is a Marker of Active Calcification and Disease Progression in Patients with Aortic Stenosis. *Circ. Cardiovasc. Imaging* **2014**, *7* (2), 371–378. https://doi.org/10.1161/CIRCIMAGING.113.001508.

(79) Tzolos, E.; Dweck, M. R. ^{18} F-Sodium Fluoride (^{18} F-NaF) for Imaging Microcalcification Activity in the Cardiovascular System. *Arterioscler. Thromb. Vasc. Biol.* **2020**, *40* (7), 1620–1626. https://doi.org/10.1161/ATVBAHA.120.313785.

(80) Kwiecinski, J.; Tzolos, E.; Adamson, P. D.; Cadet, S.; Moss, A. J.; Joshi, N.; Williams, M. C.; van Beek, E. J. R.; Dey, D.; Berman, D. S.; Newby, D. E.; Slomka, P. J.; Dweck, M. R. Coronary 18F-Sodium Fluoride Uptake Predicts Outcomes in Patients With Coronary Artery Disease. *J. Am. Coll. Cardiol.* **2020**, *75* (24), 3061–3074. https://doi.org/10.1016/j.jacc.2020.04.046.

(81) Kwiecinski, J.; Cadet, S.; Daghem, M.; Lassen, M. L.; Dey, D.; Dweck, M. R.; Berman, D. S.; Newby, D. E.; Slomka, P. J. Whole-Vessel Coronary 18F-Sodium Fluoride PET for Assessment of the Global Coronary Microcalcification Burden. *Eur. J. Nucl. Med. Mol. Imaging* **2020**, *47* (7), 1736–1745. https://doi.org/10.1007/s00259-019-04667-z.

(82) Loffek, S.; Schilling, O.; Franzke, C.-W. Biological Role of Matrix Metalloproteinases: A Critical Balance. *Eur. Respir. J.* **2011**, *38* (1), 191–208. https://doi.org/10.1183/09031936.00146510.

(83) Nagase, H.; Visse, R.; Murphy, G. Structure and Function of Matrix Metalloproteinases and TIMPs. *Cardiovasc. Res.* **2006**, *69* (3), 562–573. https://doi.org/10.1016/j.cardiores.2005.12.002.

(84) Laronha, H.; Caldeira, J. Structure and Function of Human Matrix Metalloproteinases. *Cells* **2020**, *9* (5), 1076. https://doi.org/10.3390/cells9051076.

(85) Sternlicht, M. D.; Werb, Z. HOW MATRIX METALLOPROTEINASES REGULATE CELL BEHAVIOR. *Annu. Rev. Cell Dev. Biol.* **2001**, *17*, 463–516. https://doi.org/10.1146/annurev.cellbio.17.1.463.

(86) Van Wart, H. E.; Birkedal-Hansen, H. The Cysteine Switch: A Principle of Regulation of Metalloproteinase Activity with Potential Applicability to the Entire Matrix Metalloproteinase Gene Family. *Proc. Natl. Acad. Sci. U. S. A.* **1990**, *87* (14), 5578–5582. https://doi.org/10.1073/pnas.87.14.5578.

(87) Somerville, R. P.; Oblander, S. A.; Apte, S. S. Matrix Metalloproteinases: Old Dogs with New Tricks. *Genome Biol.* **2003**, *4* (6), 216. https://doi.org/10.1186/gb-2003-4-6-216.

(88) Bode, W. A Helping Hand for Collagenases: The Haemopexin-like Domain. *Structure* **1995**, *3* (6), 527–530. https://doi.org/10.1016/S0969-2126(01)00185-X.

(89) Klein, T.; Bischoff, R. Physiology and Pathophysiology of Matrix Metalloproteases. *Amino Acids* **2011**, *41* (2), 271–290. https://doi.org/10.1007/s00726-010-0689-x.

(90) Cabral-Pacheco, G. A.; Garza-Veloz, I.; Castruita-De la Rosa, C.; Ramirez-Acuña, J. M.; Perez-Romero, B. A.; Guerrero-Rodriguez, J. F.; Martinez-Avila, N.; Martinez-Fierro, M. L. The Roles of Matrix Metalloproteinases and Their Inhibitors in Human Diseases. *Int. J. Mol. Sci.* **2020**, *21* (24), 9739. https://doi.org/10.3390/ijms21249739.

(91) Ruddy, J. M.; Ikonomidis, J. S.; Jones, J. A. Multidimensional Contribution of Matrix Metalloproteinases to Atherosclerotic Plaque Vulnerability: Multiple Mechanisms of Inhibition to Promote Stability. *J. Vasc. Res.* **2016**, *53* (1–2), 1–16. https://doi.org/10.1159/000446703.

(92) Olejarz, W.; Łacheta, D.; Kubiak-Tomaszewska, G. Matrix Metalloproteinases as Biomarkers of Atherosclerotic Plaque Instability. *Int. J. Mol. Sci.* **2020**, *21* (11), 3946. https://doi.org/10.3390/ijms21113946.

(93) Hu, J.; Van den Steen, P. E.; Sang, Q.-X. A.; Opdenakker, G. Matrix Metalloproteinase Inhibitors as Therapy for Inflammatory and Vascular Diseases. *Nat. Rev. Drug Discov.* **2007**, *6* (6), 480–498. https://doi.org/10.1038/nrd2308.

(94) Egeblad, M.; Werb, Z. New Functions for the Matrix Metalloproteinases in Cancer Progression. *Nat. Rev. Cancer* **2002**, *2* (3), 161–174. https://doi.org/10.1038/nrc745.

(95) Das, S.; Amin, S. A.; Jha, T. Inhibitors of Gelatinases (MMP-2 and MMP-9) for the Management of Hematological Malignancies. *Eur. J. Med. Chem.* **2021**, *223*, 113623. https://doi.org/10.1016/j.ejmech.2021.113623.

(96) Cerofolini, L.; Fragai, M.; Luchinat, C. Mechanism and Inhibition of Matrix Metalloproteinases. *Curr. Med. Chem.* **2019**, *26* (15), 2609–2633. https://doi.org/10.2174/0929867325666180326163523.

(97) Castelhano, A. L.; Billedeau, R.; Dewdney, N.; Donnelly, S.; Horne, S.; Kurz, L. J.; Liak, T. J.; Martin, R.; Uppington, R.; Zhengyu Yuan; Krantz, A. Novel Indolactam-Based Inhibitors of Matrix Metalloproteinases. *Bioorg. Med. Chem. Lett.* **1995**, *5* (13), 1415–1420. https://doi.org/10.1016/0960-894X(95)00233-J.

(98) Rasmussen, H. S.; McCann, P. P. Matrix Metalloproteinase Inhibition as a Novel Anticancer Strategy: A Review with Special Focus on Batimastat and Marimastat. *Pharmacol. Ther.* **1997**, *75* (1), 69–75. https://doi.org/10.1016/s0163-7258(97)00023-5.

(99) Davies, B.; Brown, P. D.; East, N.; Crimmin, M. J.; Balkwill, F. R. A Synthetic Matrix Metalloproteinase Inhibitor Decreases Tumor Burden and Prolongs Survival of Mice Bearing Human Ovarian Carcinoma Xenografts. *Cancer Res.* **1993**, *53* (9), 2087–2091.

(100) Chirivi, R. G.; Garofalo, A.; Crimmin, M. J.; Bawden, L. J.; Stoppacciaro, A.; Brown, P. D.; Giavazzi, R. Inhibition of the Metastatic Spread and Growth of B16-BL6 Murine

Melanoma by a Synthetic Matrix Metalloproteinase Inhibitor. *Int. J. Cancer* **1994**, *58* (3), 460–464. https://doi.org/10.1002/ijc.2910580326.

(101) Watson, S. A.; Morris, T. M.; Robinson, G.; Crimmin, M. J.; Brown, P. D.; Hardcastle, J. D. Inhibition of Organ Invasion by the Matrix Metalloproteinase Inhibitor Batimastat (BB-94) in Two Human Colon Carcinoma Metastasis Models. *Cancer Res.* **1995**, *55* (16), 3629–3633.

(102) Sledge, G. W.; Qulali, M.; Goulet, R.; Bone, E. A.; Fife, R. Effect of Matrix Metalloproteinase Inhibitor Batimastat on Breast Cancer Regrowth and Metastasis in Athymic Mice. *J. Natl. Cancer Inst.* **1995**, *87* (20), 1546–1550. https://doi.org/10.1093/jnci/87.20.1546.

(103) Wojtowicz-Praga, S.; Low, J.; Marshall, J.; Ness, E.; Dickson, R.; Barter, J.; Sale, M.; McCann, P.; Moore, J.; Cole, A.; Hawkins, M. J. Phase I Trial of a Novel Matrix Metalloproteinase Inhibitor Batimastat (BB-94) in Patients with Advanced Cancer. *Invest. New Drugs* **1996**, *14* (2), 193–202. https://doi.org/10.1007/BF00210790.

(104) Grobelny, D.; Poncz, L.; Galardy, R. E. Inhibition of Human Skin Fibroblast Collagenase, Thermolysin, and Pseudomonas Aeruginosa Elastase by Peptide Hydroxamic Acids. *Biochemistry* **1992**, *31* (31), 7152–7154. https://doi.org/10.1021/bi00146a017.

(105) Agren, M. S.; Mirastschijski, U.; Karlsmark, T.; Saarialho-Kere, U. K. Topical Synthetic Inhibitor of Matrix Metalloproteinases Delays Epidermal Regeneration of Human Wounds. *Exp. Dermatol.* **2001**, *10* (5), 337–348. https://doi.org/10.1034/j.1600-0625.2001.100506.x.

(106) Wong, T. T. L.; Mead, A. L.; Khaw, P. T. Matrix Metalloproteinase Inhibition Modulates Postoperative Scarring after Experimental Glaucoma Filtration Surgery. *Invest. Ophthalmol. Vis. Sci.* **2003**, *44* (3), 1097–1103. https://doi.org/10.1167/iovs.02-0366.

(107) Bencsik, P.; Pálóczi, J.; Kocsis, G. F.; Pipis, J.; Belecz, I.; Varga, Z. V.; Csonka, C.; Görbe, A.; Csont, T.; Ferdinandy, P. Moderate Inhibition of Myocardial Matrix Metalloproteinase-2 by Ilomastat Is Cardioprotective. *Pharmacol. Res.* **2014**, *80*, 36–42. https://doi.org/10.1016/j.phrs.2013.12.007.

(108) Hao, J. L.; Nagano, T.; Nakamura, M.; Kumagai, N.; Mishima, H.; Nishida, T. Effect of Galardin on Collagen Degradation by Pseudomonas Aeruginosa. *Exp. Eye Res.* **1999**, *69* (6), 595–601. https://doi.org/10.1006/exer.1999.0755.

(109) Hao, J. L.; Nagano, T.; Nakamura, M.; Kumagai, N.; Mishima, H.; Nishida, T. Galardin Inhibits Collagen Degradation by Rabbit Keratocytes by Inhibiting the Activation of Pro-Matrix Metalloproteinases. *Exp. Eye Res.* **1999**, *68* (5), 565–572. https://doi.org/10.1006/exer.1998.0637.

(110) Winding, B.; NicAmhlaoibh, R.; Misander, H.; Høegh-Andersen, P.; Andersen, T. L.; Holst-Hansen, C.; Heegaard, A.-M.; Foged, N. T.; Brünner, N.; Delaissé, J.-M. Synthetic Matrix Metalloproteinase Inhibitors Inhibit Growth of Established Breast Cancer Osteolytic Lesions and Prolong Survival in Mice. *Clin. Cancer Res. Off. J. Am. Assoc. Cancer Res.* **2002**, *8* (6), 1932–1939.

(111) Galardy, R. E.; Cassabonne, M. E.; Giese, C.; Gilbert, J. H.; Lapierre, F.; Lopez, H.; Schaefer, M. E.; Stack, R.; Sullivan, M.; Summers, B. Low Molecular Weight Inhibitors in Corneal Ulceration. *Ann. N. Y. Acad. Sci.* **1994**, *732*, 315–323. https://doi.org/10.1111/j.1749-6632.1994.tb24746.x.

(112) Rothenberg, M. L.; Nelson, A. R.; Hande, K. R. New Drugs on the Horizon: Matrix Metalloproteinase Inhibitors. *Stem Cells* **1999**, *17* (4), 237–240. https://doi.org/10.1002/stem.170237.

(113) Millar, A. W.; Brown, P. D.; Moore, J.; Galloway, W. A.; Cornish, A. G.; Lenehan, T. J.; Lynch, K. P. Results of Single and Repeat Dose Studies of the Oral Matrix Metalloproteinase Inhibitor Marimastat in Healthy Male Volunteers. *Br. J. Clin. Pharmacol.* **1998**, *45* (1), 21–26. https://doi.org/10.1046/j.1365-2125.1998.00639.x.

(114) Nemunaitis, J.; Poole, C.; Primrose, J.; Rosemurgy, A.; Malfetano, J.; Brown, P.; Berrington, A.; Cornish, A.; Lynch, K.; Rasmussen, H.; Kerr, D.; Cox, D.; Millar, A. Combined Analysis of Studies of the Effects of the Matrix Metalloproteinase Inhibitor Marimastat on Serum Tumor Markers in Advanced Cancer: Selection of a Biologically Active and Tolerable Dose for Longer-Term Studies. *Clin. Cancer Res. Off. J. Am. Assoc. Cancer Res.* **1998**, *4* (5), 1101–1109.

(115) Wojtowicz-Praga, S.; Torri, J.; Johnson, M.; Steen, V.; Marshall, J.; Ness, E.; Dickson, R.; Sale, M.; Rasmussen, H. S.; Chiodo, T. A.; Hawkins, M. J. Phase I Trial of Marimastat, a Novel Matrix Metalloproteinase Inhibitor, Administered Orally to Patients with Advanced Lung Cancer. *J. Clin. Oncol.* **1998**, *16* (6), 2150–2156. https://doi.org/10.1200/JCO.1998.16.6.2150.

(116) Goffin, J. R.; Anderson, I. C.; Supko, J. G.; Eder, J. P.; Shapiro, G. I.; Lynch, T. J.; Shipp, M.; Johnson, B. E.; Skarin, A. T. Phase I Trial of the Matrix Metalloproteinase Inhibitor Marimastat Combined with Carboplatin and Paclitaxel in Patients with Advanced Non-Small Cell Lung Cancer. *Clin. Cancer Res. Off. J. Am. Assoc. Cancer Res.* **2005**, *11* (9), 3417–3424. https://doi.org/10.1158/1078-0432.CCR-04-2144.

(117) Tierney, G. M.; Griffin, N. R.; Stuart, R. C.; Kasem, H.; Lynch, K. P.; Lury, J. T.; Brown, P. D.; Millar, A. W.; Steele, R. J.; Parsons, S. L. A Pilot Study of the Safety and Effects of the Matrix Metalloproteinase Inhibitor Marimastat in Gastric Cancer. *Eur. J. Cancer Oxf. Engl. 1990* **1999**, *35* (4), 563–568. https://doi.org/10.1016/s0959-8049(99)00007-6.

(118) Quirt, I.; Bodurtha, A.; Lohmann, R.; Rusthoven, J.; Belanger, K.; Young, V.; Wainman, N.; Steward, W.; Eisenhauer, E. Phase II Study of Marimastat (BB-2516) in Malignant Melanoma – A Clinical and Tumor Biopsy Study of the National Cancer Institute of Canada Clinical Trials Group. *Invest. New Drugs* **2002**, *20* (4), 431–437. https://doi.org/10.1023/A:1020625423524.

(119) Miller, K. D.; Gradishar, W.; Schuchter, L.; Sparano, J. A.; Cobleigh, M.; Robert, N.; Rasmussen, H.; Sledge, G. W. A Randomized Phase II Pilot Trial of Adjuvant Marimastat in Patients with Early-Stage Breast Cancer. *Ann. Oncol. Off. J. Eur. Soc. Med. Oncol.* **2002**, *13* (8), 1220–1224. https://doi.org/10.1093/annonc/mdf199.

(120) Bramhall, S. R.; Hallissey, M. T.; Whiting, J.; Scholefield, J.; Tierney, G.; Stuart, R. C.; Hawkins, R. E.; McCulloch, P.; Maughan, T.; Brown, P. D.; Baillet, M.; Fielding, J. W. L. Marimastat as Maintenance Therapy for Patients with Advanced Gastric Cancer: A Randomised Trial. *Br. J. Cancer* **2002**, *86* (12), 1864–1870. https://doi.org/10.1038/sj.bjc.6600310.

(121) Sparano, J. A.; Bernardo, P.; Stephenson, P.; Gradishar, W. J.; Ingle, J. N.; Zucker, S.; Davidson, N. E. Randomized Phase III Trial of Marimastat versus Placebo in Patients with Metastatic Breast Cancer Who Have Responding or Stable Disease after First-Line Chemotherapy: Eastern Cooperative Oncology Group Trial E2196. *J. Clin. Oncol. Off. J.*

Am. Soc. Clin. Oncol. **2004**, *22* (23), 4683–4690. https://doi.org/10.1200/JCO.2004.08.054.

(122) Bramhall, S. R.; Schulz, J.; Nemunaitis, J.; Brown, P. D.; Baillet, M.; Buckels, J. a. C. A Double-Blind Placebo-Controlled, Randomised Study Comparing Gemcitabine and Marimastat with Gemcitabine and Placebo as First Line Therapy in Patients with Advanced Pancreatic Cancer. *Br. J. Cancer* **2002**, *87* (2), 161–167. https://doi.org/10.1038/sj.bjc.6600446.

(123) Steward, W. P.; Thomas, A. L. Marimastat: The Clinical Development of a Matrix Metalloproteinase Inhibitor. *Expert Opin. Investig. Drugs* **2000**, *9* (12), 2913–2922. https://doi.org/10.1517/13543784.9.12.2913.

(124) Fields, G. B. The Rebirth of Matrix Metalloproteinase Inhibitors: Moving Beyond the Dogma. *Cells* **2019**, *8* (9), 984. https://doi.org/10.3390/cells8090984.

(125) Adhikari, N.; Mukherjee, A.; Saha, A.; Jha, T. Arylsulfonamides and Selectivity of Matrix Metalloproteinase-2: An Overview. *Eur. J. Med. Chem.* **2017**, *129*, 72–109. https://doi.org/10.1016/j.ejmech.2017.02.014.

(126) Cheng, X.-C.; Wang, Q.; Fang, H.; Xu, W.-F. Role of Sulfonamide Group in Matrix Metalloproteinase Inhibitors. *Curr. Med. Chem.* **2008**, *15* (4), 368–373. https://doi.org/10.2174/092986708783497300.

(127) MacPherson, L. J.; Bayburt, E. K.; Capparelli, M. P.; Carroll, B. J.; Goldstein, R.; Justice, M. R.; Zhu, L.; Hu, S.; Melton, R. A.; Fryer, L.; Goldberg, R. L.; Doughty, J. R.; Spirito, S.; Blancuzzi, V.; Wilson, D.; O'Byrne, E. M.; Ganu, V.; Parker, D. T. Discovery of CGS 27023A, a Non-Peptidic, Potent, and Orally Active Stromelysin Inhibitor That Blocks

Cartilage Degradation in Rabbits. *J. Med. Chem.* **1997**, *40* (16), 2525–2532. https://doi.org/10.1021/jm960871c.

(128) Scozzafava, A.; Supuran, C. T. Protease Inhibitors: Synthesis of Potent Bacterial Collagenase and Matrix Metalloproteinase Inhibitors Incorporating N-4-Nitrobenzylsulfonylglycine Hydroxamate Moieties. *J. Med. Chem.* **2000**, *43* (9), 1858–1865. https://doi.org/10.1021/jm990594k.

(129) O'Byrne, E. M.; Parker, D. T.; Roberts, E. D.; Goldberg, R. L.; MacPherson, L. J.; Blancuzzi, V.; Wilson, D.; Singh, H. N.; Ludewig, R.; Ganu, V. S. Oral Administration of a Matrix Metalloproteinase Inhibitor, CGS 27023A, Protects the Cartilage Proteoglycan Matrix in a Partial Meniscectomy Model of Osteoarthritis in Rabbits. *Inflamm. Res.* **1995**, *44* (2), S117–S118. https://doi.org/10.1007/BF01778290.

(130) Levitt, N. C.; Eskens, F. A.; O'Byrne, K. J.; Propper, D. J.; Denis, L. J.; Owen, S. J.; Choi, L.; Foekens, J. A.; Wilner, S.; Wood, J. M.; Nakajima, M.; Talbot, D. C.; Steward, W. P.; Harris, A. L.; Verweij, J. Phase I and Pharmacological Study of the Oral Matrix Metalloproteinase Inhibitor, MMI270 (CGS27023A), in Patients with Advanced Solid Cancer. *Clin. Cancer Res. Off. J. Am. Assoc. Cancer Res.* **2001**, *7* (7), 1912–1922.

(131) Eatock, M.; Cassidy, J.; Johnson, J.; Morrison, R.; Devlin, M.; Blackey, R.; Owen, S.; Choi, L.; Twelves, C. A Dose-Finding and Pharmacokinetic Study of the Matrix Metalloproteinase Inhibitor MMI270 (Previously Termed CGS27023A) with 5-FU and Folinic Acid. *Cancer Chemother. Pharmacol.* **2005**, *55* (1), 39–46. https://doi.org/10.1007/s00280-004-0856-4.

(132) Vandenbroucke, R. E.; Libert, C. Is There New Hope for Therapeutic Matrix Metalloproteinase Inhibition? *Nat. Rev. Drug Discov.* **2014**, *13* (12), 904–927. https://doi.org/10.1038/nrd4390.

(133) Santos, O.; McDermott, C. D.; Daniels, R. G.; Appelt, K. Rodent Pharmacokinetic and Anti-Tumor Efficacy Studies with a Series of Synthetic Inhibitors of Matrix Metalloproteinases. *Clin. Exp. Metastasis* **1997**, *15* (5), 499–508. https://doi.org/10.1023/A:1018418725453.

(134) Shalinsky, D. R.; Brekken, J.; Zou, H.; Kolis, S.; Wood, A.; Webber, S.; Appelt, K. Antitumor Efficacy of AG3340 Associated with Maintenance of Minimum Effective Plasma Concentrations and Not Total Daily Dose, Exposure or Peak Plasma Concentrations. *Invest. New Drugs* **1998**, *16* (4), 303–313. https://doi.org/10.1023/a:1006204901140.

(135) Price, A.; Shi, Q.; Morris, D.; Wilcox, M. E.; Brasher, P. M.; Rewcastle, N. B.; Shalinsky, D.; Zou, H.; Appelt, K.; Johnston, R. N.; Yong, V. W.; Edwards, D.; Forsyth, P. Marked Inhibition of Tumor Growth in a Malignant Glioma Tumor Model by a Novel Synthetic Matrix Metalloproteinase Inhibitor AG3340. *Clin. Cancer Res. Off. J. Am. Assoc. Cancer Res.* **1999**, *5* (4), 845–854.

(136) Shalinsky, D. R.; Brekken, J.; Zou, H.; McDermott, C. D.; Forsyth, P.; Edwards, D.; Margosiak, S.; Bender, S.; Truitt, G.; Wood, A.; Varki, N. M.; Appelt, K. Broad Antitumor and Antiangiogenic Activities of AG3340, a Potent and Selective MMP Inhibitor Undergoing Advanced Oncology Clinical Trials. *Ann. N. Y. Acad. Sci.* **1999**, *878*, 236–270. https://doi.org/10.1111/j.1749-6632.1999.tb07689.x.

(137) Shalinsky, D. R.; Brekken, J.; Zou, H.; Bloom, L. A.; McDermott, C. D.; Zook, S.; Varki, N. M.; Appelt, K. Marked Antiangiogenic and Antitumor Efficacy of AG3340 in Chemoresistant Human Non-Small Cell Lung Cancer Tumors: Single Agent and Combination Chemotherapy Studies. *Clin. Cancer Res. Off. J. Am. Assoc. Cancer Res.* **1999**, *5* (7), 1905–1917.

(138) Bissett, D.; O'Byrne, K. J.; von Pawel, J.; Gatzemeier, U.; Price, A.; Nicolson, M.; Mercier, R.; Mazabel, E.; Penning, C.; Zhang, M. H.; Collier, M. A.; Shepherd, F. A. Phase III Study of Matrix Metalloproteinase Inhibitor Prinomastat in Non-Small-Cell Lung Cancer. *J. Clin. Oncol. Off. J. Am. Soc. Clin. Oncol.* **2005**, *23* (4), 842–849. https://doi.org/10.1200/JCO.2005.03.170.

(139) Hande, K. R.; Collier, M.; Paradiso, L.; Stuart-Smith, J.; Dixon, M.; Clendeninn, N.; Yeun, G.; Alberti, D.; Binger, K.; Wilding, G. Phase I and Pharmacokinetic Study of Prinomastat, a Matrix Metalloprotease Inhibitor. *Clin. Cancer Res. Off. J. Am. Assoc. Cancer Res.* **2004**, *10* (3), 909–915. https://doi.org/10.1158/1078-0432.ccr-0981-3.

(140) Heath, E. I.; Burtness, B. A.; Kleinberg, L.; Salem, R. R.; Yang, S. C.; Heitmiller, R. F.; Canto, M. I.; Knisely, J. P. S.; Topazian, M.; Montgomery, E.; Tsottles, N.; Pithavala, Y.; Rohmiller, B.; Collier, M.; Forastiere, A. A. Phase II, Parallel-Design Study of Preoperative Combined Modality Therapy and the Matrix Metalloprotease (Mmp) Inhibitor Prinomastat in Patients with Esophageal Adenocarcinoma. *Invest. New Drugs* **2006**, *24* (2), 135–140. https://doi.org/10.1007/s10637-006-5934-5.

(141) Nozaki, S.; Sissons, S.; Chien, D.-S.; Sledge, G. W. Activity of Biphenyl Matrix Metalloproteinase Inhibitor BAY 12-9566 in a Human Breast Cancer Orthotopic Model. *Clin. Exp. Metastasis* **2003**, *20* (5), 407–412. https://doi.org/10.1023/a:1025473709656.

(142) Gatto, C.; Rieppi, M.; Borsotti, P.; Innocenti, S.; Ceruti, R.; Drudis, T.; Scanziani, E.; Casazza, A. M.; Taraboletti, G.; Giavazzi, R. BAY 12-9566, a Novel Inhibitor of Matrix Metalloproteinases with Antiangiogenic Activity. *Clin. Cancer Res. Off. J. Am. Assoc. Cancer Res.* **1999**, *5* (11), 3603–3607.

(143) Rowinsky, E. K.; Humphrey, R.; Hammond, L. A.; Aylesworth, C.; Smetzer, L.; Hidalgo, M.; Morrow, M.; Smith, L.; Garner, A.; Sorensen, J. M.; Von Hoff, D. D.; Eckhardt, S. G. Phase I and Pharmacologic Study of the Specific Matrix Metalloproteinase Inhibitor BAY 12-9566 on a Protracted Oral Daily Dosing Schedule in Patients with Solid Malignancies. *J. Clin. Oncol. Off. J. Am. Soc. Clin. Oncol.* **2000**, *18* (1), 178–186. https://doi.org/10.1200/JCO.2000.18.1.178.

(144) Erlichman, C.; Adjei, A. A.; Alberts, S. R.; Sloan, J. A.; Goldberg, R. M.; Pitot, H. C.; Rubin, J.; Atherton, P. J.; Klee, G. G.; Humphrey, R. Phase I Study of the Matrix Metalloproteinase Inhibitor, BAY 12-9566. *Ann. Oncol. Off. J. Eur. Soc. Med. Oncol.* **2001**, *12* (3), 389–395. https://doi.org/10.1023/a:1011183905848.

(145) Heath, E. I.; O'Reilly, S.; Humphrey, R.; Sundaresan, P.; Donehower, R. C.; Sartorius, S.; Kennedy, M. J.; Armstrong, D. K.; Carducci, M. A.; Sorensen, J. M.; Kumor, K.; Kennedy, S.; Grochow, L. B. Phase I Trial of the Matrix Metalloproteinase Inhibitor BAY12-9566 in Patients with Advanced Solid Tumors. *Cancer Chemother. Pharmacol.* **2001**, *48* (4), 269–274. https://doi.org/10.1007/s002800100330.

(146) Denham, C. O-107 Adjuvant Targeted Therapy in Unresectable Lung Cancer: The Results of Two Randomized Placebo-Controlled Trials of BAY 12-9566, a Matrix Metalloproteinase Inhibitor (MMPI). *Lung Cancer* **2003**.

(147) Moore, M. J.; Hamm, J.; Dancey, J.; Eisenberg, P. D.; Dagenais, M.; Fields, A.; Hagan, K.; Greenberg, B.; Colwell, B.; Zee, B.; Tu, D.; Ottaway, J.; Humphrey, R.; Seymour, L.; National Cancer Institute of Canada Clinical Trials Group. Comparison of Gemcitabine versus the Matrix Metalloproteinase Inhibitor BAY 12-9566 in Patients with Advanced or Metastatic Adenocarcinoma of the Pancreas: A Phase III Trial of the National Cancer Institute of Canada Clinical Trials Group. *J. Clin. Oncol. Off. J. Am. Soc. Clin. Oncol.* **2003**, *21* (17), 3296–3302. https://doi.org/10.1200/JCO.2003.02.098.

(148) Hirte, H.; Vergote, I. B.; Jeffrey, J. R.; Grimshaw, R. N.; Coppieters, S.; Schwartz, B.; Tu, D.; Sadura, A.; Brundage, M.; Seymour, L. A Phase III Randomized Trial of BAY 12-9566 (Tanomastat) as Maintenance Therapy in Patients with Advanced Ovarian Cancer Responsive to Primary Surgery and Paclitaxel/Platinum Containing Chemotherapy: A National Cancer Institute of Canada Clinical Trials Group Study. *Gynecol. Oncol.* **2006**, *102* (2), 300–308. https://doi.org/10.1016/j.ygyno.2005.12.020.

(149) Lombard, M. A.; Wallace, T. L.; Kubicek, M. F.; Petzold, G. L.; Mitchell, M. A.; Hendges, S. K.; Wilks, J. W. Synthetic Matrix Metalloproteinase Inhibitors and Tissue Inhibitor of Metalloproteinase (TIMP)-2, but Not TIMP-1, Inhibit Shedding of Tumor Necrosis Factor-Alpha Receptors in a Human Colon Adenocarcinoma (Colo 205) Cell Line. *Cancer Res.* **1998**, *58* (17), 4001–4007.

(150) Naglich, J. G.; Jure-Kunkel, M.; Gupta, E.; Fargnoli, J.; Henderson, A. J.; Lewin, A. C.; Talbott, R.; Baxter, A.; Bird, J.; Savopoulos, R.; Wills, R.; Kramer, R. A.; Trail, P. A. Inhibition of Angiogenesis and Metastasis in Two Murine Models by the Matrix Metalloproteinase Inhibitor, BMS-275291. *Cancer Res.* **2001**, *61* (23), 8480–8485.

(151) Rizvi, N. A.; Humphrey, J. S.; Ness, E. A.; Johnson, M. D.; Gupta, E.; Williams, K.; Daly, D. J.; Sonnichsen, D.; Conway, D.; Marshall, J.; Hurwitz, H. A Phase I Study of Oral BMS-275291, a Novel Nonhydroxamate Sheddase-Sparing Matrix Metalloproteinase Inhibitor, in Patients with Advanced or Metastatic Cancer. *Clin. Cancer Res.* **2004**, *10* (6), 1963–1970. https://doi.org/10.1158/1078-0432.CCR-1183-02.

(152) Brinker, B. T.; Krown, S. E.; Lee, J. Y.; Cesarman, E.; Chadburn, A.; Kaplan, L. D.; Henry, D. H.; Von Roenn, J. H. Phase 1/2 Trial of BMS-275291 in Patients with Human Immunodeficiency Virus-Related Kaposi Sarcoma: A Multicenter Trial of the AIDS Malignancy Consortium. *Cancer* **2008**, *112* (5), 1083–1088. https://doi.org/10.1002/cncr.23108.

(153) Lara, P. N., Jr.; Stadler, W. M.; Longmate, J.; Quinn, D. I.; Wexler, J.; Van Loan, M.; Twardowski, P.; Gumerlock, P. H.; Vogelzang, N. J.; Vokes, E. E.; Lenz, H. J.; Doroshow, J. H.; Gandara, D. R. A Randomized Phase II Trial of the Matrix Metalloproteinase Inhibitor BMS-275291 in Hormone-Refractory Prostate Cancer Patients with Bone Metastases. *Clin. Cancer Res.* **2006**, *12* (5), 1556–1563. https://doi.org/10.1158/1078-0432.CCR-05-2074.

(154) Miller, K. D.; Saphner, T. J.; Waterhouse, D. M.; Chen, T.-T.; Rush-Taylor, A.; Sparano, J. A.; Wolff, A. C.; Cobleigh, M. A.; Galbraith, S.; Sledge, G. W. A Randomized Phase II Feasibility Trial of BMS-275291 in Patients with Early Stage Breast Cancer. *Clin. Cancer Res.* **2004**, *10* (6), 1971–1975. https://doi.org/10.1158/1078-0432.CCR-03-0968.

(155) Douillard, J.-Y.; Peschel, C.; Shepherd, F.; Paz-Ares, L.; Arnold, A.; Davis, M.; Tonato, M.; Smylie, M.; Tu, D.; Voi, M.; Humphrey, J.; Ottaway, J.; Young, K.; Vreckem, A. V.; Seymour, L. Randomized Phase II Feasibility Study of Combining the Matrix

Metalloproteinase Inhibitor BMS-275291 with Paclitaxel plus Carboplatin in Advanced Non-Small Cell Lung Cancer. *Lung Cancer Amst. Neth.* **2004**, *46* (3), 361–368. https://doi.org/10.1016/j.lungcan.2004.05.009.

(156) Leighl, N. B.; Paz-Ares, L.; Douillard, J.-Y.; Peschel, C.; Arnold, A.; Depierre, A.; Santoro, A.; Betticher, D. C.; Gatzemeier, U.; Jassem, J.; Crawford, J.; Tu, D.; Bezjak, A.; Humphrey, J. S.; Voi, M.; Galbraith, S.; Hann, K.; Seymour, L.; Shepherd, F. A. Randomized Phase III Study of Matrix Metalloproteinase Inhibitor BMS-275291 in Combination with Paclitaxel and Carboplatin in Advanced Non-Small-Cell Lung Cancer: National Cancer Institute of Canada-Clinical Trials Group Study BR.18. *J. Clin. Oncol. Off. J. Am. Soc. Clin. Oncol.* **2005**, *23* (12), 2831–2839. https://doi.org/10.1200/JCO.2005.04.044.

(157) Lewis, E. J.; Bishop, J.; Bottomley, K. M. K.; Bradshaw, D.; Brewster, M.; Broadhurst, M. J.; Brown, P. A.; Budd, J. M.; Elliott, L.; Greenham, A. K.; Johnson, W. H.; Nixon, J. S.; Rose, F.; Sutton, B.; Wilson, K. Ro 32-3555, an Orally Active Collagenase Inhibitor, Prevents Cartilage Breakdown in Vitro and in Vivo. *Br. J. Pharmacol.* **1997**, *121* (3), 540–546. https://doi.org/10.1038/sj.bjp.0701150.

(158) Brewster, M.; Lewis, J. E.; Wilson, K. L.; Greenham, A. K.; Bottomley, K. M. K. Ro 32-3555, an Orally Active Collagenase Selective Inhibitor, Prevents Structural Damage in the STR/ORT Mouse Model of Osteoarthritis. *Arthritis Rheum.* **1998**, *41* (9), 1639–1644. https://doi.org/10.1002/1529-0131(199809)41:9<1639::AID-ART15>3.0.CO;2-0.

(159) *Tolerability and pharmacokinetics of the collagenase-selective inhibitor Trocade™ in patients with rheumatoid arthritis | Rheumatology | Oxford Academic*. https://academic.oup.com/rheumatology/article/40/5/537/1784136 (accessed 2024-09-06).

(160) Close, D. R. Matrix Metalloproteinase Inhibitors in Rheumatic Diseases. *Ann. Rheum. Dis.* **2001**, *60 Suppl 3* (Suppl 3), iii62-67. https://doi.org/10.1136/ard.60.90003.iii62.

(161) Mitchell, P. G.; Magna, H. A.; Reeves, L. M.; Lopresti-Morrow, L. L.; Yocum, S. A.; Rosner, P. J.; Geoghegan, K. F.; Hambor, J. E. Cloning, Expression, and Type II Collagenolytic Activity of Matrix Metalloproteinase-13 from Human Osteoarthritic Cartilage. *J. Clin. Invest.* **1996**, *97* (3), 761–768. https://doi.org/10.1172/JCI118475.

(162) Hu, Q.; Ecker, M. Overview of MMP-13 as a Promising Target for the Treatment of Osteoarthritis. *Int. J. Mol. Sci.* **2021**, *22* (4), 1742. https://doi.org/10.3390/ijms22041742.

(163) Davidson, R. K.; Waters, J. G.; Kevorkian, L.; Darrah, C.; Cooper, A.; Donell, S. T.; Clark, I. M. Expression Profiling of Metalloproteinases and Their Inhibitors in Synovium and Cartilage. *Arthritis Res. Ther.* **2006**, *8* (4), R124. https://doi.org/10.1186/ar2013.

(164) Borden, P.; Solymar, D.; Sucharczuk, A.; Lindman, B.; Cannon, P.; Heller, R. A. Cytokine Control of Interstitial Collagenase and Collagenase-3 Gene Expression in Human Chondrocytes. *J. Biol. Chem.* **1996**, *271* (38), 23577–23581. https://doi.org/10.1074/jbc.271.38.23577.

(165) Shlopov, B. V.; Lie, W. R.; Mainardi, C. L.; Cole, A. A.; Chubinskaya, S.; Hasty, K. A. Osteoarthritic Lesions: Involvement of Three Different Collagenases. *Arthritis Rheum.* **1997**, *40* (11), 2065–2074. https://doi.org/10.1002/art.1780401120.

(166) Chen, J. M.; Nelson, F. C.; Levin, J. I.; Mobilio, D.; Moy, F. J.; Nilakantan, R.; Zask, A.; Powers, R. Structure-Based Design of a Novel, Potent, and Selective Inhibitor for MMP-13 Utilizing NMR Spectroscopy and Computer-Aided Molecular Design. *J. Am. Chem. Soc.* **2000**, *122* (40), 9648–9654. https://doi.org/10.1021/ja001547g.

(167) Wu, J.; Rush, T. S.; Hotchandani, R.; Du, X.; Geck, M.; Collins, E.; Xu, Z.-B.; Skotnicki, J.; Levin, J. I.; Lovering, F. E. Identification of Potent and Selective MMP-13 Inhibitors. *Bioorg. Med. Chem. Lett.* **2005**, *15* (18), 4105–4109. https://doi.org/10.1016/j.bmcl.2005.06.019.

(168) Reiter, L. A.; Freeman-Cook, K. D.; Jones, C. S.; Martinelli, G. J.; Antipas, A. S.; Berliner, M. A.; Datta, K.; Downs, J. T.; Eskra, J. D.; Forman, M. D.; Greer, E. M.; Guzman, R.; Hardink, J. R.; Janat, F.; Keene, N. F.; Laird, E. R.; Liras, J. L.; Lopresti-Morrow, L. L.; Mitchell, P. G.; Pandit, J.; Robertson, D.; Sperger, D.; Vaughn-Bowser, M. L.; Waller, D. M.; Yocum, S. A. Potent, Selective Pyrimidinetrione-Based Inhibitors of MMP-13. *Bioorg. Med. Chem. Lett.* **2006**, *16* (22), 5822–5826. https://doi.org/10.1016/j.bmcl.2006.08.066.

(169) Engel, C. K.; Pirard, B.; Schimanski, S.; Kirsch, R.; Habermann, J.; Klingler, O.; Schlotte, V.; Weithmann, K. U.; Wendt, K. U. Structural Basis for the Highly Selective Inhibition of MMP-13. *Chem. Biol.* **2005**, *12* (2), 181–189. https://doi.org/10.1016/j.chembiol.2004.11.014.

(170) Baragi, V. M.; Becher, G.; Bendele, A. M.; Biesinger, R.; Bluhm, H.; Boer, J.; Deng, H.; Dodd, R.; Essers, M.; Feuerstein, T.; Gallagher, B. M.; Gege, C.; Hochgürtel, M.; Hofmann, M.; Jaworski, A.; Jin, L.; Kiely, A.; Korniski, B.; Kroth, H.; Nix, D.; Nolte, B.; Piecha, D.; Powers, T. S.; Richter, F.; Schneider, M.; Steeneck, C.; Sucholeiki, I.; Taveras, A.; Timmermann, A.; Van Veldhuizen, J.; Weik, J.; Wu, X.; Xia, B. A New Class of Potent Matrix Metalloproteinase 13 Inhibitors for Potential Treatment of Osteoarthritis: Evidence of Histologic and Clinical Efficacy without Musculoskeletal Toxicity in Rat Models. *Arthritis Rheum.* **2009**, *60* (7), 2008–2018. https://doi.org/10.1002/art.24629.

(171) Gege, C.; Bao, B.; Bluhm, H.; Boer, J.; Brian M. Gallagher, J.; Korniski, B.; Powers, T. S.; Steeneck, C.; Taveras, A. G.; Baragi, V. M. *Discovery and Evaluation of a Non-Zn Chelating, Selective Matrix Metalloproteinase 13 (MMP-13) Inhibitor for Potential Intra-articular Treatment of Osteoarthritis*. *J Med Chem*. **2012,** 55 (2), 709-716. https://doi.org/10.1021/jm201152u.

(172) Ruminski, P. G.; Massa, M.; Strohbach, J.; Hanau, C. E.; Schmidt, M.; Scholten, J. A.; Fletcher, T. R.; Hamper, B. C.; Carroll, J. N.; Shieh, H. S.; Caspers, N.; Collins, B.; Grapperhaus, M.; Palmquist, K. E.; Collins, J.; Baldus, J. E.; Hitchcock, J.; Kleine, H. P.; Rogers, M. D.; McDonald, J.; Munie, G. E.; Messing, D. M.; Portolan, S.; Whiteley, L. O.; Sunyer, T.; Schnute, M. E. Discovery of N-(4-Fluoro-3-Methoxybenzyl)-6-(2-(((2S,5R)-5-(Hydroxymethyl)-1,4-Dioxan-2-Yl)Methyl)-2H-Tetrazol-5-Yl)-2-Methylpyrimidine-4-Carboxamide. A Highly Selective and Orally Bioavailable Matrix Metalloproteinase-13 Inhibitor for the Potential Treatment of Osteoarthritis. *J. Med. Chem.* **2016**, *59* (1), 313–327. https://doi.org/10.1021/acs.jmedchem.5b01434.

(173) Quillard, T.; Tesmenitsky, Y.; Croce, K.; Travers, R.; Shvartz, E.; Koskinas, K. C.; Sukhova, G. K.; Aikawa, E.; Aikawa, M.; Libby, P. Selective Inhibition of Matrix Metalloproteinase-13 Increases Collagen Content of Established Mouse Atherosclerosis. *Arterioscler. Thromb. Vasc. Biol.* **2011**, *31* (11), 2464–2472. https://doi.org/10.1161/ATVBAHA.111.231563.

(174) Piecha, D.; Weik, J.; Kheil, H.; Becher, G.; Timmermann, A.; Jaworski, A.; Burger, M.; Hofmann, M. W. Novel Selective MMP-13 Inhibitors Reduce Collagen Degradation in Bovine Articular and Human Osteoarthritis Cartilage Explants. *Inflamm. Res.* **2010**, *59* (5), 379–389. https://doi.org/10.1007/s00011-009-0112-9.

(175) Li, J. J.; Nahra, J.; Johnson, A. R.; Bunker, A.; O'Brien, P.; Yue, W.-S.; Ortwine, D. F.; Man, C.-F.; Baragi, V.; Kilgore, K.; Dyer, R. D.; Han, H.-K. Quinazolinones and Pyrido[3,4-d]Pyrimidin-4-Ones as Orally Active and Specific Matrix Metalloproteinase-13 Inhibitors for the Treatment of Osteoarthritis. *J. Med. Chem.* **2008**, *51* (4), 835–841. https://doi.org/10.1021/jm701274v.

(176) Nara, H.; Sato, K.; Naito, T.; Mototani, H.; Oki, H.; Yamamoto, Y.; Kuno, H.; Santou, T.; Kanzaki, N.; Terauchi, J.; Uchikawa, O.; Kori, M. Thieno[2,3-d]Pyrimidine-2-Carboxamides Bearing a Carboxybenzene Group at 5-Position: Highly Potent, Selective, and Orally Available MMP-13 Inhibitors Interacting with the S1″ Binding Site. *Bioorg. Med. Chem.* **2014**, *22* (19), 5487–5505. https://doi.org/10.1016/j.bmc.2014.07.025.

(177) Nara, H.; Sato, K.; Naito, T.; Mototani, H.; Oki, H.; Yamamoto, Y.; Kuno, H.; Santou, T.; Kanzaki, N.; Terauchi, J.; Uchikawa, O.; Kori, M. Discovery of Novel, Highly Potent, and Selective Quinazoline-2-Carboxamide-Based Matrix Metalloproteinase (MMP)-13 Inhibitors without a Zinc Binding Group Using a Structure-Based Design Approach. *J. Med. Chem.* **2014**, *57* (21), 8886–8902. https://doi.org/10.1021/jm500981k.

(178) Laleu, B.; Akao, Y.; Ochida, A.; Duffy, S.; Lucantoni, L.; Shackleford, D. M.; Chen, G.; Katneni, K.; Chiu, F. C. K.; White, K. L.; Chen, X.; Sturm, A.; Dechering, K. J.; Crespo, B.; Sanz, L. M.; Wang, B.; Wittlin, S.; Charman, S. A.; Avery, V. M.; Cho, N.; Kamaura, M. Discovery and Structure–Activity Relationships of Quinazolinone-2-Carboxamide Derivatives as Novel Orally Efficacious Antimalarials. *J. Med. Chem.* **2021**, *64* (17), 12582–12602. https://doi.org/10.1021/acs.jmedchem.1c00441.

(179) Cai, H.; Agrawal, A. K.; Putt, D. A.; Hashim, M.; Reddy, A.; Brodfuehrer, J.; Surendran, N.; Lash, L. H. Assessment of the Renal Toxicity of Novel Anti-Inflammatory

Compounds Using Cynomolgus Monkey and Human Kidney Cells. *Toxicology* **2009**, *258* (1), 56–63. https://doi.org/10.1016/j.tox.2009.01.006.

(180) Settle, S.; Vickery, L.; Nemirovskiy, O.; Vidmar, T.; Bendele, A.; Messing, D.; Ruminski, P.; Schnute, M.; Sunyer, T. Cartilage Degradation Biomarkers Predict Efficacy of a Novel, Highly Selective Matrix Metalloproteinase 13 Inhibitor in a Dog Model of Osteoarthritis: Confirmation by Multivariate Analysis That Modulation of Type II Collagen and Aggrecan Degradation Peptides Parallels Pathologic Changes. *Arthritis Rheum.* **2010**, *62* (10), 3006–3015. https://doi.org/10.1002/art.27596.

(181) Fuerst, R.; Choi, J. Y.; Knapinska, A. M.; Cameron, M. D.; Ruiz, C.; Delmas, A.; Sundrud, M. S.; Fields, G. B.; Roush, W. R. Development of a Putative Zn^{2+}-Chelating but Highly Selective MMP-13 Inhibitor. *Bioorg. Med. Chem. Lett.* **2022**, *76*, 129014. https://doi.org/10.1016/j.bmcl.2022.129014.

(182) Huang, S.; Feng, K.; Ren, Y. Molecular Modelling Studies of Quinazolinone Derivatives as MMP-13 Inhibitors by QSAR, Molecular Docking and Molecular Dynamics Simulations Techniques. *MedChemComm* **2019**, *10* (1), 101–115. https://doi.org/10.1039/C8MD00375K.

(183) Choi, J. Y.; Fuerst, R.; Knapinska, A. M.; Taylor, A. B.; Smith, L.; Cao, X.; Hart, P. J.; Fields, G. B.; Roush, W. R. Structure-Based Design and Synthesis of Potent and Selective Matrix Metalloproteinase 13 Inhibitors. *J. Med. Chem.* **2017**, *60* (13), 5816–5825. https://doi.org/10.1021/acs.jmedchem.7b00514.

(184) Fuerst, R.; Yong Choi, J.; Knapinska, A. M.; Smith, L.; Cameron, M. D.; Ruiz, C.; Fields, G. B.; Roush, W. R. Development of Matrix Metalloproteinase-13 Inhibitors – A

Structure-Activity/Structure-Property Relationship Study. *Bioorg. Med. Chem.* **2018**, *26* (18), 4984–4995. https://doi.org/10.1016/j.bmc.2018.08.020.

(185) Knapinska, A. M.; Singh, C.; Drotleff, G.; Blanco, D.; Chai, C.; Schwab, J.; Herd, A.; Fields, G. B. Matrix Metalloproteinase 13 Inhibitors for Modulation of Osteoclastogenesis: Enhancement of Solubility and Stability. *ChemMedChem* **2021**, *16* (7), 1133–1142. https://doi.org/10.1002/cmdc.202000911.

(186) Nara, H.; Kaieda, A.; Sato, K.; Naito, T.; Mototani, H.; Oki, H.; Yamamoto, Y.; Kuno, H.; Santou, T.; Kanzaki, N.; Terauchi, J.; Uchikawa, O.; Kori, M. *Discovery of Novel, Highly Potent, and Selective Matrix Metalloproteinase (MMP)-13 Inhibitors with a 1,2,4-Triazol-3-yl Moiety as a Zinc Binding Group Using a Structure-Based Design Approach*. ACS Publications. https://doi.org/10.1021/acs.jmedchem.6b01007.

(187) Nara, H.; Sato, K.; Kaieda, A.; Oki, H.; Kuno, H.; Santou, T.; Kanzaki, N.; Terauchi, J.; Uchikawa, O.; Kori, M. Design, Synthesis, and Biological Activity of Novel, Potent, and Highly Selective Fused Pyrimidine-2-Carboxamide-4-One-Based Matrix Metalloproteinase (MMP)-13 Zinc-Binding Inhibitors. *Bioorg. Med. Chem.* **2016**, *24* (23), 6149–6165. https://doi.org/10.1016/j.bmc.2016.09.009.

(188) Rangasamy, L.; Di Geronimo, B.; Ortín, I.; Coderch, C.; Zapico, J. M.; Ramos, A.; de Pascual-Teresa, B. Molecular Imaging Probes Based on Matrix Metalloproteinase Inhibitors (MMPIs). *Molecules* **2019**, *24* (16), 2982. https://doi.org/10.3390/molecules24162982.

(189) Zheng, Q. H.; Fei, X.; Liu, X.; Wang, J. Q.; Bin Sun, H.; Mock, B. H.; Lee Stone, K.; Martinez, T. D.; Miller, K. D.; Sledge, G. W.; Hutchins, G. D. Synthesis and Preliminary Biological Evaluation of MMP Inhibitor Radiotracers [11C]Methyl-Halo-CGS 27023A

Analogs, New Potential PET Breast Cancer Imaging Agents. *Nucl. Med. Biol.* **2002**, *29* (7), 761–770. https://doi.org/10.1016/S0969-8051(02)00338-4.

(190) Fei, X.; Zheng, Q.-H.; Hutchins, G. D.; Liu, X.; Stone, K. L.; Carlson, K. A.; Mock, B. H.; Winkle, W. L.; Glick-Wilson, B. E.; Miller, K. D.; Fife, R. S.; Sledge, G. W.; Sun, H. B.; Carr, R. E. Synthesis of MMP Inhibitor Radiotracers [11C]Methyl-CGS 27023A and Its Analogs, New Potential PET Breast Cancer Imaging Agents. *J. Label. Compd. Radiopharm.* **2002**, *45* (6), 449–470. https://doi.org/10.1002/jlcr.570.

(191) Fei, X.; Zheng, Q.-H.; Liu, X.; Wang, J.-Q.; Stone, K. L.; Miller, K. D.; Sledge, G. W.; Hutchins, G. D. Synthesis of MMP Inhibitor Radiotracer [11C]CGS 25966, a New Potential Pet Tumor Imaging Agent. *J. Label. Compd. Radiopharm.* **2003**, *46* (4), 343–351. https://doi.org/10.1002/jlcr.675.

(192) Zheng, Q.-H.; Fei, X.; Liu, X.; Wang, J.-Q.; Lee Stone, K.; Martinez, T. D.; Gay, D. J.; Baity, W. L.; Miller, K. D.; Sledge, G. W.; Hutchins, G. D. Comparative Studies of Potential Cancer Biomarkers Carbon-11 Labeled MMP Inhibitors (S)-2-(4′-[11C]Methoxybiphenyl-4-Sulfonylamino)-3-Methylbutyric Acid and N-Hydroxy-(R)-2-[[(4′-[11C]Methoxyphenyl)Sulfonyl]Benzylamino]-3-Methylbutanamide. *Nucl. Med. Biol.* **2004**, *31* (1), 77–85. https://doi.org/10.1016/S0969-8051(03)00111-2.

(193) Furumoto, S.; Iwata, R.; Ido, T. Design and Synthesis of Fluorine-18 Labeled Matrix Metalloproteinase Inhibitors for Cancer Imaging. *J. Label. Compd. Radiopharm.* **2002**, *45* (11), 975–986. https://doi.org/10.1002/jlcr.616.

(194) Furumoto, S.; Takashima, K.; Kubota, K.; Ido, T.; Iwata, R.; Fukuda, H. Tumor Detection Using 18F-Labeled Matrix Metalloproteinase-2 Inhibitor. *Nucl. Med. Biol.* **2003**, *30* (2), 119–125. https://doi.org/10.1016/s0969-8051(02)00393-1.

(195) Kopka, K.; Breyholz, H.-J.; Wagner, S.; Law, M. P.; Riemann, B.; Schröer, S.; Trub, M.; Guilbert, B.; Levkau, B.; Schober, O.; Schäfers, M. Synthesis and Preliminary Biological Evaluation of New Radioiodinated MMP Inhibitors for Imaging MMP Activity *in Vivo*. *Nucl. Med. Biol.* **2004**, *31* (2), 257–267. https://doi.org/10.1016/j.nucmedbio.2003.08.003.

(196) Wagner, S.; Breyholz, H.-J.; Law, M. P.; Faust, A.; Höltke, C.; Schröer, S.; Haufe, G.; Levkau, B.; Schober, O.; Schäfers, M.; Kopka, K. Novel Fluorinated Derivatives of the Broad-Spectrum MMP Inhibitors *N* -Hydroxy-2(*R*)-[[(4-Methoxyphenyl)Sulfonyl](Benzyl)- and (3-Picolyl)-Amino]-3-Methyl-Butanamide as Potential Tools for the Molecular Imaging of Activated MMPs with PET. *J. Med. Chem.* **2007**, *50* (23), 5752–5764. https://doi.org/10.1021/jm0708533.

(197) Breyholz, H. J.; Wagner, S.; Levkau, B.; Schober, O.; Schäfers, M.; Kopka, K. A 18F-Radiolabeled Analogue of CGS 27023A as a Potential Agent for Assessment of Matrix-Metalloproteinase Activity in Vivo. *Q. J. Nucl. Med. Mol. Imaging Off. Publ. Ital. Assoc. Nucl. Med. AIMN Int. Assoc. Radiopharmacol. IAR Sect. Soc. Of* **2007**, *51* (1), 24–32.

(198) Wagner, S.; Breyholz, H.-J.; Höltke, C.; Faust, A.; Schober, O.; Schäfers, M.; Kopka, K. A New 18F-Labelled Derivative of the MMP Inhibitor CGS 27023A for PET: Radiosynthesis and Initial Small-Animal PET Studies. *Appl. Radiat. Isot. Data Instrum. Methods Use Agric. Ind. Med.* **2009**, *67* (4), 606–610. https://doi.org/10.1016/j.apradiso.2008.12.009.

(199) Hugenberg, V.; Breyholz, H.-J.; Riemann, B.; Hermann, S.; Schober, O.; Schäfers, M.; Gangadharmath, U.; Mocharla, V.; Kolb, H.; Walsh, J.; Zhang, W.; Kopka, K.; Wagner, S. A New Class of Highly Potent Matrix Metalloproteinase Inhibitors Based on Triazole-

Substituted Hydroxamates: (Radio)Synthesis and in Vitro and First in Vivo Evaluation. *J. Med. Chem.* **2012**, *55* (10), 4714–4727. https://doi.org/10.1021/jm300199g.

(200) Hugenberg, V.; Riemann, B.; Hermann, S.; Schober, O.; Schäfers, M.; Szardenings, K.; Lebedev, A.; Gangadharmath, U.; Kolb, H.; Walsh, J.; Zhang, W.; Kopka, K.; Wagner, S. Inverse 1,2,3-Triazole-1-Yl-Ethyl Substituted Hydroxamates as Highly Potent Matrix Metalloproteinase Inhibitors: (Radio)Synthesis, in Vitro and First in Vivo Evaluation. *J. Med. Chem.* **2013**, *56* (17), 6858–6870. https://doi.org/10.1021/jm4006753.

(201) Schäfers, M.; Riemann, B.; Kopka, K.; Breyholz, H.-J.; Wagner, S.; Schäfers, K. P.; Law, M. P.; Schober, O.; Levkau, B. Scintigraphic Imaging of Matrix Metalloproteinase Activity in the Arterial Wall in Vivo. *Circulation* **2004**, *109* (21), 2554–2559. https://doi.org/10.1161/01.CIR.0000129088.49276.83.

(202) Zinnhardt, B.; Pigeon, H.; Thézé, B.; Viel, T.; Wachsmuth, L.; Fricke, I. B.; Schelhaas, S.; Honold, L.; Schwegmann, K.; Wagner, S.; Faust, A.; Faber, C.; Kuhlmann, M. T.; Hermann, S.; Schäfers, M.; Winkeler, A.; Jacobs, A. H. Combined PET Imaging of the Inflammatory Tumor Microenvironment Identifies Margins of Unique Radiotracer Uptake. *Cancer Res.* **2017**, *77* (8), 1831–1841. https://doi.org/10.1158/0008-5472.CAN-16-2628.

(203) Vazquez, N.; Missault, S.; Vangestel, C.; Deleye, S.; Thomae, D.; Veken, P. V. der; Augustyns, K.; Staelens, S.; Dedeurwaerdere, S.; Wyffels, L. Evaluation of [18F]BR420 and [18F]BR351 as Radiotracers for MMP-9 Imaging in Colorectal Cancer. *J. Label. Compd. Radiopharm.* **2017**, *60* (1), 69–79. https://doi.org/10.1002/jlcr.3476.

(204) Zinnhardt, B.; Viel, T.; Wachsmuth, L.; Vrachimis, A.; Wagner, S.; Breyholz, H.-J.; Faust, A.; Hermann, S.; Kopka, K.; Faber, C.; Dollé, F.; Pappata, S.; Planas, A. M.; Tavitian, B.;

Schäfers, M.; Sorokin, L. M.; Kuhlmann, M. T.; Jacobs, A. H. Multimodal Imaging Reveals Temporal and Spatial Microglia and Matrix Metalloproteinase Activity after Experimental Stroke. *J. Cereb. Blood Flow Metab.* **2015**, *35* (11), 1711–1721. https://doi.org/10.1038/jcbfm.2015.149.

(205) Yang, Y.; Rosenberg, G. A. Matrix Metalloproteinases as Therapeutic Targets for Stroke. *Brain Res.* **2015**, *1623*, 30–38. https://doi.org/10.1016/j.brainres.2015.04.024.

(206) Xue, C.-B.; He, X.; Roderick, J.; DeGrado, W. F.; Cherney, R. J.; Hardman, K. D.; Nelson, D. J.; Copeland, R. A.; Jaffee, B. D.; Decicco, C. P. Design and Synthesis of Cyclic Inhibitors of Matrix Metalloproteinases and TNF-α Production. *J. Med. Chem.* **1998**, *41* (11), 1745–1748. https://doi.org/10.1021/jm970849z.

(207) Su, H.; Spinale, F. G.; Dobrucki, L. W.; Song, J.; Hua, J.; Sweterlitsch, S.; Dione, D. P.; Cavaliere, P.; Chow, C.; Bourke, B. N.; Hu, X.-Y.; Azure, M.; Yalamanchili, P.; Liu, R.; Cheesman, E. H.; Robinson, S.; Edwards, D. S.; Sinusas, A. J. Noninvasive Targeted Imaging of Matrix Metalloproteinase Activation in a Murine Model of Postinfarction Remodeling. *Circulation* **2005**, *112* (20), 3157–3167. https://doi.org/10.1161/CIRCULATIONAHA.105.583021.

(208) Zhang, J.; Nie, L.; Razavian, M.; Ahmed, M.; Dobrucki, L. W.; Asadi, A.; Edwards, D. S.; Azure, M.; Sinusas, A. J.; Sadeghi, M. M. Molecular Imaging of Activated Matrix Metalloproteinases in Vascular Remodeling. *Circulation* **2008**, *118* (19), 1953–1960. https://doi.org/10.1161/CIRCULATIONAHA.108.789743.

(209) Jung, J.-J.; Razavian, M.; Challa, A. A.; Nie, L.; Golestani, R.; Zhang, J.; Ye, Y.; Russell, K. S.; Robinson, S. P.; Heistad, D. D.; Sadeghi, M. M. Multimodality and Molecular

Imaging of Matrix Metalloproteinase Activation in Calcific Aortic Valve Disease. *J. Nucl. Med.* **2015**, *56* (6), 933–938. https://doi.org/10.2967/jnumed.114.152355.

(210) Razavian, M.; Tavakoli, S.; Zhang, J.; Nie, L.; Dobrucki, L. W.; Sinusas, A. J.; Azure, M.; Robinson, S.; Sadeghi, M. M. Atherosclerosis Plaque Heterogeneity and Response to Therapy Detected by in Vivo Molecular Imaging of Matrix Metalloproteinase Activation. *J. Nucl. Med. Off. Publ. Soc. Nucl. Med.* **2011**, *52* (11), 1795–1802. https://doi.org/10.2967/jnumed.111.092379.

(211) Fujimoto, S.; Hartung, D.; Ohshima, S.; Edwards, D. S.; Zhou, J.; Yalamanchili, P.; Azure, M.; Fujimoto, A.; Isobe, S.; Matsumoto, Y.; Boersma, H.; Wong, N.; Yamazaki, J.; Narula, N.; Petrov, A.; Narula, J. Molecular Imaging of Matrix Metalloproteinase in Atherosclerotic Lesions: Resolution With Dietary Modification and Statin Therapy. *J. Am. Coll. Cardiol.* **2008**, *52* (23), 1847–1857. https://doi.org/10.1016/j.jacc.2008.08.048.

(212) Razavian, M.; Zhang, J.; Nie, L.; Tavakoli, S.; Razavian, N.; Dobrucki, L. W.; Sinusas, A. J.; Edwards, D. S.; Azure, M.; Sadeghi, M. M. Molecular Imaging of Matrix Metalloproteinase Activation to Predict Murine Aneurysm Expansion In Vivo. *J. Nucl. Med.* **2010**, *51* (7), 1107–1115. https://doi.org/10.2967/jnumed.110.075259.

(213) Golestani, R.; Razavian, M.; Nie, L.; Zhang, J.; Jung, J.-J.; Ye, Y.; de Roo, M.; Hilgerink, K.; Liu, C.; Robinson, S. P.; Sadeghi, M. M. Imaging Vessel Wall Biology to Predict Outcome in Abdominal Aortic Aneurysm. *Circ. Cardiovasc. Imaging* **2015**, *8* (1), 10.1161/CIRCIMAGING.114.002471 e002471. https://doi.org/10.1161/CIRCIMAGING.114.002471.

(214) Ye, Y.; Toczek, J.; Gona, K.; Kim, H.-Y.; Han, J.; Razavian, M.; Golestani, R.; Zhang, J.; Wu, T. L.; Ghosh, M.; Jung, J.-J.; Sadeghi, M. M. Novel Arginine-Containing

Macrocyclic MMP Inhibitors: Synthesis, 99mTc-Labeling, and Evaluation. *Sci. Rep.* **2018**, *8*, 11647. https://doi.org/10.1038/s41598-018-29941-2.

(215) Toczek, J.; Ye, Y.; Gona, K.; Kim, H.-Y.; Han, J.; Razavian, M.; Golestani, R.; Zhang, J.; Wu, T. L.; Jung, J.-J.; Sadeghi, M. M. Preclinical Evaluation of RYM1, a Matrix Metalloproteinase-Targeted Tracer for Imaging Aneurysm. *J. Nucl. Med. Off. Publ. Soc. Nucl. Med.* **2017**, *58* (8), 1318–1323. https://doi.org/10.2967/jnumed.116.188656.

(216) Ward, M. R.; Pasterkamp, G.; Yeung, A. C.; Borst, C. Arterial Remodeling. *Circulation* **2000**, *102* (10), 1186–1191. https://doi.org/10.1161/01.CIR.102.10.1186.

(217) Curci, J. A.; Liao, S.; Huffman, M. D.; Shapiro, S. D.; Thompson, R. W. Expression and Localization of Macrophage Elastase (Matrix Metalloproteinase-12) in Abdominal Aortic Aneurysms. *J. Clin. Invest.* **1998**, *102* (11), 1900–1910. https://doi.org/10.1172/JCI2182.

(218) Toczek, J.; Gona, K.; Liu, Y.; Ahmad, A.; Ghim, M.; Ojha, D.; Kukreja, G.; Salarian, M.; Luehmann, H.; Heo, G. S.; Guzman, R. J.; Ochoa Chaar, C. I.; Tellides, G.; Hassab, A. H. M.; Ye, Y.; Shoghi, K. I.; Zayed, M. A.; Gropler, R. J.; Sadeghi, M. M. Positron Emission Tomography Imaging of Vessel Wall Matrix Metalloproteinase Activity in Abdominal Aortic Aneurysm. *Circ. Cardiovasc. Imaging* **2023**, *16* (1), e014615. https://doi.org/10.1161/CIRCIMAGING.122.014615.

(219) Schäfers, M.; Schober, O.; Hermann, S. Matrix-Metalloproteinases as Imaging Targets for Inflammatory Activity in Atherosclerotic Plaques. *J. Nucl. Med.* **2010**, *51* (5), 663–666. https://doi.org/10.2967/jnumed.109.065698.

(220) Kuzuya, M.; Nakamura, K.; Sasaki, T.; Wu Cheng, X.; Itohara, S.; Iguchi, A. Effect of MMP-2 Deficiency on Atherosclerotic Lesion Formation in ApoE-Deficient Mice.

Arterioscler. Thromb. Vasc. Biol. **2006**, *26* (5), 1120–1125. https://doi.org/10.1161/01.ATV.0000218496.60097.e0.

(221) Johnson, J. L.; George, S. J.; Newby, A. C.; Jackson, C. L. Divergent Effects of Matrix Metalloproteinases 3, 7, 9, and 12 on Atherosclerotic Plaque Stability in Mouse Brachiocephalic Arteries. *Proc. Natl. Acad. Sci. U. S. A.* **2005**, *102* (43), 15575–15580. https://doi.org/10.1073/pnas.0506201102.

(222) Lessner, S. M.; Martinson, D. E.; Galis, Z. S. Compensatory Vascular Remodeling during Atherosclerotic Lesion Growth Depends on Matrix Metalloproteinase-9 Activity. *Arterioscler. Thromb. Vasc. Biol.* **2004**, *24* (11), 2123–2129. https://doi.org/10.1161/01.ATV.0000141840.27300.fd.

(223) Fields, G. B. Interstitial Collagen Catabolism. *J. Biol. Chem.* **2013**, *288* (13), 8785–8793. https://doi.org/10.1074/jbc.R113.451211.

(224) Sukhova, G. K.; Schönbeck, U.; Rabkin, E.; Schoen, F. J.; Poole, A. R.; Billinghurst, R. C.; Libby, P. Evidence for Increased Collagenolysis by Interstitial Collagenases-1 and -3 in Vulnerable Human Atheromatous Plaques. *Circulation* **1999**, *99* (19), 2503–2509. https://doi.org/10.1161/01.CIR.99.19.2503.

(225) Deguchi, J.-O.; Aikawa, E.; Libby, P.; Vachon, J. R.; Inada, M.; Krane, S. M.; Whittaker, P.; Aikawa, M. Matrix Metalloproteinase-13/Collagenase-3 Deletion Promotes Collagen Accumulation and Organization in Mouse Atherosclerotic Plaques. *Circulation* **2005**, *112* (17), 2708–2715. https://doi.org/10.1161/CIRCULATIONAHA.105.562041.

(226) Quillard, T.; Araújo, H. A.; Franck, G.; Tesmenitsky, Y.; Libby, P. Matrix Metalloproteinase-13 Predominates Over Matrix Metalloproteinase-8 as the Functional

Interstitial Collagenase in Mouse Atheromata. *Arterioscler. Thromb. Vasc. Biol.* **2014**, *34* (6), 1179–1186. https://doi.org/10.1161/ATVBAHA.114.303326.

(227) Kalinin, D. V.; Wagner, S.; Riemann, B.; Hermann, S.; Schmidt, F.; Becker-Pauly, C.; Rose-John, S.; Schäfers, M.; Holl, R. Novel Potent Proline-Based Metalloproteinase Inhibitors: Design, (Radio)Synthesis, and First in Vivo Evaluation as Radiotracers for Positron Emission Tomography. *J. Med. Chem.* **2016**, *59* (20), 9541–9559. https://doi.org/10.1021/acs.jmedchem.6b01291.

(228) Hugenberg, V.; Wagner, S.; Kopka, K.; Schäfers, M.; Schuit, R. C.; Windhorst, A. D.; Hermann, S. Radiolabeled Selective Matrix Metalloproteinase 13 (MMP-13) Inhibitors: (Radio)Syntheses and in Vitro and First in Vivo Evaluation. *J. Med. Chem.* **2017**, *60* (1), 307–321. https://doi.org/10.1021/acs.jmedchem.6b01284.

2.0 Chapter II - Selective Imaging of Matrix Metalloproteinase-13 to Detect Extracellular Matrix Remodeling in Atherosclerotic Lesions

Ariel Buchler[1,3], Maxime Munch[2,3], Gedaliah Farber[2,3], Xiaoling Zhao[3], Rami Al-Haddad[2,3]

Eadan Farber[3], and Benjamin H. Rotstein[1,2,3]

(1) Department of Chemistry and Biomolecular Sciences, University of Ottawa, Ottawa, Ontario, Canada, K1N 6N5

(2) Department of Biochemistry, Microbiology and Immunology, University of Ottawa, Ottawa, Ontario, Canada, K1H 8M5

(3) University of Ottawa Heart Institute, Ottawa, Ontario, Canada, K1Y 4W7

Corresponding author:

Benjamin Rotstein, PhD

40 Ruskin St, H-5219, Ottawa, ON, K1Y 4W7

613-696-7324

benjamin.rotstein@uottawa.ca

Citation: Buchler A, Munch M, Farber G, Zhao X, Al-Haddad R, Farber E, BH Rotstein. "Selective Imaging of Matrix Metalloproteinase-13 to Detect Extracellular Matrix Remodeling in Atherosclerotic Lesions." *Mol Imaging Biol*. **2022**;24(1):93-103. doi: 10.1007/s11307-021-01626-9.

2.1 Context

We initially employed [^{18}F]FMBP, as a previously developed and characterized fluorine-18 labeled MMP-13 selective PET radiotracer based on the pyrimidine-dicarboxamide inhibitor scaffold. As it had only been evaluated in healthy mice, we sought to validate the feasibility of using [^{18}F]FMBP for the detection of ECM remodeling in atherosclerotic plaques. To provide a comparison to current broad spectrum MMP imaging agents, we also employed [^{18}F]BR-351, as a fluorine-18 labeled MMP-targeted PET radiotracer based on the non-peptidic aryl sulfonamide inhibitor scaffold. *In vivo* evaluations in atherosclerotic mice served to demonstrate the potential advantages of MMP-13 selective imaging by determining radiotracer pharmacokinetics, specificity, and sensitivity.

2.2 Statement of the Manuscript

The manuscript entitled "Selective Imaging of Matrix Metalloproteinase-13 to Detect Extracellular Matrix Remodeling in Atherosclerotic Lesions" was published in the *Journal of Molecular Imaging and Biology* on February 24, 2022. In this chapter, I developed an automated radiosynthesis of [^{18}F]FMBP and assisted Dr. Maxime Munch with an automated radiosynthesis of [^{18}F]BR-351. I conducted the *in vitro* autoradiography with assistance from Dr. Maxime Munch. I led the animal studies with assistance from all other authors. Tissue sectioning was conducted by Xiaoling Zhao. I performed the histology with assistance from Xiaoling Zhao. I performed all data analysis and interpreted the data with guidance from Dr. Benjamin Rotstein. I wrote the manuscript with editing from Dr. Benjamin Rostein. All authors approved the final version.

2.3 Abstract

Purpose: Overexpression and activation of matrix metalloproteinase-13 (MMP-13) within atheroma increases susceptibility to plaque rupture, a major cause of severe cardiovascular complications. In comparison to pan-MMP targeting [^{18}F]BR-351, we evaluated the potential for [^{18}F]FMBP, a selective PET radiotracer for MMP-13, to detect extracellular matrix (ECM) remodeling in vascular plaques possessing markers of inflammation.

Procedures: [^{18}F]FMBP and [^{18}F]BR-351 were initially assessed *in vitro* by incubation with *en face* aortae from 8 month-old atherogenic *ApoE*$^{-/-}$ mice. *Ex vivo* biodistributions, plasma metabolite analyses, and *ex vivo* autoradiography were analogously performed 30 minutes after intravenous radiotracer administration in age-matched C57Bl/6 and *ApoE*$^{-/-}$ mice under baseline or homologous blocking conditions. *En face* aortae were subsequently stained with Oil Red O (ORO), sectioned, and subject to immunofluorescence staining for Mac-2 and MMP-13.

Results: High-resolution autoradiographic image analysis demonstrated target specificity and regional concordance to lipid-rich lesions. Biodistribution studies revealed hepatobiliary excretion, low accumulation of radioactivity in non-excretory organs, and few differences between strains and conditions in non-target organs. Plasma metabolite analyses uncovered that [^{18}F]FMBP exhibited excellent *in vivo* stability (≥74% intact) while [^{18}F]BR-351 was extensively metabolized (≤37% intact). *Ex vivo* autoradiography and histology of *en face* aortae revealed that [^{18}F]FMBP, relative to [^{18}F]BR-351, exhibited 2.9-fold greater lesion uptake, substantial specific binding (68%), and improved sensitivity to atherosclerotic tissue (2.9-fold vs 2.1-fold). Immunofluorescent staining of aortic *en face* cross-sections demonstrated elevated Mac-2 and MMP-13 positive areas within atherosclerotic lesions identified by [^{18}F]FMBP *ex vivo* autoradiography.

Conclusions: While both radiotracers successfully identified atherosclerotic plaques, [^{18}F]FMBP showed superior specificity and sensitivity for lesions possessing features of destructive plaque remodeling. The detection of ECM remodeling by selective targeting of MMP-13 may enable characterization of high-risk atherosclerosis featuring elevated collagenase activity.

Keywords: matrix metalloproteinases, atherosclerosis, vulnerable plaques, remodeling, inflammation, autoradiography, positron emission tomography, radiotracer

2.4 Introduction

The extracellular matrix (ECM) is a highly dynamic network responsible for maintaining tissue integrity and modulating cellular functions related to proliferation, adhesion and migration.[1] Matrix metalloproteinases (MMPs) are a class of calcium-dependent, zinc-chelating endopeptidases which play an important physiological role in ECM remodeling. Typically, the catalytic activity of MMPs is tightly controlled through transcriptional alterations, tissue-specific MMP release and activation, or inhibition by endogenous tissue inhibitors of metalloproteinases.[2] Contrarily, dysregulation of activated MMPs is associated with several pathologies including metastatic cancer, arthritis, and multiple sclerosis through inflammation-induced tissue remodeling and degradation.[3,4] Of particular interest, uncontrolled ECM remodeling in the vasculature is a hallmark of atherosclerosis.[5]

Atherosclerotic lesions constitute a distinctive feature of progressive disease and risk of acute coronary events is largely associated with molecular markers of remodeling in these plaques.[6] Nevertheless, clinical imaging investigations focus nearly exclusively on anatomical or functional imaging modalities including angiography, computed tomography, and magnetic resonance imaging to identify the extent of coronary occlusion.[7,8] On a molecular level,

inflammatory mediators stimulate MMP recruitment and augment atheroma formation by facilitating mononuclear cell infiltration of the vessel wall.[9,10] Upon differentiation, macrophages mediate MMP secretion and induce proteolytic activity in vascular smooth muscle cells (SMC), contributing directly to plaque destabilization through degradation of the fibrous cap.[9,11,12] Given that thrombosis underlies most adverse clinical outcomes including myocardial infarction and stroke, MMPs represent compelling biomarkers of plaque vulnerability for imaging by positron emission tomography (PET).[13,14]

Specifically, MMP-13 has been identified as a predominant interstitial collagenase in *ApoE*$^{-/-}$ mice and human atheroma. Elevated expression of activated MMP-13 is associated with an increase in *in vivo* collagenolysis primarily in atheromatous compared with fibrous plaques and reduces SMC accumulation in both early and established lesions.[10,15] Additionally, knockout of MMP-13 in mice abolishes lesion collagenolytic activity, while selective inhibition increases local collagen content, suggesting that MMP-13 provokes plaque instability.[16,17]

Nevertheless, current MMP-targeted nuclear medicine agents including [^{18}F]BR-351, [^{99m}Tc]RP-805, and [^{18}F]marimastat-ArBF_3 exhibit broad-spectrum activity through coordination to the active site Zn^{2+} ion, conserved across the MMP family.[18–20] These radiotracers may exhibit lower target tissue contrast due to engagement with non-pathologic MMPs expressed in contiguous tissue.[12] Given that MMP-13 expression is limited in non-infiltrated arteries and myocardium, there is tremendous potential for improved imaging contrast, sensitivity, and especially *in vivo* characterization of atherosclerosis with elevated collagenase activity.[10,21] Fortunately, selective targeting of MMP-13 has been achieved with several small molecule inhibitors by exploiting the unique structural features of its S1′ and S1′* specificity pockets, adjacent the catalytic site.[22–24] In

particular, MMP-13 inhibitors based on the pyrimidine dicarboxamide scaffold have shown no detectable inhibition of MMPs-1, -2, -3, -7, -8, -9, -10, -12, -14, and -16 up to 100 µM.[25]

The objective of this study was to evaluate the specificity and sensitivity of an MMP-13 selective radiotracer in comparison to a non-selective MMP radiotracer for the detection of atherosclerotic plaques possessing markers of inflammation and remodeling in mice. To facilitate this analysis, a radiotracer originally developed by Hugenberg *et al.* and herein entitled [^{18}F]FMBP (IC_{50} = 56 ± 2 nM, Table 2.0) with reported 10^3-fold MMP-13 selectivity has been chosen for comparison against [^{18}F]BR-351 originally developed by Wagner *et al.*, which is non-selective (2 ≤ IC_{50} ≤ 50 nM, Table 2.0) and has been previously investigated for imaging MMPs in glioma, colorectal cancer, and stroke.[18,22,26–28]

Table 2.0 Selectivity profiles of [^{18}F]FMBP and [^{18}F]BR-351

	IC_{50} (nM)*			
Radiotracer	MMP-2	MMP-8	MMP-9	MMP-13
[^{18}F]FMBP	>10^5	>10^5	>10^5	56 ± 2
[^{18}F]BR-351	4 ± 3	2 ± 1	50 ± 27	11 ± 0.3

*Values reported in Hugenberg *et al.*[22] and Wagner *et al.*[26] as the mean ± SD of three experiments.

2.5 Materials and Methods

2.5.1 Chemical Synthesis and Radiolabeling

See ESM for chemical synthesis, radiolabeling, and quality control testing (Suppl. Figs. 1 & 2).

2.5.2 Animal Model

Male and female C57Bl/6J (strain no. 000664) and *ApoE*$^{-/-}$ (strain no. 002052) mice were obtained from Jackson Laboratory, acclimated upon arrival for 1 week, housed in groups of 4, and monitored periodically until 8-12 months of age. C57Bl/6 mice were fed with normal chow while *ApoE*$^{-/-}$ mice were fed a western atherogenic diet (TD.88137, Envigo) for 16 weeks and returned to normal chow.[29] Both strains were housed in environmentally enriched cages with free access to food and water. All housing, handling, and experimental procedures were in strict accordance with the guidelines of Canadian Council on Animal Care and with approval of the University of Ottawa Animal Care Committee. (Suppl. Fig. 3)

2.5.3 Aortic *En Face*

Procedures for aortic *en face* preparations were adapted from literature.[30] Mice anesthetized with isoflurane were sacrificed by myocardial perfusion with 1× phosphate buffered saline (PBS, 10 mL), briefly fixed with 10% formalin (10 mL), and immediately flushed with additional 1× PBS (5 mL) via left ventricle cannulation. Perfusate was drained from an incision within the right atrium. The heart and aorta were harvested by severing branching arteries and detaching the descending aorta. Upon removal of the adventitia, the aorta was separated from the heart at the root and opened longitudinally.

2.5.4 *In Vitro* Autoradiography

En face aortae harvested from *ApoE*$^{-/-}$ mice (n = 4–7 per group) were sequentially washed with EtOH and tris buffer (50 mM, pH 7.4) prior to incubation with the selected tracer (45 kBq) for 1 hour. In separate experiments, non-specific binding was assessed by incubating these same samples with excess non-radioactive standard (2 μM or 10 μM) for 1 hour. Samples were washed with buffer (2 × 5 min) followed by water (1 × 5 min). Aortae were immediately exposed to a super-resolution Storage Phosphor Screen (BAS-IP SR 2025 E) in an Electrophoresis Systems Autoradiography Cassette (FBXC 810) for 15 hours. The screen was scanned with a Cyclone Plus Storage Phosphor System and images were analyzed using OptiQuant software by drawing aortic arch regions of interest (ROI) which were Oil Red O (ORO) positive.[31] Digital light units (DLU) were converted to activity (Bq) using a set of calibration standards with known activities on the same screen. Activity density (Bq/mm^2) was calculated from dividing the sample activity by the ROI area.

2.5.5 *In Vivo* Studies

Dynamic PET imaging was performed on *ApoE*$^{-/-}$ mice over 1 hour (Suppl. Figs. 3 & 4, see ESM). For biodistributions, mice (38 ± 2 g, n = 4 per group) were anesthetized with 3% isoflurane and administered non-radioactive standard (5 mg/kg, ip, 50/50 DMSO/water) or equivalently dosed vehicle control 30 minutes prior to intravenous injection of the selected tracer (15 MBq) through a lateral tail vein catheter. After 30 minutes, mice were sacrificed by myocardial perfusion, organs of interest were excised, dipped in water, weighed, and counted for radioactivity using a Hidex Automatic Gamma Counter (energy window: 350–650 keV). Counts per minute (cpm) were converted to activity (Bq) using a set of calibration standards with known activities. Percentage injected dose (%ID) was calculated from dividing the organ activity by the injected

dose (decay-corrected) and further normalized by sample mass to obtain the percentage injected dose per gram tissue (%ID·g^{-1}).

Aortae were also harvested and *en face* specimens were imaged and quantified as described for the *in vitro* autoradiography section. Briefly, percentage injected dose (%ID) was calculated by dividing the lesion activity by the injected dose (decay-corrected) and further normalized by area to obtain activity density (%ID·m^{-2}).[31]

2.5.6 Plasma Metabolite Analysis

Blood samples were further processed and analyzed for plasma metabolites as previously described.[18] Plasma samples spiked with nonradioactive standard were analyzed using the analytical HPLC conditions as described in the quality control protocol (see ESM). Fractions were collected every 2 minutes and counted for radioactivity using a gamma counter. Fractions collected before and after the parent fraction were considered as polar and non-polar metabolites, respectively. Extraction efficiency was defined as the percentage recovery of radioactivity in protein-free plasma following precipitation with acetonitrile.

2.5.7 Histology

Procedures for ORO staining were adapted from literature.[30] *En face* prepared samples were incubated with the freshly prepared ORO solution for 1.5 hours and washed with water (2 × 5 min). Bright-field images were taken using a Krüss Stereomicroscope (MSL4000-series) adapted with a smartphone camera. Aortic arches, defined by the boundary between the aortic root and the ascending aorta to the same level on the descending aorta, were cropped using Adobe Photoshop CS5. Lesion areas were expressed relative to the total aortic arch surface area (% positive area). Quantification was completed by 2 independent observers using ImageJ.

2.5.8 Immunofluorescence

Following *ex vivo* autoradiography and staining with ORO, *en face* aortic arches were embedded in paraffin wax (TissuePrep), sliced into 5 µm sections, and deparaffinized. Regions which were positive during *ex vivo* [^{18}F]FMBP autoradiography were selected for sectioning (n = 2 per aorta). Antigen retrieval was performed in citrate buffer (pH 6.0) at 100 °C for 150 seconds. Sections were covered in 10% normal goat serum (Vector Laboratories) for 10 minutes and incubated with 1:100 MMP-13 or MMP-2 primary antibody (ab39012 or ab97779, Abcam) and 1:500 Mac-2 primary antibody (CL8942AP, Cedarlane) for 16 hours at 4 °C. Samples were then incubated with secondary antibodies at 1:500 dilution for 30 minutes (MMP-13 & MMP-2: A-11037, Mac-2: A-11006, Invitrogen). Nuclei were counterstained with Hoeschst 33258 (10 mg/mL in PBS) for 8 minutes. Slides were coated with fluorescent protective mounting media (Dako), dried, and covered until imaging by fluorescent microscopy (Zeiss Axio Imager A2). Isotype control antibodies (rabbit IgG ab171870, Abcam and rat IgG CLCR2A00, Cedarlane) were also utilized to assess non-specific fluorescence at equivalent concentrations to the primary antibodies. Images were acquired with Aperio ImageScope (10× magnification), stitched using Microsoft Image Composite Editor, cropped using Adobe Photoshop CS5 and quantified by 2 independent observers using ImageJ.

2.5.9 Statistical Analysis

Statistical analysis was performed using GraphPad Prism. Data are presented as mean ± standard error. Differences between 2 groups were tested using a 2-tailed unpaired Student's t-test. Multiple groups were compared using 1-way ANOVA or 2-way ANOVA with Tukey's multiple comparison test. Data are normally distributed. Significance was set at the 0.05 level.

2.6 Results

2.6.1 Radiosyntheses of [^{18}F]FMBP and [^{18}F]BR-351

With minor modifications to previously reported conditions, automated radiosyntheses were established to produce the target radiotracers.[22,26] [^{18}F]FMBP and [^{18}F]BR-351 were obtained in decay-corrected radiochemical yields of 28 ± 1% (n = 10) and 27 ± 6% (n = 3), 60 and 80 minutes after bombardment, with radiochemical purities >99% (Fig. 1). Molar activities were determined to be 92 ± 11 GBq/μmol and 90 ± 53 GBq/μmol at the end of synthesis for [^{18}F]FMBP and [^{18}F]BR-351, respectively (Fig. 2.0).

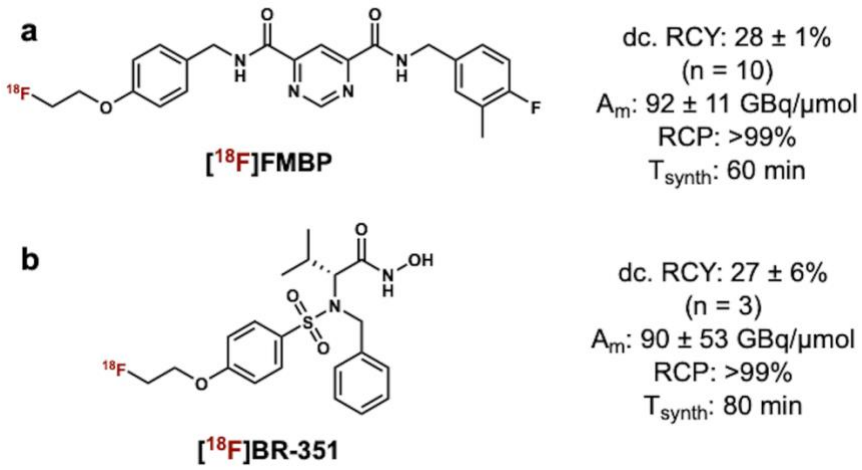

Figure 2.0 Structure of target radiotracers. **(a)** [^{18}F]FMBP **(b)** [^{18}F]BR-351.

2.6.2 *In Vitro* Autoradiographic Validation

Aortic arch autoradiographic uptake patterns of [^{18}F]FMBP and [^{18}F]BR-351 displayed colocalization with ORO-positive lipid-rich atherosclerotic lesions (Fig. 2.1a). At baseline, [^{18}F]FMBP exhibited an aortic lesion activity density of 61.45 ± 2.08 Bq/mm^2, reducible by 23% to 47.57 ± 2.04 Bq/mm^2 (P = 0.0363) and 45% to 33.79 ± 4.18 Bq/mm^2 (P = 0.0001) upon co-incubation with 2 μM and 10 μM non-radioactive FMBP, respectively (Fig. 2.1b). At baseline,

[^{18}F]BR-351 exhibited aortic lesion activity density of 37.62 ± 5.00 Bq/mm^2, reducible by 55% to 17.05 ± 3.61 Bq/mm^2 upon co-incubation with 2 µM non-radioactive BR-351 (Fig. 2.1b, P = 0.0046). Similarly, incubation with 10 µM non-radioactive BR-351 reduced aortic lesion activity density by 56% to 16.54 ± 1.94 Bq/mm^2 (Fig. 2.1b, P = 0.0017).

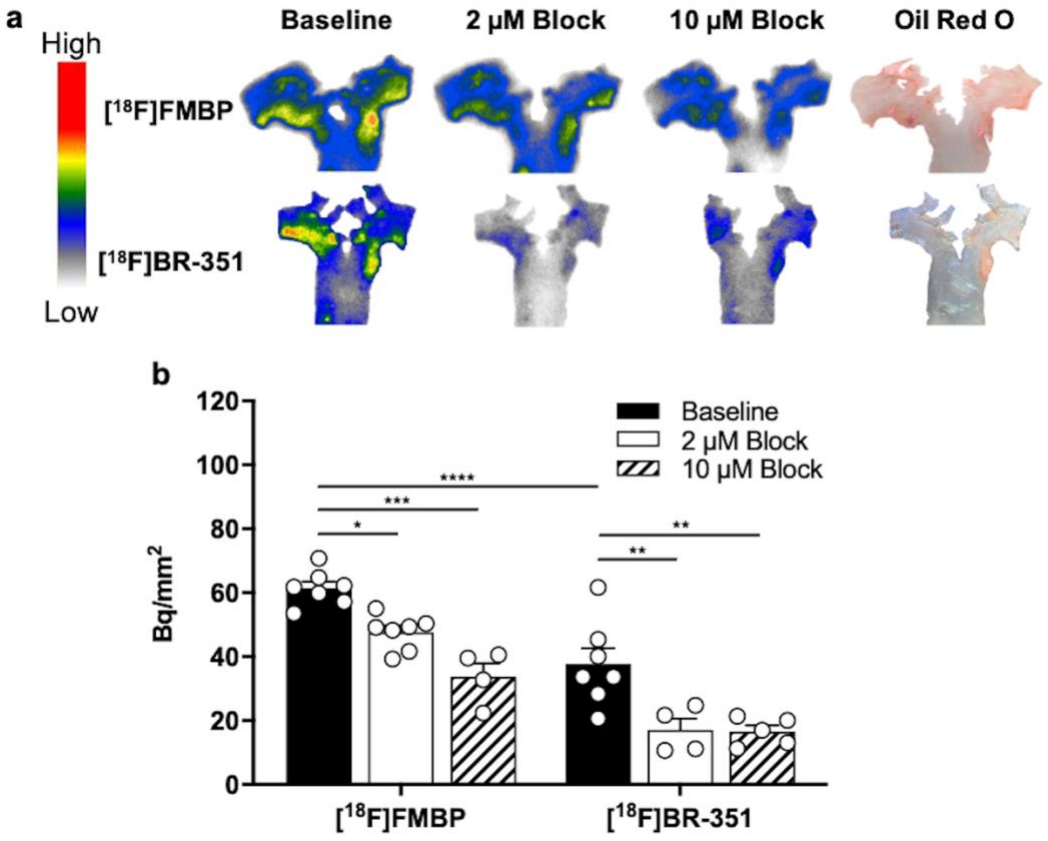

Figure 2.1 *In vitro* target specificity and co-localization with lipid content in atherosclerotic aortae. **(a)** Representative *ApoE*$^{-/-}$ aortic *en face in vitro* autoradiographs 1 h after incubation with 45 kBq [^{18}F]FMBP or [^{18}F]BR-351. Homologous blocking was performed by co-incubation of 2 µM and 10 µM non-radioactive FMBP or BR-351. Corresponding bright-field images of ORO stains are shown. Note the slight fold in the [^{18}F]BR-351 aorta under 10 µM blocking conditions. **(b)** [^{18}F]FMBP and [^{18}F]BR-351 aortic lesion uptake. Two-way ANOVA: ****P < 0.0001, ***P = 0.0001, **P < 0.0046, * P = 0.0363, n = 4–7 per group.

2.6.3 PET Imaging and Biodistribution

Under baseline conditions in *ApoE* $^{-/-}$ mice, [^{18}F]FMBP predominantly exhibited hepatic (17.22 ± 2.56 %ID·g^{-1}), intestinal (4.73 ± 0.78 %ID·g^{-1}), myocardial (4.66 ± 0.11 %ID·g^{-1}), and renal (4.04 ± 0.36 %ID·g^{-1}) retention (Fig. 2.2a). Similar to previous reports for C57Bl/6 mice and consistent with *ex vivo* findings, blood time-activity curves revealed rapid washout of radioactivity (T_{max}: 0.75 min) while myocardial uptake stabilized at 4.82 ± 0.31 %ID·cc^{-1} with slow clearance 10 minutes after injection (Suppl. Fig. 4).[22] [^{18}F]BR-351 exhibited uptake within these same organs with greater accumulation in the intestine (Fig. 2.2b, intestine: 5.79 ± 0.89 %ID·g^{-1}, kidney: 2.88 ± 0.67 %ID·g^{-1}, and liver: 2.72 ± 0.41 %ID·g^{-1}). Low levels of radioactivity (<2 %ID·g^{-1}) were observed in all other measured organs and few differences were observed between strains and conditions (Fig. 2.2). Particularly, [^{18}F]FMBP and [^{18}F]BR-351 exhibited statistically significant differences in the liver ($P < 0.0007$) and intestine ($P < 0.0011$), respectively (Fig. 2.2).

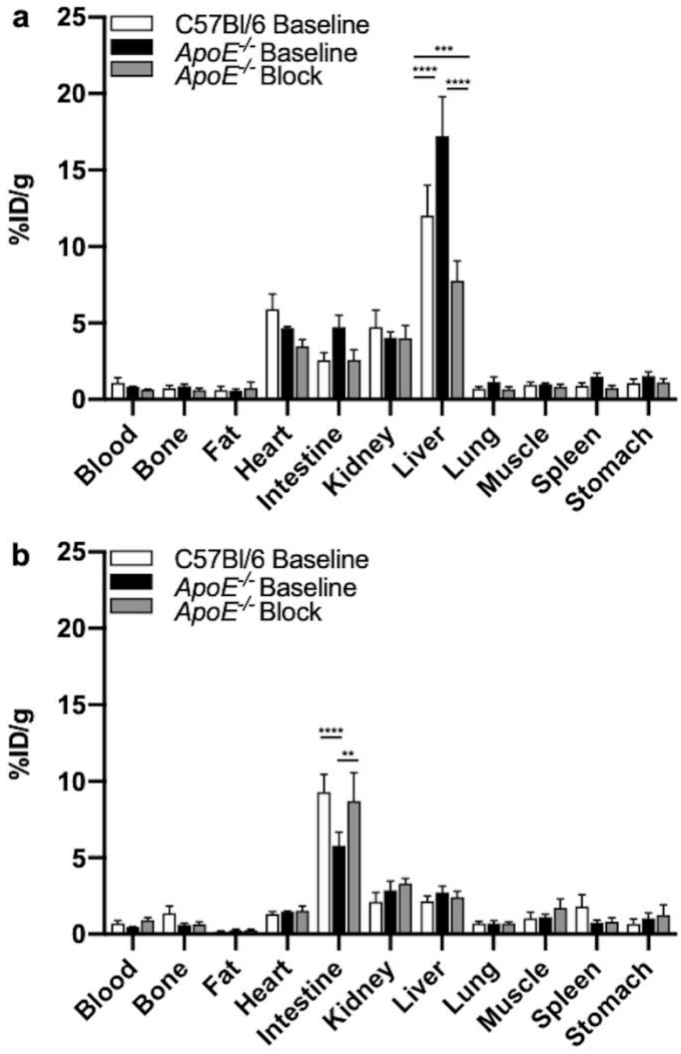

Figure 2.2. *Ex vivo* biodistributions 30 min after intravenous radiotracer administration (15 MBq) via the lateral tail vein. **(a)** [^{18}F]FMBP. Two-way ANOVA: ****P < 0.0001, ***P = 0.0007. **(b)** [^{18}F]BR-351.Two-way ANOVA: ****P <0.0001, **P = 0.0011, n = 6-7 per group (n = 2-3 for blood, heart, and muscle).

2.6.4 Plasma Metabolite Analysis

Following measurement of whole-blood radioactivity, samples were immediately pooled for plasma metabolite analysis using fractional radio-HPLC and gamma counting (Table 2.1 & Suppl. Fig. 5). In *ApoE*$^{-/-}$ mice, 79% and 74% of plasma radioactivity corresponded to intact

[^{18}F]FMBP under baseline and blocking conditions, comparable to levels observed in C57Bl/6 mice (Table 2.1). Conversely, 37% of plasma radioactivity corresponded to intact [^{18}F]BR-351 in *ApoE*$^{-/-}$ mice, with a reduction to 16% under blocking conditions and 9% in C57Bl/6 mice (Table 2.1). In both analyses, remaining radioactivity was mainly attributed to polar radio-metabolites. The observed extraction efficiencies (≥75%) suggest representative sampling of plasma radioactivity.

Table 2.1 Plasma metabolite analysis of [^{18}F]FMBP and [^{18}F]BR-351.

Fraction*	[^{18}F]FMBP			[^{18}F]BR-351		
	C57Bl/6 Baseline	*ApoE*$^{-/-}$ Baseline	*ApoE*$^{-/-}$ Block	C57Bl/6 Baseline	*ApoE*$^{-/-}$ Baseline	*ApoE*$^{-/-}$ Block
Parent Radiotracer (%)	88	79	74	9	37	16
Polar Metabolites (%)	11	19	24	88	53	82
Nonpolar Metabolites (%)	1	2	2	3	10	2
Extraction Efficiency (%)	95	95	91	85	82	75

*Values expressed as % of total radioactivity obtained for pooled blood samples 30 min after intravenous radiotracer administration, n = 2-3.

2.6.5 *Ex Vivo* Autoradiography and Oil Red O Quantification

Following intravenous administration, aortic arch uptake of [^{18}F]FMBP and [^{18}F]BR-351 was visualized by *en face* autoradiography and displayed high regional concordance with ORO-positive lipid-rich atherosclerotic lesions (Figs. 2.3a & 2.3b). At baseline, [^{18}F]FMBP exhibited significantly higher lesion activity density in the *ApoE*$^{-/-}$ cohort (244 ± 37 %ID·m^{-2}) relative to C57Bl/6 controls (Fig. 2.3c, 86 ± 22 %ID·m^{-2}, P = 0.0011). Pre-treatment with non-radioactive FMBP significantly decreased [^{18}F]FMBP aortic lesion uptake by 68% to 78 ± 24 %ID·m^{-2} (Fig.

2.3c, P = 0.0007), equivalent to levels observed in control mice, absent of vascular lesions. [^{18}F]BR-351 also exhibited elevated lesion activity density in the *ApoE*$^{-/-}$ cohort (84 ± 6 %ID·m^{-2}) relative to controls (40 ± 11 %ID·m^{-2}), however, observed differences were not statistically significant (Fig. 2.3c, P = 0.6251). No significant change in [^{18}F]BR-351 uptake was observed following pre-administration with BR-351 (Fig. 2.3c, P = 0.9935). Quantification of ORO revealed that positive areas were significantly elevated within *ApoE*$^{-/-}$ aortae (25.51 ± 3.74%) and limited in C57Bl/6 controls (0.16 ± 0.07%, Fig. 2.3d, P = 0.0002).

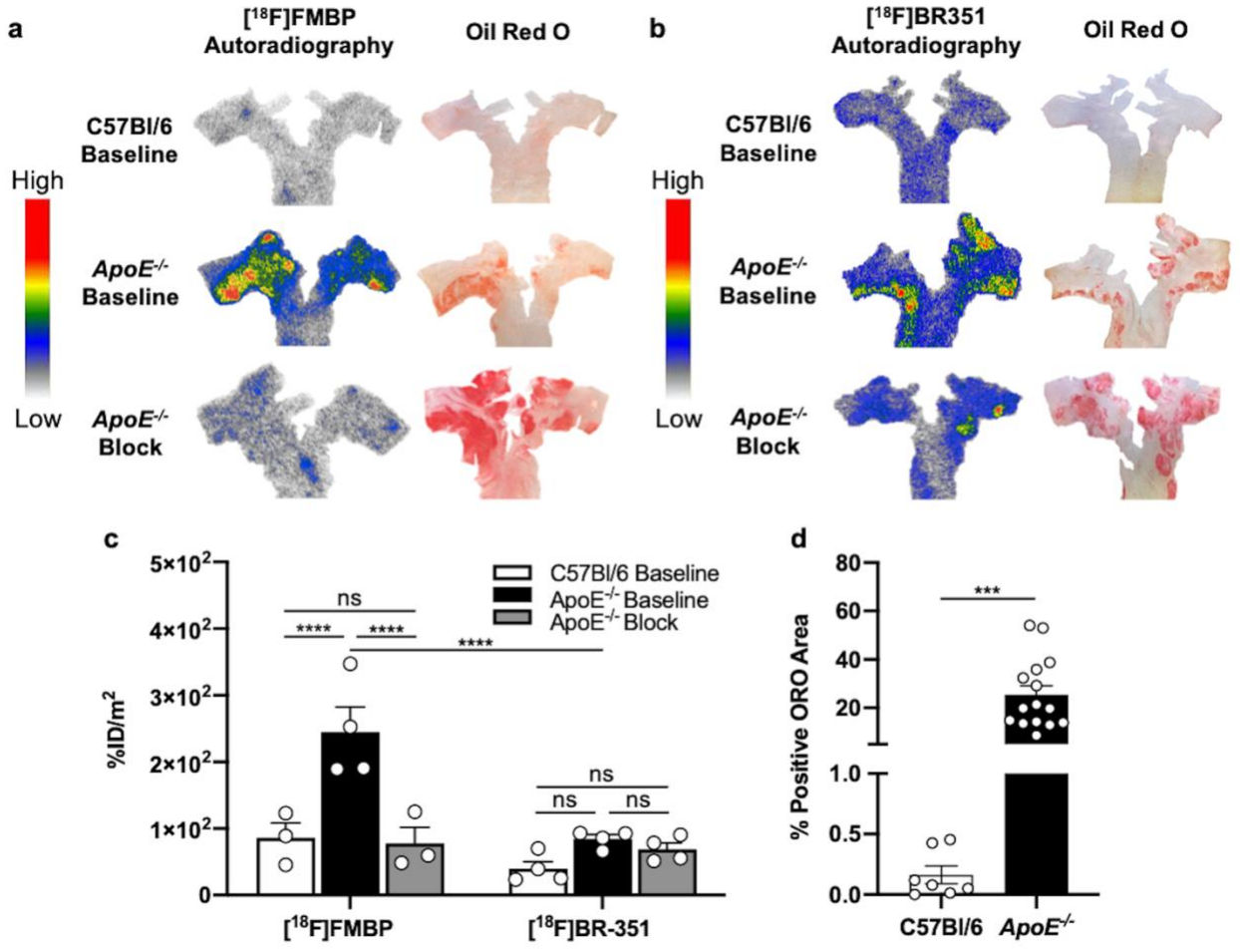

Figure 2.3 *Ex vivo* autoradiographic lesion uptake, specific binding, sensitivity to atherosclerotic tissue, and extent of lipid accumulation. **(a/b)** Representative aortic *en face ex vivo* autoradiographs 30 min after intravenous injection of 15 MBq [^{18}F]FMBP or [^{18}F]BR-351 in C57Bl/6 and *ApoE*$^{-/-}$

mice via the lateral tail vein. Blocking was performed with non-radioactive FMBP or BR-351 (5 mg/kg, IP, maximum FMBP solubility) 30 minutes prior to tracer administration. Corresponding bright-field images of ORO stains are shown. **(c)** [^{18}F]FMBP and [^{18}F]BR-351 aortic lesion uptake. Two-way ANOVA: ****P <0.0001, ns = not significant, n = 3–4 per group. **(d)** Quantification of percentage positive ORO areas in C57Bl/6 and *ApoE*$^{-/-}$ (baseline + block) mice. Unpaired t-test: ***P = 0.0002, n = 7-15 per radiotracer.

2.6.6 Markers of Inflammation and Remodeling

Percentage positive Mac-2 (7.16 ± 1.15%), MMP-13 (5.52 ± 1.54%), and MMP-2 (9.44 ± 2.14%) areas were distinctly increased within atherosclerotic lesions of *ApoE*$^{-/-}$ mice, as detected by immunofluorescence and predicted by [^{18}F]FMBP *ex vivo* autoradiography (Figs. 2.4a–l & Suppl. Fig. 6). Additionally, MMP-13 and Mac-2 positive areas colocalized (Figs. 2.4i & 2.4j). Isotype control experiments revealed a moderate extent of non-specific binding within atherosclerotic lesions, but none in C57Bl/6 controls (Suppl. Fig. 7).

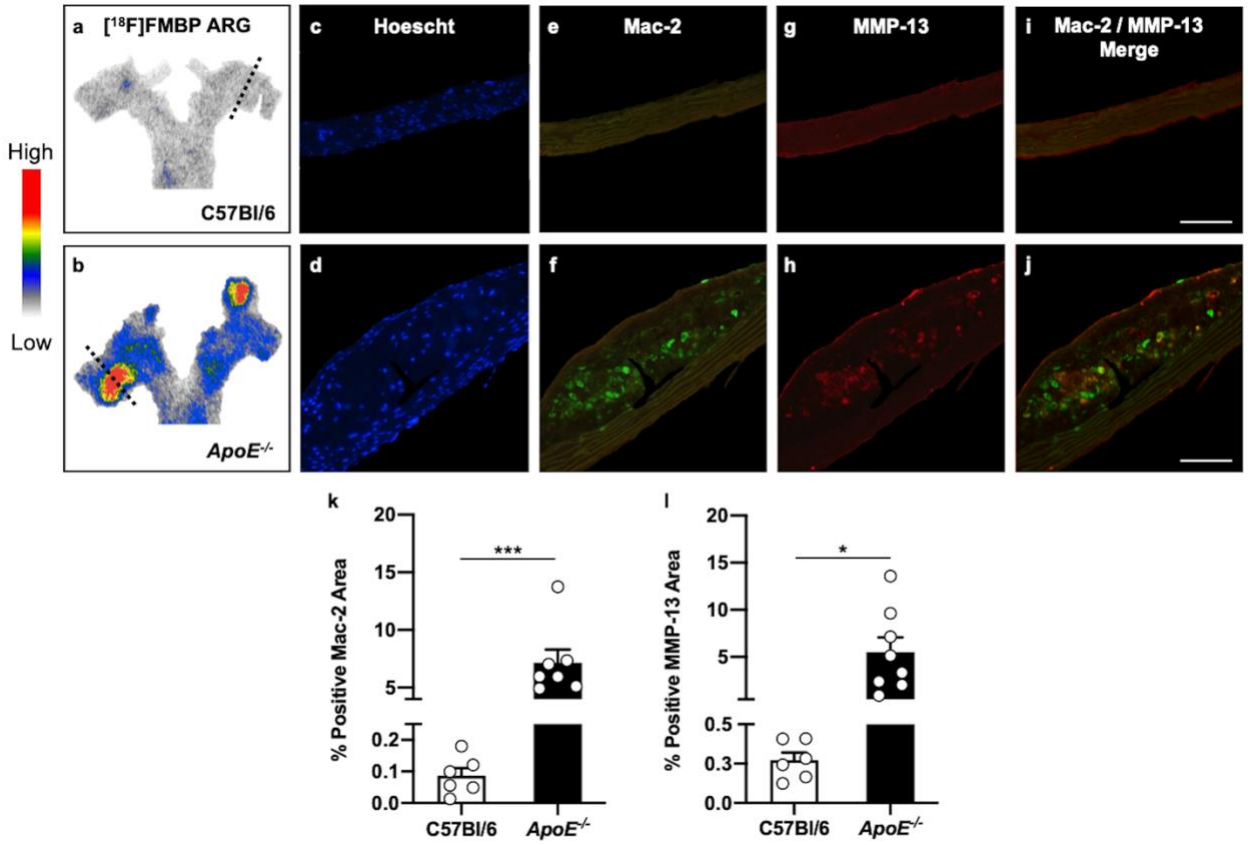

Figure 2.4 Immunofluorescent staining of atherosclerotic lesions detected by [^{18}F]FMBP *ex vivo* autoradiography. **(a/b)** Selected [^{18}F]FMBP *ex vivo* autoradiographs in C57Bl/6 and *ApoE*$^{-/-}$ mice. Corresponding composite images of cross-sections following immunofluorescent staining for **(c/d)** Hoescht, **(e/f)** Mac-2, and **(g/h)** MMP-13. **(i/j)** Mac-2 and MMP-13 merge. Scale bar = 100 µm. **(k/l)** Quantification of percentage positive Mac-2 and MMP-13 areas in *ApoE*$^{-/-}$ and C57Bl/6 mice. Unpaired t-test: ***P = 0.0001, *P = 0.0127, n = 6–8 per group.

2.7 Discussion

Few MMP-targeted radiotracers have been evaluated in mouse models of atherosclerosis, namely [^{99m}Tc]RP805, [^{111}In]RP782, [^{123}I]I-HO-CGS 27023A and [^{68}Ga]Ga-DOTA-TCTP-1.[32–38] Investigations with these radiotracers have primarily focused on colocalizing and in some cases correlating *in vivo* and *ex vivo* uptake in atherosclerosis with markers such as macrophages and

MMPs, determined by immunostaining or mRNA expression. Nevertheless, direct evidence toward the differentiation of stable from vulnerable plaques remains elusive. Limited availability of mouse models recapitulating atherosclerotic plaque rupture contribute to this shortcoming,[39] though it has also been acknowledged that quantification of broad metalloproteinase activity may not be appropriate.[32,38] The target density of a non-selective radiotracer is subject to dynamic MMP expression patterns in various tissues and diseases. While many MMPs have been shown to be upregulated in human carotid plaques, these enzymes possess varying pathophysiological roles in plaque progression.[5,12,40,41] Therefore, imaging specific subtypes which have been shown to directly contribute to atherosclerotic plaque rupture may be advantageous. The present study sought to evaluate an approach to selective targeting of MMP-13, a predominant collagenase implicated in plaque vulnerability, for sensitivity and characterization of atherosclerotic plaques possessing markers of inflammation and remodeling, in comparison to a broad-spectrum MMP radiotracer.[10,15–17]

To facilitate this comparative analysis, automated syntheses were adapted to reliably obtain [^{18}F]FMBP and [^{18}F]BR-351 with slightly improved radiochemical yield and molar activity (>90 GBq/µmol) suitable for high contrast imaging (Fig. 2.0 & Suppl. Fig 1). Initial validations were performed by high resolution *in vitro* autoradiography in *en face* aortae to visualize and quantify radioligand binding in atherosclerotic tissue without potential confounds related to target-tissue delivery and metabolism. Given the unavailability of heterologous MMP-selective inhibitors, and the aforementioned differences in target engagement, radiotracer binding specificity was assessed with the corresponding non-radioactive standard. [^{18}F]FMBP and [^{18}F]BR-351 demonstrated moderate levels of specific binding (45% and 56% displaceable, respectively) and evident colocalization to ORO-positive areas, representing lipid-laden atheromatous plaques (Fig. 2.1).

[^{18}F]FMBP demonstrated dose dependent blocking and lesion activity density was 1.6-fold greater than [^{18}F]BR-351 at baseline, while [^{18}F]BR-351 specific uptake was fully saturated at 2 μM (Fig. 2.1). Taken together, though levels of specificity were suboptimal during *in vitro* evaluation, these findings provided justification for more comprehensive investigations.

To further establish radioligand localization profiles, *ex vivo* biodistribution was performed in C57Bl/6 and *ApoE*$^{-/-}$ mice. *In vivo* PET imaging was conducted in *ApoE*$^{-/-}$ mice to select an optimal timepoint for *ex vivo* sampling (Suppl. Fig. 4). Subsequent experiments were conducted at a 30-minute timepoint following stabilization of [^{18}F]FMBP myocardial and blood time-activity curves to sufficiently allow for radiotracer circulation. Both [^{18}F]FMBP and [^{18}F]BR-351 predominantly undergo renal clearance and hepatobiliary excretion with low accumulation in non-excretory organs (Fig. 2.2), as previously reported in mice.[22,26] While the observed differences in hepatic [^{18}F]FMBP uptake are not fully understood, constitutive expression of MMP-13 and western-diet induced fibrosis suggest potential explanations.[42,43] Observed differences in intestinal [^{18}F]BR-351 uptake are suspected to be related to metabolic variations (Table 2.1). Low bone uptake indicated that radiodefluorination did not occur, offering the potential for non-invasive aortic imaging of calcific vascular lesions in close proximity to the spine in larger species using PET/CT. Most notably, distribution patterns were similar among mouse strains and few differences were observed under blocking conditions, emphasizing that target expression and specific binding are low in organs unassociated with atherosclerosis (Fig. 2.2).

A metabolic study of [^{18}F]FMBP and [^{18}F]BR-351 was conducted to assess *in vivo* stability (Table 2.1 & Suppl. Fig. 5). Analysis of blood plasma revealed high metabolic stability of [^{18}F]FMBP, with the parent fraction representing the major detectable species under all testing conditions at a 30-minute timepoint. Although metabolites were not identified, the remaining polar

radio-metabolites likely correspond to O-dealkylation or amide hydrolysis products.[22] In contrast, analysis of blood plasma revealed low metabolic stability of [^{18}F]BR-351, with polar radio-metabolites representing the major detectable species under all testing conditions at an equivalent timepoint. Differences in the extent of [^{18}F]BR-351 metabolism are consistent with the observed variability in *ex vivo* intestinal uptake (Fig. 2.2b). Similarly, polar radio-metabolites likely correspond to O-dealkylation with the sulfonamide and hydroxamate moieties representing other labile positions.[18,44]

Ex vivo autoradiography on *en face* aortae served to reinforce *in vitro* findings in atherosclerotic tissue (Figs. 2.3a & 2.3b). [^{18}F]FMBP possessed 2.9-fold greater uptake in *ApoE*$^{-/-}$ models compared to C57Bl/6 animals and exhibited regional concordance with lipid-laden ORO-positive areas. Gratifyingly, pharmacological dosing of non-radioactive FMBP completely blocked aortic lesion tracer uptake such that it was indistinguishable from controls (Fig. 2.3c). Although [^{18}F]BR-351 seemingly possessed 2.1-fold sensitivity to atherosclerotic tissue, this difference along with the slight reduction observed by pre-treatment with non-radioactive BR-351 were not statistically significant in the sample groups (Fig. 2.3c). The discrepancy between *in vitro* and *ex vivo* findings is likely attributed to the poor metabolic stability of [^{18}F]BR-351 resulting in limited MMP engagement (Table 2.1). Relative to [^{18}F]BR-351, [^{18}F]FMBP further exhibited 2.9-fold greater aortic lesion uptake (Fig. 2.3c). Quantification of ORO-positive areas highlighted that aortic lipid accumulation was elevated in *ApoE*$^{-/-}$ mice and negligible in C57Bl/6 controls (Fig. 2.3d).

En face aortae obtained during *ex vivo* analyses were subsequently embedded in paraffin, sectioned, and stained for immunofluorescent detection of Mac-2 and MMP-13 as markers of inflammation and remodeling, alongside nuclear counterstaining with Hoescht (Figs. 2.4a-j). As

expected, a negative result was obtained for C57Bl/6 samples lacking aortic lesions (Figs. 2.4a-j). In contrast, atherosclerotic lesions which were ORO-positive and detected by [^{18}F]FMBP *ex vivo* autoradiography possessed elevated Mac-2 and MMP-13 positive areas, suggesting that radiotracer uptake is sensitive to the presence of these biomarkers (Figs. 2.4a-i). Notably, MMP-13 density appears to be markedly increased within the outer curvature of the atherosclerotic lesion, consistent with localization of this enzyme within the fibrous cap, which is a major determinant of plaque destabilization (Figs. 2.4i & 2.4j).[10,15] Quantification recapitulated that Mac-2 and MMP-13 are uniquely expressed in response to atherosclerosis, consistent with macrophage mediated secretion and activation of this collagenase (Figs. 2.4k & 2.4l).

Considering that [^{18}F]BR-351 effectively binds to MMP-2, -8, -9 and -13, the contributions of each target to radiotracer uptake must be clearly identified to facilitate interpretation. While, the percentage positive area of MMP-2 was also found to be elevated in atherosclerotic plaques as detected by immunofluorescence (Suppl. Fig. 6), literature on MMP-2 deficient atherogenic mice suggests that this gelatinase imparts stability to atherosclerotic lesions by accumulating SMCs into the fibrous cap.[45] Likewise for MMP-9, inconsistent findings necessitate further elucidation of its diverse effects on cellular plaque composition.[45,46] Regarding the interstitial collagenases, MMP-13 predominates over MMP-8 in degrading intraplaque collagen, and reducing SMC accumulation in atherogenic mice.[15] Most significantly, MMP-13 colocalizes with MMP-1 in inflamed human atheromatous plaques, demonstrating that selective imaging of MMP-13 remains a promising strategy for pre-clinical evaluations.[10]

2.8 Limitations

BR-351 and FMBP bind active site zinc ions or specificity pockets adjacent the MMP active site. Although the possibility for engagement with inactive enzymes was not assessed in this study, latent MMP active sites are inaccessible to both substrate and aqueous medium prior to cleavage of the pro-peptide domain.[25,47] Therefore, it is reasonable to infer radiotracer specific binding reflects active MMP concentrations. Due to the unavailability of well-characterized selective MMP-13 inhibitors, heterologous blocking studies were not possible in the current study and target engagement of MMP-13 could not be directly evaluated. Biological variance of MMP-13 expression was insufficient to establish meaningful correlations using *ApoE*$^{-/-}$ mice, though may be possible with additional model strains.[32]

From an imaging perspective, while PET radiotracers inherently hold several advantages over SPECT analogues, accurate *in vivo* localization and quantification of small lesions in mice remains challenging due to limited spatial resolution and partial volume effects. *In vivo* PET imaging was conducted in this study to observe dynamic distribution among organs but could not be used to localize aortic uptake due to the small physical size of the vessel and significant liver uptake. It is also important to acknowledge that the employed atherogenic mouse model may lack the underlying biochemical and physiological processes necessary to truly develop rupture-prone atherosclerotic plaques.[48] As such, the present study sought to co-localize radiotracer uptake with biomarkers of inflammation and remodelling consistent with disrupted human plaques. Future studies on larger mammals with advanced human-like atherosclerosis are planned to not only localize but differentiate stable atherosclerotic plaques from those which are susceptible to rupture. Given the promising results of this approach, second generation PET radiotracers derived from

alternative inhibitor scaffolds with improved potency and selectivity are under parallel development.

2.9 Conclusion

The feasibility of imaging extracellular matrix remodeling *ex vivo* in mouse models of atherosclerosis with MMP-13 targeted PET radiotracers has been established. While both [^{18}F]BR351 and [^{18}F]FMBP successfully localized atherosclerotic lesions, MMP-13-targeted imaging with [^{18}F]FMBP showed improved binding specificity and sensitivity to atherosclerotic tissue possessing markers of destructive plaque remodeling relative to pan-selective [^{18}F]BR-351. Altogether, [^{18}F]FMBP has proven useful for the *ex vivo* detection of atherosclerotic lesions possessing markers of inflammation and extracellular matrix remodeling, suggesting that selective imaging represents a promising approach towards the characterization of high-risk atherosclerosis. Selective MMP-13-targeted radiotracers with superior specificity and pharmacokinetics may enable *in vivo* localization of collagenase activity in atherosclerotic plaques.

2.9.1 Manuscript Information

Acknowledgements

We are grateful to Dr. Rob Beanlands and Dr. Katey Rayner for illuminating discussions, Dr. Tayebeh Hadizad and Daniel Duan for isotope production, and the University of Ottawa Heart Institute Animal Care and Veterinary Services for their contributions to this work.

Author Contributions

Project design – A.B. and B.H.R.

Method development – A.B., M.M., G.F., X.Z., and R.A-H.

Data acquisition and analysis – A.B., M.M., G.F., and E.F.

Writing and revision of the manuscript - A.B., M.M., G.F., and B.H.R.

Sources of Funding

We acknowledge financial support from CIHR Project Grant 366633, CFI JELF 36848, Ontario Ministry of Research Innovation and Science ER17-13-119, and the Faculty of Medicine and Division of Cardiology at University of Ottawa. A.B. was supported by NSERC USRA and OGS. G.F. was supported by CIHR CGSM and QEII-GSST.

Conflict of Interest

The authors declare that they have no conflict of interest.

2.10 References

(1) Bonnans, C.; Chou, J.; Werb, Z. Remodelling the Extracellular Matrix in Development and Disease. *Nat. Rev. Mol. Cell Biol.* **2014**, *15* (12), 786–801. https://doi.org/10.1038/nrm3904.

(2) Löffek, S.; Schilling, O.; Franzke, C.-W. Biological Role of Matrix Metalloproteinases: A Critical Balance. *Eur. Respir. J.* **2011**, *38* (1), 191–208. https://doi.org/10.1183/09031936.00146510.

(3) Li, H.; Wang, D.; Yuan, Y.; Min, J. New Insights on the MMP-13 Regulatory Network in the Pathogenesis of Early Osteoarthritis. *Arthritis Res. Ther.* **2017**, *19* (1), 248. https://doi.org/10.1186/s13075-017-1454-2.

(4) Hu, J.; Van den Steen, P. E.; Sang, Q.-X. A.; Opdenakker, G. Matrix Metalloproteinase Inhibitors as Therapy for Inflammatory and Vascular Diseases. *Nat. Rev. Drug Discov.* **2007**, *6* (6), 480–498. https://doi.org/10.1038/nrd2308.

(5) Johnson, J. L. Metalloproteinases in Atherosclerosis. *Eur. J. Pharmacol.* **2017**, *816*, 93–106. https://doi.org/10.1016/j.ejphar.2017.09.007.

(6) Giannakou, S.; Angelidis, G.; Tsougos, I.; Valotassiou, V.; Kappas, K.; Georgoulias, P. Pet Tracers for Vulnerable Plaque Imaging. *Ann. Nucl. Med.* **2020**. https://doi.org/10.1007/s12149-020-01458-7.

(7) Heo, R.; Nakazato, R.; Kalra, D.; Min, J. K. Noninvasive Imaging in Coronary Artery Disease. *Semin. Nucl. Med.* **2014**, *44* (5), 398–409. https://doi.org/10.1053/j.semnuclmed.2014.05.004.

(8) Owen, D. R. J.; Lindsay, A. C.; Choudhury, R. P.; Fayad, Z. A. Imaging of Atherosclerosis. *Annu. Rev. Med.* **2011**, *62*, 25–40. https://doi.org/10.1146/annurev-med-041709-133809.

(9) Libby, P. Inflammation in Atherosclerosis. *Nature* **2002**, *420* (6917), 868–874. https://doi.org/10.1038/nature01323.

(10) Sukhova Galina K.; Schönbeck Uwe; Rabkin Elena; Schoen Frederick J.; Poole A. Robin; Billinghurst R. Clark; Libby Peter. Evidence for Increased Collagenolysis by Interstitial Collagenases-1 and -3 in Vulnerable Human Atheromatous Plaques. *Circulation* **1999**, *99* (19), 2503–2509. https://doi.org/10.1161/01.CIR.99.19.2503.

(11) Lessner, S. M.; Galis, Z. S. Matrix Metalloproteinases and Vascular Endothelium-Mononuclear Cell Close Encounters. *Trends Cardiovasc. Med.* **2004**, *14* (3), 105–111. https://doi.org/10.1016/j.tcm.2003.12.009.

(12) Newby, A. C. Matrix Metalloproteinase Inhibition Therapy for Vascular Diseases. *Vascul. Pharmacol.* **2012**, *56* (5–6), 232–244. https://doi.org/10.1016/j.vph.2012.01.007.

(13) Schaar, J. Terminology for High-Risk and Vulnerable Coronary Artery Plaques. *Eur. Heart J.* **2004**, *25* (12), 1077–1082. https://doi.org/10.1016/j.ehj.2004.01.002.

(14) Newby, A. C. Proteinases and Plaque Rupture: Unblocking the Road to Translation. *Curr. Opin. Lipidol.* **2014**, *25* (5), 358–366. https://doi.org/10.1097/MOL.0000000000000111.

(15) Quillard, T.; Araújo, H. A.; Franck, G.; Tesmenitsky, Y.; Libby, P. Matrix Metalloproteinase-13 Predominates Over Matrix Metalloproteinase-8 as the Functional Interstitial Collagenase in Mouse Atheromata. *Arterioscler. Thromb. Vasc. Biol.* **2014**, *34* (6), 1179–1186. https://doi.org/10.1161/ATVBAHA.114.303326.

(16) Quillard Thibaut; Tesmenitsky Yevgenia; Croce Kevin; Travers Richard; Shvartz Eugenia; Koskinas Konstantinos C.; Sukhova Galina K.; Aikawa Elena; Aikawa Masanori; Libby Peter. Selective Inhibition of Matrix Metalloproteinase-13 Increases Collagen Content of Established Mouse Atherosclerosis. *Arterioscler. Thromb. Vasc. Biol.* **2011**, *31* (11), 2464–2472. https://doi.org/10.1161/ATVBAHA.111.231563.

(17) Deguchi Jun-O; Aikawa Elena; Libby Peter; Vachon Jeffrey R.; Inada Masaki; Krane Stephen M.; Whittaker Peter; Aikawa Masanori. Matrix Metalloproteinase-13/Collagenase-3 Deletion Promotes Collagen Accumulation and Organization in Mouse Atherosclerotic Plaques. *Circulation* **2005**, *112* (17), 2708–2715. https://doi.org/10.1161/CIRCULATIONAHA.105.562041.

(18) Vazquez, N.; Missault, S.; Vangestel, C.; Deleye, S.; Thomae, D.; Veken, P. V. der; Augustyns, K.; Staelens, S.; Dedeurwaerdere, S.; Wyffels, L. Evaluation of [18F]BR420 and [18F]BR351 as Radiotracers for MMP-9 Imaging in Colorectal Cancer. *J. Label. Compd. Radiopharm.* **2017**, *60* (1), 69–79. https://doi.org/10.1002/jlcr.3476.

(19) Toczek, J.; Ye, Y.; Gona, K.; Kim, H.-Y.; Han, J.; Razavian, M.; Golestani, R.; Zhang, J.; Wu, T. L.; Jung, J.-J.; Sadeghi, M. M. Preclinical Evaluation of RYM1, a Matrix Metalloproteinase-Targeted Tracer for Imaging Aneurysm. *J. Nucl. Med. Off. Publ. Soc. Nucl. Med.* **2017**, *58* (8), 1318–1323. https://doi.org/10.2967/jnumed.116.188656.

(20) auf dem Keller, U.; Bellac, C. L.; Li, Y.; Lou, Y.; Lange, P. F.; Ting, R.; Harwig, C.; Kappelhoff, R.; Dedhar, S.; Adam, M. J.; Ruth, T. J.; Bénard, F.; Perrin, D. M.; Overall, C. M. Novel Matrix Metalloproteinase Inhibitor [18F]Marimastat-Aryltrifluoroborate as a Probe for in Vivo Positron Emission Tomography Imaging in Cancer. *Cancer Res.* **2010**, *70* (19), 7562–7569. https://doi.org/10.1158/0008-5472.CAN-10-1584.

(21) Spinale Francis G.; Coker Mytsi L.; Heung Lena J.; Bond Brian R.; Gunasinghe Himali R.; Etoh Takuma; Goldberg Aron T.; Zellner James L.; Crumbley A. Jackson. A Matrix Metalloproteinase Induction/Activation System Exists in the Human Left Ventricular Myocardium and Is Upregulated in Heart Failure. *Circulation* **2000**, *102* (16), 1944–1949. https://doi.org/10.1161/01.CIR.102.16.1944.

(22) Hugenberg, V.; Wagner, S.; Kopka, K.; Schäfers, M.; Schuit, R. C.; Windhorst, A. D.; Hermann, S. Radiolabeled Selective Matrix Metalloproteinase 13 (MMP-13) Inhibitors: (Radio)Syntheses and in Vitro and First in Vivo Evaluation. *J. Med. Chem.* **2017**, *60* (1), 307–321. https://doi.org/10.1021/acs.jmedchem.6b01284.

(23) Nara, H.; Sato, K.; Naito, T.; Mototani, H.; Oki, H.; Yamamoto, Y.; Kuno, H.; Santou, T.; Kanzaki, N.; Terauchi, J.; Uchikawa, O.; Kori, M. Discovery of Novel, Highly Potent, and Selective Quinazoline-2-Carboxamide-Based Matrix Metalloproteinase (MMP)-13 Inhibitors without a Zinc Binding Group Using a Structure-Based Design Approach. *J. Med. Chem.* **2014**, *57* (21), 8886–8902. https://doi.org/10.1021/jm500981k.

(24) Rangasamy, L.; Di Geronimo, B.; Ortín, I.; Coderch, C.; Zapico, J. M.; Ramos, A.; de Pascual-Teresa, B. Molecular Imaging Probes Based on Matrix Metalloproteinase Inhibitors (MMPIs). *Molecules* **2019**, *24* (16), 2982. https://doi.org/10.3390/molecules24162982.

(25) Engel, C. K.; Pirard, B.; Schimanski, S.; Kirsch, R.; Habermann, J.; Klingler, O.; Schlotte, V.; Weithmann, K. U.; Wendt, K. U. Structural Basis for the Highly Selective Inhibition of MMP-13. *Chem. Biol.* **2005**, *12* (2), 181–189. https://doi.org/10.1016/j.chembiol.2004.11.014.

(26) Wagner, S.; Breyholz, H.-J.; Law, M. P.; Faust, A.; Höltke, C.; Schröer, S.; Haufe, G.; Levkau, B.; Schober, O.; Schäfers, M.; Kopka, K. Novel Fluorinated Derivatives of the Broad-Spectrum MMP Inhibitors *N* -Hydroxy-2(*R*)-[[(4-Methoxyphenyl)Sulfonyl](Benzyl)- and (3-Picolyl)-Amino]-3-Methyl-Butanamide as Potential Tools for the Molecular Imaging of Activated MMPs with PET. *J. Med. Chem.* **2007**, *50* (23), 5752–5764. https://doi.org/10.1021/jm0708533.

(27) Zinnhardt, B.; Viel, T.; Wachsmuth, L.; Vrachimis, A.; Wagner, S.; Breyholz, H.-J.; Faust, A.; Hermann, S.; Kopka, K.; Faber, C.; Dollé, F.; Pappata, S.; Planas, A. M.; Tavitian, B.; Schäfers, M.; Sorokin, L. M.; Kuhlmann, M. T.; Jacobs, A. H. Multimodal Imaging Reveals Temporal and Spatial Microglia and Matrix Metalloproteinase Activity after Experimental Stroke. *J. Cereb. Blood Flow Metab.* **2015**, *35* (11), 1711–1721. https://doi.org/10.1038/jcbfm.2015.149.

(28) Zinnhardt, B.; Pigeon, H.; Thézé, B.; Viel, T.; Wachsmuth, L.; Fricke, I. B.; Schelhaas, S.; Honold, L.; Schwegmann, K.; Wagner, S.; Faust, A.; Faber, C.; Kuhlmann, M. T.; Hermann, S.; Schäfers, M.; Winkeler, A.; Jacobs, A. H. Combined PET Imaging of the Inflammatory Tumor Microenvironment Identifies Margins of Unique Radiotracer Uptake. *Cancer Res.* **2017**, *77* (8), 1831–1841. https://doi.org/10.1158/0008-5472.CAN-16-2628.

(29) Nakashima, Y.; Plump, A. S.; Raines, E. W.; Breslow, J. L.; Ross, R. ApoE-Deficient Mice Develop Lesions of All Phases of Atherosclerosis throughout the Arterial Tree. *Arterioscler. Thromb. J. Vasc. Biol.* **1994**, *14* (1), 133–140. https://doi.org/10.1161/01.atv.14.1.133.

(30) Andrés-Manzano, M. J.; Andrés, V.; Dorado, B. Oil Red O and Hematoxylin and Eosin Staining for Quantification of Atherosclerosis Burden in Mouse Aorta and Aortic Root. *Methods Mol. Biol. Clifton NJ* **2015**, *1339*, 85–99. https://doi.org/10.1007/978-1-4939-2929-0_5.

(31) Karunakaran, D.; Geoffrion, M.; Wei, L.; Gan, W.; Richards, L.; Shangari, P.; DeKemp, E. M.; Beanlands, R. A.; Perisic, L.; Maegdefessel, L.; Hedin, U.; Sad, S.; Guo, L.; Kolodgie, F. D.; Virmani, R.; Ruddy, T.; Rayner, K. J. Targeting Macrophage Necroptosis for Therapeutic and Diagnostic Interventions in Atherosclerosis. *Sci. Adv.* **2016**, *2* (7), e1600224. https://doi.org/10.1126/sciadv.1600224.

(32) Ohshima, S.; Petrov, A.; Fujimoto, S.; Zhou, J.; Azure, M.; Edwards, D. S.; Murohara, T.; Narula, N.; Tsimikas, S.; Narula, J. Molecular Imaging of Matrix Metalloproteinase Expression in Atherosclerotic Plaques of Mice Deficient in Apolipoprotein e or Low-Density-Lipoprotein Receptor. *J. Nucl. Med. Off. Publ. Soc. Nucl. Med.* **2009**, *50* (4), 612–617. https://doi.org/10.2967/jnumed.108.055889.

(33) Tavakoli, S.; Razavian, M.; Zhang, J.; Nie, L.; Marfatia, R.; Dobrucki, L. W.; Sinusas, A. J.; Robinson, S.; Edwards, D. S.; Sadeghi, M. M. Matrix Metalloproteinase Activation Predicts Amelioration of Remodeling Following Dietary Modification in Injured Arteries. *Arterioscler. Thromb. Vasc. Biol.* **2011**, *31* (1), 102–109. https://doi.org/10.1161/ATVBAHA.110.216036.

(34) Zhang, J.; Nie, L.; Razavian, M.; Ahmed, M.; Dobrucki, L. W.; Asadi, A.; Edwards, D. S.; Azure, M.; Sinusas, A. J.; Sadeghi, M. M. Molecular Imaging of Activated Matrix Metalloproteinases in Vascular Remodeling. *Circulation* **2008**, *118* (19), 1953–1960. https://doi.org/10.1161/CIRCULATIONAHA.108.789743.

(35) Razavian, M.; Tavakoli, S.; Zhang, J.; Nie, L.; Dobrucki, L. W.; Sinusas, A. J.; Azure, M.; Robinson, S.; Sadeghi, M. M. Atherosclerosis Plaque Heterogeneity and Response to Therapy Detected by in Vivo Molecular Imaging of Matrix Metalloproteinase Activation. *J. Nucl. Med. Off. Publ. Soc. Nucl. Med.* **2011**, *52* (11), 1795–1802. https://doi.org/10.2967/jnumed.111.092379.

(36) Fujimoto, S.; Hartung, D.; Ohshima, S.; Edwards, D. S.; Zhou, J.; Yalamanchili, P.; Azure, M.; Fujimoto, A.; Isobe, S.; Matsumoto, Y.; Boersma, H.; Wong, N.; Yamazaki, J.; Narula, N.; Petrov, A.; Narula, J. Molecular Imaging of Matrix Metalloproteinase in Atherosclerotic Lesions: Resolution With Dietary Modification and Statin Therapy. *J. Am. Coll. Cardiol.* **2008**, *52* (23), 1847–1857. https://doi.org/10.1016/j.jacc.2008.08.048.

(37) Schäfers Michael; Riemann Burkhard; Kopka Klaus; Breyholz Hans-Jörg; Wagner Stefan; Schäfers Klaus P.; Law Marilyn P.; Schober Otmar; Levkau Bodo. Scintigraphic Imaging of Matrix Metalloproteinase Activity in the Arterial Wall In Vivo. *Circulation* **2004**, *109* (21), 2554–2559. https://doi.org/10.1161/01.CIR.0000129088.49276.83.

(38) Kiugel, M.; Hellberg, S.; Käkelä, M.; Liljenbäck, H.; Saanijoki, T.; Li, X.-G.; Tuomela, J.; Knuuti, J.; Saraste, A.; Roivainen, A. Evaluation of [68Ga]Ga-DOTA-TCTP-1 for the Detection of Metalloproteinase 2/9 Expression in Mouse Atherosclerotic Plaques. *Molecules* **2018**, *23* (12), 3168. https://doi.org/10.3390/molecules23123168.

(39) Emini Veseli, B.; Perrotta, P.; De Meyer, G. R. A.; Roth, L.; Van der Donckt, C.; Martinet, W.; De Meyer, G. R. Y. Animal Models of Atherosclerosis. *Eur. J. Pharmacol.* **2017**, *816*, 3–13. https://doi.org/10.1016/j.ejphar.2017.05.010.

(40) Müller, A.; Krämer, S. D.; Meletta, R.; Beck, K.; Selivanova, S. V.; Rancic, Z.; Kaufmann, P. A.; Vos, B.; Meding, J.; Stellfeld, T.; Heinrich, T. K.; Bauser, M.; Hütter,

J.; Dinkelborg, L. M.; Schibli, R.; Ametamey, S. M. Gene Expression Levels of Matrix Metalloproteinases in Human Atherosclerotic Plaques and Evaluation of Radiolabeled Inhibitors as Imaging Agents for Plaque Vulnerability. *Nucl. Med. Biol.* **2014**, *41* (7), 562–569. https://doi.org/10.1016/j.nucmedbio.2014.04.085.

(41) Newby, A. C. Metalloproteinases and Vulnerable Atherosclerotic Plaques. *Trends Cardiovasc. Med.* **2007**, *17* (8), 253–258. https://doi.org/10.1016/j.tcm.2007.09.001.

(42) Schierwagen, R.; Maybüchen, L.; Zimmer, S.; Hittatiya, K.; Bäck, C.; Klein, S.; Uschner, F. E.; Reul, W.; Boor, P.; Nickenig, G.; Strassburg, C. P.; Trautwein, C.; Plat, J.; Lütjohann, D.; Sauerbruch, T.; Tacke, F.; Trebicka, J. Seven Weeks of Western Diet in Apolipoprotein-E-Deficient Mice Induce Metabolic Syndrome and Non-Alcoholic Steatohepatitis with Liver Fibrosis. *Sci. Rep.* **2015**, *5*, 12931. https://doi.org/10.1038/srep12931.

(43) Duarte, S.; Baber, J.; Fujii, T.; Coito, A. J. Matrix Metalloproteinases in Liver Injury, Repair and Fibrosis. *Matrix Biol. J. Int. Soc. Matrix Biol.* **2015**, *0*, 147–156. https://doi.org/10.1016/j.matbio.2015.01.004.

(44) Dalvie, D.; Cosker, T.; Boyden, T.; Zhou, S.; Schroeder, C.; Potchoiba, M. J. Metabolism Distribution and Excretion of a Matrix Metalloproteinase-13 Inhibitor, 4-[4-(4-Fluorophenoxy)-Benzenesulfonylamino]Tetrahydropyran-4-Carboxylic Acid Hydroxyamide (CP-544439), in Rats and Dogs: Assessment of the Metabolic Profile of CP-544439 in Plasma and Urine of Humans. *Drug Metab. Dispos. Biol. Fate Chem.* **2008**, *36* (9), 1869–1883. https://doi.org/10.1124/dmd.108.022566.

(45) Kuzuya Masafumi; Nakamura Kae; Sasaki Takeshi; Wu Cheng Xian; Itohara Shigeyoshi; Iguchi Akihisa. Effect of MMP-2 Deficiency on Atherosclerotic Lesion Formation in

ApoE-Deficient Mice. *Arterioscler. Thromb. Vasc. Biol.* **2006**, *26* (5), 1120–1125. https://doi.org/10.1161/01.ATV.0000218496.60097.e0.

(46) Johnson, J. L.; George, S. J.; Newby, A. C.; Jackson, C. L. Divergent Effects of Matrix Metalloproteinases 3, 7, 9, and 12 on Atherosclerotic Plaque Stability in Mouse Brachiocephalic Arteries. *Proc. Natl. Acad. Sci. U. S. A.* **2005**, *102* (43), 15575–15580. https://doi.org/10.1073/pnas.0506201102.

(47) Van Wart, H. E.; Birkedal-Hansen, H. The Cysteine Switch: A Principle of Regulation of Metalloproteinase Activity with Potential Applicability to the Entire Matrix Metalloproteinase Gene Family. *Proc. Natl. Acad. Sci. U. S. A.* **1990**, *87* (14), 5578–5582. https://doi.org/10.1073/pnas.87.14.5578.

(48) Jackson, C. L. Defining and Defending Murine Models of Plaque Rupture. *Arterioscler. Thromb. Vasc. Biol.* **2007**, *27* (4), 973–977. https://doi.org/10.1161/01.ATV.0000261545.53586.f0.

2.11 Supplementary Information

2.11.1 Supplementary Figures and Schemes

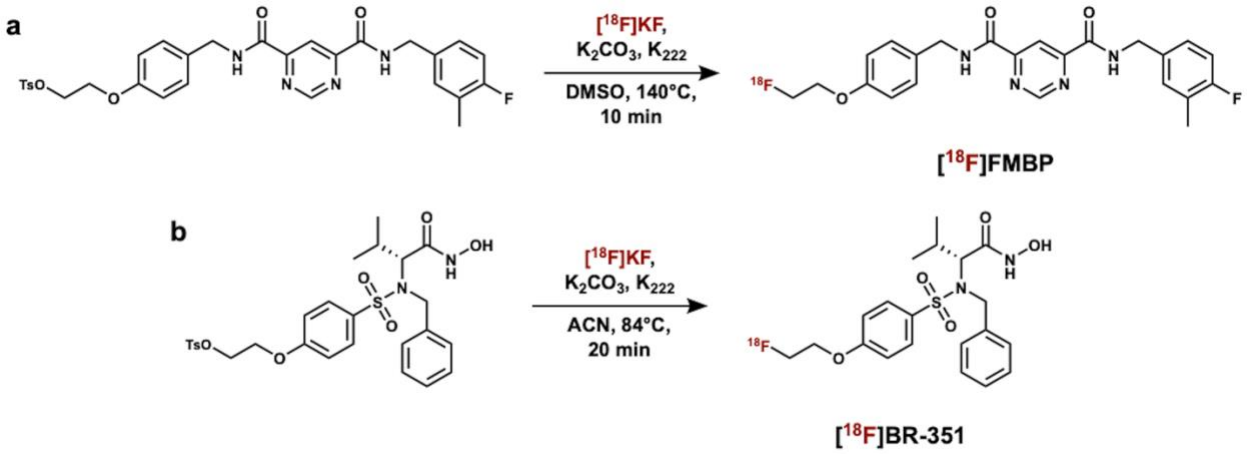

Supplemental Figure 1. Radiolabeling Schematic. (a) [^{18}F]FMBP and (b) [^{18}F]BR-351.

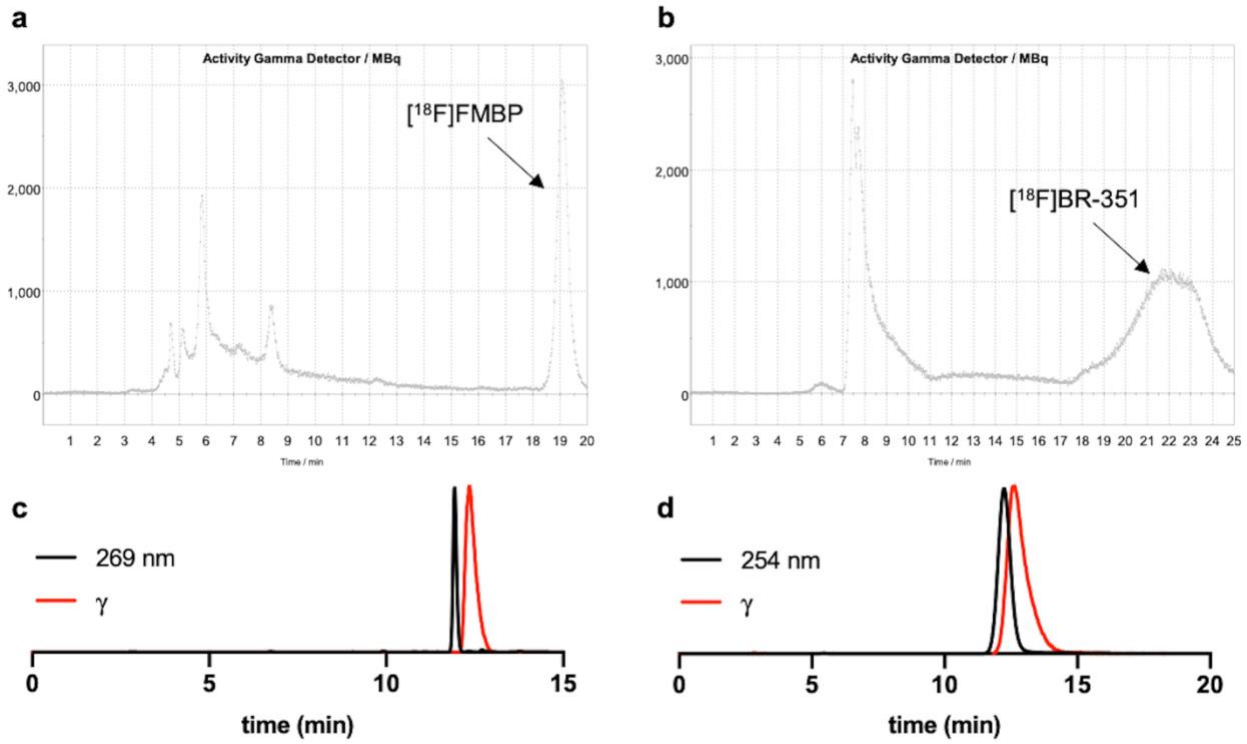

Supplemental Figure 2. Radiotracer purification and quality control. (a/b) Crude radio-HPLC chromatogram of radiolabeling reaction. (c/d) Coinjection with non-radioactive standard following isolation of (a) [^{18}F]FMBP and (b) [^{18}F]BR-351. UV and radiation detectors are connected in series.

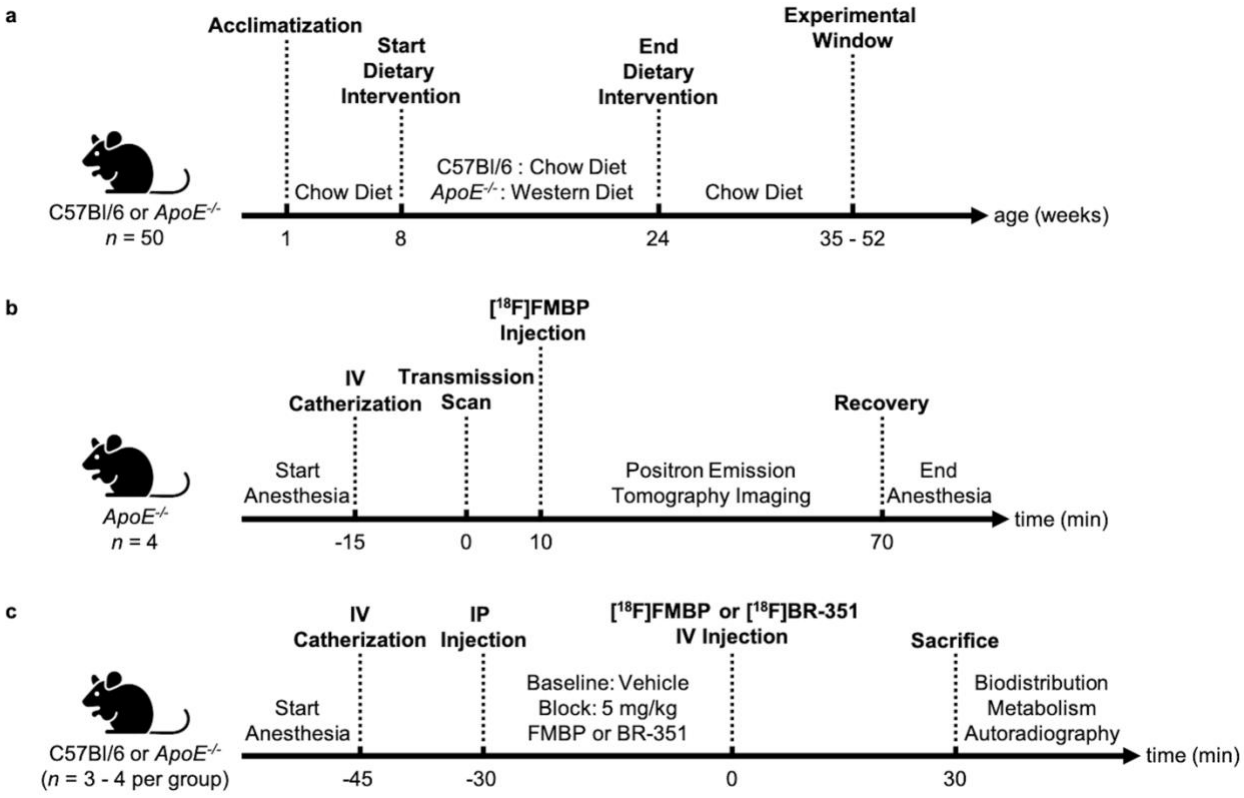

Supplemental Figure 3. Timeline of experiments. (a) Animal model dietary intervention (b) *In vivo* PET imaging (c) *Ex vivo* analyses.

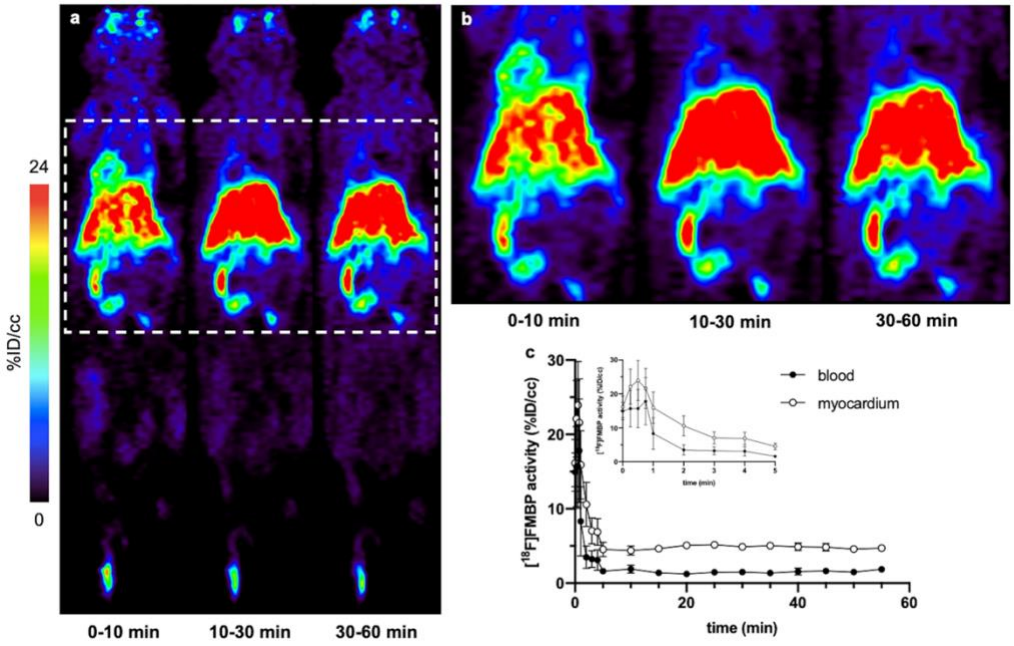

Supplemental Figure 4. *In vivo* [^{18}F]FMBP PET imaging in *ApoE*$^{-/-}$ mice. (a) Summed coronal whole-body PET images. (b) Magnified view within region of interest. (c) Mean [^{18}F]FMBP blood pool and myocardial time-activity curves derived from dynamic PET imaging (n = 4).

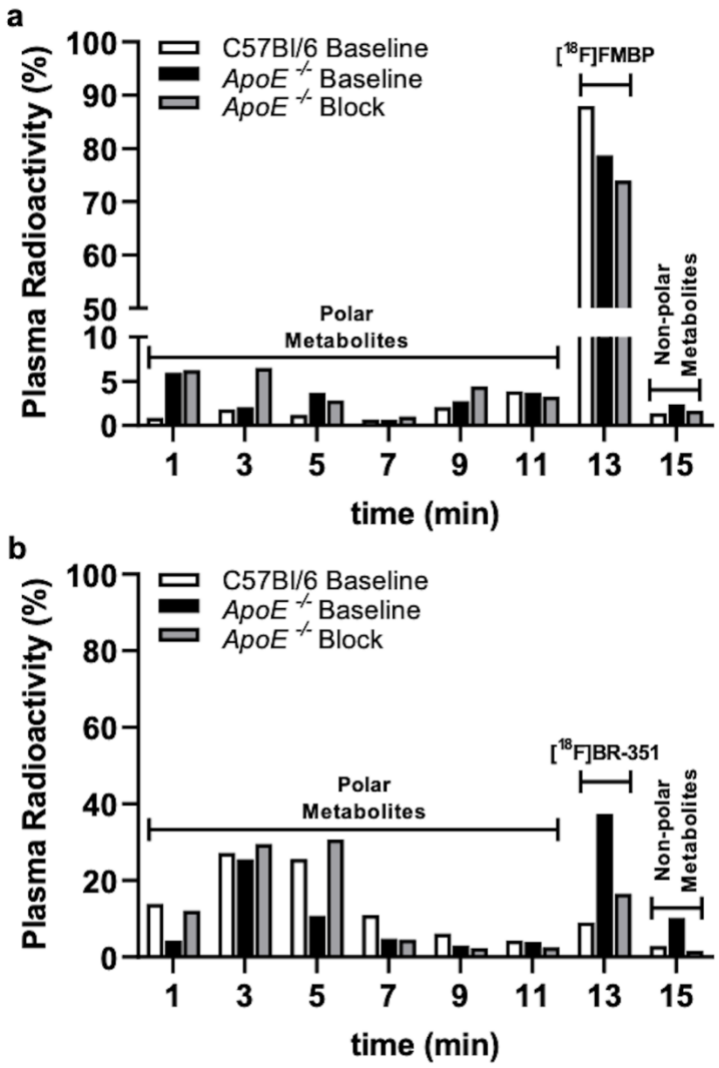

Supplemental Figure 5. Reconstructed fractional HPLC chromatograms of plasma radio-metabolites. Values represent the % of total plasma radioactivity obtained for pooled blood samples 30 min after intravenous administration of (a) [^{18}F]FMBP or (b) [^{18}F]BR-351 via the lateral tail vein (n = 2-3 per group).

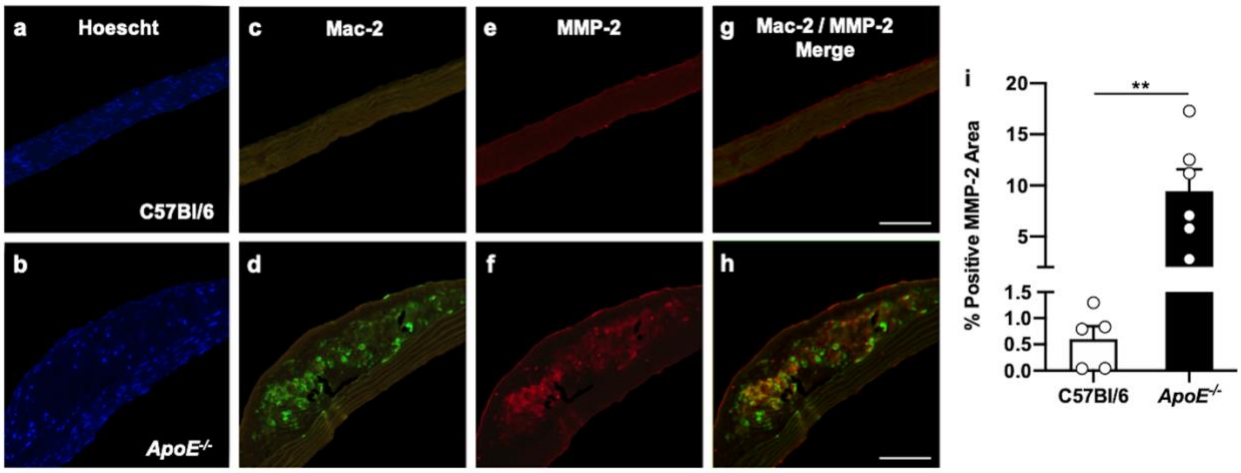

Supplemental Figure 6. Immunofluorescent staining of atherosclerotic lesions detected by [^{18}F]FMBP *ex vivo* autoradiography. Corresponding composite images of C57Bl/6 and *ApoE*$^{-/-}$ aortic *en face* cross-sections following immunofluorescent staining for (a/b) Hoescht, (c/d) Mac-2, and (e/f) MMP-2. (g/h) Mac-2 and MMP-2 merge. Scale bar = 100 µm. (i) Quantification of percentage positive MMP-2 areas in *ApoE*$^{-/-}$ and C57Bl/6 mice. Unpaired t-test: $^{**}P = 0.0048$, $n = 5$-6.

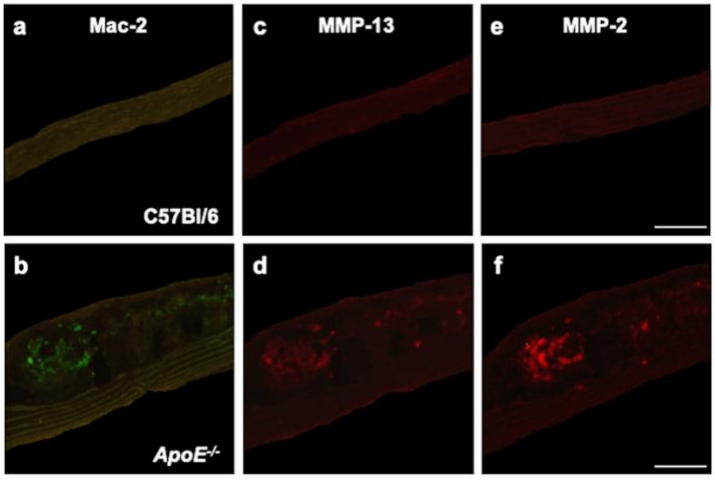

Supplemental Figure 7. Immunofluorescence signal specificity. Representative composite images of C57Bl/6 and *ApoE*$^{-/-}$ aortic *en face* cross-sections following immunofluorescent staining for (a/b) Mac-2, (c/d) MMP-13, and (e/f) MMP-2 with the corresponding isotype control antibody at an equivalent working concentration to the primary testing antibody.

2.11.2 Chemistry

Chemical reagents and solvents were obtained from commercial sources and used without further purification. Standards and precursors were prepared as previously described.[1,2] Compound characterization was completed by ^{1}H and ^{13}C NMR using a Bruker AVANCE III 400 or 600 MHz spectrometer and analyzed using MestReNova software.

2.11.3 Radiochemistry

General Radiochemical Methods

High molar activity no-carried-added aqueous [^{18}F]fluoride was prepared on a Siemens CTI Eclipse HP/RD Hybrid Cyclotron (11 MeV) via the ^{18}O(p,n)^{18}F nuclear reaction. Radiofluorination reactions were carried out on a GE TRACERlab FX2N automation system with TRACERlab FX software. In-line radio-HPLC purification was performed with a Phenomenex

Synergi Hydro-RP (C18, 80 Å, 10 μm, 250 mm × 10 mm) column. Radioactivity was quantified using a Biodex Atomlab 500 Dose Calibrator.

Synthesis of [^{18}F]FMBP and [^{18}F]BR-351

Radiochemical syntheses were adapted from the literature with minor modifications. [1,2] [^{18}F]Fluoride was captured from the [^{18}O]H_2O target solution using a Waters Sep-Pak Light Accell Plus QMA Cartridge (preconditioned with 10 mL EtOH, 10 mL water, 10 mL 0.5 M $NaHCO_3$, 10 mL water, and 1 mL air). Following [^{18}F]fluoride elution with $K_2CO_{3\,(aq)}$ ([^{18}F]FMBP: 0.05 M, 530 μL, 27 μmol or [^{18}F]BR-351: 0.075 M, 530 μL, 40 μmol), anhydrous ACN (1 mL) containing Kryptofix 2.2.2 ([^{18}F]FMBP: 22.4 mg, 60 μmol or [^{18}F]BR-351: 19 mg, 50 μmol) was dispensed into the reactor. The aqueous [^{18}F]K(K_{222})F solution was evaporated to dryness *in vacuo* (4 min at 80 °C without helium, 4 min at 60 °C with helium, and cooling to 35 °C with helium). The tosylate precursor ([^{18}F]FMBP: 4 mg, 6.8 μmol or [^{18}F]BR-351: 3 mg, 5.2 μmol), dissolved in anhydrous solvent ([^{18}F]FMBP: DMSO, 500 μL or [^{18}F]BR-351: ACN 1 mL), was added to the [^{18}F]K(K_{222})F residue and the reaction mixture was heated ([^{18}F]FMBP: 140 °C, 10 min or [^{18}F]BR-351: 84 °C, 20 min). The reaction was cooled to 40 °C, quenched with HPLC mobile phase (2 mL), loaded onto the HPLC loop, and purified by isocratic elution ([^{18}F]FMBP: 50/50, v/v, 0.1 M AMF/ACN, flow = 5 mL·min^{-1} or [^{18}F]BR-351: 55/45, v/v, 0.05 M NaOAc pH 5.5/EtOH, flow = 3 mL·min^{-1}). The product fraction ([^{18}F]FMBP: ~19 min or [^{18}F]BR-351: ~22 min) was collected in a bulk vessel pre-loaded with water (25 mL). The contents of the flask were transferred over a Waters Sep-Pak Plus Short C18 Cartridge (preconditioned with 1 mL EtOH, 5 mL water, and 1 mL air) and subsequently flushed with water (10 mL). The product was eluted with EtOH (1 mL) and diluted with saline (9 mL).

Quality Control Protocol

Radiochemical purity was determined using a Waters 2695 Alliance HPLC equipped with a Phenomenex Luna C18(2) (100 Å, 5 μm, 250 mm × 4.6 mm) column, a 996 Photodiode Array Detector (PerkinElmer), and a Carroll & Ramsey Associates 105-S high-sensitivity radiation detector. The following conditions were utilized for [^{18}F]FMBP: 80/20 for 2 minutes, linear gradient to 10/90 over 8 minutes , 10/90 for 2 minutes, linear gradient to 80/20 over 1 minute, 80/20 for 2 minutes, v/v, 0.1 M AMF/ACN, flow = 1 mL·min^{-1}, retention time: ~12 min and [^{18}F]BR-351: isocratic, 0-20 min: 55/45, v/v, 0.1 M AMF/ACN, flow = 1 mL·min^{-1}, retention time: ~11.5 min. Radiochemical product identity was confirmed by coinjection of the labeled compound and corresponding non-radioactive standard. Molar activity was determined by measurement of the UV absorbance of a known amount of radioactivity under identical HPLC conditions used to generate a calibration curve for the corresponding non-radioactive standard. All quality control was completed using Empower software.

PET Imaging Protocol

Mice (45 ± 2 g, n = 4) were anesthetized with 2-3% isoflurane, positioned in the PET scanner, and maintained under anesthesia during the imaging protocol. Following a transmission scan, animals were injected with [^{18}F]FMBP (5 MBq) as a bolus over 30 sec via intravenous lateral tail vein injection. The whole body was imaged for 60 min (4 × 15 sec frames; 4 × 1 min frames; 10 × 5 min frames). PET imaging was performed using a Siemens DPET scanner. Emission data were corrected for attenuation and scatter, then reconstructed using the 3D-OSEM/MAP algorithm. Volumetric regions of interest (ROIs) were drawn for the myocardium and cardiac blood pool. Uptake values obtained in nCi/cc were converted to %ID·cc^{-1} using the injected dose and presented as time-activity curves.

2.11.4 References

1. Hugenberg V, Wagner S, Kopka K, et al (2017) Radiolabeled Selective Matrix Metalloproteinase 13 (MMP-13) Inhibitors: (Radio)Syntheses and in Vitro and First in Vivo Evaluation. J Med Chem 60:307–321.
2. Wagner S, Breyholz H-J, Law MP, et al (2007) Novel Fluorinated Derivatives of the Broad-Spectrum MMP Inhibitors *N* -Hydroxy-2(*R*)-[[(4-methoxyphenyl)sulfonyl](benzyl)- and (3-picolyl)-amino]-3-methyl-butanamide as Potential Tools for the Molecular Imaging of Activated MMPs with PET. J Med Chem 50:5752–5764.

3.0 Chapter III - Quinazoline-2-Carboxamides as Selective PET Radiotracers for Matrix Metalloproteinase-13 Imaging in Atherosclerosis

Ariel Buchler,[1,2] Uzair S. Ismailani,[2,3] Nicole MacMullin,[2] Faduma Abdirahman,[1,2] Myriam Adi,[1,2] Christina Bi,[1,2] Catherine Jany,[2] Jeffrey W. Keillor,[1] Benjamin H. Rotstein[1,2,3]*

[1] Department of Chemistry and Biomolecular Sciences, University of Ottawa, Ottawa, Ontario, K1N 9B4, Canada.

[2] University of Ottawa Heart Institute, Ottawa, Ontario, K1Y 4W7, Canada.

[3] Department of Biochemistry, Microbiology and Immunology, University of Ottawa, Ottawa, Ontario, K1H 8M5, Canada

Correspondence: Benjamin H. Rotstein, PhD

University of Ottawa Heart Institute

40 Ruskin Street, H-5219

Ottawa, Ontario, Canada

K1Y 4W7

Phone: 613-696-7324

Email: benjamin.rotstein@uottawa.ca

Citation: Buchler A, Ismailani US, MacMullin N, Abdirahman F, Adi M, Bi C, Jany C, Keillor JW, Rotstein BH. "Quinazoline-2-Carboxamides as Selective PET Radiotracers for Matrix Metalloproteinase-13 Imaging in Atherosclerosis." *J. Med.Chem*. **2023**;66(10):6682-6696. doi: 10.1021/acs.jmedchem.2c02107.

3.1 Context

Initial evaluations of [^{18}F]FMBP demonstrated the capability to detect atherosclerotic mouse plaques *ex vivo* using an MMP-13 selective PET radiotracer with superior specificity and sensitivity to broad spectrum MMP imaging with [^{18}F]BR351. However, the significant retention of radioactivity observed in the liver and heart hindered non-invasive atherosclerotic plaque imaging and highlighted a need for new MMP-13 selective PET radiotracers with superior pharmacokinetics for vascular imaging. This prompted an exploration of the quinazoline-2-carboxamide core, representing the most potent and selective inhibitor scaffold reported to date, for MMP-13 PET radiotracer development in atherosclerosis.

3.2 Statement of the Manuscript

The manuscript entitled "Quinazoline-2-Carboxamides as Selective PET Radiotracers for Matrix Metalloproteinase-13 Imaging in Atherosclerosis" was published in the *Journal of Medicinal Chemistry* on May 25, 2023. In this chapter, I completed all the chemical synthesis and established automated radiosyntheses. I completed *in vitro* enzyme assays with assistance from Catherine Jany and Christina Bi. Uzair Ismailani performed all radiotracer productions and conducted *ex vivo* biodistributions with assistance from Nicole MacMullin and Myriam Adi. Faduma Abdirahman conducted radio-metabolite analyses. I conducted *ex vivo* aortic autoradiography and ORO staining. I performed all data analysis and interpreted the data with guidance from Dr. Benjamin Rotstein. I wrote the manuscript with editing from Dr. Benjamin Rostein. All authors approved the final version.

3.3 Abstract

Matrix metalloproteinase-13 (MMP-13) plays a critical role in the progression of unstable atherosclerosis. A series of highly potent and selective MMP-13 inhibitors were synthesized around a quinazoline-2-carboxamide scaffold to facilitate radiolabeling with fluorine-18 or carbon-11 positron-emitting nuclides and visualization of atherosclerotic plaques. *In vitro* enzyme inhibition assays identified 3 compounds as promising radiotracer candidates. Efficient automated radiosyntheses provided **[^{11}C]5b**, **[^{11}C]5f** and **[^{18}F]5j** and enabled pharmacokinetic characterization in atherosclerotic mice. The radiotracers displayed substantial differences in their distribution and excretion. Most favourably for vascular imaging, **[^{18}F]5j** exhibited low uptake in metabolic organs with minimal retention of myocardial radioactivity, substantial renal clearance, and high metabolic stability in plasma. *Ex vivo* aortic autoradiography and competition studies revealed that **[^{18}F]5j** specifically binds to MMP-13 within atherosclerotic plaques and localizes to lipid-rich regions. This study demonstrates the utility of the quinazoline-2-carboxamide scaffold for MMP-13 selective PET radiotracer development and identifies **[^{18}F]5j** for imaging atherosclerosis.

Keywords

matrix metalloproteinase-13, positron emission tomography, radiotracer, atherosclerosis, extracellular matrix, collagenase, aortic autoradiography

3.4 Introduction

Matrix metalloproteinases (MMPs) represent a family of zinc-containing endopeptidases that play a critical role in embryonic development, cell migration, and tissue remodeling by degradation of extracellular matrix proteins.[1,2] Although the catalytic domain of MMPs is highly conserved, these enzymes have several physiological roles and are classified based on their distinct substrate specificities and cellular localizations.[1–3] Typically, MMPs are secreted as zymogens whose activation is tightly controlled, while dysregulation of MMP activity is implicated in the pathogenesis of several inflammatory processes.[3–6] Given the functional diversity observed across the MMP family and their variable contribution to disease progression, selective targeting of individual MMPs is an advantageous approach for therapy and diagnosis.

MMP-13, also known as collagenase-3, is highly conserved among humans and mice and possesses substrate specificity for fibrillar collagen, a major component of the extracellular matrix that imparts biomechanical stability and tensile strength to connective tissues and vasculature.[7] Constitutive physiological expression of MMP-13 is restricted to skeletal tissue where it is secreted by chondrocytes and plays an important role in the development of growth plate cartilage and ossification.[8,9] Meanwhile, aberrant activation of MMP-13 is associated with the progression of osteoarthritis[10–12], breast cancer[13,14], and atherosclerosis.[15–18] Several preclinical studies have indicated that activation of MMP-13 within atherosclerotic plaques induces an unstable phenotype by decreasing fibrous cap thickness, reducing collagen content and organization, and hindering smooth muscle cell migration.[15,16] Densitometric analysis further revealed that MMP-13 was upregulated >5-fold in atheromatous compared with fibrous plaques and non-detectable in healthy arteries, supporting the potential for differentiation of stable and unstable forms of disease.[15] Additionally, deletion or selective inhibition of MMP-13 confers plaque stability.[17,18] Taken

together, these findings suggest that this enzyme represents a potential *in vivo* biomarker for molecular imaging by positron emission tomography (PET) that contributes to pathology and could enable early detection of unstable plaques prior to rupture and prevent subsequent acute ischemic events.

Currently, atherosclerosis imaging is most commonly conducted using [^{18}F]FDG and [^{18}F]NaF to detect inflammation and microcalcification within the vasculature.[19,20] Vascular [^{18}F]FDG imaging is hampered by the relatively indiscriminate nature of its signal and significant non-specific uptake in other metabolically active cells such as the myocardium, which restricts its utility to the carotid arteries.[21] In contrast, the feasibility of detecting coronary artery atherosclerosis has been successfully demonstrated with [^{18}F]NaF and appears highly promising for identification of culprit plaques.[21] Previously developed MMP-targeted radiotracers, including [^{99m}Tc]RYM-1[22,23] and [^{18}F]BR-351,[24,25] and therapeutic agents such as marimastat[26] are based on hydroxamate-containing inhibitors that coordinate the active site zinc(II) ion, common to all MMPs. However, considering that many clinical trials using broad-spectrum MMP inhibitors have been discontinued due to the onset of musculoskeletal syndrome attributed to inhibition of non-pathological MMPs, there is a clear need for inhibitors with improved selectivity.[27–29] Substantial efforts toward this end have uncovered several highly potent small molecule MMP-13 inhibitors that retain significant selectivity by exploiting structural differences in binding pockets adjacent to the active site.[30–40] Among them, inhibitors based on pyrimidine-dicarboxamide and quinazoline-2-carboxamide scaffolds are promising candidates for radiotracer development as they possess reliable handles for radiolabeling with fluorine-18 or carbon-11.

Our group recently substantiated the feasibility of detecting inflammatory plaques in mouse models of atherosclerosis with an MMP-13 selective PET radiotracer ([^{18}F]FMBP) derived from

the pyrimidine-dicarboxamide inhibitor class.[41] In this comparative evaluation, [^{18}F]FMBP exhibited substantially greater plaque uptake, improved sensitivity to atherosclerotic tissue, and displayed suitable specific binding relative to the aforementioned non-selective radiotracer, [^{18}F]BR-351. Nevertheless, significant challenges remain in quantifying atherosclerotic plaques non-invasively due to retention of radioactivity in the myocardium and liver, requiring alternative MMP-13 targeted radiotracers with improved pharmacokinetics for vascular imaging.

Lead compounds based on these scaffolds achieve their target affinity through hydrogen bonding interactions between their central scaffolds and amino acid residues Ala238, Leu239, Thr245, Thr247, and Met253 found within the S_1' specificity pocket (Figure 3.0).[30,32] Both pyrimidine- and quinazoline-based MMP-13 inhibitors adopt a U-shaped binding mode anchored by *N*-benzylamides occupying a hydrophobic pocket formed by Phe241 and His222. Meanwhile, selectivity is further improved by occupying the distal S_1'' side pocket, which is not observed among other MMPs.[32] In particular, the lead quinazoline-2-carboxamide compound originally reported by Nara *et al*. (herein entitled **5b**) features a carboxylate that extends deeply within the S_1'' side pocket, forming additional hydrogen bonding and ionic interactions with Asn215 and Lys140 and represents the most potent and selective MMP-13 inhibitor reported to date.[32] Additionally, this compound is metabolically stable *in vitro*, and possesses favourable clearance profiles across various species. As of yet, no quinazoline-based MMP-13 inhibitors have been radiolabeled and evaluated as imaging agents.[32]

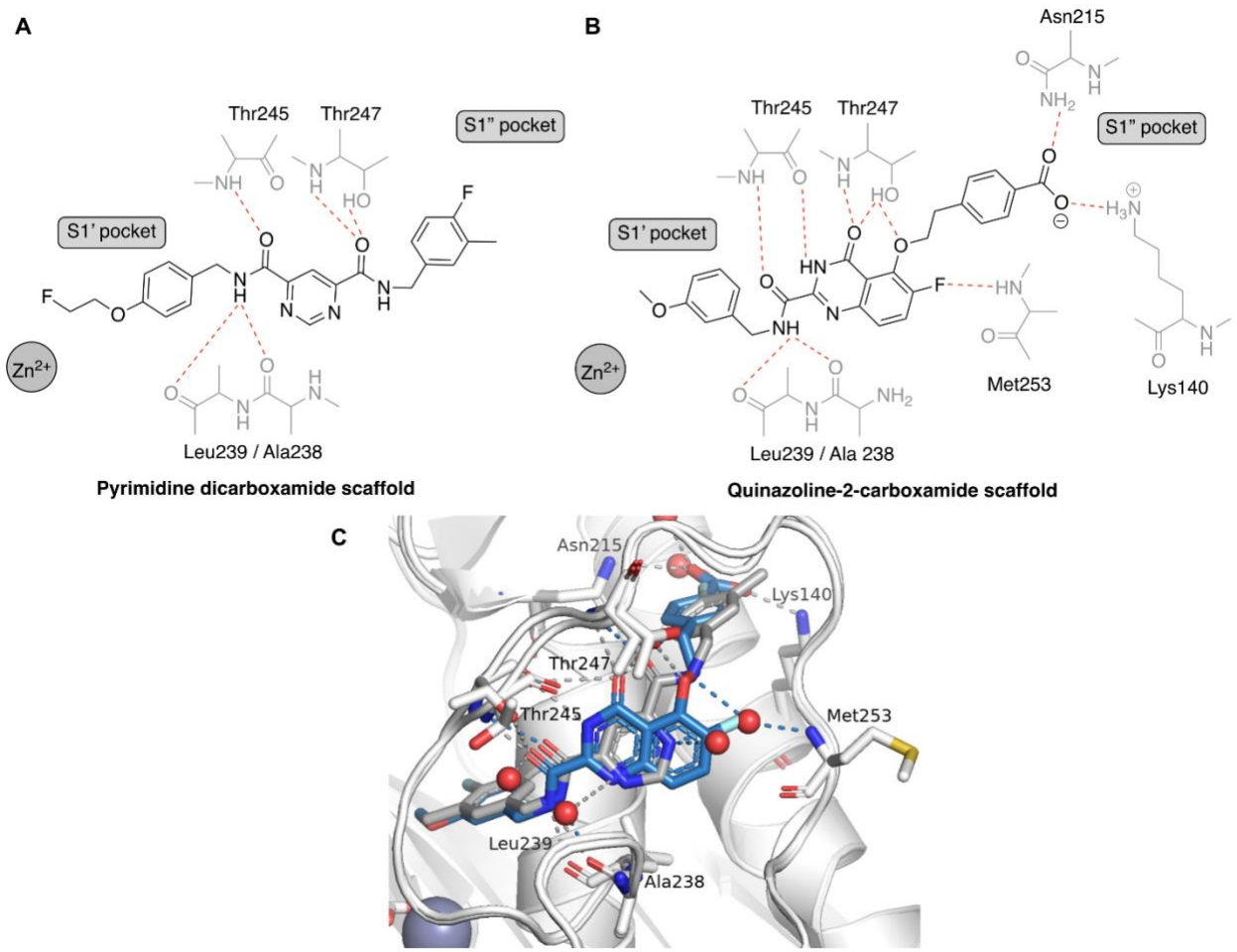

Figure 3.0 Putative binding mode of lead inhibitors with MMP-13. Hydrogen bonding and ionic interactions of (A) a pyrimidine dicarboxamide scaffold inhibitor and (B) quinazoline-2-carboxamide scaffold inhibitor (5b) within the S_1' and S_1'' pockets are indicated by dashed lines. (C) Overlay of FMBP and 5b binding modes to MMP-13. Adapted from MMP-13 – inhibitor complexes (PDB: 1XUD and 3WV1).

Here, we describe the development and evaluation of carbon-11 and fluorine-18 labeled MMP-13 selective PET radiotracers based on a quinazoline-2-carboxamide scaffold. To expand upon the structure-activity relationships of this inhibitor class, 10 novel compounds were generated by divergent synthesis with a particular focus on structural modifications that would enable late-

stage radiolabeling. An enzyme inhibition assay was employed to assess inhibitor potency and selectivity against related MMPs. Based on *in vitro* findings, three candidates including the original lead compound **5b**, were selected for radiolabeling and *in vivo* assessment in atherosclerotic *ApoE*$^{-/-}$ mice. Radiotracer pharmacokinetics were characterized by dynamic PET imaging, biodistribution, and plasma radio-metabolite analysis, while atherosclerotic plaque uptake was quantified by *ex vivo* autoradiography. The specificity of the radiotracer demonstrating the best *in vivo* performance was further assessed by homologous and heterologous pre-treatment experiments.

3.5 Results and Discussion

3.5.1 Synthesis of Quinazoline-2-carboxamide Inhibitors

The central quinazolinone scaffold **3** was obtained as previously outlined with minor modifications (Scheme 3.0).[32] Initially, *tert*-butyloxycarbonyl (Boc) protection of 3,4-difluoroaniline afforded compound **1** (84%). In the presence of 2 equivalents of *n*-butyllithium, ethyl chloroformate was selectively added at the 2-position to generate intermediate **2**, upon removal of the Boc group (64% over two steps). Under acidic conditions, a cyclization with ethyl cyanoformate formed the quinazoline scaffold **3** (73%), which represents a common intermediate with reactive handles for further conjugation.

Scheme 3.0 Synthesis of Ethyl 5,6-Difluoro-4-oxo-3,4-dihydroquinazoline-2-carboxylate (3)

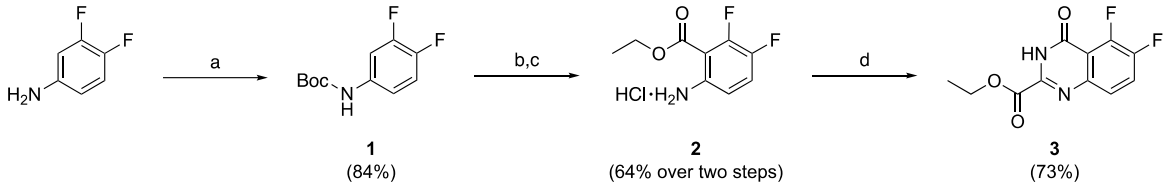

Reagents and conditions: (a) Boc_2O, THF, 60 °C, 16 h (b) *n*-BuLi, THF, -78 °C, 1 h, $ClCO_2Et$, THF, -78–0 °C, 1 h (c) 4 N HCl in dioxane, EtOAc, rt, 4 h (d) $NCCO_2Et$, 1 N HCl in AcOH, 80 °C, 3 h.

To investigate the functional group tolerance of the S_1' binding moiety, ethyl ester aminolysis of **3** was performed with several benzylamines to produce the amide intermediates **4a-d** (46-51%, Scheme 3.1). Higher benzylamine loadings improved conversion but also promoted nucleophilic aromatic substitution at the 5-position and by-products that were difficult to separate by chromatography. The 3-hydroxy- and 3-methoxy-substituted derivatives **4a** and **4b** represent intermediates toward the synthesis of phenolic precursor (**5a**) for subsequent radiolabeling with [^{11}C]iodomethane ([^{11}C]CH_3I) to obtain [^{11}C]**5b** and the corresponding standard compound (**5b**), respectively. The 4-methoxybenzyl and 4-fluoro-3-methylbenzyl intermediates **4c** and **4d** were synthesized on the basis of modifications that were well-tolerated for the pyrimidine-dicarboxamide inhibitor class.[25]

Scheme 3.1 Synthesis of Intermediates (4a-d) and 5-Substituted Derivatives (5a-k)

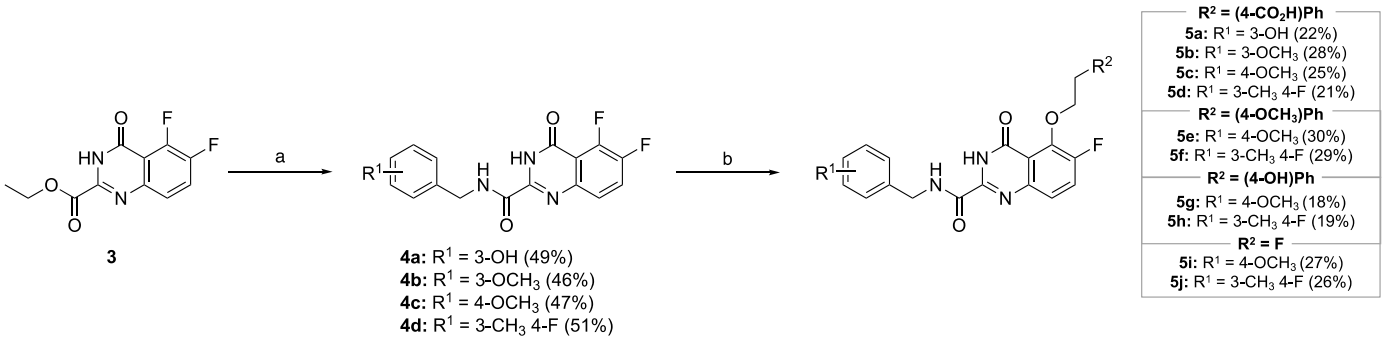

Reagents and conditions: (a) benzylamine, EtOH, 80 °C, 15 h; (b) alcohol, NaH, DMA, 80 °C, 1 h.

To further explore the structure-activity relationships of the S_1'' binding moiety, a divergent approach was employed based on nucleophilic aromatic substitution (S_NAr) at the quinazoline 5-fluoro position by various ethyl alcohols (18-30%, Scheme 3.1). Coupling of 4-(2-hydroxyethyl)benzoic acid afforded the carboxylic acid containing derivatives **5a-d**, which includes the original lead compound **5b** and the radiolabeling precursor **5a**. Replacement of the carboxylic acid with methoxy or hydroxyl groups was envisioned to circumvent potential liability for the organic anion transporter (OAT) and simultaneously represents a convenient strategy for radiolabeling with [^{11}C]CH_3I. Likewise, fluoroethyl derivatives **5i** and **5j** were proposed as alternatives amenable to radiofluorination of the corresponding tosylate precursors.

3.5.2 *In vitro* MMP Inhibition Assays

To establish inhibitor potency, the half-maximal inhibitory concentrations (IC_{50}) of all intermediates and 5-substituted derivatives were measured against activated MMP-13 (Table 3.0). Carboxamides **4** exhibit IC_{50} values in the 100 nM range, with the exception of 4-methoxy intermediate **4c**, which was ~3-fold less potent. In line with previous literature, substitutions at the

3-position are well tolerated with a preference toward smaller substituents at the 4-position, as demonstrated for the most potent 4-fluoro-3-methylbenzyl intermediate **4d**.[39] These trends persisted across the remaining derivatives with diminished potency among all compounds containing 4-methoxybenzylamine (**5c**, **5e**, **5g**, **5i**) and a marked improvement for compounds containing 4-fluoro-3-methylbenzylamine (**5d**, **5f**, **5h**, **5j**). Regarding the 5-substituted derivatives, the carboxylic acid containing compounds **5a**, **5b**, and **5d** were most potent and approached the lower limit of detection of the enzyme assay. Under the specified assay conditions, compound **5b** gave an IC_{50} of 1.3 ± 0.2 nM, which represents a ~100-fold increase in potency over the corresponding unsubstituted intermediate **4b** and highlights the contribution of the carboxylate-Lys140 ionic interaction within the S_1'' pocket. Although replacement of the carboxylic acid with methoxy or hydroxyl groups decreased potency, inhibitors **5f** and **5h** were nonetheless still potent, displaying IC_{50} values of 24 ± 1 nM and 12 ± 1 nM, respectively. Furthermore, removal of the arene as demonstrated for the fluoroalkyl derivative **5j** resulted in an IC_{50} of 16 ± 3 nM, comparable to that of the non-carboxylic acid containing derivatives. Taken together, these findings suggest that potent inhibition of MMP-13 can be achieved with quinazoline-2-carboxamides possessing an ethyl ether linkage at the 5-position, irrespective of the presence of an arene. Still, phenethyl derivatives that incorporate a strong hydrogen bond acceptor at the 4-position with sufficient size to deeply occupy the bottom of the S_1'' pocket and exploit the Lys140 interaction are optimal.

Table 3.0 MMP-13 Inhibitory Activity

Compound	R^1	R^2	MMP-13 IC_{50} (nM)[a]
4a	3-OH	-	149 ± 6
4b	3-OCH_3		118 ± 10
4c	4-OCH_3		313 ± 5
4d	3-CH_3 4-F		106 ± 8
5a	3-OH	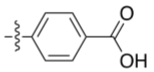	1.3 ± 0.1
5b	3-OCH_3		1.3 ± 0.2
5c	4-OCH_3		2.9 ± 0.5
5d	3-CH_3 4-F		1.2 ± 0.1
5e	4-OCH_3	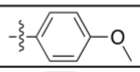	113 ± 5
5f	3-CH_3 4-F		24 ± 1
5g	4-OCH_3	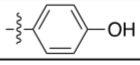	48 ± 7
5h	3-CH_3 4-F		12 ± 1
5i	4-OCH_3	F	127 ± 11
5j	3-CH_3 4-F		16 ± 3
FMBP		-	52 ± 5
Marimastat			2.0 ± 0.2

[a] Measured as the mean ± SEM from a single experiment performed in triplicate.

Using the pyrimidine-dicarboxamide based inhibitor FMBP as a benchmark (MMP-13 IC_{50}: 52 ± 5 nM), the selectivity profiles among inhibitors with greater MMP-13 potency were evaluated against MMP-1, -2, -8, -9, and -10 (Table 3.1). Remarkably, no appreciable inhibition of MMP-1, -2 or -9 was detected below 10 μM. Consistent with previous reports, collagenase MMP-8 and stromelysin MMP-10 represent the primary off-targets for this inhibitor class.[32] Among inhibitors with identical substituents at the 5-position, a significant decrease in MMP-13 selectivity was observed for derivatives containing 4-methoxybenzylamine (*i.e.*, **5c** and **5g**). Regarding modifications at the 5-position, the carboxylic acid and hydroxyl containing derivatives **5a-d** and **5h** displayed greater selectivity with respect to MMP-8 (IC_{50}: ≥1400 ± 200 nM), in comparison to the methoxyphenyl or fluoroalkyl derivatives **5f** and **5j** (IC_{50}: 780 ± 80 nM and 1200 ± 100 nM). While each of the synthesized compounds were highly selective against MMP-10 (IC_{50}: ≥2500 ± 300 nM), methoxyphenyl and hydroxyl containing derivatives **5f-h** (IC_{50}: ≥6800 ± 1000 nM) were least potent towards this off-target.

Table 3.1 MMP Selectivity Profiles

	IC_{50} (nM)[a]					
Compound	MMP-1	MMP-2	MMP-8	MMP-9	MMP-10	MMP-13 Fold Selectivity[c]
5a	$>10^4$	$>10^4$	2100 ± 160	$>10^4$	2800 ± 200	1600 ± 175
5b	$>10^4$	$>10^4$	2400 ± 130	$>10^4$	3200 ± 240	1800 ± 300
5c	$>10^4$	$>10^4$	1400 ± 140	$>10^4$	2700 ± 320	483 ± 96
5d	$>10^4$	$>10^4$	1700 ± 190	$>10^4$	2500 ± 220	1400 ± 200
5f	$>10^4$	$>10^4$	780 ± 80	$>10^4$	9100 ± 920	33 ± 3.4
5g	$>10^4$	$>10^4$	1500 ± 100	$>10^4$	6800 ± 980	32 ± 4.8
5h	$>10^4$	$>10^4$	2200 ± 240	$>10^4$	6900 ± 760	183 ± 25
5j	$>10^4$	$>10^4$	1200 ± 70	$>10^4$	3100 ± 400	75 ± 15
FMBP[b]	$>10^4$	$>10^5$	$>10^5$	$>10^5$	$>10^4$	>1900
Marimastat	1.0 ± 0.04	5.6 ± 0.2	1.3 ± 0.1	4.7 ± 0.2	69 ± 2.5	-

[a]Measured as the mean ± SEM from a single experiment performed in triplicate.

[b]FMBP IC_{50} values for MMP-2, -8, -9 obtained from the literature under similar assay conditions.[30]

[c]Fold selectivity calculated as a ratio of the MMP-13 IC_{50} / MMP-8 IC_{50} ± SEM.

In line with previous reports, the carboxylic acid containing inhibitor **5b** represented the most promising candidate of the quinazoline-2-carboxamide inhibitor class, with significantly greater potency and comparable MMP-13 selectivity to FMBP (1900 vs 1800 ± 300-fold).[32] However, as a potential substrate of the OAT, as discovered for several carboxylate-containing MMP-13 inhibitors[39,42], non-carboxylic acid derivatives were additionally synthesized. Moreover, in pursuit of optimizing radiotracer pharmacokinetics for vascular imaging, we hypothesized that evaluating structural diversity and varying lipophilicities would be informative. The remaining compounds retained adequate MMP-13 selectivity (32 ± 5 to 183 ± 25-fold) while simultaneously providing a robust strategy for radiolabeling with carbon-11 or fluorine-18. Taking these factors into consideration, compounds **5b**, **5f**, and **5j** were selected as candidates for radiolabeling and subsequent biological evaluations.

3.5.3 Synthesis of Fluorine-18 Radiolabeling Precursors (9 and 10)

We proposed to radiolabel **5j** by ^{18}F-fluorination of the corresponding tosylate precursor (Scheme 3.2). Initially, mono-tetrahydropyranyl (THP) protection of ethylene glycol was performed to afford 2-[(tetrahydro-2*H*-pyran-2-yl)oxy]ethan-1-ol (compound **6,** 79%).[43] The THP protecting group was selected for its stability under strongly basic conditions, as in the following S_NAr reaction, mediated by sodium hydride. Coupling of **6** to intermediate **4d** was conducted under identical conditions used for the formation of the 5-substituted derivatives **5a-j** to obtain compound **7** (75%). THP ether hydrolysis was achieved under mild conditions employing catalytic *para*-toluenesulfonic acid in methanol to yield compound **8** (75%). Tosylation of the resulting free alcohol was completed by activation of tosyl chloride with pyridine to give precursor **9** (84%). A DMF-aminal protection strategy was further employed to form an imidazolidine ring under Vilsmeier conditions and provide precursor **10** (85%).[32]

Scheme 3.2 Synthesis of the Fluorine-18 Radiolabeling Precursors (9 and 10)

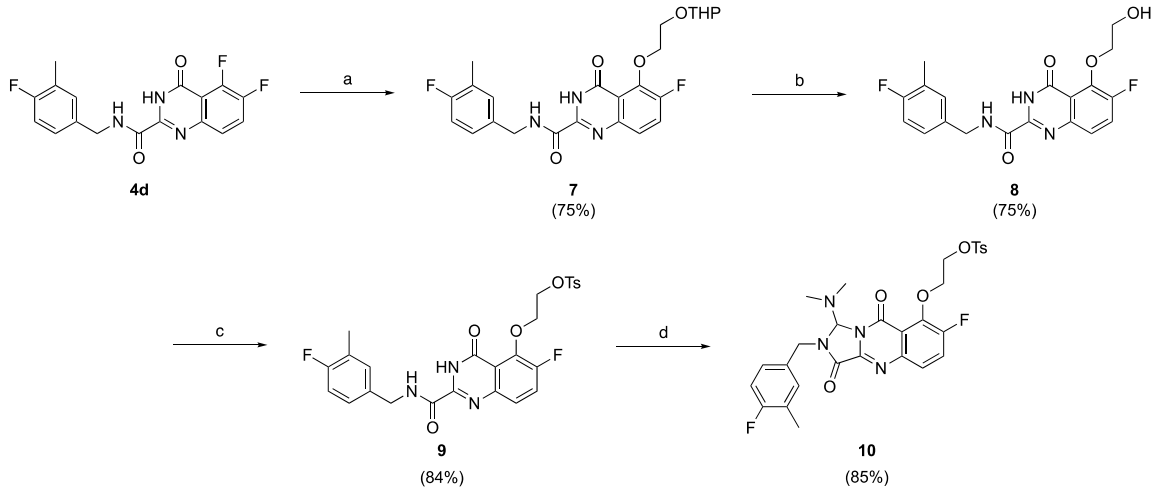

Reagents and conditions: (a) $HO(CH_2)_2OTHP$ (**6**), NaH, DMA, 80 °C, 1 h (b) TsOH, MeOH, rt, 1 h (c) TsCl, pyridine, 0 °C, 4 h (d) $(COCl)_2$, DMF, THF, 0 °C to rt, 2 h.

3.5.4 Radiolabeling Optimization

Radiolabeling of **5b** and **5f** was proposed by ^{11}C-methylation of the corresponding phenolic precursors **5a** and **5h** with [^{11}C]CH_3I (Table 3.2). Regioselective ^{11}C-methylation was achieved using predicted pK_a values and adjusting the equivalents of tetrabutylammonium hydroxide (TBAOH) required to deprotonate the desired phenol. For precursor **5a**, addition of 3 equivalents of TBAOH was expected to yield **[^{11}C]5b** in the presence of the unprotected carboxylic acid and pyrimidine ring system (Entry 1). Indeed, fewer equivalents of TBAOH was detrimental to selectivity (Entry 2) and additional equivalents did not appreciably improve radiochemical conversion (RCC, Entries 3 and 4). Maintaining this quantity of base, 80 °C afforded the highest conversion, with lower temperatures slowing reaction rates (Entry 5) and higher temperatures likely having deleterious effects on precursor stability (Entry 6). Prolonging the reaction time from 2 to 3 min led to a marginal improvement and optimally afforded **[^{11}C]5b** in 64% RCC (Entry 7). Applying the same approach for precursor **5h**, which lacks the carboxylic acid, 2 equivalents of TBAOH was predicted to deprotonate the desired phenol. Under the optimal conditions identified for the formation of **[^{11}C]5b** with 1 fewer equivalent of base, **[^{11}C]5f** was obtained in 69% RCC (Entry 1). Additional TBAOH led to selective formation of an unidentified side product (Entry 2). Radiochemical identities of **[^{11}C]5b** and **[^{11}C]5f** were confirmed using radio-HPLC by co-injection of unlabelled **5b** and **5f**, respectively (Figures S5 & S6).

Table 3.2 [^{11}C]5b and [^{11}C]5f Methylation Optimization

Entry	Prec.[a]	TBAOH (equiv.)	Temp. (°C)	Time (min)	RCC (%)
1	**5a**	3	80	2	59
2		2	80	2	10
3		3.5	80	2	61
4		4	80	2	61
5		3	60	2	35
6		3	100	2	32
7		3	80	3	64
1	**5h**	2	80	3	69
2		3			0

[a]10 mM precursor, 106 μL DMSO, dc. RCC determined by radio-HPLC (n = 1).

As previously indicated, formation of **[^{18}F]5j** was proposed by radiofluorination of the corresponding tosylate precursor **9** (Table 3.3). Initial attempts using K_2CO_3 and Kryptofix® (K_{222}) at varying concentrations were unsuccessful due to base-mediated precursor decomposition (Entry 1). To this end, weak bases such as tetrabutylammonium mesylate (Bu_4NOMs) and tetrabutylammonium triflate (Bu_4NOTf) were employed as recommended for base-sensitive scaffolds[44], but only afforded trace amounts of product (Entries 2 and 3). Attempts at radiofluorination of precursor **9** with the fewer equivalents of a moderately weak base such as tetraethylammonium bicarbonate (TEAB) proved to be more effective but yields remained insufficient (Entry 4). As an alternative strategy, precursor **10** was synthesized with a DMF-aminal protecting group to reduce base-sensitivity and improve reactivity towards [^{18}F]fluoride. Using 2 equivalents of TEAB, the DMF-protected **[^{18}F]5j** intermediate was optimally formed within 10 min in 59% RCC and slow progression thereafter (Entry 5). Lesser or greater quantities of TEAB had deleterious effects on RCC (Entries 6 and 7). Higher reaction temperatures caused product decomposition at prolonged reaction times (Entry 8). Quantitative deprotection was achieved with 6 M HCl at 100 °C for 10 min, as determined by the disappearance of the DMF-protected radio-

fluorinated intermediate and formation of **[^{18}F]5j**, confirmed by co-injection of unlabelled **5j** using radio-HPLC (Figure S7).

Table 3.3 [^{18}F]5j Fluorination Optimization

Entry	Prec.[a]	Base	Base equiv.	Temp. (°C)	RCC (%) 10 min	RCC (%) 20 min
1	**9**	K_2CO_3/K_{222}[b]	4 or 8	100	0	0
2		Bu_4NOMs	4 or 8	100	<1	<1
3		Bu_4NOTf	4 or 8	100	<1	<1
4		TEAB	2 or 4	100	2	2
5	**10**	TEAB	2	100	59	61
6			1	100	43	45
7			4	100	51	53
8			2	120	56	46

[a]13.5 mM precursor, 250 μL DMSO, RCC determined by radio-TLC (n = 1)

[b] 1:2.2 molar ratio of K_2CO_3:K_{222}

3.5.5 Radiotracer Automation, Formulation Stability and Lipophilicity

Automated radiosyntheses were developed for **[^{11}C]5b** and **[^{11}C]5f** using a Synthra MeIPlus Research module, while a two-step production of **[^{18}F]5j** was performed using the GE TRACERlab FX2 N (Figure 3.1). Radiotracers were labelled under the optimized conditions, purified with in-line semi-preparative HPLC, and reformulated in 10% EtOH/saline suitable for *in vivo* evaluation. **[^{11}C]5b** was obtained in radiochemical yields of 32 ± 2% (from [^{11}C]CH_3I) within 48 ± 2 min, >99% radiochemical purity, and a molar activity of 11 ± 2 GBq·μmol^{-1} at the end of synthesis (EoS) (n = 5). **[^{11}C]5f** was obtained in radiochemical yields of 35 ± 5 % (from [^{11}C]CH_3I) within 55 ± 10 min, >99% radiochemical purity, and a molar activity of 12 ± 3 GBq·μmol^{-1} at EoS (n = 6). **[^{18}F]5j** was obtained in radiochemical yields of 44 ± 3% within 92 ± 8 min, >99% radiochemical purity, and a molar activity of 53 ± 5 GBq·μmol^{-1} at EoS (n = 8). Radiotracer stability in formulation was assessed up to 75 min with no observable degradation during this period (Figure S9).

Radiotracer lipophilicity was assessed by determination of the octanol-PBS distribution coefficient (log*D*, n = 2). Due to the anionic nature of the carboxylate at physiological pH, **[^{11}C]5b** was least lipophilic (1.16 ± 0.03), while sequential increases were observed for **[^{18}F]5j** (3.09 ± 0.03) and **[^{11}C]5f** (3.76 ± 0.32) upon removal and replacement of the terminal arene, respectively.

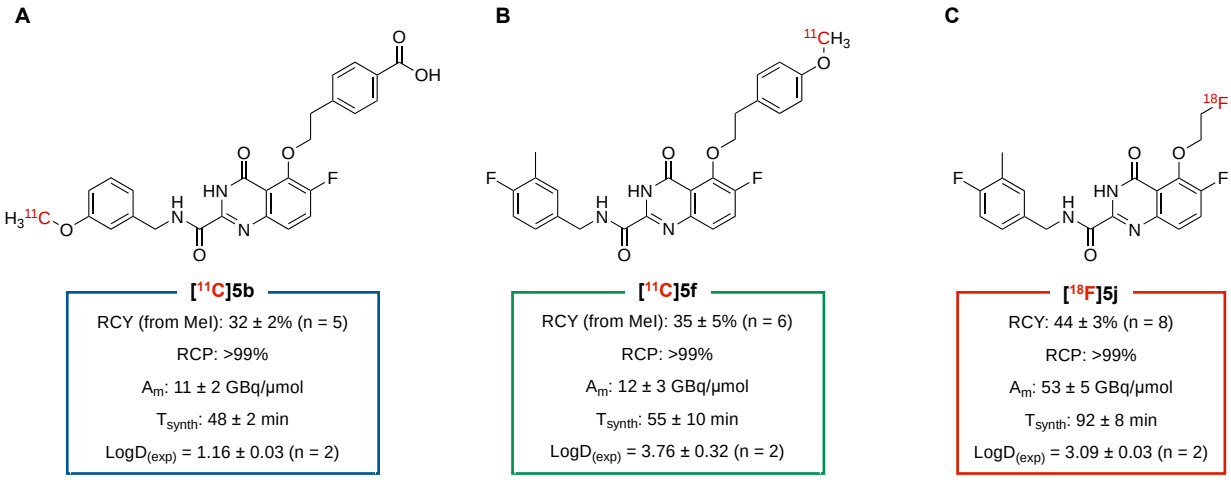

Figure 3.1 Chemical structures and automated radiosyntheses. (A) **[^{11}C]5b**, (B) **[^{11}C]5f**, (C) **[^{18}F]5j**.

3.5.6 Dynamic PET imaging and Radiotracer Kinetics

With the target radiotracers in hand, dynamic PET imaging was conducted over 60 minutes to establish *in vivo* pharmacokinetics in atherosclerotic *ApoE*$^{-/-}$ mice (Figure 3.2). Following intravenous administration, **[^{11}C]5b**, **[^{11}C]5f**, **[^{18}F]5j** cleared from the blood pool (t_{max} = 0.625 min) with prolonged washout after 30 minutes (Fig. 3.2B). Myocardial retention fell below 0.5 %ID·cc^{-1} for all 3 candidates and was greatly reduced relative to the first generation MMP-13 selective radiotracer [^{18}F]FMBP (~5 %ID·cc^{-1}). Low cardiac activity is an important property for reducing spillover and permitting quantification of the surrounding vasculature (Figures 3.2A & 3.2C). Uniquely, **[^{11}C]5b** immediately accumulated in the liver with peak uptake reaching 25.29

± 2.04 %ID·cc^{-1} (Figures 3.2A & 3.2D). Accelerated washout from the liver was subsequently observed with concomitant increase in intestinal uptake over the course of the scan, in accordance with a hepatobiliary excretion route (Figure 3.2A). In contrast to **[^{11}C]5b** and [^{18}F]FMBP, which is retained in the liver (~12 %ID·cc^{-1}), peak liver uptake of **[^{11}C]5f** and **[^{18}F]5j** reached 9.30 ± 1.33 %ID·cc^{-1} and 6.43 ± 0.08 %ID·cc^{-1}, respectively, with continual washout thereafter (Figures 3.2A & 3.2D). This marked decrease greatly reduces radioactivity in the thoracic cavity to facilitate vascular imaging and addresses a key limitation of MMP-13 targeted radiotracers based on a pyrimidine-dicarboxamide scaffold (Figure 3.2A).[30] Notably, peak kidney uptake of **[^{11}C]5b** reached 21.01 ± 1.48 %ID·cc^{-1} and was largely sustained without clearance into the bladder (Figures 3.2A & 3.2E). This suggests the possibility for OAT-mediated accumulation, as previously demonstrated for several carboxylic acid-containing MMP-13 selective inhibitors[39], and is consistent with the predominant expression of this transporter in renal proximal tubule cells.[42] Accordingly, the non-carboxylic acid derivatives **[^{11}C]5f** and **[^{18}F]5j** displayed distinct kinetics with peak kidney uptake reaching 7.40 ± 0.48 %ID·cc^{-1} and 4.42 ± 0.44 %ID·cc^{-1}, respectively, with substantial clearance over time (Figure 3.2E). Moreover, **[^{18}F]5j** preferentially exhibited renal clearance as demonstrated by urinary excretion (Figure 3.2A).

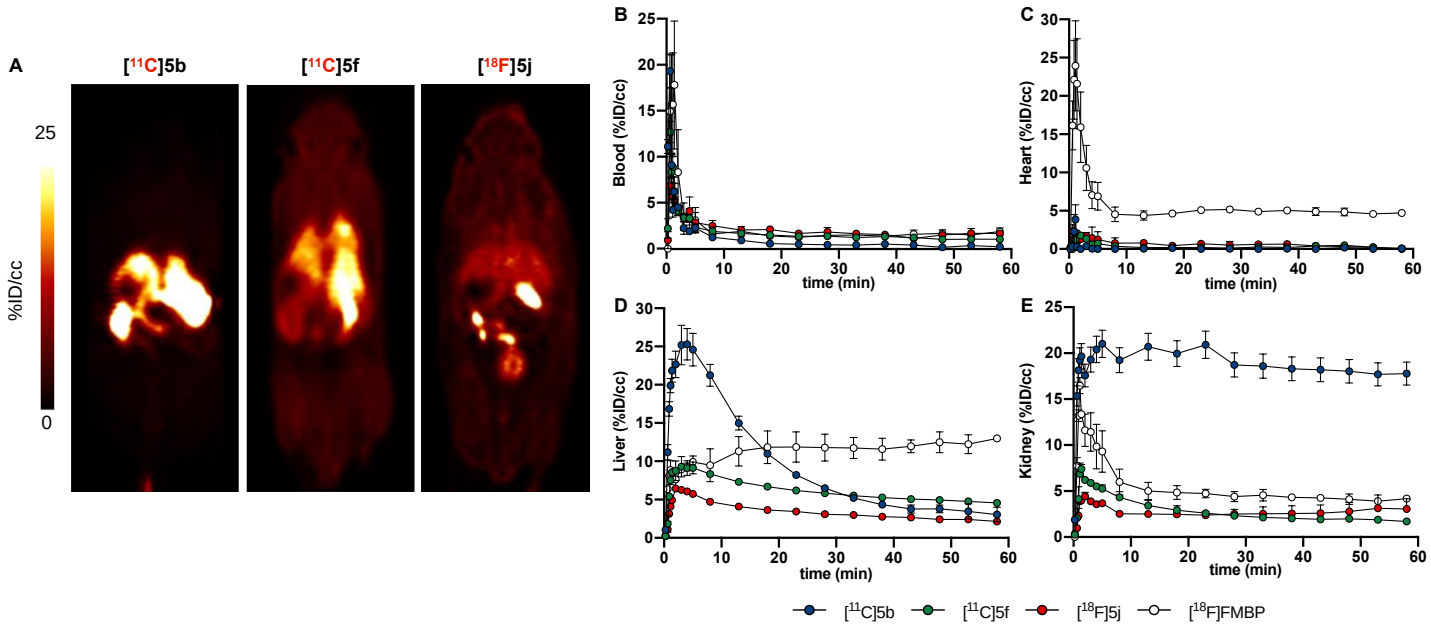

Figure 3.2 Radiotracer distribution in *ApoE*$^{-/-}$ mice. (A) Representative dynamic PET images (summed 0-60 minutes, coronal axis). (B-E) Comparative time-activity curves for the blood, heart, liver, and kidney (n = 2 per group).

3.5.7 Biodistribution and Plasma Metabolism

The biodistribution of each radiotracer was assessed by dissection at 30-minutes post-injection in *ApoE*$^{-/-}$ mice (Figure 3.3A). Consistent with *in vivo* findings, **[^{11}C]5b** rapidly cleared from the blood with 0.49 ± 0.20 %ID·g^{-1} remaining while **[^{11}C]5f** and **[^{18}F]5j** were relatively slower with 1.83 ± 0.19 %ID·g^{-1} and 3.28 ± 0.42 %ID·g^{-1}, respectively, at this timepoint (*P < 0.03). In a separate time-course experiment, **[^{18}F]5j** blood radioactivity continued to decrease between 30 and 60 minutes and stabilized thereafter (Figure S11). Minimal accumulation of myocardial activity was observed across all radiotracers with ~1 %ID·g^{-1} remaining. Regarding metabolic and excretory organs, **[^{11}C]5b** liver uptake was moderate at 7.29 ± 0.73 %ID·g^{-1} with predominant accumulation in the kidney and intestine at 30.95 ± 4.64 %ID·g^{-1} and 53.05 ± 5.95 %ID·g^{-1}, respectively. In contrast, **[^{11}C]5f** had significantly decreased uptake in the kidney and

intestine (<7 %ID·g^{-1}, **** $P < 0.0001$). **[^{18}F]5j** further displayed a significant reduction in liver uptake (3.32 ± 0.41 %ID·g^{-1}, ***$P < 0.0002$). Relatively low levels of radioactivity (~2 %ID·g^{-1}) were observed in all other measured organs except for the pancreas (**[^{11}C]5f**: 3.27 ± 1.12 %ID·g^{-1} and **[^{18}F]5j**: 2.14 ± 0.48 %ID·g^{-1}) and spleen (**[^{11}C]5b**: 2.11 ± 0.69 %ID·g^{-1}).

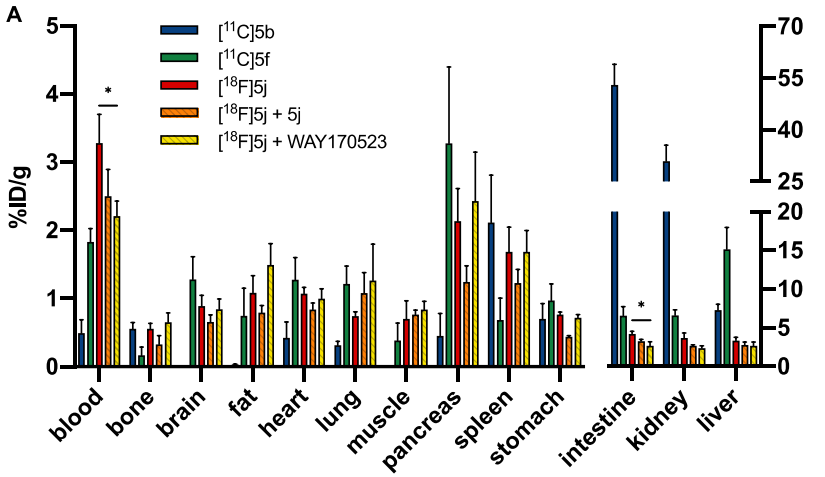

B

Fraction (%)	[^{11}C]5b	[^{11}C]5f	[^{18}F]5j	[^{18}F]5j + 5j	[^{18}F]5j + WAY170523
Parent Radiotracer	86 ± 3	70 ± 4	78 ± 3	78 ± 1	87± 2
Polar Metabolites	6 ± 3	22 ± 3	18 ± 4	21 ± 1	9 ± 1
Non-polar Metabolites	9 ± 1	8 ± 1	4 ± 1	2 ± 1	4 ± 1
Extraction Efficiency	91 ± 1	76 ± 2	92 ± 1	95 ± 1	92 ± 1

Figure 3.3 Radiotracer distribution and plasma stability in *ApoE*$^{-/-}$ mice. (A) Ex vivo biodistribution and (B) plasma radio-metabolite analysis 30 min after intravenous radiotracer administration. 2-way ANOVA: *$P < 0.039$. n = 4 for all groups except **[^{11}C]5f**, n = 6.

Considering the favourable distribution of **[^{18}F]5j**, additional blocking studies were conducted by pre-treatment with non-radioactive **5j** (2.5 mg/kg, IV) or WAY170523 (7.5 mg/kg, IV), a potent and selective commercially available MMP-13 inhibitor.[45,46] Only minor differences were measured upon homologous blocking with **5j**, although limited aqueous solubility restricted the administrable dose. Upon heterologous blocking with WAY170523, blood and intestinal radioactivity were significantly reduced by 33% and 36% (*$P < 0.04$) with no further differences in peripheral organs, reflecting low target expression in these tissues.

In parallel, radiotracer stability in plasma was also assessed at the same timepoint in *ApoE*$^{-/-}$ mice (Figure 3.3B). Radio-metabolite analysis revealed that all 3 tracers were largely intact with 70–86% of total plasma radioactivity representing the unmetabolized parent fraction after 30 minutes with an apparent dependence on lipophilicity. Remaining radioactivity was mainly attributed to polar radio-metabolites. No differences in **[^{18}F]5j** metabolism were detected under homologous blocking conditions, while a significant increase in the parent fraction was observed under heterologous blocking conditions (***P* = 0.003). This presumably suggests that homologous blocking did not saturate metabolic enzymes, while WAY170523 inhibited degradation or modification of **[^{18}F]5j**. The measured extraction efficiencies (≥76%) suggest representative sampling of plasma radioactivity.

3.5.8 Aortic Autoradiography and Oil Red O Staining

Considering the challenges associated with accurate non-invasive detection and quantification of aortic plaques in mice, *ex vivo* aortic autoradiography was employed to provide higher resolution images and enable histological colocalization (Figure 3.4). **[^{11}C]5b** did not accumulate in atherosclerotic plaques indicated by Oil Red O (ORO) positive lipid-rich regions as indicated by homogenous and comparatively low aortic uptake at 52.97 ± 9.83 %ID·m^{-2}. Conceivably, rapid excretion provides insufficient time for radiotracer circulation. Replacement of the carboxylic acid with a methyl ether, as for **[^{11}C]5f**, restored *in vivo* functionality as focal uptake could be detected in ORO positive regions, albeit with moderate uptake at 129.8 ± 42.05 %ID·m^{-2}. While the carboxylic acid has been shown to significantly drive *in vitro* target affinity and selectivity, this molecule is likely susceptible to OAT transport *in vivo* and is unsuitable as an MMP-13 targeted radiotracer for atherosclerosis. Most favourably, **[^{18}F]5j** displayed the highest overall uptake at 270.0 ± 8.06 %ID·m^{-2} and greatest co-localization to ORO positive regions. To

further assess the specificity of the signal, *in vivo* homologous and heterologous blocking was performed. Pre-treatment with non-radioactive **5j**, 15 minutes prior to intravenous radiotracer administration, resulted in a 23% decrease in aortic plaque uptake to 208.2 ± 13.27 %ID·m^{-2}, indicating an extent of saturable binding (*P = 0.047). Gratifyingly, pre-treatment with WAY170523 further reduced aortic plaque uptake by 36% to 173.4 ± 27.38 %ID·m^{-2}, providing evidence of specific binding to MMP-13 (**P = 0.0041).

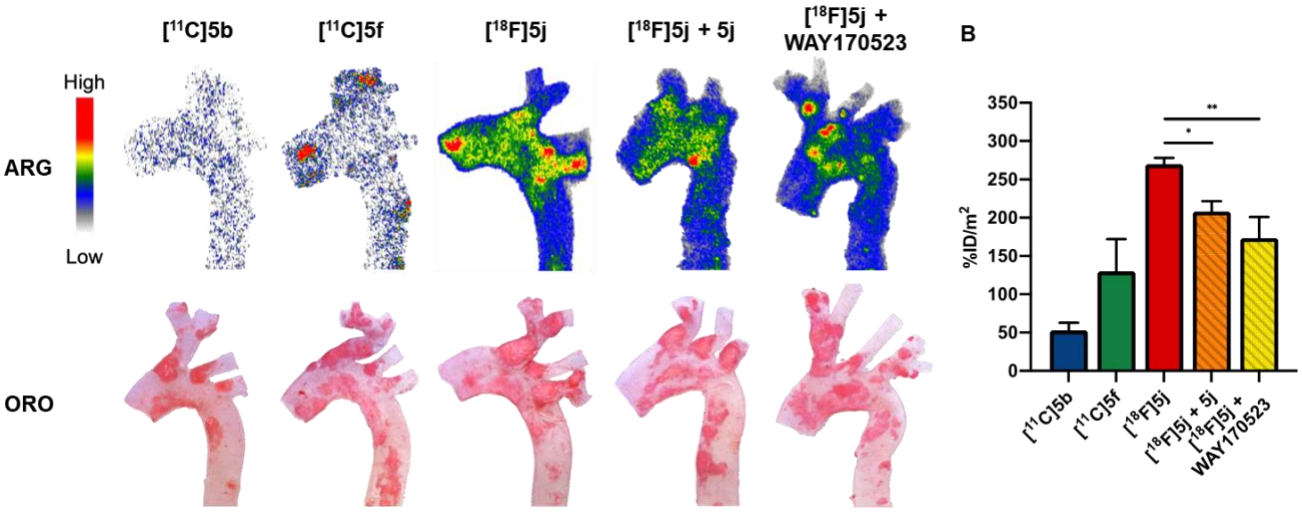

Figure 3.4 Autoradiography and Oil Red O (ORO) staining of *ApoE*$^{-/-}$ aortae. (A) Representative *ex vivo* aortic autoradiographs 30 min after intravenous radiotracer administration with corresponding ORO staining. (B) Aortic plaque uptake. 1-way ANOVA: **P = 0.0041, *P = 0.047. n = 4 per group except [^{18}F]5j, n = 5.

3.6 Conclusion

In the current study, we sought to develop and evaluate MMP-13 selective PET radiotracers based on quinazoline-2-carboxamide inhibitors for imaging extracellular matrix remodeling in atherosclerotic plaques. Several novel inhibitors were synthesized to further explore the structure-activity relationships of this class of molecules with an eye towards molecular imaging. *In vitro*

enzyme assays revealed that modifications within the S_1'-interacting arene are well tolerated, except for larger groups at the *para*-position. In line with other reports, a substantial increase in potency and selectivity can be achieved by occupying the S_1'' pocket with an ethyl ether linkage conjugated to the quinazoline scaffold at the 5-position. Most notably, phenethyl derivatives bearing a carboxylic acid at the 4-position are potent and selective *in vitro* as they can exploit an additional interaction with Lys140 at the bottom of the S_1'' pocket. However, these molecules can be substrates of the OAT *in vivo*, and alternative inhibitors were synthesized. Despite replacement of the carboxylic acid or removal of the terminal S_1''-interacting arene, these derivatives still retained significant MMP-13 potency and selectivity and facilitated late-stage radiolabeling. Based on these findings, high yielding automated radio-syntheses with carbon-11 and fluorine-18 were established for inhibitors **5b**, **5f,** and **5j** to enable *in vivo* assessments in atherosclerotic *ApoE*$^{-/-}$ mice and characterization of radiotracer pharmacokinetics.

Dynamic PET imaging and *ex vivo* biodistribution revealed that the carboxylic acid containing radiotracer **[^{11}C]5b** exhibited rapid hepatobiliary excretion with retention of radioactivity in the kidney, suggestive of OAT mediated transport. *Ex vivo* aortic autoradiography further revealed that **[^{11}C]5b** does not accumulate in atherosclerotic plaques, rendering it unsuitable as an MMP-13 targeted radiotracer for this application. In contrast, the non-carboxylic acid alternatives **[^{11}C]5f** and **[^{18}F]5j** exhibited vastly improved pharmacokinetic profiles with low uptake in metabolic organs, and minimal retention of radioactivity in the myocardium, addressing a previous limitation of first generation MMP-13 targeted radiotracers based on a pyrimidine-dicarboxamide scaffold. Most importantly, *in vivo* utility was restored as focal uptake of **[^{11}C]5f** and **[^{18}F]5j** could be detected in atherosclerotic plaques, with **[^{18}F]5j** displaying the highest overall uptake and greatest colocalization to lipid-rich ORO-positive regions. Furthermore, homologous

and heterologous MMP-13 blocking studies with **[^{18}F]5j** significantly reduced atherosclerotic plaque uptake, confirming specific target engagement. Overall, we have demonstrated that the quinazoline-2-carboxamide core represents an excellent scaffold for MMP-13 selective PET radiotracer development and identified **[^{18}F]5j** as a promising lead candidate which possesses favourable pharmacokinetics properties for vascular imaging. Future studies will focus on increasing inhibitor selectivity and reducing lipophilicity to improve the extent of specific binding and accelerate blood clearance.

3.7 Experimental Section

3.7.1 General Information

Chemical reagents and solvents were purchased from commercial sources and used without further purification. All moisture or air sensitive reactions were performed under inert atmosphere in flame dried glassware. Reaction progress was monitored by thin layer chromatography on silica gel-coated plates and visualized directly with UV light (254 and 280 nm) or following staining with a potassium permanganate solution. Products were purified by flash column chromatography using a Biotage Isolera One system. Compound identity was confirmed with a Magritek Spinsolve 80 MHz Spectrometer and characterization was completed by ^{1}H/^{13}C NMR with a Bruker AVANCE III 400 or 600 MHz spectrometer using DMSO-d_6 or $CDCl_3$ as a solvent (reference: 2.54 or 7.26 ppm) and analyzed using Mnova software. High resolution mass spectrometry data was acquired using a Waters Synapt G1, HRes and Ion Mobility, Time of Flight Mass Spectrometer or a Kratos Concept – Magnetic Sector Electron Impact Mass Spectrometer. All target compounds are >95% pure according to analysis using a Waters Xevo TQD with an Acquity UPLC H-Class Plus system.

3.7.2 Chemical Synthesis

*tert-Butyl N-(3,4-difluorophenyl)carbamate (**1**).* To a solution of 3,4-difluoroaniline (3.00 mL, 30.3 mmol, 1.0 equiv.) in anhydrous THF (30.0 mL) was added di-*tert*-butyl dicarbonate (7.65 mL, 33.3 mmol, 1.1 equiv.). The mixture was refluxed at 60 °C for 16 h. The solution was then cooled to room temperature and concentrated under reduced pressure. The residue was re-suspended in EtOAc and washed with 0.1 M HCl followed by saturated $NaHCO_3$. The organic layer was collected, dried over Na_2SO_4, filtered, and concentrated under reduced pressure. The residue was crystallized from hexanes to obtain the title compound as a white solid (5.85 g, 25.52 mmol, 84%). ^{1}H-NMR (80 MHz, $CDCl_3$): δ 7.57-7.28 (1H, ddd, J = 12.8, 7.2, 3.2 Hz), 7.24-6.78 (2H, m), 6.44 (1H, br), 1.51 (9H, s) ppm. HRMS (EI, m/z): $[M]^+$ calculated $C_{11}H_{13}F_2NO_2$ as 229.0914, found as 229.0899. Spectrum in accordance with literature.[47]

*Ethyl 6-amino-2,3-difluorobenzoate hydrochloride (**2**).* To a solution of **1** (3.89 g, 16.98 mmol, 1.0 equiv.) in anhydrous THF (38.6 mL), was added dropwise *n*-butyl lithium (1.6 M in hexane, 23.4 mL, 37.4 mmol, 2.2 equiv.) at -78 °C. The mixture was stirred at -78 °C for 1 h before a solution of ethyl chloroformate (1.79 mL, 18.72 mmol, 1.1 equiv.) in anhydrous THF (11.7 mL) was added dropwise over 30 min. The reaction was warmed to 0 °C and stirred for an additional 1 h. The reaction was then quenched by dropwise addition of saturated NH_4Cl (40 mL) and extracted with EtOAc. The combined organics were washed with brine, dried over Na_2SO_4, filtered, and concentrated under reduced pressure to obtain yellow oil. The crude product was utilized in the following reaction without further purification. To a solution of the yellow oil in EtOAc (7.57 mL) was added 4 N HCl in dioxane (30.3 mL). The mixture was stirred at room temperature for 4 h before diethyl ether was added and the precipitate was collected by filtration to obtain the title compound as a white solid (2.59 g, 10.90 mmol, 64% over 2 steps). ^{1}H-NMR (80 MHz, $(CD_3)_2SO$):

δ 8.16 (3H, br), 7.55-7.19 (1H, m), 6.72-6.53 (1H, ddd, J = 8.8, 4.0, 1.6 Hz), , 4.34 (2H, q, J = 7.2 Hz), 1.33 (3H, t, J = 7.2 Hz) ppm. ^{13}C-NMR (150 MHz, $(CD_3)_2SO$): δ 164.8, 149.2 (dd, J = 254, 14 Hz) 146.6, 141.2 (dd, J = 234, 14 Hz) 122.0 (dd, J = 19, 2 Hz), 118.6 (d, J = 19 Hz), 112.1, 60.9, 14.1 ppm. HRMS (EI, m/z): $[M]^+$ calculated $C_9H_9F_2NO_2$ as 201.0601, found as 201.0610.

*Ethyl 5,6-difluoro-4-oxo-3,4-dihydroquinazoline-2-carboxylate (**3**).* To a solution of **2** (2.59 g, 10.90 mmol, 1.0 equiv.) in 1 N HCl in acetic acid (52.0 mL) was added ethyl cyanoformate (1.18 mL, 11.94 mmol, 1.1 equiv.). The mixture was stirred at 80 °C for 3 h before removal of the solvent under reduced pressure. The residue was re-suspended in EtOH and the precipitate was collected by filtration. The solid was further washed with EtOH to obtain the title compound as a white solid (2.03 g, 7.99 mmol, 73%). ^{1}H-NMR (400 MHz, $(CD_3)_2SO$): δ 12.78 (1H, br), 8.05-7.98 (1H, m), 7.76-7.72 (1H, m), 4.42 (2H, q, J = 7.0 Hz), 1.38 (3H, t, J = 7.0 Hz) ppm. ^{13}C-NMR (600 MHz, $(CD_3)_2SO$): δ 159.8, 158.3, 148.4 (dd, J = 12.0, 246 Hz), 147.5 (dd, J = 15, 264 Hz), 144.8 (d, J = 1.5 Hz), 143.8 (d, J = 1.5 Hz), 125.2 (dd, J = 6.0, 7.5 Hz), 123.8 (d, J = 20 Hz), 113.9 (d, J = 3.0 Hz), 62.8, 13.9 ppm. HRMS (EI, m/z): $[M]^+$ calculated $C_{11}H_8F_2N_2O_3$ as 254.0503, found as 254.0522.

*5,6-Difluoro-N-[(3-hydroxyphenyl)methyl]-4-oxo-3,4-dihydroquinazoline-2-carboxamide (**4a**).* To a solution of **3** (363 mg, 1.43 mmol, 1.0 equiv.) in anhydrous EtOH (7.15 mL) was added 3-hydroxybenzylamine (264 mg, 2.15 mmol, 1.5 equiv.). The reaction mixture stirred at 80 °C for 15 h before removal of the solvent under reduced pressure. The residue was re-suspended in EtOAc and extracted with 0.1 M HCl. The combined organics were washed with brine, dried over Na_2SO_4, filtered, and concentrated under reduced pressure. The crude mixture was purified by column chromatography (10-50% EtOAc/hexane) to obtain the title compound as a white solid (232 mg, 0.70 mmol, 49%). ^{1}H-NMR (600 MHz, $(CD_3)_2SO$): δ 12.46 (1H, br), 9.51 (1H, t, J = 6.4 Hz), 9.36

(1H, s), 7.98-7.94 (1H, m), 7.63-7.60 (1H, m), 7.11-7.09 (1H, m), 6.76-6.74 (2H, m), 6.64-6.63 (1H, m), 4.38 (2H, d, J = 6.4 Hz) ppm. ^{13}C-NMR (150 MHz, $(CD_3)_2SO$): δ 159.1, 158.2, 157.4, 148.0 (dd, J = 11, 245 Hz), 147.6 (dd, J = 14, 263 Hz), 146.1, 144.7, 140.1, 129.3, 124.3, 123.6 (d, J = 19 Hz), 118.1, 114.3, 113.9, 113.6, 42.6 ppm. HRMS (EI, m/z): $[M]^+$ calculated $C_{16}H_{11}F_2N_3O_3$ as 331.0768, found as 331.0760.

5,6-Difluoro-N-[(3-methoxyphenyl)methyl]-4-oxo-3,4-dihydroquinazoline-2-carboxamide ***(4b)***. Following the procedure described for **4a**, compound **4b** was prepared from compound **3** and 3-methoxybenzylamine. The crude mixture was purified by column chromatography (10-40% EtOAc/hexane) to obtain the title compound as a white solid (314 mg, 0.91 mmol, 46%). ^{1}H NMR (600 MHz, $(CD_3)_2SO$): δ 9.26 (1H, t, J = 6.0 Hz), 7.62 - 7.59 (1H, m), 7.53 – 7.50 (1H, m), 7.28 – 7.25 (1H, m), 6.94 – 6.92 (2H, m), 6.85 – 6.83 (1H, m), 4.47 (2H, d, 6.0 Hz), 3.77 (3H, s) ppm. ^{13}C-NMR (150 MHz, $(CD_3)_2SO$): δ 168.8, 165.6, 159.3, 156.7, 149.4, 146.9 (dd, J = 14, 243 Hz), 145.3 (dd, J = 14, 240 Hz), 141.1, 129.3, 123.0 (dd, J = 3.0, 6.0 Hz), 119.9 (d, J = 18 Hz), 119.5, 113.4 (d, J = 3.0 Hz), 113.1, 112.1, 55.0, 42.5 ppm. HRMS (EI, m/z): $[M]^+$ calculated $C_{17}H_{13}F_2N_3O_3$ as 345.0925, found as 345.0916.

5,6-Difluoro-N-[(4-methoxyphenyl)methyl]-4-oxo-3,4-dihydroquinazoline-2-carboxamide ***(4c)***. Following the procedure described for **4a**, compound **4c** was prepared from compound **3** and 4-methoxybenzylamine. The crude mixture was purified by column chromatography (10-40% EtOAc/hexane) to obtain the title compound as a white solid (563 mg, 1.63 mmol, 47%). ^{1}H-NMR (600 MHz, $(CD_3)_2SO$): δ 12.43 (1H, br), 9.49 (1H t, J = 6.1 Hz), 7.98-7.93 (1H, m), 7.62-7.59 (1H, m), 7.28-7.26 (2H, m), 6.90-6.87 (2H, m), 4.39 (2H, d, J = 6.4 Hz), 3.72 (3H, s) ppm. ^{13}C-NMR (150 MHz, $(CD_3)_2SO$): δ 159.1, 158.4, 158.2, 147.9 (dd, J = 11, 245 Hz), 147.6 (dd, J = 14, 263

Hz), 146.2, 144.7, 130.7, 129.0, 124.3, 123.6 (d, J = 19 Hz), 113.7, 113.6, 55.1, 42.2 ppm. HRMS (EI, m/z): $[M]^+$ calculated $C_{17}H_{13}F_2N_3O_3$ as 345.0925, found as 345.0917.

*5,6-Difluoro-N-[(4-fluoro-3-methylphenyl)methyl]-4-oxo-3,4-dihydroquinazoline-2-carboxamide (**4d**).* Following the procedure for described **4a**, compound **4d** was prepared from compound **3** and 4-fluoro-3-methylbenzylamine. The crude mixture was purified by column chromatography (10-40% EtOAc/hexane) to obtain the title compound as a white solid (524 mg, 1.51 mmol, 51%). ^{1}H-NMR (600 MHz, $(CD_3)_2SO$): δ 12.48 (1H, s), 9.59 (1H, t, J = 6.2 Hz), 8.02-7.97 (1H, m), 7.66-7.64 (1H, m), 7.30-7.28 (1H, m), 7.24-7.21 (1H, m), 7.14-7.10 (1H, m), 4.45 (2H, d, J = 6.4 Hz), 2.25 (3H, d, J = 1.7 Hz) ppm. ^{13}C-NMR (150 MHz, $(CD_3)_2SO$): δ 159.8 (d, J = 241 Hz), 159.2, 158.2, 148.0 (dd, J = 11, 245 Hz), 147.7 (dd, J = 14, 263Hz), 146.1, 144.7, 134.6 (d, J = 3.4 Hz), 130.8 (d, J = 5.1 Hz), 126.9 (d, J = 8.1 Hz), 124.3, 123.9 (d, J = 17 Hz), 123.6 (d, J = 19 Hz), 114.7 (d, J = 22 Hz), 113.6, 42.1, 14.2 (d, J = 3.3 Hz) ppm. HRMS (EI, m/z): $[M]^+$ calculated $C_{17}H_{12}F_3N_3O_2$ as 347.0882, found as 347.0876.

*4-{2-[(6-Fluoro-2-{[(3-hydroxyphenyl)methyl]carbamoyl}-4-oxo-3,4-dihydroquinazolin-5-yl)oxy]ethyl}benzoic acid (**5a**).* To a solution of 4-(2-hydroxyethyl)benzoic acid (137 mg, 0.83 mmol, 1.5 equiv.) in anhydrous DMA (5.53 mL) was added sodium hydride (60% oil dispersion, 164 mg, 4.09 mmol, 7.5 equiv), and the mixture was stirred at room temperature for 30 min. Compound **4a** (181 mg, 0.55 mmol, 1.0 equiv.) was added and the mixture was stirred at 80 °C for 1 h. The reaction was cooled to room temperature, acidified with 0.1 M HCl to pH 3−4 and extracted with EtOAc. The combined organics were washed with brine, dried over Na_2SO_4, filtered, and concentrated under reduced pressure. The crude mixture was purified by preparative TLC (10% MeOH/DCM + 1% formic acid) to obtain the title compound as a white solid (58 mg, 0.12 mmol, 22%). ^{1}H-NMR (600 MHz, $(CD_3)_2SO$): δ 12.87 (1H, br), 12.19 (1H, br), 9.50 (1H, t,

J = 6.4 Hz), 9.39 (1H, br), 7.92-7.90 (2H, m), 7.84-7.81 (1H, m), 7.58-7.56 (1H, m), 7.51-7.49 (2H, m), 7.16-7.13 (1H,m), 6.80-6.77 (2H, m), 6.68-6.66 (1H, m), 4.43 (2H, d, J = 6.4 Hz), 4.36 (2H, t, J = 6.9 Hz), 3.23 (2H, t, J = 6.9 Hz) ppm. ^{13}C-NMR (150 MHz, $(CD_3)_2SO$): δ 167.3, 159.3, 158.8, 157.4, 153.8 (d, J = 245Hz), 145.3, 145.2, 145.1, 143.6, 140.1, 129.3, 129.1, 129.0, 128.9, 124.3, 123.1 (d, J = 22Hz), 118.2, 118.0, 114.2, 113.9, 75.2, 42.6, 35.7 ppm. HRMS (ESI+, m/z): calculated $[M+Na]^+$ $C_{25}H_{20}FN_3O_6Na$ as 500.1234, found as 500.1222.

*4-{2-[(6-Fluoro-2-{[(3-methoxyphenyl)methyl]carbamoyl}-4-oxo-3,4-dihydroquinazolin-5-yl)oxy]ethyl}benzoic acid (**5b**).* Following the procedure described for **5a**, compound **5b** was prepared from compound **4b** and 4-(2-hydroxyethyl)benzoic acid. The crude reaction mixture was purified by preparative TLC (10% MeOH/DCM + 1% formic acid) to obtain the title compound as a white solid (79 mg, 0.16 mmol, 28%). ^{1}H-NMR (600 MHz, $(CD_3)_2SO$): δ 12.86 (1H br), 12.18 (1H, s), 9.54 (1H, t, J = 6.4 Hz), 7.92-7.90 (2H, m), 7.84-7.81 (1H, m), 7.58-7.56 (1H, m), 7.51-7.49 (2H, m) 7.30-7.27 (1H, m), 6.95-6.94 (2H, m), 6.87-6.85 (1H, m), 4.48 (2H, d, J = 6.4 Hz), 4.35 (2H, t, J = 6.9 Hz), 3.77 (3H, s), 3.22 (2H, t, J = 6.9 Hz) ppm. ^{13}C-NMR (150 MHz, $(CD_3)_2SO$): δ 167.3, 159.4, 159.3, 158.8, 153.8 (d, J = 245Hz), 145.3, 145.2, 145.1, 143.6, 140.3, 129.4, 129.3, 129.2, 128.8, 124.3, 123.1 (d, J = 21 Hz), 119.6, 118.2, 113.3, 112.3, 75.2, 55.0, 42.6, 35.7 ppm. HRMS (ESI+, m/z): calculated $[M+Na]^+$ $C_{26}H_{22}FN_3O_6Na$ as 514.1390, found as 514.1412.

*4-{2-[(6-Fluoro-2-{[(4-methoxyphenyl)methyl]carbamoyl}-4-oxo-3,4-dihydroquinazolin-5-yl)oxy]ethyl}benzoic acid (**5c**).* Following the procedure described for **5a**, compound **5c** was prepared from compound **4c** and 4-(2-hydroxyethyl)benzoic acid. The crude reaction mixture was purified by preparative TLC (10% MeOH/DCM + 1% formic acid) to obtain the title compound as a white solid (36 mg, 0.073 mmol, 25%). ^{1}H-NMR (600 MHz, $(CD_3)_2SO$): δ 12.83 (1H, br),

12.12 (1H, br), 9.45 (1H, t, J = 6.1 Hz), 7.87-7.86 (2H, m), 7.79-7.76 (1H, m), 7.53-7.51 (1H, m), 7.46-7.45 (2H, m), 7.28-7.25 (2H, m), 6.90-6.87 (2H, m), 4.39 (2H, d, J = 6.4 Hz), 4.31 (2H, t, J = 6.9 Hz), 3.72 (3H, s), 3.17 (2H, t, J = 6.9 Hz) ppm. ^{13}C-NMR (150 MHz, $(CD_3)_2SO$): δ 167.3, 159.2, 158.8, 158.4, 153.8 (d, J = 244 Hz), 145.3, 145.2, 145.1, 143.6, 130.7, 129.3, 129.2, 129.0, 128.8, 124.2 (d, J = 6.8 Hz), 123.1 (d, J = 22 Hz), 118.2, 113.7, 75.2, 55.1, 42.1, 35.7 ppm. HRMS (ESI+, m/z): calculated $[M+Na]^+$ $C_{26}H_{22}FN_3O_6Na$ as 514.1390, found as 514.1387.

*4-{2-[(6-Fluoro-2-{[(4-fluoro-3-methylphenyl)methyl]carbamoyl}-4-oxo-3,4-dihydroquinazolin-5-yl)oxy]ethyl}benzoic acid (**5d**).* Following the procedure described for **5a**, compound **5d** was prepared from compound **4d** and 4-(2-hydroxyethyl)benzoic acid. The crude mixture was purified by preparative TLC (10% MeOH/DCM + 1% formic acid) to obtain the title compound as a white solid (30 mg, 0.061 mmol, 21%). ^{1}H-NMR (600 MHz, $(CD_3)_2SO$): δ 12.87 (1H, br), 12.18 (1H, br), 9.56 (1H, t, J = 6.0 Hz), 7.92-7.88 (2H, m), 7.85-7.81 (1H, m), 7.58-7.56 (1H, m), 7.51-7.49 (2H, m), 7.30-7.28 (1H, m), 7.24-7.22 (1H, m), 7.14-7.11 (1H, m), 4.46 (2H, d, J = 6 Hz), 4.36 (2H, t, J = 6 Hz), 3.22 (2H, t, J = 6 Hz), 2.26 (3H, d, J = 6 Hz) ppm. ^{13}C-NMR (150 MHz, $(CD_3)_2SO$): δ 167.3, 159.8 (d, J = 240 Hz), 159.4, 158.8, 153.8 (d, J = 245 Hz), 145.3, 145.2, 145.1, 143.6, 134.6 (d, J = 4.5 Hz), 130.8 (d, J = 6.0 Hz), 129.3, 129.2, 128.8, 126.8 (d, J = 9 Hz), 124.3 (d, J = 7.5 Hz), 123.9 (d, J = 17 Hz), 123.1 (d, J = 21 Hz), 118.2, 114.7 (d, J = 23 Hz), 75.2 (d, J = 1.5 Hz), 42.0, 35.8, 14.2 (d, J = 3.0 Hz) ppm. HRMS (ESI+, m/z): calculated $[M+Na]^+$ $C_{26}H_{21}F_2N_3O_5Na$ as 516.1347, found as 516.1365.

*6-Fluoro-5-[2-(4-methoxyphenyl)ethoxy]-N-[(4-methoxyphenyl)methyl]-4-oxo-3,4-dihydroquinazoline-2-carboxamide (**5e**).* Following the procedure described for **5a**, compound **5e** was prepared from compound **4c** and 2-(4-methoxyphenyl)ethanol. The crude mixture was purified by preparative TLC (20% EtOAc/hexane + 1% formic acid) to obtain the title compound

as a white solid (42 mg, 0.088 mmol, 30%). ^{1}H-NMR (600 MHz, $(CD_3)_2SO$): δ 12.10 (1H, br), 9.44 (1H, t, J = 6.4 Hz), 7.80-7.77 (1H, m), 7.52-7.50 (1H, m), 7.28-7.26 (2H, m), 7.23-7.20 (2H, m), 6.90-6.87 (2H, m), 6.85-6.82 (2H,m), 4.39 (2H, d, J = 6.4 Hz), 4.22 (2H, t, J = 7.3 Hz), 3.72 (3H, s), 3.71 (3H, s), 3.02 (2H, t, J = 7.3 Hz) ppm. ^{13}C-NMR (150 MHz, $(CD_3)_2SO$): δ 159.2, 158.8, 158.8, 158.4, 157.8, 153.8 (d, J = 244 Hz), 145.4, 145.3, 145.2, 130.7, 129.9, 129.8, 129.0, 124.1 (d, J = 7.5 Hz) 123.1 (d, J = 22Hz), 118.2, 113.7, 75.9, 55.1, 55.0, 42.1, 34.9 ppm. HRMS (ESI+, m/z): calculated $[M+Na]^+$ $C_{26}H_{24}FN_3O_5Na$ as 500.1598, found as 500.1602.

*6-Fluoro-N-[(4-fluoro-3-methylphenyl)methyl]-5-[2-(4-methoxyphenyl)ethoxy]-4-oxo-3,4-dihydroquinazoline-2-carboxamide (**5f**).* Following the procedure described for **5a**, compound **5f** was prepared from compound **4d** and 2-(4-methoxyphenyl)ethanol. The crude mixture was purified by preparative TLC (30% EtOAc/hexane + 1% formic acid) to obtain the title compound as a white solid (40 mg, 0.083 mmol, 29%). ^{1}H-NMR (600 MHz, $(CD_3)_2SO$): δ 12.10 (1H, s), 9.51 (1H, t, J = 6.2 Hz), 7.80-7.77 (1H, m), 7.53-7.51 (1H, m), 7.25-7.24 (1H, m), 7.23-7.20 (2H, m), 7.19-7.17 (1H, m), 7.09-7.06 (1H, m), 6.85-6.83 (2H, m), 4.41 (2H, d, J = 6.2 Hz), 4.22 (2H, t, J = 7.3 Hz), 3.71 (3H, s), 3.03 (2H, t, J = 7.3 Hz), 2.21 (3H, d, J = 1.7 Hz) ppm. ^{13}C-NMR (150 MHz, $(CD_3)_2SO$): δ 159.8 (d, J = 240 Hz), 159.4, 158.8, 157.8, 153.8 (d, J = 244 Hz), 145.4 (d, J = 14 Hz), 145.3, 145.2, 134.6 (d, J = 3.0 Hz), 130.8 (d, J = 4.5 Hz), 129.9, 129.8, 126.8 (d, J = 8.3 Hz), 124.1 (d, J = 7.0 Hz), 123.9 (d, J = 18 Hz), 123.1 (d, J = 21 Hz), 118.2, 114.7 (d, J = 23 Hz), 113.7, 75.9, 55.0, 42.0, 34.9, 14.2 (d, J = 3.0 Hz) ppm. HRMS (ESI+, m/z): calculated $[M+Na]^+$ $C_{26}H_{23}F_2N_3O_4Na$ as 502.1554, found as 502.1581.

*6-Fluoro-5-[2-(4-hydroxyphenyl)ethoxy]-N-[(4-methoxyphenyl)methyl]-4-oxo-3,4-dihydroquinazoline-2-carboxamide (**5g**).* Following the procedure described for **5a**, compound **5g** was prepared from compound **4c** and 2-(4-hydroxyphenyl)ethanol. The crude mixture was purified

by preparative TLC (30% EtOAc/hexane + 1% formic acid) to obtain the title compound as a white solid (24mg, 0.052 mmol, 18%). ^{1}H-NMR (600 MHz, $(CD_3)_2SO$): δ 12.09 (1H, br), 9.44 (1H, t, J = 6.4 Hz), 9.19 (1H, s), 7.80-7.77 (1H, m), 7.52-7.50 (1H, m), 7.28-7.26 (2H, m), 7.09-7.07 (2H, m), 6.89-6.88 (2H, m), 6.67-6.65 (2H, m), 4.39 (2H, d, J = 6.4 Hz), 4.18 (2H, t, J = 7.4 Hz), 3.72 (3H, s), 2.97 (2H, t, J = 7.4 Hz) ppm. ^{13}C-NMR (150 MHz, $(CD_3)_2SO$): δ 159.2, 158.8, 158.4, 155.7, 153.8 (d, J = 244 Hz), 145.4, 145.3, 145.3, 130.7, 129.8, 129.0, 127.8, 124.1 (d, J = 7.2 Hz), 123.1 (d, J = 21 Hz), 118.2, 115.1, 113.7, 76.1, 55.1, 42.1, 35.0 ppm. HRMS (ESI+, m/z): calculated $[M+Na]^+$ $C_{25}H_{22}FN_3O_5Na$ as 486.1441, found as 486.1452.

*6-Fluoro-N-[(4-fluoro-3-methylphenyl)methyl]-5-[2-(4-hydroxyphenyl)ethoxy]-4-oxo-3,4-dihydroquinazoline-2-carboxamide (**5h**).* Following the procedure described for **5a**, compound **5h** was prepared from compound **4d** and 2-(4-hydroxyphenyl)ethanol. The crude reaction mixture was purified by preparative TLC (30% EtOAc/hexane + 1% formic acid) to obtain the title compound as a white solid (26 mg, 0.056 mmol, 19%). ^{1}H-NMR (600 MHz, $(CD_3)_2SO$): δ 12.10 (1H, br), 9.51 (1H, t, J = 6.3 Hz), 9.19 (1H, s), 7.80-7.77 (1H, m), 7.52-7.51 (1H, m), 7.25-7.23 (1H, m), 7.20-7.17 (1H, m), 7.09-7.06 (3H, m), 6.67-6.65 (2H, m), 4.41 (2H,d, J = 6.4 Hz), 4.18 (2H, t, J = 7.4 Hz), 2.97 (2H, t, J = 7.4 Hz), 2.21 (3H, d, J = 1.8 Hz) ppm. ^{13}C-NMR (150 MHz, $(CD_3)_2SO$): δ 159.8 (d, J = 240 Hz), 159.4, 158.8, 155.8, 153.8 (d, J = 244 Hz), 145.4, 145.3, 145.2 134.6 (d, J = 3.4 Hz), 130.8 (d, J = 5.3 Hz), 129.8, 127.8, 126.8 (d, J = 7.9 Hz) 124.1 (d, J = 7.0 Hz), 123.9 (d, J = 17 Hz), 123.1 (d, J = 21 Hz), 118.2, 115.1, 114.7 (d, J = 22 Hz), 76.1, 42.0, 34.9, 14.2 (d, J = 3.2 Hz) ppm. HRMS (ESI+, m/z): calculated $[M+Na]^+$ $C_{25}H_{21}F_2N_3O_4Na$ as 488.1398, found as 488.1419.

*6-Fluoro-5-(2-fluoroethoxy)-N-[(4-methoxyphenyl)methyl]-4-oxo-3,4-dihydroquinazoline-2-carboxamide (**5i**).* Following the procedure described for **5a**, compound **5i** was prepared from compound **4c** and 2-fluoroethanol. The crude mixture was purified by preparative TLC (20% EtOAc/hexane + 1% formic acid) to obtain the title compound as a white solid (30 mg, 0.077 mmol, 27%). ^{1}H-NMR (600 MHz, $(CD_3)_2SO$) δ 12.16 (1H, br), 9.45 (1 H, t, J = 6.2 Hz), 7.83-7.80 (1H, m), 7.56-7.54 (1H, m), 7.28-7.26 (2H, m), 6.90-6.87 (2H, m), 4.78-4.69 (2H, m), 4.39 (2H, d, J = 6.4 Hz), 4.36-4.30 (2H, m), 3.72 (3H, s) ppm. ^{13}C-NMR (150 MHz, $(CD_3)_2SO$): δ 159.2, 158.8, 158.4, 153.8 (d, J = 245 Hz), 145.3, 145.2, 145.1, 130.7, 129.0, 124.5 (d, J = 7.5 Hz), 123.1 (d, J = 22 Hz), 118.1, 113.7, 83.1 (d, J = 166 Hz), 74.4 (d, J = 18 Hz), 55.1, 42.1 ppm. HRMS (ESI+, m/z): calculated $[M+Na]^+$ $C_{19}H_{17}F_2N_3O_4Na$ as 412.1085, found as 412.1098.

*6-Fluoro-N-[(4-fluoro-3-methylphenyl)methyl]-5-(2-fluoroethoxy)-4-oxo-3,4-dihydroquinazoline-2-carboxamide (**5j**).* Following the procedure described for **5a**, compound **5j** was prepared from compound **4d** and 2-fluoroethanol. The crude mixture was purified by preparative TLC (20% EtOAc/hexane + 1% formic acid) to obtain the title compound as a white solid (29 mg, 0.074 mmol, 26%). ^{1}H-NMR (600 MHz, $(CD_3)_2SO$): δ 12.17 (1H, s), 9.52 (1H, t, J = 6.2 Hz), 7.84-7.80 (1H, m), 7.56-7.54 (1H, m), 7.25-7.24 (1H, m), 7.20-7.17 (1H, m), 7.09-7.06 (1H, m), 4.78-4.69 (2H, m), 4.41 (2H, d, J = 6.4 Hz), 4.36-4.30 (2H, m), 2.21 (3H, d, J = 1.7 Hz) ppm. ^{13}C-NMR (150 MHz, $(CD_3)_2SO$): δ 159.8 (d, J = 240 Hz), 159.4, 158.8, 153.8 (d, J = 245 Hz), 145.3, 145.2, 145.0 (d, J = 14 Hz), 134.6 (d, J = 3.3 Hz), 130.8 (d, J = 4.7 Hz), 126.8 (d, J = 8.3 Hz), 124.5 (d, J = 6.5 Hz), 123.9 (d, J = 17 Hz), 123.1 (d, J = 21 Hz), 118.1, 114.7 (d, J = 22 Hz), 83.1 (d, J = 165 Hz), 74.4 (d, J = 19 Hz), 42.0, 14.2 (d, J = 3.3 Hz) ppm. HRMS (ESI+, m/z): calculated $[M+Na]^+$ $C_{19}H_{16}F_3N_3O_3Na$ as 414.1041, found as 414.1056.

*2-[(Tetrahydro-2H-pyran-2-yl)oxy]ethan-1-ol (**6**).* To a solution of *p*-toluenesulfonic acid monohydrate (312 mg, 1.64 mmol, 5 mol%) in ethylene glycol (14.0 mL, 250 mmol, 7.6 equiv.) was added dihydropyran (3.00 mL, 32.9 mmol, 1.0 equiv.) dropwise over 30 min at 0 °C. The solution was stirred at 0 °C for 2 h and then at room temperature for an additional 4 h. The reaction was then diluted with DCM and extracted with 0.1 M NaOH. The combined organics were dried over Na_2SO_4, filtered, and concentrated under reduced pressure. The crude mixture was purified by column chromatography (0-50% EtOAc/hexane) to obtain the title compound as a colorless oil (3.80 g, 26.0 mmol, 79%). ^{1}H-NMR (600 MHz, $CDCl_3$): δ 4.56-4.55 (1H, m), 3.93-3.89 (1H, m), 3.78-3.67 (4H, m), 3.55-3.51 (1H, m), 2.90 (1H, br), 1.85-1.80 (1H, m), 1.77-1.73 (1H, m), 1.60-1.50 (4H, m) ppm. ^{13}C-NMR (150 MHz, $CDCl_3$): δ 100.3, 70.9, 63.4, 62.4, 30.9, 25.3, 20.1 ppm. HRMS (EI, m/z): $[M-H]^+$ calculated $C_7H_{14}O_3$ as 145.0859, found as 145.0846. Spectrum in accordance with literature.[43]

*6-Fluoro-N-[(4-fluoro-3-methylphenyl)methyl]-5-[2-(oxan-2-yloxy)ethoxy]-4-oxo-3,4-dihydroquinazoline-2-carboxamide (**7**).* Following the procedure described for **5a**, compound **7** was prepared from compound **4d** and compound **6**. The crude mixture was purified by column chromatography (0-40% EtOAc/hexane) to obtain the title compound as a white solid (376 mg, 0.79 mmol, 75%). ^{1}H-NMR (600 MHz, $(CD_3)_2SO$): δ 12.14 (1H, br), 9.55 (1H, t, J = 6.0 Hz), 7.84-7.81 (1H, m), 7.57-7.55 (1H, m), 7.29-7.27(1H, m), 7.23-7.21 (1H, m), 7.13-7.10 (1H, m), 4.65-4.63 (1H, m), 4.45 (2H, d, J = 6.0 Hz), 4.32-4.25 (2H, m), 3.96-3.93 (1H, m), 3.78-3.72 (2H, m), 3.45-3.36 (1H, m), 2.24 (3H, d, J = 6.0 Hz), 1.68-1.55 (2H, m), 1.51-1.36 (4H, m). ^{13}C-NMR (150 MHz, $(CD_3)_2SO$) 159.8 (d, J = 240 Hz), 159.4, 158.9, 153.8 (d, J = 245 Hz), 145.7 (d, J = 14 Hz), 145.3, 145.2, 134.6 (d, J = 4.5 Hz), 130.8 (d, J = 4.5 Hz), 126.9 (d, J = 7.5 Hz), 124.1, 123.9 (d, J = 17 Hz), 123.0 (d, J = 23 Hz), 118.1, 114.7 (d, J = 21 Hz), 98.0, 74.4 (d, J = 3.0 Hz), 66.4, 61.1,

42.1, 30.1, 25.0, 18.9, 14.2 (d, J = 3.0 Hz) ppm. HRMS (ESI+, m/z): calculated $[M+Na]^+$ $C_{24}H_{25}F_2N_3O_5Na$ as 496.1660, found as 496.1653.

6-Fluoro-N-[(4-fluoro-3-methylphenyl)methyl]-5-(2-hydroxyethoxy)-4-oxo-3,4-dihydroquinazoline-2-carboxamide (8). To a solution of compound **7** (376 mg, 0.79 mmol, 1.0 equiv.) in MeOH (7.94 mL) was added *p*-toluenesulfonic acid monohydrate (12.2 mg, 0.064 mmol, 8 mol%). The solution was stirred at room temperature for 1 h before removal of the solvent under reduced pressure. The residue was re-suspended in DCM and extracted with water. The combined organics were dried over Na_2SO_4, filtered, and concentrated under reduced pressure. The crude mixture was purified by column chromatography (20-60% EtOAc/hexane) to obtain the title compound as a white solid (230 mg, 0.59 mmol, 75%). ^{1}H-NMR (600 MHz, $(CD_3)_2SO$): δ 12.27 (1H, br), 9.56 (1H, t, J = 6.0 Hz), 7.87-7.84 (1H, m), 7.59-7.57 (1H, m), 7.29-7.27 (1H, m), 7.24-7.21 (1H, m), 7.13-7.10 (1H, m) 4.95 (1H, t, J = 6.0 Hz), 4.45 (2H, d, J = 6.0 Hz), 4.20 (2H, t, J = 6.0 Hz), 3.76 (2H, q, J = 6.0 Hz), 2.25 (3H, d, J = 6.0 Hz) ppm. ^{13}C-NMR (150 MHz, $(CD_3)_2SO$): δ 159.8 (d, J = 240 Hz), 159.7, 159.3, 153.8 (d, J = 245 Hz), 145.7 (d, J = 14 Hz), 145.3, 145.1, 134.6 (d, J = 3.0 Hz), 130.8 (d, J = 4.5 Hz), 126.8 (d, J = 9.0 Hz), 124.0, 123.9 (d, J = 18 Hz), 123.3 (d, J = 21 Hz), 117.7, 114.7 (d, J = 21 Hz), 77.0 (d, J = 3.0 Hz), 60.2, 42.1, 14.2 (d, J = 3.0 Hz) ppm. HRMS (ESI+, m/z): calculated $[M+Na]^+$ $C_{19}H_{17}F_2N_3O_4Na$ as 412.1085, found as 412.1069.

*2-[(6-Fluoro-2-{[(4-fluoro-3-methylphenyl)methyl]carbamoyl}-4-oxo-3,4-dihydroquinazolin-5-yl)oxy]ethyl 4-methylbenzene-1-sulfonate (**9**).* To a solution of compound **8** (200 mg, 0.51 mmol, 1.0 equiv.) in pyridine (1.14 mL) was added *p*-toluenesulfonyl chloride (294 mg, 1.54 mmol, 3.0 equiv.) portionwise at 0 °C over 30 min. The solution was stirred for 4 h at 0 °C, diluted with EtOAc and extracted with 1 M HCl followed by water. The combined organics

were dried over Na_2SO_4, filtered, and concentrated under reduced pressure. The crude mixture was purified by column chromatography (20-70% EtOAc/hexane) to obtain the title compound as a white solid (233 mg, 0.43 mmol, 84%). ^{1}H-NMR (600 MHz, $(CD_3)_2SO$): δ 12.19 (1H, br), 9.57 (1H, t, J = 6.0 Hz), 7.84-7.81 (1H, m), 7.78-7.76 (2H, m), 7.59-7.57 (1H, m), 7.48-7.46 (2H, m), 7.29-7.28 (1H, m), 7.24-7.21 (1H, m), 7.13-7.10 (1H, m), 4.45 (2H, d, J = 6.0 Hz) 4.40-4.39 (2H, m), 4.30-4.29 (2H, m), 2.42 (3H, s), 2.25 (3H, d, J = 6.0 Hz) ppm. ^{13}C-NMR (150 MHz, $(CD_3)_2SO$): δ 159.8 (d, J = 240 Hz), 159.4, 158.8, 153.6 (d, J = 246 Hz), 145.3, 145.2 145.0, 144.7 (d, J = 14 Hz), 134.6 (d, J = 4.5 Hz), 132.2, 130.8 (d, J = 6.0 Hz), 130.1, 127.6, 126.9 (d, J = 9.0 Hz), 124.6, 123.9 (d, J = 17 Hz), 123.2 (d, J = 23 Hz), 117.9, 114.7 (d, J = 23 Hz), 72.5 (d, J = 1.5 Hz), 70.2, 42.1, 21.1, 14.2 (d, J = 3.0 Hz) ppm. HRMS (ESI+, m/z): calculated $[M+Na]^+$ $C_{26}H_{23}F_2N_3O_6SNa$ as 566.1173, found as 566.1166.

*2-{[1-(Dimethylamino)-7-fluoro-2-[(4-fluoro-3-methylphenyl)methyl]-3,9-dioxo-1H,2H,3H,9H-imidazo[4,3-b]quinazolin-8-yl]oxy}ethyl 4-methylbenzene-1-sulfonate (**10**).* To a solution of compound **9** (71 mg, 0.13 mmol, 1.0 equiv.) in anhydrous DMF (0.20 mL) and THF (0.42 mL) was added oxalyl chloride (33 uL, 0.39 mmol, 3.0 equiv.) dropwise at 0 °C. The solution was stirred at room temperature for 2 h before removal of the solvent under reduced pressure. The residue was re-suspended in EtOAc and extracted with water. The combined organics were dried over Na_2SO_4, filtered, and concentrated under reduced pressure. The crude mixture was purified by column chromatography (0-60% EtOAc/hexane) to obtain the title compound as a bright yellow solid (66 mg, 0.11 mmol, 85%). ^{1}H-NMR (600 MHz, $(CD_3)_2SO$): δ 7.90-7.86 (1H, m), 7.78 (2H, d, J = 8.2 Hz), 7.71-7.69 (1H, m), 7.47 (2H, d, J = 8.2 Hz), 7.33-7.30 (1H, m), 7.27-7.23 (1H, m), 7.17-7.14 (1H, m), 6.15 (1H, s), 4.87 (1H, d, J = 15 Hz), 4.42-4.28 (5H, m), 2.43 (3H, s), 2.34 (6H, br), 2.26 (3H, s) ppm. ^{13}C-NMR (150 MHz, $CDCl_3$): δ 161.4 (d, J = 245 Hz), 157.4, 157.3, 154.8

(d, J = 250 Hz), 146.5, 145.8 (d, J = 14 Hz), 145.0, 144.4, 133.0, 132.3 (d, J = 6.0 Hz), 130.5 (d, J = 3.0 Hz), 129.9, 128.2, 128.1, 126.0 (d, J = 7.5 Hz), 125.9 (d, J = 18 Hz), 123.6 (d, J = 21 Hz), 117.6, 115.6 (d, J = 23 Hz), 105.8, 87.0, 72.6 (d, J = 3.0 Hz), 68.9, 43.2, 21.8, 14.7 ppm. HRMS (ESI+, m/z): calculated $[M+Na]^+$ $C_{29}H_{28}F_2N_4O_6SNa$ as 621.1595, found as 621.1578.

3.7.3 MMP Enzyme Inhibition Assay

Inhibitor potency against human recombinant MMP-1,-2,-8,-9, and -13 (R&D Systems) was measured using the fluorogenic substrate Mca-Lys-Pro-Leu-Gly-Leu-Dpa-Ala-Arg-NH_2 (Sigma Aldrich, MMP-13 K_M = 5.2 μM)[48] or Mca-Arg-Pro-Lys-Pro-Val-Glu-Nval-Trp-Arg-Lys(Dnp)-NH_2 (R&D Systems) for human recombinant MMP-10 (R&D Systems). Enzymes were activated with *para*-aminophenylmercuric acetate (1 mM) at 37 °C for the time indicated by the provider and diluted in assay buffer (pH 7.5) containing Tris (50 mM), NaCl (0.15 M), $CaCl_2$ (5 mM), $ZnSO_4$ (20 μM) and Brij 35 (0.05% w/v). Inhibitor solutions (45 μL) were prepared in DMSO, diluted to varying concentrations spanning 2 orders of magnitude in assay buffer (<5% DMSO final), and incubated with the active enzyme (45 μL, 4.44 nM) at 37°C for 30 min. The reaction was initiated with the addition of substrate (10 μL, 50 μM). Final concentrations of the enzyme and substrate were 2 nM and 5 μM, respectively. Changes in fluorescence were monitored using a BioTek Synergy Mx multi-mode plate reader with excitation and emission wavelengths of 320 and 405 nm, respectively. Initial rates were measured over the linear range (0-10 min), normalized to the observed reaction rates for no enzyme (0% activity) and no inhibitor (100% activity) control wells, and plotted as a function of inhibitor concentration on a logarithmic scale. The IC_{50} values were calculated by nonlinear regression analysis according to the following equation using GraphPad Prism software:

$$Y = \frac{100}{1+10^{(\mathrm{LogIC_{50}}-X)*\mathrm{HillSlope}}} \qquad (1)$$

3.7.4 Radiochemistry

*Automated Radiosynthesis – [^{11}C]**5b.*** A fully automated sequence including the generation of [^{11}C]CH_3I and radiolabeling were performed on a Synthra MeIPlus Research system. [^{11}C]CO_2 was prepared on a Siemens CTI Eclipse HP/RD Hybrid Cyclotron (11 MeV) via the $^{14}N(p,\alpha)^{11}C$ nuclear reaction. [^{11}C]CO_2 (~27 GBq) was transferred from the target, delivered into the module, and trapped on a steel coil at -180 °C. The trap was then heated to 50 °C, [^{11}C]CO_2 was released by H_2 gas flow (40 mL·min^{-1}) and reduced using a nickel catalyst (99.999% purity, C < 100 ppm) at 425 °C. The generated [^{11}C]CH_4 was trapped on a Carboxen® column (60-80 mesh) at -140 °C. The trap was then heated to 160 °C, [^{11}C]CH_4 was released by He gas flow (100 mL·min^{-1}), directed over iodine at 95 °C (99.999% purity, -10 mesh, anhydrous beads) and heated in a high temperature oven at 720 °C. The generated [^{11}C]CH_3I was trapped on a Porapak™ Q column (50-80 mesh), while unreacted [^{11}C]CH_4 was re-circulated in a closed system with a gas pump. When conversion was complete, the Porapak™ Q column was heated at 200 °C, [^{11}C]CH_3I was released by He gas flow (30 mL·min^{-1}) and bubbled into the reactor containing precursor (10 mM) and TBAOH (6.29 μL, 3 equiv.) dissolved in anhydrous DMSO (209 μL). The reactor was then heated at 80°C for 3 min, immediately cooled to 30 °C, and quenched with water (500 μL). The crude mixture was purified with a Phenomenex Synergi Hydro-RP column (C18, 80Å, 10 μm, 250 mm × 10 mm), mobile phase: 65/35 0.1 M ammonium formate / ACN (isocratic), flowrate: 5 mL·min^{-1}. The product fraction (retention time: ~9.5 min) was collected into a bulk vessel containing water (40 mL). The contents of the flask were transferred over a Waters Sep-Pak Plus Short C18 cartridge (preconditioned with 1 mL EtOH, 5 mL water, and 1 mL air) and subsequently washed with water (10 mL). The product was eluted with EtOH (1 mL) and diluted with saline (9 mL, 0.9%).

*Automated Radiosynthesis – [^{11}C]**5f***. An automated synthesis of **[^{11}C]5f** was performed according to the procedure described for **[^{11}C]5b** with TBAOH (4.19 μL, 2 equiv.). The crude mixture was purified with a Phenomenex Synergi Hydro-RP column (C18, 80Å, 10 μm, 250 mm × 10 mm), mobile phase: 35/65 0.1 M ammonium formate / ACN (isocratic), flowrate: 5 mL·min^{-1}. The product fraction (retention time: ~11 min) was collected and reformulated in 10% EtOH/saline (0.9%).

*Automated Radiosynthesis – [^{18}F]**5j***. A fully automated sequence was developed on a GE TRACERlab FX2N automation system. No-carrier-added aqueous [^{18}F]fluoride was prepared on a Siemens CTI Eclipse HP/RD Hybrid Cyclotron (11 MeV) via the ^{18}O(p,n)^{18}F nuclear reaction. [^{18}F]Fluoride (~13 GBq) was captured from the [^{18}O]H_2O target solution using a Waters Sep-Pak Light Accell Plus QMA Cartridge (preconditioned with 10 mL EtOH, 10 mL water, 10 mL 0.5 M $NaHCO_3$, 10 mL water, and 1 mL air) and eluted into the reactor with aqueous tetraethylammonium bicarbonate (800μL 3.23 mg/mL). Anhydrous ACN (1 mL) was also added and the reactor was heated at 80 °C for 5 min and 120 °C for 3 min under a nitrogen stream to yield dried [^{18}F]TEAF. The reactor was then cooled to 40 °C with compressed air, before adding the precursor (3.66 mg) in anhydrous DMSO (500 μL). The radiofluorination was performed at 100 °C for 10 min, and returned to 50 °C. Subsequently, hydrochloric acid (6M, 500 μL) was added and the deprotection was performed at 100 °C for 10 min. Following cooling with compressed air, the reaction was quenched with sodium hydroxide (6M, 400 μL) and HPLC mobile phase (1 mL) and loaded onto the HPLC loop. The crude mixture was purified with a Phenomenex Synergi Hydro-RP column (C18, 80Å, 10 μm, 250 mm × 10 mm), mobile phase: 50% 0.1 M ammonium formate / ACN (isocratic), flowrate: 5 mL·min^{-1}. The product fraction (retention time: ~15 min) was collected into a bulk vessel containing water (25 mL). The contents of the flask were

transferred over a Waters Sep-Pak Plus Short C18 cartridge (preconditioned with 1 mL EtOH, 5 mL water, and 1 mL air) and subsequently washed with water (10 mL). The product was eluted with EtOH (1 mL) and diluted with saline (9 mL, 0.9%).

*Manual Optimization – [^{11}C]**5b** and [^{11}C]**5f**.* ^{11}C-Methylation conditions were optimized on the Synthra MeIPlus Research system. [^{11}C]CH_3I was generated as previously described and bubbled into the reactor containing precursor (0.5 mg) and the indicated amount of TBAOH (1-4 equiv.) dissolved in anhydrous DMSO (10 mM). The reactor was then heated at the indicated temperature for the indicated time, immediately cooled to 30 °C, and quenched with water (250 μL). The crude reaction mixture was transferred to a sealed vial and analyzed by radio-HPLC using the conditions in the radiotracer quality control section. Radiochemical conversion was defined as the percentage of total radioactivity corresponding to the desired product (decay-corrected). Radiochemical identity was confirmed by co-injection of the corresponding non-radioactive standard.

*Manual Optimization – [^{18}F]**5j**.* Radiofluorination conditions were manually optimized in sealed conical vials. Azeotropic drying of aqueous [^{18}F]fluoride (~37 MBq) containing the indicated amount of base (1-8 equiv.), and anhydrous ACN (3 × 1 mL) was performed at 100 °C under nitrogen gas dried over a P_2O_5 column. A solution of the precursor (13.5 mM) in anhydrous DMSO (250 μL) was then added and the reaction mixture was heated at the indicated temperature (100 or 120 °C). Samples were withdrawn for radio-TLC analysis after 10, and 20 min, spotted on a silica-coated TLC plate, and developed in a chamber containing EtOAc until the solvent front reached 2 cm from the top of the plate. Incorporation of [^{18}F]fluoride was quantified using a Bioscan AR-2000 radio-TLC imaging scanner and WinScan software by integration of product peaks and unreacted [^{18}F]fluoride. Quantitative deprotection was observed with hydrochloric acid

(6M, 500 μL) at 100°C for 10 min by radio-HPLC using the conditions in the radiotracer quality control section. Radiochemical identity was confirmed by co-injection of the corresponding non-radioactive standard.

*Radiotracer Quality Control – [^{11}C]**5b**, [^{11}C]**5f**, and [^{18}F]**5j**.* Radiochemical purity and identity were confirmed by analytical radio-HPLC using a Phenomenex Luna C18 column (100 Å, 5 μm, 250 mm × 4.6 mm), a 996 Photodiode Array Detector (PerkinElmer), and a Carroll & Ramsey Associates 105-S high-sensitivity radiation detector. HPLC solvent A: 0.1 M ammonium formate, HPLC solvent B: ACN, flowrate: 1 mL·min^{-1}. **[^{11}C]5b** method: 0-2 min 25% B, 2-10 min 25-95% B, 10-12 min 95% B, 12-13 min 95-25% B, 13-15 25% B, retention time: 9.5 min. **[^{11}C]5f** method: 0-2 min 50% B, 2-8 min 50-95% B, 8-10 min 95% B, 10-13 min 95-50% B, 13-15 min 50% B, retention time: 9.5 min. **[^{18}F]5j** method: 0-2 min 20% B, 2-10 min 20-90% B, 10-12 min 90% B, 12-13 min 90-20% B, 13-15 min 20% B, retention time: 11.5 min. Molar activity was determined by measuring the UV absorbance of a known amount of radioactivity under identical HPLC conditions used to generate a calibration curve for the corresponding non-radioactive standard. The ratio of radioactivity (GBq) to moles (μmol) provided the molar activity (GBq·μmol^{-1}), which was decay corrected to the end of synthesis (EoS).

3.7.5 Formulation Stability

Radiotracer stability in 10% EtOH/saline (0.9%) was assessed at room temperature up to 75 min by analytical radio-HPLC using the conditions described in the radiotracer quality control section. Radiochemical purity was >99% for all radiotracers immediately following reformulation.

3.7.6 Distribution Coefficient (logD)

Radiotracer lipophilicity was measured by determination of the 1-octanol - 1× PBS (pH 7.4) distribution coefficient (logD) as previously described[49]. Data represent the mean ± standard error of two independent experiments performed in quadruplicate.

3.7.7 Animal Model

Male *ApoE*$^{-/-}$ (strain no. 002052) mice were obtained from Jackson Laboratory and housed in groups of 4. Mice were fed a western atherogenic diet (TD.88137, Envigo) beginning at 8 weeks of age for a total of 13-16 weeks. Animals were monitored periodically and housed in environmentally enriched cages with free access to food and water. All housing, handling, and experimental procedures were in strict accordance with the guidelines of Canadian Council on Animal Care and with approval of the University of Ottawa Animal Care Committee.

3.7.8 PET Imaging

ApoE$^{-/-}$ mice (41 ± 2 g, n = 2 per group) were anesthetized with 2% isoflurane, positioned in the PET scanner, and maintained under anesthesia during the imaging protocol. Following a 10 min transmission scan, animals were intravenously injected with radiotracer (~7.5 MBq) as a bolus over 30 sec via the lateral tail vein. The whole body was imaged for 60 min (4 × 15 sec frames; 4 × 1 min frames; 11 × 5 min frames). PET imaging was performed using a Siemens DPET scanner. Emission data were corrected for attenuation and scatter, then reconstructed using the 3D-OSEM/MAP algorithm. Volumetric regions of interest (ROIs) were drawn over target organs. Uptake values obtained in nCi·cc^{-1} were converted to %ID·cc^{-1} using the injected dose (nCi) and presented as time-activity curves.

3.7.9 Biodistribution

ApoE$^{-/-}$ mice (39 ± 5 g, n = 4-6 per group) were anesthetized with 2% isoflurane and intravenously injected with radiotracer (~7.5 MBq, 100-200 μL) as a bolus over 30 sec via the lateral tail vein. For pharmacological treatments, **5j** (2.5 mg/kg, 3 mg/mL, 16% DMA/ 32% propylene glycol/ 32% PEG400/ 20% sterile water), or WAY170523 (7.5 mg/kg, 3.5 mg/mL, 10% DMSO, 40% PEG400, 50% sterile water), were intravenously administered 15 min prior to the radiotracer. Isoflurane was maintained for 30 min, blood was collected by cardiac puncture, and animals were sacrificed by myocardial perfusion (10 mL 1× PBS, 10 mL 10% formalin, 5 mL 1× PBS). Perfusate was drained from an incision within the right atrium. Organs of interest were harvested, weighed, and counted for radioactivity using a Hidex Automatic Gamma Counter (energy window: 480−558 keV). Counts per minute (CPM) were converted to activity using a set of calibration standards with known activities. Percentage injected dose (%ID) was calculated by dividing the organ activity by the injected dose (decay-corrected) and further normalized by sample mass (g) to obtain the percentage injected dose per gram tissue (%ID·g^{-1}).

3.7.10 Plasma Radio-Metabolite Analysis

Blood samples were withdrawn by cardiac puncture into K_2EDTA-coated blood collection tubes 30 minutes after intravenous radiotracer administration. Protein-free plasma samples were obtained as previously described.[25] Pooled plasma samples were then spiked with non-radioactive standard and analyzed by radio-HPLC using the analytical methods described in the radiotracer quality control section. Fractions were collected each minute and counted for radioactivity using a gamma counter. Polar and non-polar radio-metabolites were defined by the radioactivity collected before and after the parent fraction, respectively. Extraction efficiency was defined as the percentage recovery of radioactivity in plasma following protein precipitation.

3.7.11 Autoradiography and Oil Red O Staining

Following removal of residual blood by myocardial perfusion, aortae and branching arteries were carefully dissected under a microscope and exposed to a super-resolution GE Storage Phosphor Screen (BAS-IP SR 2025 E) for 10 half-lives. The screen was scanned with a Cyclone Plus Storage Phosphor System and quantified using OptiQuant software by drawing aortic arch regions of interest (ROI) which were Oil Red O (ORO) positive. Digital light units (DLU) were converted to activity (Bq) using a set of calibration standards with known activities on the same screen. Percentage injected dose (%ID) was calculated by dividing the ROI activity (Bq) by the injected dose (Bq) and further normalized by ROI area (mm^2) to obtain ROI activity density ($\%ID \cdot mm^{-2}$). ORO staining was performed as previously described.[50] Bright-field images were taken using a Krüss Stereomicroscope (MSL4000-series) adapted with a smartphone camera and cropped.

3.7.12 Statistical Analysis

Statistical analysis was performed using GraphPad Prism. Data are presented as mean ± standard error. Multiple groups were compared using 1-way or 2-way ANOVA with Dunnett's or Tukey's multiple comparison test. Significance was set at the 0.05 level.

3.7.13 Manuscript Information

Corresponding author

Benjamin H. Rotstein; Phone: 613-696-7324; Email: benjamin.rotstein@uottawa.ca

Author contributions

A.B. and B.H.R. designed the project, directed research, performed experiments, analyzed data, and wrote the manuscript. J.W.K. guided enzyme inhibition assays. All other authors performed experiments. All authors approved of the manuscript.

Notes

The authors declare no competing financial interest.

Acknowledgments

The authors thank the staff of the University of Ottawa Heart Institute (UOHI) PET Radiochemistry Laboratory, Biomedical Engineering, and Animal Care and Veterinary Services for cyclotron, PET scanner, and animal care support. Support for this work was provided by CIHR (PJT 148968), CFI (JELF 36848 & 39358), and the Ontario Ministry for Research, Innovation and Science (ER17-13-119). A.B. was supported by OGS, QEII-GSST, and a UOHI Endowed Research Scholarship. U.S.I. was supported by QEII-GSST and the University of Ottawa Cardiac Endowment Fund. M.A. was supported by NSERC USRA and University of Ottawa UROP.

Abbreviations Used

A_M, molar activity; ARG, autoradiography; CPM, counts per minute; DLU, digital light units; Dnp, 2,4-dinitrophenol; EoS, end-of-synthesis; %ID, percentage of injected dose; Mca, 7-methoxycoumarin-4-acetic acid; Nval, norvaline; OAT, organic anion transporter; ORO, Oil Red O; QMA, quaternary methyl ammonium; RCC, radiochemical conversion; RCY, radiochemical yield; ROI, region of interest; SEM, standard error of the mean; S_NAr, nucleophilic aromatic substitution; TBAOH, tetrabutylammonium hydroxide; TEAB, tetraethylammonium bicarbonate.

3.8 References

1) Loffek, S.; Schilling, O.; Franzke, C.-W. Biological Role of Matrix Metalloproteinases: A Critical Balance. *Eur. Respir. J.* **2011**, *38* (1), 191–208. https://doi.org/10.1183/09031936.00146510.

(2) Laronha, H.; Caldeira, J. Structure and Function of Human Matrix Metalloproteinases. *Cells* **2020**, *9* (5), 1076. https://doi.org/10.3390/cells9051076.

(3) Sternlicht, M. D.; Werb, Z. How Matrix Metalloproteinases Regulate Cell Behavior. *Annu. Rev. Cell Dev. Biol.* **2001**, *17*, 463–516. https://doi.org/10.1146/annurev.cellbio.17.1.463.

(4) Cabral-Pacheco, G. A.; Garza-Veloz, I.; Castruita-De la Rosa, C.; Ramirez-Acuña, J. M.; Perez-Romero, B. A.; Guerrero-Rodriguez, J. F.; Martinez-Avila, N.; Martinez-Fierro, M. L. The Roles of Matrix Metalloproteinases and Their Inhibitors in Human Diseases. *Int. J. Mol. Sci.* **2020**, *21* (24), 9739. https://doi.org/10.3390/ijms21249739.

(5) Klein, T.; Bischoff, R. Physiology and Pathophysiology of Matrix Metalloproteases. *Amino Acids* **2011**, *41* (2), 271–290. https://doi.org/10.1007/s00726-010-0689-x.

(6) Nissinen, L.; Kähäri, V.-M. Matrix Metalloproteinases in Inflammation. *Biochim. Biophys. Acta BBA - Gen. Subj.* **2014**, *1840* (8), 2571–2580. https://doi.org/10.1016/j.bbagen.2014.03.007.

(7) Kular, J. K.; Basu, S.; Sharma, R. I. The Extracellular Matrix: Structure, Composition, Age-Related Differences, Tools for Analysis and Applications for Tissue Engineering. *J. Tissue Eng.* **2014**, *5*, 2041731414557112. https://doi.org/10.1177/2041731414557112.

(8) Inada, M.; Wang, Y.; Byrne, M. H.; Rahman, M. U.; Miyaura, C.; López-Otín, C.; Krane, S. M. Critical Roles for Collagenase-3 (Mmp13) in Development of Growth Plate

Cartilage and in Endochondral Ossification. *Proc. Natl. Acad. Sci. U. S. A.* **2004**, *101* (49), 17192–17197. https://doi.org/10.1073/pnas.0407788101.

(9) Yamamoto, K.; Okano, H.; Miyagawa, W.; Visse, R.; Shitomi, Y.; Santamaria, S.; Dudhia, J.; Troeberg, L.; Strickland, D. K.; Hirohata, S.; Nagase, H. MMP-13 Is Constitutively Produced in Human Chondrocytes and Co-Endocytosed with ADAMTS-5 and TIMP-3 by the Endocytic Receptor LRP1. *Matrix Biol.* **2016**, *56*, 57–73. https://doi.org/10.1016/j.matbio.2016.03.007.

(10) Wang, M.; Sampson, E. R.; Jin, H.; Li, J.; Ke, Q. H.; Im, H.-J.; Chen, D. MMP13 Is a Critical Target Gene during the Progression of Osteoarthritis. *Arthritis Res. Ther.* **2013**, *15* (1), R5. https://doi.org/10.1186/ar4133.

(11) Kamekura, S.; Hoshi, K.; Shimoaka, T.; Chung, U.; Chikuda, H.; Yamada, T.; Uchida, M.; Ogata, N.; Seichi, A.; Nakamura, K.; Kawaguchi, H. Osteoarthritis Development in Novel Experimental Mouse Models Induced by Knee Joint Instability. *Osteoarthritis Cartilage* **2005**, *13* (7), 632–641. https://doi.org/10.1016/j.joca.2005.03.004.

(12) Little, C. B.; Barai, A.; Burkhardt, D.; Smith, S. M.; Fosang, A. J.; Werb, Z.; Shah, M.; Thompson, E. W. Matrix Metalloproteinase 13-Deficient Mice Are Resistant to Osteoarthritic Cartilage Erosion but Not Chondrocyte Hypertrophy or Osteophyte Development. *Arthritis Rheum.* **2009**, *60* (12), 3723–3733. https://doi.org/10.1002/art.25002.

(13) Pivetta, E.; Scapolan, M.; Pecolo, M.; Wassermann, B.; Abu-Rumeileh, I.; Balestreri, L.; Borsatti, E.; Tripodo, C.; Colombatti, A.; Spessotto, P. MMP-13 Stimulates Osteoclast Differentiation and Activation in Tumour Breast Bone Metastases. *Breast Cancer Res.* **2011**, *13* (5), R105. https://doi.org/10.1186/bcr3047.

(14) Zhang, B.; Cao, X.; Liu, Y.; Cao, W.; Zhang, F.; Zhang, S.; Li, H.; Ning, L.; Fu, L.; Niu, Y.; Niu, R.; Sun, B.; Hao, X. Tumor-Derived Matrix Metalloproteinase-13 (MMP-13) Correlates with Poor Prognoses of Invasive Breast Cancer. *BMC Cancer* **2008**, *8*, 83. https://doi.org/10.1186/1471-2407-8-83.

(15) Sukhova, G. K.; Schönbeck, U.; Rabkin, E.; Schoen, F. J.; Poole, A. R.; Billinghurst, R. C.; Libby, P. Evidence for Increased Collagenolysis by Interstitial Collagenases-1 and -3 in Vulnerable Human Atheromatous Plaques. *Circulation* **1999**, *99* (19), 2503–2509. https://doi.org/10.1161/01.CIR.99.19.2503.

(16) Quillard, T.; Araújo, H. A.; Franck, G.; Tesmenitsky, Y.; Libby, P. Matrix Metalloproteinase-13 Predominates Over Matrix Metalloproteinase-8 as the Functional Interstitial Collagenase in Mouse Atheromata. *Arterioscler. Thromb. Vasc. Biol.* **2014**, *34* (6), 1179–1186. https://doi.org/10.1161/ATVBAHA.114.303326.

(17) Deguchi, J.-O.; Aikawa, E.; Libby, P.; Vachon, J. R.; Inada, M.; Krane, S. M.; Whittaker, P.; Aikawa, M. Matrix Metalloproteinase-13/Collagenase-3 Deletion Promotes Collagen Accumulation and Organization in Mouse Atherosclerotic Plaques. *Circulation* **2005**, *112* (17), 2708–2715. https://doi.org/10.1161/CIRCULATIONAHA.105.562041.

(18) Quillard, T.; Tesmenitsky, Y.; Croce, K.; Travers, R.; Shvartz, E.; Koskinas, K. C.; Sukhova, G. K.; Aikawa, E.; Aikawa, M.; Libby, P. Selective Inhibition of Matrix Metalloproteinase-13 Increases Collagen Content of Established Mouse Atherosclerosis. *Arterioscler. Thromb. Vasc. Biol.* **2011**, *31* (11), 2464–2472. https://doi.org/10.1161/ATVBAHA.111.231563.

(19) Cocker, M. S.; Spence, J. D.; Hammond, R.; deKemp, R. A.; Lum, C.; Wells, G.; Bernick, J.; Hill, A.; Nagpal, S.; Stotts, G.; Alturkustani, M.; Adeeko, A.; Yerofeyeva, Y.; Rayner,

K.; Peterson, J.; Khan, A. R.; Naidas, A. C.; Garrard, L.; Yaffe, M. J.; Leung, E.; Prato, F. S.; Tardif, J.-C.; Beanlands, R. S. B. [18F]-Fluorodeoxyglucose PET/CT Imaging as a Marker of Carotid Plaque Inflammation: Comparison to Immunohistology and Relationship to Acuity of Events. *Int. J. Cardiol.* **2018**, *271*, 378–386. https://doi.org/10.1016/j.ijcard.2018.05.057.

(20) Tzolos, E.; Dweck, M. R. 18F-Sodium Fluoride (18F-NaF) for Imaging Microcalcification Activity in the Cardiovascular System. *Arterioscler. Thromb. Vasc. Biol.* **2020**, *40* (7), 1620–1626. https://doi.org/10.1161/atvbaha.120.313785.

(21) MacAskill, M. G.; Newby, D. E.; Tavares, A. A. S. Frontiers in Positron Emission Tomography Imaging of the Vulnerable Atherosclerotic Plaque. *Cardiovasc. Res.* **2019**, *115* (14), 1952–1962. https://doi.org/10.1093/cvr/cvz162.

(22) Toczek, J.; Ye, Y.; Gona, K.; Kim, H.-Y.; Han, J.; Razavian, M.; Golestani, R.; Zhang, J.; Wu, T. L.; Jung, J.-J.; Sadeghi, M. M. Preclinical Evaluation of RYM1, a Matrix Metalloproteinase-Targeted Tracer for Imaging Aneurysm. *J. Nucl. Med.* **2017**, *58* (8), 1318–1323. https://doi.org/10.2967/jnumed.116.188656.

(23) Ye, Y.; Toczek, J.; Gona, K.; Kim, H.-Y.; Han, J.; Razavian, M.; Golestani, R.; Zhang, J.; Wu, T. L.; Ghosh, M.; Jung, J.-J.; Sadeghi, M. M. Novel Arginine-Containing Macrocyclic MMP Inhibitors: Synthesis, 99mTc-Labeling, and Evaluation. *Sci. Rep.* **2018**, *8*, 11647. https://doi.org/10.1038/s41598-018-29941-2.

(24) Wagner, S.; Breyholz, H.-J.; Law, M. P.; Faust, A.; Höltke, C.; Schröer, S.; Haufe, G.; Levkau, B.; Schober, O.; Schäfers, M.; Kopka, K. Novel Fluorinated Derivatives of the Broad-Spectrum MMP Inhibitors N-Hydroxy-2(R)-[[(4-Methoxyphenyl)Sulfonyl](Benzyl)- and (3-Picolyl)-Amino]-3-Methyl-Butanamide as

Potential Tools for the Molecular Imaging of Activated MMPs with PET. *J. Med. Chem.* **2007**, *50* (23), 5752–5764. https://doi.org/10.1021/jm0708533.

(25) Vazquez, N.; Missault, S.; Vangestel, C.; Deleye, S.; Thomae, D.; Veken, P. V. der; Augustyns, K.; Staelens, S.; Dedeurwaerdere, S.; Wyffels, L. Evaluation of [18F]BR420 and [18F]BR351 as Radiotracers for MMP-9 Imaging in Colorectal Cancer. *J. Label. Compd. Radiopharm.* **2017**, *60* (1), 69–79. https://doi.org/10.1002/jlcr.3476.

(26) Steward, W. P.; Thomas, A. L. Marimastat: The Clinical Development of a Matrix Metalloproteinase Inhibitor. *Expert Opin. Investig. Drugs* **2000**, *9* (12), 2913–2922. https://doi.org/10.1517/13543784.9.12.2913.

(27) Fields, G. B. The Rebirth of Matrix Metalloproteinase Inhibitors: Moving Beyond the Dogma. *Cells* **2019**, *8* (9), 984. https://doi.org/10.3390/cells8090984.

(28) Peterson, J. T. The Importance of Estimating the Therapeutic Index in the Development of Matrix Metalloproteinase Inhibitors. *Cardiovasc. Res.* **2006**, *69* (3), 677–687. https://doi.org/10.1016/j.cardiores.2005.11.032.

(29) Vandenbroucke, R. E.; Libert, C. Is There New Hope for Therapeutic Matrix Metalloproteinase Inhibition? *Nat. Rev. Drug Discov.* **2014**, *13* (12), 904–927. https://doi.org/10.1038/nrd4390.

(30) Hugenberg, V.; Wagner, S.; Kopka, K.; Schäfers, M.; Schuit, R. C.; Windhorst, A. D.; Hermann, S. Radiolabeled Selective Matrix Metalloproteinase 13 (MMP-13) Inhibitors: (Radio)Syntheses and in Vitro and First in Vivo Evaluation. *J. Med. Chem.* **2017**, *60* (1), 307–321. https://doi.org/10.1021/acs.jmedchem.6b01284.

(31) Engel, C. K.; Pirard, B.; Schimanski, S.; Kirsch, R.; Habermann, J.; Klingler, O.; Schlotte, V.; Weithmann, K. U.; Wendt, K. U. Structural Basis for the Highly Selective Inhibition

of MMP-13. *Chem. Biol.* **2005**, *12* (2), 181–189. https://doi.org/10.1016/j.chembiol.2004.11.014.

(32) Nara, H.; Sato, K.; Naito, T.; Mototani, H.; Oki, H.; Yamamoto, Y.; Kuno, H.; Santou, T.; Kanzaki, N.; Terauchi, J.; Uchikawa, O.; Kori, M. Discovery of Novel, Highly Potent, and Selective Quinazoline-2-Carboxamide-Based Matrix Metalloproteinase (MMP)-13 Inhibitors without a Zinc Binding Group Using a Structure-Based Design Approach. *J. Med. Chem.* **2014**, *57* (21), 8886–8902. https://doi.org/10.1021/jm500981k.

(33) Nara, H.; Kaieda, A.; Sato, K.; Naito, T.; Mototani, H.; Oki, H.; Yamamoto, Y.; Kuno, H.; Santou, T.; Kanzaki, N.; Terauchi, J.; Uchikawa, O.; Kori, M. Discovery of Novel, Highly Potent, and Selective Matrix Metalloproteinase (MMP)-13 Inhibitors with a 1,2,4-Triazol-3-yl Moiety as a Zinc Binding Group Using a Structure-Based Design Approach. *J. Med. Chem.* **2017,** *60* (2), 608–626. https://doi.org/10.1021/acs.jmedchem.6b01007.

(34) Nara, H.; Sato, K.; Naito, T.; Mototani, H.; Oki, H.; Yamamoto, Y.; Kuno, H.; Santou, T.; Kanzaki, N.; Terauchi, J.; Uchikawa, O.; Kori, M. Thieno[2,3-d]Pyrimidine-2-Carboxamides Bearing a Carboxybenzene Group at 5-Position: Highly Potent, Selective, and Orally Available MMP-13 Inhibitors Interacting with the S1″ Binding Site. *Bioorg. Med. Chem.* **2014**, *22* (19), 5487–5505. https://doi.org/10.1016/j.bmc.2014.07.025.

(35) Choi, J. Y.; Fuerst, R.; Knapinska, A. M.; Taylor, A. B.; Smith, L.; Cao, X.; Hart, P. J.; Fields, G. B.; Roush, W. R. Structure-Based Design and Synthesis of Potent and Selective Matrix Metalloproteinase 13 Inhibitors. *J. Med. Chem.* **2017**, *60* (13), 5816–5825. https://doi.org/10.1021/acs.jmedchem.7b00514.

(36) Knapinska, A. M.; Singh, C.; Drotleff, G.; Blanco, D.; Chai, C.; Schwab, J.; Herd, A.; Fields, G. B. Matrix Metalloproteinase 13 Inhibitors for Modulation of

Osteoclastogenesis: Enhancement of Solubility and Stability. *ChemMedChem* **2021**, *16* (7), 1133–1142. https://doi.org/10.1002/cmdc.202000911.

(37) Gege, C.; Bao, B.; Bluhm, H.; Boer, J.; Brian M. Gallagher, J.; Korniski, B.; Powers, T. S.; Steeneck, C.; Taveras, A. G.; Baragi, V. M. *Discovery and Evaluation of a Non-Zn Chelating, Selective Matrix Metalloproteinase 13 (MMP-13) Inhibitor for Potential Intra-articular Treatment of Osteoarthritis*. *J Med Chem*. **2012,** 55 (2), 709-716. https://doi.org/10.1021/jm201152u.

(38) Reiter, L. A.; Freeman-Cook, K. D.; Jones, C. S.; Martinelli, G. J.; Antipas, A. S.; Berliner, M. A.; Datta, K.; Downs, J. T.; Eskra, J. D.; Forman, M. D.; Greer, E. M.; Guzman, R.; Hardink, J. R.; Janat, F.; Keene, N. F.; Laird, E. R.; Liras, J. L.; Lopresti-Morrow, L. L.; Mitchell, P. G.; Pandit, J.; Robertson, D.; Sperger, D.; Vaughn-Bowser, M. L.; Waller, D. M.; Yocum, S. A. Potent, Selective Pyrimidinetrione-Based Inhibitors of MMP-13. *Bioorg. Med. Chem. Lett.* **2006**, *16* (22), 5822–5826. https://doi.org/10.1016/j.bmcl.2006.08.066.

(39) Ruminski, P. G.; Massa, M.; Strohbach, J.; Hanau, C. E.; Schmidt, M.; Scholten, J. A.; Fletcher, T. R.; Hamper, B. C.; Carroll, J. N.; Shieh, H. S.; Caspers, N.; Collins, B.; Grapperhaus, M.; Palmquist, K. E.; Collins, J.; Baldus, J. E.; Hitchcock, J.; Kleine, H. P.; Rogers, M. D.; McDonald, J.; Munie, G. E.; Messing, D. M.; Portolan, S.; Whiteley, L. O.; Sunyer, T.; Schnute, M. E. Discovery of N-(4-Fluoro-3-Methoxybenzyl)-6-(2-(((2S,5R)-5-(Hydroxymethyl)-1,4-Dioxan-2-Yl)Methyl)-2H-Tetrazol-5-Yl)-2-Methylpyrimidine-4-Carboxamide. A Highly Selective and Orally Bioavailable Matrix Metalloproteinase-13 Inhibitor for the Potential Treatment of Osteoarthritis. *J. Med. Chem.* **2016**, *59* (1), 313–327. https://doi.org/10.1021/acs.jmedchem.5b01434.

(40) Taylor, S. J.; Abeywardane, A.; Liang, S.; Xiong, Z.; Proudfoot, J. R.; Farmer, B. S.; Gao, D. A.; Heim-Riether, A.; Smith-Keenan, L. L.; Muegge, I.; Yu, Y.; Zhang, Q.; Souza, D.; Panzenbeck, M.; Goldberg, D.; Hill-Drzewi, M.; Margarit, M.; Collins, B.; Li, J. X.; Zuvela-Jelaska, L.; Li, J.; Farrow, N. A. Indole Inhibitors of MMP-13 for Arthritic Disorders. *ACS Omega* **2021**, *6* (29), 18635–18650. https://doi.org/10.1021/acsomega.1c01320.

(41) Buchler, A.; Munch, M.; Farber, G.; Zhao, X.; Al-Haddad, R.; Farber, E.; Rotstein, B. H. Selective Imaging of Matrix Metalloproteinase-13 to Detect Extracellular Matrix Remodeling in Atherosclerotic Lesions. *Mol. Imaging Biol.* **2021**. https://doi.org/10.1007/s11307-021-01626-9.

(42) Cai, H.; Agrawal, A. K.; Putt, D. A.; Hashim, M.; Reddy, A.; Brodfuehrer, J.; Surendran, N.; Lash, L. H. Assessment of the Renal Toxicity of Novel Anti-Inflammatory Compounds Using Cynomolgus Monkey and Human Kidney Cells. *Toxicology* **2009**, *258* (1), 56–63. https://doi.org/10.1016/j.tox.2009.01.006.

(43) Kreibich, M.; Petrović, D.; Brückner, R. Mechanistic Studies of the Deslongchamps Annulation. *J. Org. Chem.* **2018**, *83* (3), 1116–1133. https://doi.org/10.1021/acs.joc.7b02341.

(44) Bratteby, K.; Shalgunov, V.; Battisti, U. M.; Petersen, I. N.; van den Broek, S. L.; Ohlsson, T.; Gillings, N.; Erlandsson, M.; Herth, M. M. Insights into Elution of Anion Exchange Cartridges: Opening the Path toward Aliphatic 18F-Radiolabeling of Base-Sensitive Tracers. *ACS Pharmacol. Transl. Sci.* **2021**, *4* (5), 1556–1566. https://doi.org/10.1021/acsptsci.1c00133.

(45) Chen, J. M.; Nelson, F. C.; Levin, J. I.; Mobilio D.; Moy F. J.; Nilakantan R.; Zask, A.; Powers, R. Structure-Based Design of a Novel, Potent, and Selective Inhibitor for MMP-13 Utilizing NMR Spectroscopy and Computer-Aided Molecular Design. *J. Am. Chem. Soc.* **2000,** *122* (40), 9648–9654. https://doi.org/10.1021/ja001547g.

(46) Jaffré, F.; Friedman, A. E.; Hu, Z.; Mackman, N.; Blaxall, B. C. β-Adrenergic Receptor Stimulation Transactivates Protease-Activated Receptor 1 via Matrix Metalloproteinase 13 in Cardiac Cells. *Circulation* **2012**, *125* (24), 2993–3003. https://doi.org/10.1161/circulationaha.111.066787.

(47) Carretero, J. C.; García Ruano, J. L.; Vicioso, M. A Practical Route to C-8 Substituted Fluoroquinolones. *Tetrahedron* **1992**, *48* (35), 7373–7382. https://doi.org/10.1016/S0040-4020(01)88273-9.

(48) Neumann, U.; Kubota, H.; Frei, K.; Ganu, V.; Leppert, D. Characterization of Mca-Lys-Pro-Leu-Gly-Leu-Dpa-Ala-Arg-NH2, a Fluorogenic Substrate with Increased Specificity Constants for Collagenases and Tumor Necrosis Factor Converting Enzyme. *Anal. Biochem.* **2004**, *328* (2), 166–173. https://doi.org/10.1016/j.ab.2003.12.035.

(49) Wilson, A. A.; Jin, L.; Garcia, A.; DaSilva, J. N.; Houle, S. An Admonition When Measuring the Lipophilicity of Radiotracers Using Counting Techniques. *Appl. Radiat. Isot.* **2001**, *54* (2), 203–208. https://doi.org/10.1016/S0969-8043(00)00269-4.

(50) Andrés-Manzano, M. J.; Andrés, V.; Dorado, B. Oil Red O and Hematoxylin and Eosin Staining for Quantification of Atherosclerosis Burden in Mouse Aorta and Aortic Root. *Methods Mol. Biol. Clifton NJ* **2015**, *1339*, 85–99. https://doi.org/10.1007/978-1-4939-2929-0_5.

3.9 Supporting information

3.9.1 ^{1}H NMR and ^{13}C NMR spectra for all synthesized compounds (1–10)

Compound 1

^{1}H-NMR (80 MHz, $CDCl_3$)

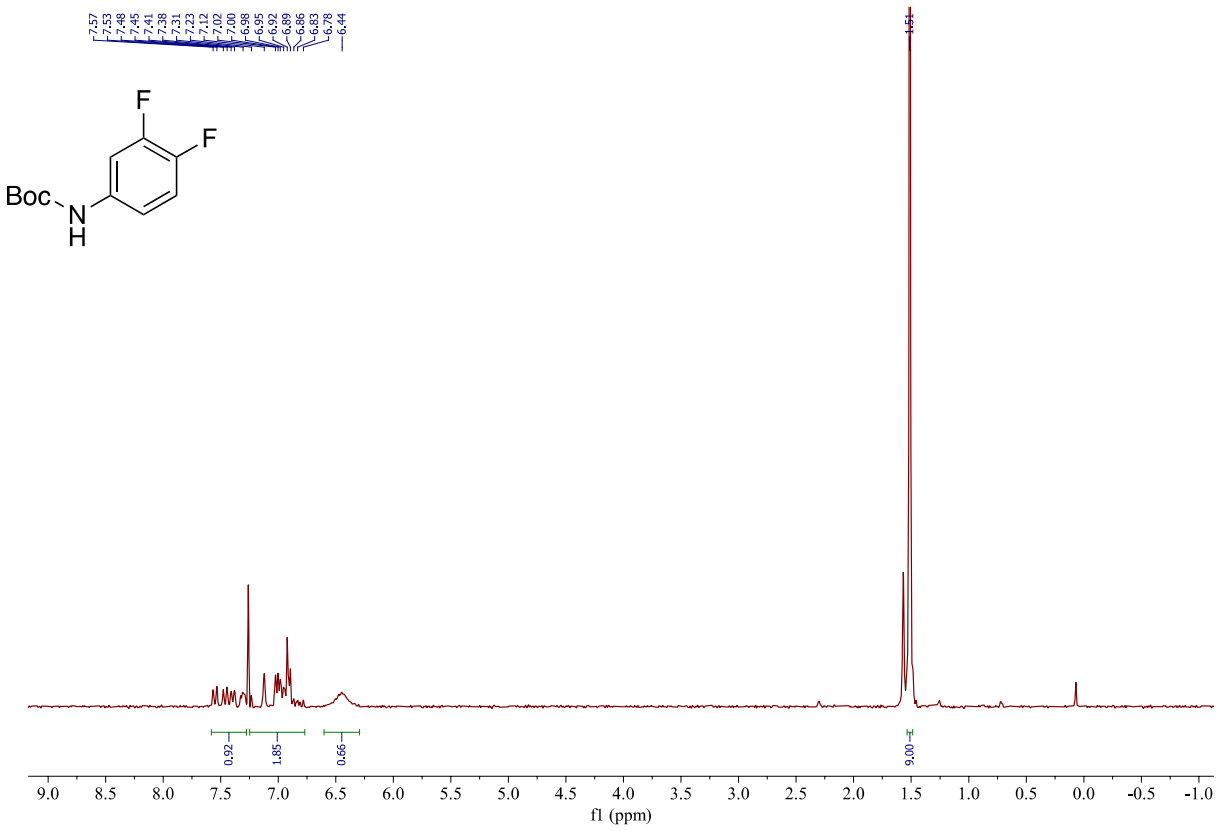

Compound 2

^{1}H-NMR (80 MHz, $(CD_3)_2SO$)

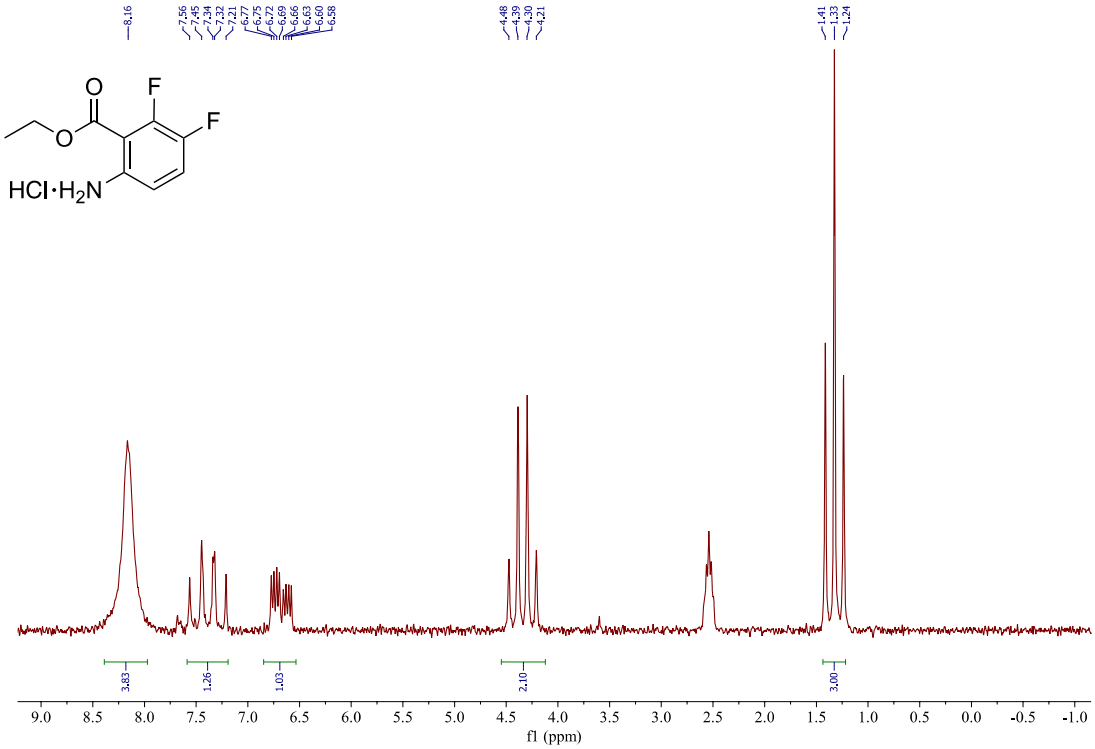

^{13}C-NMR (150 MHz, $(CD_3)_2SO$)

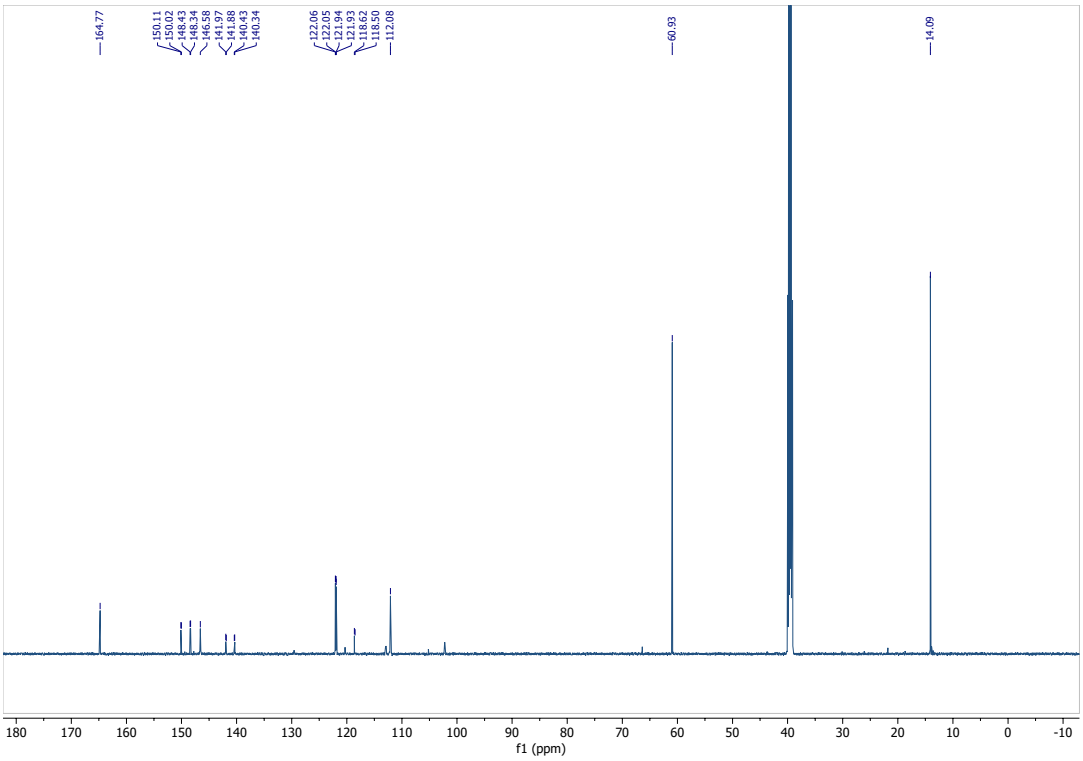

Compound 3

^{1}H-NMR (400 MHz, $(CD_3)_2SO$)

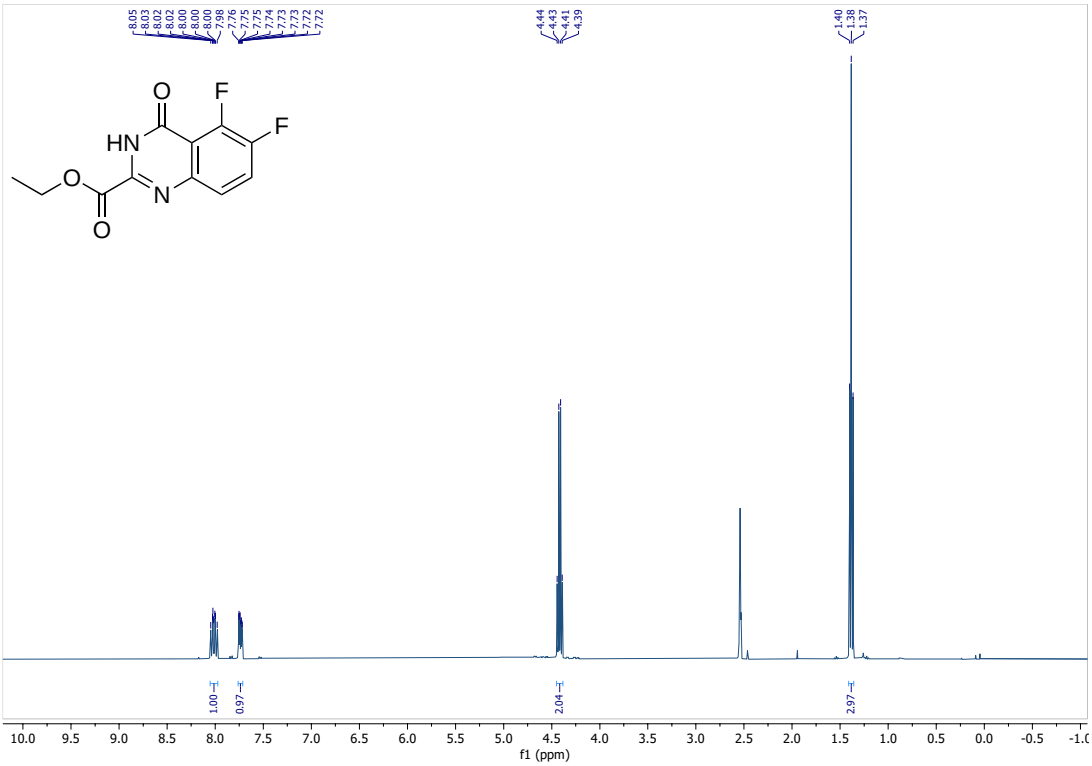

^{13}C-NMR (150 MHz, $(CD_3)_2SO$)

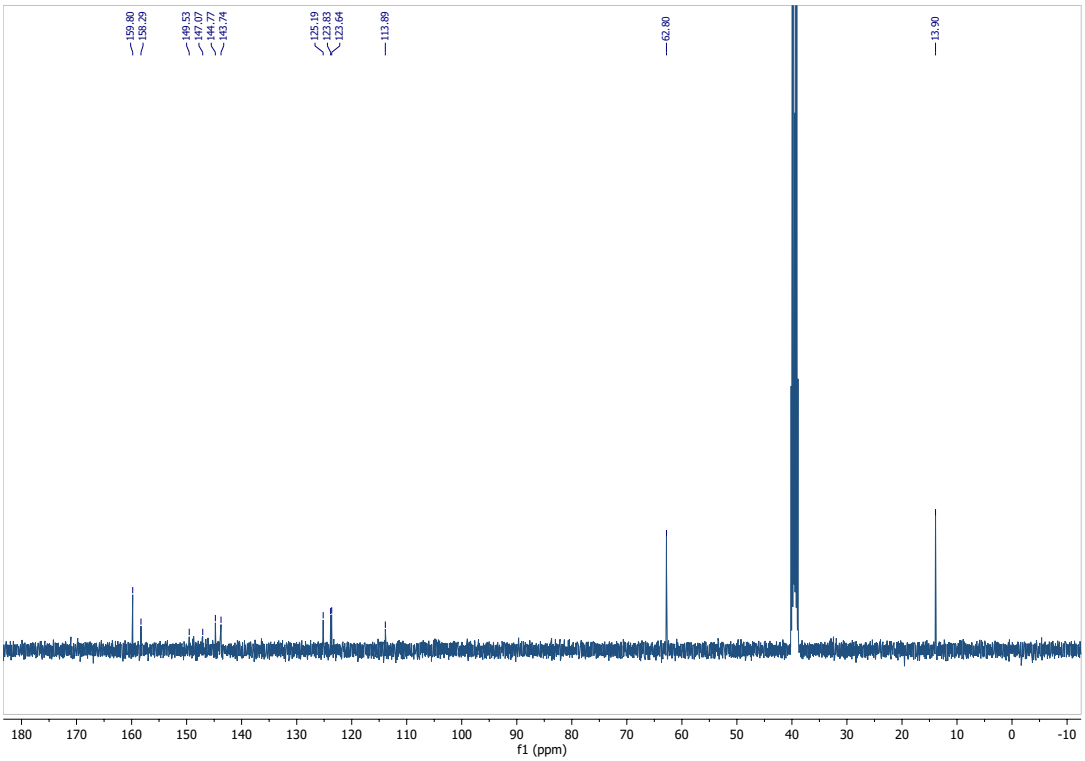

Compound 4a

^{1}H-NMR (600 MHz, $(CD_3)_2SO$)

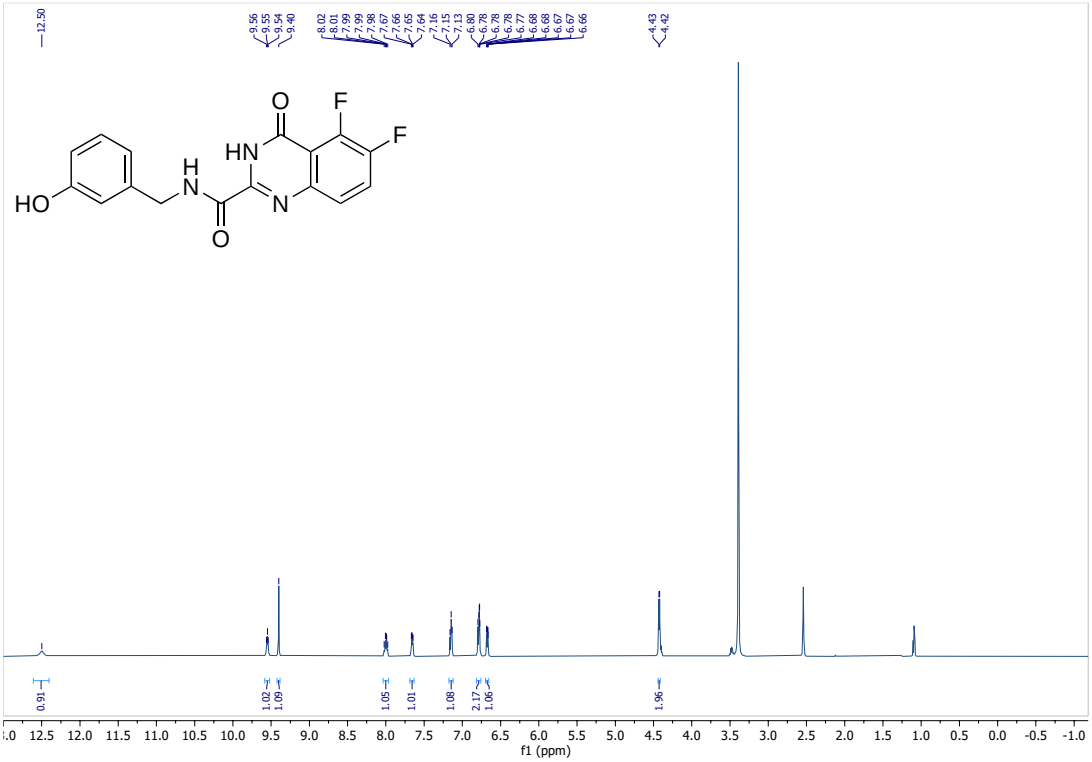

^{13}C-NMR (150 MHz, $(CD_3)_2SO$)

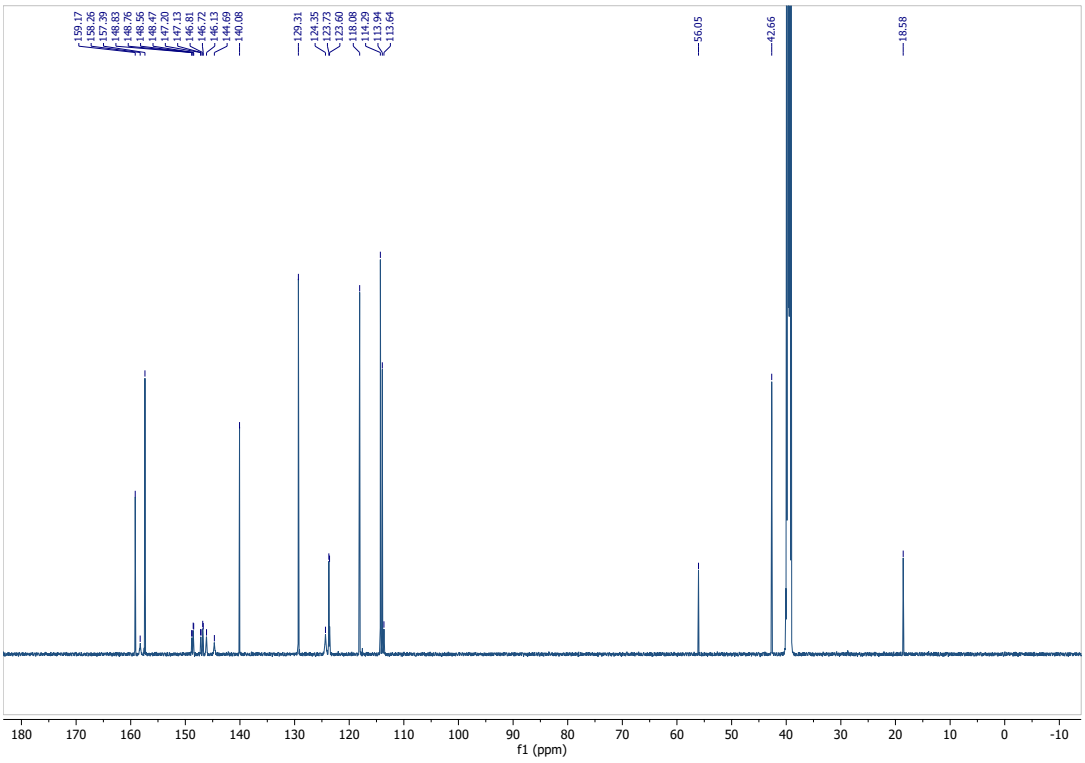

Compound 4b

^{1}H-NMR (600 MHz, $(CD_3)_2SO$)

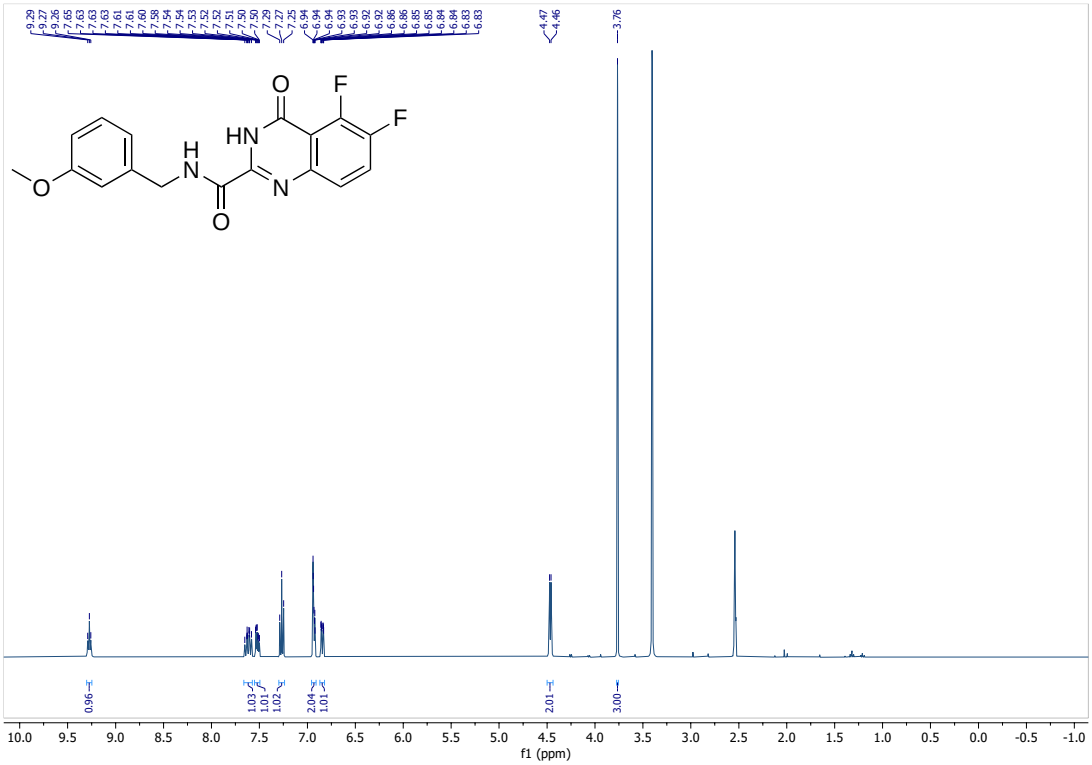

^{13}C-NMR (150 MHz, $(CD_3)_2SO$)

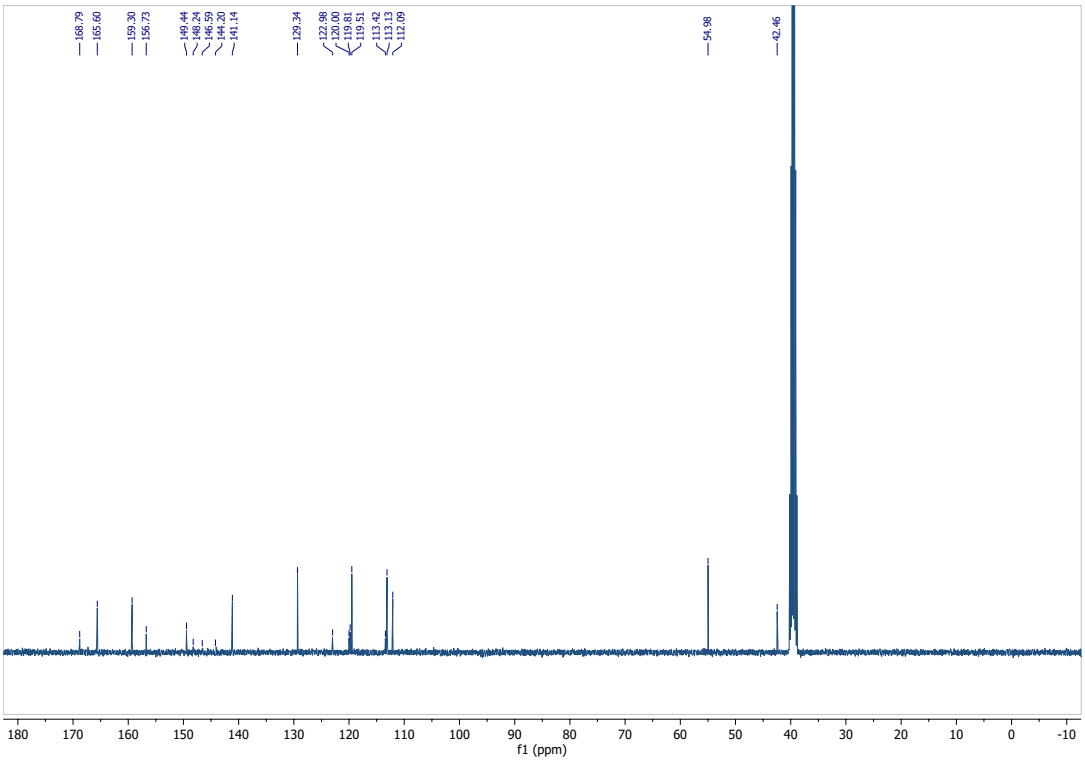

Compound 4c

^{1}H-NMR (600 MHz, $(CD_3)_2SO$)

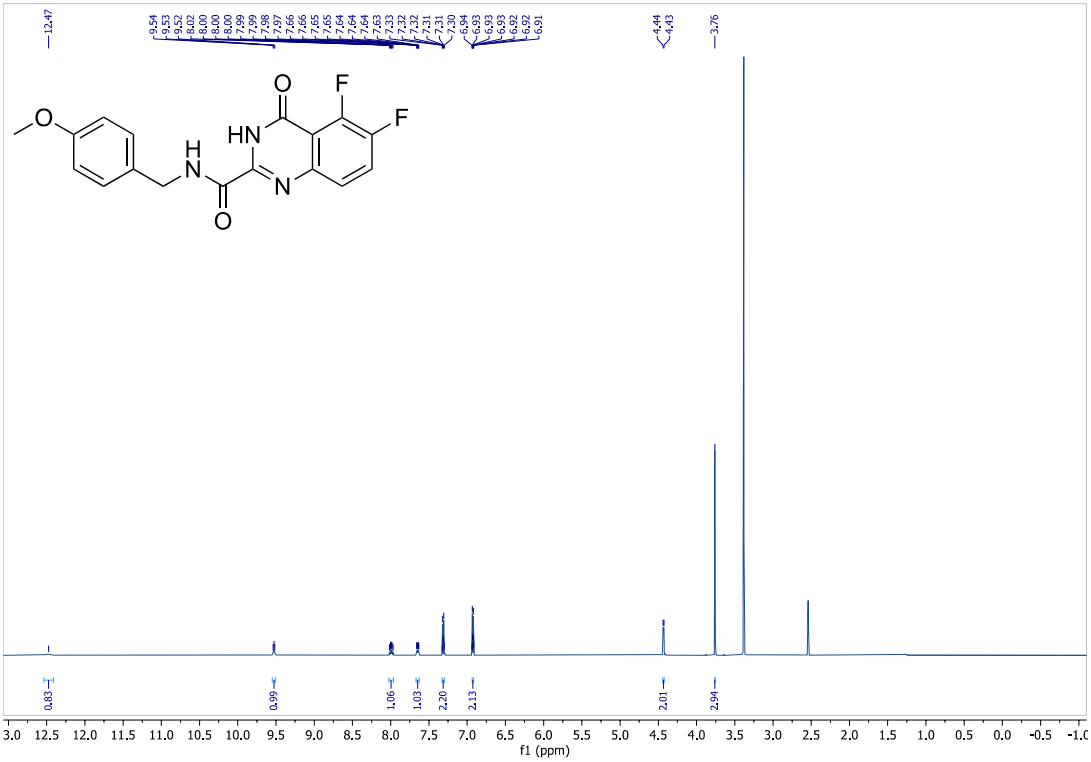

^{13}C-NMR (150 MHz, $(CD_3)_2SO$)

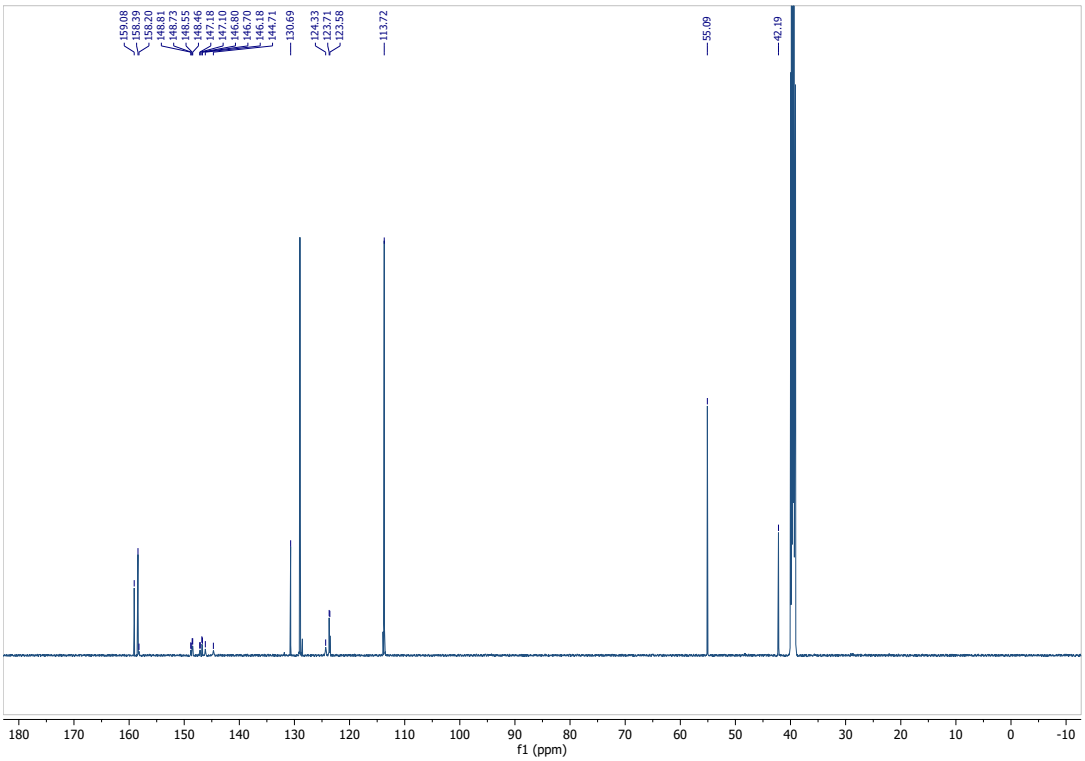

Compound 4d

^{1}H-NMR (600 MHz, $(CD_3)_2SO$)

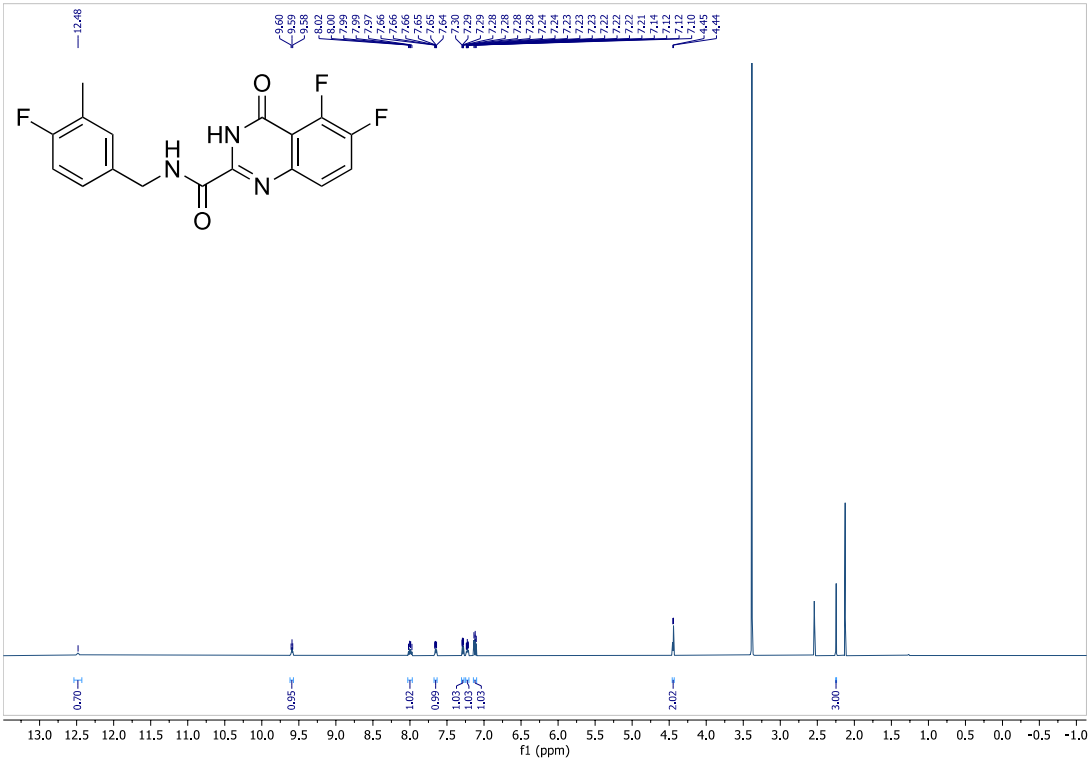

^{13}C-NMR (150 MHz, $(CD_3)_2SO$)

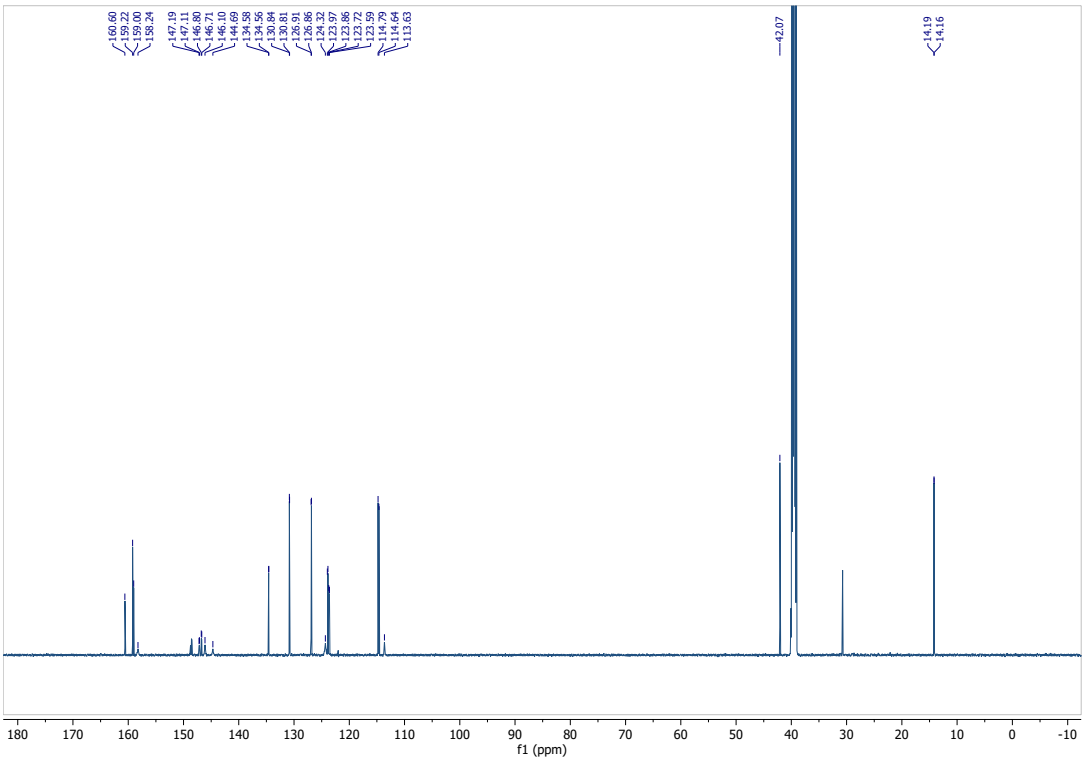

Compound 5a

^{1}H-NMR (600 MHz, $(CD_3)_2SO$)

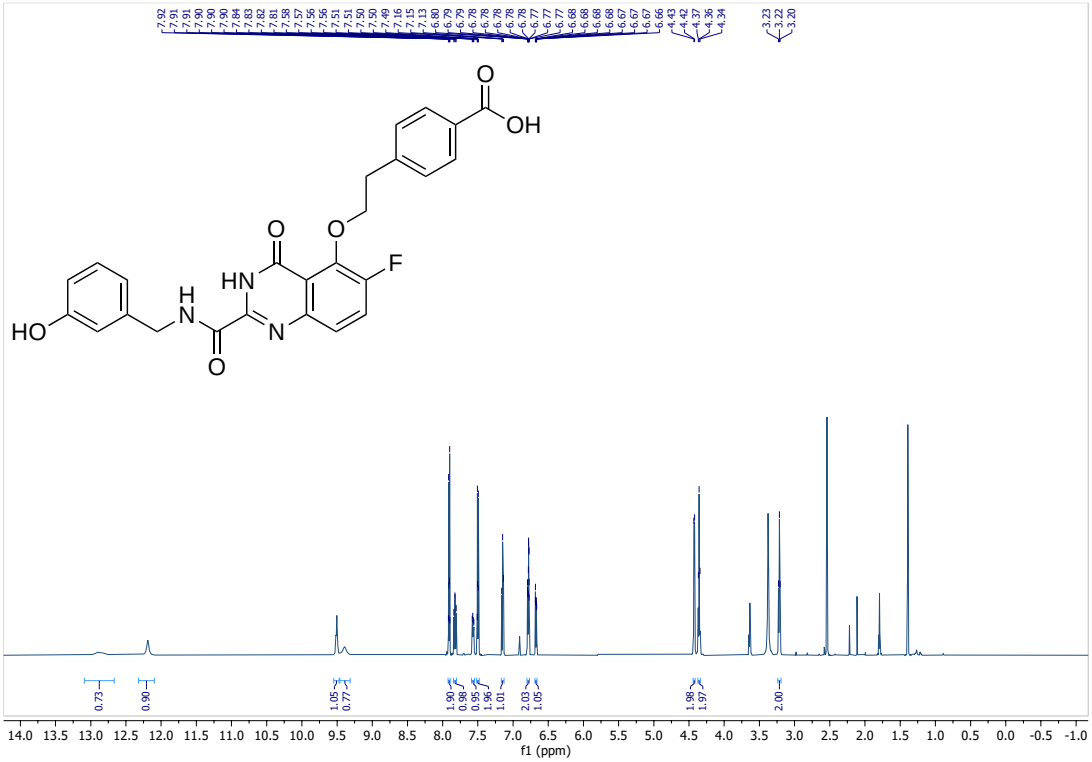

^{13}C-NMR (150 MHz, $(CD_3)_2SO$)

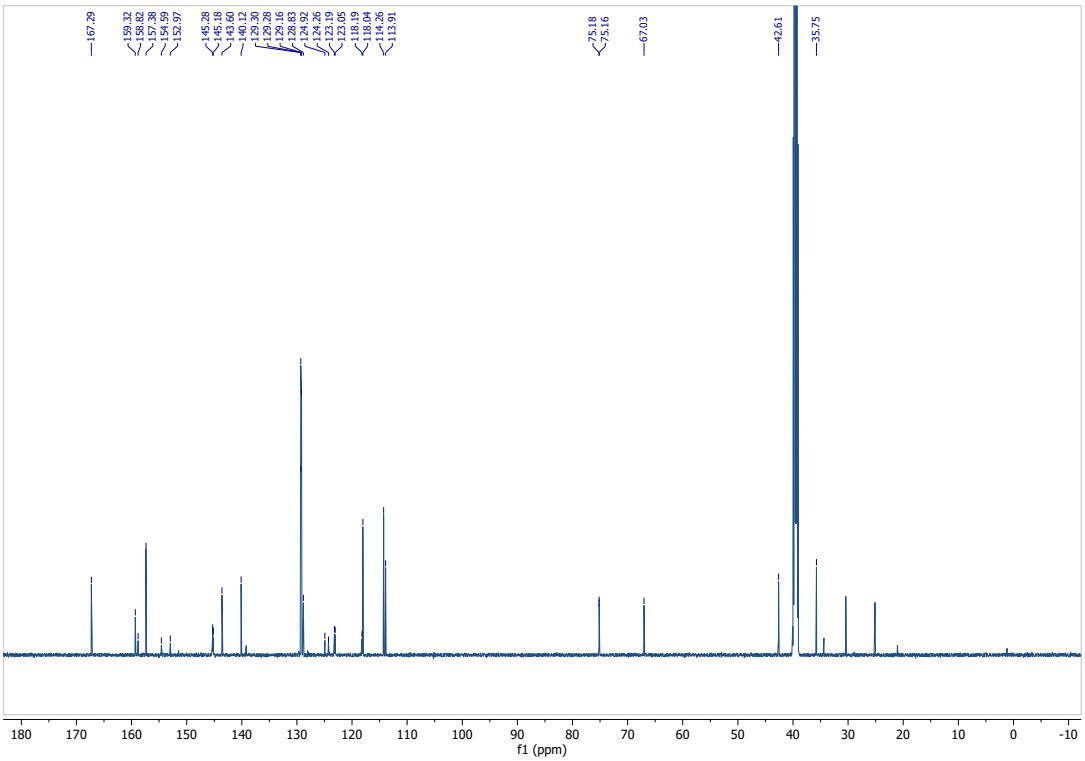

Compound 5b

^{1}H-NMR (600 MHz, $(CD_3)_2SO$)

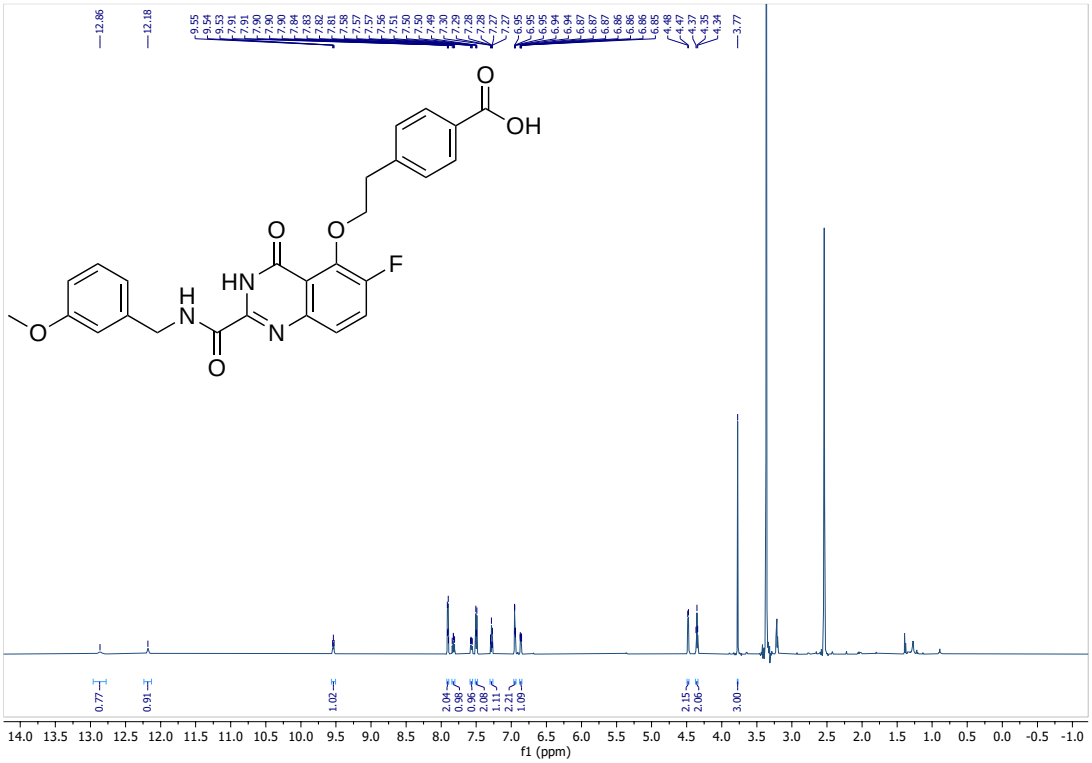

^{13}C-NMR (150 MHz, $(CD_3)_2SO$)

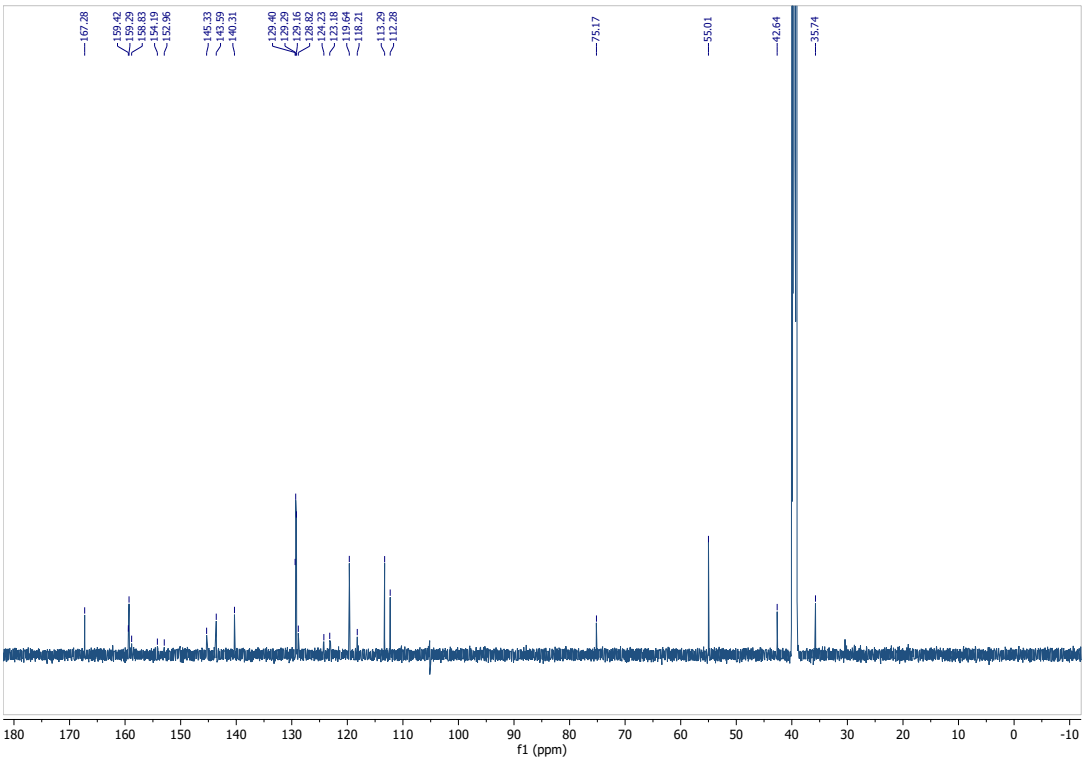

Compound 5c

^{1}H-NMR (600 MHz, $(CD_3)_2SO$)

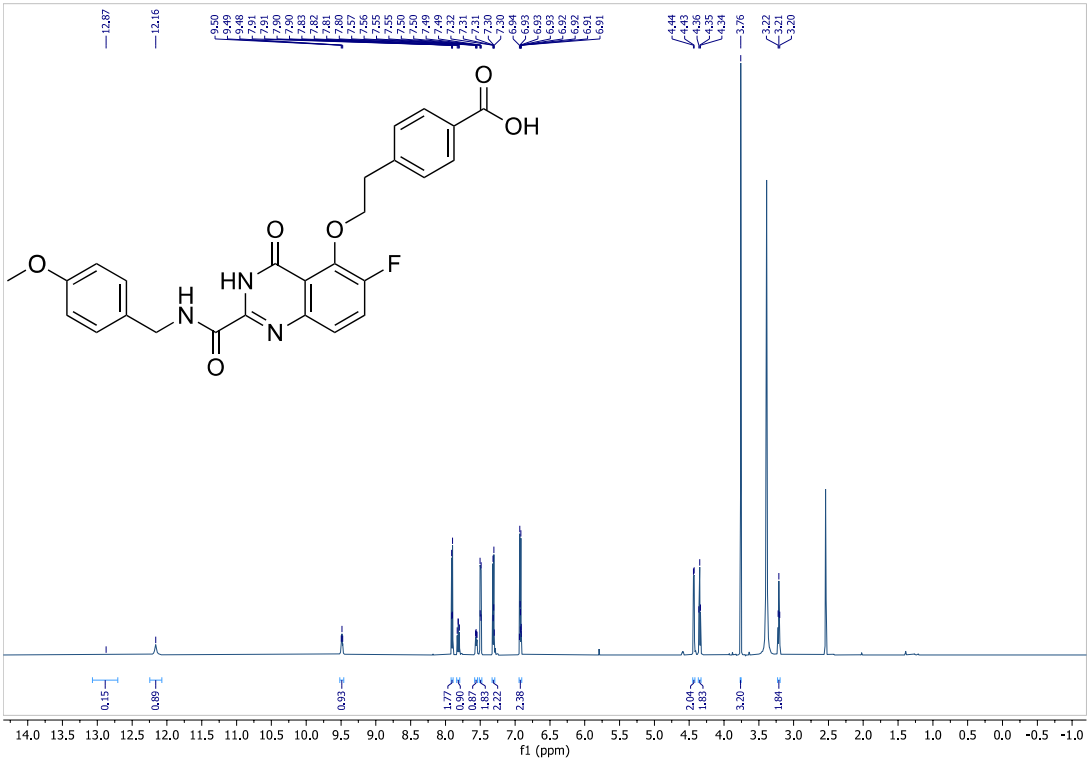

^{13}C-NMR (150 MHz, $(CD_3)_2SO$)

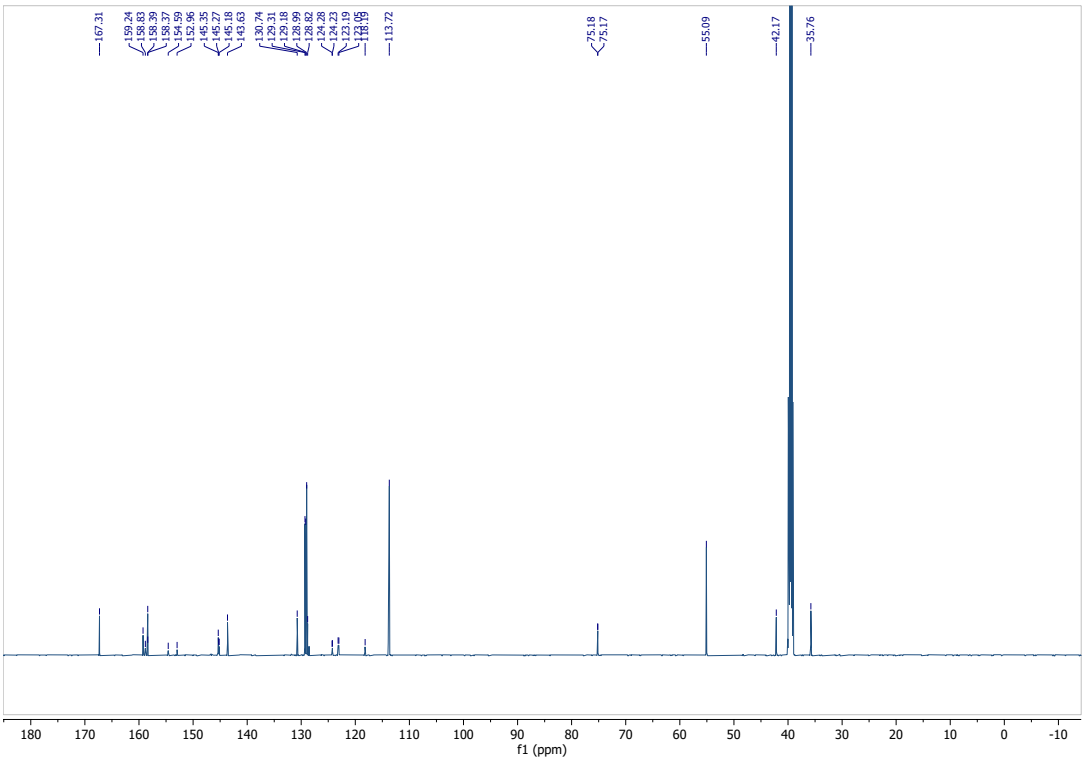

Compound 5d

^{1}H-NMR (600 MHz, $(CD_3)_2SO$)

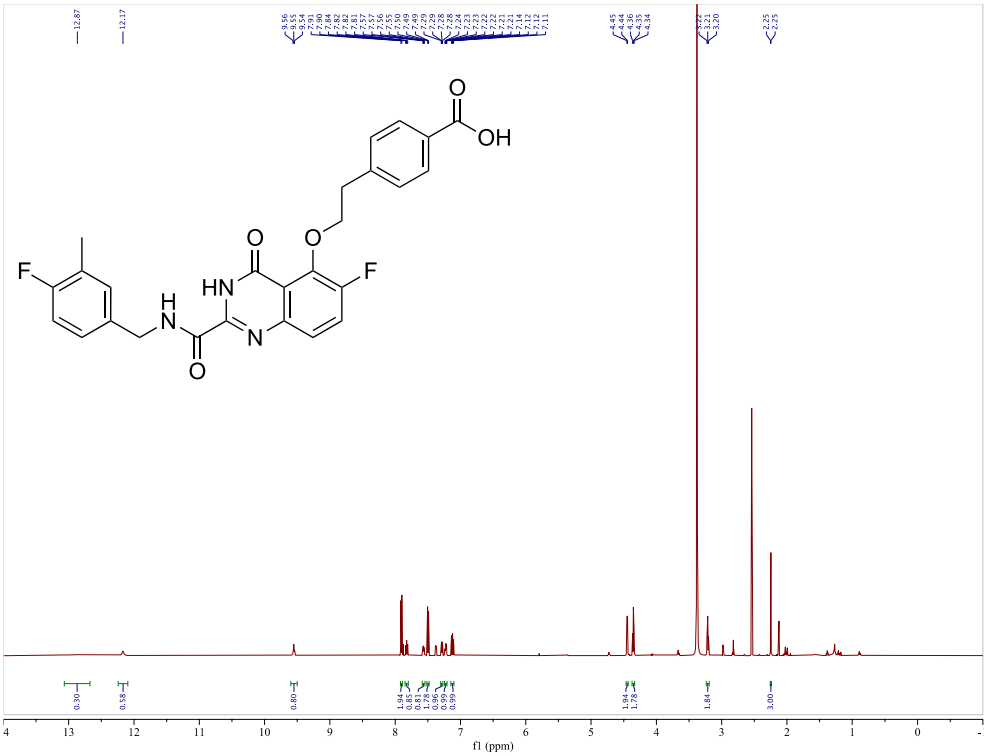

^{13}C-NMR (150 MHz, $(CD_3)_2SO$)

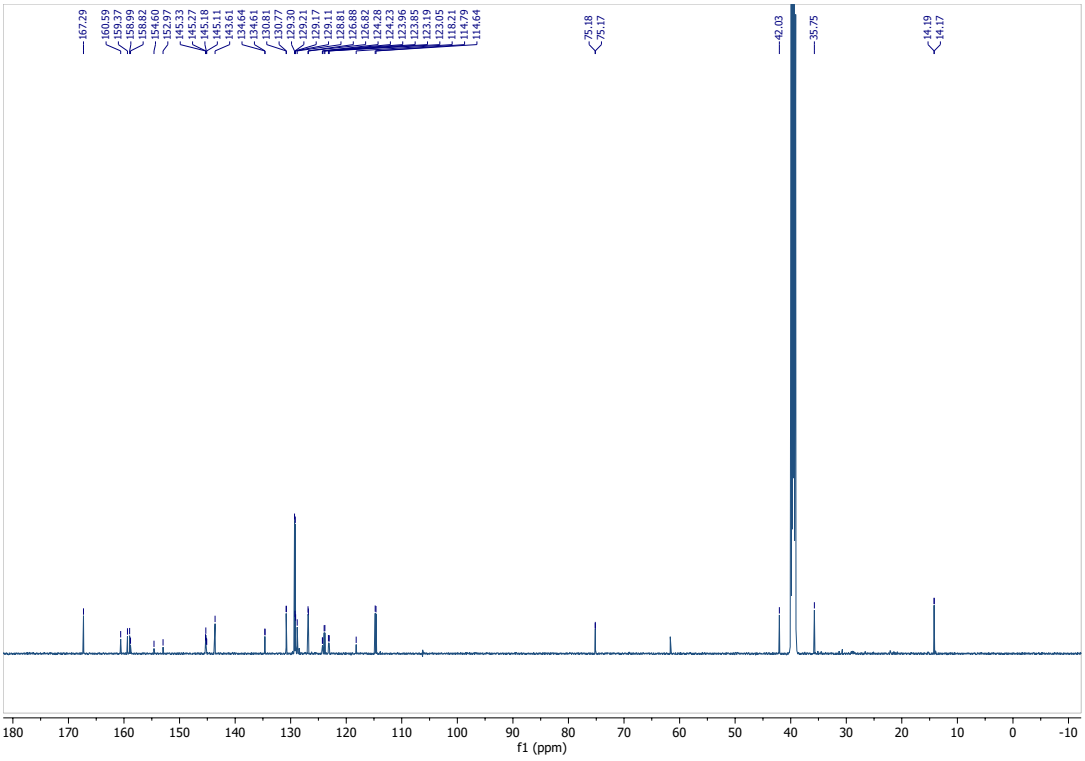

Compound 5e

^{1}H-NMR (600 MHz, $(CD_3)_2SO$)

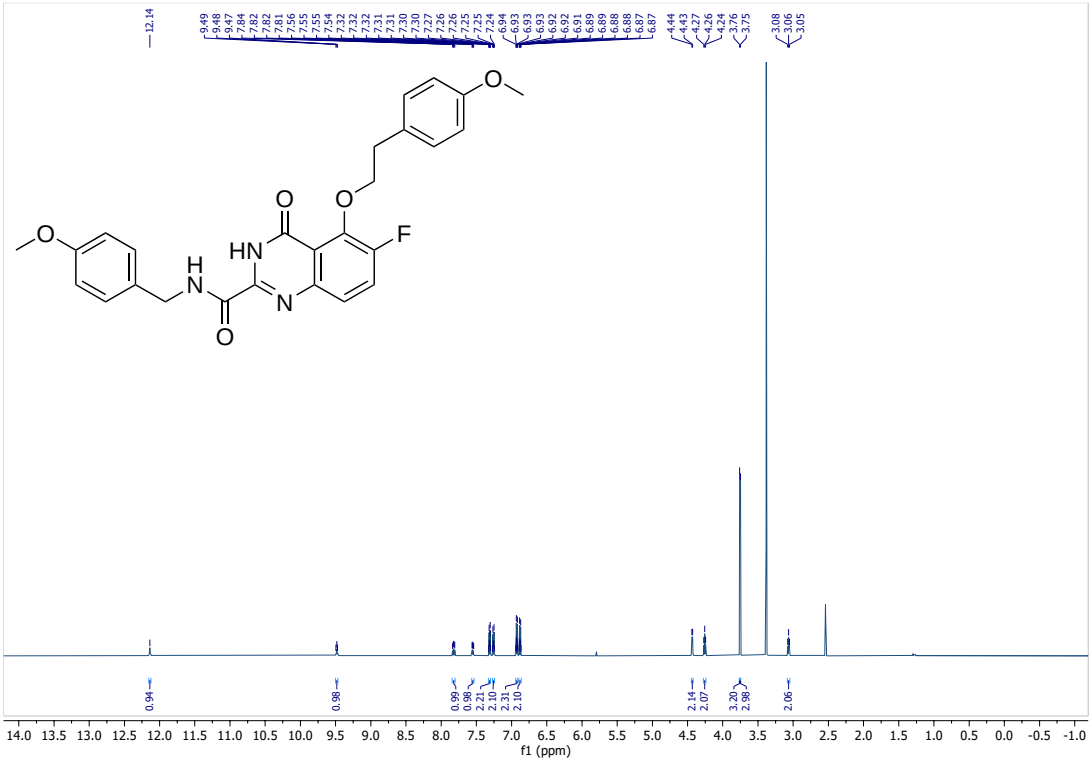

^{13}C-NMR (150 MHz, $(CD_3)_2SO$)

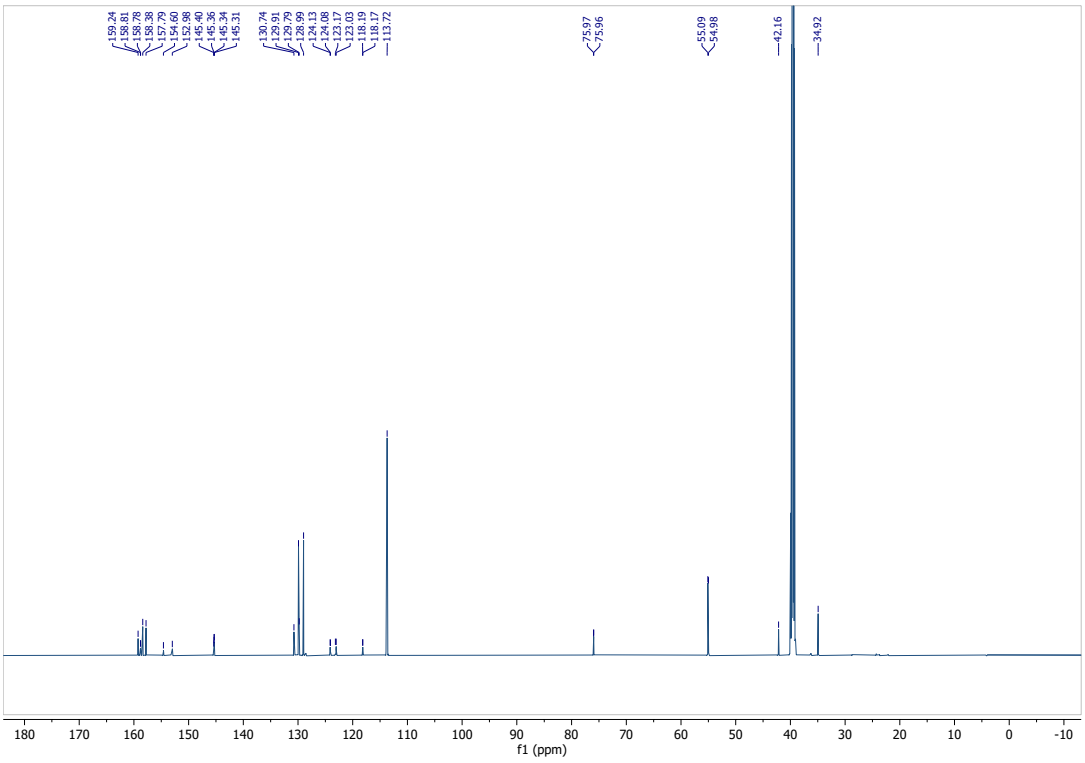

Compound 5f

^{1}H-NMR (600 MHz, $(CD_3)_2SO$)

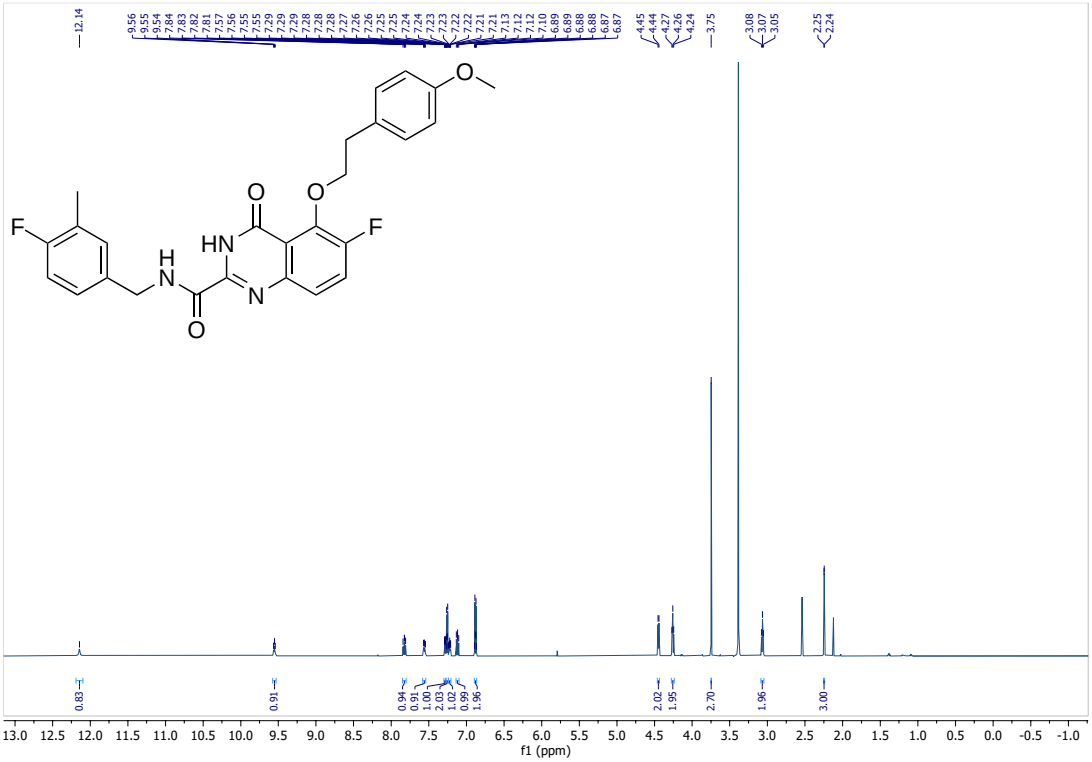

^{13}C-NMR (150 MHz, $(CD_3)_2SO$)

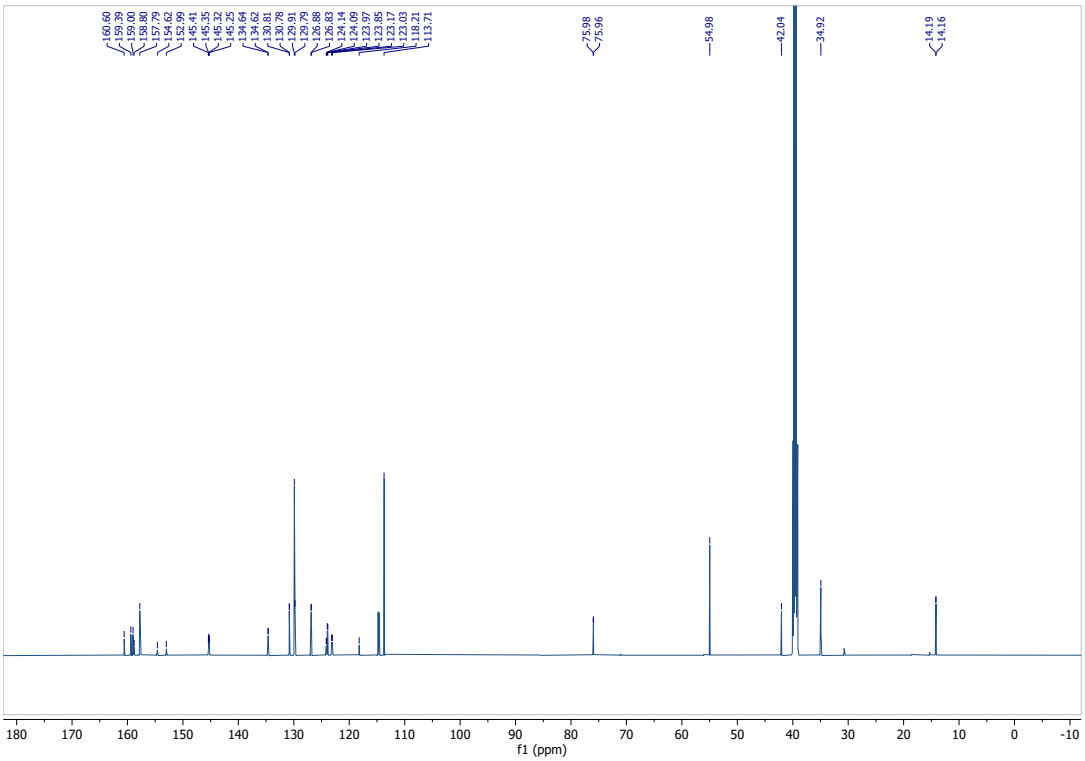

Compound 5g

^{1}H-NMR (600 MHz, $(CD_3)_2SO$)

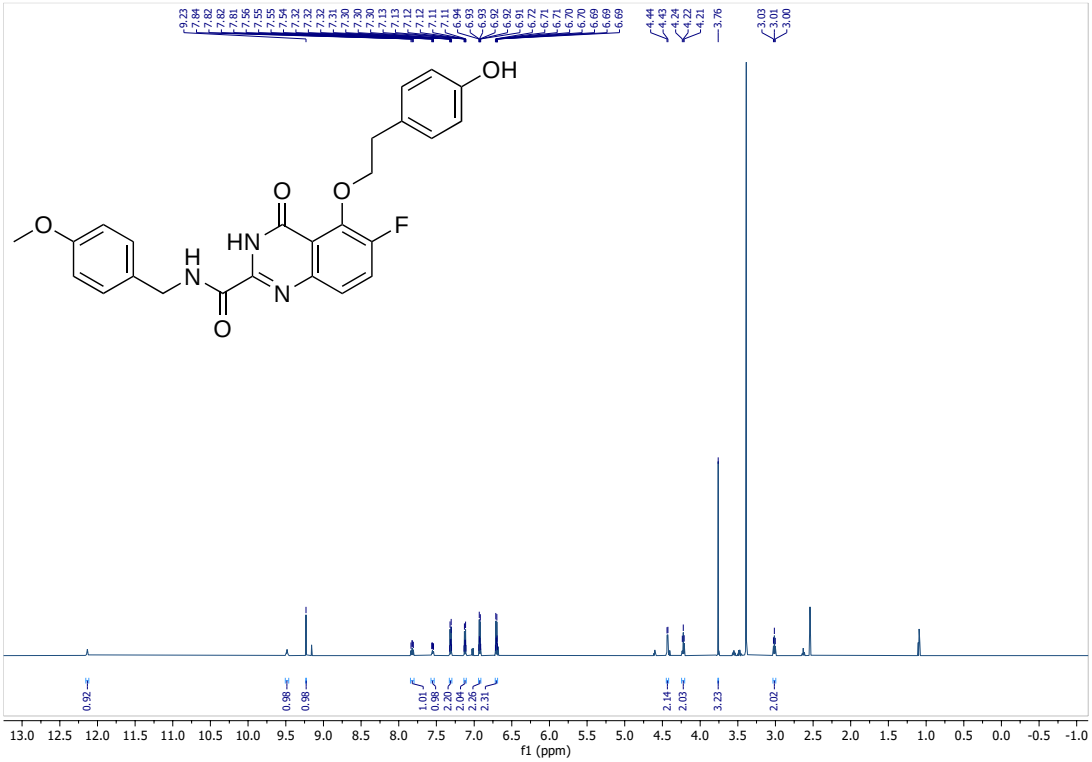

^{13}C-NMR (150 MHz, $(CD_3)_2SO$)

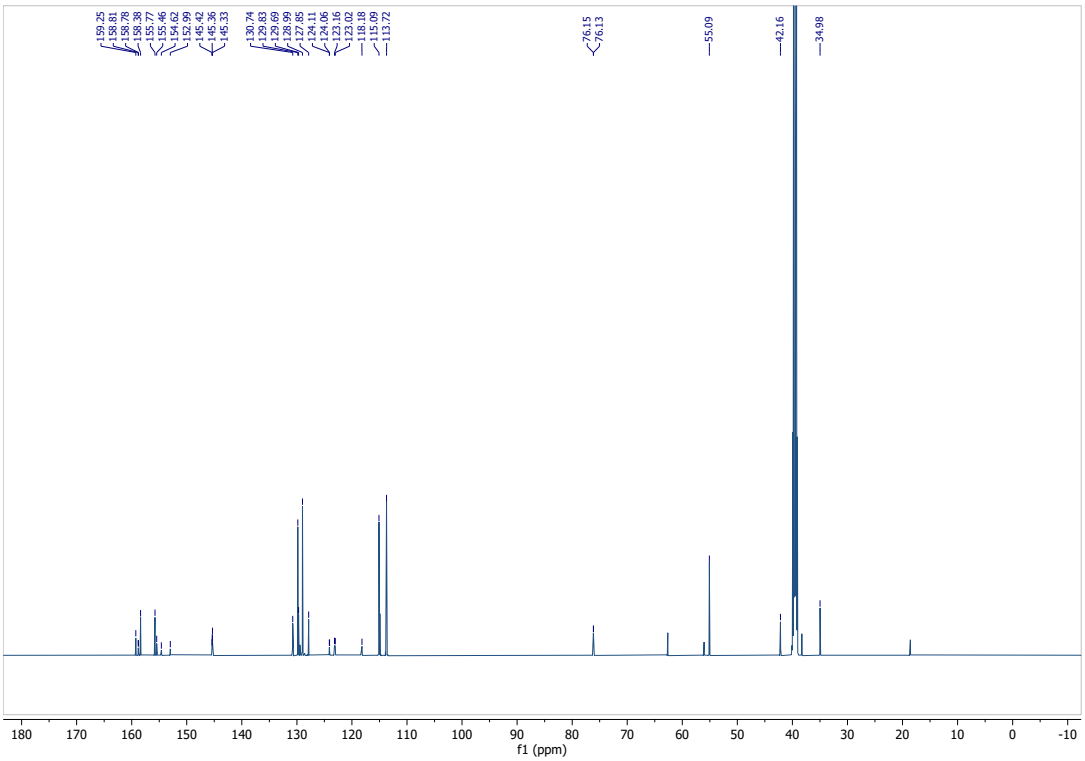

Compound 5h

^{1}H-NMR (600 MHz, $(CD_3)_2SO$)

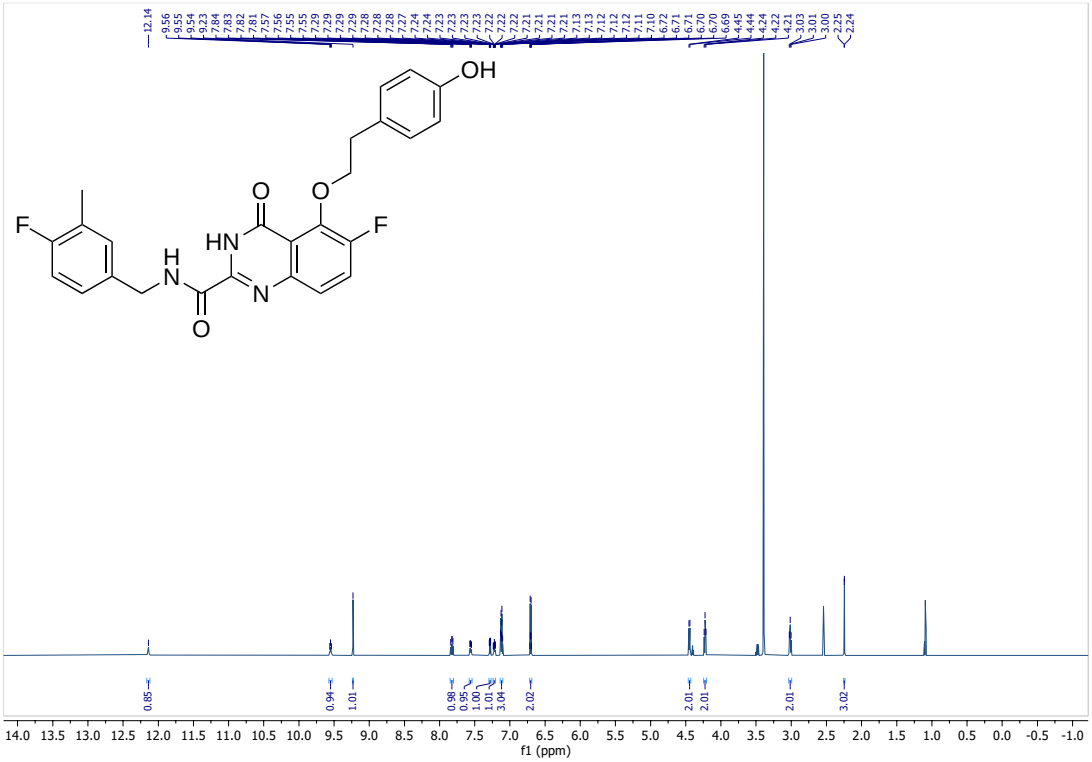

^{13}C-NMR (150 MHz, $(CD_3)_2SO$)

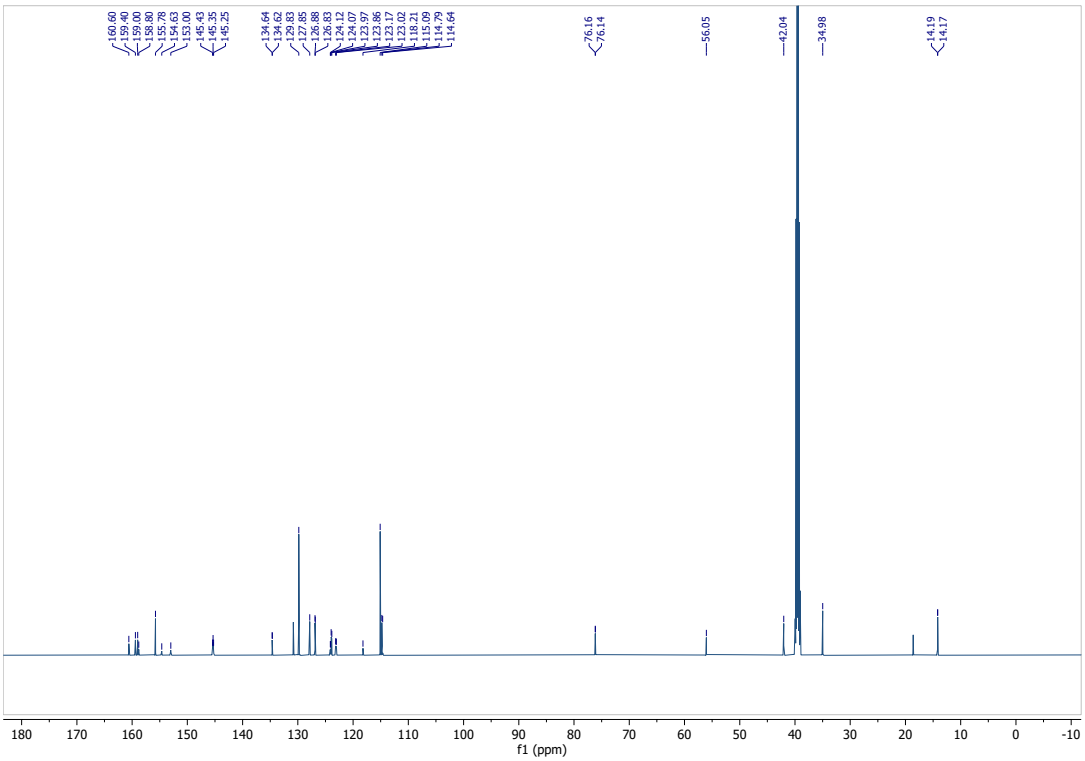

Compound 5i

^{1}H-NMR (600 MHz, $(CD_3)_2SO$)

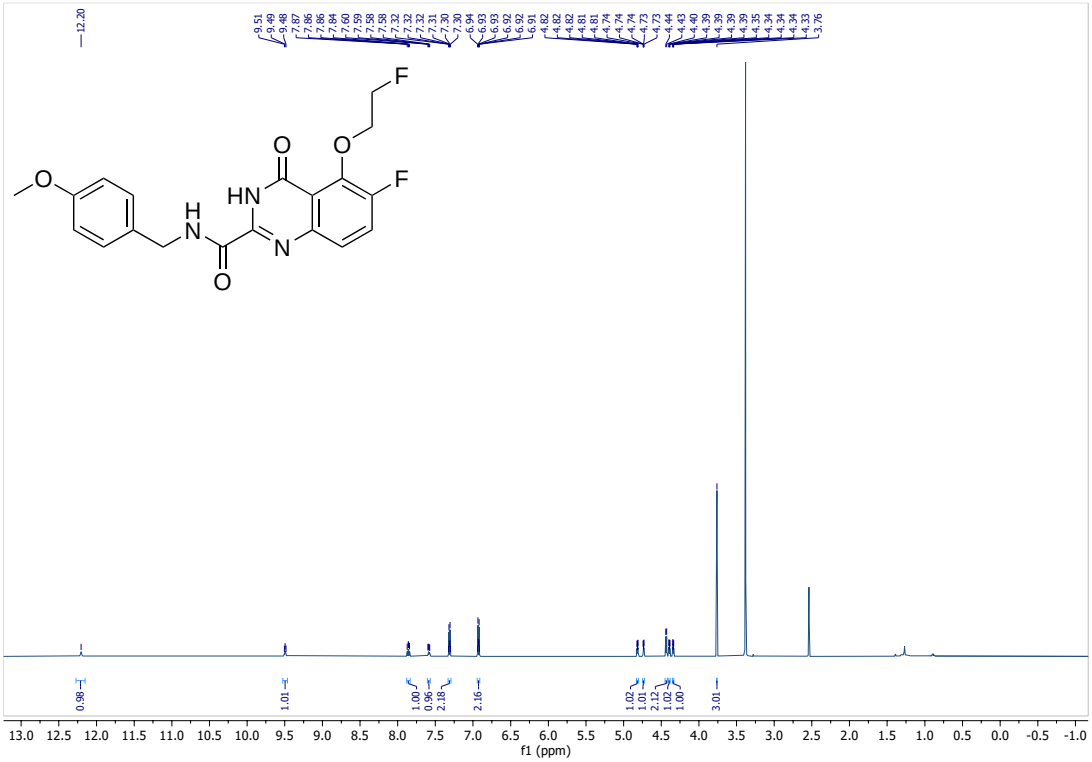

^{13}C-NMR (150 MHz, $(CD_3)_2SO$)

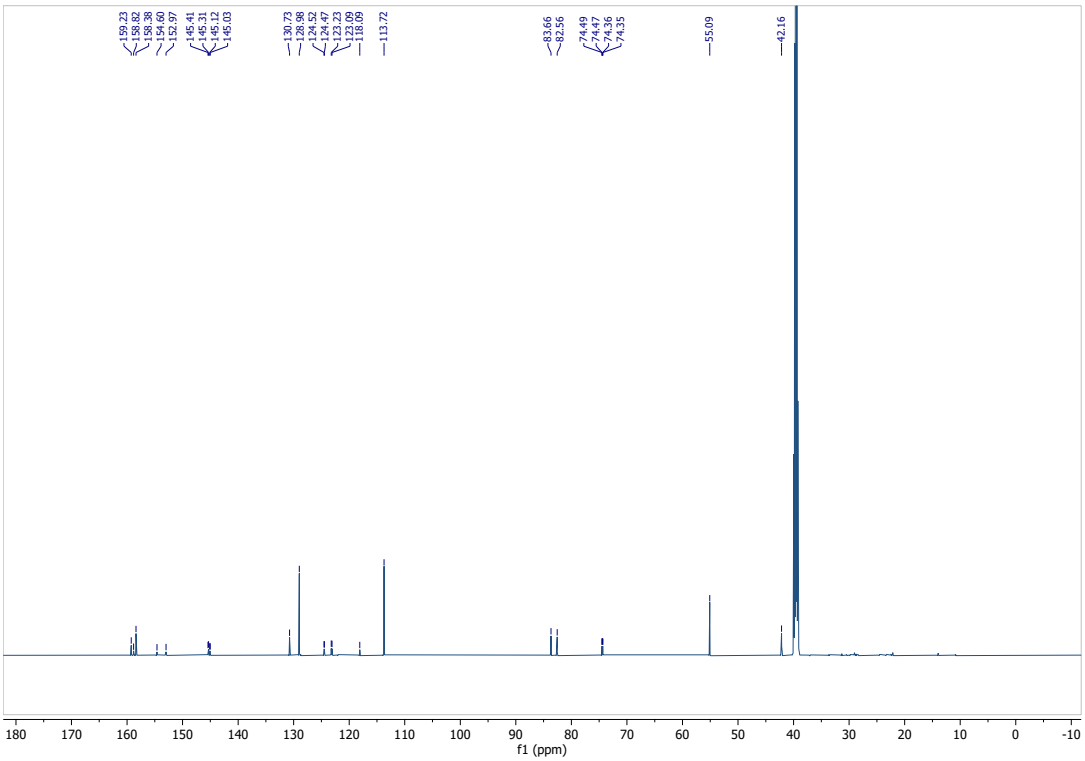

Compound 5j

^{1}H-NMR (600 MHz, $(CD_3)_2SO$)

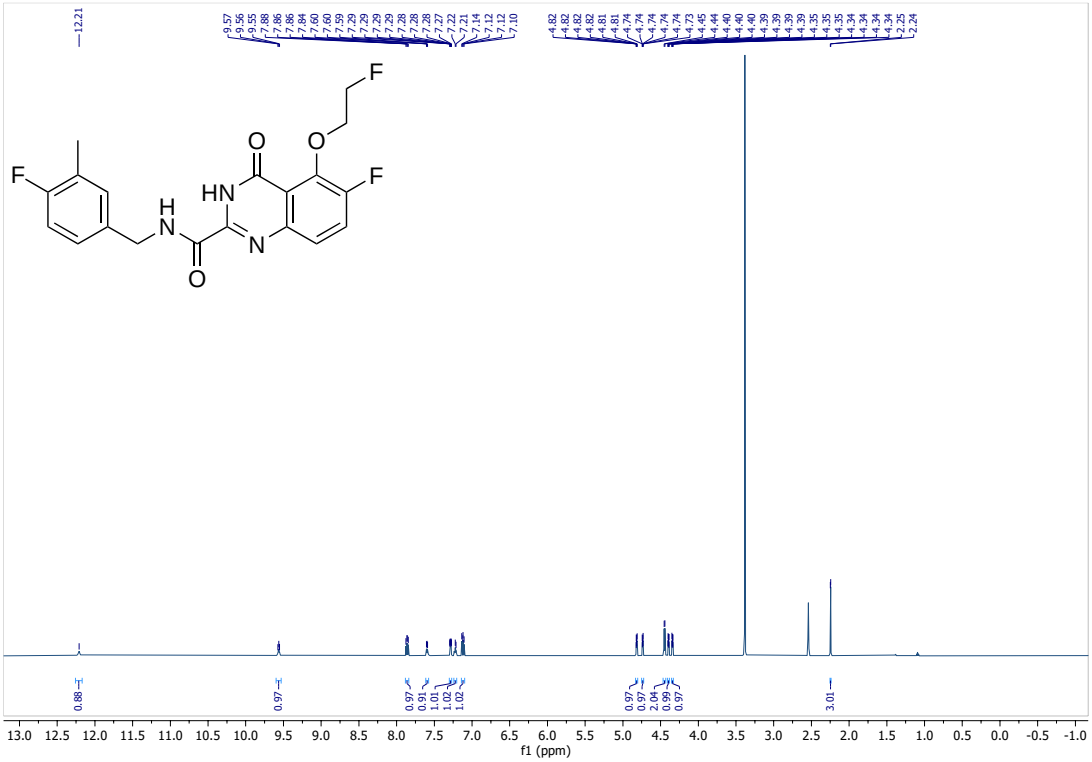

^{13}C-NMR (150 MHz, $(CD_3)_2SO$)

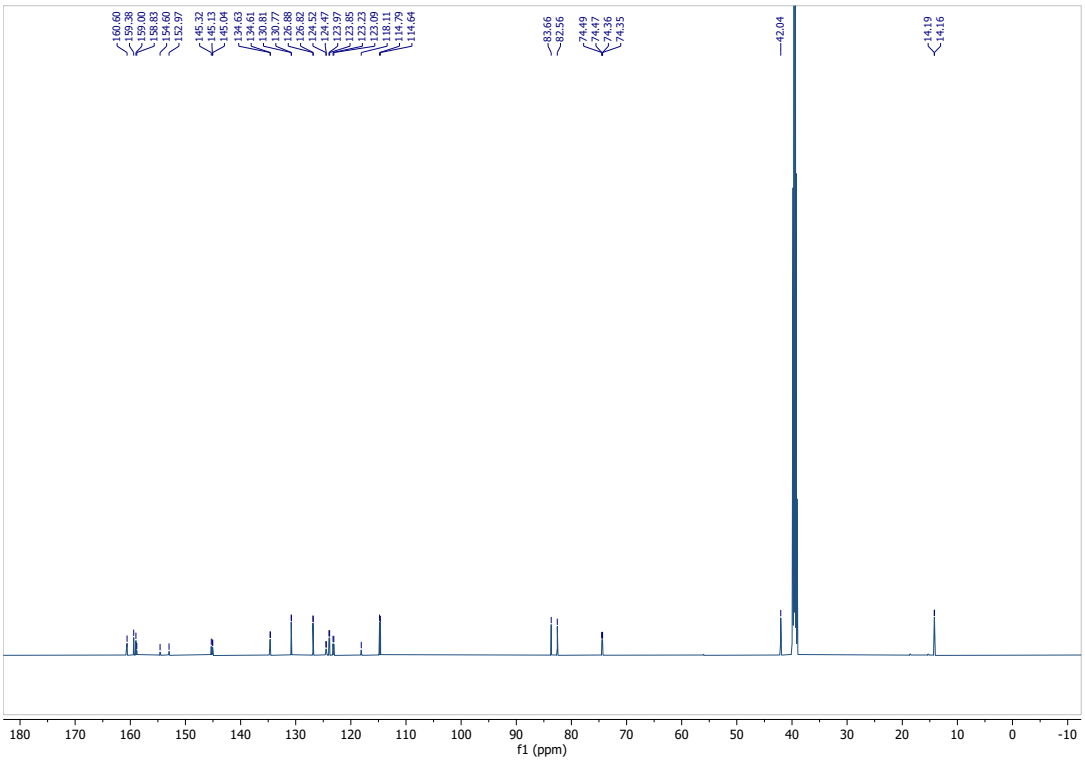

Compound 6

^{1}H-NMR (600 MHz, $CDCl_3$)

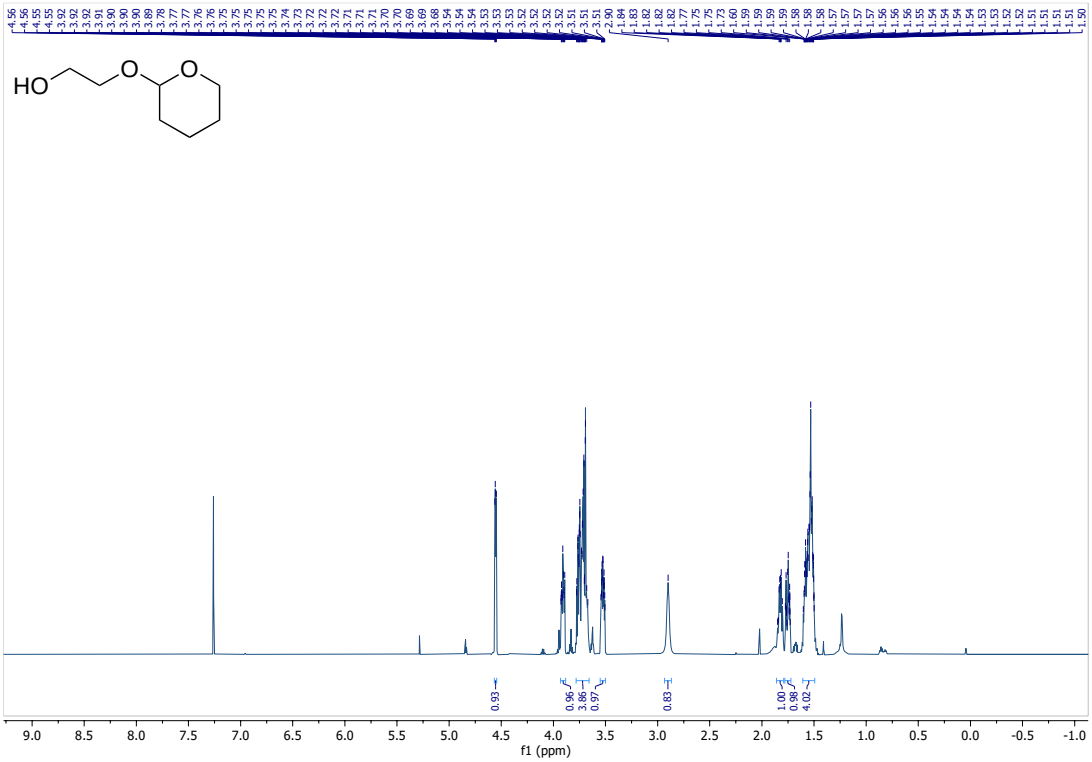

^{13}C-NMR (150 MHz, $CDCl_3$)

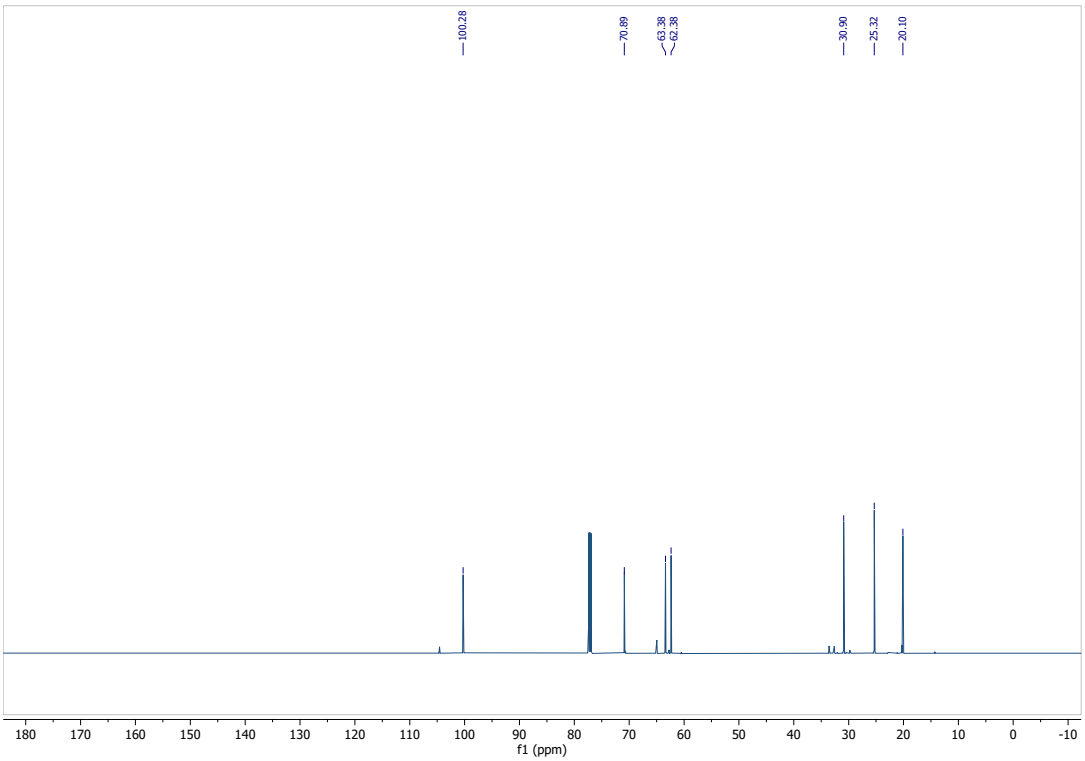

Compound 7

^{1}H-NMR (600 MHz, $(CD_3)_2SO$)

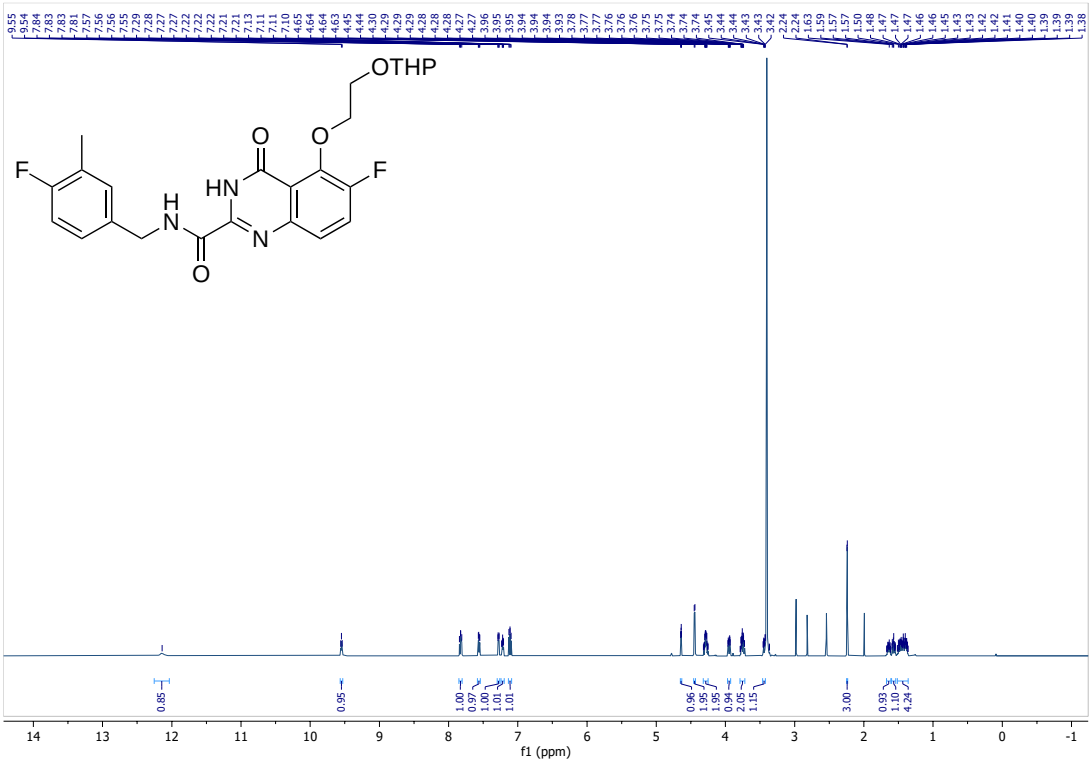

^{13}C-NMR (150 MHz, $(CD_3)_2SO$)

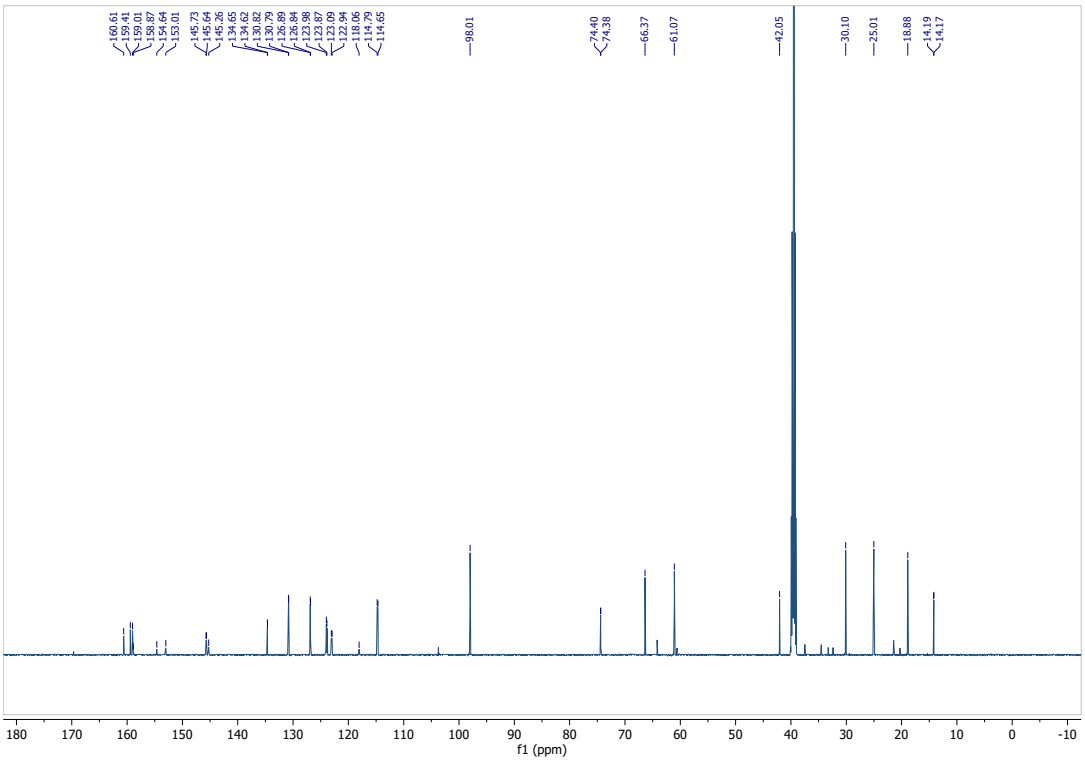

Compound 8

^{1}H-NMR (600 MHz, $(CD_3)_2SO$)

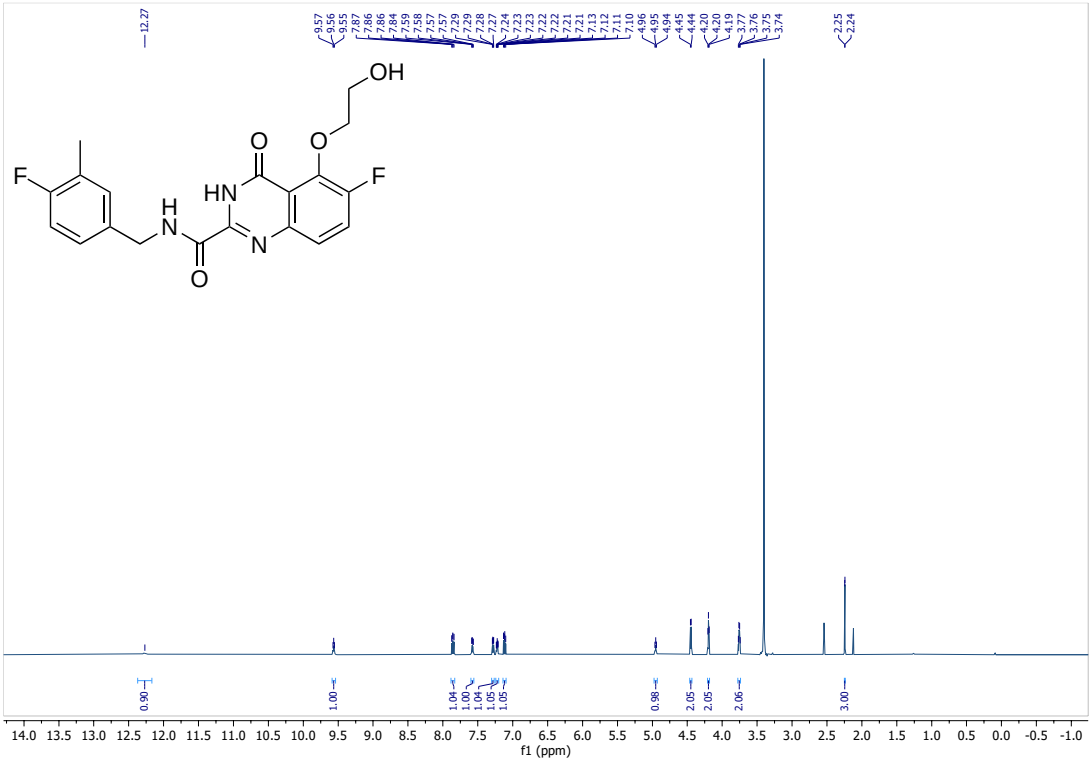

^{13}C-NMR (150 MHz, $(CD_3)_2SO$)

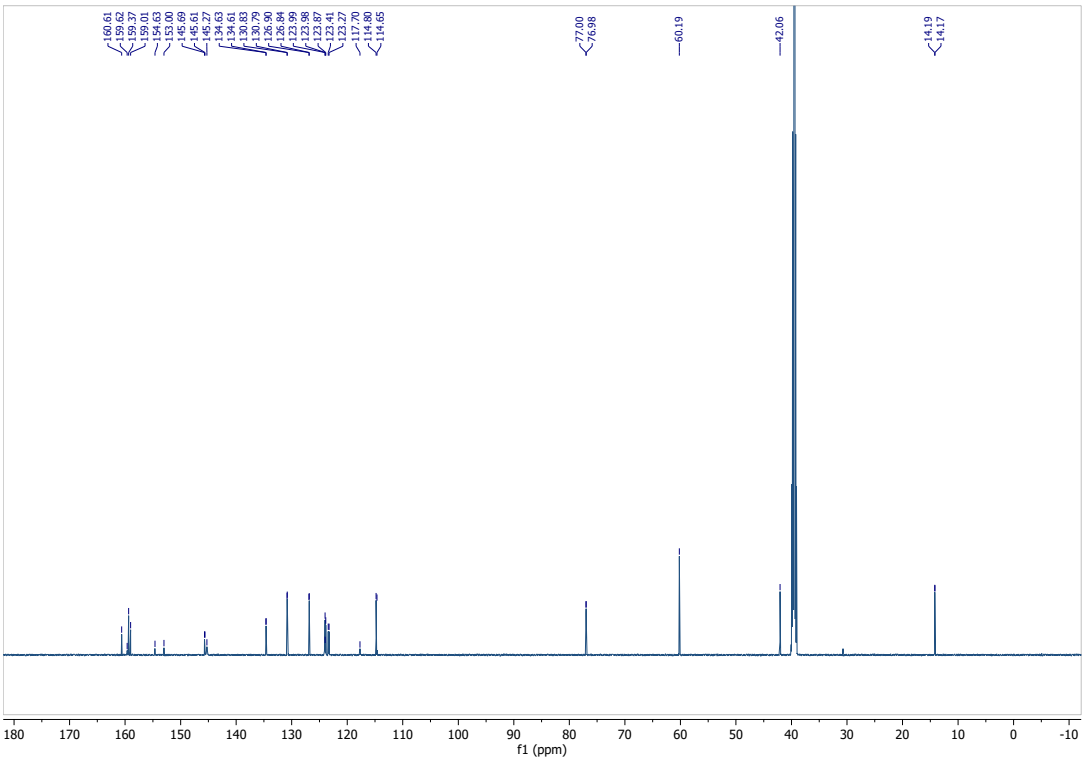

Compound 9

^{1}H-NMR (600 MHz, $(CD_3)_2SO$)

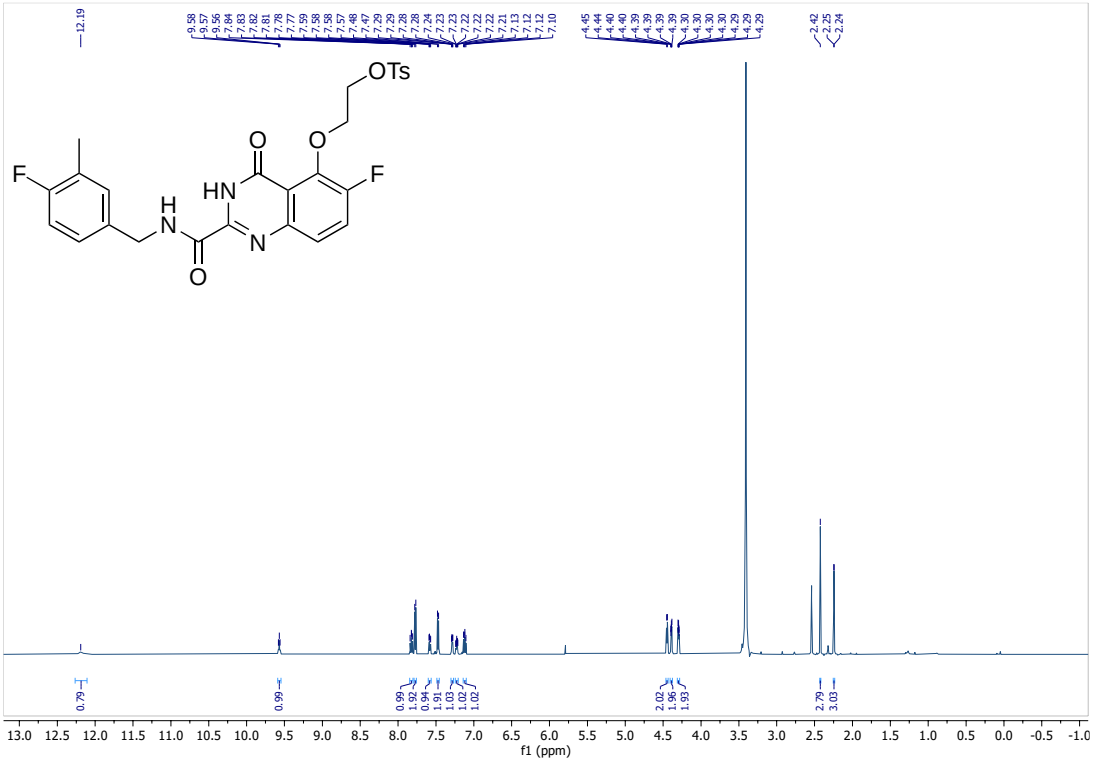

^{13}C-NMR (150 MHz, $(CD_3)_2SO$)

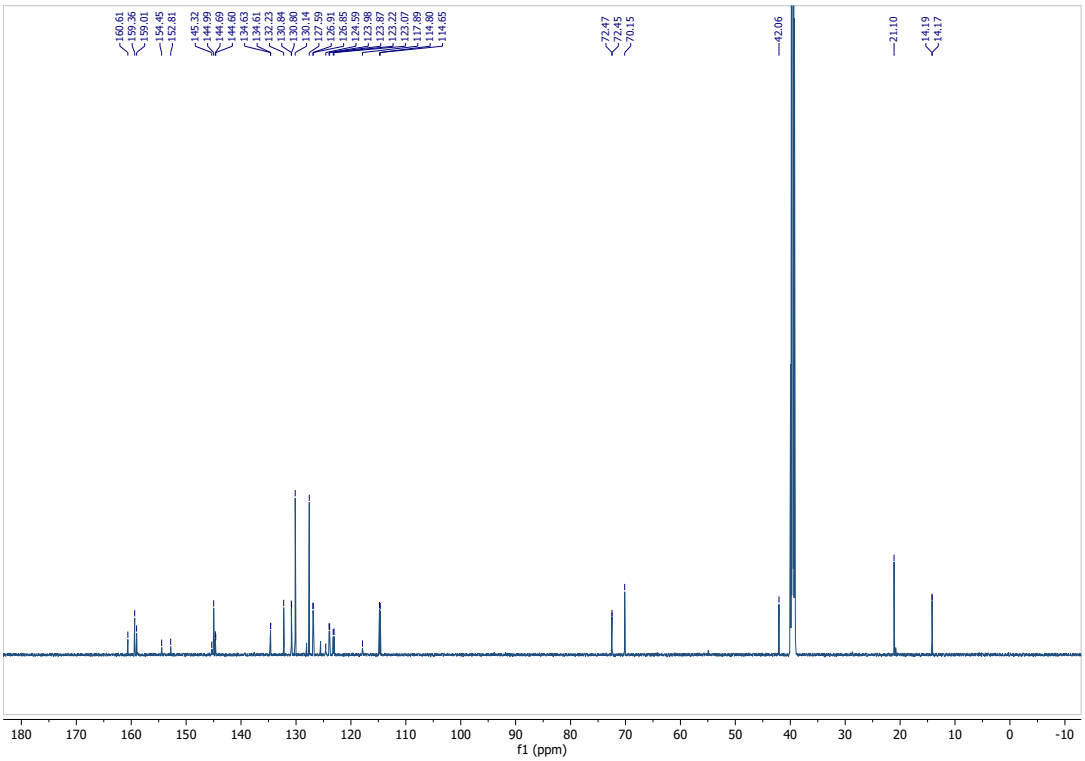

Compound 10

^{1}H-NMR (600 MHz, $(CD_3)_2SO$)

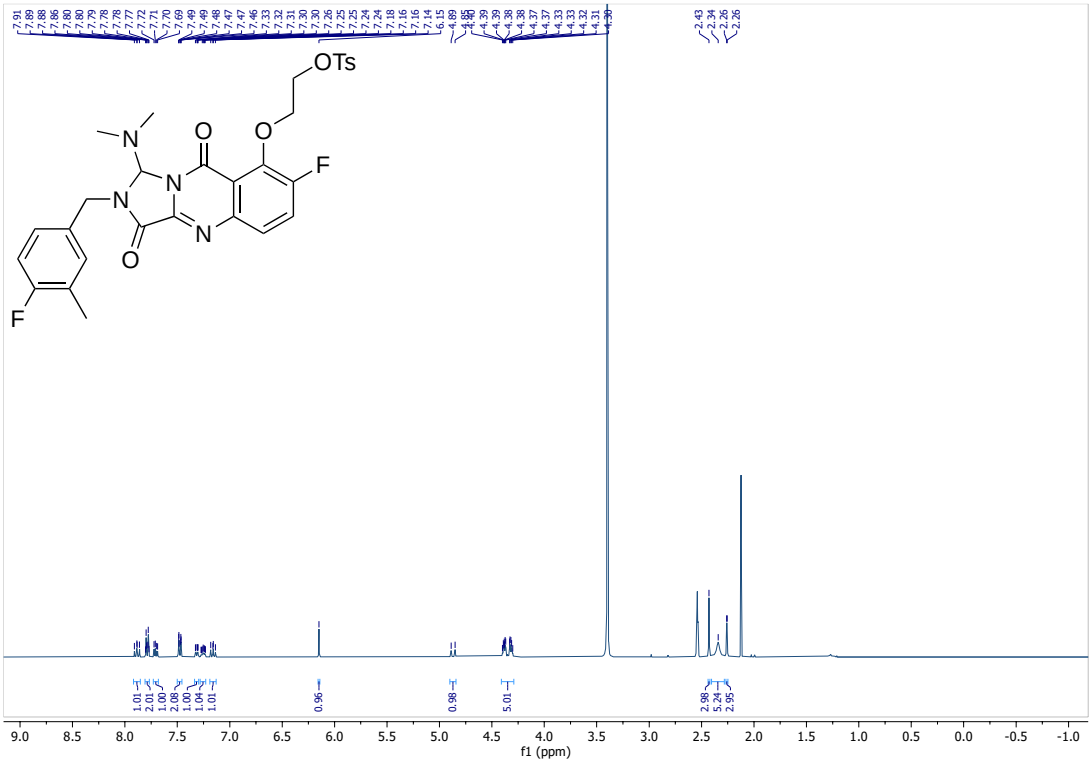

^{13}C-NMR (150 MHz, $CDCl_3$)

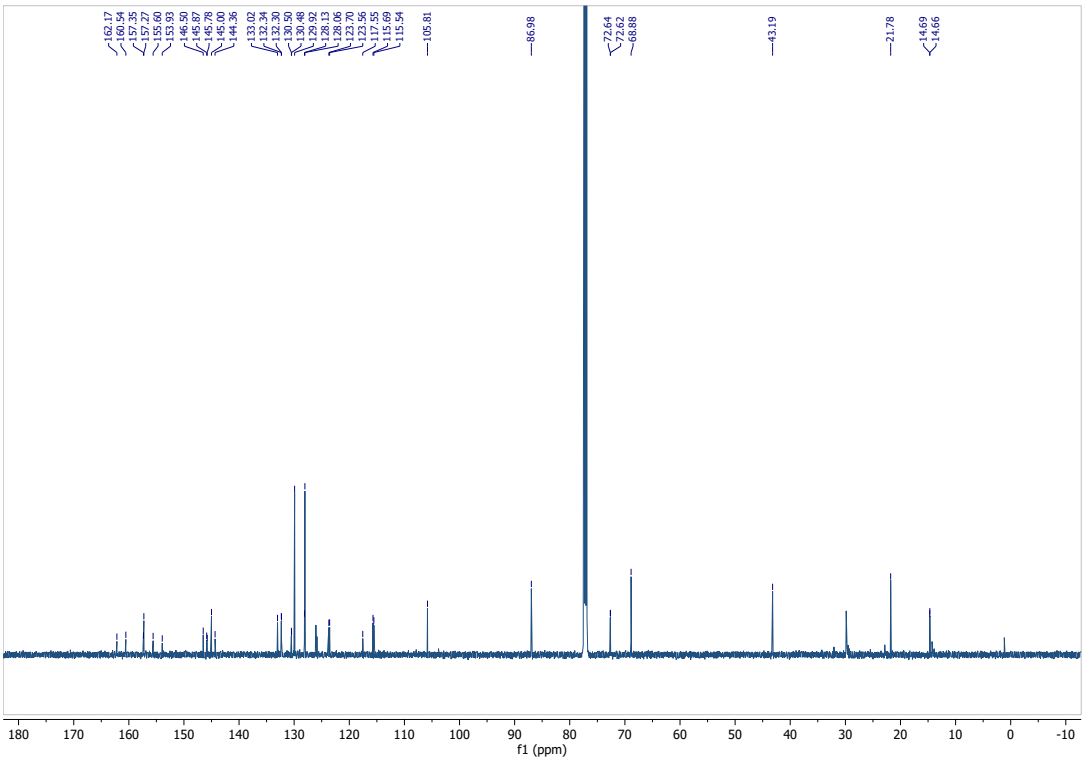

3.9.2 Supplementary Figures and Tables

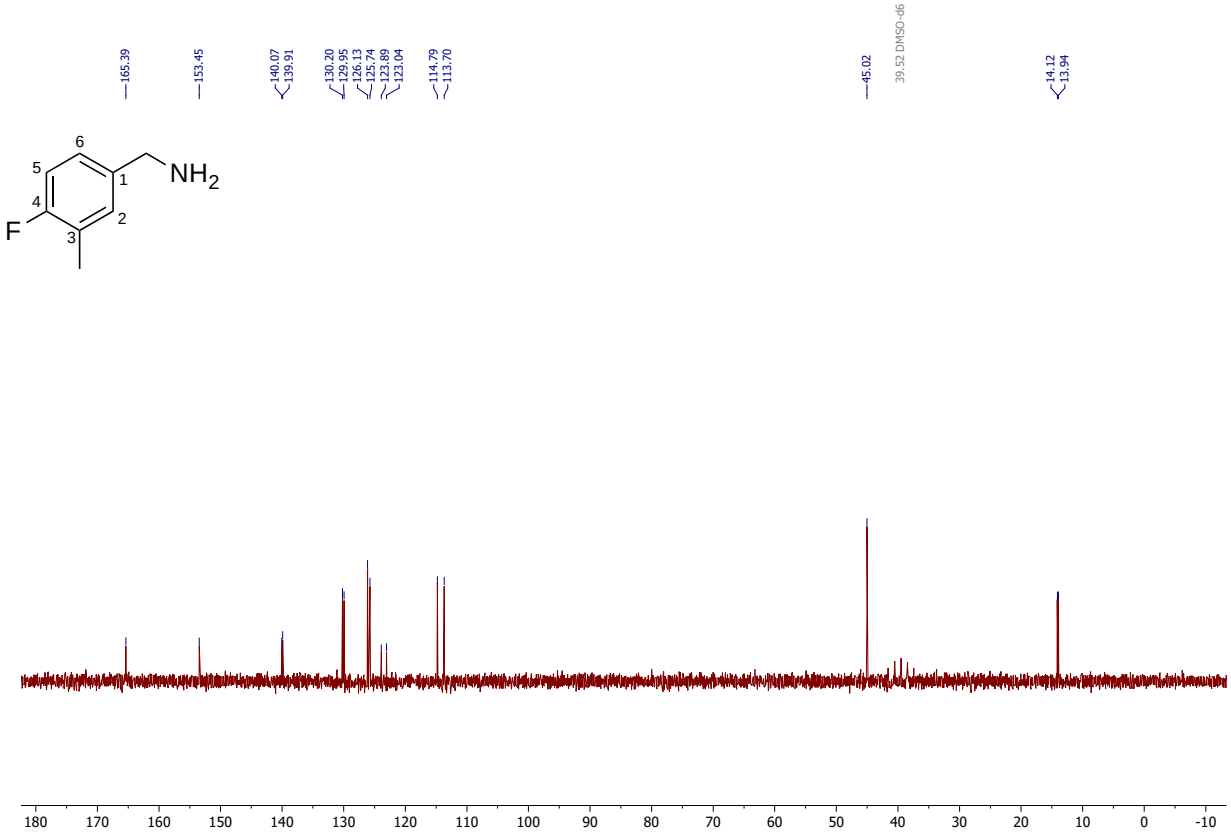

Figure S1. ^{13}C NMR spectrum of 4-fluoro-3-methylbenzylamine (20 MHz, $(CD_3)_2SO$))

Table S1. ^{13}C NMR assignments for 4-fluoro-3-methylbenzylamine.[a]

Carbon Position	δ Chemical Shift (ppm)	J Value (Hz)	C-F Coupling
1	140.0	3.3	*para*
2	125.9	7.7	*meta*
3	123.5	17	*ortho*
4	159.4	241	*ipso*
5	114.2	22	*ortho*
6	130.1	5.1	*meta*

[a] For C–F coupling constants of fluorobenzenes, see reference 2.

Table S2. ^{13}C NMR assignments for compound 5d.

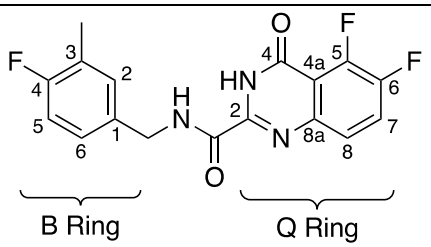

Carbon Position	δ Chemical Shift (ppm)	J Value(s) (Hz)	C-F Coupling
B1	134.6	3.4	*para*
B2	126.9	8.1	*meta*
B3	123.9	17	*ortho*
B4	159.8	241	*ipso*
B5	114.7	22	*ortho*
B6	130.8	5.1	*meta*
Q2	146.1	-	-
Q4	158.2	-	-
Q4a	113.6	-	-
Q5	147.7	263, 14	*ipso*, *ortho*
Q6	148.0	245, 11	*ipso*, *ortho*
Q7	123.6	19	*ortho*
Q8	124.3	br	-
Q8a	144.7	-	-

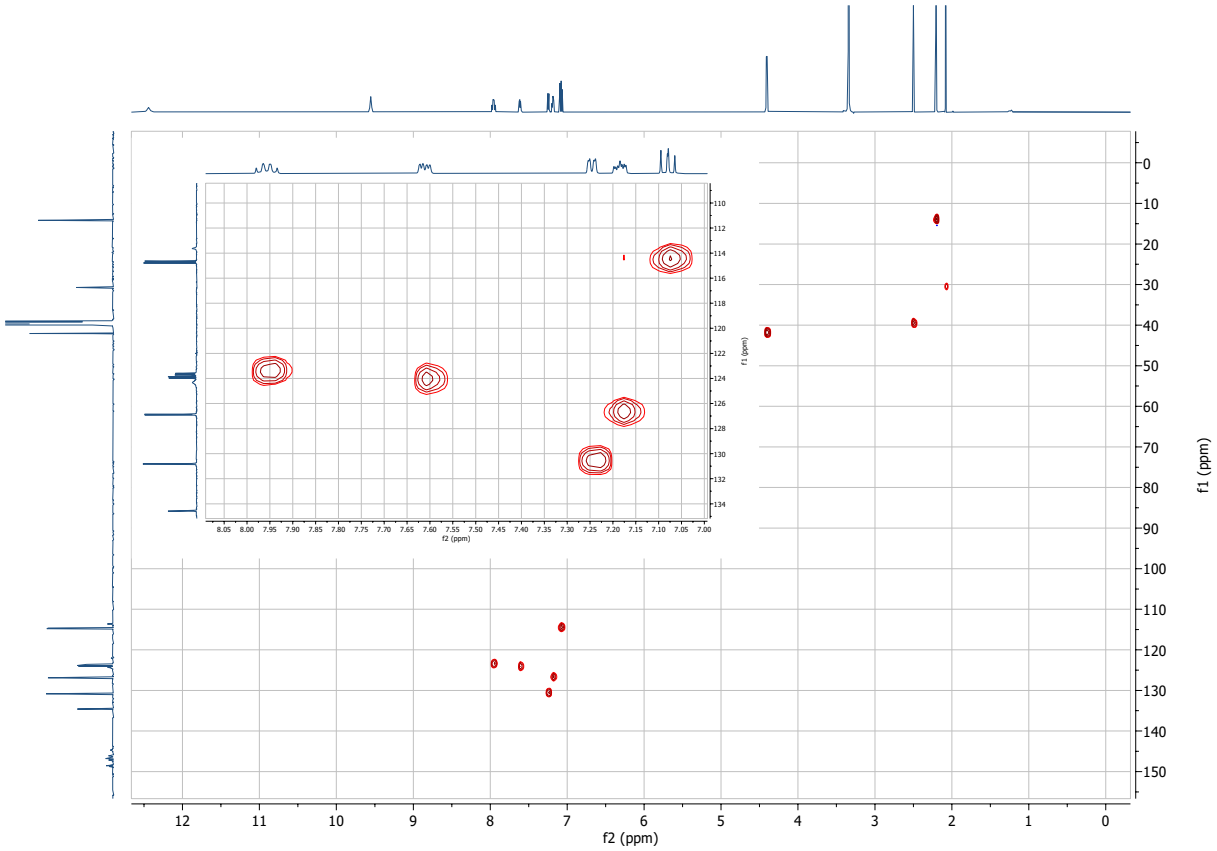

Figure S2. HSQC analysis of compound 5d (^{1}H (600 MHz) vs ^{13}C (150 MHz), $(CD_3)_2SO$). ^{13}C NMR signals from the B ring are maintained. Remaining aromatic carbon signals which are HSQC positive correspond to Q7 and Q8 on the Q ring. Q7 (123.6, J = 19 Hz, C-F *ortho* coupling) corresponds to signal at 8.02–7.97 (1H, m). Q8 (124.3, br, C-F *meta* coupling) corresponds to signal at 7.66–7.64 (1H, m).

Table S3. ^{13}C NMR assignments for compound 5j.

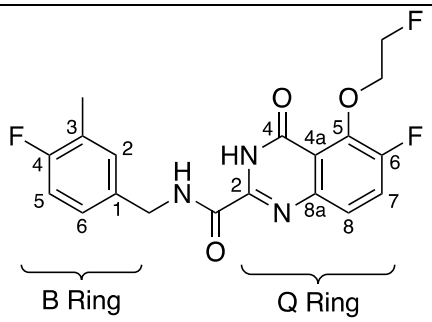

Carbon Position	δ Chemical Shift (ppm)	J Value(s) (Hz)	C-F Coupling
B1	134.6	3.3	*para*
B2	126.8	8.3	*meta*
B3	123.9	17	*ortho*
B4	159.8	240	*ipso*
B5	114.7	22	*ortho*
B6	130.8	4.7	*meta*
Q2	145.3	-	-
Q4	158.8	-	-
Q4a	118.1	-	-
Q5	145.0	14	*ortho*
Q6	153.8	245	*ipso*
Q7	123.1	21	*ortho*
Q8	124.5	6.5	*meta*
Q8a	145.2	-	-

Q7 and Q8 *J*-values are consistent with SNAr at the 5-position on the Q-ring as *ortho* and *meta* C-F coupling is maintained (J = 21 Hz and 6.5 Hz, respectively).

Table S4. ^{13}C NMR assignments for compound 7.

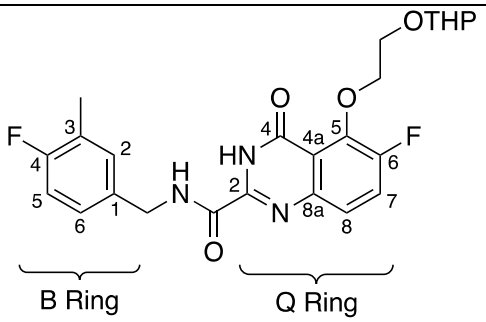

Carbon Position	Chemical Shift (ppm)	J Value(s) (Hz)	C-F Coupling
B1	134.6	4.5	*para*
B2	126.9	7.5	*meta*
B3	123.9	17	*ortho*
B4	159.8	240	*ipso*
B5	114.7	21	*ortho*
B6	130.8	4.5	*meta*
Q2	145.3	-	-
Q4	158.9	-	-
Q4a	118.1	-	-
Q5	145.7	14	*ortho*
Q6	153.8	245	*ipso*
Q7	123.0	23	*ortho*
Q8	124.1	br	-
Q8a	145.2	-	-

Q7 *J*-value is consistent with S_NAr at 5-position on the Q ring as *ortho* C-F coupling is maintained (J = 23 Hz).

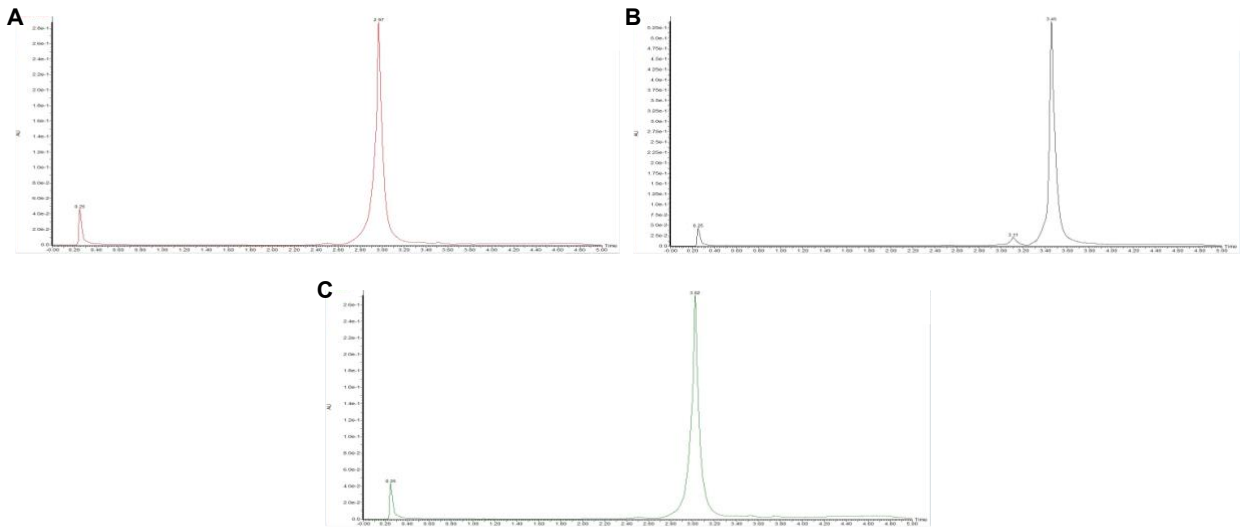

Figure S3. UPLC chromatograms for compounds (A) 5b, (B) 5f and (C) 5j (254 nm). Solvent A: water, solvent B: ACN, solvent C: 5% formic acid, flowrate: 0.5 mL·min^{-1}. Method: 0-0.5 min 93% A 5% B 2% C, 0.5-3.5 min gradient to 5% A 93% B 2% C, 3.5-4.0 min 5% A 93% B 2%, 4.0-4.2 min gradient to 93% A 5% B 2% C, 4.2-5.0 min 93% A 5% B 2% C.

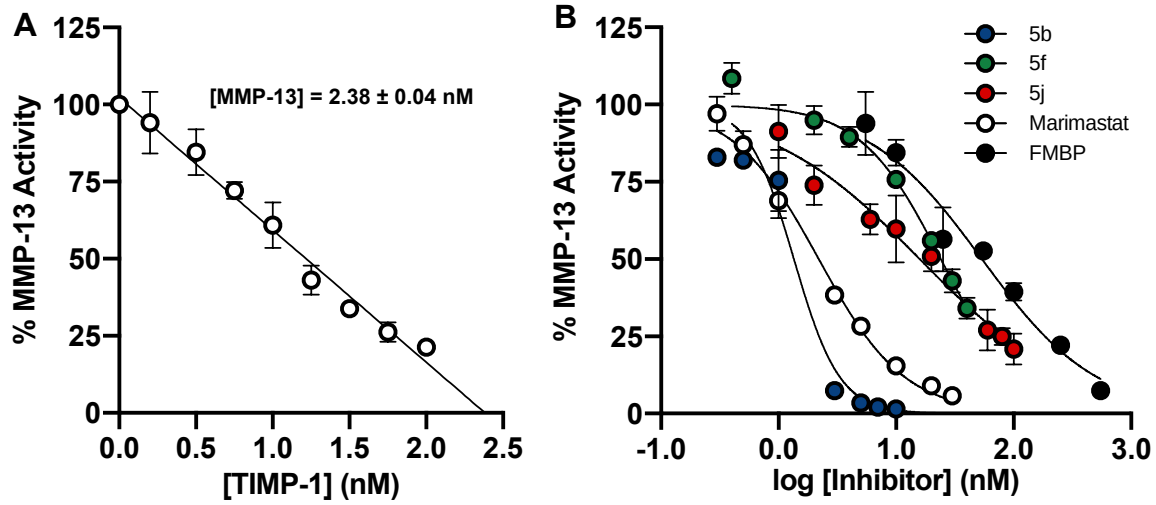

Figure S4. MMP-13 inhibition assays. (A) MMP-13 active site titration with TIMP-1 (R&D Systems).[1] (B) Representative MMP-13 IC_{50} curves.

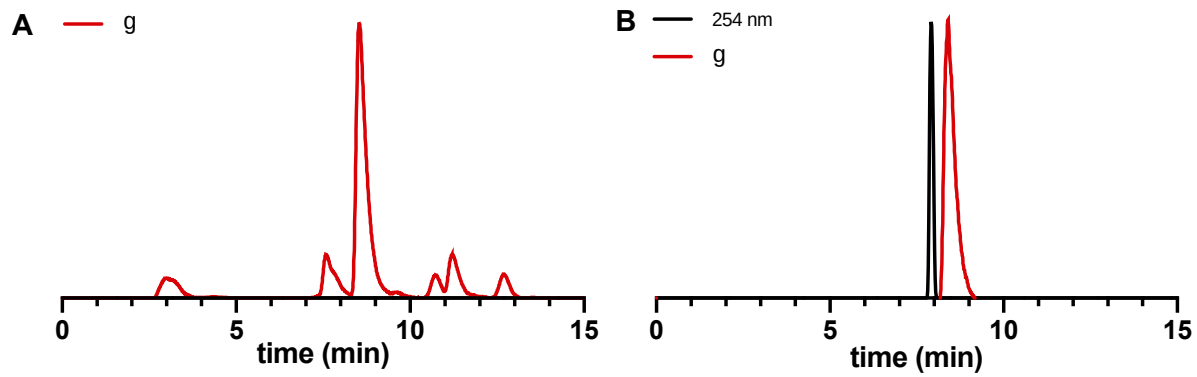

Figure S5. RadioHPLC chromatograms for synthesis of [^{11}C]5b. (A) Crude [^{11}C]methylation of precursor 5a and (B) Purified [^{11}C]5b with co-injection of 5b.

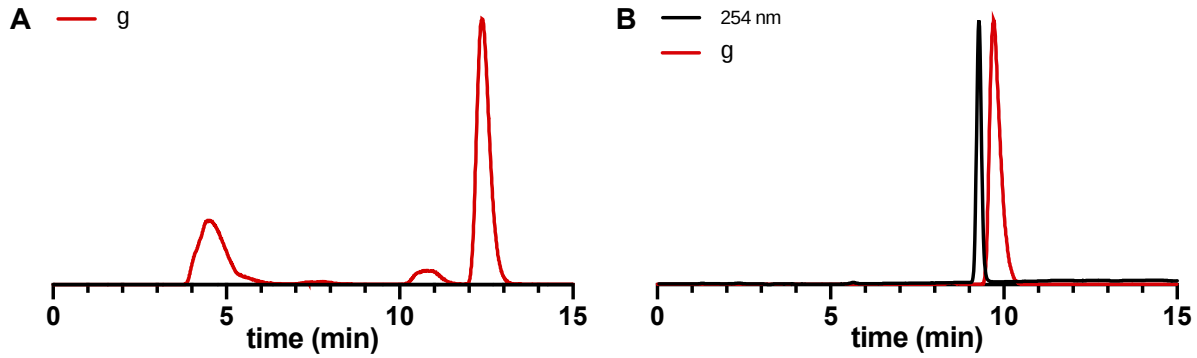

Figure S6. RadioHPLC chromatograms for synthesis of [^{11}C]5f. (A) Crude [^{11}C]methylation of precursor 5h and (B) Purified [^{11}C]5f with co-injection of 5f. *Note: the retention time of the product shifted following HPLC maintenance.

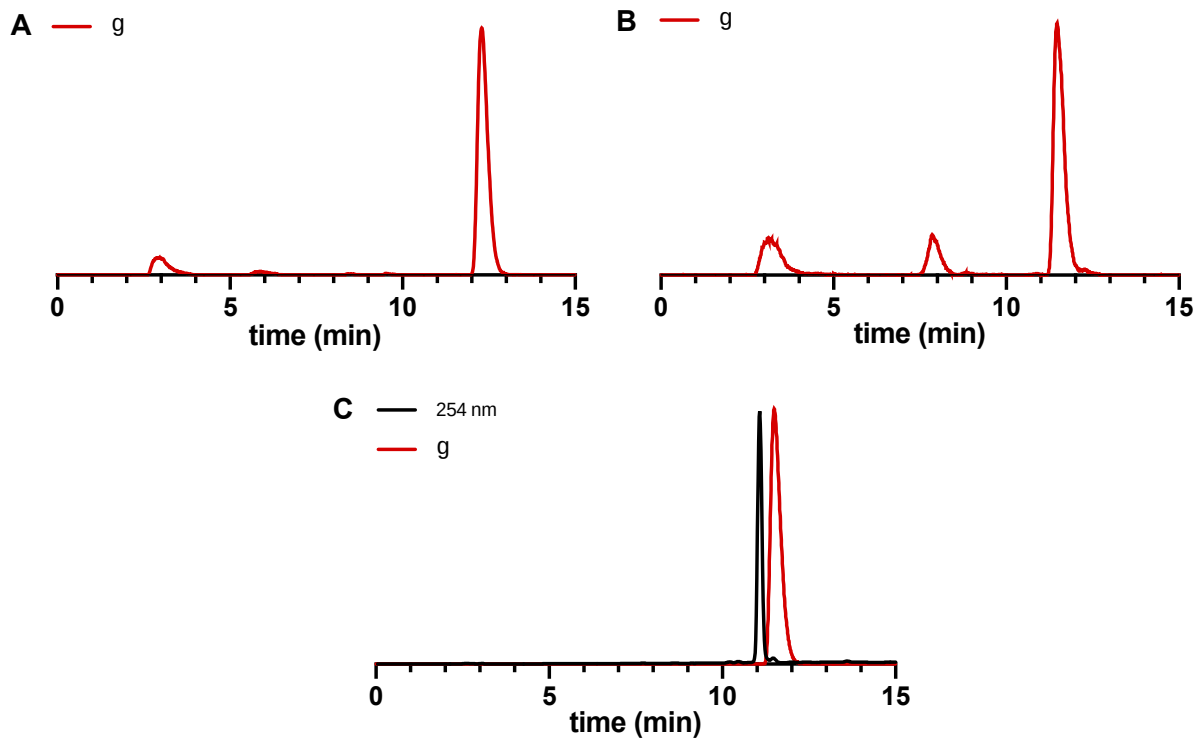

Figure S7. RadioHPLC chromatograms for synthesis of [^{18}F]5j. (A) Crude radiofluorination of precursor 10 (B) Crude deprotection and (C) Purified [^{18}F]5j with co-injection of 5j.

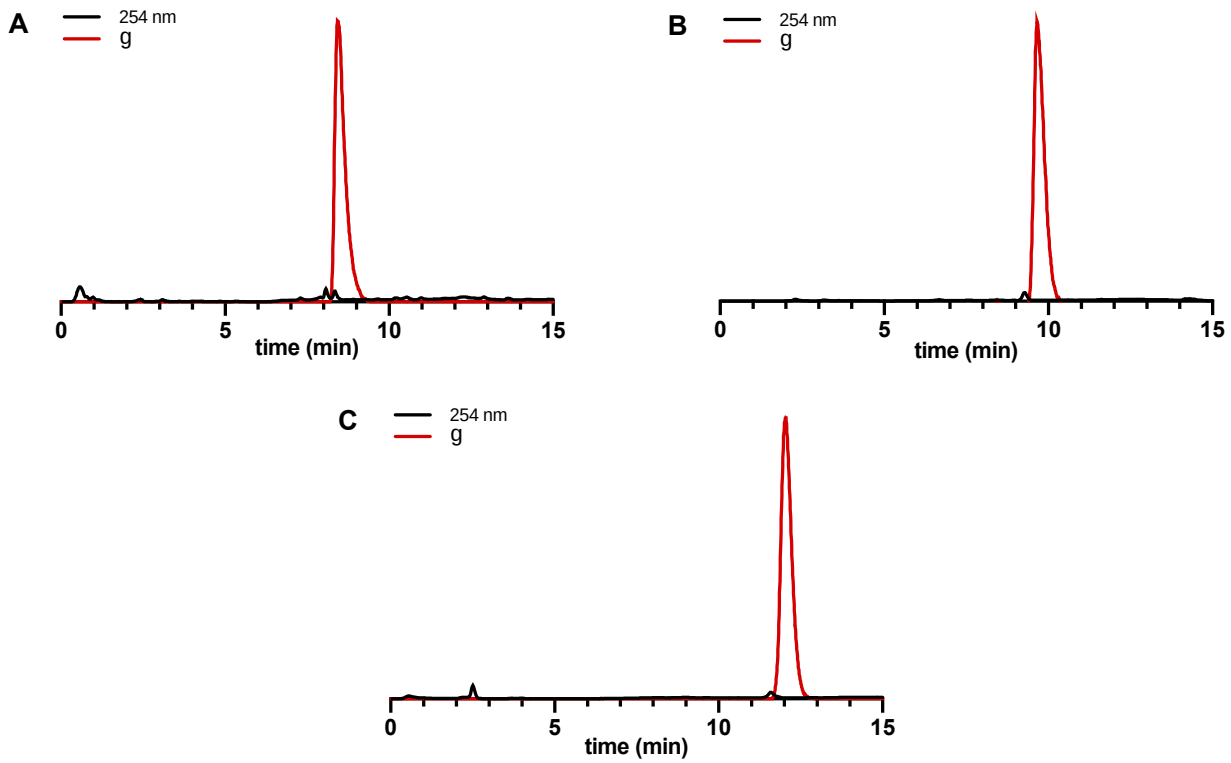

Figure S8. RadioHPLC chromatograms without coinjection. (A) [^{11}C]5b. (B) [^{11}C]5f. (C) [^{18}F]5j.

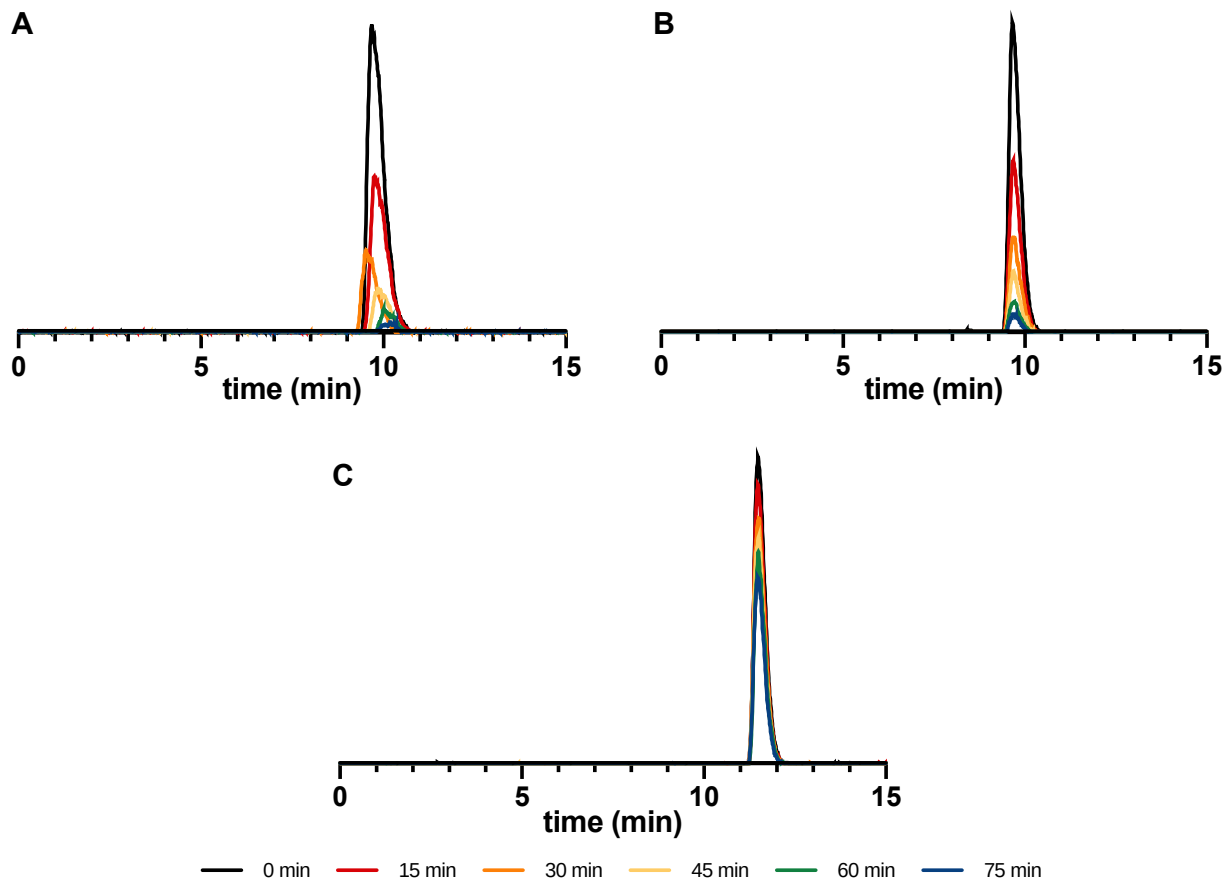

Figure S9. Radiotracer stability following reformulation in 10% EtOH/saline (0.9%). (A) [^{11}C]5b. (B) [^{11}C]5f. (C) [^{18}F]5j.

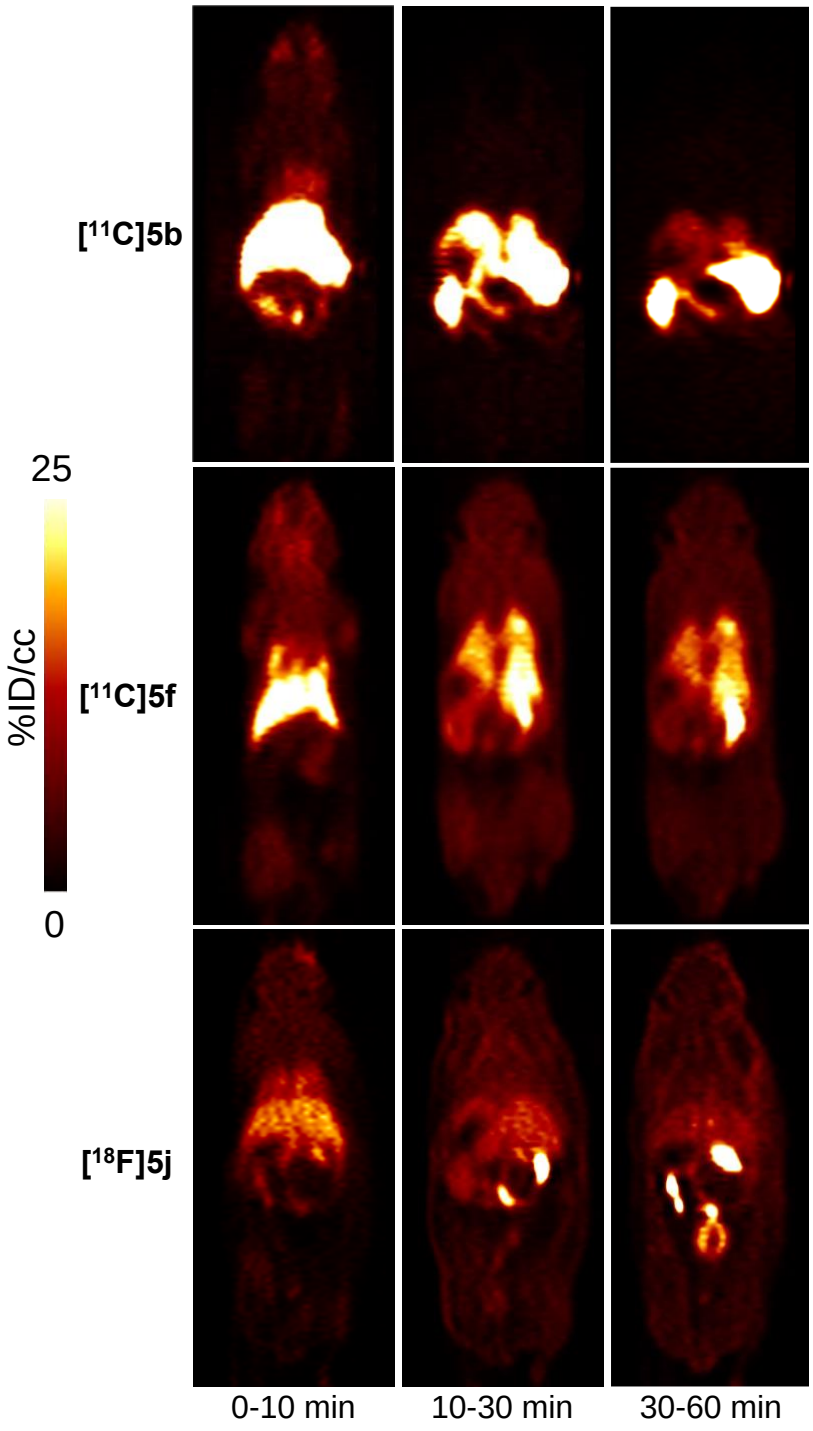

Figure S10. Representative summed coronal whole-body PET images in *ApoE*$^{-/-}$ mice.

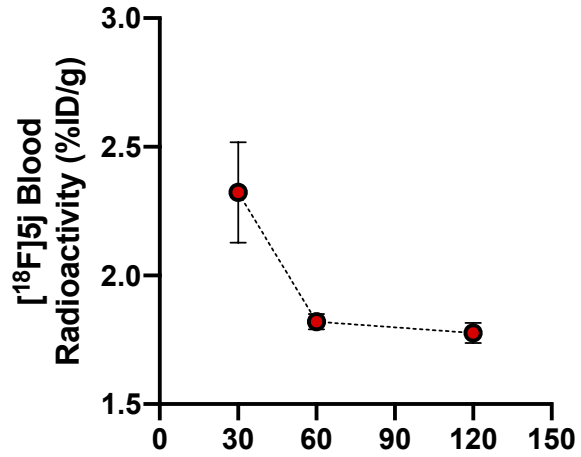

Figure S11. [^{18}F]5j blood radioactivity time-course. Anesthetized *ApoE*$^{-/-}$ mice were intravenously administered with [^{18}F]5j (15 ± 1 MBq) via the lateral tail vein and immediately returned to their cages. Mice were sacrificed by CO_2 asphyxiation at the indicated time (30, 60 or 120 min) and blood was collected by cardiac puncture. Samples were weighed and counted for radioactivity using a gamma counter (n = 2–3 per group).

References

(1) Knight, C. G.; Willenbrock, F.; Murphy, G. A Novel Coumarin-Labelled Peptide for Sensitive Continuous Assays of the Matrix Metalloproteinases. *FEBS Lett.* **1992**, *296* (3), 263–266. https://doi.org/10.1016/0014-5793(92)80300-6.

(2) Roberts, J. D.; Weigert, F. J. ^{13}C Nuclear Magnetic Resonance Spectroscopy. Determination of Carbon-Fluorine Couplings. *J. Am. Chem. Soc.* **1971**, *93* (10), 2361–2369. https://doi.org/10.1021/ja00739a001.

4.0 Chapter IV – Neutral 5-functionalized Quinazoline-2-Carboxamides as Matrix Metalloproteinase-13 Selective PET Radiotracers

Ariel Buchler,[1,2] Myriam Adi,[1,2] Braeden A. Mair[1,2], Uzair S. Ismailani,[2,3] Christina Bi,[1,2]

Marcelo Muñoz,[2] Emilio I. Alarcon,[2,3] Benjamin H. Rotstein[1,2,3]*

[1] Department of Chemistry and Biomolecular Sciences, University of Ottawa, Ottawa, Ontario, K1N 9B4, Canada.

[2] University of Ottawa Heart Institute, Ottawa, Ontario, K1Y 4W7, Canada.

[3] Department of Biochemistry, Microbiology and Immunology, University of Ottawa, Ottawa, Ontario, K1H 8M5, Canada

Correspondence: Benjamin H. Rotstein, PhD
University of Ottawa Heart Institute
40 Ruskin Street, H-5219
Ottawa, Ontario, Canada
K1Y 4W7
Phone: 613-696-7324
Email: benjamin.rotstein@uottawa.ca

4.1 Context

Our investigation of MMP-13 selective PET radiotracers based on the quinazoline-2-carboxamide scaffold demonstrated that the most potent and selective carboxylate-containing derivative, [^{11}C]5b was susceptible to OAT-mediated transport. Upon replacement of this functional group, as conducted for derivatives [^{11}C]5f or [^{18}F]5j, *in vivo* functionality was restored and vascular pharmacokinetics were markedly superior to [^{18}F]FMBP. The identified lead candidate [^{18}F]5j, detected atherosclerotic plaques *ex vivo* and demonstrated MMP-13 specific binding. However, non-invasive imaging remained challenging due prolonged circulation of blood radioactivity. Moreover, while the carboxylate proved detrimental for *in vivo* imaging, its removal resulted in a significant reduction *in vitro* MMP-13 potency and selectivity. As such, we sought to design optimized second-generation MMP-13 selective PET radiotracers based on the quinazoline-2-carboxamide.

4.2 Statement of the Manuscript

This manuscript has been prepared for submission to the *Journal of Medicinal Chemistry.* In this chapter, I conducted all the chemical synthesis with Myriam Adi. Dr. Marcelo Muñoz assisted with preparative HPLC purification. I completed *in vitro* enzyme assays with assistance from Myriam Adi and Christina Bi. Uzair Ismailani conducted molecular docking experiments. Braeden Mair performed all radiotracer productions and plasma radio-metabolite analyses. Myriam Adi conducted *ex vivo* biodistributions. I conducted *ex vivo* aortic autoradiography and ORO staining. I performed all data analysis and interpreted the data with guidance from Dr. Benjamin Rotstein. I wrote the manuscript with editing from Dr. Benjamin Rostein. All authors approved the final version.

4.3 Abstract

Matrix metalloproteinase-13 (MMP-13) has been implicated with the development of unstable atherosclerosis and represents a molecular biomarker for positron emission tomography (PET) radiotracer development. A series of neutral 5-functionalized MMP-13 inhibitors based on a quinazoline-2-carboxamide scaffold were designed and synthesized to incorporate a potential site for radiolabeling within the S1' pocket and establish S1" binding interactions while maintaining favourable pharmacokinetics for atherosclerotic plaque imaging. *In vitro* enzyme assays identified compound **29f** as a promising lead radiotracer candidate with an MMP-13 IC_{50} of 2.6 ± 1.9 nM and >3800-fold selectivity over related MMPs. A high-yielding automated radiosynthesis of **[^{11}C]29f** was established to enable characterization of radiotracer pharmacokinetics in atherosclerotic mice. *In vivo* PET/CT imaging and *ex vivo* biodistributions revealed accelerated washout of **[^{11}C]29f** from the blood and myocardium with mixed hepatobiliary and renal clearance mechanisms. Radio-metabolite analyses showed that **[^{11}C]29f** was highly stable in plasma. Despite these properties, quantification of *ex vivo* aortic autoradiography under baseline and MMP-13 blocking conditions revealed relatively low and non-specific uptake in atherosclerotic plaques. Although **[^{11}C]29f** is unsuitable for atherosclerotic plaque imaging, it may find an alternative application in other MMP-13 related diseases such as osteoarthritis.

Keywords

matrix metalloproteinase-13, positron emission tomography, radiotracer, atherosclerosis, extracellular matrix, collagenase, aortic autoradiography

4.4 Introduction

Matrix metalloproteinases (MMPs) constitute a class of zinc-dependent enzymes that collectively process and degrade extracellular matrix (ECM) proteins.[1–3] Matrix metalloproteinase-13 (MMP-13), also known as collagenase 3, efficiently cleaves fibrillar collagen which represents a major structural component of joint cartilage and the vasculature.[4–6] Dysregulation of MMP-13 activity in atherosclerosis increases susceptibility to plaque rupture through uncontrolled collagen degradation within the fibrous cap and weakening of its structural integrity.[7–10] Given that rupture of atherosclerotic plaques is closely associated with heart attack and stroke,[11–14] characterization of disease severity with an MMP-13 targeted positron emission tomography (PET) radiotracer could assist in the prevention of acute cardiovascular events.

Extensive high-throughput screenings and structure-activity relationship (SAR) studies have discovered several highly potent and selective MMP-13 inhibitors.[15–25] Most notably, small molecules based on pyrimidine-dicarboxamide and quinazoline-2-carboxamide scaffolds are highly potent MMP-13 inhibitors with minimal off-target binding, representing promising leads for PET radiotracer development.[16,19,23] To obtain selectivity over related MMPs, these inhibitors occupy the unique S1' and S1" specificity pockets adjacent the active site without coordination to the highly conserved catalytic Zn^{2+} ion.[16,19,23] The pharmacophores serve as the central anchoring point and form key hydrogen bonding interactions with the backbones and sidechains of Ala238, Leu239, Thr245, Thr247 and Met253 spanning the S1' pocket.[16,19,23] The proximal inhibitor arm, directed toward the entrance of the S1' pocket, appears less influential but demonstrates a preference for (hetero)aryl rings due to participation in hydrophobic stacking with His222.[16,19,22,23,26,27] To obtain selectivity, both inhibitor classes adopt bent conformations that enable their distal inhibitor arms to deeply occupy the S1" side pocket, not described for other

MMPs.[16,19,23] Molecular modelling indicated the possibility to exploit additional interactions at the bottom of the S1" pocket.[19] Distinctive of the quinazoline-2-carboxamide class, this was performed by attachment of a phenethyl linker at the 5-position and incorporation of appropriate functional groups at the 4-position on the terminal phenyl ring. The lead compound previously identified by Nara *et al.* possesses a carboxylate which gains hydrogen bonding and ionic interactions with Asn215 and Lys140 critical for achieving sub-nanomolar IC_{50} values and conferring best-in-class selectivity across a panel of related MMPs.[19]

Our group has previously developed and evaluated fluorine-18 and carbon-11 labeled radiotracers based on these two major MMP-13 selective inhibitor classes and conducted the first *in vivo* PET imaging studies in mouse models of atherosclerosis (Figure 4.0).[28,29] Evaluation of [^{18}F]FMBP, a previously developed MMP-13 selective pyrimidine-dicarboxamide radiotracer (MMP-13 IC_{50}: 52 ± 5 nM, >1900-fold selectivity), demonstrated the feasibility and superior *ex vivo* performance of MMP-13 selective imaging as compared to broad-spectrum MMP imaging for atherosclerosis.[28] However, significant radiotracer accumulation in the heart and liver prompted the discovery of alternative MMP-13 selective PET radiotracers based on the quinazoline-2-carboxamide class.[29]

A carbon-11 radiosynthesis was originally established for the most potent (MMP-13 IC_{50}: 1.3 ± 0.2 nM) and selective (1800 ± 300-fold) lead carboxylate-containing quinazoline-2-carboxamide inhibitor 21k (therein entitled [^{11}C]5b). Preliminary *in vivo* evaluations in atherosclerotic mice revealed rapid hepatobiliary excretion and extensive uptake in the kidneys, without accumulation in plaques. These findings align with reports that the anionic nature of carboxylate-containing MMP-13 selective inhibitors renders these molecules substrates of the

organic anion transporter (OAT) and are consistent with the predominant expression of this transporter in the kidneys.[22,30] To circumvent this *in vivo* liability, a series of non-carboxylate containing quinazoline-2-carboxamide inhibitor derivatives were synthesized with reliable handles for radiolabeling.[29] Among them, derivative [^{18}F]5j (MMP-13 IC_{50}: 16 ± 3 nM, 75 ± 15-fold selectivity), bearing a fluoroethyl linker, possessed a vastly improved pharmacokinetic profile for vascular imaging including minimal retention of radioactivity in the heart, low uptake in metabolic or off-target organs, and renal clearance. Importantly, functionality was successfully restored as focal radiotracer uptake in atherosclerotic plaques was observed and MMP-13 target engagement was confirmed by *ex vivo* aortic autoradiography. Still, *in vivo* imaging was hindered by suboptimal clearance of radioactivity from the blood pool, and the relatively moderate extent of specific binding may be attributed to the observed reduction in potency and selectivity upon removal of the carboxylic acid and lack of S1" pocket interactions.

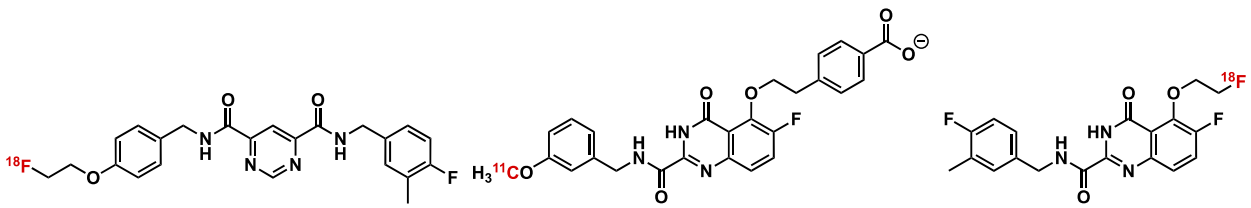

Figure 4.0 Chemical structures of previously developed MMP-13 selective PET radiotracers.

Accordingly, we hypothesized that second-generation MMP-13 selective PET radiotracers based on the quinazoline-2-carboxamide core with reduced lipophilicity and superior potency and selectivity would accelerate blood clearance to enhance contrast for *in vivo* imaging and improve the extent of MMP-13 specific uptake in atherosclerotic plaques (Figure 4.1). We envisioned that the former could be accomplished by adding heteroatoms and polar functional groups into the proximal and distal inhibitor arms, while also providing sites for ^{18}F or ^{11}C radiolabeling.

Meanwhile, the latter could be achieved by reincorporating phenethyl linkers bearing strong hydrogen bond acceptors that are neutral at physiological pH to restore critical interactions with Asn215/Lys140 at the back of the S1" pocket and avoid OAT-mediated transport.

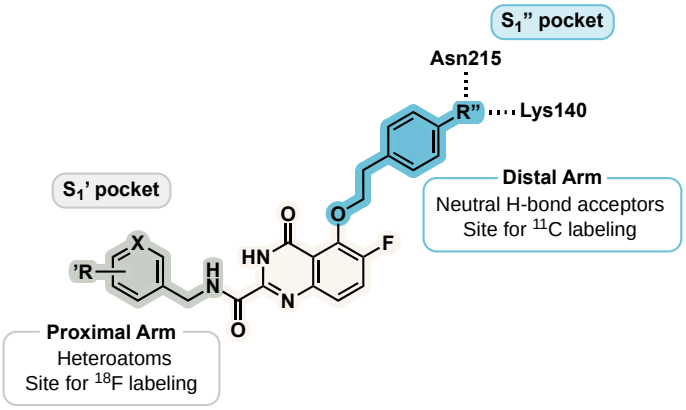

Figure 4.1 Strategy for structural modification of MMP-13 quinazoline-2-carboxamide inhibitors.

In this study, we synthesized several novel compounds based on the quinazoline-2-carboxamide scaffold and conducted SAR studies to optimize the proximal inhibitor and distal inhibitor arms which occupy the S1' and S1" pockets, respectively. We employed an *in vitro* enzyme inhibition assay to characterize MMP-13 potency and determine the selectivity profiles of the most potent inhibitors. Based on these screenings, a promising lead candidate was selected for carbon-11 radiolabeling and *in vivo* evaluations in atherosclerotic *ApoE*$^{-/-}$ mice. Radiotracer pharmacokinetics were assessed by dynamic PET/CT imaging. Organ accumulation and plasma stability were determined by *ex vivo* biodistributions and radio-metabolite analysis. Atherosclerotic plaque uptake and specificity were quantified under baseline and MMP-13 blocking conditions.

4.5 Results and Discussion

4.5.1 Synthesis of Amide Intermediates 5a-e

The central quinazoline scaffold **1** was initially synthesized over 4 steps according to previously published protocols and possesses reactive handles that enable rapid structural diversification by successive attachment of proximal and distal inhibitors arms (Scheme 4.0).[19,29] As the S1' pocket is largely hydrophobic and generally more tolerant toward modifications, it was hypothesized that the proximal arm would be a suitable site for eventual incorporation of fluorine-18 and additional heteroatoms that would reduce lipophilicity. Accordingly, various (2-fluoropyridine)methanamine regioisomers and (3-(2-fluoroethoxy)phenyl)methanamine **4** were coupled by ethyl ester aminolysis to produce the amide derivatives **5a-e** (Scheme 4.0). 2-fluoropyridines **5a-d** were selected due to their widespread utility in radiopharmaceuticals as prosthetic groups for direct incorporation of fluorine-18 by nucleophilic aromatic substitution of reactive 2-halo, 2-nitro-, or 2-trimethylammonium-substituted pyridine precursors.[31] Concurrently, pyridine is a common nitrogen-containing and water soluble isostere of benzene, offering a convenient approach to reduce lipophilicity by replacement of the benzylamine found in earlier quinazoline-2-carboxamide inhibitors.[32] Based on previously tolerated aryl substitutions, a *meta*-substituted 2-fluoroethyloxy derivative **5e** was also obtained from **4**, separately synthesized over 4 steps (Scheme 4.1).[19,23,29] *Tert*-butyloxycarbonyl (Boc) protection of 3-hydroxybenzylamine with di-*tert*-butyl dicarbonate afforded **2** (98%). Coupling of 2-fluoroethyltosylate under basic conditions provided **3** (69%), followed by acidic Boc deprotection to give **4** (90%). This linker was envisioned to provide an indirect and robust method for incorporation of fluorine-18 by nucleophilic substitution of the corresponding tosylate precursor and to a lesser extent, contribute to lowering lipophilicity.[33]

Scheme 4.0 Synthesis of amide intermediates (5a-e)

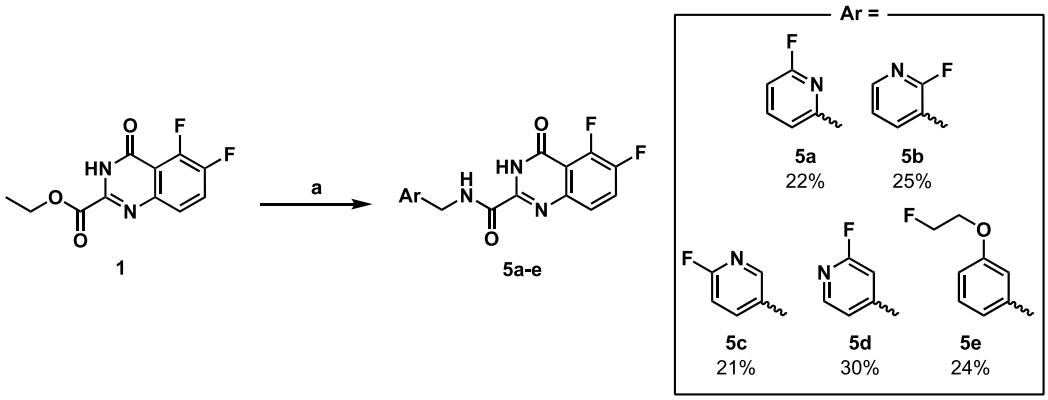

Reagents and Conditions: (a) RNH_2, Et_3N, DMA, 80 °C, 16 h.

Scheme 4.1 Synthesis of (3-(2-fluoroethoxy)phenyl)methanamine hydrochloride (4)

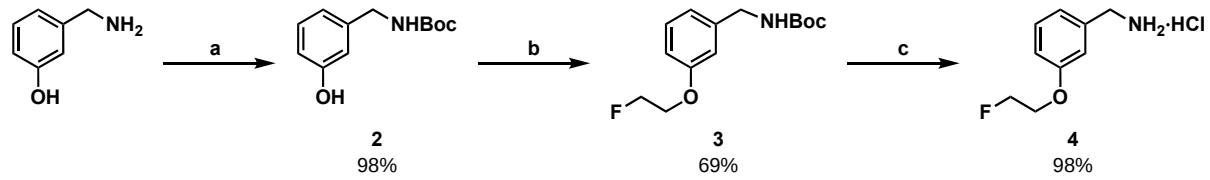

Reagents and Conditions: (a) Boc_2O, $NaHCO_3$, THF, rt, 2 h (b) $F(CH_2)_2OTs$, K_2CO_3, DMF, 120 °C, 16 h (c) 4 M HCl in dioxane, rt, 2 h.

4.5.2 Structure-Activity Relationships of Amide Intermediates (5a-e)

To assess whether these structural modifications were well-tolerated, the half-maximal inhibitory concentrations (IC_{50}) of all amide intermediates **5a-e** were measured against active recombinant human MMP-13 (Table 4.0).[29] Interestingly, initial screenings revealed a stark preference for the (2-fluoropyridin-4-yl)methanamine derivative **5d** which displayed an IC_{50} of 121 ± 11 nM, while all other 2-fluoropyridine regioisomers were not tolerated (IC_{50}: > 1000 nM). The determined MMP-13 potency of derivative **5d** is comparable to that of previous compounds containing 4-fluoro-3-methyl (IC_{50}: 106 ± 8 nM) or 3-methoxy benzylamines (IC_{50}: 118 ± 10 nM),

while greatly reducing the calculated lipophilicity (cLogP) to 1.68 from 3.03 and 2.26, representing 22- and 4-fold changes, respectively.[29] While the extent of intolerance for other 2-fluoropyridine regioisomers is surprising, electronic and steric repulsion in the hydrophobic S1' pocket could explain these observations. Additionally, these findings align with others reports suggesting that the 4-position is the preferred site for the pyridine nitrogen on this arene.[27,34] Derivative **5e** was also identified as a hit with an IC_{50} of 193 ± 5 nM, albeit with slightly lower potency and higher lipophilicity (cLogP: 2.45) as compared to **5d**.

Table 4.0 MMP-13 inhibitory activity of amide intermediates (5a-e)

Compound	**Ar**	**MMP-13 IC_{50} (nM)[a]**	**cLogP[b]**
5a		>1000	2.10
5b		>1000	1.68
5c	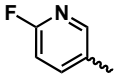	>1000	1.68
5d	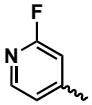	121 ± 11	1.68
5e	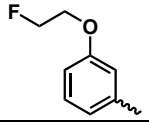	193 ± 5	2.45
4b from ref[c]	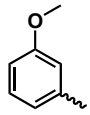	118 ± 10	2.26
4d from ref[c]	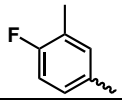	106 ± 8	3.03

[a]Measured as the mean ± SEM from a single experiment performed in triplicate.

[b]Calculated using Chemdraw Professional 22.0.

[c]IC_{50} values obtained under identical conditions as previously described.[29]

As the most potent and least lipophilic intermediate identified, the (2-fluoropyridin-4-yl)methanamine moeity of **5d** was maintained throughout subsequent structure-activity relationship studies focusing on the distal inhibitor arm. Several functionalized phenethyl alcohols bearing neutral and strong hydrogen bond acceptors were synthesized to obtain S1" interactions without rendering these molecules substrates for the OAT. To verify that they are well-accommodated in the presence of the newly introduced 2-fluoropyridine moiety, phenethyl alcohol was coupled to **5d** by nucleophilic aromatic substitution to provide compound **6**, under previously reported conditions (Scheme 4.2).[19,29] Indeed, this unfunctionalized control compound possesses an IC_{50} of 46 ± 12 nM, suggesting that the MMP-13 binding conformation has not been significantly altered by the proximal 2-fluoropyridine and that further functionalization of the distal arene may offer additional improvements.

Scheme 4.2 Synthesis of the 5-phenethyl alcohol substituted quinazoline-2-carboxamide inhibitor (6)

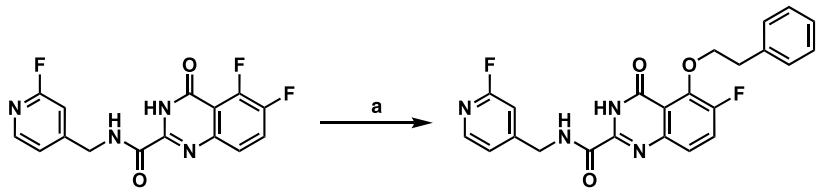

Reagents and conditions: (a) Phenethyl alcohol, NaH, DMA, 80 °C, 1 h.

4.5.3 Synthesis of the Phenethyl Alcohol Derivatives (9, 12a, 12b, 14, 17, 18 and 20)

In total, 7 phenethyl alcohols bearing amide, sulfonamide, *N*-acetyl, and benzyl alcohol functionalities were separately synthesized (Schemes 4.3-4.7). The primary amide **9** was synthesized by tetrahydropyranyl (THP) protection of 4-(2-hydroxyethyl)benzonitrile with 3,4-dihydropyran and catalytic *para*-toluenesulfonic acid (PTSA) to afford **7** (73%, Scheme 4.3). The

nitrile was then oxidized to the primary amide using hydrogen peroxide to give **8** (94%). THP ether hydrolysis using catalytic PTSA in methanol provided **9** (70%). Secondary and tertiary amides **12a** and **12b** were synthesized using a common strategy (Scheme 4.4). Dual *tert*-butyl(dimethyl)silyl (TBS) protection of 4-(2-hydroxyethyl)benzoic acid with *tert*-butyldimethylsilyl chloride and imidazole followed by selective removal of the silyl ester using potassium carbonate in methanol gave **10** (93% over two steps). Thereafter, the carboxylic acid was converted to the acyl chloride with thionyl chloride and activated with pyridine prior to addition of the corresponding alkylamine to obtain **11a** (methylamine, 83% over two steps) and **11b** (dimethylamine, 88% over two steps). Cleavage of the TBS ether with PTSA in methanol provided **12a** (92%) and **12b** (86%). *N*-acetyl and *N*-mesyl compounds **14** and **17** were synthesized from the same starting material (Scheme 4.5). For the *N*-acetyl derivative, dual acetylation of 2-(4-aminophenyl)ethanol using acetic anhydride with pyridine afforded **13** (84%) before removal of the acetyl ester with potassium carbonate in methanol to yield **14** (70%). The *N*-mesyl derivative was produced by TBS protection of the alcohol to afford **15** (85%). The sulfonamide **16** was then formed by pyridine-mediated addition of methanesulfonyl chloride to the aniline (85%). The sulfonamide was then Boc protected using DMAP before selective TBS ether cleavage with PTSA in methanol to give **17** (60% over two steps). The tertiary sulfonamide **18** was directly obtained by reduction of 2-(4-(*N*,*N*-dimethylsulfamoyl)phenyl)acetic acid with lithium aluminum hydride ($LiAlH_4$) (42%, Scheme 4.6). The benzyl alcohol **20** was synthesized by dual TBS protection of 2-(4-(hydroxymethyl)phenyl)acetic acid and selective removal of the silyl ester to give **19** (80% over two steps, Scheme 4.7). Then, the carboxylic acid was reduced with $LiAlH_4$ to provide **20** (71%).

Scheme 4.3 Synthesis of the primary amide fragment (9)

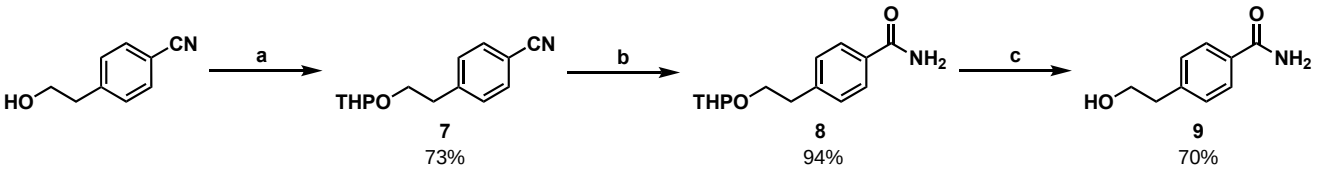

Reagents and conditions: (a) 3,4-Dihydropyran, PTSA, DCM, rt, 12 h (b) 30% $H_2O_{2\,(aq)}$, K_2CO_3, DMSO, 0 °C to rt, 12 h (c) PTSA, MeOH, rt, 2 h.

Scheme 4.4 Synthesis of the secondary and tertiary amide fragments (12a and 12b)

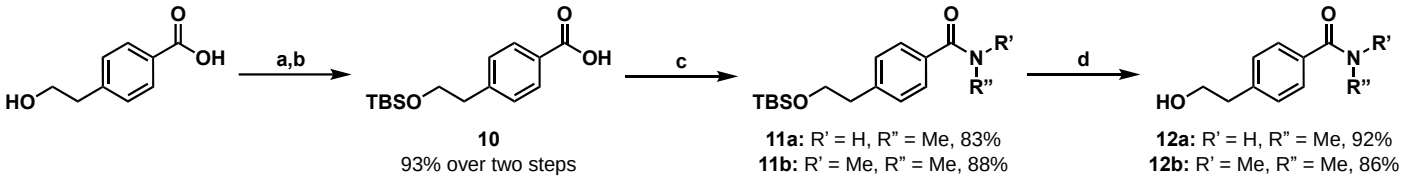

Reagents and conditions: (a) TBSCl, imidazole, THF, 0 °C to rt, 2 h (b) K_2CO_3, MeOH, rt, 2 h (c) $SOCl_2$, reflux, 3 h, 2 M NHMe or NMe_2 in THF, pyridine, DCM, rt, 1 h (d) K_2CO_3, MeOH, rt, 2 h.

Scheme 4.5 Synthesis of the *N*-acetyl and *N*-mesyl fragments (14 and 17)

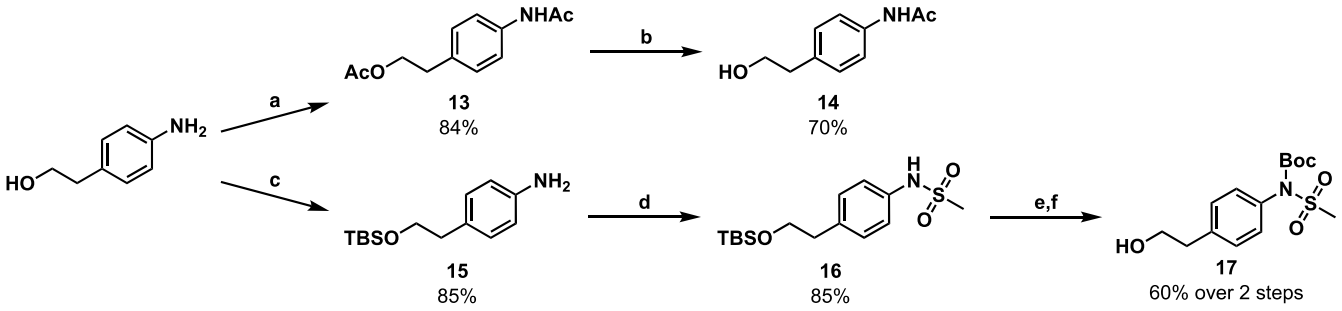

Reagents and conditions: (a) Ac_2O, pyridine, DCM, 0°C to rt, 1 h (b) K_2CO_3, MeOH, rt, 1 h (c) TBSCl, imidazole, DCM, rt, 12 h (d) MsCl, pyridine, DCM, 0°C to rt, 12 h (e) Boc_2O, DMAP, DCM, rt, 2 h (f) PTSA, MeOH, rt, 1 h.

Scheme 4.6 Synthesis of the tertiary sulfonamide fragment (18)

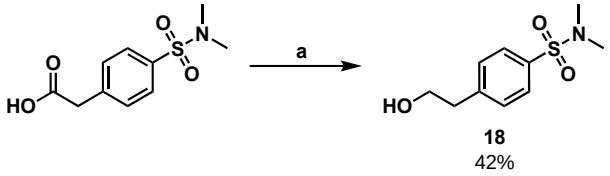

Reagents and conditions: (a) 1 M $LiAlH_4$ in THF, 0 °C to rt, 1 h.

Scheme 4.7 Synthesis of the benzyl alcohol fragment (20)

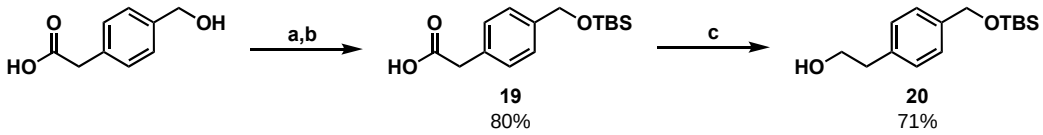

Reagents and conditions: (a) TBSCl, imidazole, THF, rt, 2 h (b) K_2CO_3, MeOH, rt, 2 h (c) 1 M $LiAlH_4$ in THF, 0 °C to rt, 1 h.

With the functionalized phenethyl alcohol derivatives in hand, coupling of **9** at the 5-fluoro position was attempted by nucleophilic aromatic substitution (S_NAr), as reported for previously developed inhibitors of this class.[19,29] However, low conversion and poor selectivity were observed during preliminary small-scale reactions as determined by ultra-performance liquid chromatography mass spectrometry (UPLC-MS, data not shown). In line with previous reports, this harsh reaction requires the use of a large excess of sodium hydride at elevated temperature and is notoriously inefficient with isolated yields often below 30%.[19,29] It is presumed that competing side reactions including β-elimination of phenethyl alcohols and S_NAr at the 2-fluoropyridine ring, as well as limited tolerance for unprotected acidic functional groups, and poor stability under highly basic conditions contributed to this observation. To test whether the unprotected quinazoline scaffold was problematic, a DMF-aminal protecting group was installed under Vilsmeier conditions with the potential to reduce base sensitivity and enhance reactivity (data not shown).[19,29] Nevertheless, reaction conversion remained low, demonstrating that this

approach is unsuitable, particularly for highly functionalized molecules, and an alternative is needed.

Mitsunobu etherification represents a highly versatile method for dehydrogenative coupling of an alcohol (nucleophile) and phenol (pronucleophile) using an azodicarboxylate and phosphine.[35] Importantly, this reaction is revered for its wide functional group tolerance by virtue of the mild conditions employed at room temperature. Good reaction yields rely on a pronucleophile of sufficient acidity (pKa < 10) to minimize competing side reactions with the azodicarboxylate.[36,37] As several phenethyl alcohols had already been synthesized, it was envisioned that this strategy could be conveniently employed by producing the 5-hydroxy (5-OH) derivative of **5d**. As the phenol is flanked by electron-withdrawing fluoro and carbonyl groups, it was expected to serve as an excellent pronucleophile (calculated pKa of 6). To provide confidence in this new strategy, Mitsunobu etherification was performed using phenethyl alcohol and Boc-protected 5-amino-2-fluorophenol as a model substrate of the quinazoline scaffold (Scheme S1). The desired product, *tert*-butyl (4-fluoro-3-phenethoxyphenyl)carbamate, was obtained in an isolated yield of 77%. Despite these promising results, numerous efforts to directly introduce a hydroxyl group at the 5-fluoro position on the original quinazoline scaffold failed. Conditions employing strong nucleophiles such as sodium hydroxide, tetrabutylammonium hydroxide (TBAOH), or sodium methoxide and forcing conditions to add and eliminate phenethyl alcohol or 2-bromoethanol were attempted but proved unsuccessful. As such, a novel synthesis of the quinazoline-2-carboxamide scaffold already bearing a 5-OH group was required.

4.5.4 Synthesis of the 5-Hydroxy Quinazoline-2-Carboxamide Scaffold (27)

Analogous to the original route, a synthesis starting from 4-fluoro-3-methoxyaniline was proposed to obtain the 5-OH containing quinazoline-2-carboxamide scaffold (Scheme 4.8). This starting material was selected as it features an aryl methyl ether protecting group for late-stage demethylation to the desired phenol. Additionally, its general stability toward acidic or basic conditions is desirable and its relatively small size does not impose significant electronic or steric constraints on subsequent reactions. After Boc protection of 4-fluoro-3-methoxyaniline, selective lithiation and addition of ethyl chloroformate at the 2-position proved ineffective. Based on the predicted acidity of the 2-position (pKa ~47), it was suspected that *n*-butyl lithium (pKaH ~50) could not sufficiently deprotonate the desired site. Utilization of the more reactive *tert*-butyl lithium (pKaH ~53) was also unproductive. Instead, pivaloyl (Piv) protection of 4-fluoro-3-methoxyaniline was conducted by treatment with trimethylacetyl chloride catalyzed by 4-dimethylaminopyridine (DMAP) to afford **21** (84%). Together with the comparably greater withdrawing effect of Piv, which lowered the predicted acidity of the 2-position (pKa ~42), and its role as a strong directing group for *ortho*-metalation, selective addition of ethyl chloroformate was achieved using 2 equivalents of *n*-BuLi to provide **22** (82%).[38,39] Cleavage of the pivaloyl ester by refluxing with concentrated hydrochloric acid (HCl) in ethanol afforded **23** (66%).[38] Under previously described conditions, the quinazoline scaffold **24** was formed by acid-catalyzed cyclization with ethyl cyanoformate (71%) and the identified proximal arm was conjugated to core by ethyl ester aminolysis with (2-fluoropyridin-4-yl)methanamine to give **25** (90%). A DMF-aminal protecting group was then installed to fully protect the quinazoline core and yield **26** (85%) and avoid the potential for multiple sites of addition during subsequent Mitsunobu etherification. While boron tribromide and trimethylsilyl iodide were initially tested as common reagents for *O*-

demethylation, **26** was unstable or unreactive to these conditions, respectively. However, the aryl methyl ether was effectively cleaved by refluxing with lithium chloride in dimethylformamide to finally obtain the desired 5-hydroxy quinazoline-2-carboxamide scaffold **27** (50%).

Scheme 4.8 Synthesis of the 5-hydroxy quinazoline-2-carboxamide scaffold (27)

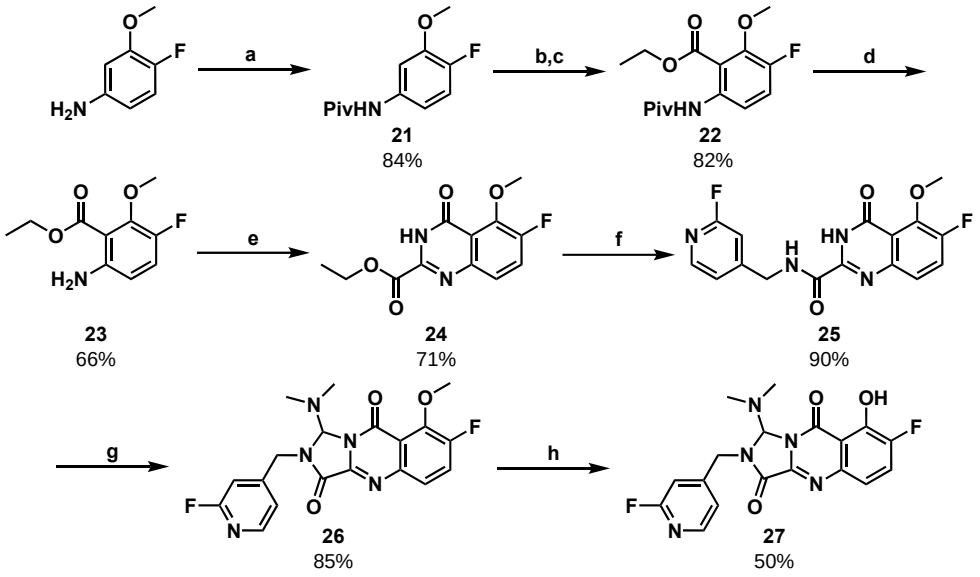

Reagents and conditions: (a) PivCl, DMAP, pyridine, DCM, rt, 1 h (b) 1.6 M *n*-BuLi in hexanes, THF, 0 °C, 4 h, (c) $ClCO_2Et$, THF, -78 °C to -50 °C, 2 h (d) 12 M HCl, EtOH, reflux, 16 h (e) $NCCO_2Et$, 4 M HCl in dioxane, 80 °C, 3 h (f) (2-fluoropyridin-4-yl)methanamine, Et_3N, EtOH, 80 °C, 12 h (g) $(COCl)_2$, DMF, THF, 0 °C to rt, 2 h (h) LiCl, DMF, reflux, 16 h.

4.5.5 Synthesis of the 5-Substituted Inhibitor Derivatives (29a-g)

Now that a synthesis of the 5-hydroxy quinazoline-2-carboxamide scaffold **27** was achieved, the functionalized phenethyl alcohol derivatives (distal inhibitor arms) could be coupled via Mitsunobu etherification. This was accomplished using diisopropyl azodicarboxylate (DIAD) and triphenylphosphine to give intermediates **28a-g** in moderate to good yields (39-73%, Scheme 4.9). Finally, deprotection of the DMF-aminal protecting group was carried out using a mixture of

6 M HCl and acetic acid to provide the final inhibitors **29a-g** (19-46%). Reaction progress had to be closely monitored as the 2-fluoropyridine was gradually hydrolyzed to the corresponding 2-hydroxypyridine after DMF-aminal deprotection, as detected by UPLC-MS. As such, the reaction needed to be stopped within a narrow time frame, during which maximum conversion to the desired product occurred (50-60% by UPLC-MS, Figure S1). Ultimately, this two-step procedure provided critical access to the desired products in sufficient quantities that were previously unattainable with existing methods.

Scheme 4.9 Synthesis of the 5-substituted quinazoline-2-carboxamide inhibitors (29a-g)

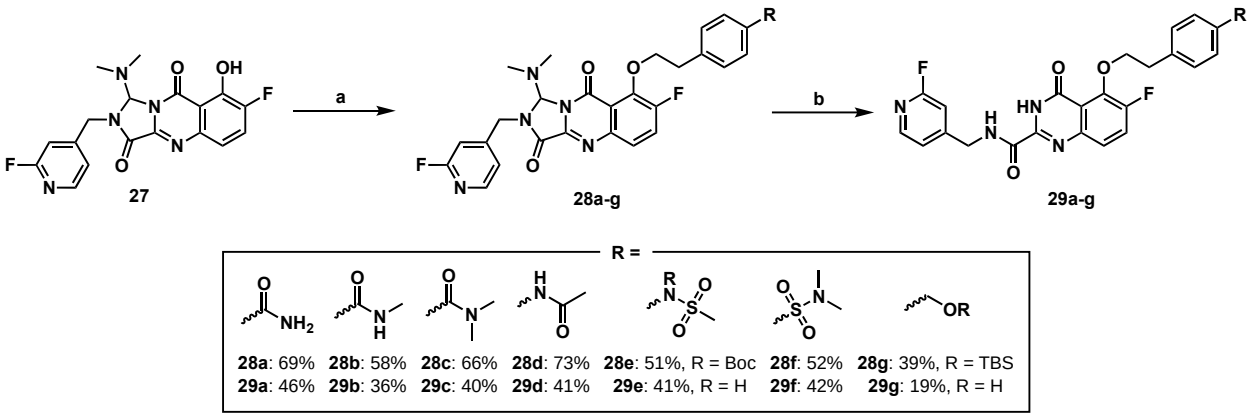

Reagents and conditions: (a) ROH, DIAD, PPh_3, THF, 0 °C to rt, 1 h (b) 6 M HCl, AcOH, 40 °C, 4 h.

4.5.6 Structure-Activity Relationships of the 5-Substituted Inhibitor Derivatives (29a-g)

To evaluate the structure-activity relationships of the distal inhibitor arm occupying the S1" pocket and determine the potency of all 5-substituted inhibitor derivatives **29a-g**, the IC_{50} values for MMP-13 were measured (Table 4.1). Strikingly, most of the functionalized inhibitors, possessed IC_{50} values in the single digit nanomolar range. As compared to unsubstituted intermediate **5d** and the unfunctionalized inhibitor **6**, these compounds exhibit remarkable

improvements in potency up to ~50- and ~20-fold, respectively. Comparison of the amide derivatives **29a-c** revealed a trend towards improved potency with increasing methylation of the terminal amide (**29a** IC_{50}: 14 ± 2 nM vs **29b** IC_{50}: 6.6 ± 0.4 nM vs **29c** IC_{50}: 5.4 ± 1.3 nM). Successive *N*-methylation of the amide is expected to increase electron density at the carbonyl oxygen and provide stronger interactions with Lys140 or Asn215. The *N*-acetyl derivative **29d**, containing an amide in the reversed orientation, exhibits similar potency (IC_{50}: 5.5 ± 1.8 nM) to amides **29b** and **29c**. Analysis of the *N*-mesyl derivative **29e** and tertiary sulfonamide **29f** provided further evidence to support the trend that increased methylation confers superior potency (**29e** IC_{50}: 5.2 ± 0.4 nM vs **29f** IC_{50}: 2.6 ± 1.9 nM). Gratifyingly, the potency of **29f** approached that of previous carboxylic acid containing inhibitors (IC_{50}: 1.2-1.3 ± 0.1 nM) characterized under identical assay conditions.

This validates the inhibitor design strategy and confirms the hypothesis that appropriate functional groups, such as sulfonamides, which are neutral at physiological pH, can achieve similar binding efficiency to anionic carboxylates. To rationalize these trends, molecular docking of **29a-g** with MMP-13 was performed (Figure S2 and S3). Based on the expected binding conformation of **29a-e,** the benzylic carbonyl and sulfonyl groups are optimally positioned to form a single hydrogen bond with the side chain of either Asn215 or Lys140 (Figure S3). Uniquely, the tertiary sulfonamide derivative **29f** contains a benzylic sulfonyl group along with an electron-rich terminal dimethylamine moiety, making it optimally positioned to interact with both Asn215 and Lys140 via its two oxygen atoms (Figure S3). The benzyl alcohol derivative **29g** exhibits weaker potency, comparable to that of the primary amide **29a** (IC_{50}: 11 ± 2 nM). The absence of functionality in the benzylic position and relatively lower electron-density of the alcohol are possible explanations for this finding (Figure S3).

Table 4.1 MMP-13 inhibitory activity of 5-Subsituted quinazoline-2-carboxamide inhibitors (29a-g)

Compound	R	MMP-13 IC_{50} (nM)[a]	cLogP[b]
6	H	46 ± 12	3.40
29a		14 ± 2	2.31
29b		6.6 ± 0.4	2.55
29c		5.4 ± 1.3	2.78
29d		5.5 ± 1.8	2.31
29e		5.2 ± 0.8	1.63
29f		2.6 ± 1.9	2.68
29g		11 ± 2	2.83
5b from ref[d]		1.3 ± 0.2	1.16 ± 0.03[c]
5j from ref[d]	-	16 ± 3	3.09 ± 0.03[c]

[a]Measured as the mean ± SEM from a single experiment performed in triplicate.

[b]Calculated using Chemdraw Professional 22.0.

[c]LogD determined experimentally.

[d]IC_{50} and LogD values obtained under identical conditions as previously described.[29,40]

Compounds **29c-f** were identified as the most potent MMP-13 inhibitors and selected for further determination of their selectivity against MMP-1, -2, -8, -9, and -10 (Table 4.2). Remarkably, no appreciable inhibition of MMP-1, -2, or -9 was detected below 10 μM. Meanwhile, inhibition of MMP-8 and -10 only was observed at elevated inhibitor concentrations (IC_{50}'s > 6100 nM). Consistent with earlier reports, the collagenase MMP-8, and stromelysin MMP-10, have been identified as the major off-targets for the quinazoline-2-carboxamide inhibitor class.[19,29] This new series of compounds **29c-f** significantly reduced off-target affinity for MMP-

8 and MMP-10.[29] Together with the improved MMP-13 potency, this marks a tremendous increase in MMP selectivity, similar to carboxylate-containing inhibitors (1100-3800-fold selectivity). While the structural basis for this selectivity is not fully understood, it is possible that the 2-fluoropyridin-4-yl ring occupying the S1' is not tolerated by other MMPs, as exemplified by the selectivity of MMP-13 for only a single 2-fluoropyridine regioisomer. It is also reasonable to suggest that the newly introduced amides and sulfonamides on terminal phenyl ring deeply occupying the S1" pocket, unique to MMP-13, cannot be accommodated by other MMPs possessing shallower binding pockets.[41] Nevertheless, these marked improvements are expected to enhance the extent of MMP-13 target engagement and specificity.

Table 4.2 MMP selectivity profiles of 29c-f

	IC_{50} (nM)[a]					
Compound	**MMP-1**	**MMP-2**	**MMP-8**	**MMP-9**	**MMP-10**	**MMP-13 fold-selectivity[b]**
29c	$>10^4$	$>10^4$	7900 ± 920	$>10^4$	6100 ± 870	1100 ± 320
29d	$>10^4$	$>10^4$	7400 ± 1100	$>10^4$	8000 ± 1100	1300 ± 480
29e	$>10^4$	$>10^4$	$>10^4$	$>10^4$	8700 ± 740	1700 ± 300
29f	$>10^4$	$>10^4$	$>10^4$	$>10^4$	$>10^4$	>3800
5b[c]	$>10^4$	$>10^4$	2400 ± 130	$>10^4$	3200 ± 240	1800 ± 300
5j[c]	$>10^4$	$>10^4$	1200 ± 70	$>10^4$	3100 ± 400	75 ± 15

[a]Measured as the mean ± SEM from a single experiment performed in triplicate.

[b]Calculated as a ratio of the MMP-13 IC_{50}/MMP-10 IC_{50} ± SEM.

[c]IC_{50} values obtained under identical conditions.[29]

As the most potent (IC_{50}: 2.6 ± 1.9 nM) and selective (3800-fold) MMP-13 inhibitor identified, **29f** was advanced as a lead candidate for radiolabeling. This discovery represents a ~6-fold and ~50-fold improvement in MMP-13 potency and selectivity over the aforementioned fluorine-18 labeled radiotracer based on this scaffold [^{18}F]5j.[29] The tertiary sulfonamide is desirable as its high polarity further contributed to lowering lipophilicity (cLogP: 2.68) which is anticipated to accelerate blood clearance for non-invasive PET imaging. Conveniently, this methylated functional group is also amenable to robust and late-stage carbon-11 *N*-methylation strategies and would expedite *in vivo* assessment of radiotracer pharmacokinetics.[42]

4.5.7 Synthesis of the Carbon-11 Radiolabeling Precursor 32

We proposed that synthesis of **[^{11}C]29f** could be accomplished by ^{11}C-methylation of the corresponding secondary sulfonamide precursor. Using the same approach, the carboxylic of 2-(4-(N-methylsulfamoyl)phenyl)acetic acid was reduced with $LiAlH_4$ to afford the corresponding phenethyl alcohol **30** (55%, scheme 4.10). Under established Mitsunobu conditions, this fragment was coupled to the 5-hydroxy quinazoline-2-carboxamide scaffold to give **31** (67%, Scheme 4.11). Acidic removal of the DMF-aminal protecting group afforded the desired radiolabeling precursor **32** (40%).

Scheme 4.10 Synthesis of the secondary sulfonamide phenethyl alcohol (30)

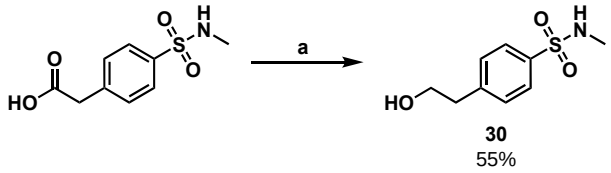

Reagents and conditions: (a) 1 M $LiAlH_4$ in THF, 0 °C to rt, 1 h.

Scheme 4.11 Synthesis of the carbon-11 radiolabeling precursor (32)

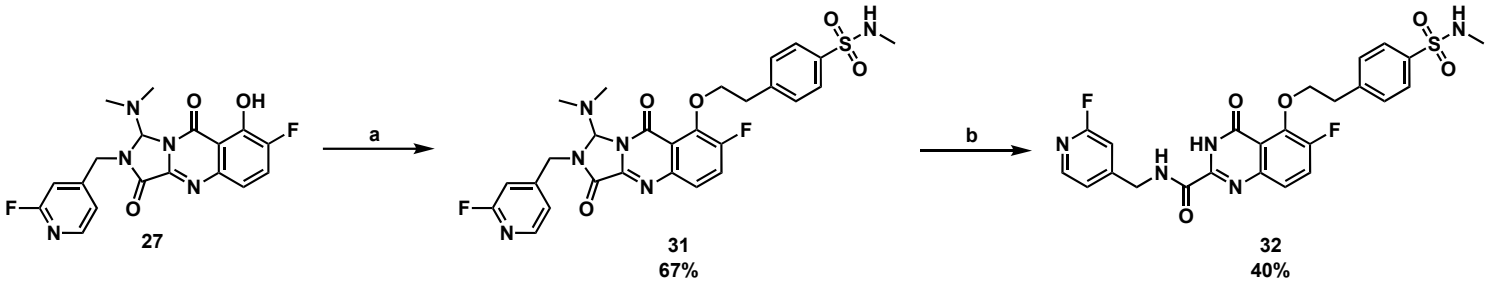

Reagents and conditions: (a) **30**, DIAD, PPh_3, THF, 0 °C to rt, 1 h (b) 6 M HCl, AcOH, 40 °C, 4 h.

4.5.8 Radiotracer Automation, Formulation Stability, and Lipophilicity

As optimized for other ^{11}C-labeled quinazoline-2-carboxamides, methylation can be achieved using [^{11}C]methyl iodide ([^{11}C]CH_3I) and TBAOH in DMSO at 80 °C in under 3 min.[29] Regioselective ^{11}C-methylation can be achieved using predicted pKa values without protecting groups by adjusting the equivalents of TBAOH required to deprotonate the desired position. In the presence of the unprotected pyrimidine ring system, 2 equivalents of TBAOH were expected to fully deprotonate the secondary sulfonamide. Unlike previous carbon-11 *O*-methylations for this inhibitor class, *N*-methylation of arylamines and less nucleophilic conjugated amines such as sulfonamides, can be sluggish using [^{11}C]CH_3I.[43] In such cases, [^{11}C]methyl triflate is frequently employed due its greater reactivity, and accordingly utilized for this synthesis. Indeed, an initial attempt with this strategy proved highly effective as the desired **[^{11}C]29f** was produced with [^{11}C]methyl triflate and 2 equivalents of TBAOH in DMSO at 80 °C for 1 min in decay-corrected radiochemical conversions of 82% (n = 1, Figure S4). Next, an automated radiosynthesis for **[^{11}C]29f** was developed using a GE TracerLab FXC module (Scheme 4.12). **[^{11}C]29f** was labeled under these conditions, purified by semi-preparative high-performance liquid chromatography, and reformulated as a 10% ethanol solution in saline, suitable for intravenous injection. **[^{11}C]29f**

was obtained in radiochemical yields of 29 ± 3 % within 30 ± 1 min, >99% radiochemical purity, and a molar activity of 65 ± 5 GBq·µmol^{-1} at the time of injection (n = 6, Figure S5). Radiotracer stability in formulation was assessed up to 75 min with no observable decomposition (Figure S6). The logD of **[^{11}C]29f** is 2.37 ± 0.05 (n = 2), determined experimentally as the octanol-PBS distribution coefficient (pH 7.4). This represents a >5-fold reduction in lipophilicity as compared to [^{18}F]5j (LogD: 3.09 ± 0.03) and is expected to markedly improve contrast for cardiovascular imaging.[29]

Scheme 4.12 Radiosynthesis and quality control of [^{11}C]29f

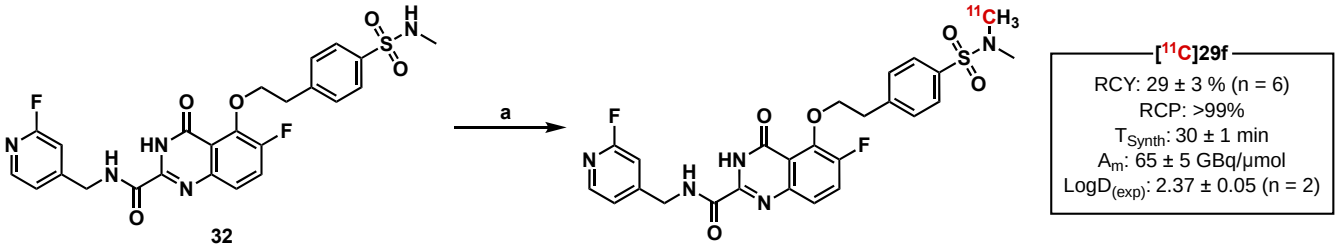

Reagents and conditions: [^{11}C]CH_3OTf, 1 M TBAOH, DMSO, 80 °C, 1 min.

4.5.9 *In Vivo* Dynamic PET/CT Imaging

Initial *in vivo* pharmacokinetic screenings were conducted by dynamic PET/CT imaging over 60 min following intravenous administration of **[^{11}C]29f** in atherosclerotic *ApoE*$^{-/-}$ mice via the lateral tail vein (n = 4, Figure 4.2). Radioactivity rapidly cleared from the blood pool (t_{max}: 0.625 min) stabilizing at ~1% %ID·cc^{-1} after 10 min. This marks a ~3-fold reduction in blood radioactivity, critical for enhancing vessel/blood contrast for cardiovascular imaging applications and addresses a previous limitation of the first-generation quinazoline-2-carboximde radiotracer [^{18}F]5j.[29,44,45] Myocardial kinetics were similar with relatively slower washout to ~1%ID·cc^{-1} after 30 min. Low myocardial retention is another essential feature that minimizes spillover and

facilitates quantification of radiotracer uptake within the coronary arteries.[46] The observed washout of radioactivity from the liver (8.67 ± 1.57 %ID·cc^{-1} at peak) and corresponding increases in the gall bladder and intestine over time suggest that **[^{11}C]29f** is predominantly eliminated via a hepatobiliary clearance route. Washout from the kidneys (7.82 ± 0.7 %ID·cc^{-1} at peak) into the urinary bladder was also observed, indicating an extent of renal clearance. While renal clearance is generally considered preferable for aortic imaging as it reduces radioactivity within the thoracic cavity**, [^{11}C]29f** experiences significant clearance from the liver down to 5.94 ± 0.32 %ID·cc^{-1} and the observed intestinal uptake within the abdominal cavity is not expected to impede quantification. Overall, **[^{11}C]29f** retains the low myocardial and liver retention characteristic of the quinazoline-2-carboxamide class, and maintains superior pharmacokinetics over the first-generation pyrimidine-dicarboxamide radiotracer [^{18}F]FMBP.[28]

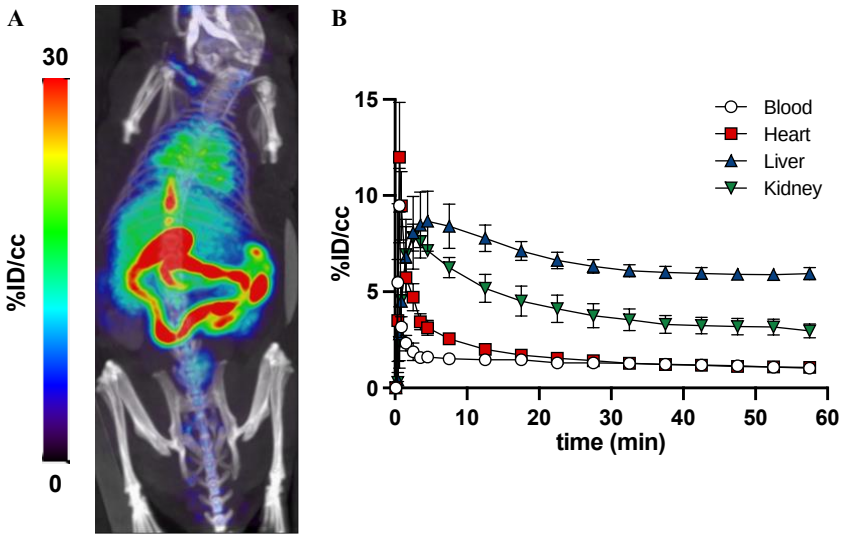

Figure 4.2 Dynamic PET/CT [^{11}C]29f imaging in *ApoE*$^{-/-}$ mice. (A) Representative PET/CT maximum intensity projection (MIP, coronal axis). (B) Time−activity curves for the blood, heart, liver, and kidney (n = 4 per group).

4.5.10 *Ex Vivo* Biodistribution and Plasma Metabolism

To provide additional support for these *in vivo* findings, *ex vivo* biodistributions were conducted by counting organs of interest for radioactivity 30 min after intravenous administration of **[^{11}C]29f** in atherosclerotic *ApoE*$^{-/-}$ mice via the lateral tail vein (n = 4-5 per group, Figure 4.3A). In line with the PET images, **[^{11}C]29f** blood and myocardial radioactivity cleared quickly with 1.06 ± 0.07 %ID·g^{-1} and 1.13 ± 0.41 %ID·g^{-1} remaining at this timepoint, respectively. Meanwhile, liver and kidney uptake were comparable to [^{18}F]5j at 4.26 ± 0.99 %ID·g^{-1} and 2.85 ± 0.74 %ID·g^{-1}, respectively. Intestinal accumulation was significantly higher with 7.93 ± 0.87 %ID·g^{-1}, confirming hepatobiliary clearance as the major route of excretion. Elevated, albeit variable, urinary uptake was also detected at 4.71 ± 2.13 %ID·g^{-1}, indicating a lesser extent of renal clearance. Relatively low levels of radioactivity (~2 %ID·g^{-1}) were observed in all other measured organs. To assess the specificity of **[^{11}C]29f** in these tissues, heterologous blocking with WAY17053, representing a commercially available and structurally unrelated MMP-13 selective inhibitor, was administered intravenously (7.5 mg/kg) 10 min prior to the radiotracer.[15,29,47,48] No statistical differences were observed upon blocking, reflecting low target expression in these off-target organs.

Simultaneously, *in vivo* radiotracer stability was evaluated by analyzing plasma for radio-metabolites (Figure 4.3B). **[^{11}C]29f** demonstrated excellent stability with 86 ± 6% remaining intact after 30 mins. This is mainly attributed to the reduced lipophilicity of **[^{11}C]29f** and possible lower affinity for metabolic enzymes due to their propensity to metabolize lipophilic compounds. No differences were detected under WAY17053 blocking conditions with 88 ± 2% corresponding to the parent radiotracer (P > 0.05). The measured extraction efficiencies (89 ± 1%) suggest representative sampling of plasma radioactivity.

A

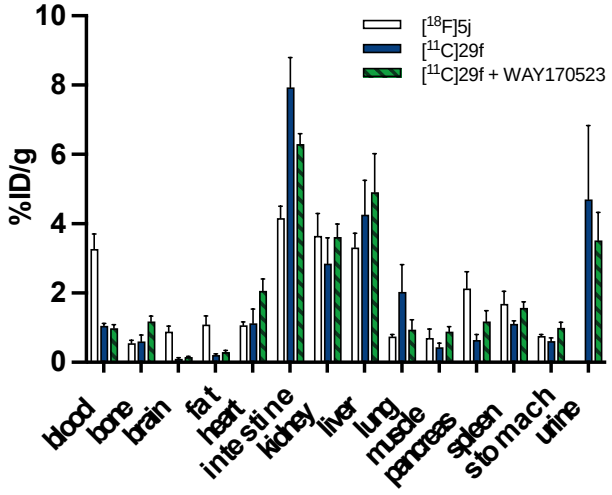

B

Fraction (%)	[^{11}C]29f	[^{11}C]29f + WAY170523
Parent Radiotracer	86 ± 6	88 ± 2
Polar metabolites	14 ± 6	12 ± 2
Extraction Efficiency	90 ± 1	89 ± 2

Figure 4.3 [^{11}C]29f biodistribution and metabolism in *ApoE*$^{-/-}$ mice. (A) *Ex vivo* biodistribution and (B) plasma radio-metabolite analysis 30 min after intravenous radiotracer administration. ANOVA. n = 4 - 5 per group. The biodistribution of [^{18}F]5j is provided for comparison.[29]

4.5.11 *Ex Vivo* Aortic Autoradiography and Oil Red O Staining

Despite significant improvements over previous MMP-13 selective PET radiotracers, non-invasive atherosclerotic plaque imaging in mice remains an ongoing challenge due to the small anatomical size of the aorta which approaches the spatial resolution limit of PET.[49–51] To obtain high-resolution images and ensure accurate quantification of aortic plaque uptake, *ex vivo* aortic autoradiography was performed (Figure 4.4). Under baseline conditions, **[^{11}C]29f** primarily accumulated within the aortic arch and carotid arteries and significantly colocalized with Oil Red O (ORO) positives areas, indicating lipid-rich atherosclerotic plaques. Quantification of **[^{11}C]29f** uptake in ORO-positive regions revealed 67 ± 3 %ID·m^{-2}, which is ~4-fold lower than [^{18}F]5j. No statistical differences were observed under WAY170523 blocking conditions with **[^{11}C]29f** uptake remaining at 79 ± 11 %ID·m^{-2} ($P > 0.05$). This data suggests that the observed **[^{11}C]29f** uptake in atherosclerotic plaques is likely non-specific. While clearance from the blood is critical to achieve

sufficient contrast for vascular imaging, this approach relies on high affinity radioligands to enable rapid target binding. Despite the tremendous improvements in potency and selectivity, and favorable pharmacokinetics of **[^{11}C]29f**, it appears that fast blood clearance provided insufficient time for radiotracer circulation and MMP-13 specific accumulation in atherosclerotic plaques.

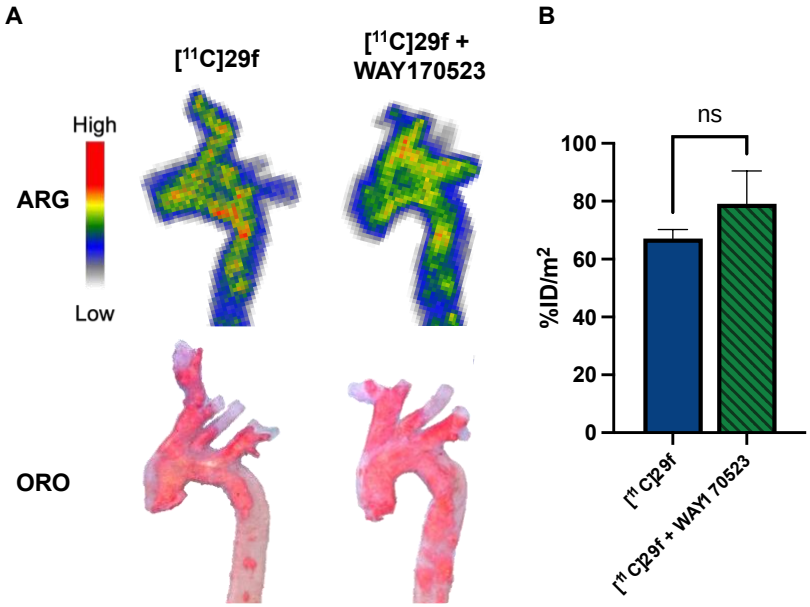

Figure 4.4 *Ex vivo* aortic autoradiography in *ApoE*$^{-/-}$ mice. (A) Representative autoradiographs 30 min after intravenous radiotracer administration with corresponding Oil Red O staining. (B) Aortic plaque uptake. Unpaired t-test: $P > 0.05$, n = 4 - 5 per group.

4.6 Conclusion

The goal of this study was to design a second-generation MMP-13 targeted PET radiotracer based on the quinazoline-2-carboxamide scaffold with improved potency and selectivity, and reduced lipophilicity to confer better specificity and contrast for atherosclerosis imaging. To accomplish this, the central quinazoline core was maintained and SAR studies were performed on a new series of inhibitors focusing on the proximal and distal inhibitor arms which occupy the S1' and S1" pockets, respectively. Addition of a 2-fluoropyridin-4-yl in the S1' pocket maintained

MMP-13 potency and provided a convenient strategy to simultaneously reduce lipophilicity and introduce a site for eventual fluorine-18 radiolabeling. To deeply occupy and restore interactions with Lys140/Asn215 at the back of the S1" pocket without susceptibility for the OAT, several distal inhibitor arms, comprised of neutral functionalized phenethyl alcohols were synthesized. As conventional methods employing S_NAr for attachment of these fragments to the 5-position on the quinazoline scaffold were ineffective, an alternate synthesis of the quinazoline core was developed. Mitsunobu etherification provided access to highly functionalized 5-substituted quinazoline-2-carboxamide inhibitors in suitable yields. Among them, derivatives **29c-f**, bearing amides and sulfonamides, possessed MMP-13 IC_{50}'s between 2.6 – 6.6 nM, superior to first-generation inhibitors and in range of best-in-class carboxylate-containing inhibitors. SAR and docking experiments further indicated a preference for benzylic carbonyl or sulfonyl groups and an electron-rich terminal dimethylamine moiety to increase the strength of interaction with Asn215 or Lys140. Remarkably, these inhibitors displayed exceptional selectivity against a panel of related MMPs. Notably, affinity for MMP-8 and MMP-10, representing the primary off-targets for this inhibitor class, was greatly reduced, and significantly enhanced MMP-13 selectivity (1100-3800-fold). Based on these findings, **29f** was selected as a lead candidate for radiolabeling and *in vivo* evaluations in atherosclerotic mice. Most conveniently, the tertiary sulfonamide of **29f** was an excellent candidate for carbon-11 methylation and a high-yielding automated radiosynthesis was established. *In vivo* PET imaging and *ex vivo* biodistributions revealed that **[^{11}C]29f** exhibits accelerated clearance from the blood and minimal retention in the myocardium, offering improved vascular contrast, and addressing a significant limitation of previous MMP-13 selective PET radiotracers. **[^{11}C]29f** is primarily excreted via a hepatobiliary route, albeit with low liver accumulation. Some contribution from renal clearance was also observed. Plasma radio-metabolite

analysis demonstrated that **[^{11}C]29f** is highly stable *in vivo*. Despite these collective improvements, *ex vivo* aortic autoradiography under baseline and heterologous blocking conditions revealed relatively low and non-specific uptake of **[^{11}C]29f** in atherosclerotic plaques. Therefore, **[^{11}C]29f** is not suitable for selective imaging of MMP-13 in atherosclerosis. Nevertheless, **[^{11}C]29f** may prove useful for alternative disease applications in which MMP-13 is the primary target.

4.7 Experimental Section

4.7.1 General Information

Chemical reagents and solvents were purchased from commercial sources and used without further purification. All moisture or air sensitive reactions were performed under inert atmosphere in flame dried glassware. Reaction progress was monitored by thin layer chromatography on silica gel-coated plates and visualized directly with UV light (254 and 280 nm) or following staining with a potassium permanganate solution. Products were purified by flash column chromatography using a Biotage Isolera One system or by preparative HPLC using an Agilent 1290 Infinity II Preparative LC/MSD System (Solvents: ACN / water). Compound characterization was completed by ^{1}H/^{13}C NMR with a Magritek Spinsolve 80 MHz Spectrometer, or Bruker AVANCE III 400/600 MHz spectrometers using DMSO-d_6 or $CDCl_3$ as a solvent (reference: 2.54 / 39.52 or 7.26 / 77.16 ppm) and analyzed using Mnova software. High resolution mass spectrometry data was acquired using a Waters Synapt G1, HRes and Ion Mobility, Time of Flight Mass Spectrometer or a Kratos Concept – Magnetic Sector Electron Impact Mass Spectrometer. All target compounds are >95% pure according to analysis using a Waters Xevo TQD with an Acquity UPLC H-Class Plus system.

4.7.2 Chemical Synthesis

Ethyl 5,6-difluoro-4-oxo-3,4-dihydroquinazoline-2-carboxylate (1)

Synthesized over 4 steps under previously established conditions.[19,29] Spectra in accordance with literature.^{1}H-NMR (600 MHz, $(CD_3)_2SO$): 12.83 (1H, br), 8.04-7.99 (1H, m), 7.75-7.73 (1H, m), 4.42 (2H, q, J = 6.0 Hz), 1.39 (3H, t, J = 6.0 Hz) ppm. ^{13}C-NMR (150 MHz, $(CD_3)_2SO$): 159.8, 158.3, 148.4 (dd, J = 12, 246 Hz), 147.5 (dd, J=15, 264 Hz), 144.8 (d, J = 1.5 Hz), 143.8 (d, J =1.5 Hz), 125.2 (dd, J = 6.0, 7.5 Hz), 123.8 (d, J = 20 Hz), 113.9 (d, J = 3.0 Hz), 62.8, 13.9 ppm. HRMS (EI+, m/z): calculated $[M]^+$ $C_{11}H_8F_2N_2O_3$ as 254.0503, found as 254.04856.

***tert*-butyl (3-hydroxybenzyl)carbamate (2)**

To a solution of 3-hydroxybenzylamine (250 mg, 2.03 mmol, 1.0 equiv.) in THF (4.1 mL) was added $NaHCO_3$ (501 mg, 6.09, 3.0 equiv.) in water (4.06 mL), followed by Boc_2O (0.52 mL, 2.23 mmol, 1.1 equiv.). The mixture was stirred at room temperature for 2 h, diluted with EtOAc and extracted with water. The combined organics were washed with brine, dried over Na_2SO_4, filtered, and concentrated under reduced pressure. The crude mixture was purified by column chromatography (0-40% EtOAc/hexane) to obtain the title compound as a colorless oil (469 mg, 2.24 mmol, 98%).^{1}H-NMR (600 MHz, DMSO-d_6) 9.35 (1H, s), 7.37 (1H, t, J = 6.2 Hz), 7.14-7.10 (1H, m), 6.68-6.62 (3H, m), 4.07 (2H, d, J= 6.2Hz), 1.43 (9H, s) ppm. ^{13}C-NMR (150 MHz, DMSO-d_6): 157.8, 156.2, 142.1, 129.6, 117.9, 114.2, 114.0, 78.2, 43.7, 28.7 ppm. HRMS (EI+, m/z): calculated $[M-C_5H_8O_2]^+$ C_7H_9NO as 123.0684, found as 123.0691.

***tert*-butyl (3-(2-fluoroethoxy)benzyl)carbamate (3)**

To a solution of 2-fluoroethyltosylate (189 mg, 0.848 mmol, 1.0 equiv.) in DMF (4.6 mL) was added K_2CO_3 (234 mg, 1.70 mmol, 2.0 equiv.), followed by **2** (185 mg, 0.848 mmol, 1.0 equiv.).

The mixture was stirred at 120 °C for 16 h, diluted with EtOAc and extracted with water. The combined organics were washed with brine, dried over Na_2SO_4, filtered, and concentrated under reduced pressure. The crude mixture was purified by column chromatography (0-25% EtOAc/hexane) to obtain the title compound as a white solid (158 mg, 0.587 mmol, 69%). ^{1}H-NMR (600 MHz, $(CD_3)_2SO$): δ 7.42 (1H, t, J = 6 .1 Hz), 7.29-7.25 (1H, m), 6.87-6.85 (3H, m), 4.84-4.82 (1H, m), 4.72-4.70 (1H, m), 4.28-4.26 (1H, m), 4.21-4.19 (1H, m), 4.13 (2H, d, J = 6.1 Hz), 1.43 (9H, s) ppm. ^{13}C-NMR (150 MHz, $(CD_3)_2SO$): 158.2, 141.9, 129.4, 119.4, 113.2, 112.5, 82.2 (d, J = 166 Hz), 77.8, 66.9 (d, J = 19 Hz), 43.3, 28.3 ppm. HRMS (EI+, m/z): calculated $[M-C_5H_8O_2]^+$ $C_9H_{12}FNO$ as 169.0903, found as 169.0910.

(3-(2-fluoroethoxy)phenyl)methanamine hydrochloride (4)

A solution of 9 (151 mg, 0.561 mmol, 1.0 equiv.) in 4 M HCl in dioxane (4.3 mL) was stirred at room temperature for 2 h. The solvent was removed under reduced pressure to afford the title compound without further purification as a white solid (113 mg, 0.550 mmol, 98%). ^{1}H-NMR (600 MHz, $(CD_3)_2SO$): δ 8.53 (3H, br), 7.39-7.35 (1H, m), 7.22-7.21 (1H, m), 7.12-7.10 (1H, m), 7.03-7.00 (1H, m), 4.86-4.84 (1H, m), 4.74-4.72 (1H, m), 4.33-4.31 (1H, m), 4.26-4.24 (1H, m), 4.02 (2H, s) ppm. ^{13}C-NMR (150 MHz, $(CD_3)_2SO$): 158.2, 135.7, 129.8, 121.3, 115.2, 114.4, 82.1 (d, J = 166 Hz), 67.1 (d, J = 19 Hz), 42.1 ppm. HRMS (EI+, m/z): calculated $[M-HCl]^+$ $C_9H_{12}FNO$ as 169.0903, found as 169.0911.

5,6-difluoro-*N*-((6-fluoropyridin-2-yl)methyl)-4-oxo-3,4-dihydroquinazoline-2-carboxamide (5a)

To a solution of **1** (110 mg, 0.433 mmol, 1.0 equiv.) in DMA (2.2 mL) was added (6-fluoropyridin-2-yl)methanamine hydrochloride (98 mg, 0.477 mmol, 1.1 equiv.), followed by triethylamine (72 µL, 0.520 mmol, 1.2 equiv.). The mixture was stirred at 80 °C for 12 h. The reaction was cooled

to room temperature, diluted with EtOAc and extracted with 0.1 M HCl and water. The combined organics were washed with brine, dried over Na_2SO_4, filtered, and concentrated under reduced pressure.The crude mixture was purified by column chromatography (30% EtOAc/$CHCl_3$) to obtain the title compound as a pale-yellow solid (29 mg, 0.086 mmol, 22%).^{1}H-NMR (600 MHz, $(CD_3)_2SO$): 12.53 (1H, br), 9.65 (1H, t, J = 6.3 Hz), 8.04-7.98 (2H, m), 7.69-7.67 (1H, m), 7.36-7.35 (1H, m), 7.11-7.10 (1H, m), 4.58 (2H, d, J = 6.3 Hz). ^{13}C-NMR (150 MHz, $(CD_3)_2SO$): 162.4 (d, J = 234 Hz), 159.5, 158.1, 157.0 (d, J = 14 Hz), 148.1 (dd, J = 12, 246 Hz), 147.6 (dd, J = 14, 263 Hz), 145.8, 144.7, 142.7 (d, J=7.5 Hz), 124.4, 123.7 (d, J =18 Hz), 119.0 (d, J=4.5 Hz), 113.7, 107.7 (d, J = 37 Hz), 43.9 ppm. HRMS (ESI+, m/z): calculated $[M+Na]^+$ $C_{15}H_9F_3N_4O_2Na$ as 357.0575, found as 357.0575.

5,6-difluoro-*N*-((2-fluoropyridin-3-yl)methyl)-4-oxo-3,4-dihydroquinazoline-2-carboxamide (5b)

Following the procedure described for **5a**, compound **5b** was prepared from compound **1** and (2-fluoropyridin-3-yl)methanamine hydrochloride. The crude mixture was purified by preparative HPLC to obtain the title compound as a pale-yellow solid (41 mg, 0.123 mmol, 25%).^{1}H-NMR (600 MHz, $(CD_3)_2SO$): δ 12.52 (1H, s), 9.66 (1H, s), 8.19-8.18 (1H, m), 8.03-7.94 (2H, m), 7.67-7.65 (1H, m), 7.39-7.37 (1H, m) 4.55 (2H, d, J = 6.2 Hz) ppm. ^{13}C-NMR (150 MHz, $(CD_3)_2SO$): 160.6 (d, J = 236 Hz), 159.6, 158.1, 148.0 (dd, J = 246, 11 Hz), 147.6 (dd, J = 263, 14 Hz), 146.1 (d, J = 15 Hz), 145.8, 144.7, 140.7 (d, J = 5.0 Hz), 124.4, 123.7 (d, J = 19 Hz), 122.1 (d, J = 4.0 Hz), 120.2 (d, J = 30 Hz), 113.7, 36.6 ppm. HRMS (ESI+, m/z): calculated $[M+Na]^+$ $C_{15}H_9F_3N_4O_2Na$ as 357.0575, found as 357.0575.

5,6-difluoro-*N*-((6-fluoropyridin-3-yl)methyl)-4-oxo-3,4-dihydroquinazoline-2-carboxamide (5c)

Following the procedure described for **5a**, compound **5c** was prepared from compound **1** and (6-fluoropyridin-3-yl)methanamine dihydrochloride with an additional equivalent of Et_3N (2.2 equiv.). The crude mixture was purified by column chromatography (20-30% EtOAc/DCM) to obtain the title compound as a pale-yellow solid (27 mg, 0.081 mmol, 21%).^{1}H-NMR (400 MHz, $(CD_3)_2SO$): 12.51 (1H, br), 9.70 (1H, t, J=6.3 Hz), 8.27-8.26 (1H, m), 8.04-7.97 (2H, m), 7.66-7.63 (1H, m), 7.22-7.19 (1H, m), 4.53 (d, 2H, J = 6.3 Hz).^{13}C-NMR (100 MHz, $(CD_3)_2SO$): 162.2 (d, J = 235 Hz), 159.4, 158.2, 148.1 (dd, J =12, 246 Hz), 147.6 (dd, J=14, 263 Hz), 146.7 (d, J=15 Hz), 145.9, 144.7, 141.7 (d, J = 8.0 Hz), 132.6 (d, J = 4.0 Hz), 124.4, 123.7 (d, J = 18 Hz), 113.7, 109.3 (d, J = 37 Hz), 39.6 ppm. HRMS (ESI+, m/z): calculated $[M+Na]^+$ $C_{15}H_9F_3N_4O_2Na$ as 357.0575, found as 357.0575.

5,6-difluoro-*N*-((2-fluoropyridin-4-yl)methyl)-4-oxo-3,4-dihydroquinazoline-2-carboxamide (5d)

Following the procedure described for **5a**, compound **5d** was prepared from compound **1** and (2-fluoropyridin-4-yl)methanamine hydrochloride. The crude mixture was purified by column chromatography (10-40% EtOAc/DCM) to obtain the title compound as a pale-yellow solid (39 mg, 0.117 mmol, 30%).^{1}H-NMR (400 MHz, $(CD_3)_2SO$): 12.54 (1H, br), 9.74 (1H, t, J = 6.3 Hz), 8.23-8.22 (1H, m), 8.05-7.98 (1H, m), 7.69-7.65 (1H, m), 7.36-7.34 (1H, m), 7.16-7.15 (1H, m), 4.59 (2H, d, J = 6.3 Hz). ^{13}C-NMR (100 MHz, $(CD_3)_2SO$): 163.4 (d, J = 234 Hz), 159.7, 158.2, 154.5 (d, J = 8.0 Hz), 148.1 (dd, J = 11, 246 Hz), 147.7 (dd, J =14, 263 Hz), 147.5 (d, J = 16 Hz), 145.8, 144.7, 124.4, 123.7 (d, J = 20 Hz), 120.6 (d, J = 3.8 Hz), 113.7, 107.6 (d, J = 39 Hz), 41.7 ppm. HRMS (ESI+, m/z): calculated $[M+Na]^+$ $C_{15}H_9F_3N_4O_2Na$ as 357.0575, found as 357.0575.

5,6-difluoro-*N*-(3-(2-fluoroethoxy)benzyl)-4-oxo-3,4-dihydroquinazoline-2-carboxamide (5e)

Following the procedure described for **5a**, compound **5e** was prepared from compounds **1** and **4**. The crude mixture was purified by column chromatography (20-60% EtOAc/hexane) to obtain the title compound as a white solid (39 mg, 0.103 mmol, 24%).^{1}H-NMR (400 MHz, $(CD_3)_2SO$): δ 12.49 (1H, br), 9.59 (1H, t, J=6.3 Hz), 8.03-7.96 (1H, m), 7.67-7.63 (1H, m), 7.31-7.27 (1H, m), 6.98-6.96 (2H, m), 6.91-6.88 (1H, m), 4.83-4.82 (1H, m), 4.72-4.70 (1H, m), 4.49 (2H, d, J = 6.3 Hz), 4.29-4.27 (1H, m), 4.22-4.20 (1H, m). ^{13}C-NMR (150 MHz, $(CD_3)_2SO$): 160.1, 159.8, 158.2, 147.7, 147.6 (dd, J = 12, 246 Hz), 147.5 (dd, J = 14, 263 Hz), 145.2, 140.5, 129.5, 123.9, 123.0 (d, J = 19 Hz), 120.0, 113.9, 113.6, 112.7, 82.2 (d, J = 167 Hz), 67.0 (d, J = 19 Hz), 42.6 ppm. HRMS (ESI+, m/z): calculated $[M+Na]^+$ $C_{18}H_{14}F_3N_3O_3Na$ as 400.0885, found as 400.0885.

6-fluoro-*N*-((2-fluoropyridin-4-yl)methyl)-4-oxo-5-phenethoxy-3,4-dihydroquinazoline-2-carboxamide (6)

To a solution of 2-phenylethanol (13 μL, 0.112 mmol, 1.5 equiv.) in DMA (0.50 mL) was added sodium hydride (60% oil dispersion, 22 mg, 0.561 mmol, 7.5 equiv.), and the mixture was stirred at room temperature for 30 min. Compound **5d** (25 mg, 0.075 mmol, 1.0 equiv.) was added and the mixture was stirred at 80 °C for 1 h. The reaction was cooled to room temperature, acidified with 0.1 M HCl to pH 3−4 and extracted with EtOAc. The combined organics were washed with brine, dried over Na2SO4, filtered, and concentrated under reduced pressure. The crude mixture was purified by preparative HPLC to obtain the title compound as a white solid (10 mg, 0.023 mmol, 30%). ^{1}H-NMR (600 MHz, $(CD_3)_2SO$): δ 12.21 (1H, br), 9.70 (1H, t, J = 6.3 Hz), 8.23-8.22 (1H, m), 7.86-7.83 (1H, m), 7.60-7.57 (1H, m), 7.37-7.32 (5H, m), 7.26-7.23 (1H, m), 7.15-7.14 (1H, m), 4.59 (2H, d, J = 6.3 Hz), 4.32 (2H, t, J=7.2 Hz), 3.15 (2H, t, J=7.2 Hz). ^{13}C-NMR (150

MHz, $(CD_3)_2SO$): 163.4 (d, J = 235 Hz), 160.0, 158.8, 154.6 (d, J = 7.8 Hz), 153.0, 147.5 (d, J= 16 Hz), 145.4 (d, J =14 Hz), 145.3, 145.1, 138.0, 128.9, 128.3, 126.3, 124.2, 123.1 (d, J = 22 Hz), 120.6 (d, J = 3.8 Hz), 118.3, 107.6 (d, J = 38 Hz), 75.7, 41.6 (d, J = 3.0 Hz), 35.8 ppm. HRMS (ESI+, m/z): calculated $[M+Na]^+$ $C_{23}H_{18}F_2N_4O_3Na$ as 459.1245, found as 459.1245.

4-(2-((tetrahydro-2*H*-pyran-2-yl)oxy)ethyl)benzonitrile (7)

To a solution of 4-(2-hydroxyethyl)benzonitrile (50 mg, 0.340 mmol, 1.0 equiv.) in DCM (1.4 mL) was added p-toluenesulfonic acid monohydrate (70 mg, 0.374 mmol, 1.1 equiv.) and 3,4-dihydro-2H-pyran (34 μL, 0.374 mmol, 1.1 equiv.). The mixture was stirred at room temperature for 12 h, diluted with DCM and extracted with 1 M NaOH. The combined organics were washed with brine, dried over Na_2SO_4, filtered, and concentrated under reduced pressure. The crude mixture was purified by column chromatography (0-20% EtOAc/hexane) to obtain the title compound as a yellow oil (57 mg, 0.248 mmol, 73%).^{1}H-NMR (400 MHz, $CDCl_3$): δ 7.57 (2H, d, J = 8.3 Hz), 7.35 (2H, d, J = 8.3 Hz), 4.57-4.56 (1H, m), 3.99-3.93 (1H, dt, J = 9.9, 6.8 Hz), 3.70-3.58 (2H, m), 3.47-3.41 (1H, m), 2.95 (2H, t, J = 6.6 Hz), 1.82-1.44 (6H, m) ppm. ^{13}C-NMR (100 MHz, $CDCl_3$): 145.3, 132.2, 130.0, 119.2, 110.2, 98.9, 67.4, 62.3, 36.6, 30.7, 25.5, 19.5 ppm. HRMS (EI+, m/z): calculated $[M]^+$ $C_{14}H_{17}NO_2$ as 231.1259, found as 231.1268.

4-(2-((tetrahydro-2*H*-pyran-2-yl)oxy)ethyl)benzamide (8)

To a solution of **7** (190 mg, 0.821 mmol, 1.0 equiv.) in DMSO (0.3 mL) was added K_2CO_3 (34 mg, 0.246 mmol, 0.3 equiv.) and a 30% hydrogen peroxide solution in water (0.12 mL). The mixture was stirred at room temperature for 12 h, quenched with water and extracted with DCM. The combined organics were washed with brine, dried over Na_2SO_4, filtered, and concentrated under reduced pressure to obtain the title compound as a white solid (192 mg, 0.772 mmol, 94%).^{1}H-NMR (80 MHz, $CDCl_3$): δ 7.74 (2H, d, J=8.2 Hz), 7.31 (2H, d, J=8.5 Hz), 5.95 (2H, br),

4.57 (1H, s), 4.12-3.35 (4H, m), 3.03-2.86 (2H, m), 1.60-1.45 (6H, m) ppm. ^{13}C-NMR (100 MHz, $CDCl_3$): 169.5, 144.0, 131.3, 129.4, 127.5, 98.9, 67.8, 62.3, 36.4, 30.7, 25.5, 19.6 ppm. HRMS (EI+, m/z): calculated $[M]^+$ $C_{14}H_{19}NO_3$ as 249.1365, found as 249.1372.

4-(2-hydroxyethyl)benzamide (9)

To a solution of **8** (236 mg, 0.947 mmol, 1.0 equiv.) in MeOH (9.5 mL) was added p-toluenesulfonic acid monohydrate (14 mg, 0.076 mmol, 0.08 equiv.). The mixture was stirred at room temperature for 2 h, before removal of the solvent under reduced pressure. The residue was resuspended in 3:1 $CHCl_3$:IPA and extracted with brine. The combined organics were dried over Na_2SO_4, filtered, and concentrated under reduced pressure. The crude mixture was purified by column chromatography (0-8% MeOH/DCM) to obtain the title compound as a yellow oil (110 mg, 0.665 mmol, 70%).^{1}H-NMR (400 MHz, $(CD_3)_2SO$): δ 7.94 (2H, br), 7.82 (2H, d, J = 8.3 Hz), 7.32 (2H, d, J = 8.2 Hz), 3.65 (2H, q, J = 6.9 Hz), 3.39 (1H, br), 2.80 (2H, t, J = 6.9 Hz) ppm. ^{13}C-NMR (100 MHz, $(CD_3)_2SO$): 167.8, 143.1, 132.0, 128.7, 127.4, 61.8, 38.8 ppm. HRMS (EI+, m/z): calculated $[M]^+$ $C_9H_{11}NO_2$ as 165.0790, found as 165.07883.

4-(2-((*tert*-butyldimethylsilyl)oxy)ethyl)benzoic acid (10)

To a solution of 4-(2-hydroxyethyl)benzoic acid (125 mg, 0.752 mmol, 1.0 equiv.) in THF (1.9 mL) was added imidazole (128 mg, 1.88 mmol, 2.5 equiv.). The mixture was cooled to 0 °C and *tert*-butyldimethylsilyl chloride (238 mg, 1.58, 2.1 equiv.) was added dropwise in THF (0.4 mL). The reaction was stirred at room temperature for 2 h, before removal of the solvent under reduced pressure. The residue was re-suspended in THF (0.40 mL) and MeOH (0.75 mL), and K_2CO_3 (375 mg, 2.71 mmol, 3.6 equiv.) was added. The reaction was stirred at room temperature for another 2 h, before removal of the solvent under reduced pressure. The residue was re-suspended in DCM and washed with 1 M HCl. The combined organics were washed with brine, dried over Na_2SO_4,

filtered, and concentrated under reduced pressure. The crude mixture was purified by column chromatography (0-15% EtOAc/hexane) to obtain the title compound as a yellow oil (196 mg, 0.70 mmol, 93%). ^{1}H-NMR (600 MHz, $(CD_3)_2SO$): δ 12.88 (1H, br), 7.89-7.88 (2H, m), 7.38-7.27 (2H, m), 3.84 (2H, t, J = 6.6 Hz), 2.85 (2H, t, J = 6.6 Hz), 0.84 (9H, s), -0.03 (6H, s) ppm. ^{13}C-NMR (150 MHz, $(CD_3)_2SO$): 167.3, 144.6, 129.3, 129.1, 128.6, 63.3, 38.7, 25.8, 17.9, -5.5 ppm. HRMS (EI+, m/z): calculated $[M-C_4H_9]^+$ $C_{11}H_{15}O_3Si$ as 223.0790, found as 223.0804.

4-(2-((*tert*-butyldimethylsilyl)oxy)ethyl)-*N*-methylbenzamide (11a)

A solution of **10** (125 mg, 0.446 mmol, 1.0 equiv.) in thionyl chloride (1.8 mL) was refluxed for 3 h at 90 °C, before removal of the solvent under reduced pressure. The residue was resuspended in DCM (1.8 mL) and cooled to 0 °C before addition of pyridine (47 μL, 0.579 mmol, 1.3 equiv.) and 2 M methylamine in THF (0.45 mL, 0.891 mmol, 2.0 equiv.). The reaction was stirred at room temperature for 1 h, quenched with saturated NH_4Cl and extracted with water. The combined organics were washed with brine, dried over Na_2SO_4, filtered, and concentrated under reduced pressure. The crude mixture was purified by column chromatography (0-20% EtOAc/DCM) to obtain the title compound as a yellow oil (108 mg, 0.368 mmol, 83%). ^{1}H-NMR (80 MHz, $CDCl_3$): δ 7.73-7.63 (2H, m), 7.31-7.20 (2H, m), 6.14 (1H, br), 3.81 (2H, t, J = 6.0 Hz), 3.0 (d, J = 6.0 Hz), 2.84 (2H, t, J = 6.0 Hz), 0.85 (9H, s), -0.04 (6H, s) ppm. HRMS (EI+, m/z): calculated $[M-C_4H_9]^+$ $C_{12}H_{18}NO_2Si$ as 236.1107, found as 236.1112.

4-(2-((*tert*-butyldimethylsilyl)oxy)ethyl)-*N*,*N*-dimethylbenzamide (11b)

Following the procedure described for **11a**, compound **11b** was prepared from compound **10** and 2 M dimethylamine in THF. The crude mixture was purified by column chromatography (0-20% EtOAc/DCM) to obtain the title compound as a yellow oil (116 mg, 0.377 mmol, 88%).^{1}H-NMR (80 MHz, $(CD_3)_2SO$): δ 7.33 (4H, s), 3.83 (2H, t, J = 6.0 Hz), 2.97 (6H, br), 2.81 (2H, t, J = 6.0

Hz), 0.84 (9H, s), -0.03 (6H, s) ppm. HRMS (EI+, m/z): calculated $[M\text{-}C_4H_9]^+$ $C_{13}H_{20}NO_2Si$ as 250.1263, found as 250.1270.

4-(2-hydroxyethyl)-*N*-methylbenzamide (12a)

To a solution of **11a** (103 mg, 0.351 mmol, 1.0 equiv.) in MeOH (3.5 mL) was added p-toluenesulfonic acid monohydrate (6.7 mg, 0.035 mmol, 0.01 equiv.). The mixture was stirred at room temperature for 2 h, before removal of the solvent under reduced pressure. The crude mixture was directly purified by column chromatography (0-5% MeOH/DCM) to obtain the title compound as a white solid (58 mg, 0.323 mmol, 92%). ^{1}H-NMR (600 MHz, $(CD_3)_2SO$): δ 8.38 (1H, s), 7.77 (2H, d, J = 8.3 Hz), 7.32 (2H, d, J = 8.3 Hz), 4.70 (1H, t, J = 5.2 Hz), 3.67-3.64 (2H, m), 2.81-2.78 (5H, m) ppm. ^{13}C-NMR (150 MHz, $(CD_3)_2SO$): 167.0, 143.4, 132.7, 129.3, 127.4, 62.3, 39.3, 26.7 ppm. HRMS (EI+, m/z): calculated $[M]^+$ $C_{10}H_{13}NO_2$ as 179.0946, found as 179.0945.

4-(2-hydroxyethyl)-*N*,*N*-dimethylbenzamide (12b)

Following the procedure described for **12a**, compound **12b** was prepared from compound **11b**. The crude mixture was directly purified by column chromatography (0-5% MeOH/DCM) to obtain the title compound as a white solid (60 mg, 0.310 mmol, 86%).^{1}H-NMR (600 MHz, $(CD_3)_2SO$): δ 7.34 (2H, d, J = 8.1 Hz), 7.30 (2H, d, J = 8.1 Hz), 4.70 (1H, br), 3.66 (2H, t, J = 7.0 Hz), 3.00 (3H, s), 2.95 (3H, s), 2.79 (2H, t, J = 7.0 Hz) ppm. ^{13}C-NMR (150 MHz, $(CD_3)_2SO$): 170.2, 141.0, 134.0, 128.7, 126.9, 61.9, 38.8, 34.8 ppm. HRMS (EI+, m/z): calculated $[M]^+$ $C_{11}H_{15}NO_2$ as 193.1103, found as 193.1111.

4-acetamidophenethyl acetate (13)

To a solution of 4-aminophenethyl alcohol (250 mg, 1.82 mmol, 1.0 equiv.) in DCM (0.91 mL) was added pyridine (0.44 mL, 5.47 mmol, 3.0 equiv.). The mixture was cooled to 0 °C and acetic anhydride (0.52 mL, 5.47 mmol, 3.0 equiv.) was added dropwise. The reaction was allowed to stir at room temperature for 1 h, before removal of the solvent under reduced pressure. The residue was resuspended in EtOAc and consecutively washed with 1 M HCl and $NaHCO_3$. The combined organics were washed with brine, dried over Na_2SO_4, filtered, and concentrated under reduced pressure to obtain the title compound as a white solid (338 mg, 1.53 mmol, 84%).^{1}H-NMR (600 MHz, $(CD_3)_2SO$): δ 9.91 (1H, s), 7.53 (2H, d, J = 8.4 Hz), 7.19 (2H, d, J = 8.4 Hz), 4.20 (2H, t, J = 7.0 Hz), 2.85 (2H, t, J = 7.0 Hz), 2.06 (3H, s), 2.01 (3H, s) ppm. ^{13}C-NMR (150 MHz, $(CD_3)_2SO$): 170.3, 168.1, 137.7, 132.4, 129.0, 119.0, 64.4, 33.8, 24.0, 20.7 ppm. HRMS (EI+, m/z): calculated $[M]^+$ $C_{12}H_{15}NO_3$ as 221.1052, found as 221.1065.

***N*-(4-(2-hydroxyethyl)phenyl)acetamide (14)**

To a solution of **13** (330 mg, 1.49 mmol, 1.0 equiv.) in MeOH (6.0 mL) was added K_2CO_3 (309 mg, 2.24 mmol, 1.5 equiv.). The mixture was stirred at room temperature for 1 h, before removal of the solvent under reduced pressure. The residue was resuspended in EtOAc and extracted with water. The combined organics were wash with brine, dried over Na_2SO_4, filtered, and concentrated under reduced pressure. The crude mixture was purified by column chromatography (50% EtOAc/DCM) to obtain the title compound as a white solid (188 mg, 1.05 mmol, 70%). ^{1}H-NMR (600 MHz, $(CD_3)_2SO$): δ 9.87 (1H, s), 7.49 (2H, d, J = 8.4 Hz), 7.15 (2H, d, J = 8.4 Hz), 4.64 (1H, t, J = 5.2 Hz), 3.61-3.58 (2H, m), 2.69 (2H, t, J = 7.1 Hz), 2.05 (3H, s) ppm. ^{13}C-NMR (150 MHz, $(CD_3)_2SO$): 168.0, 137.3, 134.1, 129.0, 118.9, 62.3, 38.5, 23.9 ppm. HRMS (EI+, m/z): calculated $[M]^+$ $C_{10}H_{13}NO_2$ as 179.0946, found as 179.0948.

4-(2-((*tert*-butyldimethylsilyl)oxy)ethyl)aniline (15)

To a solution of 4-aminophenethyl alcohol (250 mg, 1.82 mmol, 1.0 equiv.) in DCM (4.5 mL) was added imidazole (136 mg, 2.00 mmol, 1.1 equiv.) and *tert*-butyldimethylsilyl chloride (275 mg, 1.82, 1.0 equiv.). The mixture was stirred at room temperature for 12 h, diluted with DCM and extracted with water. The combined organics were washed with brine, dried over Na_2SO_4, filtered, and concentrated under reduced pressure. The crude mixture was purified by column chromatography (10% EtOAc/hexane) to obtain the title compound as a colorless oil (386 mg, 1.54 mmol, 85%).^{1}H-NMR (600 MHz, $(CD_3)_2SO$): δ 6.88 (2H, d, J = 8.3 Hz), 6.51 (2H, d, J = 8.3 Hz), 4.89 (2H, s), 3.69 (2H, t, J = 7.1 Hz), 2.60 (2H, t, J = 7.1), 0.88 (9H, s), 0.00 (6H, s) ppm. ^{13}C-NMR (150 MHz, $(CD_3)_2SO$): 146.7, 129.4, 125.7, 113.8, 64.5, 38.2, 25.8, 18.0, -5.4 ppm. HRMS (EI+, m/z): calculated $[M]^+$ $C_{14}H_{25}NOSi$ as 251.1705, found as 251.1710.

N-(4-(2-((tert-butyldimethylsilyl)oxy)ethyl)phenyl)methanesulfonamide (16)

To a solution of **15** (359 mg, 1.43 mmol, 1.0 equiv.) in DCM (14 mL) was added pyridine (0.28 mL, 3.43 mmol, 2.4 equiv.). The mixture was cooled to 0 °C and methanesulfonyl chloride (0.12 mL, 1.57 mmol, 1.1 equiv.) was added. The reaction was allowed to stir at room temperature for 12 h, before quenching with 1 M HCl and extracted with EtOAc followed by water. The combined organics were washed with brine, dried over Na_2SO_4, filtered, and concentrated under reduced pressure to obtain the title compound as a white solid (401 mg, 1.22 mmol, 85%). ^{1}H-NMR (80 MHz, $(CD_3)_2SO$): δ 9.60 (1H, s), 7.18 (1H, s), 3.78 (2H, t, J = 6.0 Hz), 2.95 (3H, s), 2.73 (2H, t, J = 6.0 Hz), 0.85 (9H, s), -0.02 (6H, s) ppm. ^{13}C-NMR (150 MHz, $(CD_3)_2SO$): δ 138.2, 135.4, 129.7, 120.3, 62.1, 39.0, 38.3, 25.8, 17.8, -5.4 ppm. HRMS (EI+, m/z): calculated $[M\text{-}C_4H_9]^+$ $C_{11}H_{18}NO_3SSi$ as 272.0777, found as 272.0781.

tert-butyl (4-(2-hydroxyethyl)phenyl)(methylsulfonyl)carbamate (17)

To a solution of **16** (460 mg, 1.40, 1.0 equiv.) in DCM (28 mL) was added DMAP (188 mg, 1.54 mmol, 1.1 equiv.) and Boc_2O (0.35 mL, 1.54 mmol, 1.1 equiv.). The solution was stirred at room temperature for 2 h and extracted with 1 M HCl followed by water. The combined organics were washed with brine, dried over Na_2SO_4, filtered, and concentrated under reduced pressure. The solid was resuspended in methanol (14 mL) and p-toluenesulfonic acid monohydrate (27 mg, 0.14 mmol, 0.1 equiv.) was added. The mixture was stirred at room temperature for 1 h, before removal of the solvent under reduced pressure. The crude mixture was purified by column chromatography (0-15% EtOAc/DCM) to obtain the title compound as a white solid (265 mg, 0.84 mmol, 60% over 2 steps). ^{1}H-NMR (600 MHz, $(CD_3)_2SO$): δ 7.31-7.30 (2H, m), 7.25-7.23 (2H, m), 4.72 (1H, t, J = 6.0 Hz), 3.68-3.65 (2H, m), 3.55 (3H, s), 2.79 (2H, t, J = 6.0 Hz), 1.45 (9H, s) ppm. ^{13}C-NMR (150 MHz, $(CD_3)_2SO$): δ 151.0, 140.4, 133.7, 129.4, 129.3, 83.9, 61.8, 41.5, 38.5, 27.5 ppm. HRMS (EI+, m/z): calculated $[M-C_5H_8O_2]^+$ $C_9H_{13}NO_3S$ as 215.0616, found as 215.0641.

4-(2-hydroxyethyl)-*N*,*N*-dimethylbenzenesulfonamide (18)

To a solution of 2-(4-(*N*,*N*-dimethylsulfamoyl)phenyl)acetic acid (100 mg, 0.41 mmol, 1.0 equiv.) in THF (0.82 mL) was added 1 M lithium aluminum hydride in THF (0.45 mL, 0.45 mmol, 1.1 equiv.) at 0 °C. The mixture was stirred at room temperature for 1 h, quenched slowly with methanol, and concentrated under reduced pressure. The crude mixture was purified by column chromatography (0-20% EtOAc/hexane) to obtain the title compound as a colorless oil (40 mg, 0.17 mmol, 42%). ^{1}H-NMR (600 MHz, $(CD_3)_2SO$): δ 7.70-7.69 (2H, m), 7.68-7.67 (2H, m), 4.75 (1H, t, J = 6.0 Hz), 3.71-3.68 (2H, m), 2.86 (2H, t, J = 6.0 Hz), 2.63 (6H, s) ppm. ^{13}C-NMR (150 MHz, $(CD_3)_2SO$): δ 145.5, 132.3, 129.8, 127.4, 61.4, 38.6, 37.6 ppm. HRMS (EI+, m/z): calculated $[M]^+$ $C_{10}H_{15}NO_3S$ as 229.0773, found as 229.0755.

2-(4-(((*tert*-butyldimethylsilyl)oxy)methyl)phenyl)acetic acid (19)

To a solution of 2-[4-(hydroxymethyl)phenyl]acetic acid (250 mg, 1.50 mmol, 1.0 equiv.) in THF (3.8 mL) was added imidazole (256 mg, 3.76 mmol, 2.5 equiv.). The mixture was cooled to 0 °C and *tert*-butyldimethylsilyl chloride (476 mg, 3.76, 2.1 equiv.) was added dropwise as a solution in THF (0.75 mL). The reaction was stirred at room temperature for 2 h, before removal of the solvent under reduced pressure. The residue was resuspended in THF (0.75 mL) and MeOH (1.5 mL), and K_2CO_3 (750 mg, 5.43 mmol, 3.6 equiv.) was added. The reaction was stirred at room temperature for another 2 h, before removal of the solvent under reduced pressure. The residue was resuspended in DCM and washed with 1 M HCl. The combined organics were washed with brine, dried over Na_2SO_4, filtered, and concentrated under reduced pressure. The crude mixture was purified by column chromatography (0-15% EtOAc/hexane) to obtain the title compound as a white solid (338 mg, 1.20 mmol, 80%). ^{1}H-NMR (80 MHz, $CDCl_3$): δ 10.68 (1H, br), 7.31 (4H, s), 4.77 (2H, s), 3.68 (2H, s), 0.98 (9H, s), 0.14 (6H, s) ppm. ^{13}C-NMR (100 MHz, $CDCl_3$): 177.7, 140.7, 132.0, 129.4,126.5, 64.8, 40.9, 26.1, 18.6, -5.1 ppm. HRMS (EI+, m/z): calculated $[M-C_4H_9]^+$ $C_{11}H_{15}O_3Si$ as 223.0790, found as 223.0803.

2-(4-(((*tert*-butyldimethylsilyl)oxy)methyl)phenyl)ethan-1-ol (20)

To a solution of **19** (291 mg, 1.04 mmol, 1.0 equiv.) in THF (1.0 mL) was added 1 M lithium aluminum hydride in THF (2.08 mL, 2.08 mmol, 2.0 equiv.) at 0 °C. The mixture was stirred at room temperature for 1 h, quenched with saturated NH_4Cl and extracted with 3:1 $CHCl_3$:IPA. The combined organics were washed with brine, dried over Na_2SO_4, filtered, and concentrated under reduced pressure. The crude mixture was purified by column chromatography (0-20% EtOAc/hexane) to obtain the title compound as a colorless oil (197 mg, 0.738 mmol, 71%). ^{1}H-NMR (600 MHz, $(CD_3)_2SO$): δ 7.24-7.20 (4H, m), 4.70 (2H, s), 4.65 (1H, d, J = 6.0 Hz), 3.64-

3.60 (2H, m), 2.74 (2H, t, J = 6.0 Hz), 0.94 (9H, s), 0.11 (6H, s) ppm. ^{13}C-NMR (150 MHz, $(CD_3)_2SO$): δ 138.6, 138.1, 128.6, 125.9, 64.2, 62.2, 38.8, 25.8, 18.0, -5.3 ppm. HRMS (EI+, m/z): calculated $[M\text{-}C_4H_9]^+$ $C_{11}H_{17}O_2Si$ as 209.0998, found as 209.0987.

***N*-(4-fluoro-3-methoxyphenyl)pivalamide (21)**

To a solution of 4-fluoro-3-methoxyaniline (5.0 g, 35.4 mmol, 1.0 equiv.) in DCM (44 mL) was added pyridine (5.7 mL, 70.9 mmol, 2.0 equiv.) and 4-dimethylaminopyridine (432 mg, 3.54 mmol, 0.1 equiv.), followed by trimethylacetyl chloride (4.4 mL, 36.1 mmol, 1.02 equiv.). The mixture was stirred at room temperature for 1 h and extracted with 1 M HCl. The combined organics were washed brine, dried over Na_2SO_4, filtered, and concentrated under reduced pressure. The crude mixture was recrystallized from DCM/hexane to obtain the title compound as a light-purple solid (6.7 g, 29.9 mmol, 84%). ^{1}H-NMR (400 MHz, $CDCl_3$): δ 7.64-7.61 (1H, m), 7.31 (1H, br), 7.01-6.95 (1H, m), 6.74-6.70 (1H, m), 3.89 (1H, s), 1.31 (9H, s) ppm. ^{13}C-NMR (100 MHz, $CDCl_3$): 176.8, 149.1 (d, J = 241 Hz), 147.8 (d, J = 14 Hz), 134.7 (d, J = 2.4 Hz),115.8 (d, J = 19 Hz), 111.5 (d, J = 7.0 Hz), 106.3, 56.3, 39.8, 27.7 ppm. HRMS (EI+, m/z): calculated $[M]^+$ $C_{12}H_{16}FNO_2$ as 225.1165, found as 225.1194.

Ethyl 3-fluoro-2-methoxy-6-pivalamidobenzoate (22)

To a solution of **21** (3.1 g, 13.7 mmol, 1.0 equiv.) in anhydrous THF (31 mL), was added n-butyllithium (1.6 M in hexane, 19.0 mL, 30.1 mmol, 2.2 equiv.) dropwise at 0 °C. The mixture was stirred for 4 h before a solution of ethyl chloroformate (1.4 mL, 15.1 mmol, 1.1 equiv.) in anhydrous THF (9.4 mL) was slowly added at -78 °C. The reaction was stirred at -78 °C for 15 min, warmed to -50 °C, and stirred for an additional 2 h. The reaction was then quenched by addition of saturated NH_4Cl (40 mL) and extracted with EtOAc. The combined organics were washed with brine, dried over Na_2SO_4, filtered, and concentrated under reduced pressure. The

crude mixture was purified by column chromatography (0-10% EtOAc/hexane) to obtain the title compound as a white solid (3.3 g, 11.2 mmol, 82%). ^{1}H-NMR (400 MHz, $CDCl_3$): δ 9.66 (1H, br), 8.14-8.10 (1H, m), 7.21-7.16 (1H, m), 4.45-4.39 (2H, m), 3.93 (3H, s), 1.44-1.40 (3H, m), 1.29 (9H, s) ppm. ^{13}C-NMR (100 MHz, $CDCl_3$): 177.4, 167.3 (d, J = 3.0 Hz), 152.2 (d, J = 243 Hz), 147.1 (d, J = 13 Hz), 135.1 (d, J = 3.0 Hz), 120.2 (d, J = 19 Hz), 117.4 (d, J = 7.0 Hz), 116.4 (d, J = 5.0 Hz), 62.2, 62.1, 40.1, 27.6, 14.3 ppm. HRMS (EI+, m/z): calculated $[M]^+$ $C_{15}H_{20}FNO_4$ as 297.1376, found as 297.1347.

Ethyl 6-amino-3-fluoro-2-methoxybenzoate hydrochloride (23)

To a solution of **22** (392 mg, 1.32 mmol, 1.0 equiv.) in EtOH (1.3 mL) was added 12 M HCl (0.43 mL). The mixture was stirred at 80 °C for 16 h before addition of diethyl ether. The precipitate was collected by filtration to obtain the title compound as a white solid (218 mg, 0.873 mmol, 66%). ^{1}H-NMR (400 MHz, $(CD_3)_2SO$): δ 7.33-7.28 (1H, m), 6.80-6.77 (1H, m), 6.80 (2H, br), 4.34 (2H, q, J = 4.0 Hz), 3.86 (3H, d, J = 4.0 Hz), 1.34 (3H, t, J = 8.0 Hz) ppm. ^{13}C-NMR (100 MHz, $(CD_3)_2SO$): δ 165.2, 148.8 (d, J = 235 Hz), 146.1 (d, J = 13 Hz), 139.8, 120.1 (d, J = 21 Hz), 113.8, 113.6, 61.8 (d, J = 4.0 Hz), 61.09, 14.0 ppm. HRMS (EI+, m/z): calculated $[M\text{-}HCl]^+$ $C_{10}H_{12}FNO_3$ as 213.0801, found as 213.0809.

Ethyl 6-fluoro-5-methoxy-4-oxo-3,4-dihydroquinazoline-2-carboxylate (24)

To a solution of **23** (215 mg, 0.862 mmol, 1.0 equiv.) in 4 M HCl in dioxane (7.2 mL) was added ethyl cyanoformate (0.10 mL, 1.03 mmol, 1.2 equiv.). The mixture was stirred at 80 °C for 3 h, diluted with EtOAc and extracted with water. The combined organics were washed with brine, dried over Na_2SO_4, filtered, and concentrated under reduced pressure. The crude mixture was purified by column chromatography (20-50% EtOAc/hexane) to obtain the title compound as a white solid (163 mg, 0.612 mmol, 71%).^{1}H-NMR (400 MHz, $CDCl_3$): δ 10.08 (1H, br), 7.69-7.66

(1H, m), 7.60-7.54 (1H, m), 4.56 (2H, q, J = 8.0 Hz), 4.08 (3H, s), 1.47 (3H, t, J = 8.0 Hz) ppm. ^{13}C-NMR (100 MHz, $CDCl_3$): 160.4, 158.8, 155.2 (d, J = 250 Hz), 147.6 (d, J = 13 Hz), 145.5, 141.4, 125.5 (d, J = 7.0 Hz), 123.8 (d, J = 21 Hz), 118.5, 64.3, 62.9 (d, J = 4.0 Hz), 14.3 ppm. HRMS (EI+, m/z): calculated $[M]^+$ $C_{12}H_{11}FN2O_4$ as 266.0703, found as 266.0714.

6-fluoro-*N*-((2-fluoropyridin-4-yl)methyl)-5-methoxy-4-oxo-3,4-dihydroquinazoline-2-carboxamide (25)

To a solution of **24** (500 mg, 1.88 mmol, 1.0 equiv.) in EtOH (9.4 mL) was added (2-fluoropyridin-4-yl)methanamine hydrochloride (459 mg, 2.82 mmol, 1.5 equiv.), followed by triethylamine (0.45 mL, 3.20 mmol, 1.7 equiv.). The mixture was stirred at 80 °C for 12 h and cooled to room temperature. The precipitate was collected by filtration and washed with cold diethyl ether to obtain the title compound as a white solid (588 mg, 1.69 mmol, 90%). ^{1}H-NMR (80 MHz, $(CD_3)_2SO$): δ.12.21 (1H, br), 9.70 (1H, m), 8.26-8.20 (1H, m), 7.89-7.61 (2H, m), 7.44-7.27 (1H, m), 7.15 (1H, m), 4.63 (2H, d, J = 6.4 Hz), 3.94 (3H, s) ppm. ^{13}C-NMR (150 MHz, $(CD_3)_2SO$): δ 164.1 (d, J = 234 Hz), 160.8, 160.0, 155.2 (d, J = 7.5 Hz), 154.6 (d, J = 246 Hz), 148.2 (d, J = 15 Hz), 147.1 (d, J = 14 Hz), 145.9, 145.4, 125.4 (d, J = 5 Hz), 124.4 (d, J = 21 Hz), 121.4 (d, J = 3.0 Hz), 118.5, 108.3 (d, J = 38 Hz), 63.2 (d, J = 3.0 Hz), 42.4 (d, J = 3.0 Hz) ppm. HRMS (ESI+, m/z): calculated $[M+H]^+$ $C_{16}H_{13}F_2N_4O_3$ as 347.0956, found as 347.0956.

1-(dimethylamino)-7-fluoro-2-((2-fluoropyridin-4-yl)methyl)-8-methoxy-1,2 dihydroimidazo[5,1-*b*]quinazoline-3,9-dione (26)

To a solution of **25** (250 mg, 0.722 mmol, 1.0 equiv.) in THF (2.35 mL) was added oxalyl chloride (0.185 mL, 0.x mmol, 3.0 equiv.) and DMF (1.13 mL) at 0 °C. The mixture was stirred at room temperature for 2 h, before removal of the solvent under reduced pressure. The residue was resuspended in EtOAc and extracted with water. The combined organics were washed with brine,

dried over Na_2SO_4, filtered, and concentrated under reduced pressure. The crude mixture was purified by column chromatography (0-20% EtOAc/DCM) to obtain the title compound as a pale-yellow solid (246 mg, 0.614 mmol, 85%).^{1}H-NMR (600 MHz, $(CD_3)_2SO$): δ 8.26-8.25 (1H, m), 7.94-7.91 (1H, m), 7.73-7.70 (1H, m), 7.42-7.41 (1H, m), 7.26 (1H, s), 6.36 (1H, s), 4.94-4.91 (2H, m), 3.96 (3H, s), 2.38 (6H, br) ppm. ^{13}C-NMR (150 MHz, $(CD_3)_2SO$): δ 164.2 (d, J = 236 Hz), 158.5, 157.6 (d, J = 4.5 Hz), 154.8 (d, J = 245 Hz), 152.3 (d, J = 7.5 Hz), 148.3 (d, J = 15 Hz), 147.5 (d, J = 14 Hz), 146.8 (d, J = 1.5 Hz), 145.3 (d, J = 3 Hz), 125.6 (d, J = 7.5 Hz), 124.5 (d, J = 21 Hz), 122.0 (d, J = 3 Hz), 117.8 (d, J = 3 Hz), 109.0 (d, J = 38 Hz), 88.7, 63.2 (d, J = 3 Hz), 43.1 (d, J = 3 Hz) ppm. HRMS (ESI+, m/z): calculated $[M+H]^+$ $C_{19}H_{18}F_2N_5O_3$ as 402.1378, found as 402.1378.

1-(dimethylamino)-7-fluoro-2-((2-fluoropyridin-4-yl)methyl)-8-hydroxy-1,2-dihydroimidazo[5,1-*b*]quinazoline-3,9-dione (27)

To a solution of **26** (226 mg, 0.563 mmol, 1.0 equiv.) in DMF (9.1 mL) was added lithium chloride (72 mg, 1.69 mmol, 4.0 equiv.). The solution was refluxed for 16 h and cooled to room temperature. The mixture was diluted with EtOAc and extracted with 10% aqueous LiCl followed by saturated NH_4Cl. The combined organics were washed with brine, dried over Na_2SO_4, filtered, and concentrated under reduced pressure. The crude mixture was purified by column chromatography (0-25% EtOAc/DCM) and further washed with ethanol to obtain the title compound as a white solid (109 mg, 0.282 mmol, 50%). ^{1}H-NMR (600 MHz, $CDCl_3$): δ 11.16 (1H, s), 8.25-8.24 (1H, m), 7.60-7.57 (1H, m), 7.46-7.43 (1H, m), 7.18-7.17 (1H, m), 6.92 (1H, m), 6.08 (1H, s), 5.13 (1H, d, J = 12 Hz), 4.39 (1H, d, J = 12 Hz), 2.46 (6H, br) ppm. ^{13}C-NMR (150 MHz, $CDCl_3$): δ 163.4 (d, J = 240 Hz), 163.4 (d, J = 4.5 Hz), 157.5, 149.6 (d, J = 7.5 Hz), 149.2 (d, J = 249 Hz), 148.8 (d, J = 15 Hz), 148.0 (d, J = 14 Hz), 144.3 (d, J = 3.0 Hz), 142.5 (d, J

= 1.5 Hz), 124.4 (d, J = 20 Hz), 121.1 (d, J = 3.0 Hz), 119.5 (d, J = 6.0 Hz), 109.5 (d, J = 38 Hz), 109.4 (d, J = 6.0 Hz), 87.6, 42.6 (d, J = 3.0 Hz) ppm. HRMS (ESI+, m/z): calculated $[M+Na]^+$ $C_{18}H_{15}F_2N_5O_3Na$ as 410.1041, found as 410.1041.

4-(2-((1-(dimethylamino)-7-fluoro-2-((2-fluoropyridin-4-yl)methyl)-3,9-dioxo-1,2,3,9-tetrahydroimidazo[5,1-*b*]quinazolin-8-yl)oxy)ethyl)benzamide (28a)

To a solution of **9** (26 mg, 0.16 mmol, 1.0 equiv.) in THF (1.6 mL) was added **5d** (75 mg, 0.19 mmol, 1.2 equiv.) and triphenylphosphine (102 mg, 0.39 mmol, 2.4 equiv.). The mixture was cooled to 0 °C and diisopropyl azodicarboxylate (76 μL, 0.39 mmol, 2.4 equiv.) was added dropwise. The reaction was stirred at room temperature for 1 h and concentrated under reduced pressure. The crude mixture was partially purified by column chromatography (50-100% EtOAc/hexane) to remove unreacted starting materials and easily separable byproducts before complete purification by preparative HPLC to obtain the title compound as a white solid (59 mg, 0.110 mmol, 69%). ^{1}H-NMR (600 MHz, $(CD_3)_2SO$): δ 8.20 (1H, m), 8.03, (1H, br), 7.81-7.76 (3H, m), 7.65-7.63 (1H, m), 7.42-7.41 (2H, m), 7.35-7.34 (1H, m), 7.24 (1H, br), 7.17 (1H, m), 6.33 (1H, s), 4.84 (2H, d, J = 18 Hz), 4.61 (2H, d, J = 18 Hz), 4.39-4.35 (2H, m), 4.33-4.29 (2H, m), 3.15 (2H, t, J = 6.0 Hz), 2.31 (6H, br) ppm. ^{13}C-NMR (150 MHz, $(CD_3)_2SO$): δ 169.7, 164.2 (d, J = 234 Hz), 158.5, 154.8 (d, J = 246 Hz), 152.3 (d, J = 7.5 Hz), 148.3 (d, J = 14 Hz), 146.8 (d, J = 1.5 Hz), 146.3 (d, J = 14 Hz), 145.2 (d, J = 1.5 Hz), 143.1, 132.3, 129.8, 128.3, 125.7 (d, J = 7.5 Hz), 124.4 (d, J = 21 Hz), 121.9 (d, J = 3.0 Hz), 117.9 (d, J = 3.0 Hz), 109.0 (d, J = 38 Hz), 88.6, 76.1, 43.1 (d, J = 3.0 Hz), 36.3, 31.1 ppm. HRMS (ESI+, m/z): calculated $[M+Na]^+$ $C_{27}H_{24}F_2N_6O_4Na$ as 557.1725, found as 557.1725.

4-(2-((1-(dimethylamino)-7-fluoro-2-((2-fluoropyridin-4-yl)methyl)-3,9-dioxo-1,2,3,9-tetrahydroimidazo[5,1-*b*]quinazolin-8-yl)oxy)ethyl)-*N*-methylbenzamide (28b)

Following the procedure described for **28a**, compound **28b** was prepared from compound **12a** and **5d**. The crude mixture was partially purified by column chromatography (50-85% EtOAc/hexane) to remove unreacted starting materials and easily separable byproducts before complete purification by preparative HPLC to obtain the title compound as a white solid (51 mg, 0.093 mmol, 58%). ^{1}H-NMR (600 MHz, $(CD_3)_2SO$): δ 8.41-8.40 (1H, m), 8.25-8.24 (1H, m), 7.90-7.87 (1H, m), 7.79-7.77 (2H, m), 7.70-7.68 (1H, m), 7.45-7.44 (2H, m), 7.41-7.40 (1H, m), 7.25 (1H, m), 6.36 (1H, s), 4.92 (1H, d, J = 18 Hz), 4.61 (1H, d, J = 18 Hz), 4.41-4.32 (2H, m), 3.19 (2H, t, J = 6.0 Hz), 2.80 (3H, d, J = 6.0 Hz), 2.38 (6H, br) ppm. ^{13}C-NMR (150 MHz, $(CD_3)_2SO$): δ 166.8, 163.6 (d, J = 234 Hz), 157.8, 157.0 (d, J = 3.0 Hz), 154.2 (d, J = 245 Hz), 151.8 (d, J = 7.5 Hz), 147.8 (d, J = 15 Hz), 146.5 (d, J = 3.0 Hz), 145.7 (d, J = 14 Hz), 144.8 (d, J = 1.5 Hz), 141.6, 132.6, 129.0, 127.2, 125.1 (d, J = 7.5 Hz), 123.6 (d, J = 21 Hz), 121.2 (d, J = 4.5 Hz), 117.5 (d, J = 1.5 Hz), 108.2 (d, J = 38 Hz), 87.6, 75.6 (d, J = 3.0 Hz), 42.3 (d, J = 3.0 Hz), 35.7, 26.4 ppm. HRMS (ESI+, m/z): calculated $[M+Na]^+$ $C_{28}H_{26}F_2N_6O_4Na$ as 571.1881, found as 571.1881.

4-(2-((1-(dimethylamino)-7-fluoro-2-((2-fluoropyridin-4-yl)methyl)-3,9-dioxo-1,2,3,9-tetrahydroimidazo[5,1-*b*]quinazolin-8-yl)oxy)ethyl)-*N*,*N*-dimethylbenzamide (28c)

Following the procedure described for **28a**, compound **28c** was prepared from compound **12b** and **5d**. The crude mixture was partially purified by column chromatography (50-100% EtOAc/hexane) to remove unreacted starting materials and easily separable byproducts before complete purification by preparative HPLC to obtain the title compound as a white solid (65 mg, 0.116 mmol, 66%). ^{1}H-NMR (600 MHz, $(CD_3)_2SO$): δ 8.20 (1H, J = 6.0 Hz), 7.81-7.78 (1H, m), 7.65-7.62 (1H, m), 7.38-7.37 (2H, m), 7.35-7.34 (1H, m), 7.31-7.30 (2H, m), 7.17 (1H, m), 6.34

(1H, s), 4.84 (1H, d, J = 18 Hz), 4.62 (1H, d, J = 18 Hz), 4.40-4.36 (2H, m), 4.34-4.30 (2H, m), 3.13 (2H, t, J = 6.0 Hz), 2.97 (3H, s), 2.89 (3H, s), 2.32 (6H, br) ppm. ^{13}C-NMR (150 MHz, $(CD_3)_2SO$): δ 171.6, 164.2 (d, J = 234 Hz), 158.5, 157.6 (d, J = 4.5 Hz), 154.8 (d, J = 246 Hz), 152.3 (d, J = 7.5 Hz), 148.3 (d, J = 15 Hz), 146.8 (d, J = 1.5 Hz), 146.3 (d, J = 14 Hz), 145.2 (d, J = 1.5 Hz), 140.6, 134.7, 129.6, 127.7, 125.6 (d, J = 6.0 Hz), 124.4 (d, J = 23 Hz), 121.9 (d, J = 4.5 Hz), 117.9 (d, J = 3.0 Hz), 109.0 (d, J = 38 Hz), 88.6, 76.2 (d, J = 3.0 Hz), 43.1 (d, J = 3.0 Hz), 36.3, 35.7 ppm. HRMS (ESI+, m/z): calculated $[M+Na]^+$ $C_{29}H_{28}F_2N_6O_4Na$ as 585.2038, found as 585.2038.

***N*-(4-(2-((1-(dimethylamino)-7-fluoro-2-((2-fluoropyridin-4-yl)methyl)-3,9-dioxo-1,2,3,9-tetrahydroimidazo[5,1-*b*]quinazolin-8-yl)oxy)ethyl)phenyl)acetamide (28d)**

Following the procedure described for **28a**, compound **28d** was prepared from compound **14** and **5d**. The crude mixture was partially purified by column chromatography (50-80% EtOAc/hexane) to remove unreacted starting materials and easily separable byproducts before complete purification by preparative HPLC to obtain the title compound as a white solid (86 mg, 0.157 mmol, 73%). ^{1}H-NMR (600 MHz, $(CD_3)_2SO$): δ 9.97 (1H, s), 8.19 (1H, m), 7.80-7.76 (1H, m), 7.62-7.60 (1H, m), 7.43-7.41 (2H, m), 7.35-7.34 (1H, m), 7.22-7.21 (2H, m), 7.17 (1H, m), 6.33 (1H, s), 4.83 (1H, d, J = 18 Hz), 4.61 (1H, d, J = 18 Hz), 4.30-4.27 (2H, m), 4.25-4.21 (2H, m), 3.02 (2H, t, J = 6.0 Hz), 2.31 (6H, br), 2.02 (3H, s) ppm. ^{13}C-NMR (150 MHz, $(CD_3)_2SO$): δ 170.1, 164.1 (d, J = 234 Hz), 158.5, 157.6 (d, J = 4.5 Hz), 154.8 (d, J = 246 Hz), 152.3 (d, J = 9.0 Hz), 148.3 (d, J = 15 Hz), 146.8 (d, J = 1.5 Hz), 146.3 (d, J = 14 Hz), 145.2 (d, J = 1.5 Hz), 137.8, 134.0, 129.9, 125.5 (d, J = 7.5 Hz), 124.3 (d, J = 23 Hz), 121.9 (d, J = 3.0 Hz), 120.2, 117.8 (d, J = 1.5 Hz), 109.0 (d, J = 38 Hz), 88.6, 76.6 (d, J = 3.0 Hz), 43.1 (d, J = 3.0 Hz), 35.8, 24.4 ppm. HRMS (ESI+, m/z): calculated $[M+Na]^+$ $C_{28}H_{26}F_2N_6O_4Na$ as 571.1881, found as 571.1881.

***tert*-butyl (4-(2-((1-(dimethylamino)-7-fluoro-2-((2-fluoropyridin-4-yl)methyl)-3,9-dioxo-1,2,3,9-tetrahydroimidazo[5,1-b]quinazolin-8-yl)oxy)ethyl)phenyl)(methylsulfonyl)carbamate (28e)**

Following the procedure described for **28a**, compound **28e** was prepared from compound **17** and **5d**. The crude mixture was partially purified by column chromatography (0-5% MeOH/DCM) to remove unreacted starting materials and easily separable byproducts before complete purification by preparative HPLC to obtain the title compound as a white solid (56 mg, 0.0818 mmol, 51%). ^{1}H-NMR (600 MHz, $(CD_3)_2SO$): δ 8.26 (1H, m), 7.92-7.89 (1H, m), 7.72-7.70 (1H, m), 7.44-7.42 (3H, m), 7.28-7.26 (3H, m), 6.38 (1H, s), 4.94 (d, J = 18 Hz), 4.61 (1H, d, J = 18 Hz), 4.42-4.33 (2H, m), 3.55 (3H, s), 3.19 (2H, t, J = 6.0 Hz), 2.40 (6H, br), 1.44 (9H, s) ppm. ^{13}C-NMR (150 MHz, $(CD_3)_2SO$): δ 163.5 (d, J = 233 Hz), 157.6, 156.9 (d, J = 4.5 Hz), 154.0 (d, J = 245 Hz), 151.7 (d, J = 7.5 Hz), 150.9, 147.6 (d, J = 17 Hz), 146.4 (d, J = 1.5 Hz), 145.6 (d, J = 14 Hz), 144.7 (d, J = 3.0 Hz), 138.9, 134.0, 129.5, 129.4, 124.9, 123.4 (d, J = 21 Hz), 121.0 (3.0 Hz), 117.4 (d, J = 1.5 Hz), 108.1 (d, J = 38 Hz), 87.4, 83.9, 75.5 (d, J = 1.5 Hz), 41.6, 35.3, 30.4, 27.5 ppm. HRMS (ESI+, m/z): calculated $[M+Na]^+$ $C_{32}H_{34}F_2N_6O_7SNa$ as 707.2075, found as 707.2075.

4-(2-((1-(dimethylamino)-7-fluoro-2-((2-fluoropyridin-4-yl)methyl)-3,9-dioxo-1,2,3,9-tetrahydroimidazo[5,1-*b*]quinazolin-8-yl)oxy)ethyl)-*N*,*N*-dimethylbenzenesulfonamide (28f)

Following the procedure described for **28a**, compound **28f** was prepared from compound **18** and **5d**. The crude mixture was partially purified by column chromatography (50-70% EtOAc/hexane) to remove unreacted starting materials and easily separable byproducts before complete purification by preparative HPLC to obtain the title compound as a white solid (50 mg, 0.084 mmol, 52%). ^{1}H-NMR (600 MHz, $(CD_3)_2SO$): δ 8.26-8.25 (1H, m), 7.91-7.87 (1H, m), 7.71-7.69 (3H, m), 7.67-7.65 (2H, m), 7.42-7.41 (1H, m), 7.26 (1H, m), 6.36 (1H, s), 4.94 (1H, d, J = 18 Hz),

4.61 (1H, d, J = 18 Hz), 4.47-4.38 (2H, m), 3.26 (2H, t, J = 6.0 Hz), 2.62 (6H, s), 2.39 (6H, br) ppm. ^{13}C-NMR (150 MHz, $(CD_3)_2SO$): δ 163.5 (d, J = 234 Hz), 157.6, 156.8 (d, J = 3.0 Hz), 154.0 (d, J = 240 Hz), 151.7 (d, J = 7.5 Hz), 147.6 (d, J = 15 Hz), 146.4 (d, J = 1.5 Hz), 145.5 (d, J = 14 Hz), 144.7 (d, J = 1.5 Hz), 144.0, 132.6, 129.9, 127.5, 125.0 (d, J = 7.5 Hz), 123.4 (d, J = 21 Hz), 121.0 (d, J = 4.5 Hz), 117.3 (d, J = 1.5 Hz), 108.1 (d, J = 38 Hz), 87.4, 75.1 (d, J = 3.0 Hz), 42.1 (d, J = 3.0 Hz), 37.6, 35.6 ppm. HRMS (ESI+, m/z): calculated $[M+Na]^+$ $C_{28}H_{28}F_2N_6O_5SNa$ as 621.1708, found as 621.1708.

8-(4-(((*tert*-butyldimethylsilyl)oxy)methyl)phenethoxy)-1-(dimethylamino)-7-fluoro-2-((2-fluoropyridin-4-yl)methyl)-1,2-dihydroimidazo[5,1-*b*]quinazoline-3,9-dione (28g)

Following the procedure described for **28a**, compound **28g** was prepared from compound **20** and **5d**. The crude mixture was partially purified by column chromatography (50-100% EtOAc/hexane) to remove unreacted starting materials and easily separable byproducts before complete purification by preparative HPLC to obtain the title compound as a white solid (40 mg, 0.063 mmol, 39%). ^{1}H-NMR (600 MHz, $(CD_3)_2SO$): δ 8.26-8.25 (1H, m), 7.92-7.89 (1H, m), 7.71-7.69 (1H, m), 7.42-7.41 (1H, m), 7.33-7.32 (2H, m), 7.26-7.25 (2H, m), 6.37 (1H, s), 4.94 (1H, d, J = 18 Hz), 4.70 (2 H, s), 4.61 (1H, d, J = 18 Hz), 4.38-4.29 (2H, m), 3.14 (2H, t, J = 6.0 Hz), 2.39 (6H, br), 0.93 (9H, s), 0.10 (6H, s) ppm. ^{13}C-NMR (150 MHz, $(CD_3)_2SO$): δ 163.5 (d, J = 234 Hz), 157.6, 156.8 (d, J = 4.5 Hz), 154.0 (d, J = 246 Hz), 151.7 (d, J = 7.5 Hz), 147.6 (d, J = 15 Hz), 146.4 (d, J = 1.5 Hz), 145.6 (d, J = 14 Hz), 144.7 (d, J = 1.5 Hz), 139.1, 136.5, 128.7, 126.1, 124.8 (d, J = 6.0 Hz), 123.4 (d, J = 23 Hz), 121.0 (d, J = 3.0 Hz), 117.3 (d, J = 1.5 Hz), 108.1 (d, J = 38 Hz), 87.4, 75.8 (d, J = 1.5 Hz), 64.1, 42.0 (d, J = 3.0 Hz), 35.5, 25.8, 18.0, -5.3 ppm. HRMS (ESI+, m/z): calculated $[M+Na]^+$ $C_{33}H_{39}F_2N_5O_4SiNa$ as 658.2637, found as 658.2637.

5-(4-carbamoylphenethoxy)-6-fluoro-*N*-((2-fluoropyridin-4-yl)methyl)-4-oxo-3,4-dihydroquinazoline-2-carboxamide (29a)

To compound **28a** (51 mg, 0.0954 mmol, 1 equiv.) was added 6 M HCl (0.64 mL) and glacial acetic acid (0.64 mL). The mixture was heated at 40 °C for 4 h with careful monitoring by UPLC-MS. The mixture was diluted with 3:1 $CHCl_3$:IPA and extracted with water. The combined organics were washed with brine, dried over Na_2SO_4, filtered, and concentrated under reduced pressure. The crude mixture was purified by preparative HPLC to obtain the title compound as a white solid (21 mg, 0.044 mmol, 46%). ^{1}H-NMR (600 MHz, $(CD_3)_2SO$): δ 12.17 (1H, br), 9.71 (1H, t, J = 6.0 Hz), 8.22 (1H, m), 7.97 (1H, br), 7.84-7.81 (3H, m), 7.61-7.59 (1H, m), 7.45-7.43 (2H, m), 7.34-7.31 (2H, m), 7.13 (1H, s), 4.59 (2H, d, J = 6.0 Hz), 4.34 (2H, t, J = 6.0 Hz), 3.18 (2H, t, J = 6.0 Hz) ppm. ^{13}C-NMR (150 MHz, $(CD_3)_2SO$): δ 168.1, 163.5 (d, J = 234 Hz), 160.1, 159.1, 154.0 (d, J = 245 Hz), 154.7 (d, J = 7.5 Hz), 147.7 (d, J = 15 Hz), 145.5, 145.4 (d, J = 14 Hz), 145.2, 141.9, 132.3, 129.0, 127.7, 124.5, 123.3 (d, J = 21 Hz), 120.7 (d, J = 3 Hz), 118.4, 107.7 (d, J = 38 Hz), 75.5, 41.8 (d, J = 3.0 Hz), 35.7 ppm. HRMS (ESI+, m/z): calculated $[M+Na]^+$ $C_{24}H_{19}F_2N_5O_4Na$ as 502.1303, found as 502.1303.

6-fluoro-*N*-((2-fluoropyridin-4-yl)methyl)-5-(4-(methylcarbamoyl)phenethoxy)-4-oxo-3,4-dihydroquinazoline-2-carboxamide (29b)

Following the procedure described for **29a**, compound **29b** was prepared from compound **28b**. The crude mixture purified by preparative HPLC to obtain the title compound as a white solid (14 mg, 0.028 mmol, 36%). ^{1}H-NMR (600 MHz, $(CD_3)_2SO$): δ 12.17 (1H, br), 9.71 (1H, t, J = 6.0 Hz), 8.43-8.40 (1H, m), 8.22-8.21 (1H, m), 7.83-7.8 (1H, m), 7.79-7.78 (2H, m), 7.60-7.58 (1H, m), 7.45-7.43 (2H, m), 7.34-7.33 (1H, m), 7.13 (1H, m), 4.59 (2H, d, J = 6.0 Hz), 4.34 (2H, t, J = 6.0 Hz), 3.18 (2H, t, J = 6.0 Hz), 2.81 (3H, d, J = 6.0 Hz) ppm. ^{13}C-NMR (150 MHz, $(CD_3)_2SO$): δ

164.3, 163.5 (d, J = 235 Hz), 160.2, 159.3, 154.7 (d, J = 7.5 Hz), 153.9 (d, J = 245 Hz), 147.7 (d, J = 15 Hz), 145.4, 145.3 (d, J = 14 Hz), 145.2, 141.7, 132.6, 129.0, 127.2, 124.4, 123.3 (d, J = 23 Hz), 120.7 (d, J = 4.5 Hz), 118.3, 107.7 (d, J = 38 Hz), 75.5 (d, J = 3.0 Hz), 41.8 (d, J = 3.0 Hz), 35.7, 26.4 ppm. HRMS (ESI+, m/z): calculated $[M+Na]^+$ $C_{25}H_{21}F_2N_5O_4Na$ as 516.1459, found as 516.1459.

5-(4-(dimethylcarbamoyl)phenethoxy)-6-fluoro-*N*-((2-fluoropyridin-4-yl)methyl)-4-oxo-3,4-dihydroquinazoline-2-carboxamide (29c)

Following the procedure described for **29a**, compound **29c** was prepared from compound **28c**. The crude mixture purified by preparative HPLC to obtain the title compound as a white solid (20 mg, 0.039 mmol, 40%). ^{1}H-NMR (600 MHz, $(CD_3)_2SO$): δ 12.18 (1H, br), 9.71 (1H, t, J = 6.0 Hz), 8.22-8.21 (1H, m), 7.83-7.80 (1H, m), 7.60-7.58 (1H, m), 7.42-7.41 (2H, m), 7.35-7.33 (3H, m), 7.13 (1H, m), 4.59 (2H, d, J = 6.0 Hz), 4.35 (2H, t, J = 6.0 Hz), 3.17 (2H, t, J = 6.0 Hz), 2.99-2.93 (6H, m) ppm. ^{13}C-NMR (150 MHz, $(CD_3)_2SO$): δ 170.4, 163.5 (d, J = 233 Hz), 160.1, 159.1, 154.7 (d, J = 7.5 Hz), 153.9 (d, J = 245 Hz), 147.7 (d, J = 15 Hz), 145.5, 145.4 (d, J = 14 Hz), 145.2, 139.8, 134.5, 128.9, 127.1, 124.5, 123.3 (d, J = 21 Hz), 120.7 (d, J = 4.5 Hz), 118.3, 107.7 (d, J = 38 Hz), 75.6 (d, J = 3.0 Hz), 41.8 (d, J = 3.0 Hz), 35.7, 34.9 ppm. HRMS (ESI+, m/z): calculated $[M+Na]^+$ $C_{26}H_{23}F_2N_5O_4Na$ as 530.1616, found as 530.1616.

5-(4-acetamidophenethoxy)-6-fluoro-*N*-((2-fluoropyridin-4-yl)methyl)-4-oxo-3,4-dihydroquinazoline-2-carboxamide (29d)

Following the procedure described for **29a**, compound **29d** was prepared from compound **28d**. The crude mixture purified by preparative HPLC to obtain the title compound as a white solid (30 mg, 0.061 mmol, 41%).^{1}H-NMR (600 MHz, $(CD_3)_2SO$): δ 9.98 (1H, s), 9.74 (1H, t, J = 6.0 Hz), 8.17 (1H, m), 7.78-7.75 (1H, m), 7.62-7.6 (1H, m), 7.44-7.42 (2H, m), 7.30 (1H, m), 7.25-7.23

(2H, m), 7.08 (1H, s), 4.57 (2H, d, J = 6.0 Hz), 4.26 (2H, t, J = 6.0 Hz), 3.03 (2H, t, J = 6.0 Hz), 2.03 (3H, s) ppm. ^{13}C-NMR (150 MHz, $(CD_3)_2SO$): δ 170.2, 164.1 (d, J = 234 Hz), 160.8, 160.0, 155.2 (d, J = 7.5 Hz), 154.7 (d, J = 246 Hz), 148.2 (d, J = 15 Hz), 146.0 (d, J = 14 Hz), 145.3, 145.2, 137.7, 134.1, 130.0, 125.4, 124.2 (d, J = 21 Hz), 121.3 (d, J = 4.5 Hz), 120.3, 118.6, 108.3 (d, J = 38 Hz), 76.6, 42.4, 35.9, 24.4 ppm. HRMS (ESI+, m/z): calculated $[M+Na]^+$ $C_{18}H_{15}F_2N_5O_3Na$ as 516.1459, found as 516.1459.

6-fluoro-*N*-((2-fluoropyridin-4-yl)methyl)-5-(4-(methylsulfonamido)phenethoxy)-4-oxo-3,4-dihydroquinazoline-2-carboxamide (29e)

Following the procedure described for **29a**, compound **29e** was prepared from compound **28e**. The crude mixture purified by preparative HPLC to obtain the title compound as a white solid (16 mg, 0.023 mmol, 41%). ^{1}H-NMR (600 MHz, $(CD_3)_2SO$): δ 12.19 (1H, br), 9.69 (1H, t, J = 6.0 Hz), 9.64 (1H, br), 8.23-8.22 (1H, m), 7.86-7.82 (1H, m), 7.59-7.57 (1H, m), 7.35-7.34 (1H, m), 7.33-7.31 (2H, m), 7.18-7.16 (2H, m), 7.14 (1H, m), 4.59 (2H, d, J = 6.0 Hz), 4.30 (2H, t, J = 6.0 Hz), 3.10 (2H, t, J = 6.0 Hz), 2.97 (3H, s) ppm. ^{13}C-NMR (150 MHz, $(CD_3)_2SO$): δ 163.4 (d, J = 233 Hz), 159.9, 158.8 (d, J = 3.0 Hz), 154.6 (d, J = 9.0 Hz) 153.8 (d, J = 243 Hz), 147.5 (d, J = 15 Hz), 145.4 (d, J = 14 Hz), 145.3, 145.0 (d, J = 3.0 Hz), 136.5, 133.7, 129.7, 124.2 (d, J = 7.5 Hz), 123.1 (d, J = 21 Hz), 120.6 (d, J = 3.0 Hz), 120.1, 118.3, 107.5 (d, J = 38 Hz), 75.7 (d, J = 3.0 Hz), 46.5 (d, J = 3.0 Hz), 35.1, 30.4 ppm. HRMS (ESI+, m/z): calculated $[M+Na]^+$ $C_{24}H_{21}F_2N_5O_5SNa$ as 552.1129, found as 552.1129.

5-(4-(*N*,*N*-dimethylsulfamoyl)phenethoxy)-6-fluoro-*N*-((2-fluoropyridin-4-yl)methyl)-4-oxo-3,4-dihydroquinazoline-2-carboxamide (29f)

Following the procedure described for **29a**, compound **29f** was prepared from compound **28f**. The crude mixture purified by preparative HPLC to obtain the title compound as a white solid (17 mg,

0.0316 mmol, 42%). ^{1}H-NMR (600 MHz, $(CD_3)_2SO$): δ 12.22 (1H, br), 9.69 (1H, t, J = 6.0 Hz), 8.23-8.22 (1H, m), 7.83-7.80 (1H, m), 7.71-7.70 (2H, m), 7.66-7.65 (2H, m), 7.59-7.56 (1H, m), 7.35-7.34 (1H, m), 7.14 (1H, m), 4.59 (2H, d, J = 6.0 Hz), 4.40 (2H, t, J = 6.0 Hz), 3.26 (2H, t, J = 6.0 Hz), 2.62 (6H, s) ppm. ^{13}C-NMR (150 MHz, $(CD_3)_2SO$): δ 163.4 (d, J = 233 Hz), 160.0, 159.1, 154.6 (d, J = 7.5 Hz), 153.7 (d, J = 245 Hz), 147.5 (d, J = 15 Hz), 145.4, 145.3, 145.2 (d, J = 14 Hz), 144.1, 132.5, 129.8, 127.5, 124.3 (d, J = 7.5 Hz), 123.1 (d, J = 21 Hz), 120.6 (d, J = 4.5 Hz), 118.2, 107.5 (d, J = 38 Hz), 75.0 (d, J = 1.5 Hz), 41.6 (d, J = 3.0 Hz), 37.6, 35.6 ppm. HRMS (ESI+, m/z): calculated $[M+Na]^+$ $C_{25}H_{23}F_2N_5O_5SNa$ as 566.1286, found as 566.1285.

6-fluoro-*N*-((2-fluoropyridin-4-yl)methyl)-5-(4-(hydroxymethyl)phenethoxy)-4-oxo-3,4-dihydroquinazoline-2-carboxamide (29g)

Following the procedure described for **29a**, compound **29g** was prepared from compound **28g**. The crude mixture purified by preparative HPLC to obtain the title compound as a white solid (5 mg, 0.011 mmol, 19%). ^{1}H-NMR (600 MHz, $(CD_3)_2SO$): δ 12.18 (1H, br), 9.69 (1H, t, J = 6.0 Hz), 8.23-8.22 (1H, m), 7.86-7.83 (1H, m), 7.60-7.57 (1H, m), 7.37-7.33 (1H, m), 7.31-7.30 (2H, m), 7.28-7.26 (2H, m), 7.14 (1H, m), 5.15 (1H, t, J = 6.0 Hz), 4.59 (2H, d, J = 6.0 Hz), 4.50 (2H, d, J = 6.0 Hz), 4.30 (2H, t, J = 6.0 Hz), 3.13 (2H, t, J = 6.0 Hz) ppm. ^{13}C-NMR (150 MHz, $(CD_3)_2SO$): δ 163.4 (d, J = 233 Hz), 160.0, 158.8 (d, J = 3.0 Hz), 154.5 (d, J = 7.5 Hz), 153.8 (d, J = 245 Hz), 147.5 (d, J = 15 Hz), 145.4 (d, J = 14 Hz), 145.3 (d, J = 1.5 Hz), 145.1 (d, J = 1.5 Hz), 140.3, 136.2, 128.6, 126.5, 124.2 (d, J = 7.5 Hz), 123.1 (d, J = 23 Hz), 120.6 (d, J = 3.0 Hz), 118.3 (d, J = 1.5 Hz), 107.5 (d, J = 38 Hz), 75.8 (d, J = 1.5 Hz), 62.7, 41.6 (d, J = 3.0 Hz), 35.5 ppm. HRMS (ESI+, m/z): calculated $[M+Na]^+$ $C_{24}H_{20}F_2N_4O_4Na$ as 489.1350, found as 489.1350.

4-(2-hydroxyethyl)-*N*-methylbenzenesulfonamide (30)

To a solution of 2-(4-(*N*-methylsulfamoyl)phenyl)acetic acid (250 mg, 1.09 mmol, 1.0 equiv.) in THF (2.18 mL) was added 1 M lithium aluminum hydride in THF (2.18 mL, 2.18 mmol, 2.0 equiv.) at 0 °C. The mixture was stirred at room temperature for 1 h, quenched slowly with methanol, and concentrated under reduced pressure. The crude mixture was purified by column chromatography (0-20% EtOAc/hexane) to obtain the title compound as a colorless oil (130 mg, 0.60 mmol, 55%).^{1}H-NMR (600 MHz, $(CD_3)_2SO$): δ 7.72-7.70 (2H, m), 7.49-7.47 (2H, m), 7.40 (1H, q, J = 6.0 Hz), 4.74 (1H, t, J = 6.0 Hz), 3.70-3.67 (2H, m), 2.84 (2H, m), 2.44 (3H, d, J = 6.0 Hz) ppm. ^{13}C-NMR (150 MHz, $(CD_3)_2SO$): δ 144.7, 136.9, 129.7, 126.5, 61.5, 38.6, 28.7 ppm. HRMS (EI+, m/z): calculated $[M]^+$ $C_9H_{13}NO_3S$ as 215.0616, found as 215.0618.

4-(2-((1-(dimethylamino)-7-fluoro-2-((2-fluoropyridin-4-yl)methyl)-3,9-dioxo-1,2,3,9-tetrahydroimidazo[5,1-*b*]quinazolin-8-yl)oxy)ethyl)-*N*-methylbenzenesulfonamide (31)

Following the procedure described for **28a**, compound **31** was prepared from compound **30** and **5d**. The crude mixture was partially purified by column chromatography (0-50% EtOAc/DCM) to remove unreacted starting materials and easily separable byproducts before complete purification by preparative HPLC to obtain the title compound as a white solid (308 mg, 0.53 mmol, 67%). ^{1}H-NMR (600 MHz, $(CD_3)_2SO$): δ 8.26-8.25 (1H, m), 7.91-7.88 (1H, m), 7.74-7.73 (2H, m), 7.71-7.69 (1H, m), 7.62-7.61 (2H, m), 7.42-7.40 (2H, m), 7.26 (1H, m), 6.36 (1H, s), 4.94 (1H, d, J = 18 Hz), 4.61 (1H, d, J = 18 Hz), 4.45-4.36 (2H, m), 3.24 (2H, t, J = 6.0 Hz), 2.43 (3H, d, J = 6.0 Hz), 2.39 (6H, br) ppm. ^{13}C-NMR (150 MHz, $(CD_3)_2SO$): δ 163.5 (d, J = 233 Hz), 157.6, 156.9 (d, J = 3.0 Hz), 154.0 (d, J = 245 Hz), 151.7 (d, J = 7.5 Hz), 147.6 (d, J = 15 Hz), 146.4 (d, J = 1.5 Hz), 145.5 (d, J = 14 Hz), 144.7, 143.2, 137.2, 129.7, 126.6, 125.0 (d, J = 7.5 Hz), 123.4 (d, J = 23 Hz), 121.0 (d, J = 4.5 Hz), 117.3 (d, J = 3.0 Hz), 108.1 (d, J = 38 Hz), 87.5, 75.1 (d, J = 1.5 Hz),

42.1 (d, J = 3.0 Hz), 35.6, 28.7 ppm. HRMS (ESI+, m/z): calculated $[M+Na]^+$ $C_{27}H_{26}F_2N_6O_5SNa$ as 607.1551, found as 607.1551.

6-fluoro-*N*-((2-fluoropyridin-4-yl)methyl)-5-(4-(*N*-methylsulfamoyl)phenethoxy)-4-oxo-3,4-dihydroquinazoline-2-carboxamide (32)

Following the procedure described for **29a**, compound **32** was prepared from compound **31**. The crude mixture purified by preparative HPLC to obtain the title compound as a white solid (109 mg, 0.205 mmol, 40%). ^{1}H-NMR (600 MHz, $(CD_3)_2SO$): δ 12.18 (1H, br), 9.68 (1H, t, J = 6.0 Hz), 8.23-8.22 (1H, m), 7.83-7.80 (1H, m), 7.74-7.73 (2H, m), 7.62-7.61 (2H, m), 7.59-7.56 (1H, m), 7.43-7.40 (1H, m), 7.35-7.34 (1H, m), 7.14 (1H, m), 4.59 (2H, d, J = 6.0 Hz), 4.38 (2H, t, J = 6.0 Hz), 3.23 (2H, t, J = 6.0 Hz), 2.44 (3H, d, J = 6.0 Hz) ppm. ^{13}C-NMR (150 MHz, $(CD_3)_2SO$): δ 163.6 (d, J = 233 Hz), 160.2, 159.4, 154.6 (d, J = 7.5 Hz), 153.6 (d, J = 245 Hz), 147.5 (d, J = 17 Hz), 145.6, 145.4, 145.2 (d, J = 12 Hz), 143.3, 137.2, 129.8, 126.6, 124.1, 123.0 (d, J = 21 Hz), 120.6 (d, J = 4.5 Hz), 118.2, 107.5 (d, J = 38 Hz), 75.0 (d, J = 1.5 Hz), 41.6 (d, J = 3.0 Hz), 35.6, 28.7 ppm. HRMS (ESI+, m/z): calculated $[M+Na]^+$ $C_{24}H_{21}F_2N_5O_5SNa$ as 552.1129, found as 552.1129.

4.7.3 MMP Enzyme Inhibition Assay

Inhibitor potency against human recombinant MMP-1,-2,-8,-9,-10, and -13 (R&D Systems) was measured as previously described.[29] Final concentrations of the enzyme and substrate were 2 nM and 5 μM, respectively. Changes in fluorescence were monitored using a BioTek Synergy H1 multimode microplate reader with excitation and emission wavelengths of 320 and 405 nm, respectively. The half-maximal inhibitory concentration (IC_{50}) values were calculated by nonlinear regression analysis using GraphPad Prism software.

4.7.4 Molecular Docking

Docking was performed with Molecular Operating Environment (MOE) software. Human MMP-13 was prepared with MOE QuickPrep prior to docking of inhibitors **29a-g**, **6**, and 5b. 75 binding poses were sampled for each inhibitor within the MMP-13 binding pocket under the rigid docking model. Poses were scored using the Generalized-Born Volume Integral/ Weighted Surface Area (GBVI/WSA) dG force-field function and the top results (lowest S value, kcal·mol^{-1}) were visually inspected to ensure sensible binding. 2-dimensional ligand interaction maps were extracted for visual interpretation of the optimized binding pose.

4.7.5 Radiochemistry

Automated Radiosynthesis of ***[^{11}C]29f*** - A fully automated sequence including the generation of [^{11}C]CH_3OTf and radiolabeling were performed on a GE TRACERlab FXC Pro module. [^{11}C]CO_2 was prepared on a Siemens CTI Eclipse HP/RD Hybrid Cyclotron (11 MeV) via the $^{14}N(p,\alpha)^{11}C$ nuclear reaction. [^{11}C]CO_2 (20-27 GBq) was transferred from the target, delivered into the module, and trapped on a steel coil at room temperature. The trap was then heated to release [^{11}C]CO_2 with H_2 gas flow (70 mL·min^{-1}) and reduced using a nickel catalyst (99.999% purity, C < 100 ppm) at 380 °C. The generated [^{11}C]CH_4 was trapped on a Carbopack™ column (60-80 mesh) at -90 °C. The trap was then heated to 90 °C, [^{11}C]CH_4 was released by He gas flow (100 mL·min^{-1}), directed over iodine at 100 °C (>99.8% purity, EMSURE®) and heated in a high temperature oven at 720 °C. The generated [^{11}C]CH_3I was trapped on a Porapak™ Q column (50-80 mesh), while unreacted [^{11}C]CH_4 was re-circulated in a closed system with a gas pump. When conversion was complete, [^{11}C]CH_3I was released at 190 °C and passed over a AgOTf column (>99.95% purity, trace metals basis) at 190 °C with He gas flow (15 mL·min^{-1}). [^{11}C]CH_3OTf was directly bubbled into the reactor (15 mL·min^{-1}) containing precursor (10 mM)

and TBAOH (3.77 μL, 2 equiv.) dissolved in anhydrous DMSO (185 μL). The reactor was then heated at 80 °C for 1 min, immediately cooled to 30 °C, and quenched with 50/50 ACN / water (500 μL). The crude mixture was purified with a Phenomenex Synergi Hydro-RP column (C18, 80Å, 10 μm, 250 mm × 10 mm), mobile phase: 50/50 0.1 M ammonium formate / ACN (isocratic), flowrate: 5 mL·min^{-1}. The product fraction (retention time: ~8 min) was collected into a bulk vessel containing water (25 mL). The contents of the flask were transferred over a Waters Sep-Pak Plus Short C18 cartridge (preconditioned with 1 mL EtOH, 5 mL water, and 1 mL air) and subsequently washed with water (10 mL). The product was eluted with EtOH (0.5 mL) and diluted with saline (4.5 mL, 0.9%).

[^{11}C]29f *Quality Control.* Radiochemical purity and identity were confirmed by analytical radio-HPLC using a Phenomenex Luna C18 column (100 Å, 5 μm, 250 mm × 4.6 mm), a 996 Photodiode Array Detector (PerkinElmer), and a Carroll & Ramsey Associates 105-S high-sensitivity radiation detector. HPLC solvent A: 0.1 M ammonium formate, HPLC solvent B: ACN, flowrate: 1 mL·min^{-1}. Method: 0-2 min 30% B, 2-10 min 30-90% B, 10-12 min 90% B, 12-13 min 90-30% B, 13-15 min 30% B, retention time: 10 min. Molar activity was determined by measuring the UV absorbance of a known amount of radioactivity under identical HPLC conditions used to generate a calibration curve for the corresponding non-radioactive standard. The ratio of radioactivity (GBq) to moles (μmol) provided the molar activity (GBq·μmol^{-1}), which was decay corrected to the end of synthesis (EoS).

4.7.6 Formulation Stability

Radiotracer stability in 10% EtOH/saline (0.9%) was assessed as previously described.[29] See the analytical radio-HPLC method outlined in the quality control section. Radiochemical purity was >99% for **[^{11}C]29f** immediately following reformulation.

4.7.7 Distribution Coefficient (LogD)

Radiotracer lipophilicity (logD, 1-octanol - 1× PBS, pH 7.4) was determined as previously described.[29,40] Data represent the mean ± standard error of two independent experiments performed in quadruplicate.

4.7.8 Animal Model

Male *ApoE*$^{-/-}$ (strain no. 002052) mice were obtained from Jackson Laboratory and housed in groups of 4. Mice were fed a western atherogenic diet (TD.88137, Envigo) beginning at 8 weeks of age for a total of 24-30 weeks. Animals were monitored periodically and housed in environmentally enriched cages with free access to food and water. All housing, handling, and experimental procedures were in strict accordance with the guidelines of Canadian Council on Animal Care and with approval of the University of Ottawa Animal Care Committee.

4.7.9 PET/CT Imaging

ApoE$^{-/-}$ mice (41 ± 2 g, n = 4) were anesthetized with 2% isoflurane, positioned in the PET scanner, and maintained under anesthesia during the imaging protocol. Animals were intravenously injected with **[^{11}C]29f** (20 ± 1 MBq, 100-200 μL) as a bolus over 30 sec via the lateral tail vein. The whole body was imaged for 60 min (4 × 15 sec frames; 4 × 1 min frames; 10 × 5 min frames). PET/CT Imaging was performed using a Bruker Si78 scanner. Emission data were reconstructed using the using 3D maximum-likelihood expectation-maximization (3D-

MLEM) algorithm. Uptake values were quantified using PMOD software and expressed as the percentage of injected dose per cubic centimeter (%ID·cc^{-1}) over time.

4.7.10 Biodistribution

ApoE$^{-/-}$ mice (39 ± 2 g, *n* = 4-5 per group) were anesthetized with 2% isoflurane and intravenously injected with **[^{11}C]29f** (52 ± 4 MBq, 100-200 μL) as a bolus over 30 sec via the lateral tail vein. For blocking experiments, WAY170523 (7.5 mg/kg, 3.5 mg/mL, 10% DMSO, 40% PEG400, 50% sterile water), was intravenously administered 10 min prior to the radiotracer. Mice were maintained on isoflurane for 30 min and sacrificed by myocardial perfusion following blood collection by cardiac puncture as previously described.[29] Organs of interest were harvested, weighed, and counted for radioactivity using a Hidex Automatic Gamma Counter (energy window: 480−558 keV). Uptake values are expressed as the percentage injected dose per gram tissue (%ID·g^{-1}).

4.7.11 Plasma Radio-Metabolite Analysis

Pooled plasma samples were processed and analyzed as previously described.[29] See the analytical radio-HPLC method outlined in the quality control section. Polar radio-metabolites were defined by the radioactivity collected before the parent fraction, identified by co-injection of non-radioactive **29f**. Values represent the percentage of total plasma radioactivity (%).

4.7.12 Autoradiography and Oil Red O Staining

Aortic samples were harvested and exposed to a super-resolution GE Storage Phosphor Screen (BAS-IP SR 2025 E) for 3 hours. The screen was scanned with a Cyclone Plus Storage Phosphor System and quantified using OptiQuant software as previously described.[29] Uptake values are expressed as the percentage injected dose per square millimeter (%ID·mm^{-2}). ORO

staining was performed as previously described.[55] Bright-field images were acquired using a Krüss Stereomicroscope (MSL4000-series) adapted with a smartphone camera.

4.7.13 Statistical Analysis

Statistical analysis was performed using GraphPad Prism. Data are presented as mean ± standard error. Groups were compared using an unpaired t-test. Significance was set at the 0.05 level.

4.7.14 Manuscript Information

Author Contributions

A.B. and B.H.R. designed the project. A.B. directed research, performed experiments, analyzed data, and wrote the manuscript. All other authors performed experiments. All authors approved of the manuscript.

Notes

The authors declare no competing financial interest.

Acknowledgments

The authors thank Christian Umeobika of the University of Ottawa Heart Institute (UOHI) PET Radiochemistry Laboratory, and all staff from the Biomedical Engineering, and Animal Care and Veterinary Services for cyclotron, PET scanner, and animal care support. Support for this work was provided by CIHR (PJT 148968), CFI (JELF 36848 & 39358), and the Ontario Ministry for Research, Innovation and Science (ER17-13-119). A.B. was supported by CIHR CGSD, M.A. was supported by NSERC USRA, B.A.M. was supported by NSERC PGSD, C.B. was supported by NSERC USRA, M.M. was supported by CIHR (MFE-186357).

Abbreviations used

AM, molar activity; ARG, autoradiography; DIAD, diisopropyl azodicarboxylate; %ID, percentage of injected dose; OAT, organic anion transporter; ORO, Oil Red O; Piv, pivaloyl; PTSA, *p*-toluenesulfonic acid; QMA, quaternary methyl ammonium; RCY, radiochemical yield; ROI, region of interest; SAR, structure activity relationship; SEM, standard error of the mean; SNAr, nucleophilic aromatic substitution; TBAOH, tetrabutylammonium hydroxide; TBS, *tert*-butyldimethylsilyl; TEAB, tetraethylammonium bicarbonate; THP, tetrahydropyran.

4.8 References

(1) Nagase, H.; Visse, R.; Murphy, G. Structure and Function of Matrix Metalloproteinases and TIMPs. *Cardiovasc. Res.* **2006**, *69* (3), 562–573. https://doi.org/10.1016/j.cardiores.2005.12.002.

(2) Loffek, S.; Schilling, O.; Franzke, C.-W. Biological Role of Matrix Metalloproteinases: A Critical Balance. *Eur. Respir. J.* **2011**, *38* (1), 191–208. https://doi.org/10.1183/09031936.00146510.

(3) Laronha, H.; Caldeira, J. Structure and Function of Human Matrix Metalloproteinases. *Cells* **2020**, *9* (5), 1076. https://doi.org/10.3390/cells9051076.

(4) Mitchell, P. G.; Magna, H. A.; Reeves, L. M.; Lopresti-Morrow, L. L.; Yocum, S. A.; Rosner, P. J.; Geoghegan, K. F.; Hambor, J. E. Cloning, Expression, and Type II Collagenolytic Activity of Matrix Metalloproteinase-13 from Human Osteoarthritic Cartilage. *J. Clin. Invest.* **1996**, *97* (3), 761–768. https://doi.org/10.1172/JCI118475.

(5) Alcaide-Ruggiero, L.; Molina-Hernández, V.; Granados, M. M.; Domínguez, J. M. Main and Minor Types of Collagens in the Articular Cartilage: The Role of Collagens in Repair Tissue Evaluation in Chondral Defects. *Int. J. Mol. Sci.* **2021**, *22* (24), 13329. https://doi.org/10.3390/ijms222413329.

(6) Xu, J.; Shi, G.-P. Vascular Wall Extracellular Matrix Proteins and Vascular Diseases. *Biochim. Biophys. Acta* **2014**, *1842* (11), 2106–2119. https://doi.org/10.1016/j.bbadis.2014.07.008.

(7) Sukhova, G. K.; Schönbeck, U.; Rabkin, E.; Schoen, F. J.; Poole, A. R.; Billinghurst, R. C.; Libby, P. Evidence for Increased Collagenolysis by Interstitial Collagenases-1 and -3

in Vulnerable Human Atheromatous Plaques. *Circulation* **1999**, *99* (19), 2503–2509. https://doi.org/10.1161/01.CIR.99.19.2503.

(8) Deguchi, J.-O.; Aikawa, E.; Libby, P.; Vachon, J. R.; Inada, M.; Krane, S. M.; Whittaker, P.; Aikawa, M. Matrix Metalloproteinase-13/Collagenase-3 Deletion Promotes Collagen Accumulation and Organization in Mouse Atherosclerotic Plaques. *Circulation* **2005**, *112* (17), 2708–2715. https://doi.org/10.1161/CIRCULATIONAHA.105.562041.

(9) Quillard, T.; Tesmenitsky, Y.; Croce, K.; Travers, R.; Shvartz, E.; Koskinas, K. C.; Sukhova, G. K.; Aikawa, E.; Aikawa, M.; Libby, P. Selective Inhibition of Matrix Metalloproteinase-13 Increases Collagen Content of Established Mouse Atherosclerosis. *Arterioscler. Thromb. Vasc. Biol.* **2011**, *31* (11), 2464–2472. https://doi.org/10.1161/ATVBAHA.111.231563.

(10) Quillard, T.; Araújo, H. A.; Franck, G.; Tesmenitsky, Y.; Libby, P. Matrix Metalloproteinase-13 Predominates Over Matrix Metalloproteinase-8 as the Functional Interstitial Collagenase in Mouse Atheromata. *Arterioscler. Thromb. Vasc. Biol.* **2014**, *34* (6), 1179–1186. https://doi.org/10.1161/ATVBAHA.114.303326.

(11) Virmani, R.; Kolodgie, F. D.; Burke, A. P.; Farb, A.; Schwartz, S. M. Lessons from Sudden Coronary Death: A Comprehensive Morphological Classification Scheme for Atherosclerotic Lesions. *Arterioscler. Thromb. Vasc. Biol.* **2000**, *20* (5), 1262–1275. https://doi.org/10.1161/01.atv.20.5.1262.

(12) Virmani, R.; Burke, A. P.; Farb, A.; Kolodgie, F. D. Pathology of the Vulnerable Plaque. *J. Am. Coll. Cardiol.* **2006**, *47* (8 Suppl), C13-18. https://doi.org/10.1016/j.jacc.2005.10.065.

(13) Finn, A. V.; Nakano, M.; Narula, J.; Kolodgie, F. D.; Virmani, R. Concept of Vulnerable/Unstable Plaque. *Arterioscler. Thromb. Vasc. Biol.* **2010**, *30* (7), 1282–1292. https://doi.org/10.1161/ATVBAHA.108.179739.

(14) Bentzon, J. F.; Otsuka, F.; Virmani, R.; Falk, E. Mechanisms of Plaque Formation and Rupture. *Circ. Res.* **2014**, *114* (12), 1852–1866. https://doi.org/10.1161/CIRCRESAHA.114.302721.

(15) Chen, J. M.; Nelson, F. C.; Levin, J. I.; Mobilio, D.; Moy, F. J.; Nilakantan, R.; Zask, A.; Powers, R. Structure-Based Design of a Novel, Potent, and Selective Inhibitor for MMP-13 Utilizing NMR Spectroscopy and Computer-Aided Molecular Design. *J. Am. Chem. Soc.* **2000**, *122* (40), 9648–9654. https://doi.org/10.1021/ja001547g.

(16) Engel, C. K.; Pirard, B.; Schimanski, S.; Kirsch, R.; Habermann, J.; Klingler, O.; Schlotte, V.; Weithmann, K. U.; Wendt, K. U. Structural Basis for the Highly Selective Inhibition of MMP-13. *Chem. Biol.* **2005**, *12* (2), 181–189. https://doi.org/10.1016/j.chembiol.2004.11.014.

(17) Baragi, V. M.; Becher, G.; Bendele, A. M.; Biesinger, R.; Bluhm, H.; Boer, J.; Deng, H.; Dodd, R.; Essers, M.; Feuerstein, T.; Gallagher, B. M.; Gege, C.; Hochgürtel, M.; Hofmann, M.; Jaworski, A.; Jin, L.; Kiely, A.; Korniski, B.; Kroth, H.; Nix, D.; Nolte, B.; Piecha, D.; Powers, T. S.; Richter, F.; Schneider, M.; Steeneck, C.; Sucholeiki, I.; Taveras, A.; Timmermann, A.; Van Veldhuizen, J.; Weik, J.; Wu, X.; Xia, B. A New Class of Potent Matrix Metalloproteinase 13 Inhibitors for Potential Treatment of Osteoarthritis: Evidence of Histologic and Clinical Efficacy without Musculoskeletal Toxicity in Rat Models. *Arthritis Rheum.* **2009**, *60* (7), 2008–2018. https://doi.org/10.1002/art.24629.

(18) Gege, C.; Bao, B.; Bluhm, H.; Boer, J.; Brian M. Gallagher, J.; Korniski, B.; Powers, T. S.; Steeneck, C.; Taveras, A. G.; Baragi, V. M. *Discovery and Evaluation of a Non-Zn Chelating, Selective Matrix Metalloproteinase 13 (MMP-13) Inhibitor for Potential Intra-articular Treatment of Osteoarthritis*. *J Med Chem*. **2012**, *55* (2), 709-716. https://doi.org/10.1021/jm201152u.

(19) Nara, H.; Sato, K.; Naito, T.; Mototani, H.; Oki, H.; Yamamoto, Y.; Kuno, H.; Santou, T.; Kanzaki, N.; Terauchi, J.; Uchikawa, O.; Kori, M. Discovery of Novel, Highly Potent, and Selective Quinazoline-2-Carboxamide-Based Matrix Metalloproteinase (MMP)-13 Inhibitors without a Zinc Binding Group Using a Structure-Based Design Approach. *J. Med. Chem.* **2014**, *57* (21), 8886–8902. https://doi.org/10.1021/jm500981k.

(20) Nara, H.; Sato, K.; Naito, T.; Mototani, H.; Oki, H.; Yamamoto, Y.; Kuno, H.; Santou, T.; Kanzaki, N.; Terauchi, J.; Uchikawa, O.; Kori, M. Thieno[2,3-d]Pyrimidine-2-Carboxamides Bearing a Carboxybenzene Group at 5-Position: Highly Potent, Selective, and Orally Available MMP-13 Inhibitors Interacting with the S1″ Binding Site. *Bioorg. Med. Chem.* **2014**, *22* (19), 5487–5505. https://doi.org/10.1016/j.bmc.2014.07.025.

(21) Nara, H.; Sato, K.; Kaieda, A.; Oki, H.; Kuno, H.; Santou, T.; Kanzaki, N.; Terauchi, J.; Uchikawa, O.; Kori, M. Design, Synthesis, and Biological Activity of Novel, Potent, and Highly Selective Fused Pyrimidine-2-Carboxamide-4-One-Based Matrix Metalloproteinase (MMP)-13 Zinc-Binding Inhibitors. *Bioorg. Med. Chem.* **2016**, *24* (23), 6149–6165. https://doi.org/10.1016/j.bmc.2016.09.009.

(22) Ruminski, P. G.; Massa, M.; Strohbach, J.; Hanau, C. E.; Schmidt, M.; Scholten, J. A.; Fletcher, T. R.; Hamper, B. C.; Carroll, J. N.; Shieh, H. S.; Caspers, N.; Collins, B.; Grapperhaus, M.; Palmquist, K. E.; Collins, J.; Baldus, J. E.; Hitchcock, J.; Kleine, H. P.;

Rogers, M. D.; McDonald, J.; Munie, G. E.; Messing, D. M.; Portolan, S.; Whiteley, L. O.; Sunyer, T.; Schnute, M. E. Discovery of N-(4-Fluoro-3-Methoxybenzyl)-6-(2-(((2S,5R)-5-(Hydroxymethyl)-1,4-Dioxan-2-Yl)Methyl)-2H-Tetrazol-5-Yl)-2-Methylpyrimidine-4-Carboxamide. A Highly Selective and Orally Bioavailable Matrix Metalloproteinase-13 Inhibitor for the Potential Treatment of Osteoarthritis. *J. Med. Chem.* **2016**, *59* (1), 313–327. https://doi.org/10.1021/acs.jmedchem.5b01434.

(23) Hugenberg, V.; Wagner, S.; Kopka, K.; Schäfers, M.; Schuit, R. C.; Windhorst, A. D.; Hermann, S. Radiolabeled Selective Matrix Metalloproteinase 13 (MMP-13) Inhibitors: (Radio)Syntheses and in Vitro and First in Vivo Evaluation. *J. Med. Chem.* **2017**, *60* (1), 307–321. https://doi.org/10.1021/acs.jmedchem.6b01284.

(24) Nara, H.; Kaieda, A.; Sato, K.; Naito, T.; Mototani, H.; Oki, H.; Yamamoto, Y.; Kuno, H.; Santou, T.; Kanzaki, N.; Terauchi, J.; Uchikawa, O.; Kori, M. Discovery of Novel, Highly Potent, and Selective Matrix Metalloproteinase (MMP)-13 Inhibitors with a 1,2,4-Triazol-3-Yl Moiety as a Zinc Binding Group Using a Structure-Based Design Approach. *J. Med. Chem.* **2017**, *60* (2), 608–626. https://doi.org/10.1021/acs.jmedchem.6b01007.

(25) Fuerst, R.; Yong Choi, J.; Knapinska, A. M.; Smith, L.; Cameron, M. D.; Ruiz, C.; Fields, G. B.; Roush, W. R. Development of Matrix Metalloproteinase-13 Inhibitors – A Structure-Activity/Structure-Property Relationship Study. *Bioorg. Med. Chem.* **2018**, *26* (18), 4984–4995. https://doi.org/10.1016/j.bmc.2018.08.020.

(26) Huang, S.; Feng, K.; Ren, Y. Molecular Modelling Studies of Quinazolinone Derivatives as MMP-13 Inhibitors by QSAR, Molecular Docking and Molecular Dynamics Simulations Techniques. *MedChemComm* **2019**, *10* (1), 101–115. https://doi.org/10.1039/C8MD00375K.

(27) Laleu, B.; Akao, Y.; Ochida, A.; Duffy, S.; Lucantoni, L.; Shackleford, D. M.; Chen, G.; Katneni, K.; Chiu, F. C. K.; White, K. L.; Chen, X.; Sturm, A.; Dechering, K. J.; Crespo, B.; Sanz, L. M.; Wang, B.; Wittlin, S.; Charman, S. A.; Avery, V. M.; Cho, N.; Kamaura, M. Discovery and Structure–Activity Relationships of Quinazolinone-2-Carboxamide Derivatives as Novel Orally Efficacious Antimalarials. *J. Med. Chem.* **2021**, *64* (17), 12582–12602. https://doi.org/10.1021/acs.jmedchem.1c00441.

(28) Buchler, A.; Munch, M.; Farber, G.; Zhao, X.; Al-Haddad, R.; Farber, E.; Rotstein, B. H. Selective Imaging of Matrix Metalloproteinase-13 to Detect Extracellular Matrix Remodeling in Atherosclerotic Lesions. *Mol. Imaging Biol.* **2021**. https://doi.org/10.1007/s11307-021-01626-9.

(29) Buchler, A.; Ismailani, U. S.; MacMullin, N.; Abdirahman, F.; Adi, M.; Bi, C.; Jany, C.; Keillor, J. W.; Rotstein, B. H. Quinazoline-2-Carboxamides as Selective PET Radiotracers for Matrix Metalloproteinase-13 Imaging in Atherosclerosis. *J. Med. Chem.* **2023**, *66* (10), 6682–6696. https://doi.org/10.1021/acs.jmedchem.2c02107.

(30) Cai, H.; Agrawal, A. K.; Putt, D. A.; Hashim, M.; Reddy, A.; Brodfuehrer, J.; Surendran, N.; Lash, L. H. Assessment of the Renal Toxicity of Novel Anti-Inflammatory Compounds Using Cynomolgus Monkey and Human Kidney Cells. *Toxicology* **2009**, *258* (1), 56–63. https://doi.org/10.1016/j.tox.2009.01.006.

(31) Dollé, F. Fluorine-18-Labelled Fluoropyridines: Advances in Radiopharmaceutical Design. *Curr. Pharm. Des.* **2005**, *11* (25), 3221–3235. https://doi.org/10.2174/138161205774424645.

(32) Subbaiah, M. A. M.; Meanwell, N. A. Bioisosteres of the Phenyl Ring: Recent Strategic Applications in Lead Optimization and Drug Design. *J. Med. Chem.* **2021**, *64* (19), 14046–14128. https://doi.org/10.1021/acs.jmedchem.1c01215.

(33) Kniess, T.; Laube, M.; Brust, P.; Steinbach, J. 2-[18F]Fluoroethyl Tosylate – a Versatile Tool for Building 18F-Based Radiotracers for Positron Emission Tomography. *MedChemComm* **2015**, *6* (10), 1714–1754. https://doi.org/10.1039/C5MD00303B.

(34) Taylor, S. J.; Abeywardane, A.; Liang, S.; Xiong, Z.; Proudfoot, J. R.; Farmer, B. S.; Gao, D. A.; Heim-Riether, A.; Smith-Keenan, L. L.; Muegge, I.; Yu, Y.; Zhang, Q.; Souza, D.; Panzenbeck, M.; Goldberg, D.; Hill-Drzewi, M.; Margarit, M.; Collins, B.; Li, J. X.; Zuvela-Jelaska, L.; Li, J.; Farrow, N. A. Indole Inhibitors of MMP-13 for Arthritic Disorders. *ACS Omega* **2021**, *6* (29), 18635–18650. https://doi.org/10.1021/acsomega.1c01320.

(35) Swamy, K. C. K.; Kumar, N. N. B.; Balaraman, E.; Kumar, K. V. P. P. Mitsunobu and Related Reactions: Advances and Applications. *Chem. Rev.* **2009**, *109* (6), 2551–2651. https://doi.org/10.1021/cr800278z.

(36) Hain, J.; Rollin, P.; Klaffke, W.; Lindhorst, T. K. Anomeric Modification of Carbohydrates Using the Mitsunobu Reaction. *Beilstein J. Org. Chem.* **2018**, *14*, 1619–1636. https://doi.org/10.3762/bjoc.14.138.

(37) Liu, D.; Sanow, L. P.; Zhang, C. Mitsunobu Reactions of Aliphatic Alcohols and Bulky Phenols. *Tetrahedron Lett.* **2014**, *55* (19), 3090–3092. https://doi.org/10.1016/j.tetlet.2014.03.138.

(38) Sugaya, T.; Mimura, Y.; Kato, N.; Ikuta, M.; Mimura, T.; Kasai, M.; Tomioka, S. Synthesis of a 6H-Pyrazolo[4,5,1-de]Acridin-6-One Derivative: A Useful Intermediate of Antitumour Agents. *Synthesis* **2002**, *1994*, 73–76. https://doi.org/10.1055/s-1994-25408.

(39) Akama, T.; Ueno, K.; Saito, H.; Kasai, M. Synthesis of an Ethyl 6-Amino-3,5-Difluorosalicylate Derivative by Sequential Regioselective Directed Ortho-Metalation, A Practical Synthesis Of4,5-Diamino-3,6,8-Trifluoroflavone, A Potent Antitumor Agent. *Synthesis* **2000**, *1997*, 1446–1450. https://doi.org/10.1055/s-1997-1379.

(40) Wilson, A. A.; Jin, L.; Garcia, A.; DaSilva, J. N.; Houle, S. An Admonition When Measuring the Lipophilicity of Radiotracers Using Counting Techniques. *Appl. Radiat. Isot.* **2001**, *54* (2), 203–208. https://doi.org/10.1016/S0969-8043(00)00269-4.

(41) Gimeno, A.; Beltrán-Debón, R.; Mulero, M.; Pujadas, G.; Garcia-Vallvé, S. Understanding the Variability of the S1′ Pocket to Improve Matrix Metalloproteinase Inhibitor Selectivity Profiles. *Drug Discov. Today* **2020**, *25* (1), 38–57. https://doi.org/10.1016/j.drudis.2019.07.013.

(42) Pees, A.; Chassé, M.; Lindberg, A.; Vasdev, N. Recent Developments in Carbon-11 Chemistry and Applications for First-In-Human PET Studies. *Molecules* **2023**, *28* (3), 931. https://doi.org/10.3390/molecules28030931.

(43) Cai, L.; Xu, R.; Guo, X.; Pike, V. W. Rapid Room-Temperature 11C-Methylation of Arylamines with [11C]Methyl Iodide Promoted by Solid Inorganic Bases in DMF. *Eur. J. Org. Chem.* **2012**, *2012* (7), 1303–1310. https://doi.org/10.1002/ejoc.201101499.

(44) Toczek, J.; Ye, Y.; Gona, K.; Kim, H.-Y.; Han, J.; Razavian, M.; Golestani, R.; Zhang, J.; Wu, T. L.; Jung, J.-J.; Sadeghi, M. M. Preclinical Evaluation of RYM1, a Matrix

Metalloproteinase-Targeted Tracer for Imaging Aneurysm. *J. Nucl. Med. Off. Publ. Soc. Nucl. Med.* **2017**, *58* (8), 1318–1323. https://doi.org/10.2967/jnumed.116.188656.

(45) Toczek, J.; Bordenave, T.; Gona, K.; Kim, H.-Y.; Beau, F.; Georgiadis, D.; Correia, I.; Ye, Y.; Razavian, M.; Jung, J.-J.; Lequin, O.; Dive, V.; Sadeghi, M. M.; Devel, L. Novel Matrix Metalloproteinase 12 Selective Radiotracers for Vascular Molecular Imaging. *J. Med. Chem.* **2019**, *62* (21), 9743–9752. https://doi.org/10.1021/acs.jmedchem.9b01186.

(46) Joshi, N. V.; Vesey, A. T.; Williams, M. C.; Shah, A. S. V.; Calvert, P. A.; Craighead, F. H. M.; Yeoh, S. E.; Wallace, W.; Salter, D.; Fletcher, A. M.; van Beek, E. J. R.; Flapan, A. D.; Uren, N. G.; Behan, M. W. H.; Cruden, N. L. M.; Mills, N. L.; Fox, K. A. A.; Rudd, J. H. F.; Dweck, M. R.; Newby, D. E. 18F-Fluoride Positron Emission Tomography for Identification of Ruptured and High-Risk Coronary Atherosclerotic Plaques: A Prospective Clinical Trial. *The Lancet* **2014**, *383* (9918), 705–713. https://doi.org/10.1016/S0140-6736(13)61754-7.

(47) Wu, J.; Rush, T. S.; Hotchandani, R.; Du, X.; Geck, M.; Collins, E.; Xu, Z.-B.; Skotnicki, J.; Levin, J. I.; Lovering, F. E. Identification of Potent and Selective MMP-13 Inhibitors. *Bioorg. Med. Chem. Lett.* **2005**, *15* (18), 4105–4109. https://doi.org/10.1016/j.bmcl.2005.06.019.

(48) Jaffré, F.; Friedman, A. E.; Hu, Z.; Mackman, N.; Blaxall, B. C. Beta-Adrenergic Receptor Stimulation Transactivates Protease-Activated Receptor 1 via MMP-13 in Cardiac Cells. *Circulation* **2012**, *125* (24), 2993–3003. https://doi.org/10.1161/CIRCULATIONAHA.111.066787.

(49) Alavi, A.; Werner, T. J.; Høilund-Carlsen, P. F. What Can Be and What Cannot Be Accomplished with PET to Detect and Characterize Atherosclerotic Plaques. *J. Nucl.*

Cardiol. Off. Publ. Am. Soc. Nucl. Cardiol. **2018**, *25* (6), 2012–2015. https://doi.org/10.1007/s12350-017-0977-x.

(50) Alavi, A.; Werner, T. J.; Raynor, W.; Høilund-Carlsen, P. F.; Revheim, M.-E. Critical Review of PET Imaging for Detection and Characterization of the Atherosclerotic Plaques with Emphasis on Limitations of FDG-PET Compared to NaF-PET in This Setting. *Am. J. Nucl. Med. Mol. Imaging* **2021**, *11* (5), 337–351.

(51) Moses, W. W. Fundamental Limits of Spatial Resolution in PET. *Nucl. Instrum. Methods Phys. Res. Sect. Accel. Spectrometers Detect. Assoc. Equip.* **2011**, *648 Supplement 1*, S236–S240. https://doi.org/10.1016/j.nima.2010.11.092.

(52) Andrés-Manzano, M. J.; Andrés, V.; Dorado, B. Oil Red O and Hematoxylin and Eosin Staining for Quantification of Atherosclerosis Burden in Mouse Aorta and Aortic Root. *Methods Mol. Biol. Clifton NJ* **2015**, *1339*, 85–99. https://doi.org/10.1007/978-1-4939-2929-0_5.

4.9 Supporting information

4.9.1 Supplemental Figures

Tert-butyl (4-fluoro-3-phenethoxyphenyl)carbamate

To a solution of 2-phenylethanol (22 μL, 0.183 mmol, 1.0 equiv.) in THF (0.44 mL) was added *tert*-butyl (4-fluoro-3-hydroxyphenyl)carbamate (50 mg, 0.220 mmol, 1.2 equiv.) and triphenylphosphine (67 mg, 0.256 mmol, 1.4 equiv.). The mixture was cooled to 0 °C and diisopropyl azodicarboxylate (50 μL, 0.256 mmol, 1.4 equiv.) was added dropwise. The reaction was stirred at room temperature for 1 h, diluted with EtOAc and extracted with $NaHCO_3$, followed by 1 M HCl. The combined organics were washed with brine, dried over Na_2SO_4, filtered, and concentrated under reduced pressure The crude mixture was purified by column chromatography (0-8% EtOAc/hexane) to obtain the title compound as a white solid (47 mg, 0.141 mmol, 77%).^{1}H-NMR (400 MHz, $CDCl_3$): δ 7.35-7.23 (6H, m), 6.99-6.94 (1H, m), 6.65-6.62 (1H, m), 6.41 (1H, br), 4.26-4.22 (2H, m), 3.16-3.12 (2H, m), 1.51 (9H, s) ppm.

^{1}H-NMR (400 MHz, $CDCl_3$)

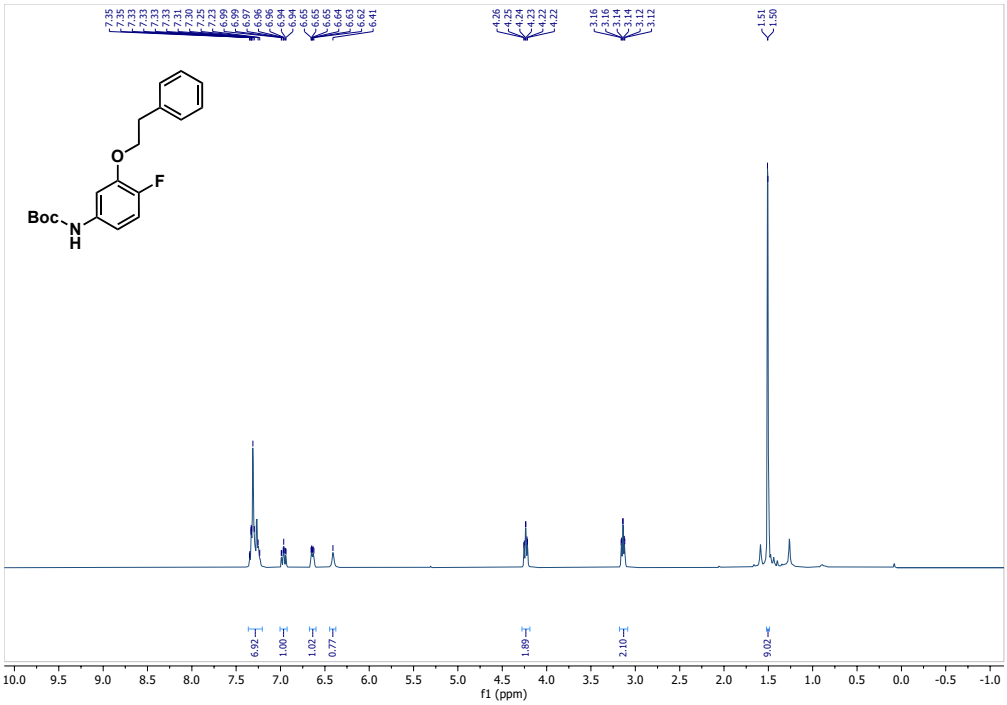

Scheme S1. Mitsunobu etherification screening.

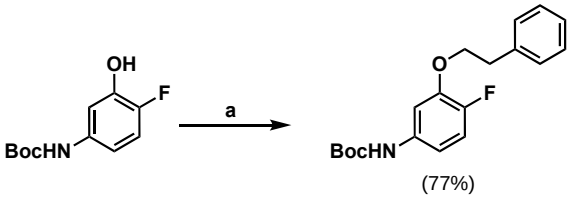

(77%)

Reagents and conditions: (a) phenethyl alcohol or **9**, DIAD, PPh_3, THF, 0 °C to rt, 1 h.

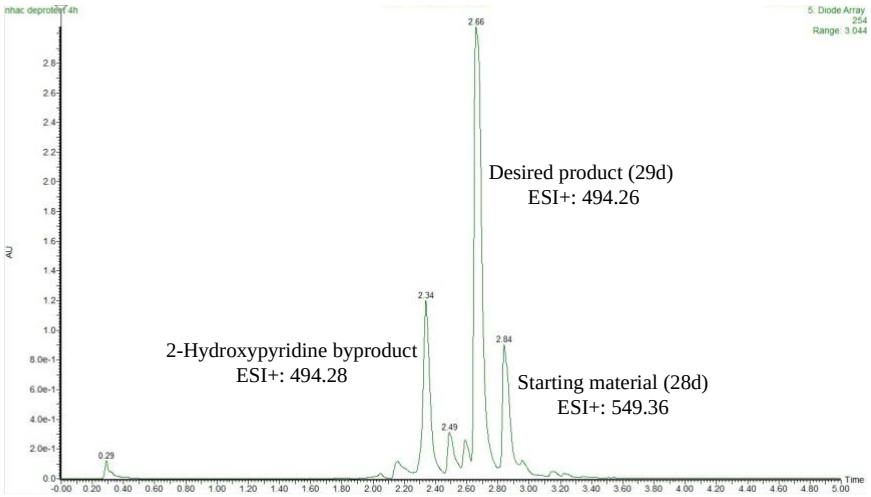

Figure S1. Representative UPLC chromatogram for the deprotection of intermediate **28d** to the final inhibitor **29d**.

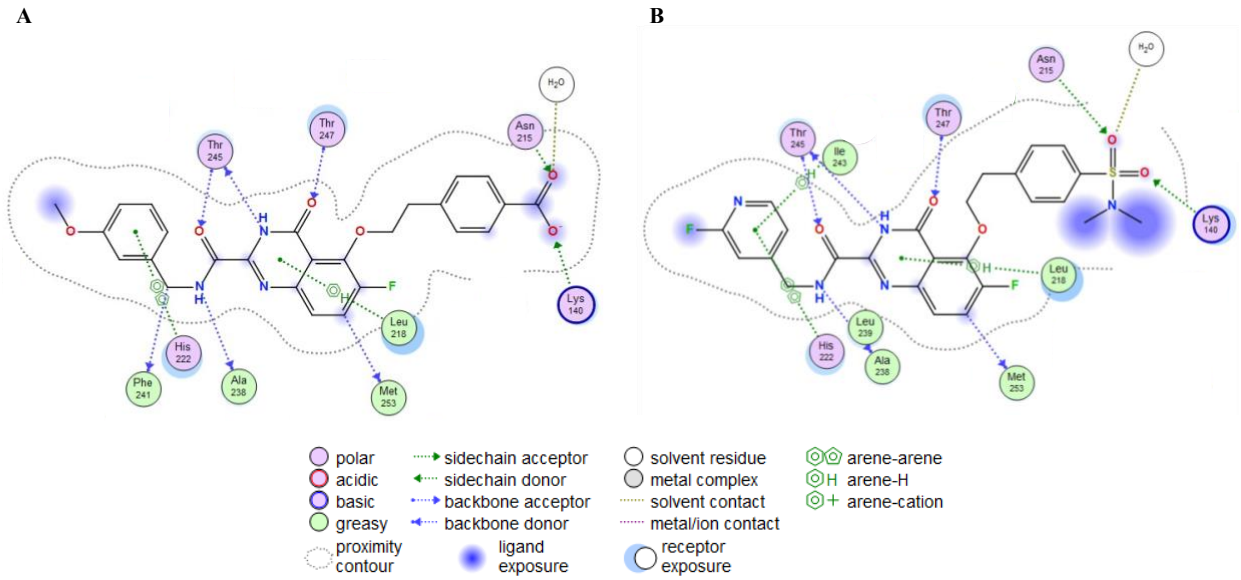

Figure S2. Molecular docking of lead quinazoline-2-carboxamide inhibitors with MMP-13. (A) 5b (from ref: *J Med Chem*. 2014 Nov 13;57(21):8886-902). (B) 29f. Only residues participating in binding interactions are shown.

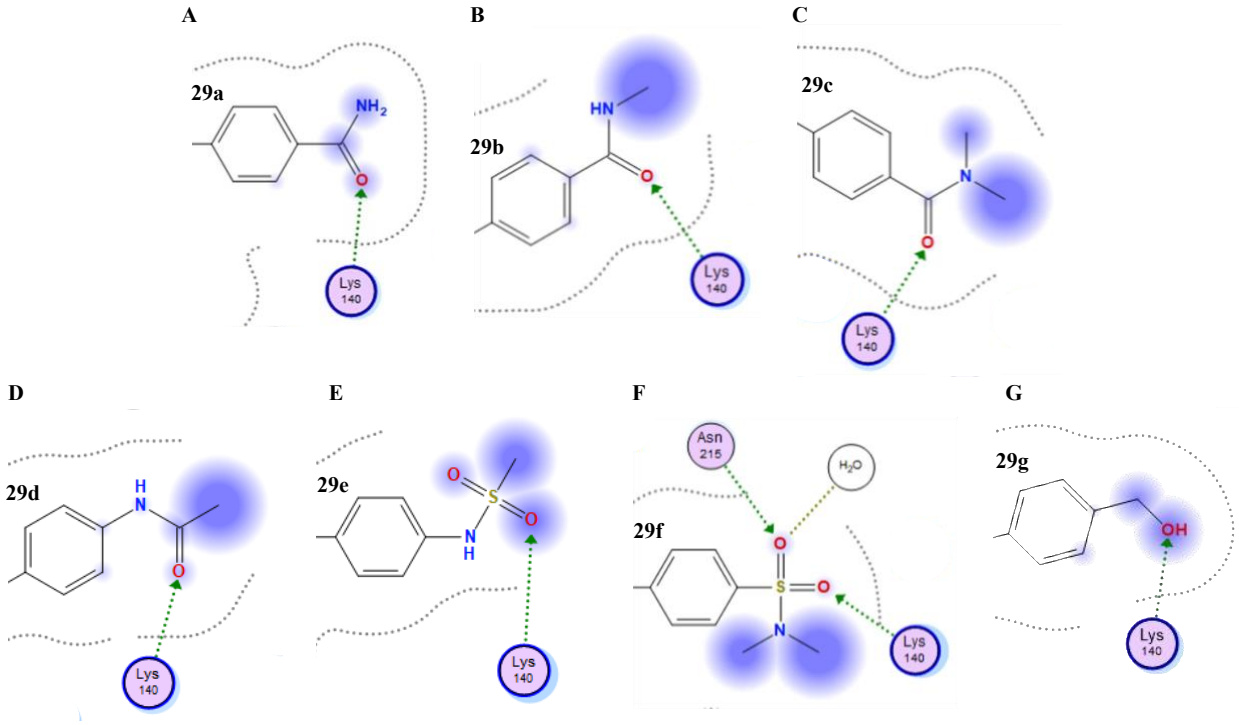

H

Compound	Docking score (S, ΔG kcal·mol^{-1})
29a	-10.02
29b	-10.43
29c	-10.67
29d	-10.40
29e	-10.49
29f	-11.44
29g	-10.81
6	-9.98
5b from ref	-11.17

Figure S3. (A-G) Binding interactions of inhibitors 29a-g within the S1" pocket of MMP-13. Only residues participating in binding interactions are shown. (H) Docking scores for all inhibitors. Compound 6 and 5b (from ref: *J Med Chem*. 2014 Nov 13;57(21):8886-902) are provided as controls. Alternate binding conformations with Asn215 are possible with similar docking scores.

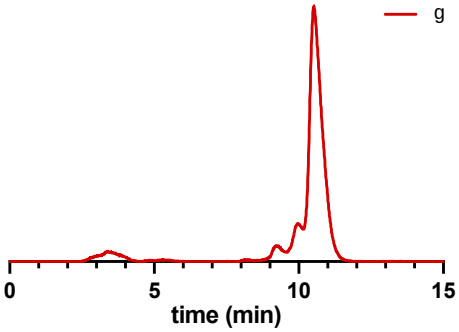

Figure S4. Crude RadioHPLC chromatogram for the synthesis of **[^{11}C]29f**.

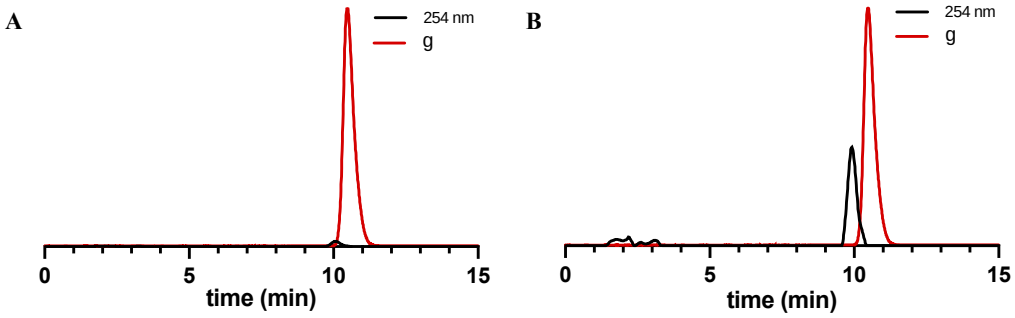

Figure S5. [^{11}C]29f quality control. (A) Purified **[^{11}C]29f** without co-injection. (B) Purified **[^{11}C]29f** with co-injection of **29f**.

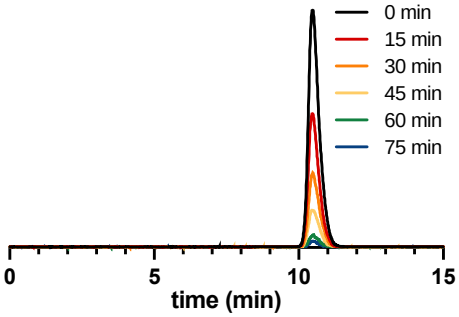

Figure S6. [^{11}C]29f stability following reformulation in 10% EtOH/saline (0.9%).

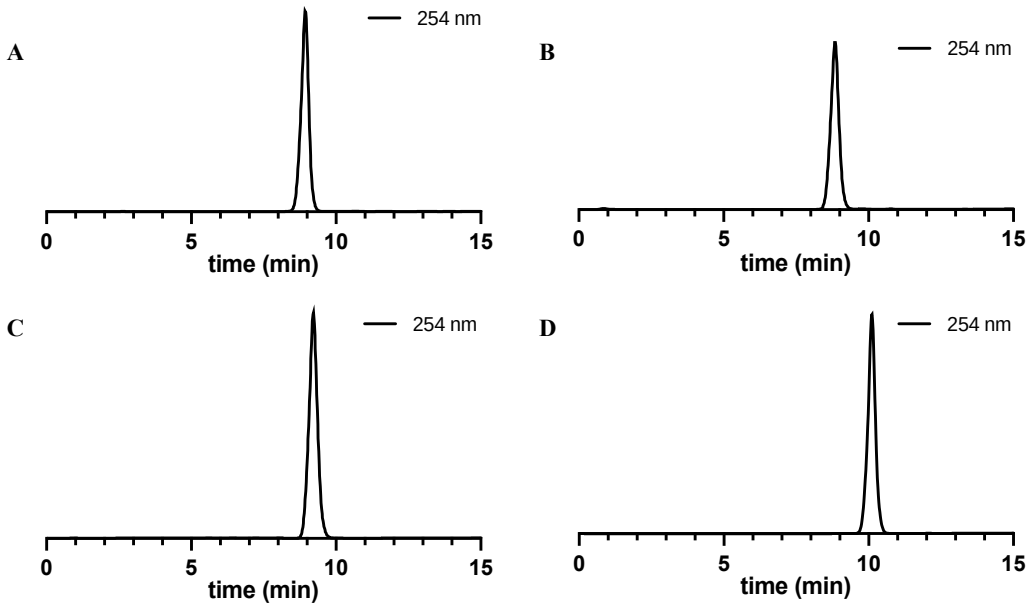

Figure S7. HPLC chromatograms for compounds (A) **29c** (B) **29d** (C) **29e** (D) **29f** (254 nm). See quality control section for HPLC method.

4.9.2 ^{1}H NMR and ^{13}C NMR spectra for all synthesized compounds

Compound 1

^{1}H-NMR (600 MHz, $(CD_3)_2SO$)

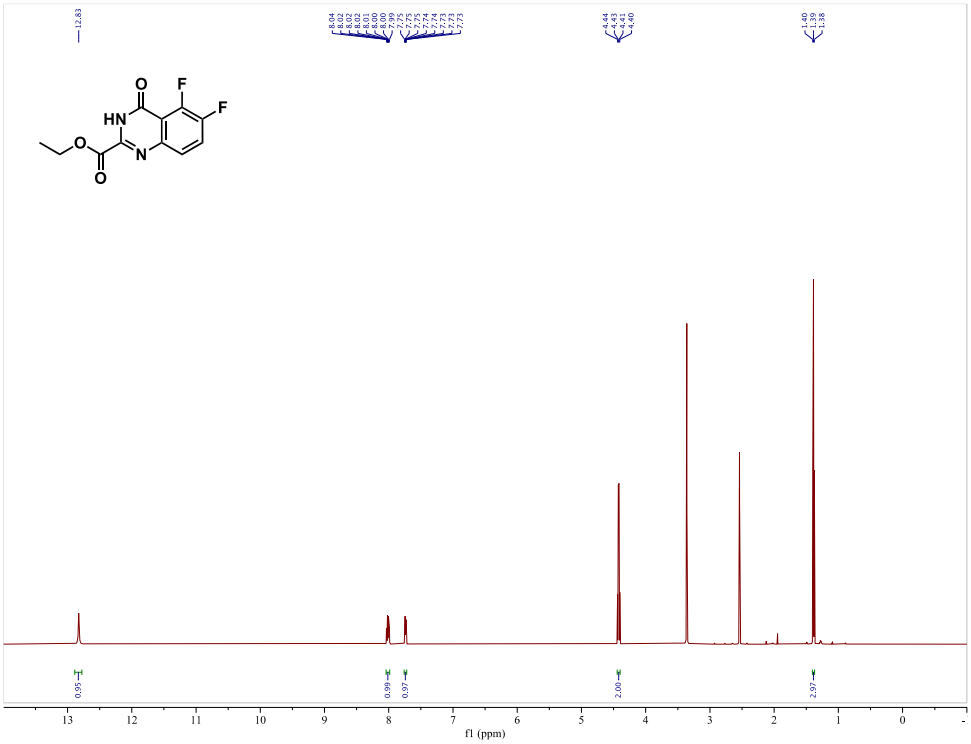

^{13}C-NMR (150 MHz, $(CD_3)_2SO$)

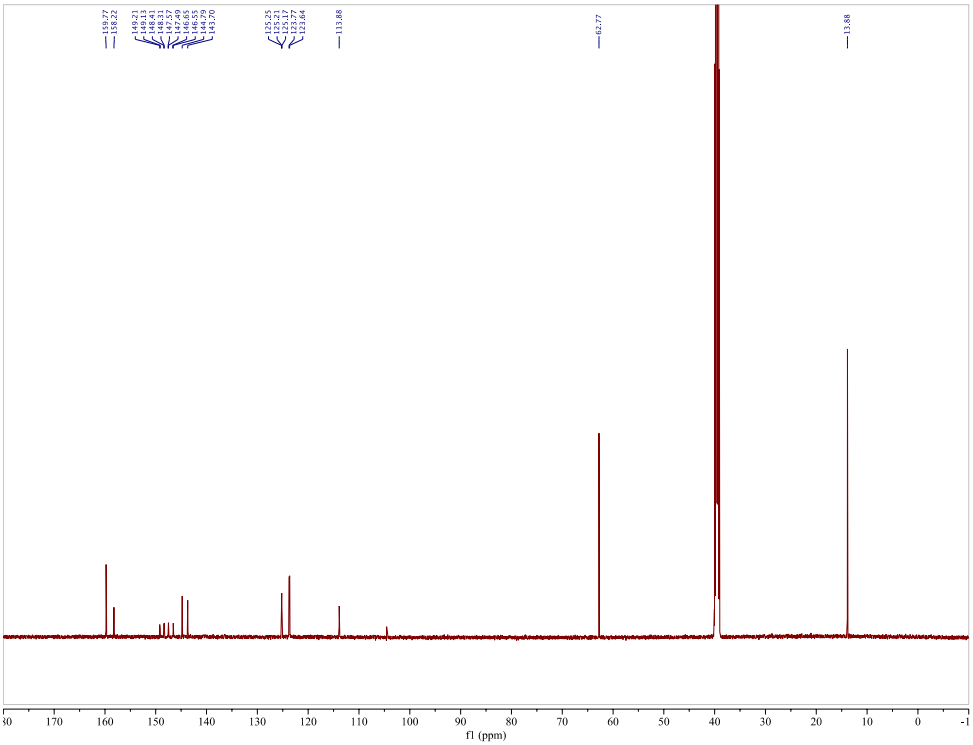

Compound 2

^{1}H-NMR (600 MHz, $(CD_3)_2SO$)

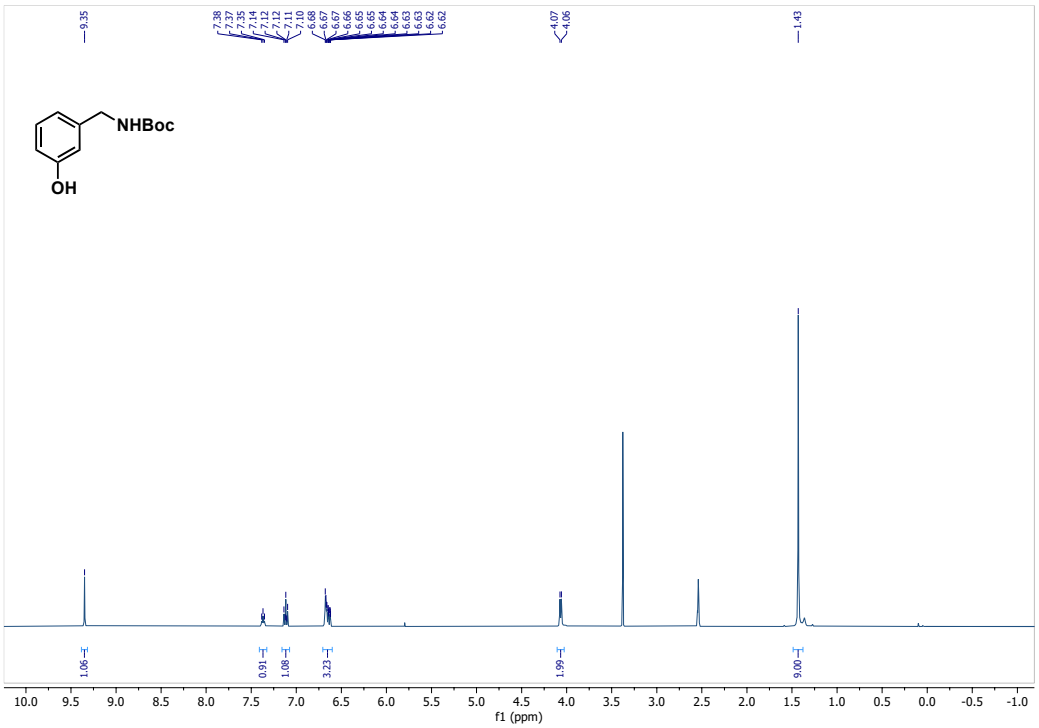

^{13}C-NMR (150 MHz, $(CD_3)_2SO$)

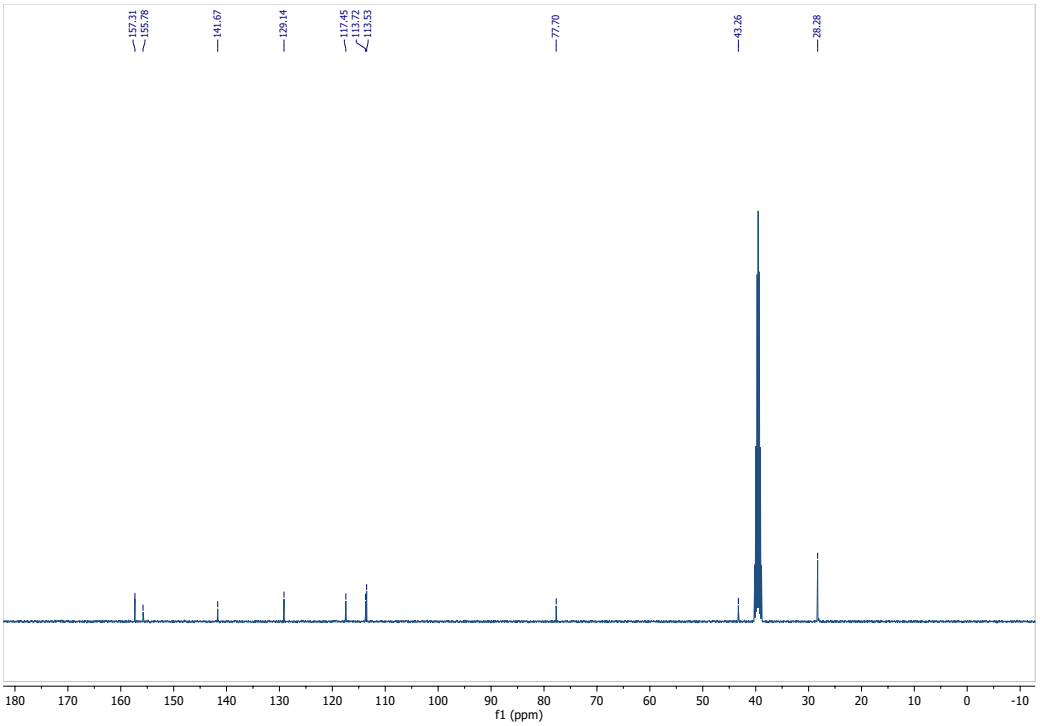

Compound 3

^{1}H-NMR (600 MHz, $(CD_3)_2SO$)

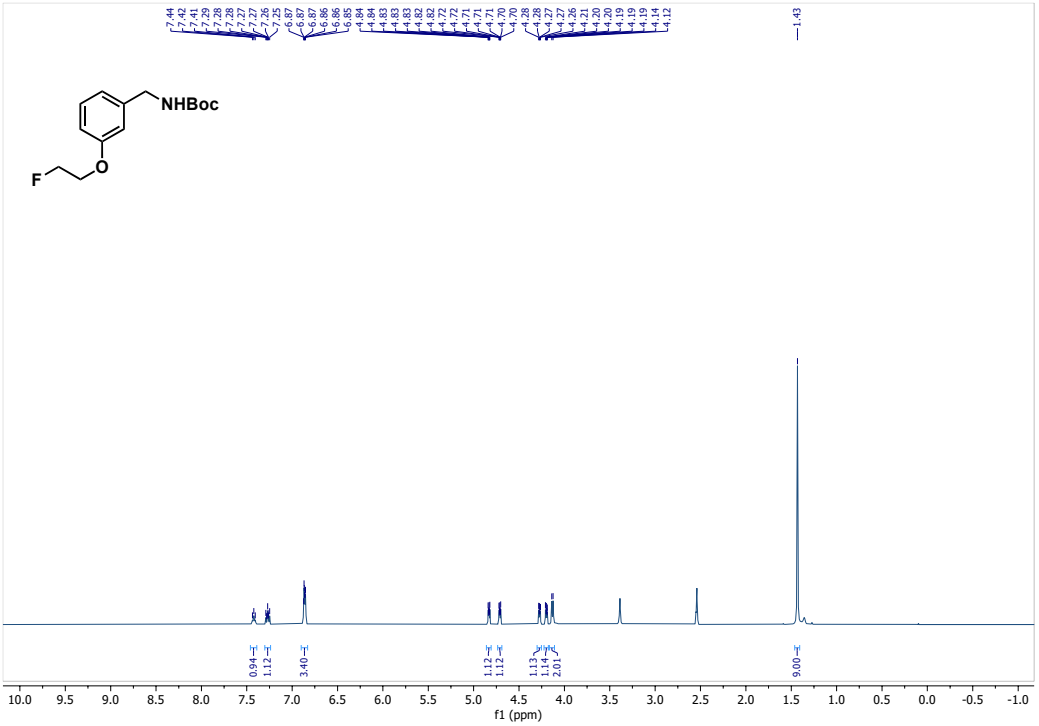

^{13}C-NMR (150 MHz, $(CD_3)_2SO$)

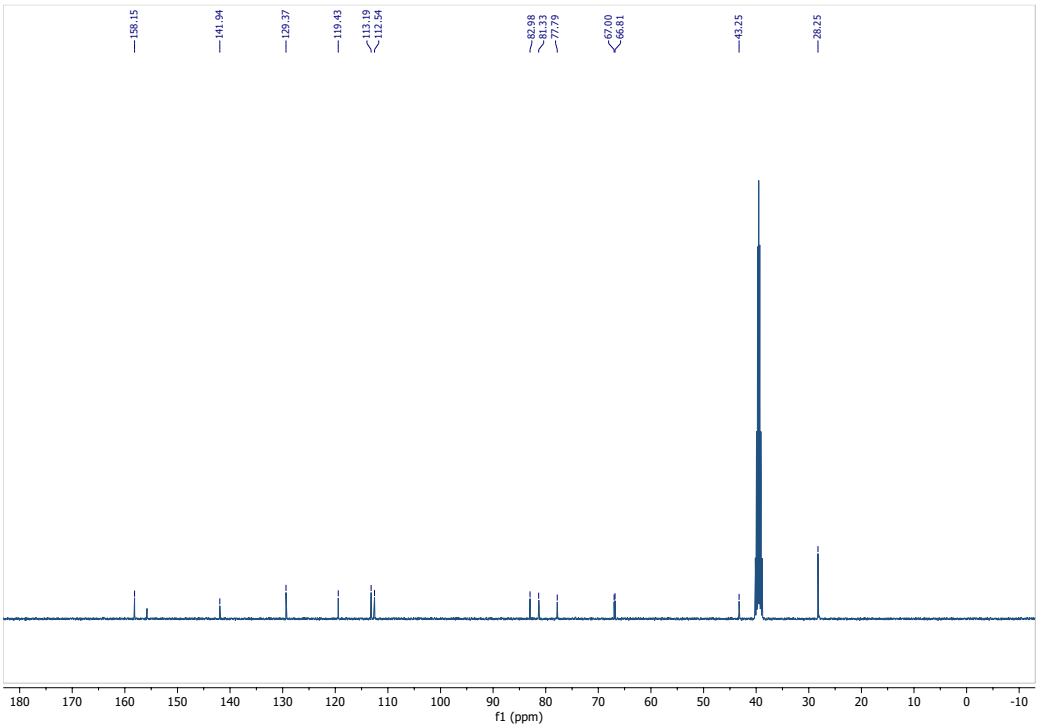

Compound 4

^{1}H-NMR (600 MHz, $(CD_3)_2SO$)

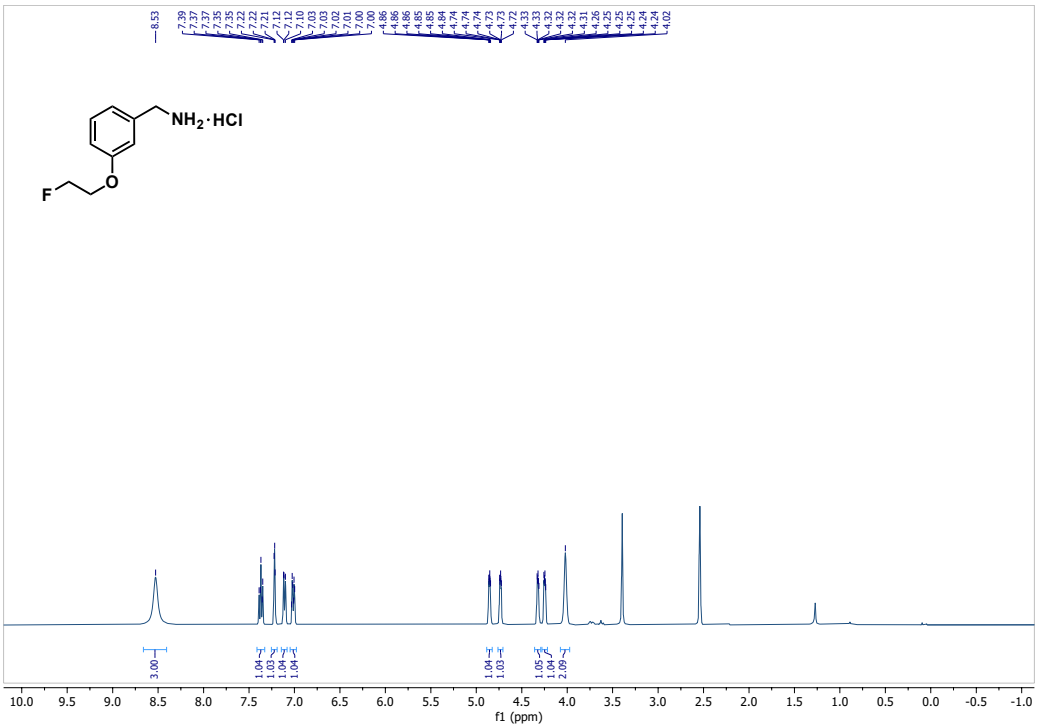

^{13}C-NMR (150 MHz, $(CD_3)_2SO$)

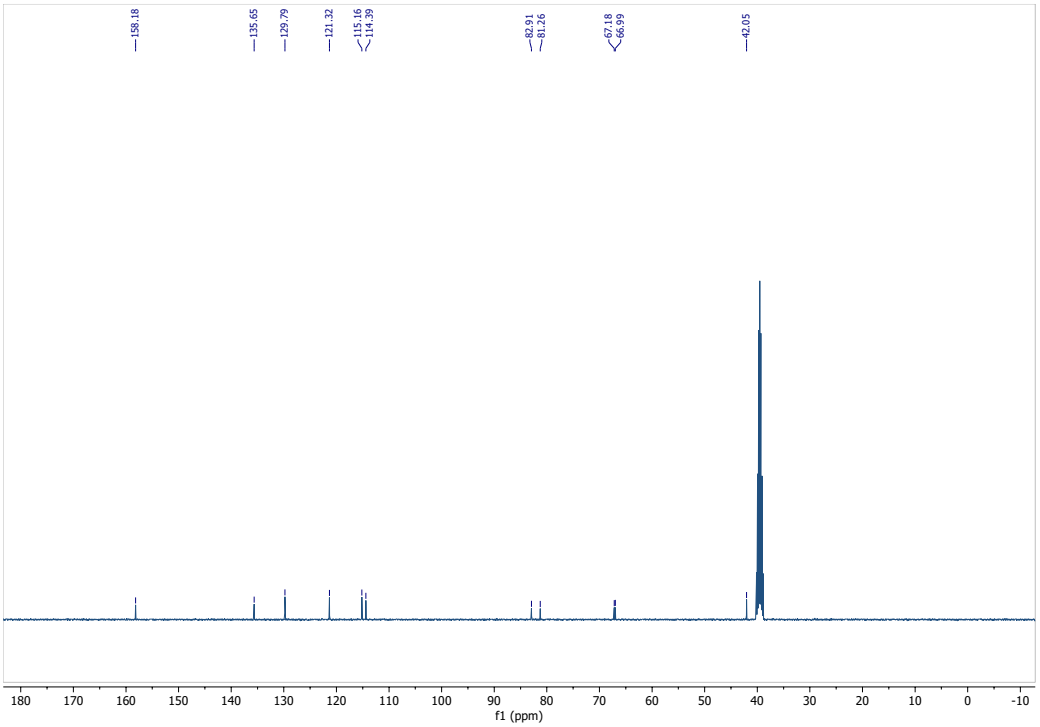

Compound 5a

^{1}H-NMR (600 MHz, $(CD_3)_2SO$)

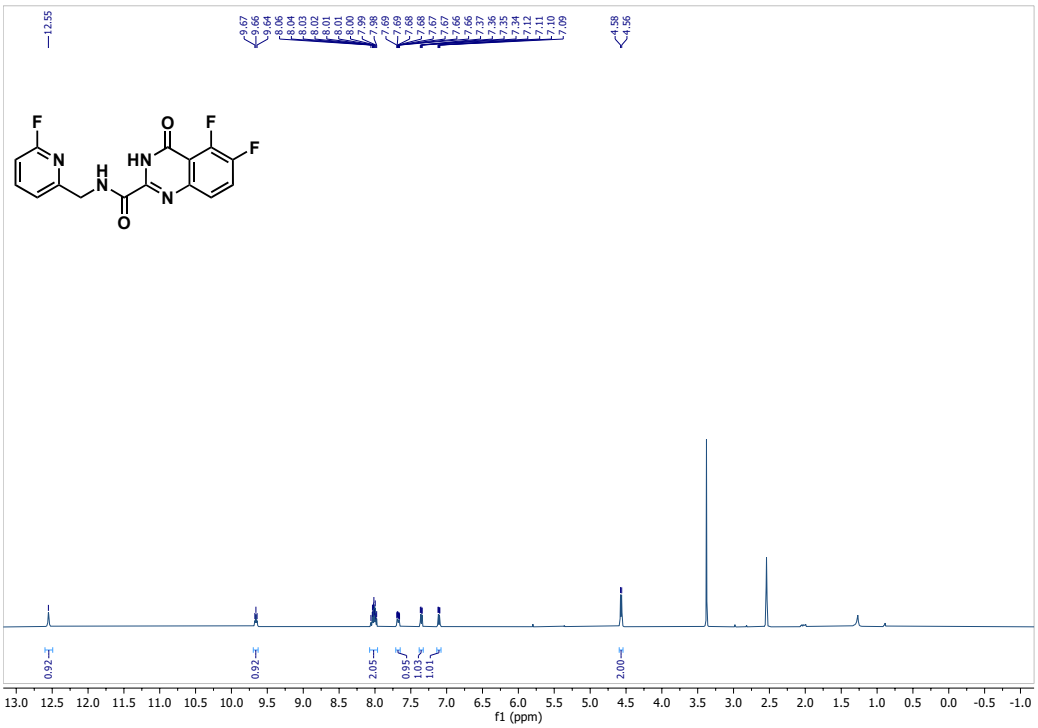

^{13}C-NMR (150 MHz, $(CD_3)_2SO$)

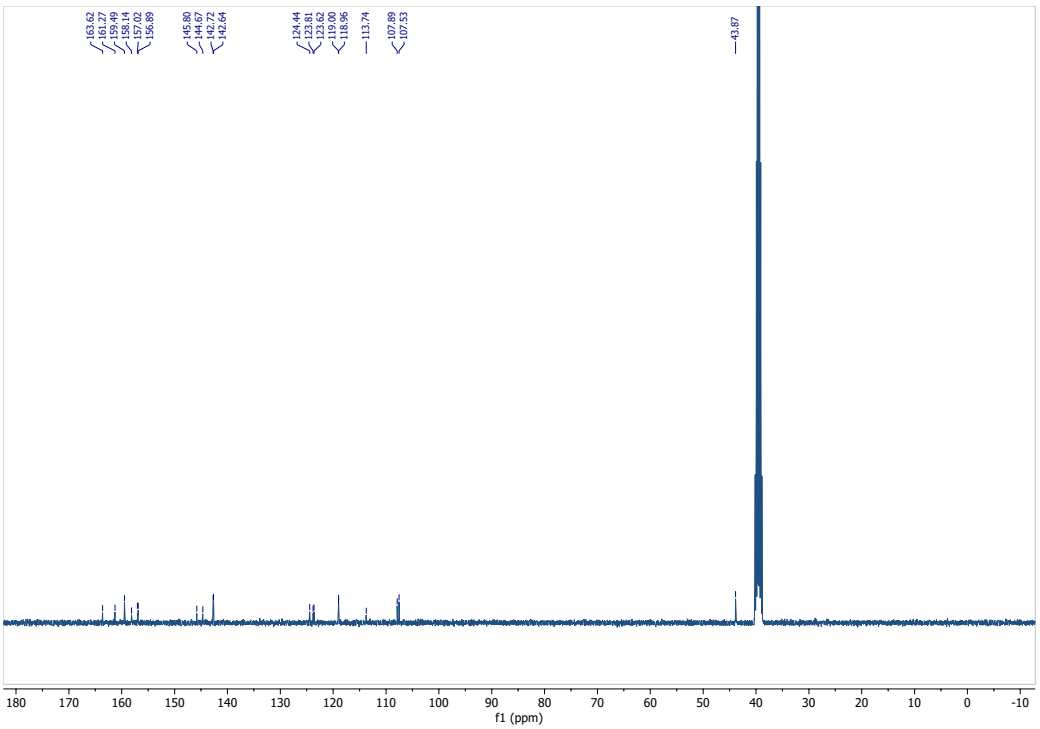

Compound 5b

^{1}H-NMR (400 MHz, $(CD_3)_2SO$)

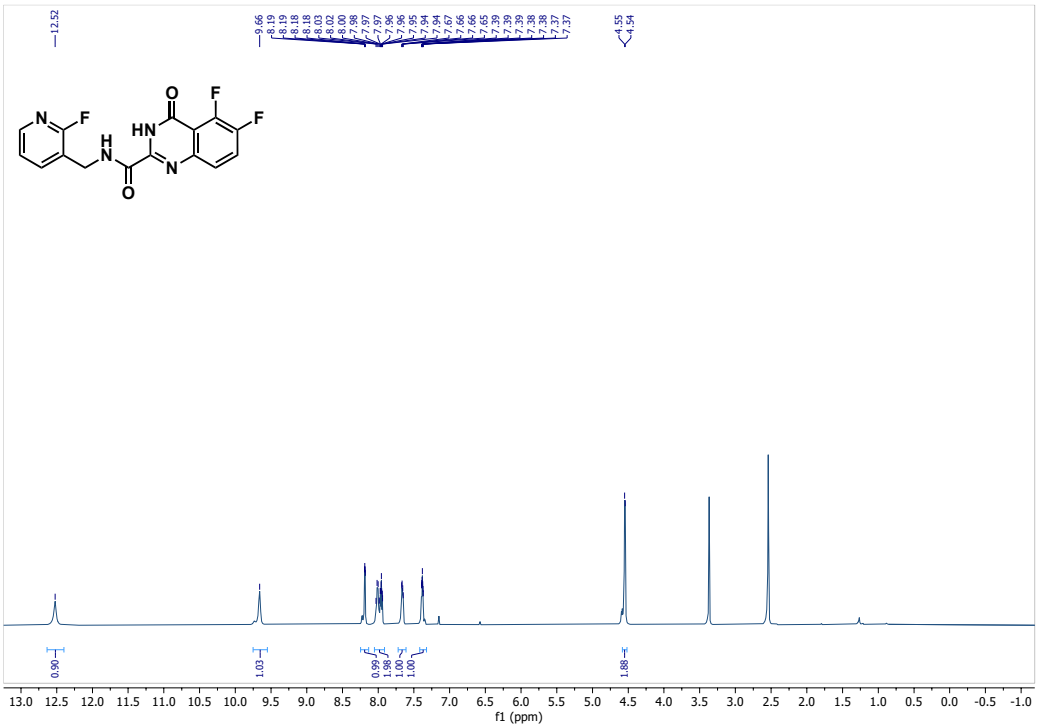

^{13}C-NMR (100 MHz, $(CD_3)_2SO$)

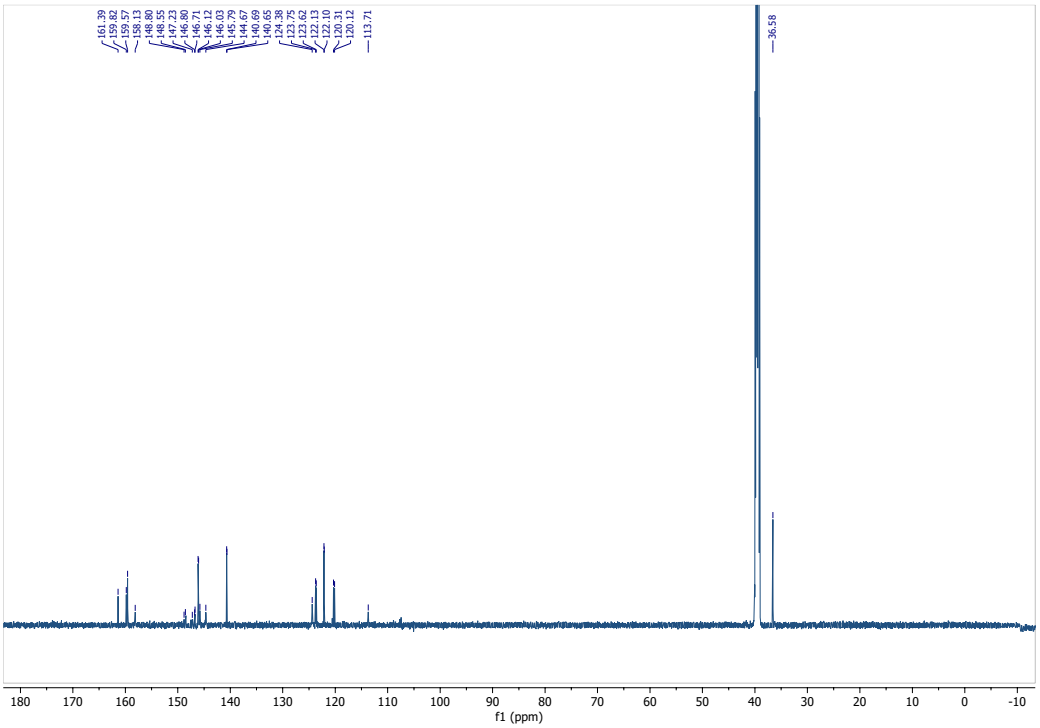

Compound 5c

^{1}H-NMR (400 MHz, $(CD_3)_2SO$)

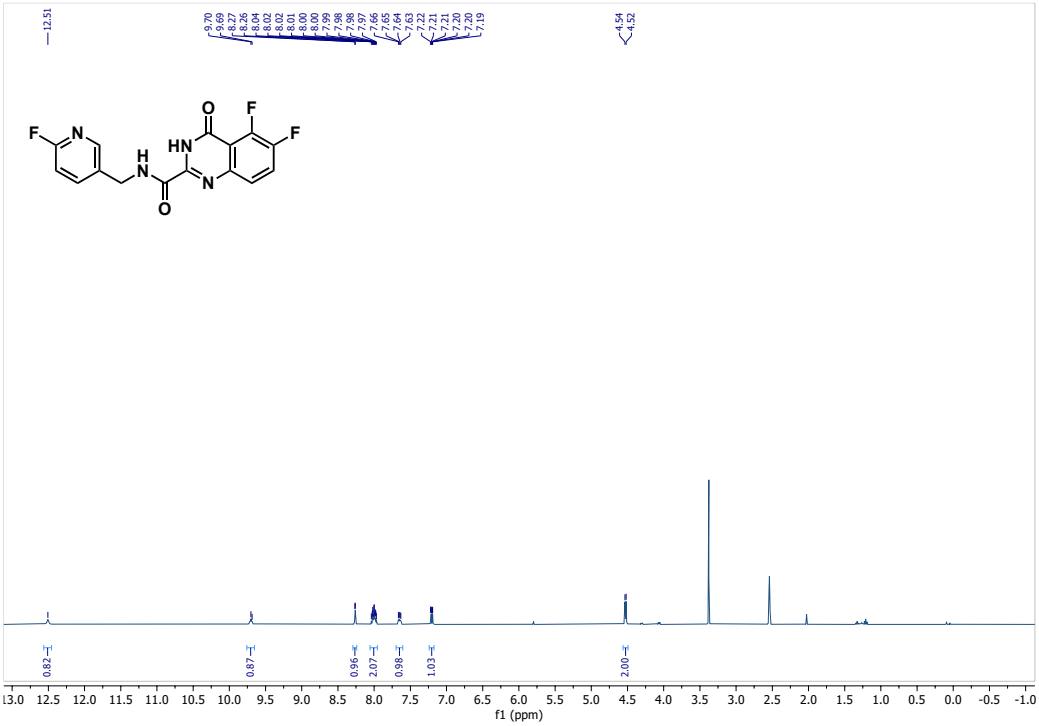

^{13}C-NMR (100 MHz, $(CD_3)_2SO$)

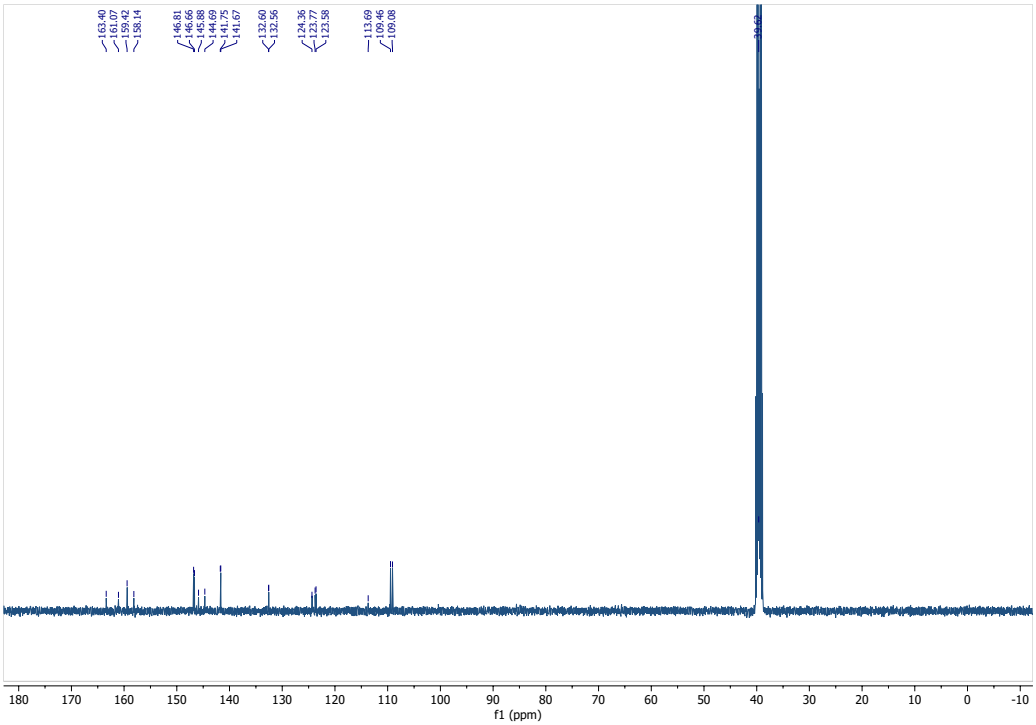

Compound 5d

^{1}H-NMR (400 MHz, $(CD_3)_2SO$)

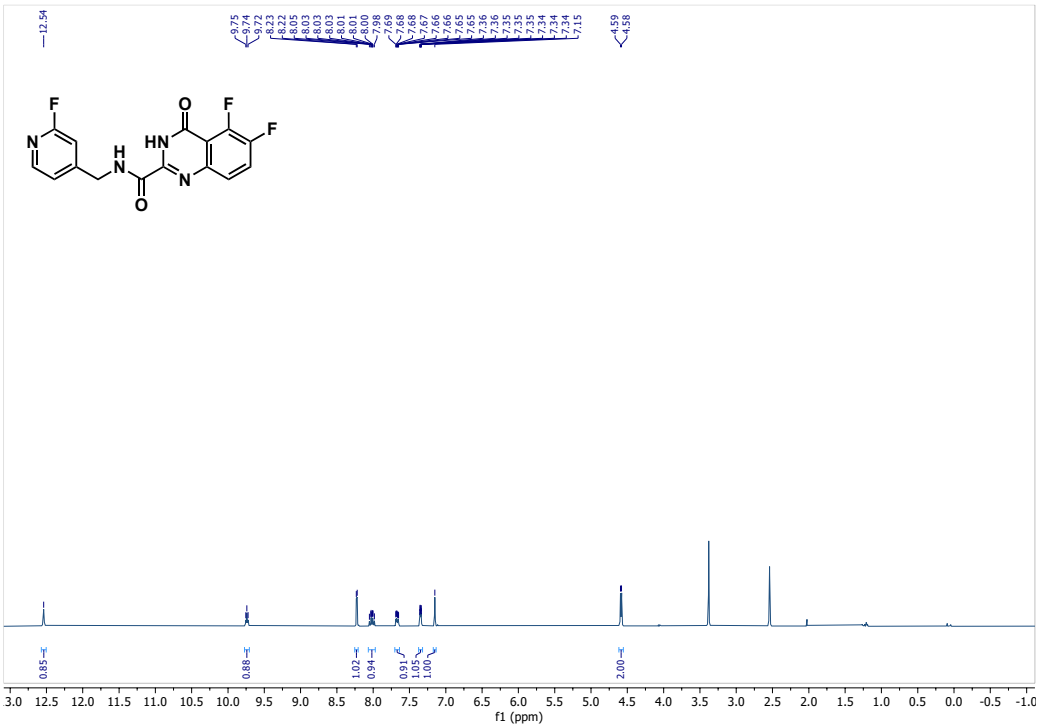

^{13}C-NMR (100 MHz, $(CD_3)_2SO$)

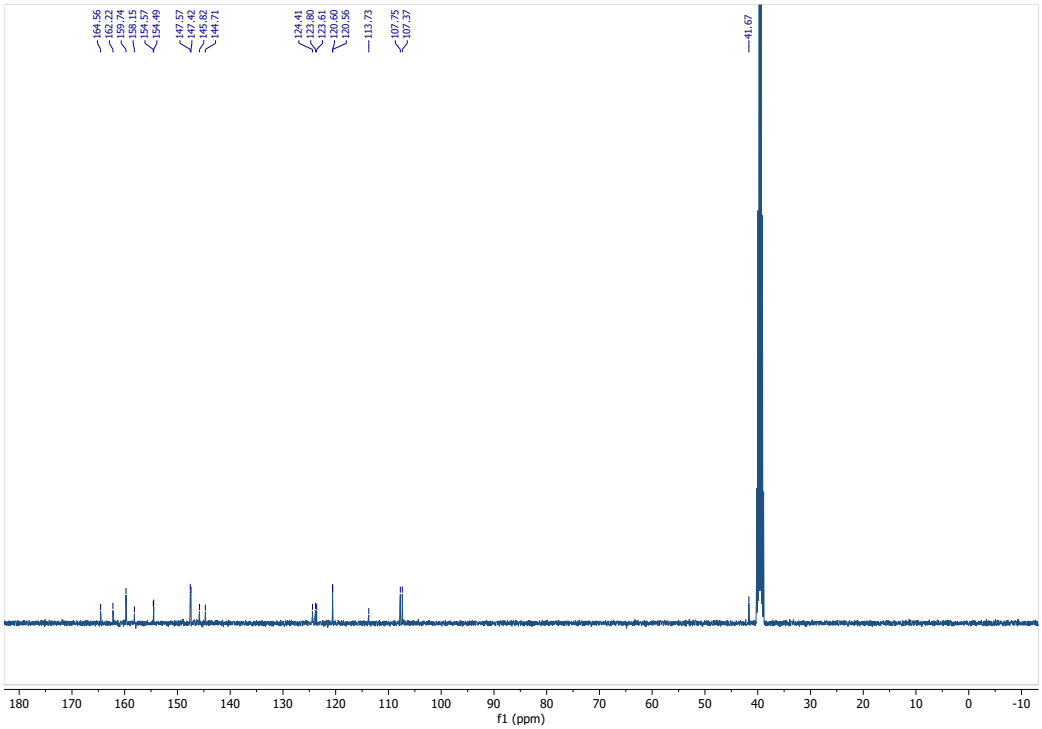

Compound 5e

^{1}H-NMR (400 MHz, $(CD_3)_2SO$)

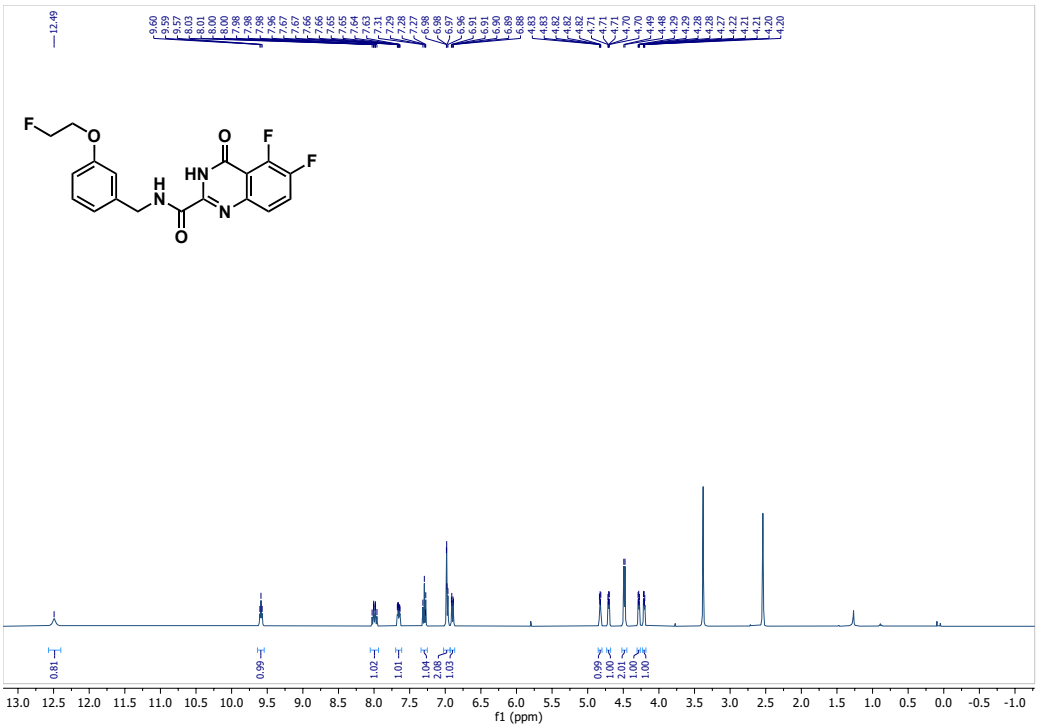

^{13}C-NMR (150 MHz, $(CD_3)_2SO$)

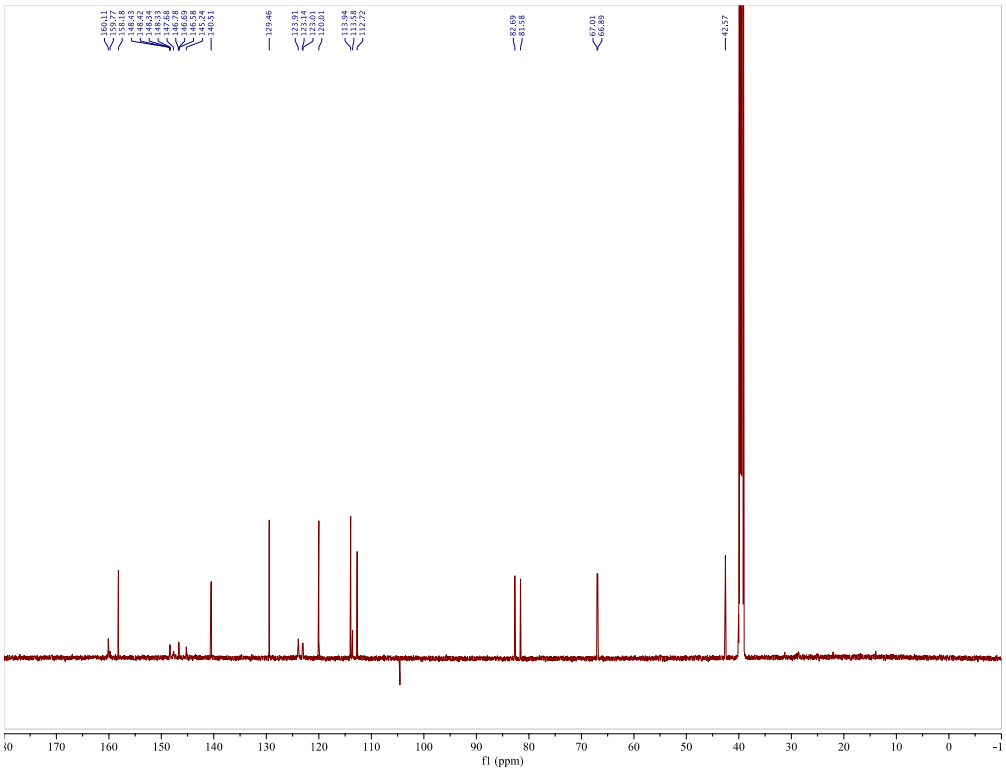

Compound 6

^{1}H-NMR (600 MHz, $(CD_3)_2SO$)

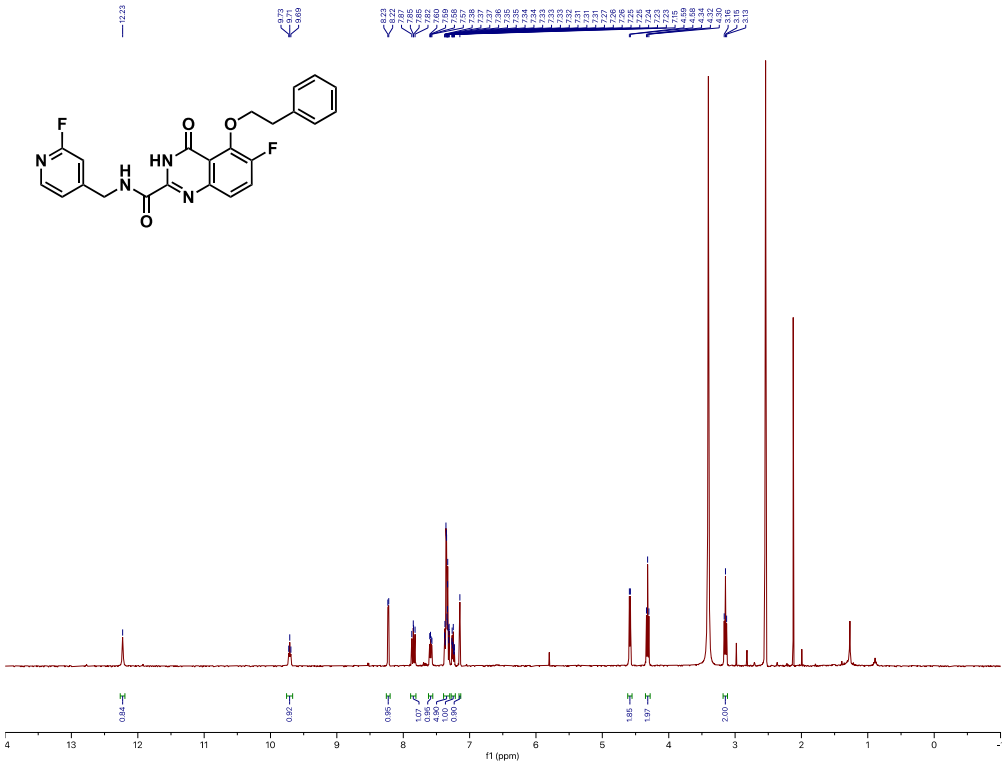

^{13}C-NMR (150 MHz, $(CD_3)_2SO$)

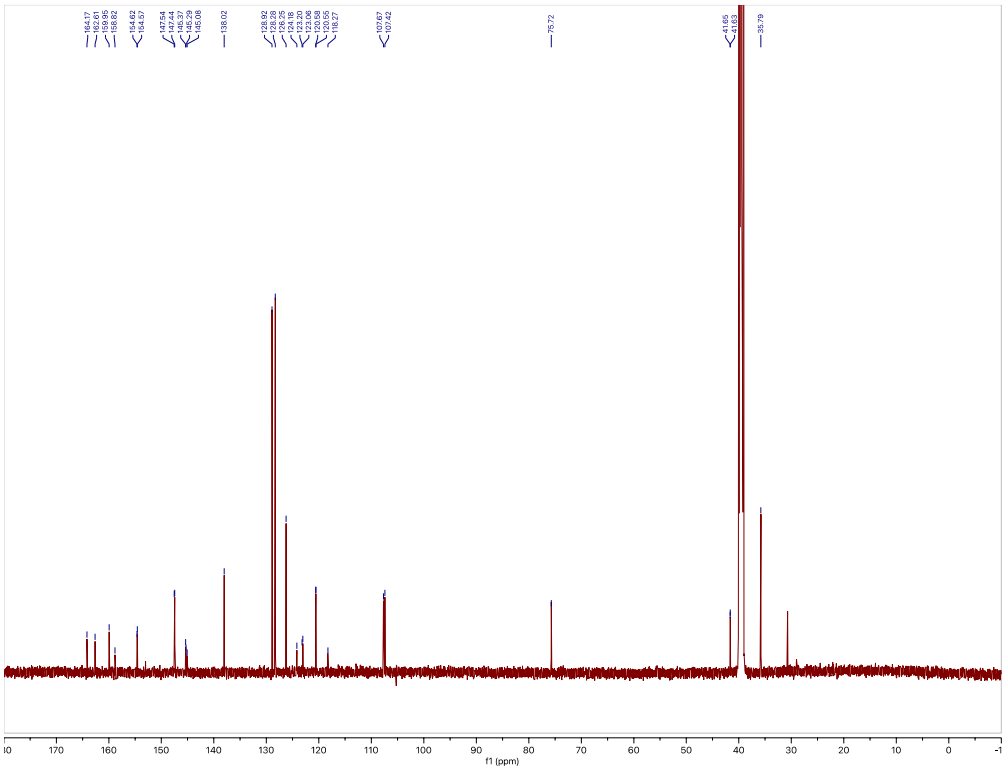

Compound 7

^{1}H-NMR (400 MHz, $CDCl_3$)

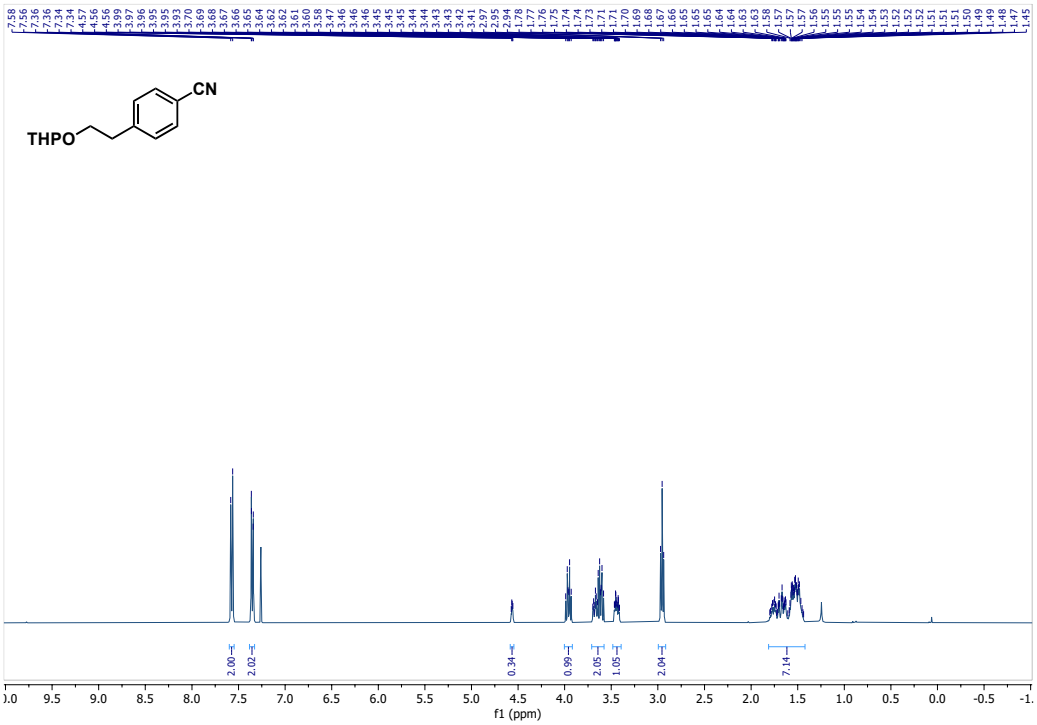

^{13}C-NMR (100 MHz, $CDCl_3$)

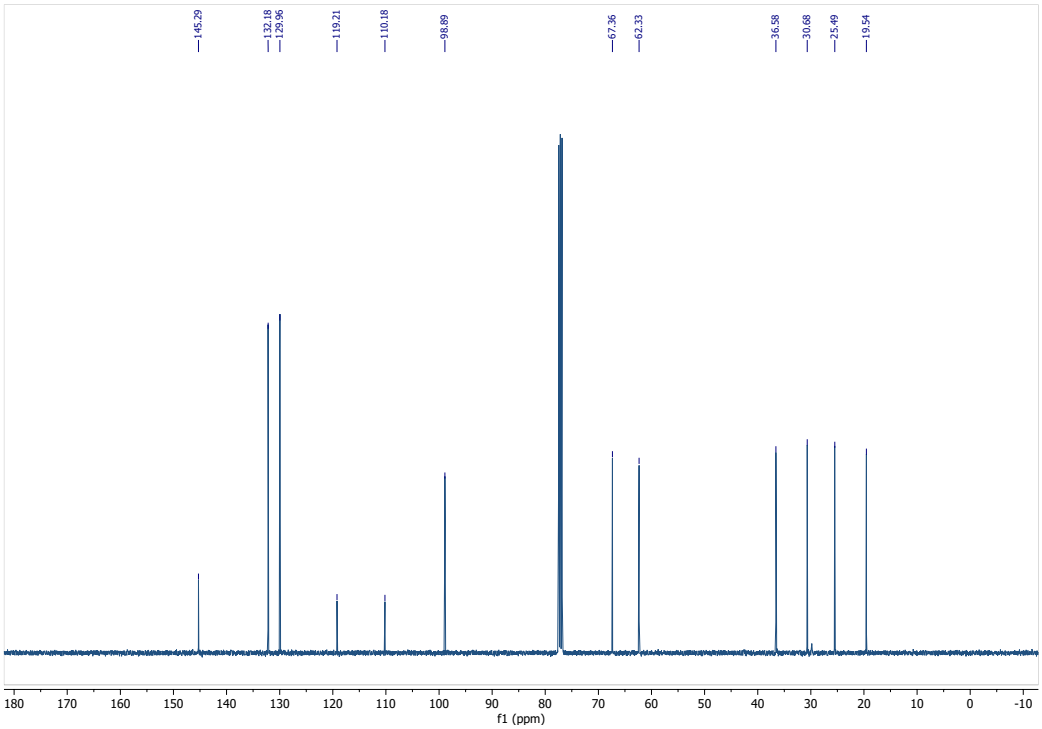

Compound 8

^{1}H-NMR (80 MHz, $(CD_3)_2SO$)

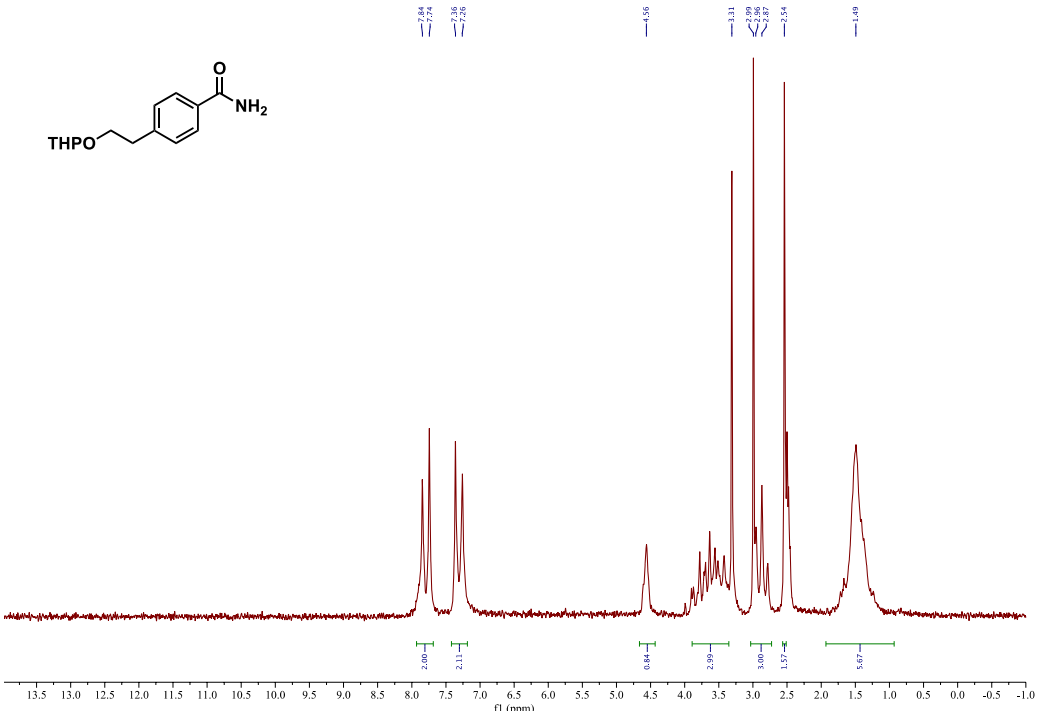

^{13}C-NMR (100 MHz, $CDCl_3$)

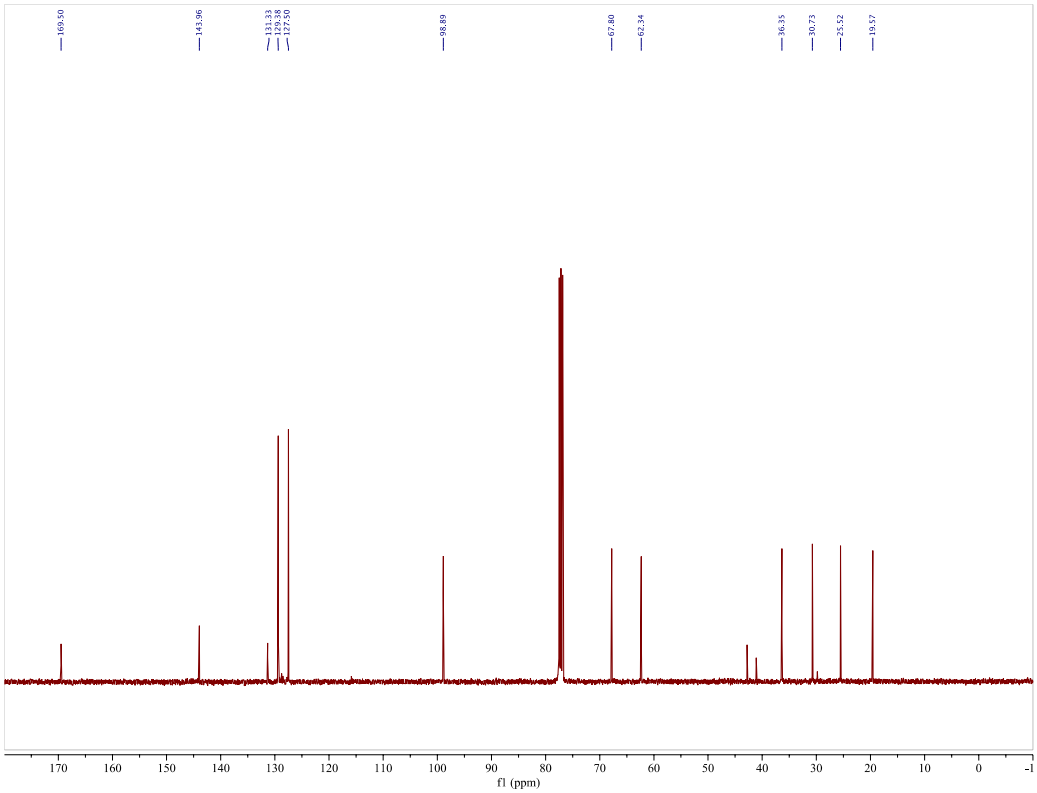

Compound 9

^{1}H-NMR (400 MHz, $(CD_3)_2SO$)

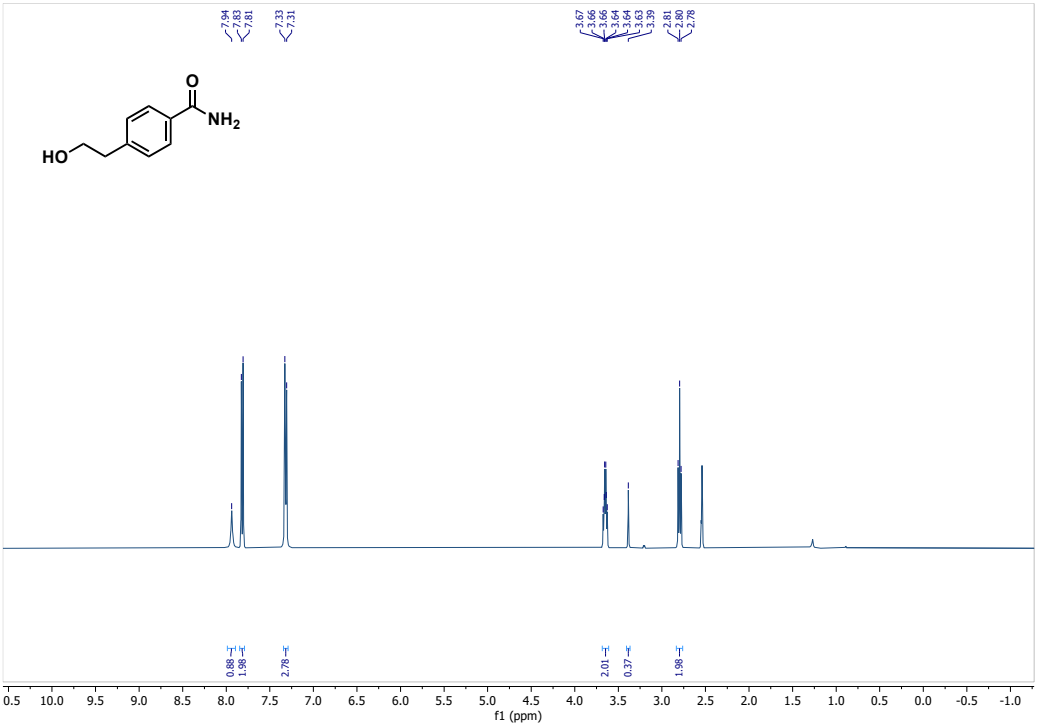

^{13}C-NMR (100 MHz, $(CD_3)_2SO$)

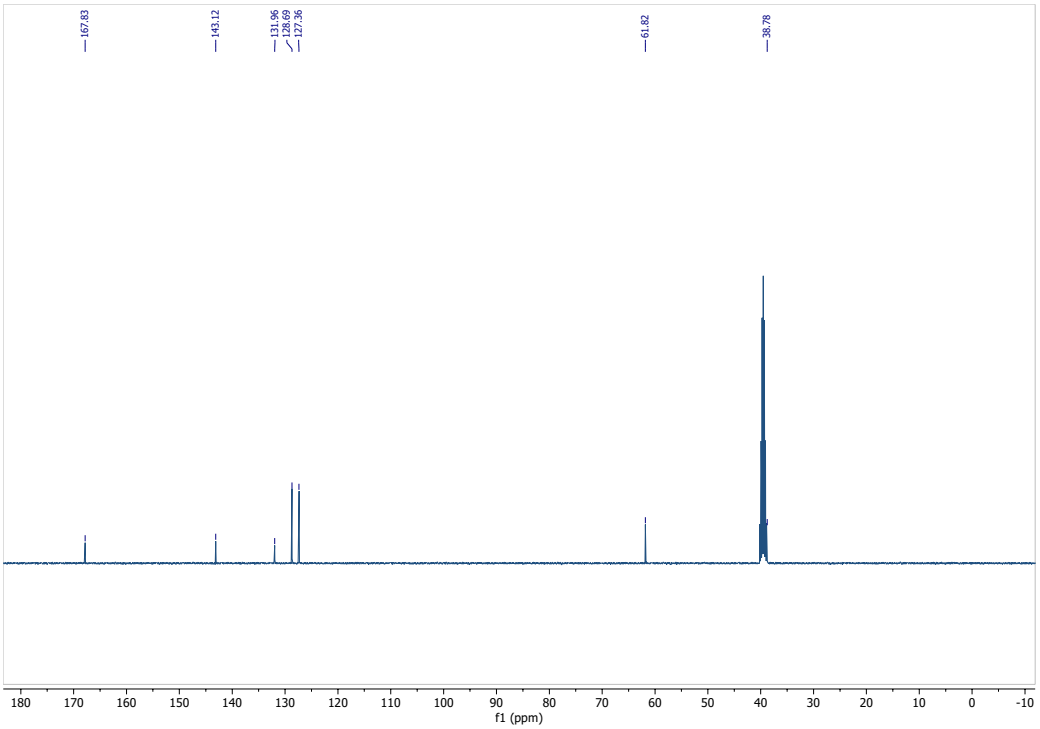

Compound 10

^{1}H-NMR (600 MHz, $(CD_3)_2SO$)

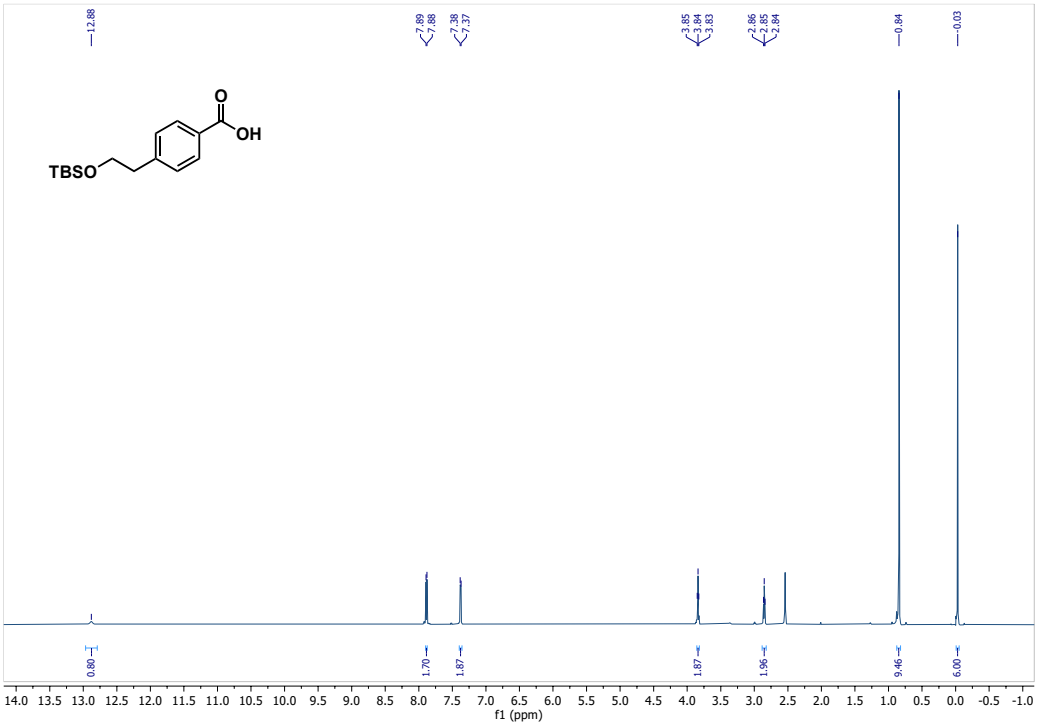

^{13}C-NMR (150 MHz, $(CD_3)_2SO$)

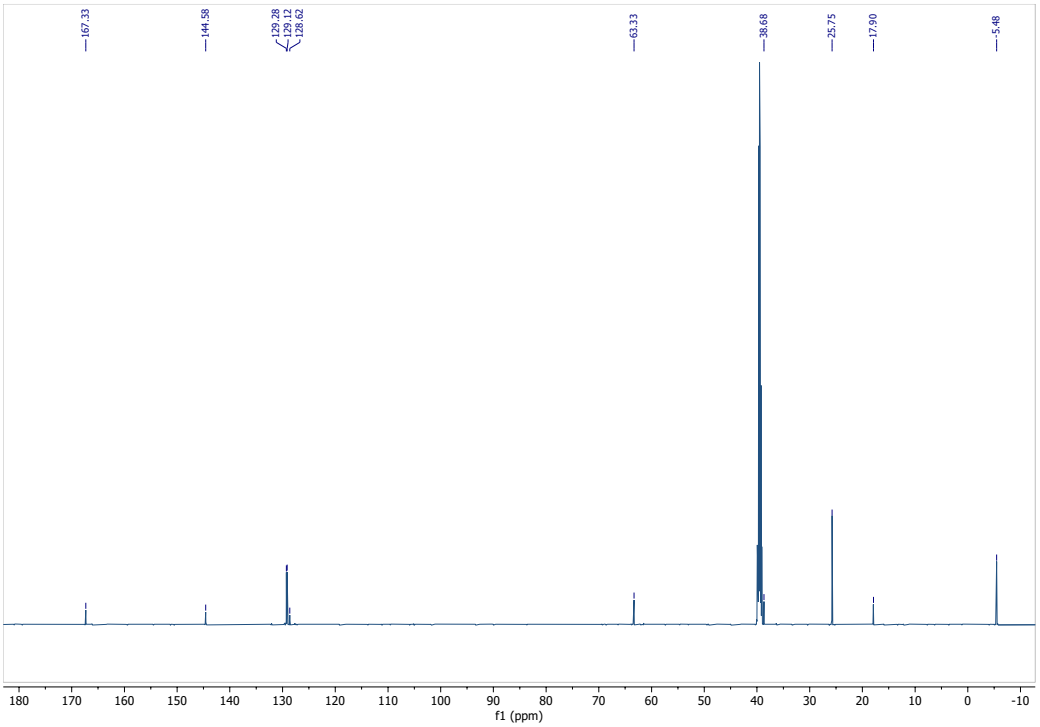

Compound 11a

^{1}H-NMR (80 MHz, $CDCl_3$)

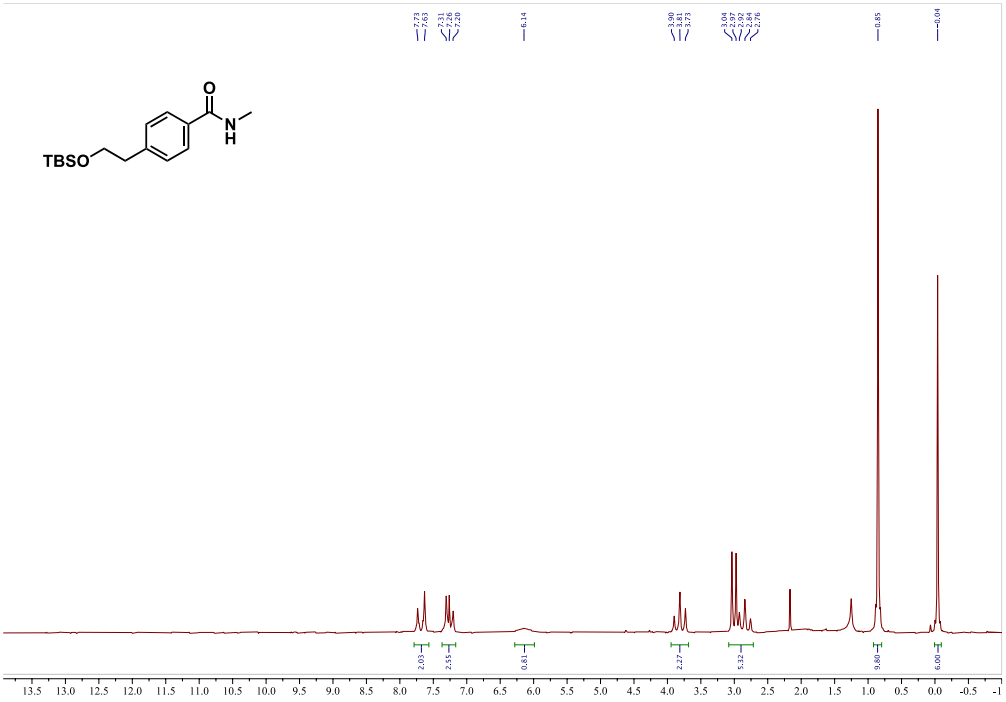

Compound 11b

^{1}H-NMR (80 MHz, $(CD_3)_2SO$)

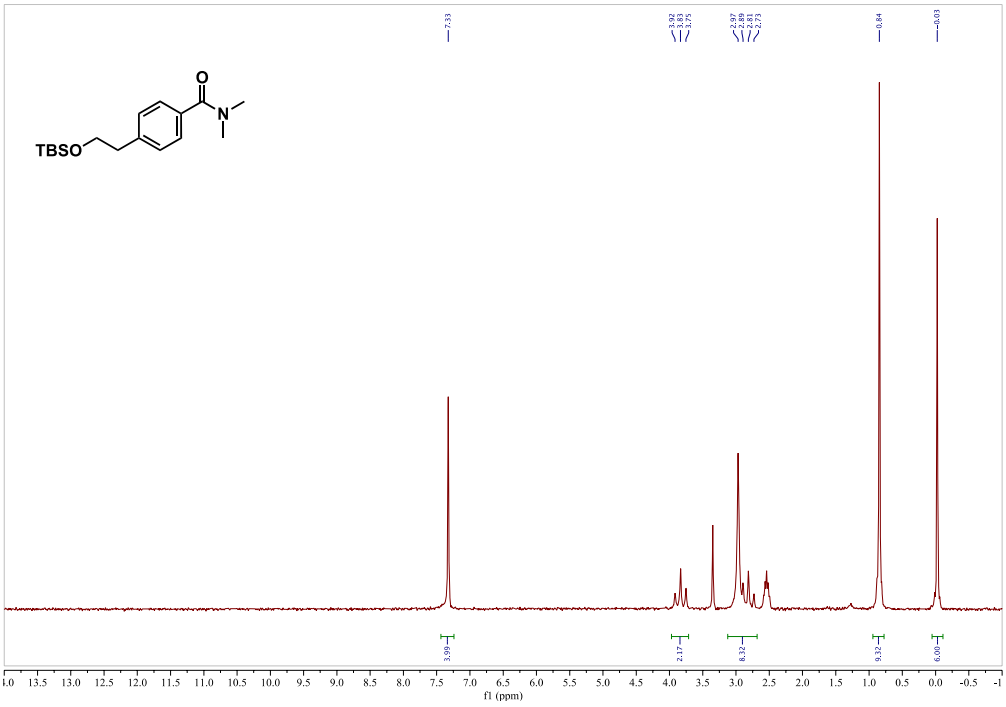

Compound 12a

^{1}H-NMR (600 MHz, $(CD_3)_2SO$)

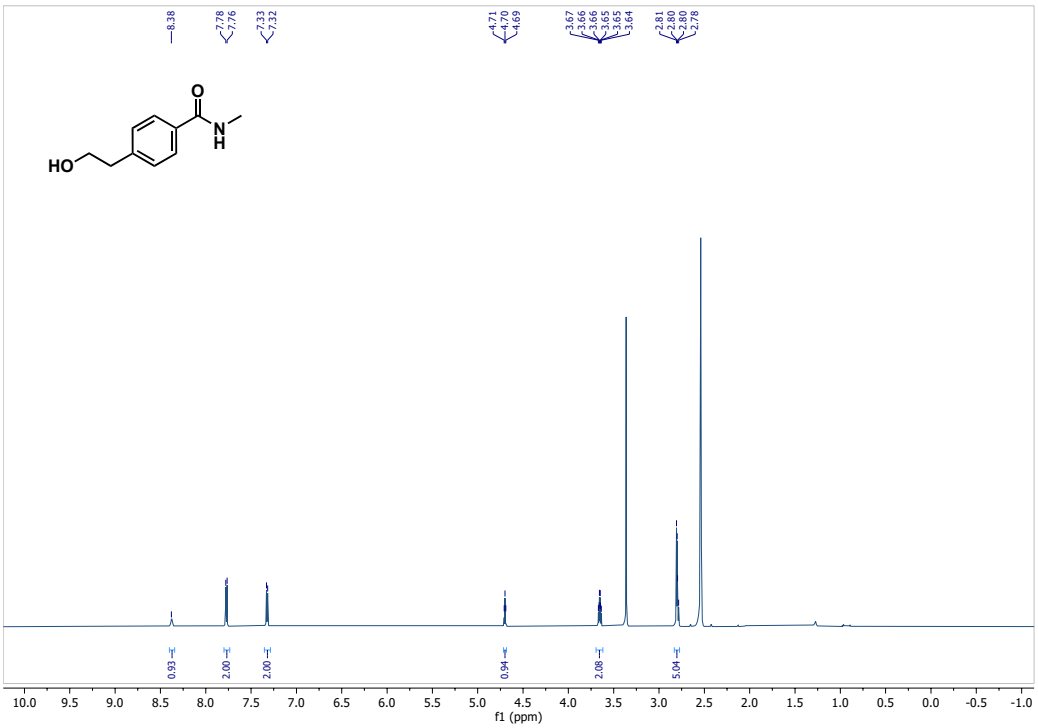

^{13}C-NMR (150 MHz, $(CD_3)_2SO$)

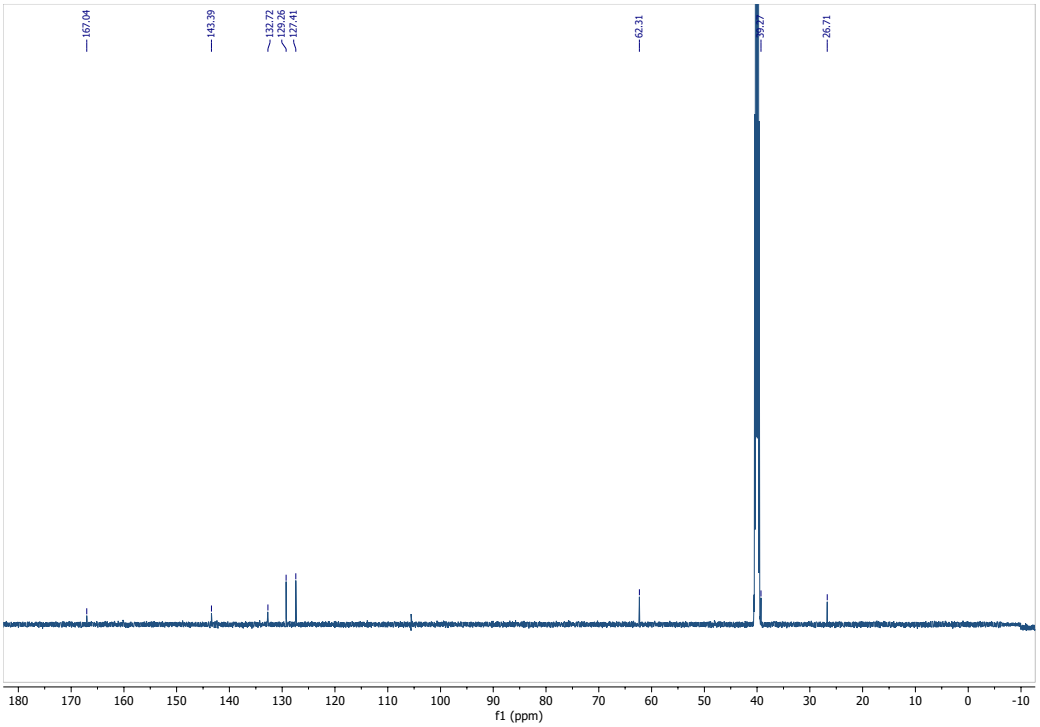

Compound 12b

^{1}H-NMR (600 MHz, $(CD_3)_2SO$)

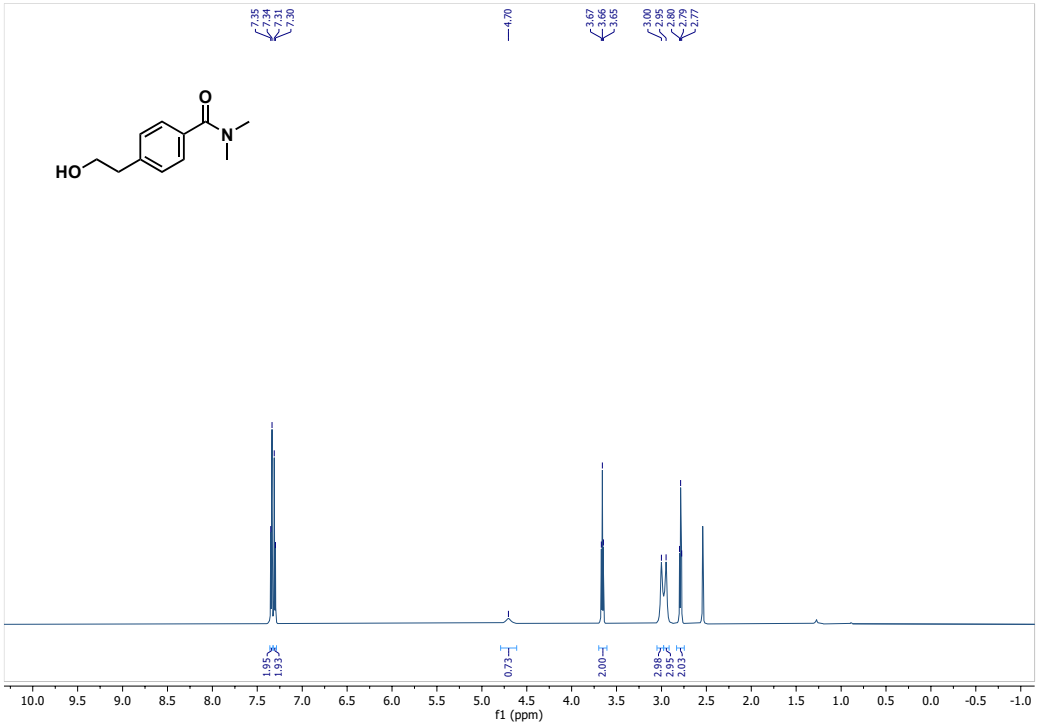

^{13}C-NMR (150 MHz, $(CD_3)_2SO$)

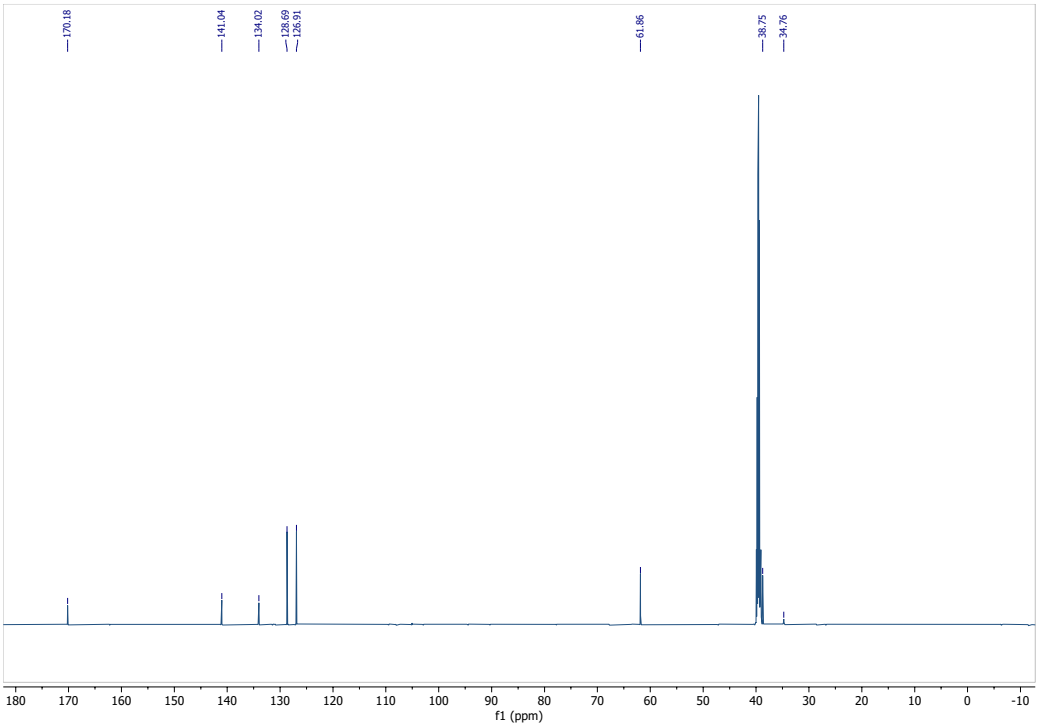

Compound 13

^{1}H-NMR (600 MHz, $(CD_3)_2SO$)

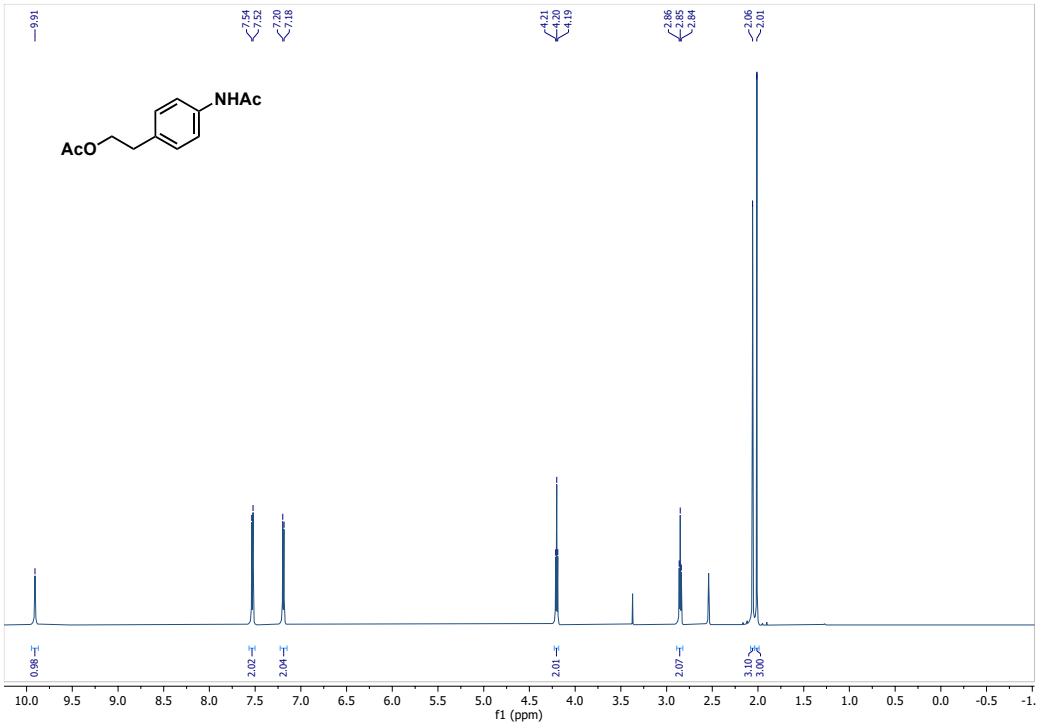

^{13}C-NMR (150 MHz, $(CD_3)_2SO$)

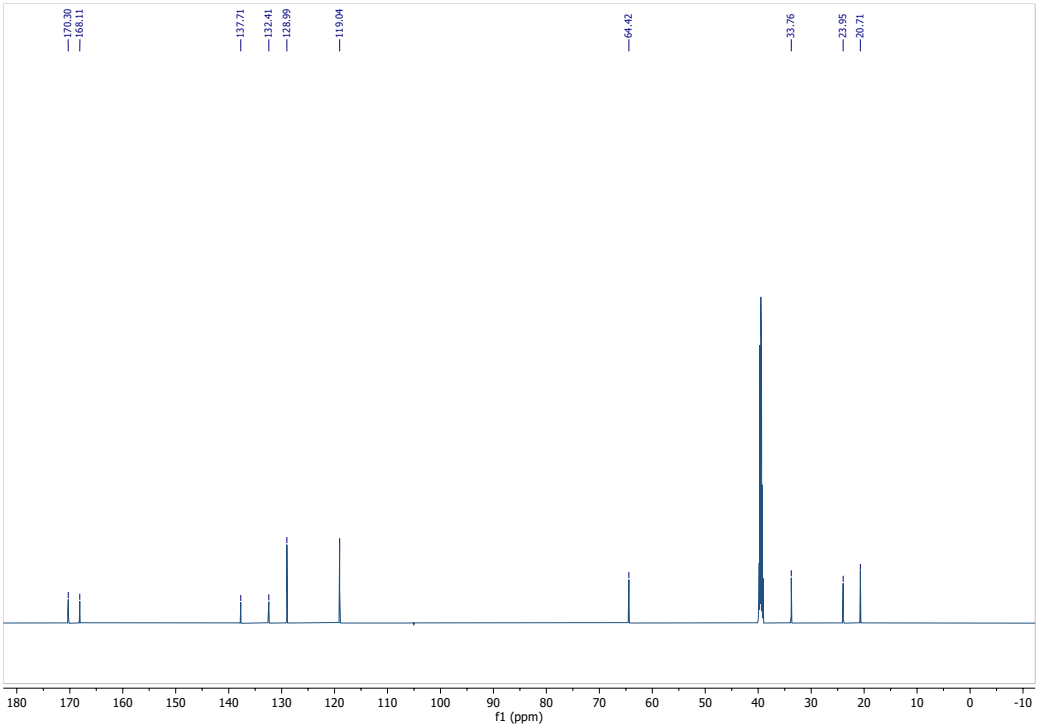

Compound 14

^{1}H-NMR (600 MHz, $(CD_3)_2SO$)

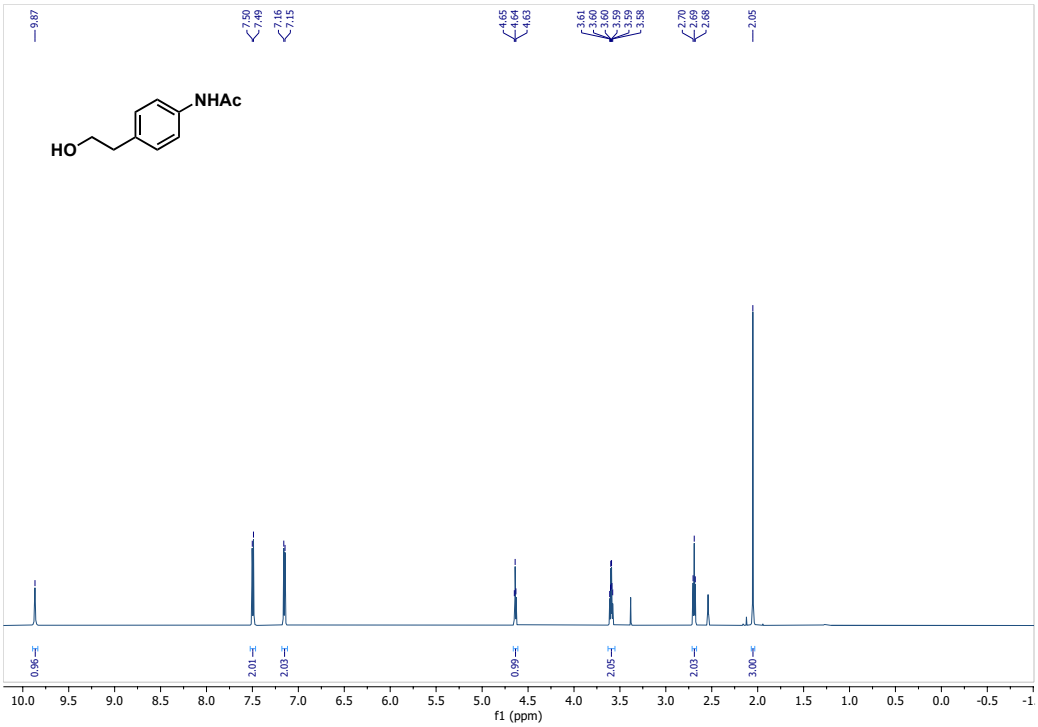

^{13}C-NMR (150 MHz, $(CD_3)_2SO$)

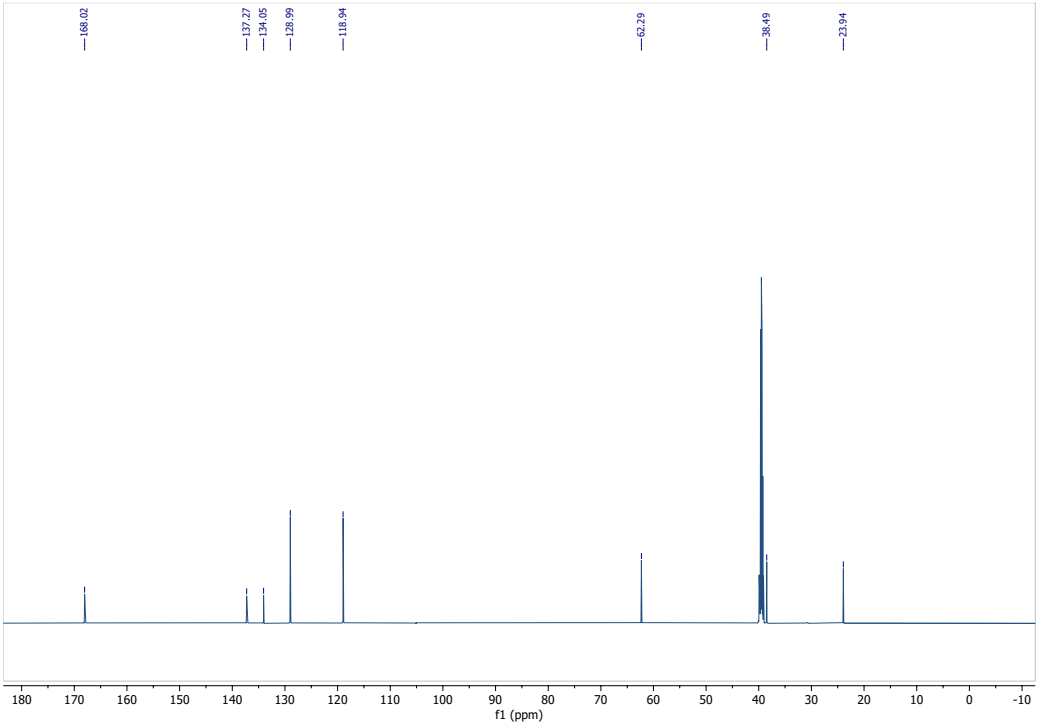

Compound 15

^{1}H-NMR (600 MHz, $(CD_3)_2SO$)

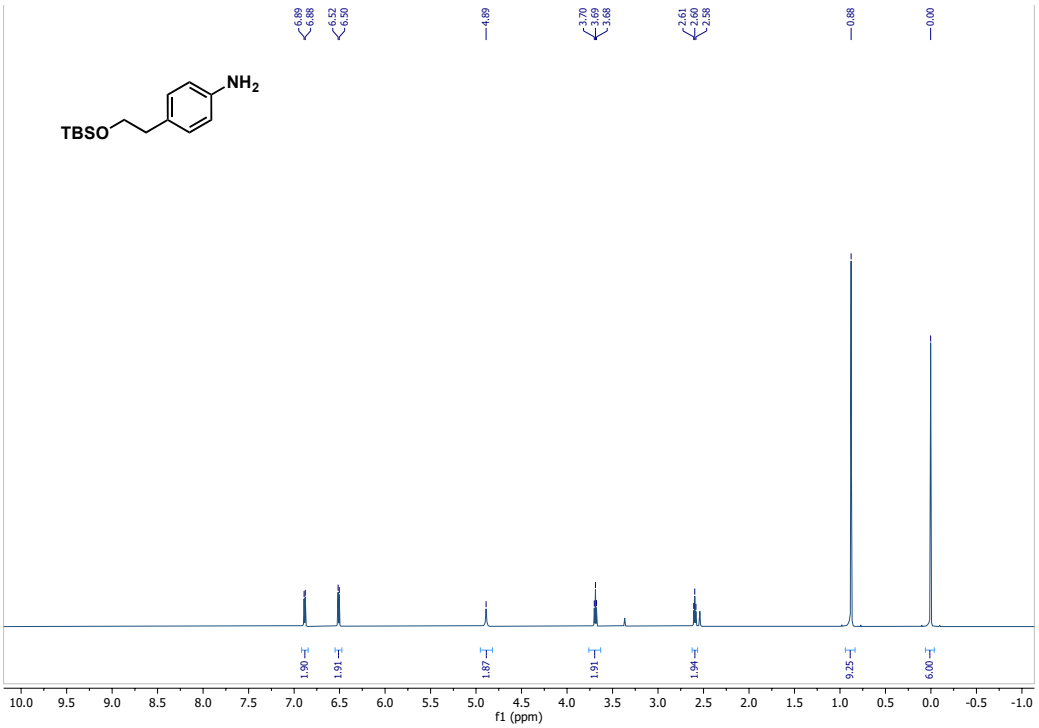

^{13}C-NMR (150 MHz, $(CD_3)_2SO$)

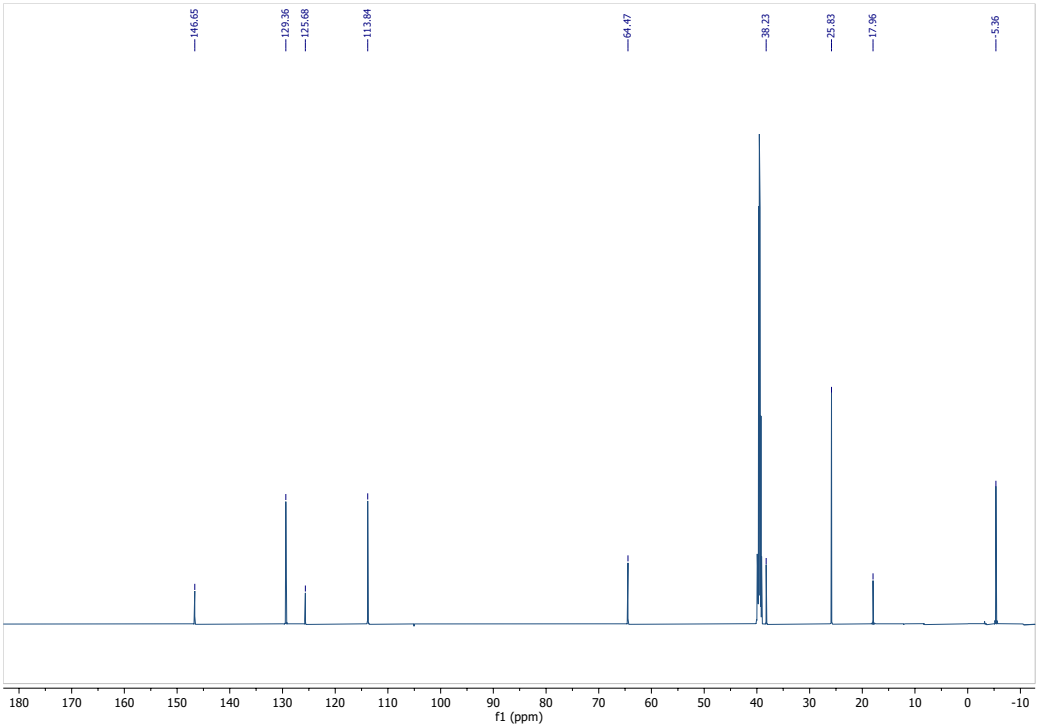

Compound 16

^{1}H-NMR (80 MHz, $(CD_3)_2SO$)

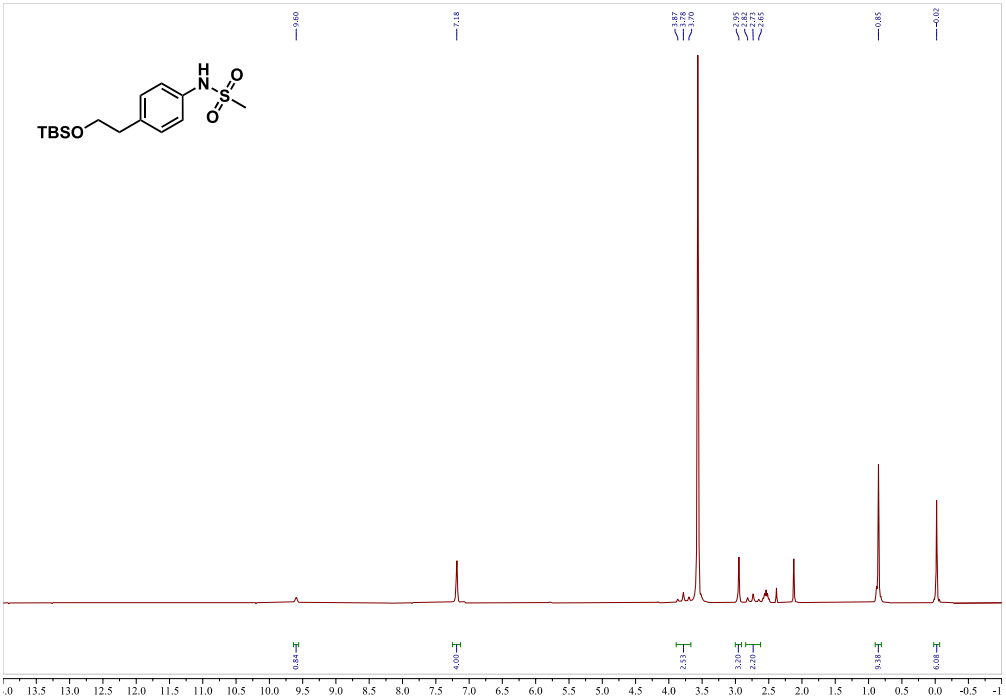

^{13}C-NMR (150 MHz, $(CD_3)_2SO$)

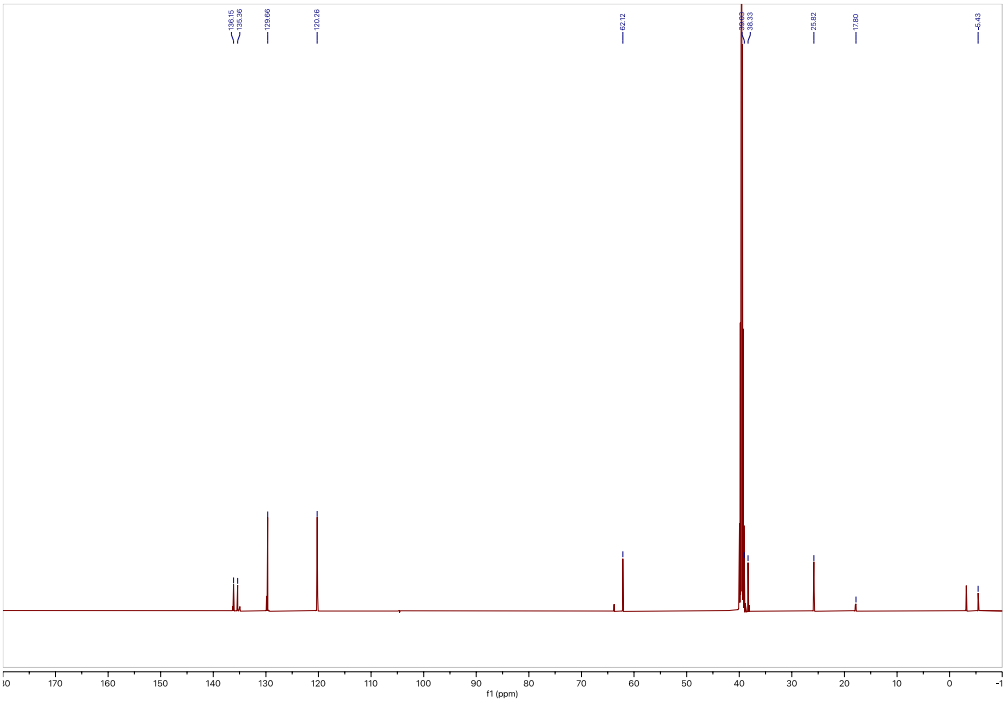

Compound 17

^{1}H-NMR (600 MHz, $(CD_3)_2SO$)

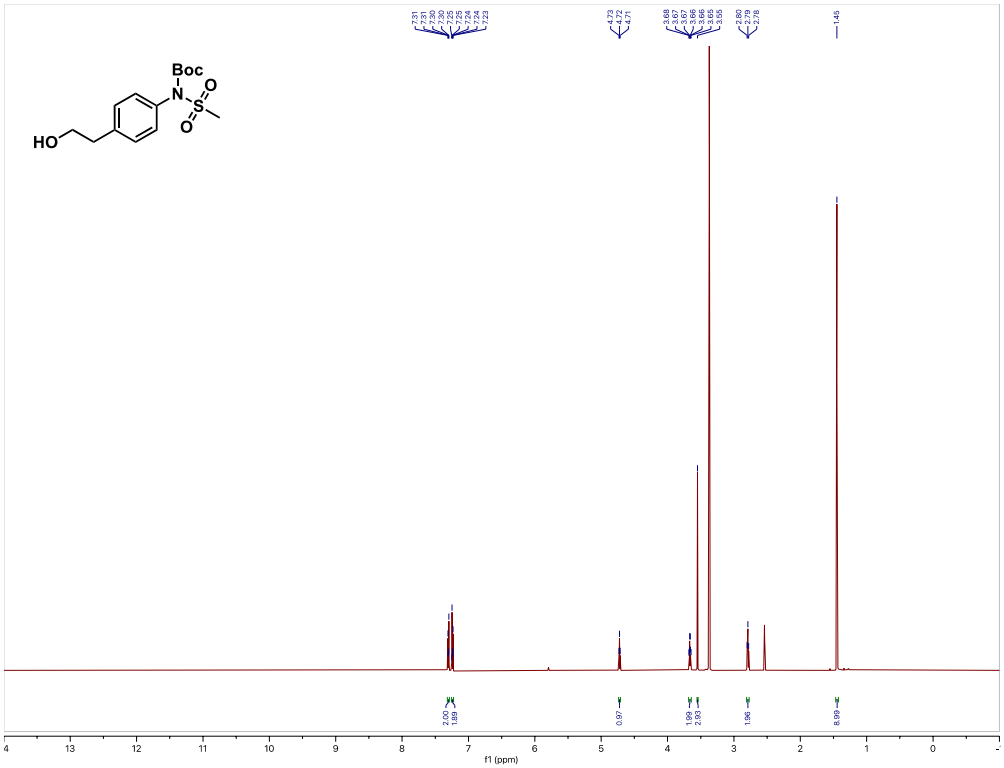

^{13}C-NMR (150 MHz, $(CD_3)_2SO$)

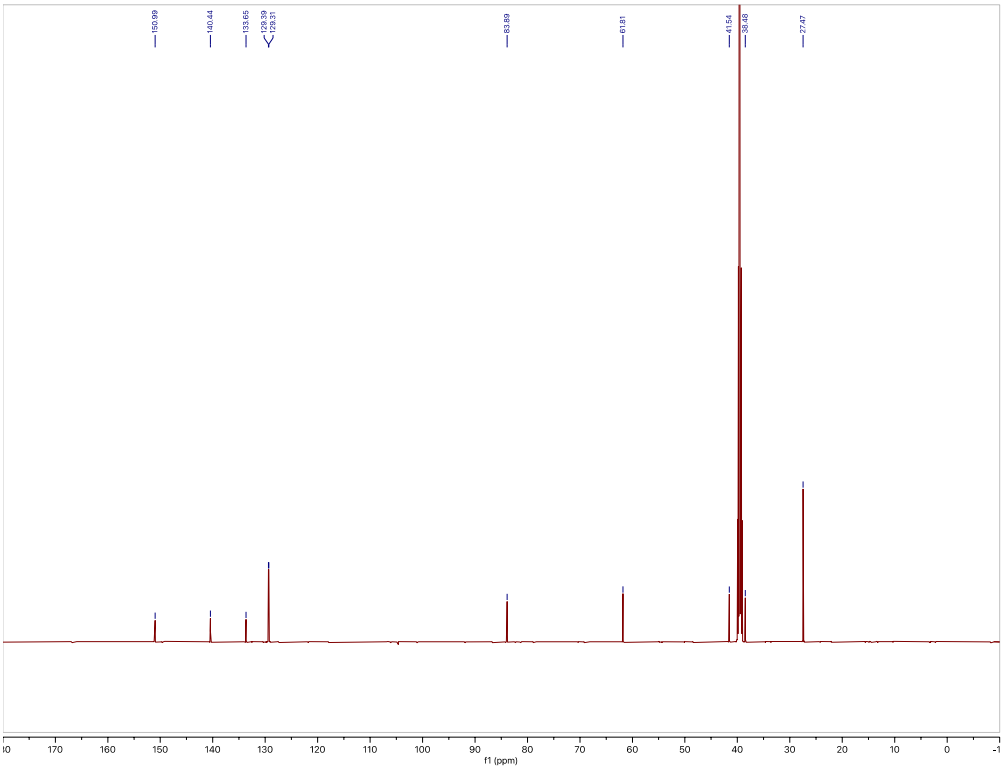

Compound 18

^{1}H-NMR (600 MHz, $(CD_3)_2SO$)

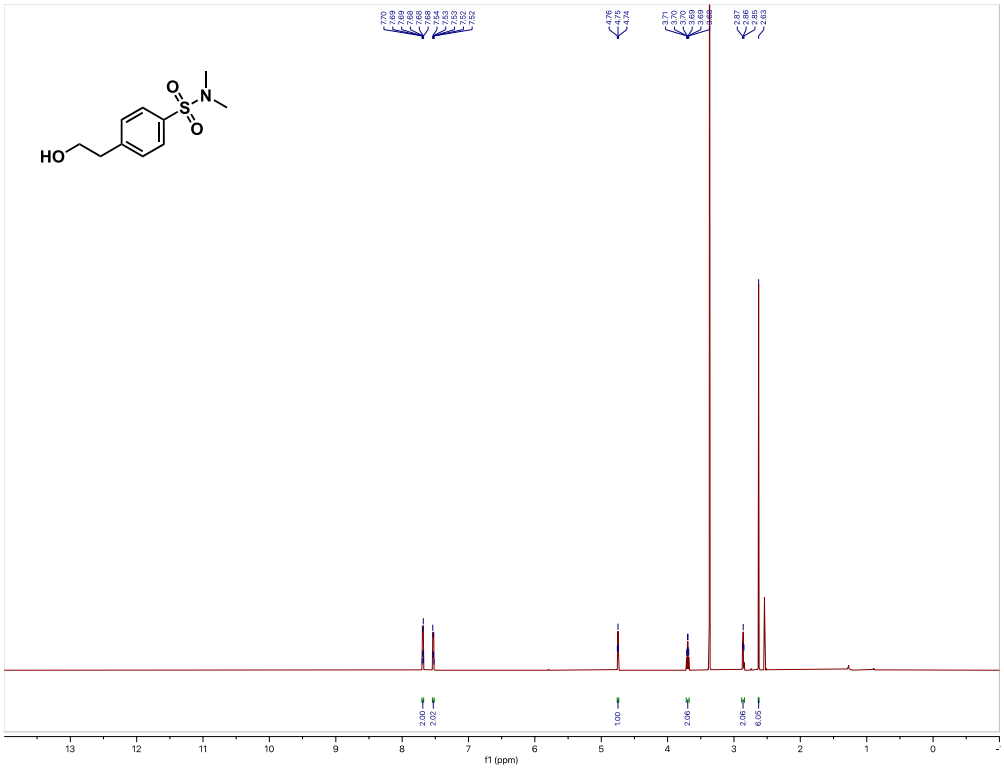

^{13}C-NMR (150 MHz, $(CD_3)_2SO$)

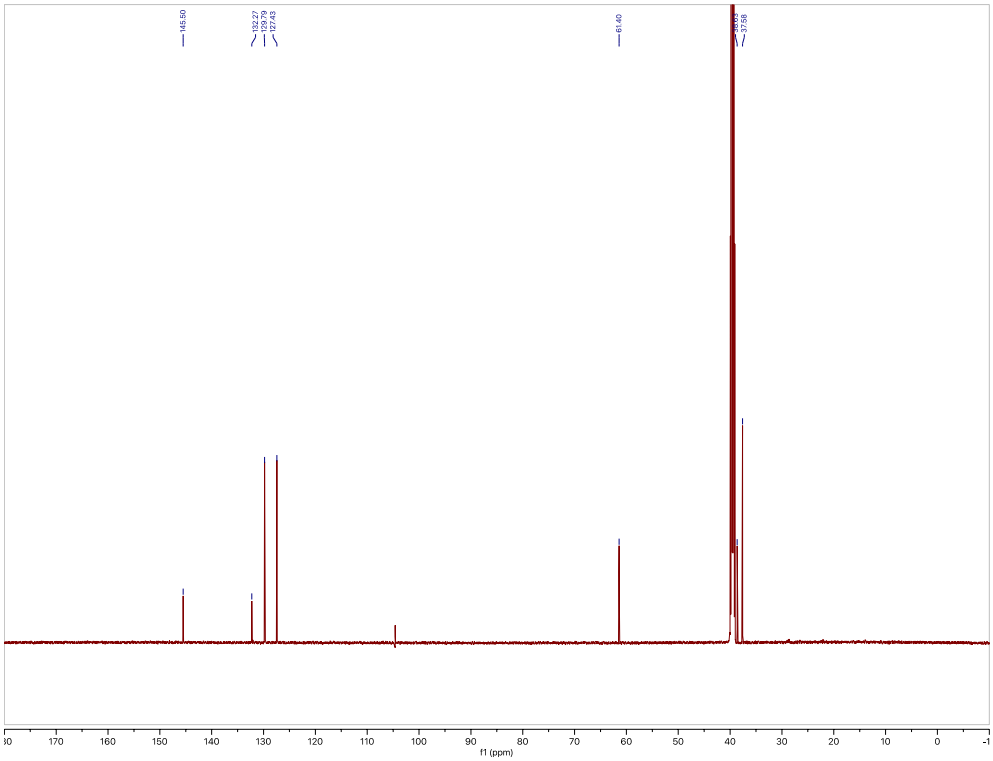

Compound 19

^{1}H-NMR (80 MHz, $CDCl_3$)

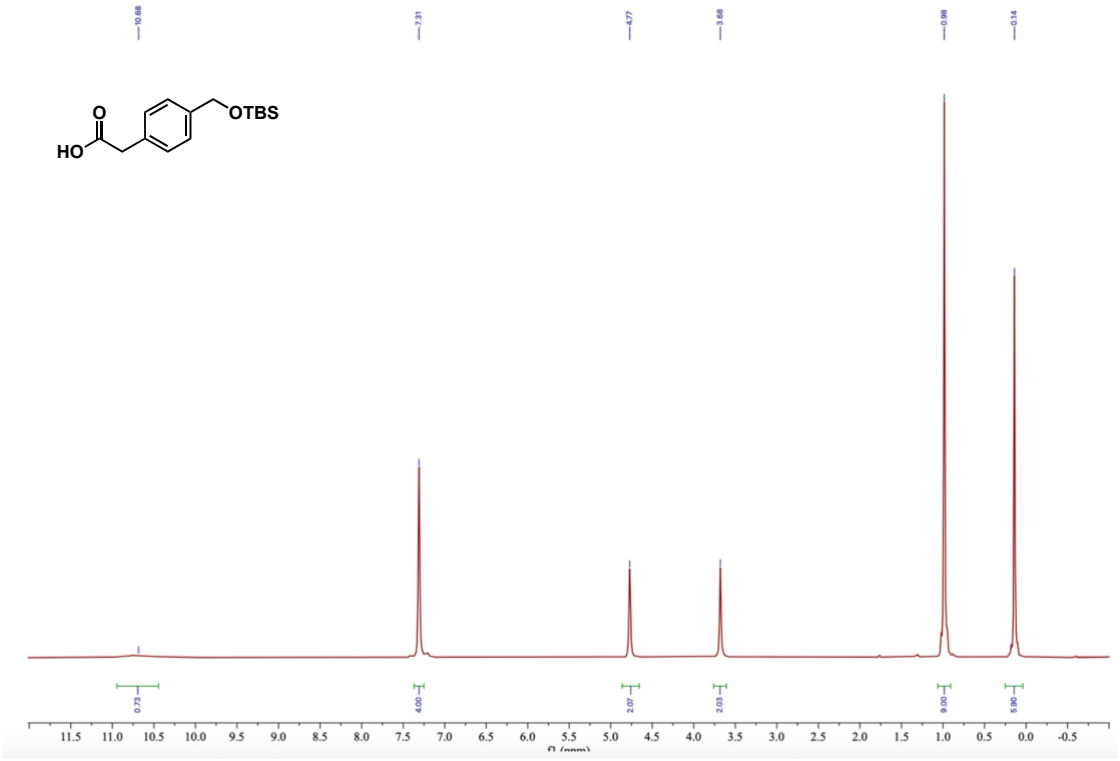

^{13}C-NMR (100 MHz, $CDCl_3$)

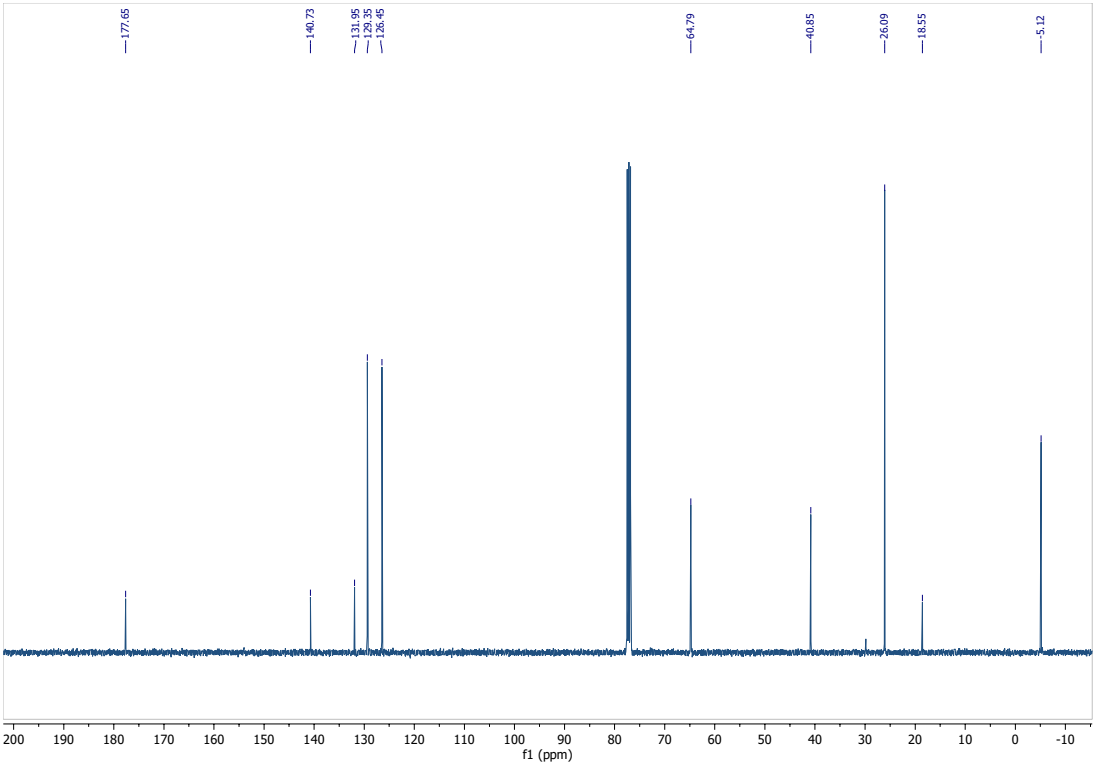

Compound 20

^{1}H-NMR (600 MHz, $(CD_3)_2SO$)

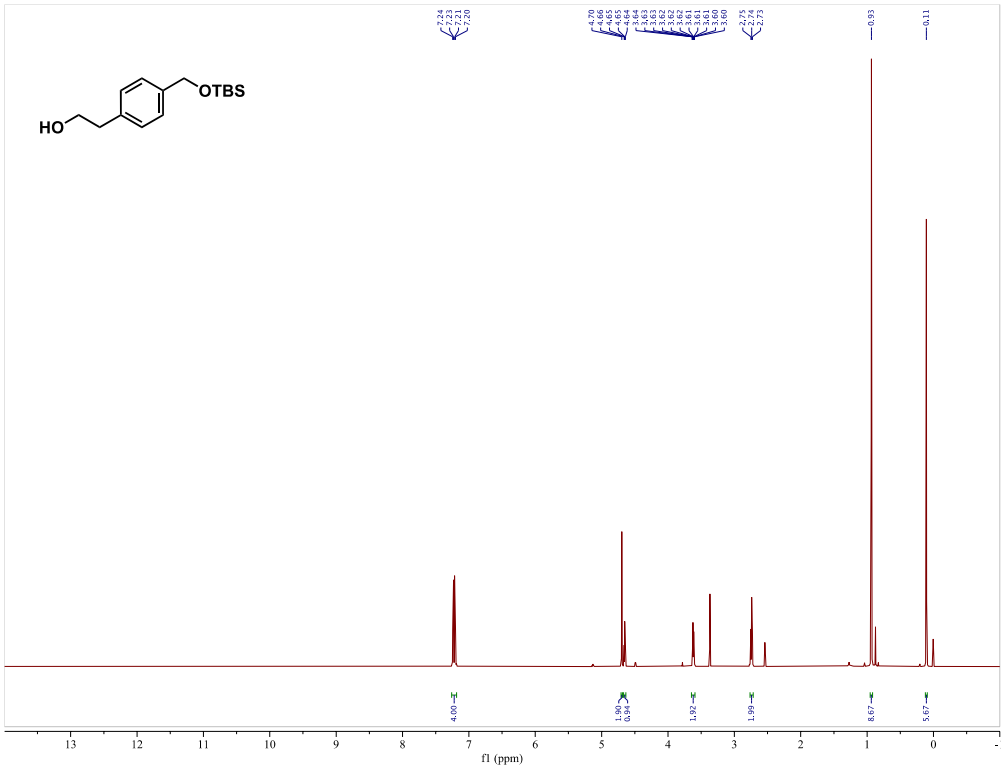

^{13}C-NMR (150 MHz, $(CD_3)_2SO$)

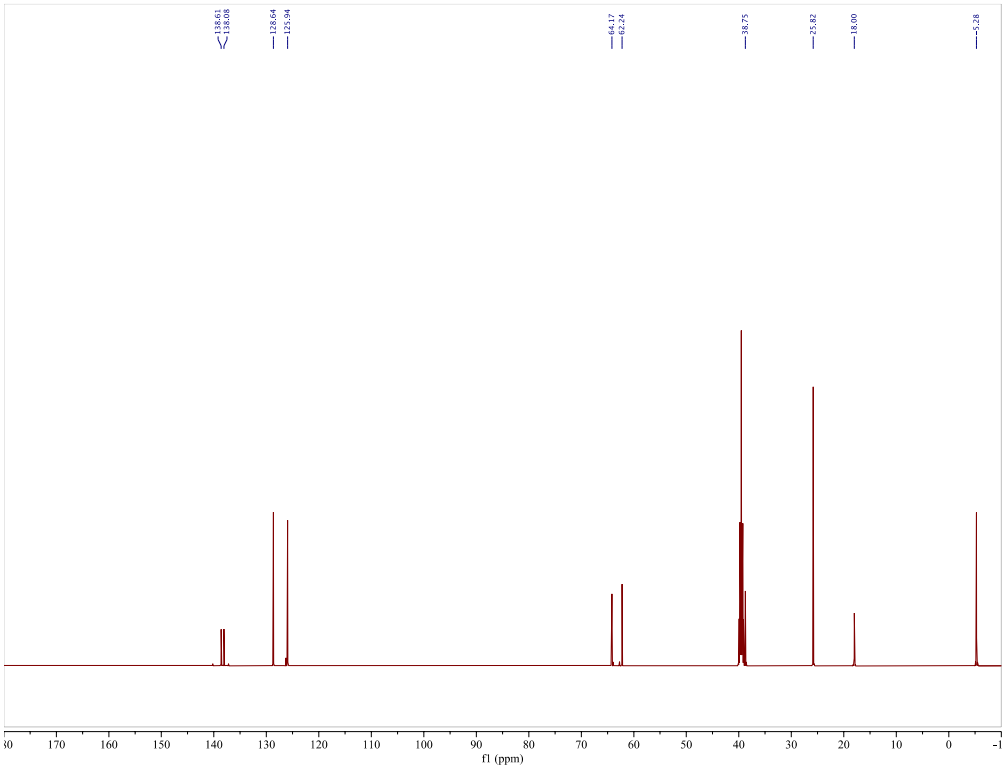

Compound 21

^{1}H-NMR (400 MHz, $CDCl_3$)

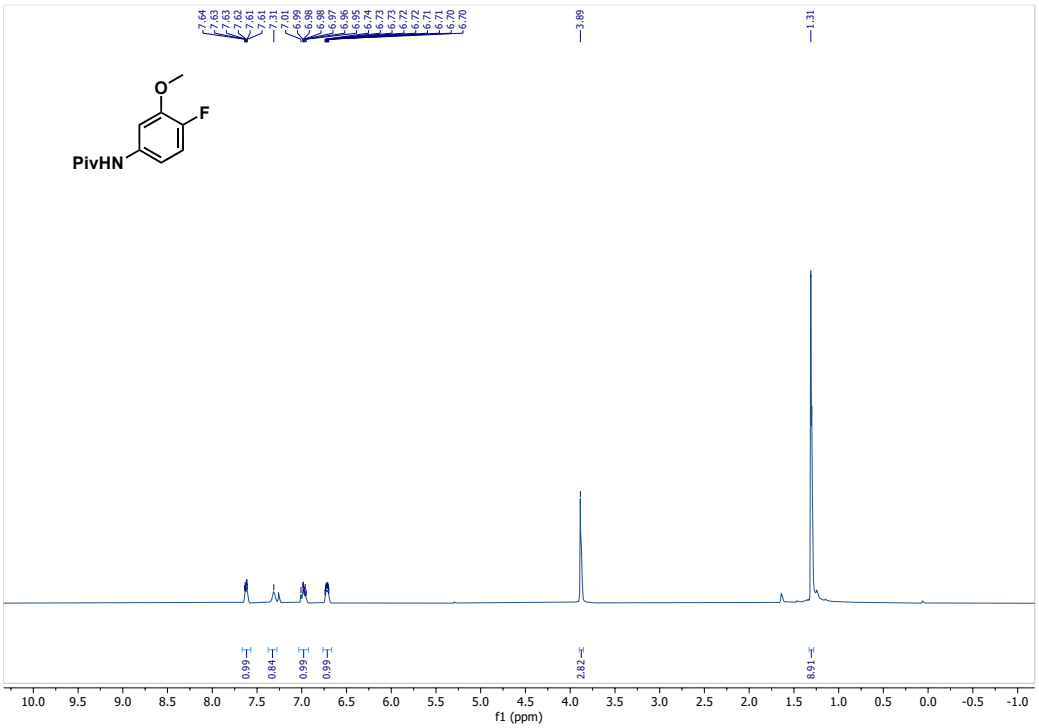

^{13}C-NMR (100 MHz, $CDCl_3$)

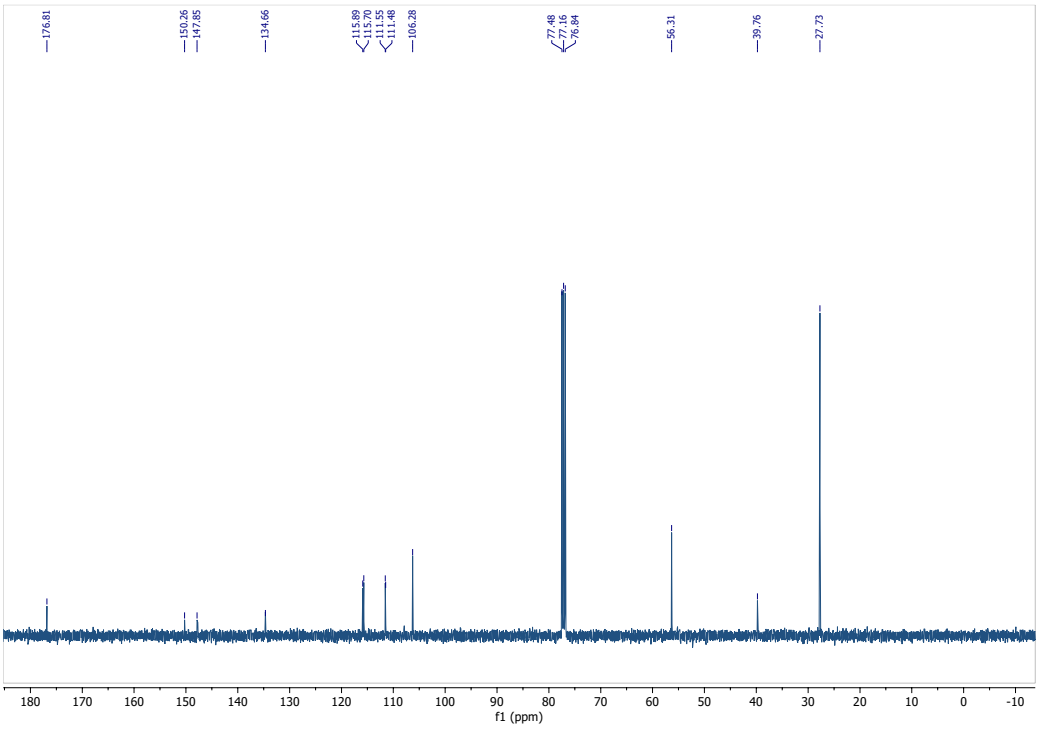

Compound 22

^{1}H-NMR (400 MHz, $CDCl_3$)

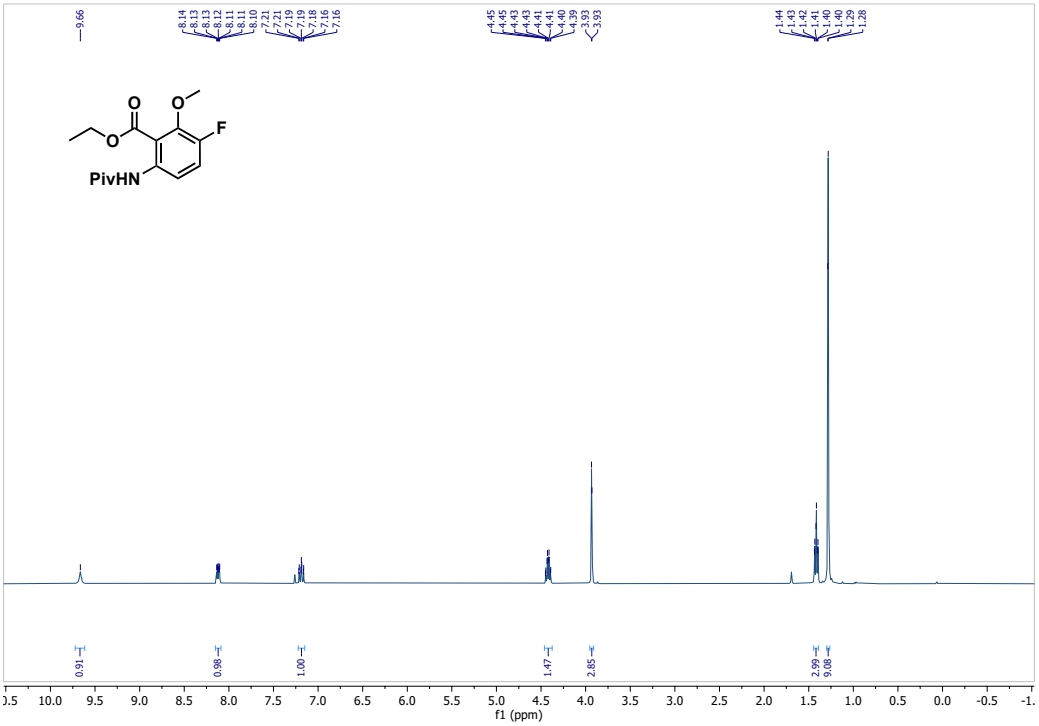

^{13}C-NMR (100 MHz, $CDCl_3$)

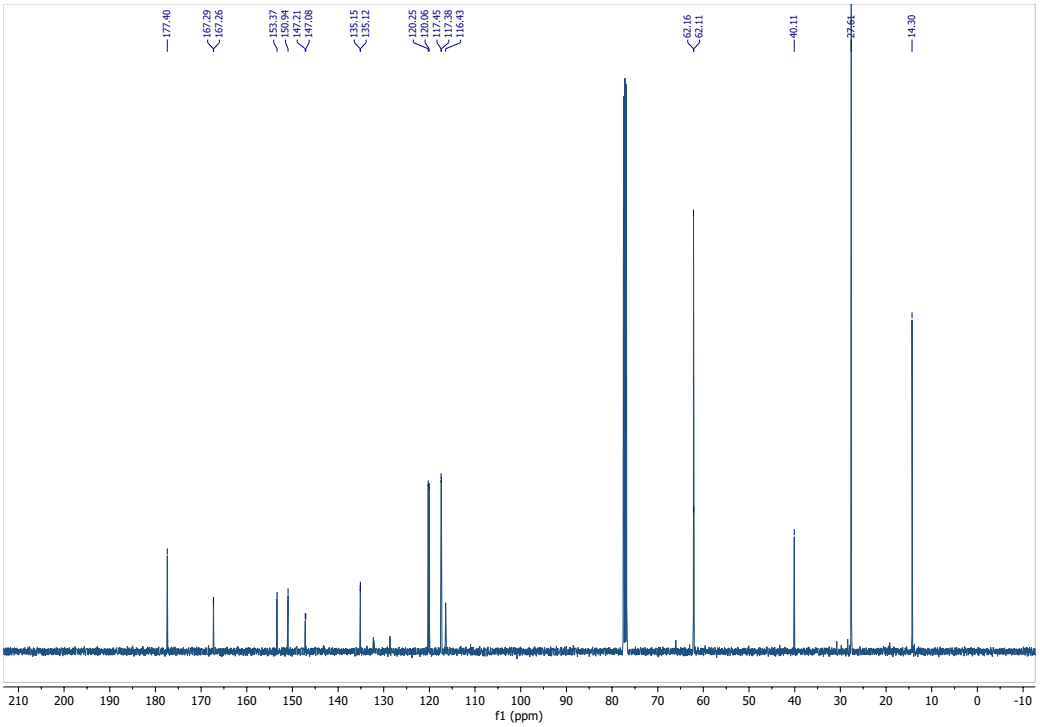

Compound 23

^{1}H-NMR (400 MHz, $(CD_3)_2SO$)

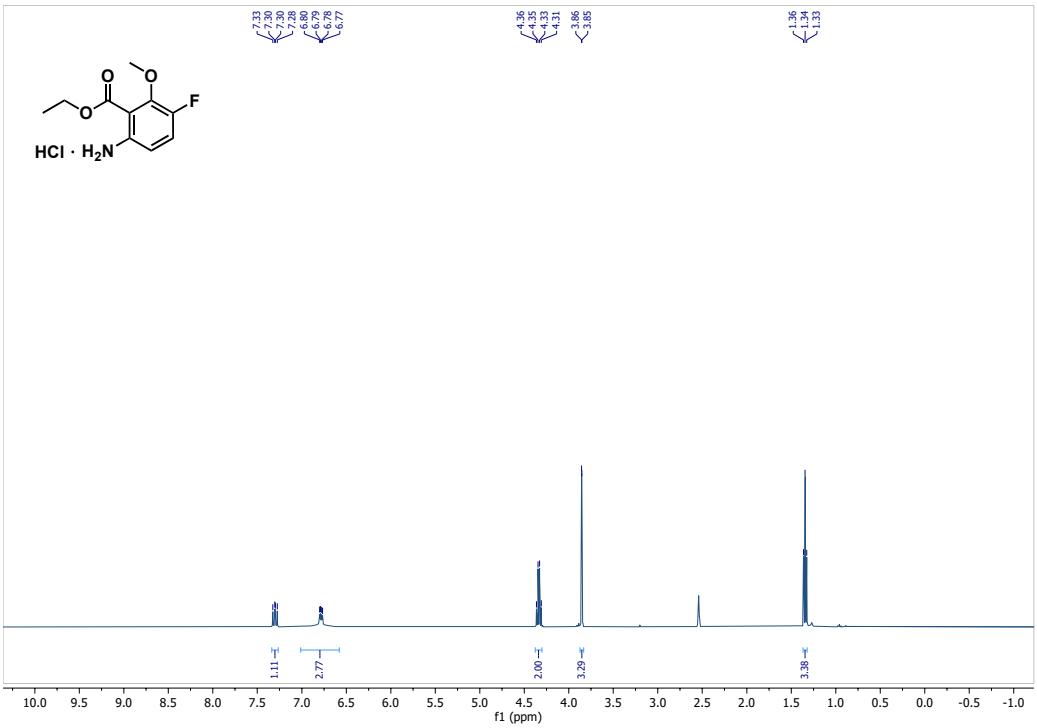

^{13}C-NMR (100 MHz, $(CD_3)_2SO$)

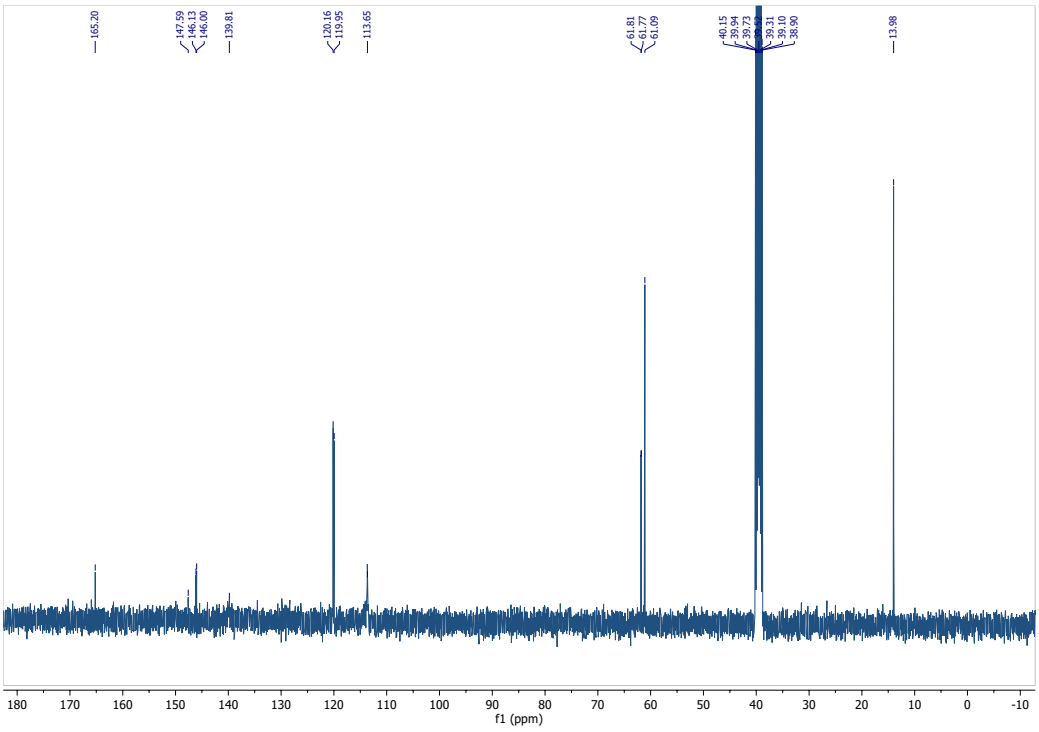

Compound 24

^{1}H-NMR (400 MHz, $CDCl_3$)

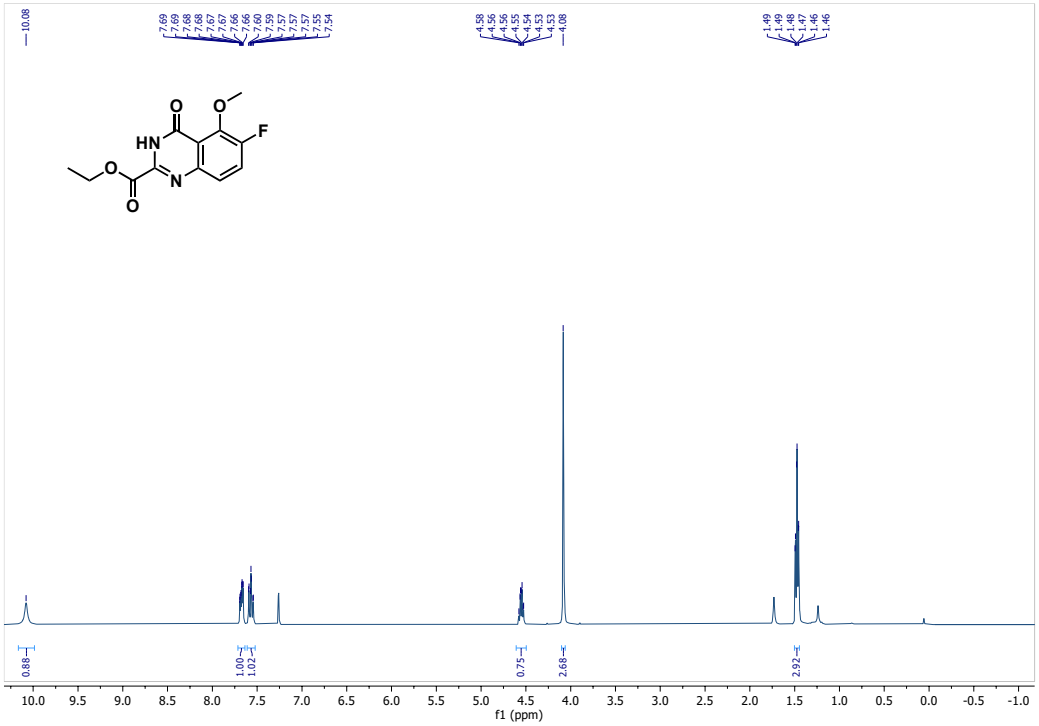

^{13}C-NMR (100 MHz, $CDCl_3$)

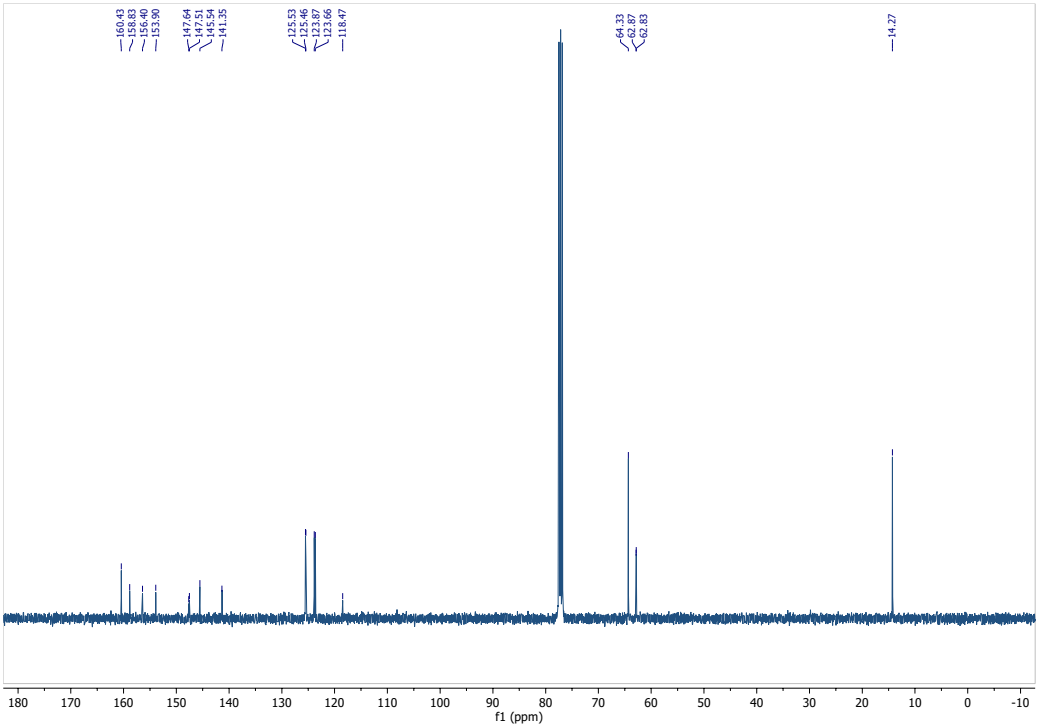

Compound 25

^{1}H-NMR (80 MHz, $(CD_3)_2SO$)

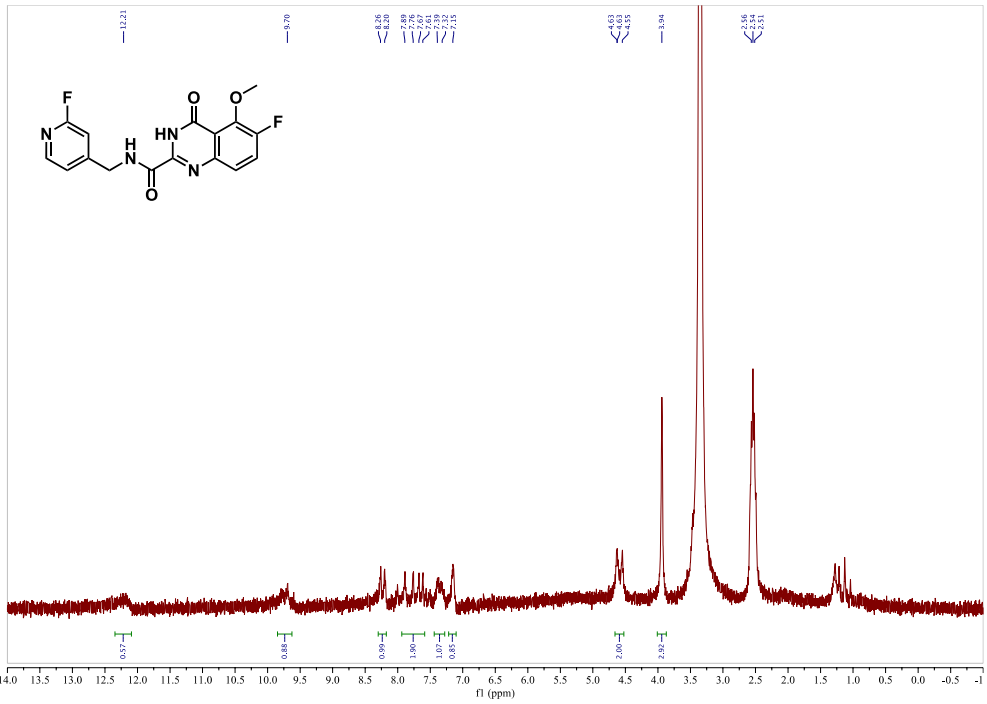

^{13}C-NMR (150 MHz, $(CD_3)_2SO$)

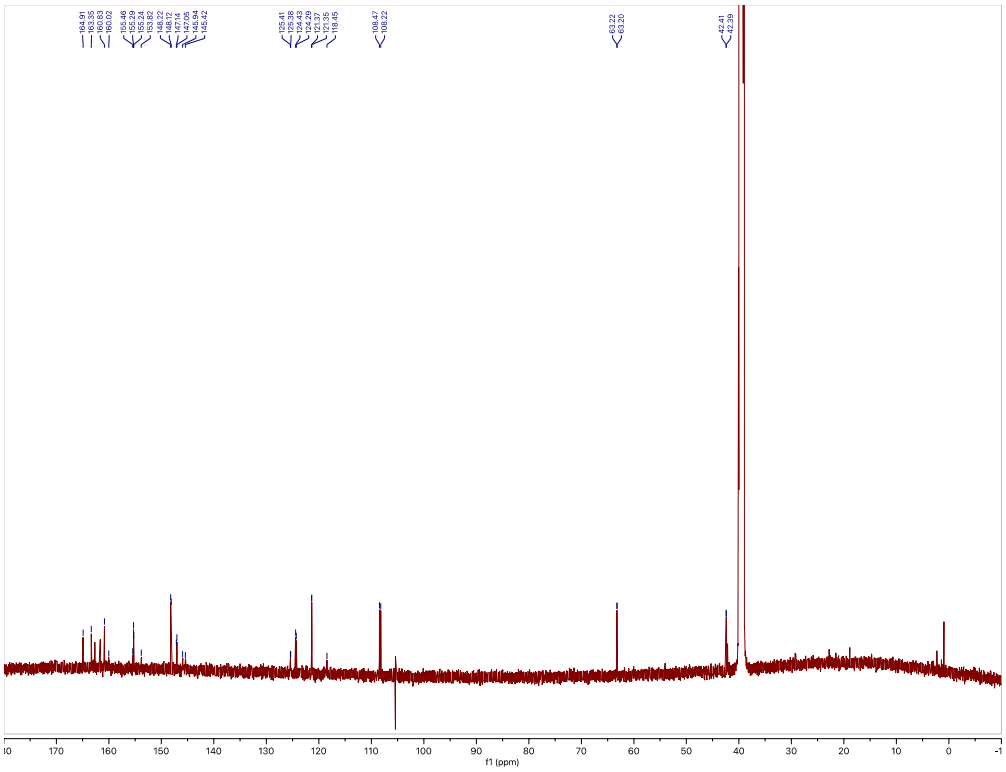

Compound 26

^{1}H-NMR (600 MHz, $(CD_3)_2SO$)

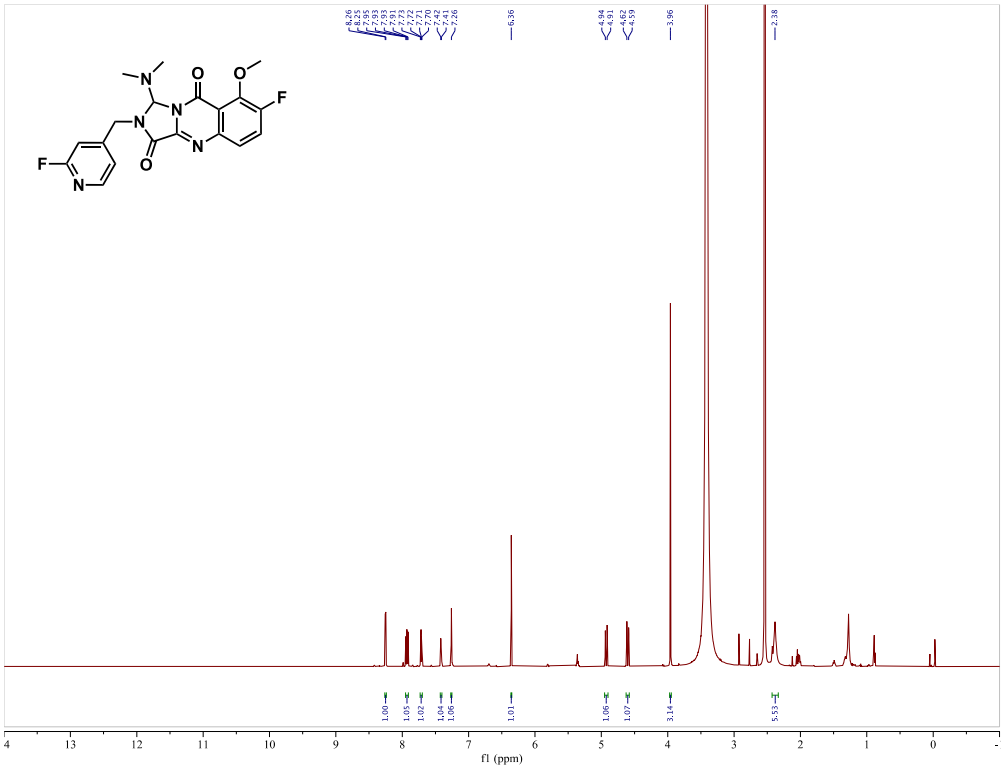

^{13}C-NMR (150 MHz, $(CD_3)_2SO$)

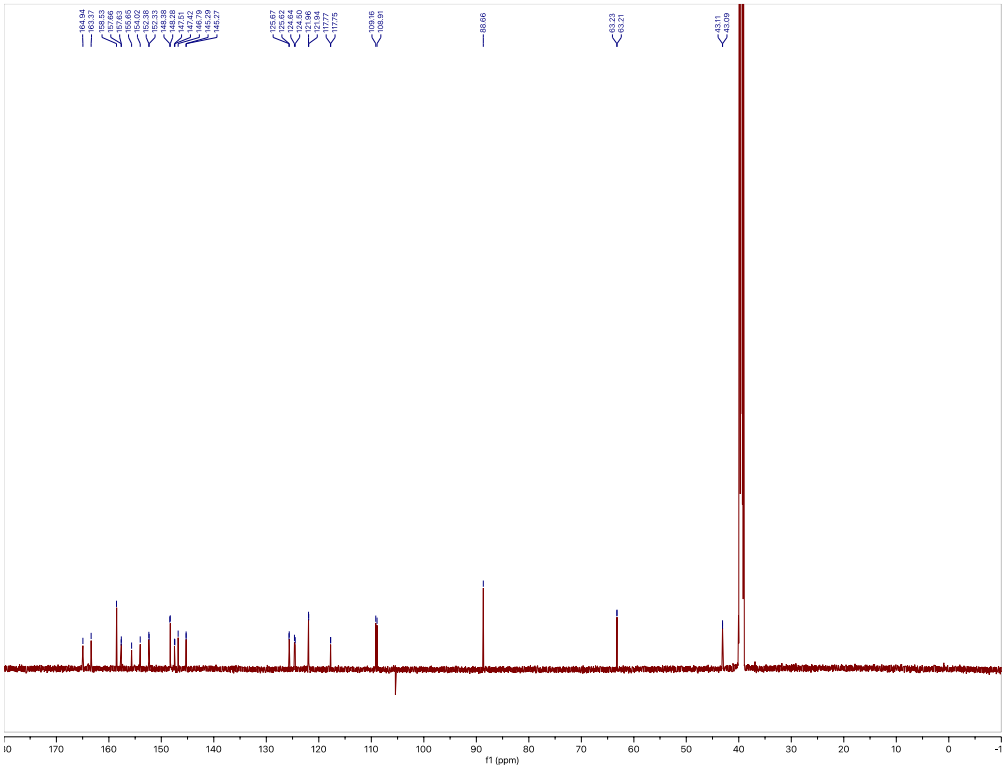

Compound 27

^{1}H-NMR (600 MHz, $CDCl_3$)

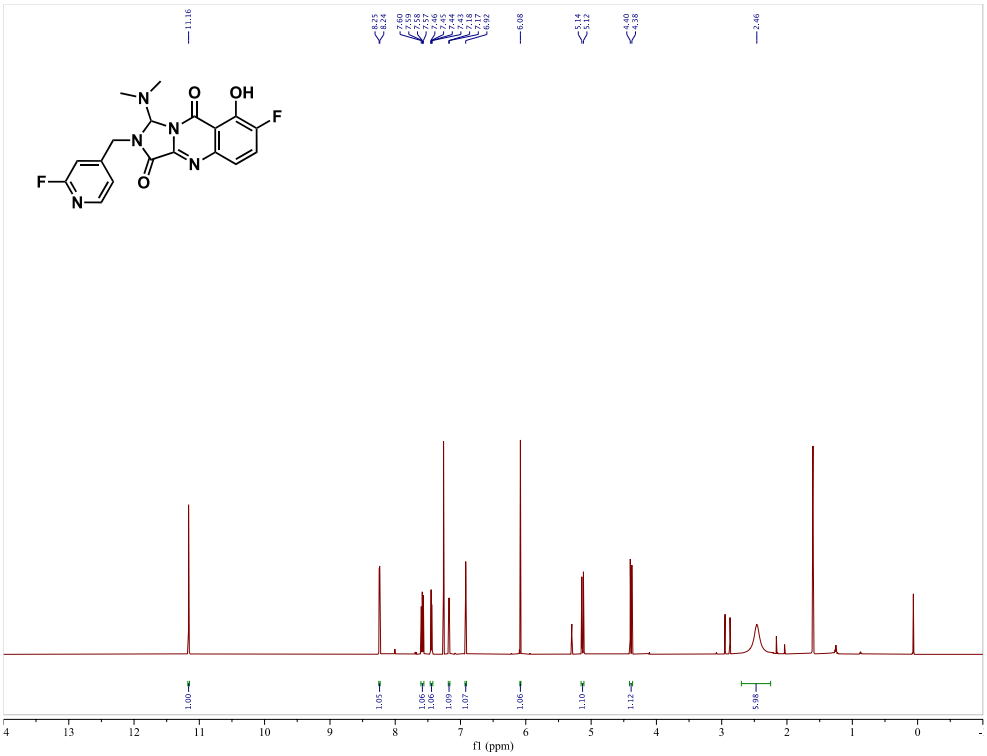

^{13}C-NMR (150 MHz, $CDCl_3$)

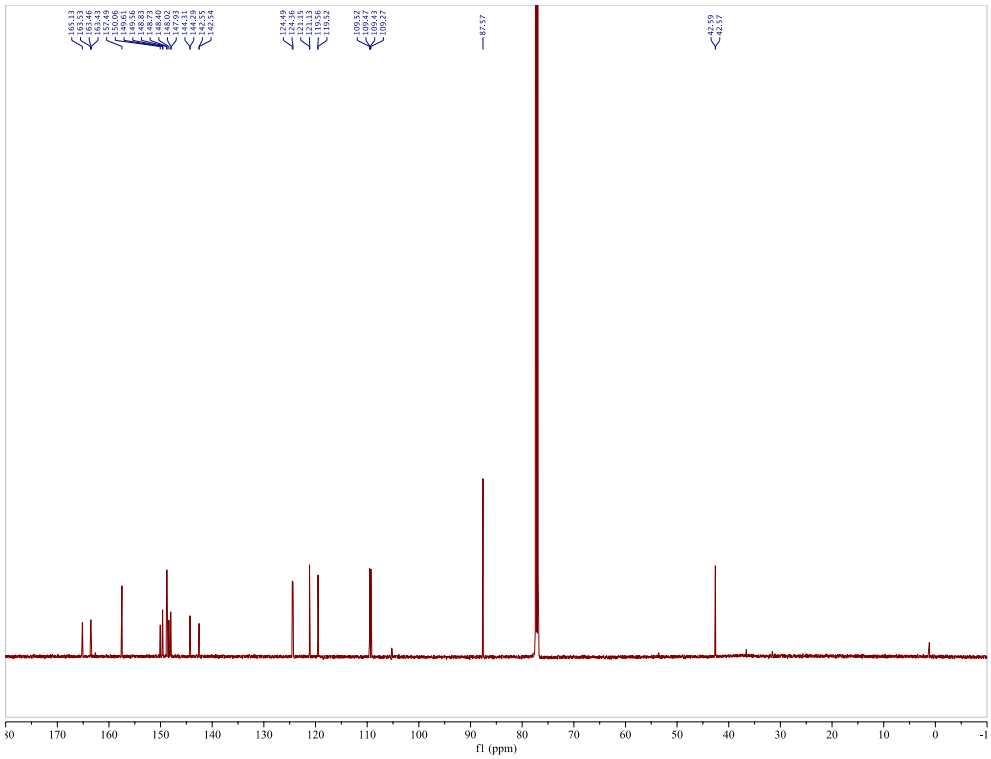

Compound 28a

^{1}H-NMR (600 MHz, $(CD_3)_2SO$)

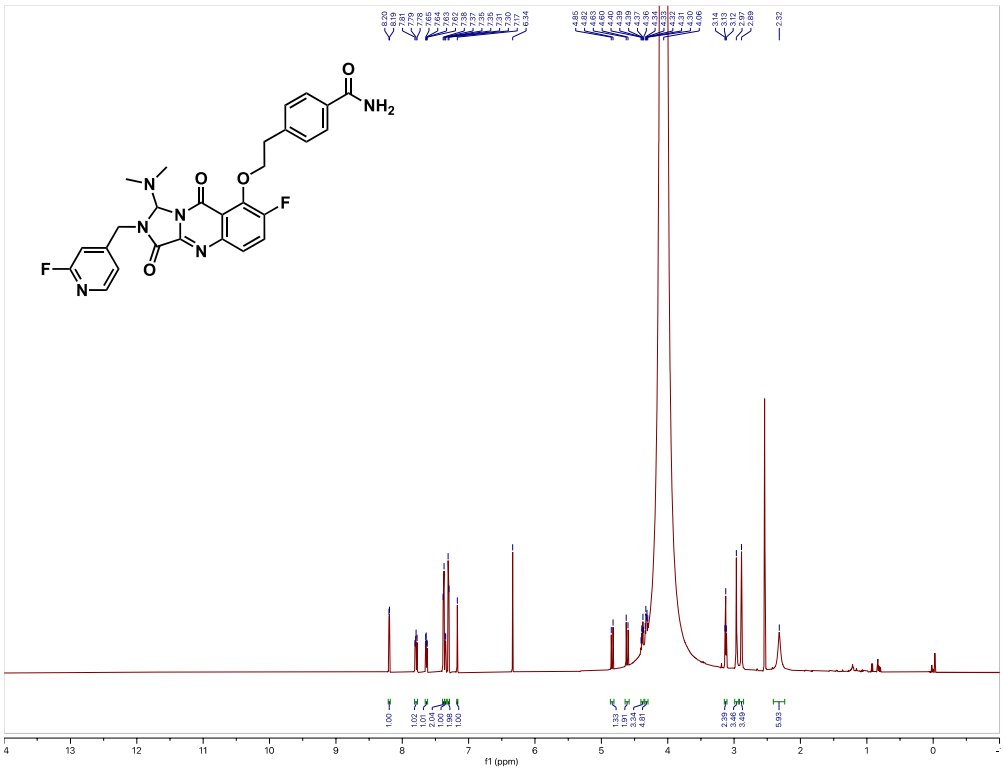

^{13}C-NMR (150 MHz, $(CD_3)_2SO$)

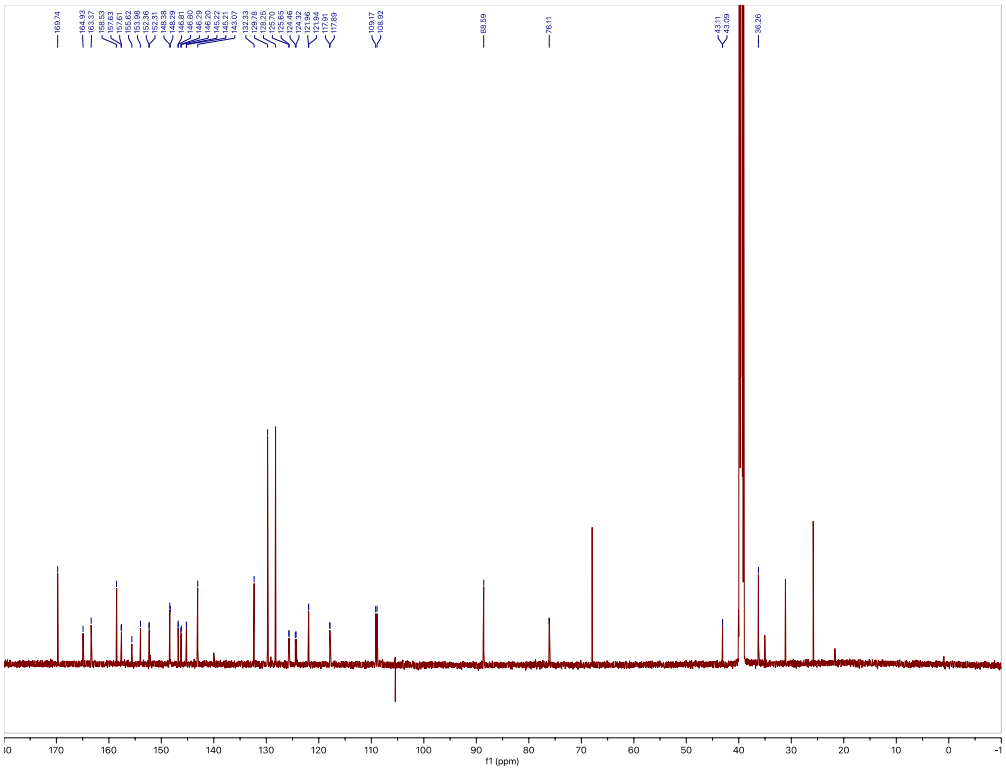

Compound 28b

^{1}H-NMR (600 MHz, $(CD_3)_2SO$)

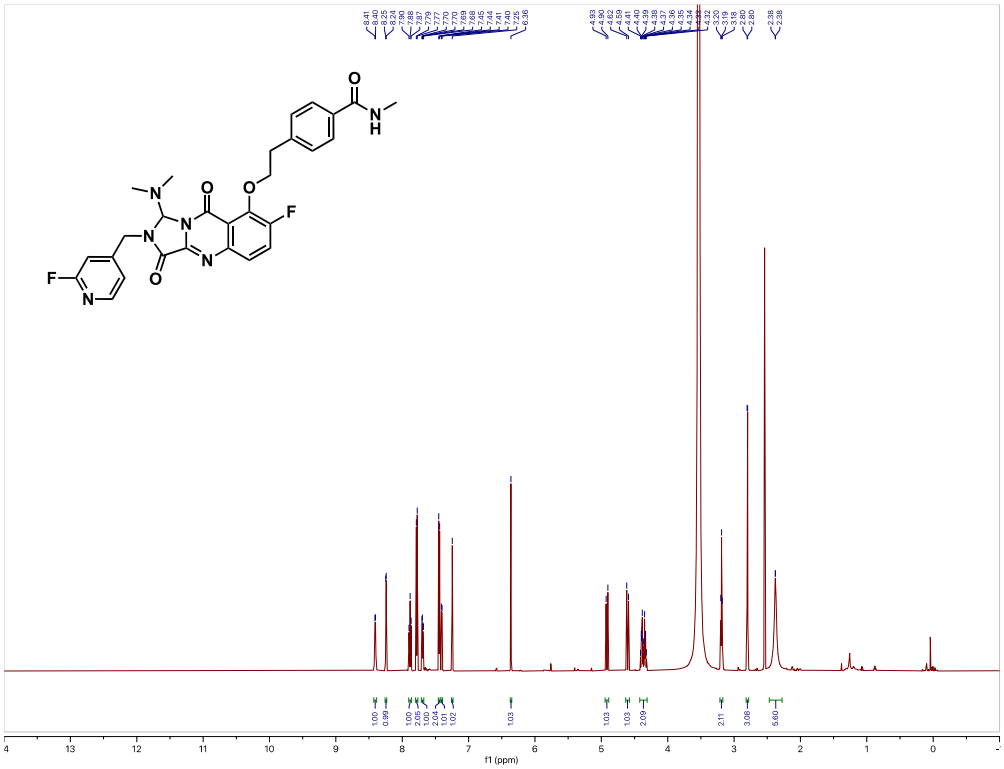

^{13}C-NMR (150 MHz, $(CD_3)_2SO$)

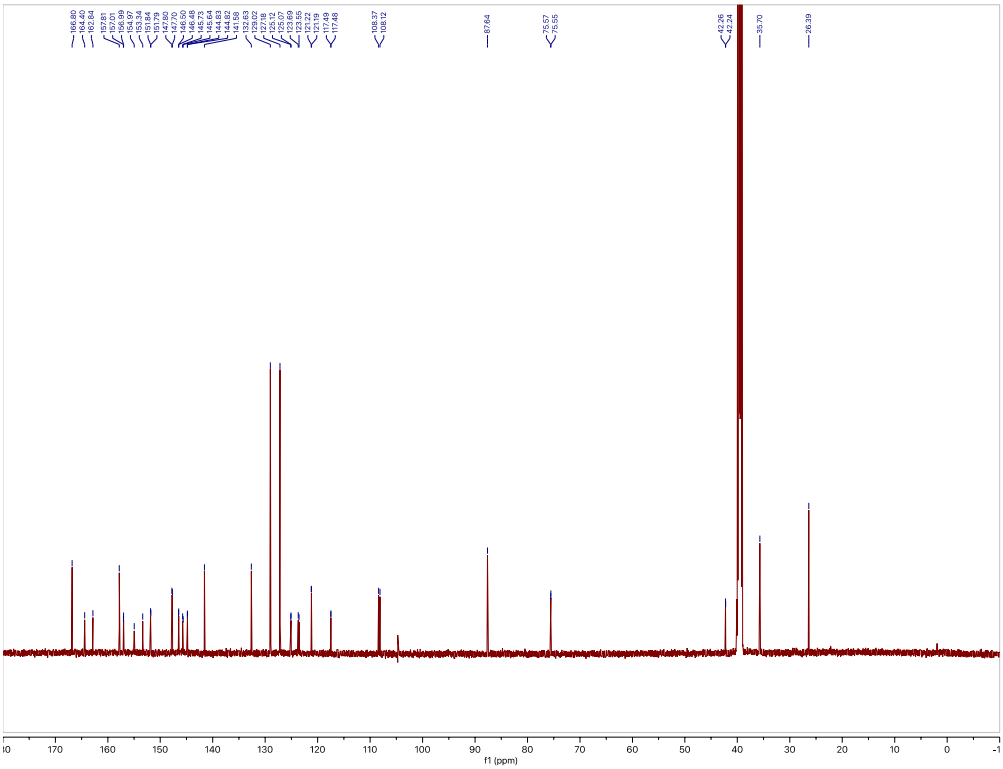

Compound 28c

^{1}H-NMR (600 MHz, $(CD_3)_2SO$)

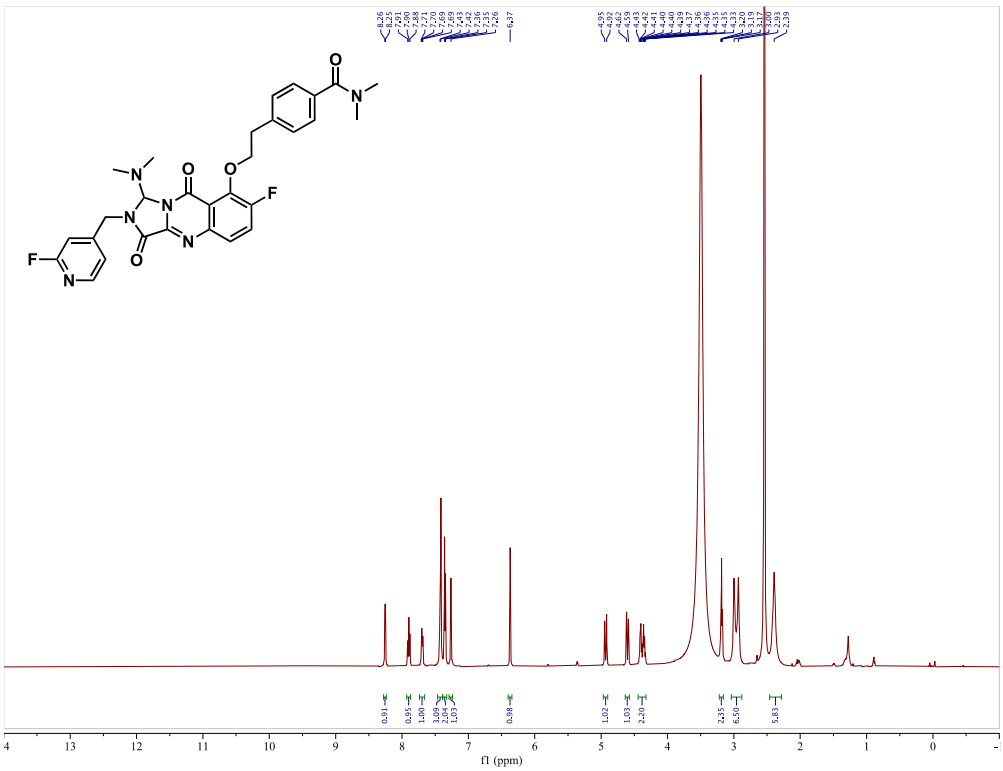

^{13}C-NMR (150 MHz, $(CD_3)_2SO$)

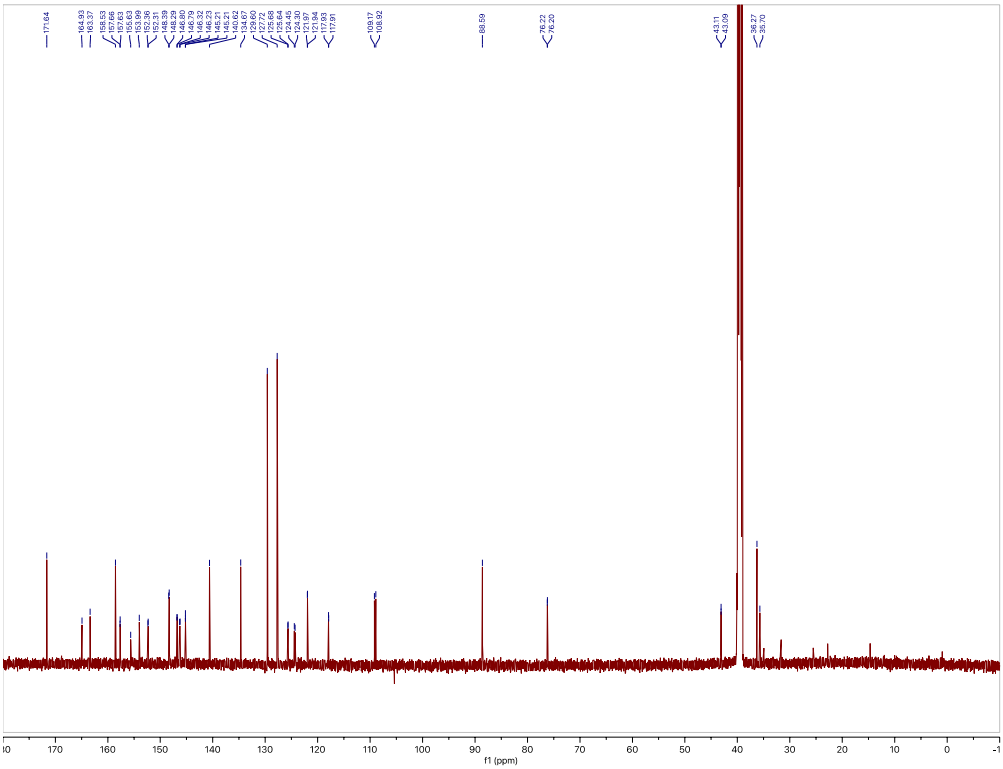

Compound 28d

^{1}H-NMR (600 MHz, $(CD_3)_2SO$)

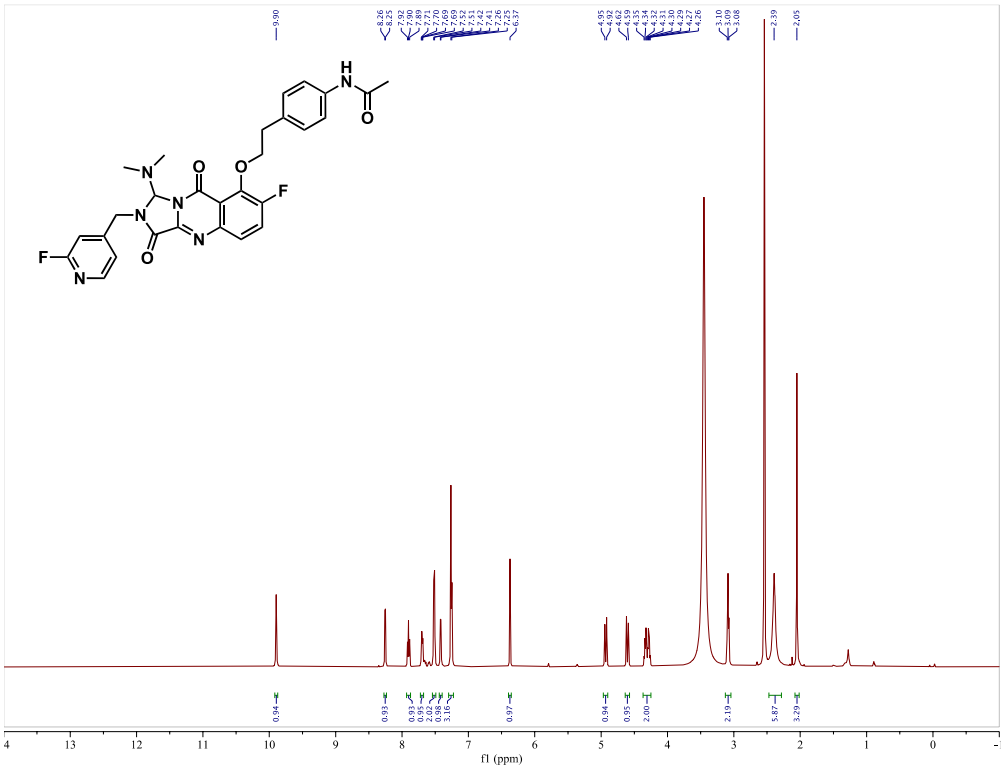

^{13}C-NMR (150 MHz, $(CD_3)_2SO$)

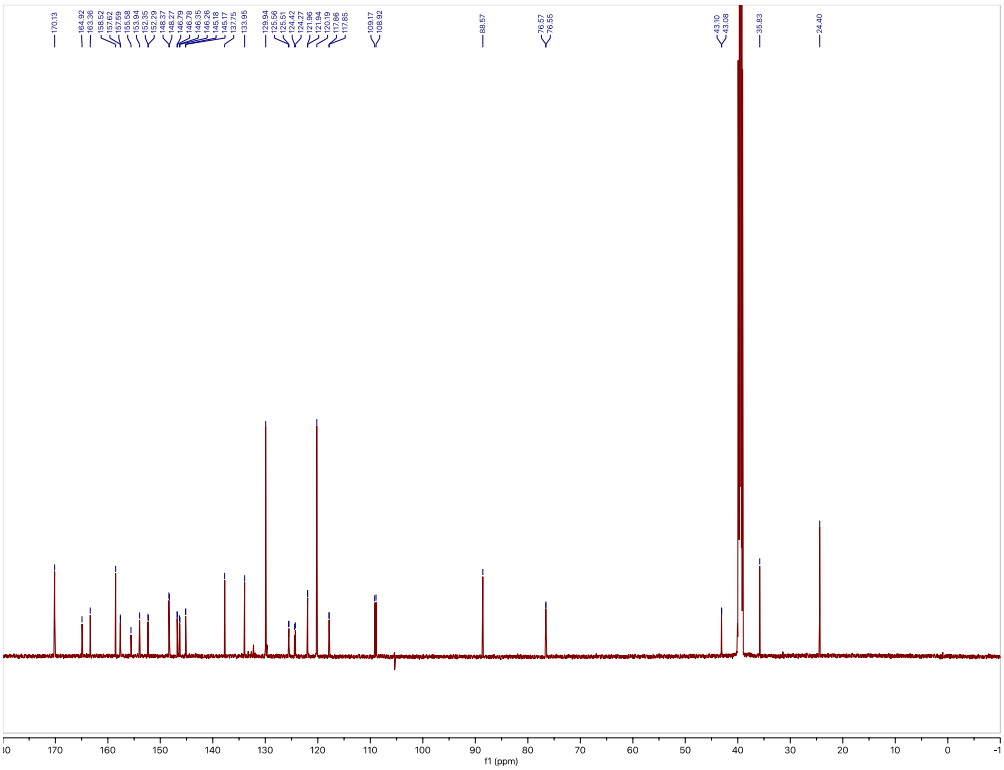

Compound 28e

^{1}H-NMR (600 MHz, $(CD_3)_2SO$)

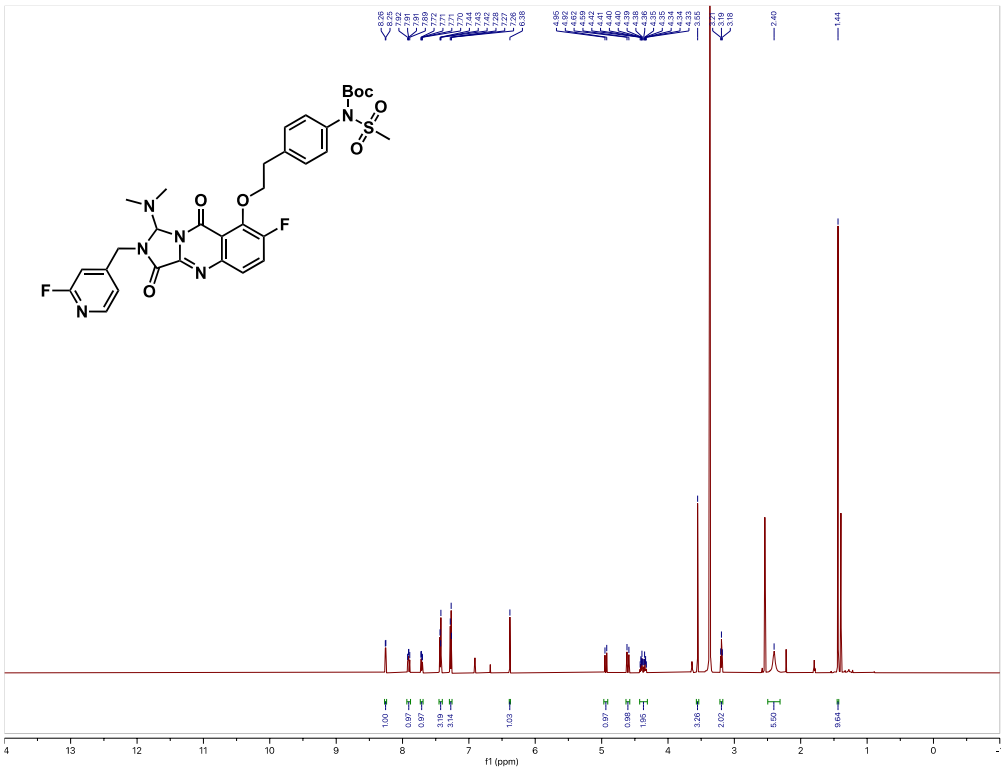

^{13}C-NMR (150 MHz, $(CD_3)_2SO$)

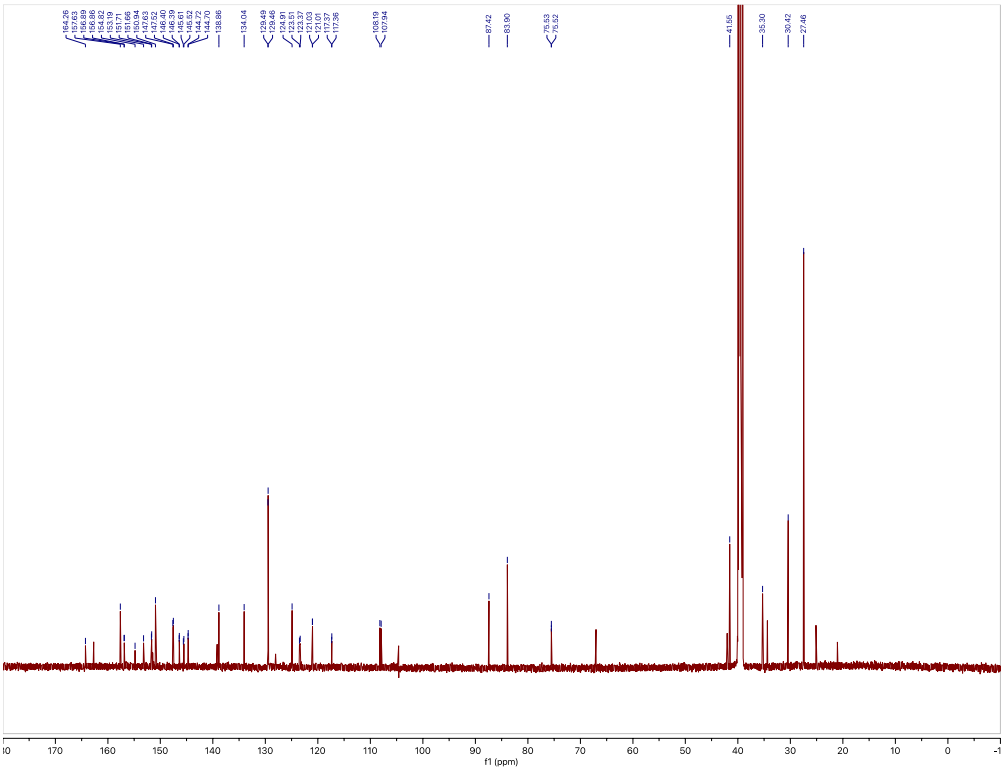

Compound 28f

^{1}H-NMR (600 MHz, $(CD_3)_2SO$)

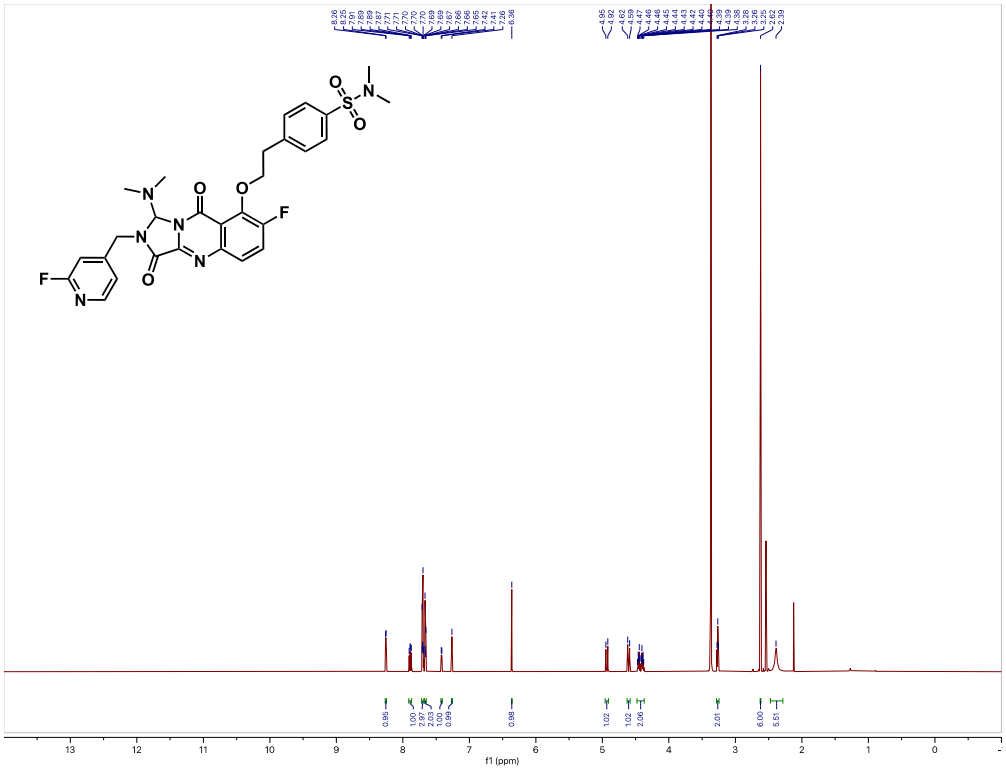

^{13}C-NMR (150 MHz, $(CD_3)_2SO$)

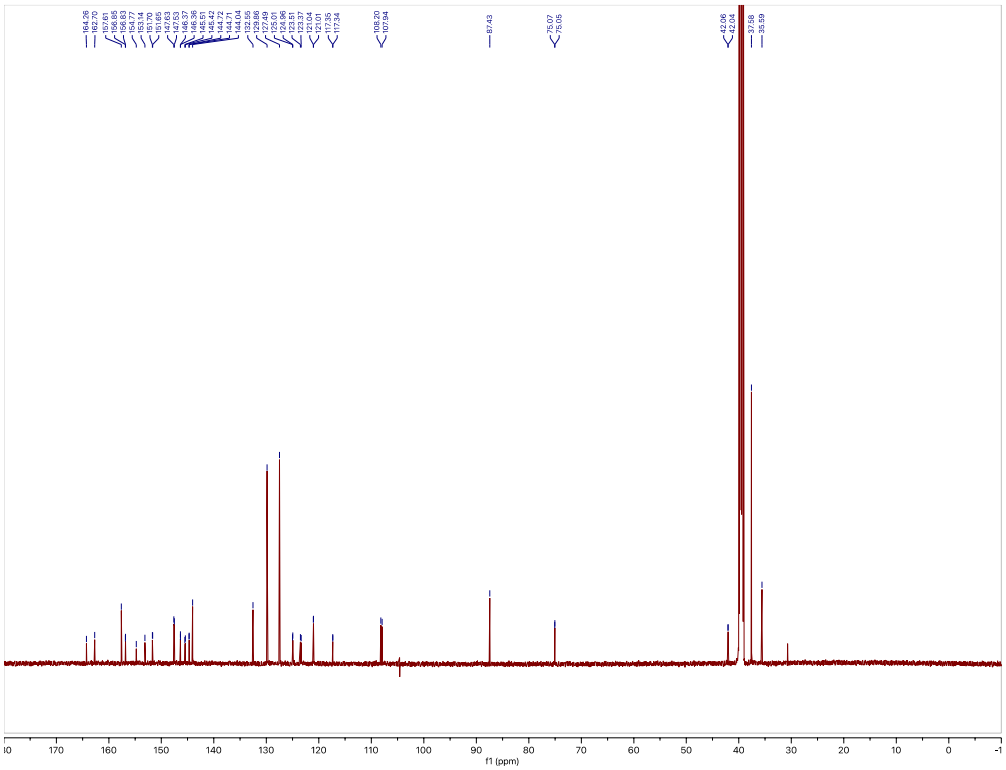

Compound 28g

^{1}H-NMR (600 MHz, $(CD_3)_2SO$)

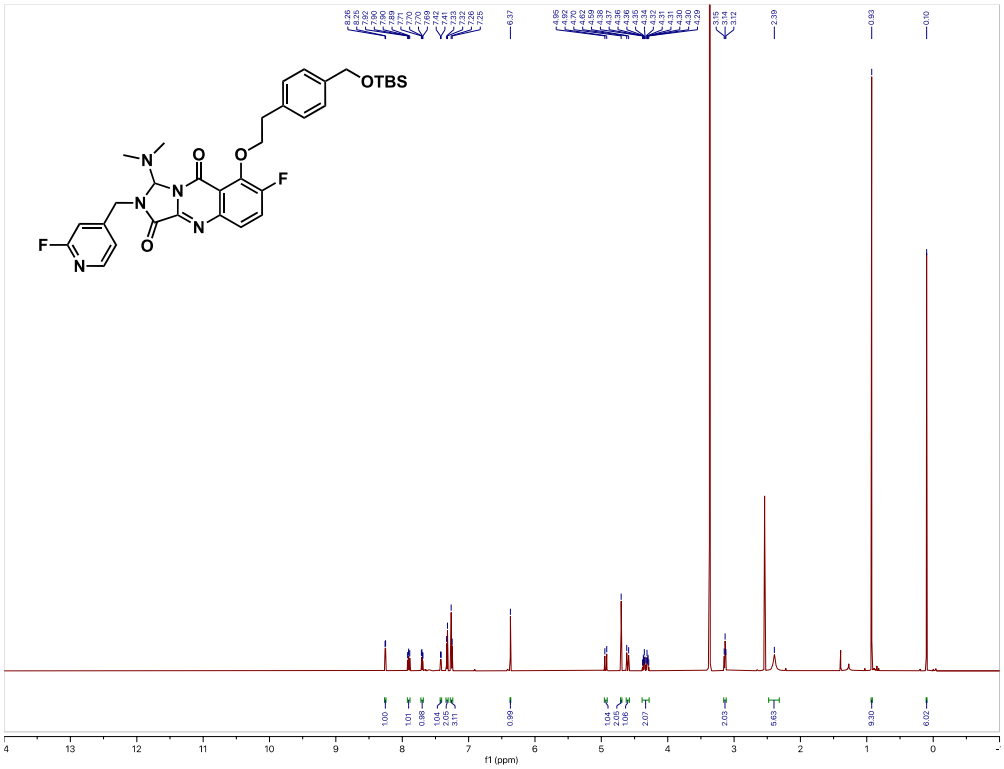

^{13}C-NMR (150 MHz, $(CD_3)_2SO$)

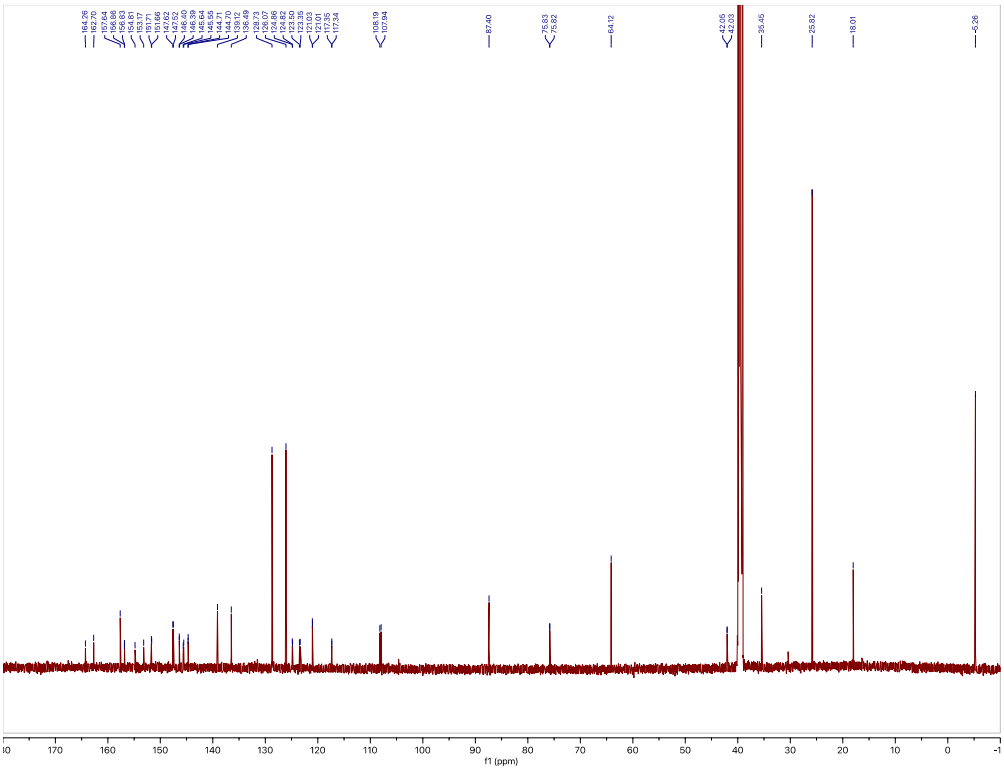

Compound 29a

^{1}H-NMR (600 MHz, $(CD_3)_2SO$)

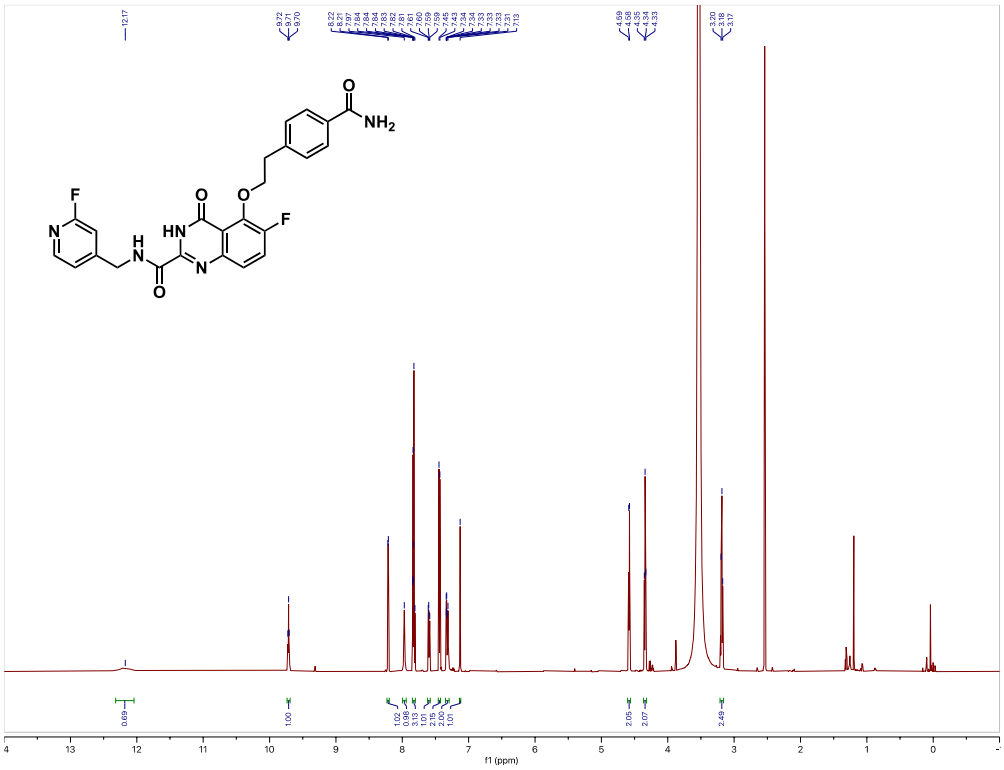

^{13}C-NMR (150 MHz, $(CD_3)_2SO$)

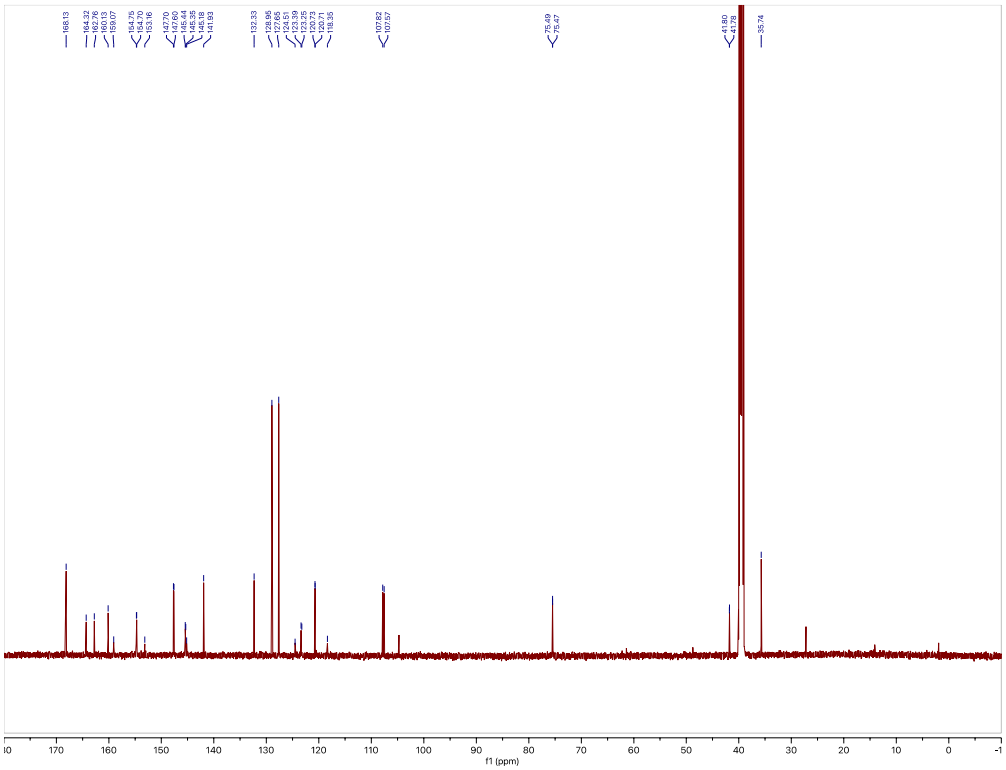

Compound 29b

^{1}H-NMR (600 MHz, $(CD_3)_2SO$)

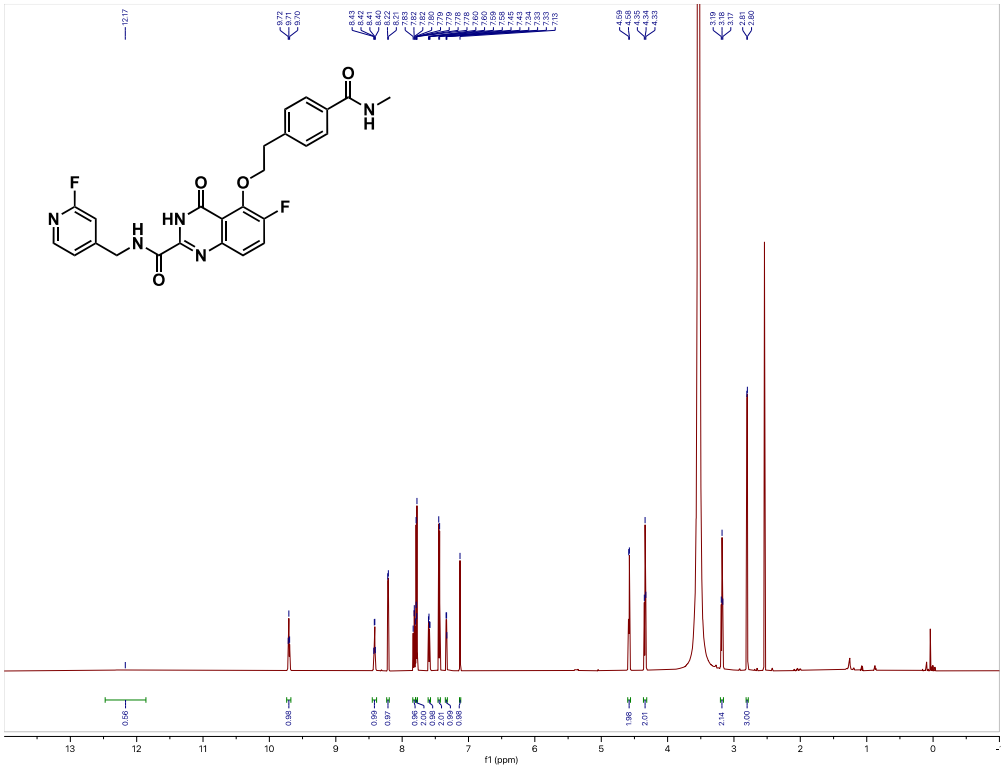

^{13}C-NMR (150 MHz, $(CD_3)_2SO$)

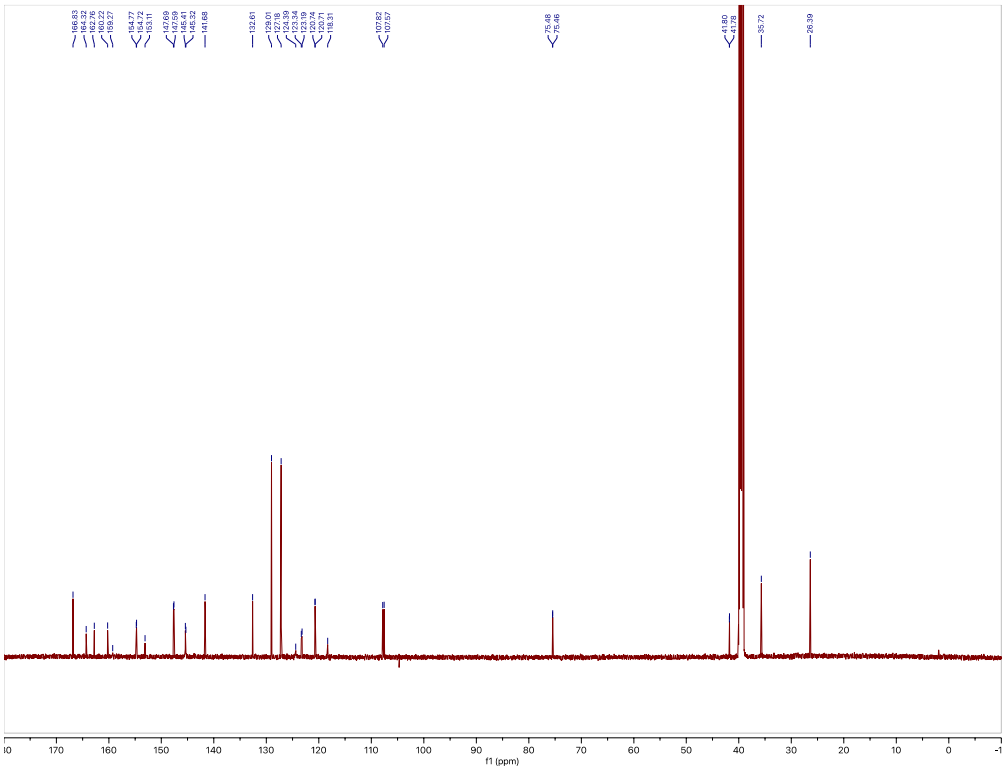

Compound 29c

^{1}H-NMR (600 MHz, $(CD_3)_2SO$)

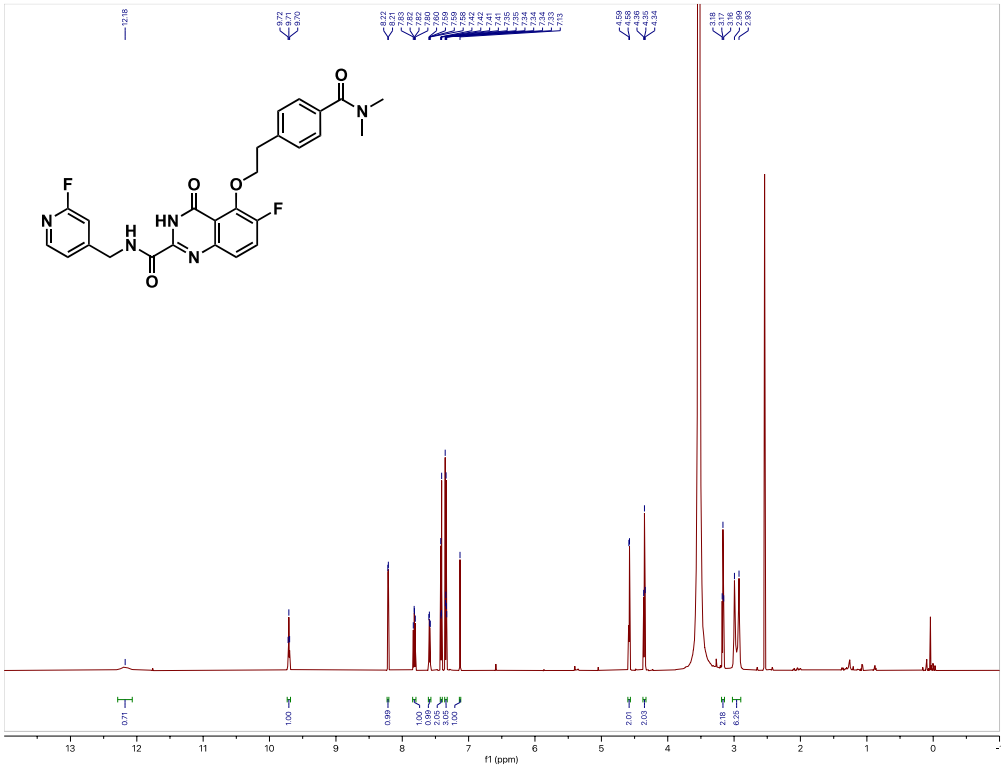

^{13}C-NMR (150 MHz, $(CD_3)_2SO$)

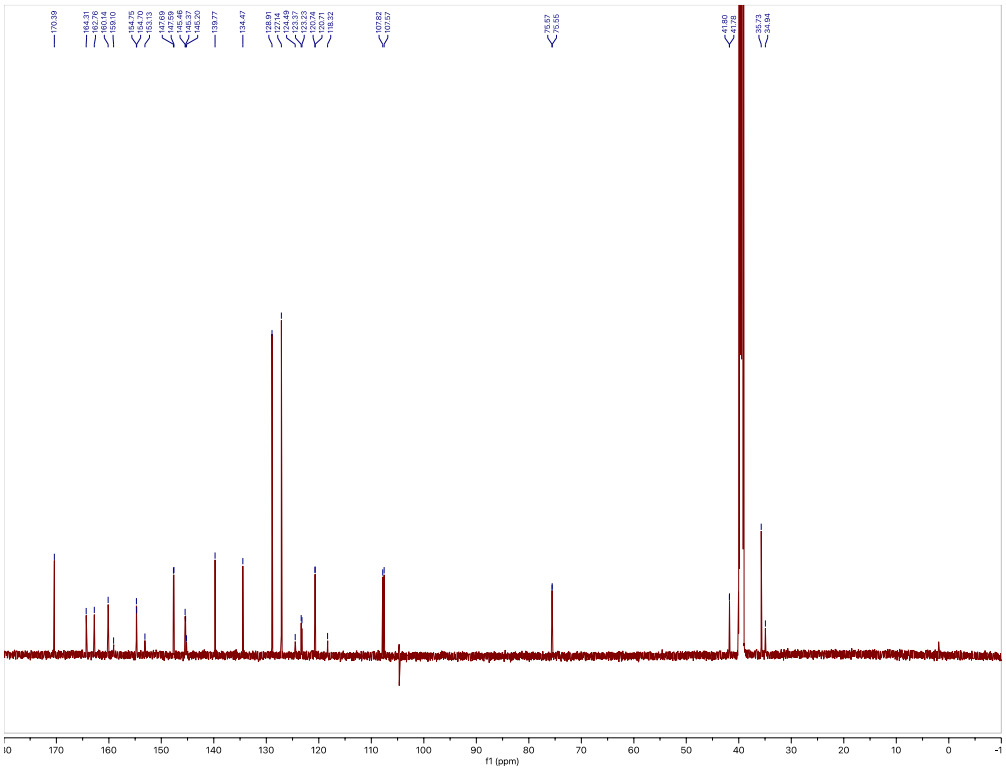

Compound 29d

^{1}H-NMR (600 MHz, $(CD_3)_2SO$)

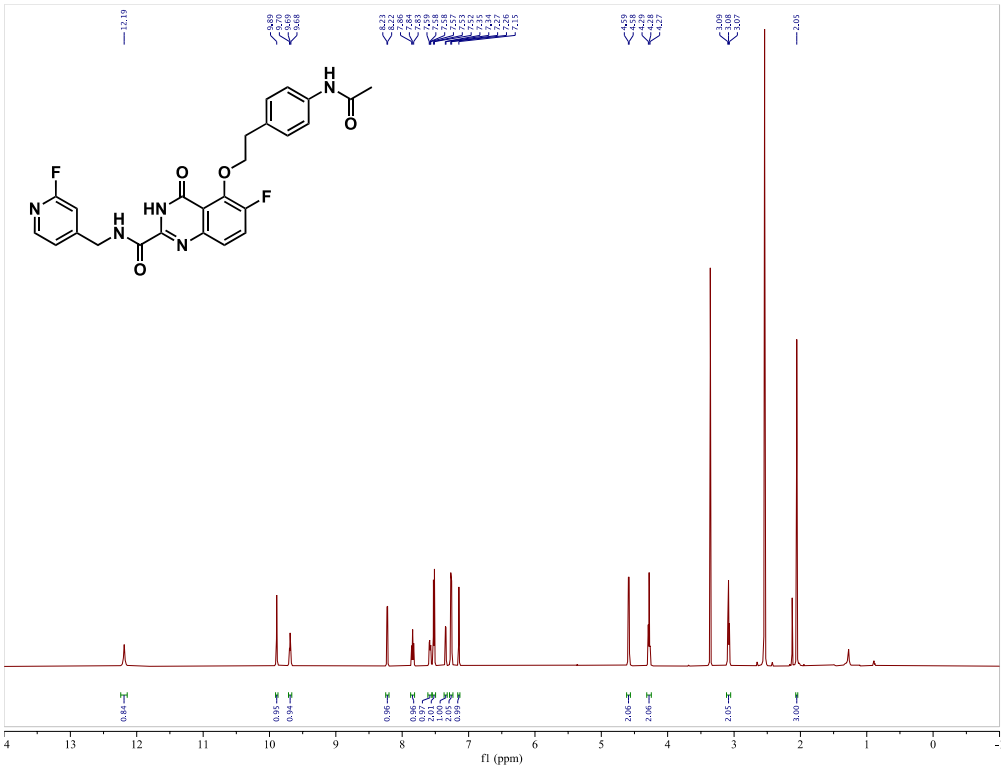

^{13}C-NMR (150 MHz, $(CD_3)_2SO$)

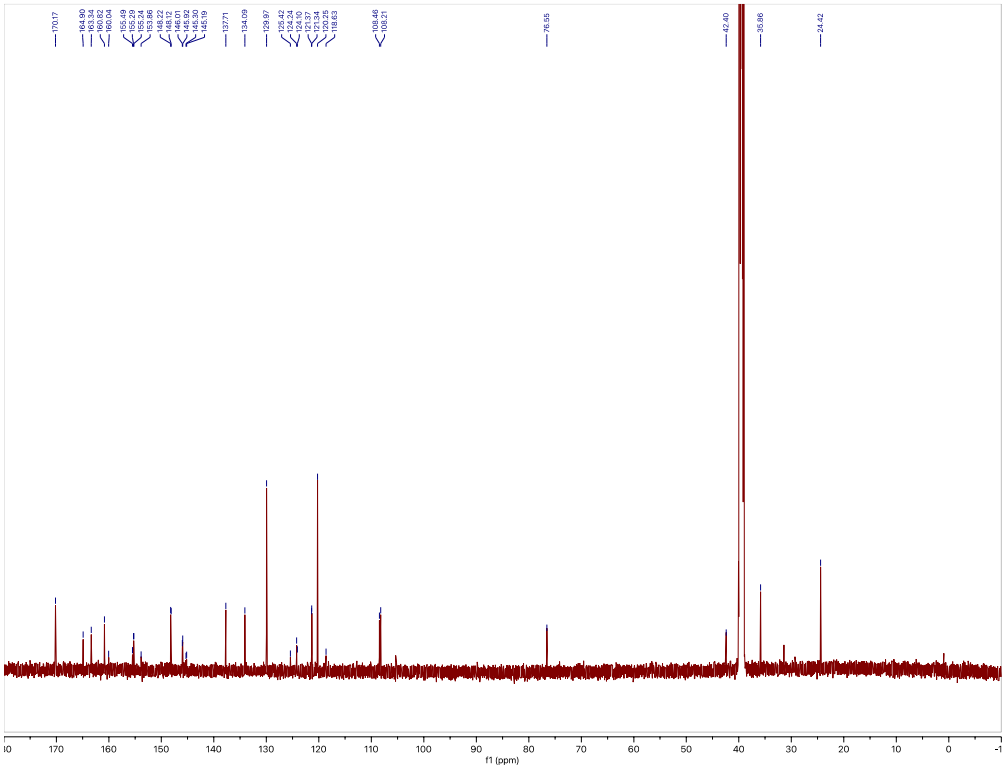

Compound 29e

^{1}H-NMR (600 MHz, $(CD_3)_2SO$)

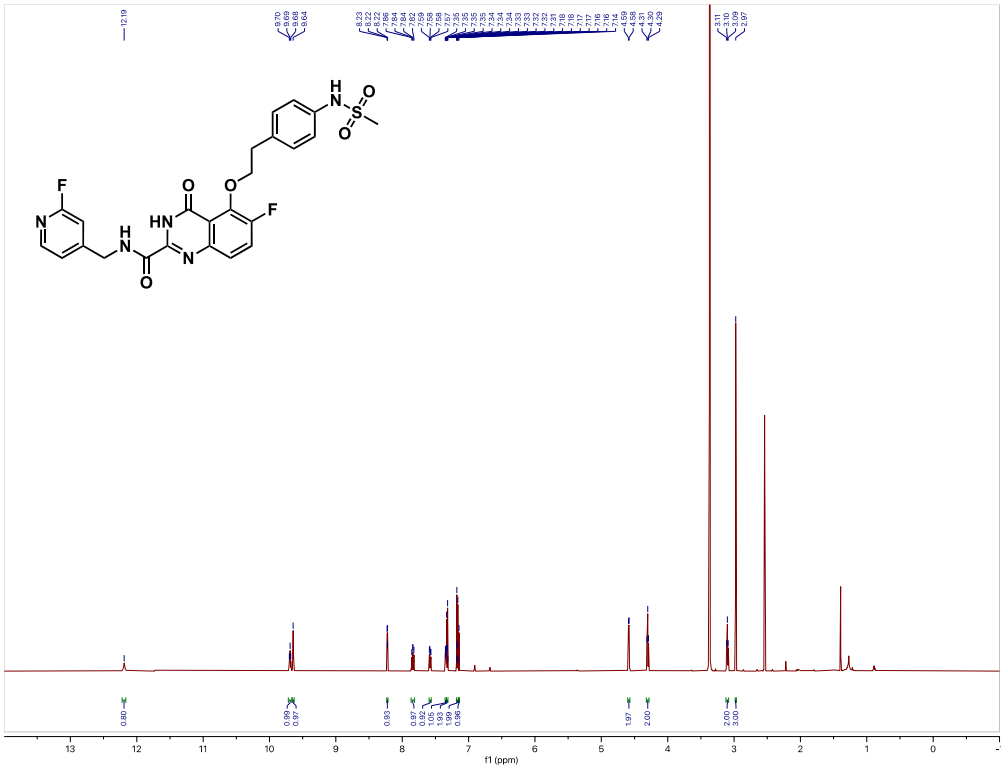

^{13}C-NMR (150 MHz, $(CD_3)_2SO$)

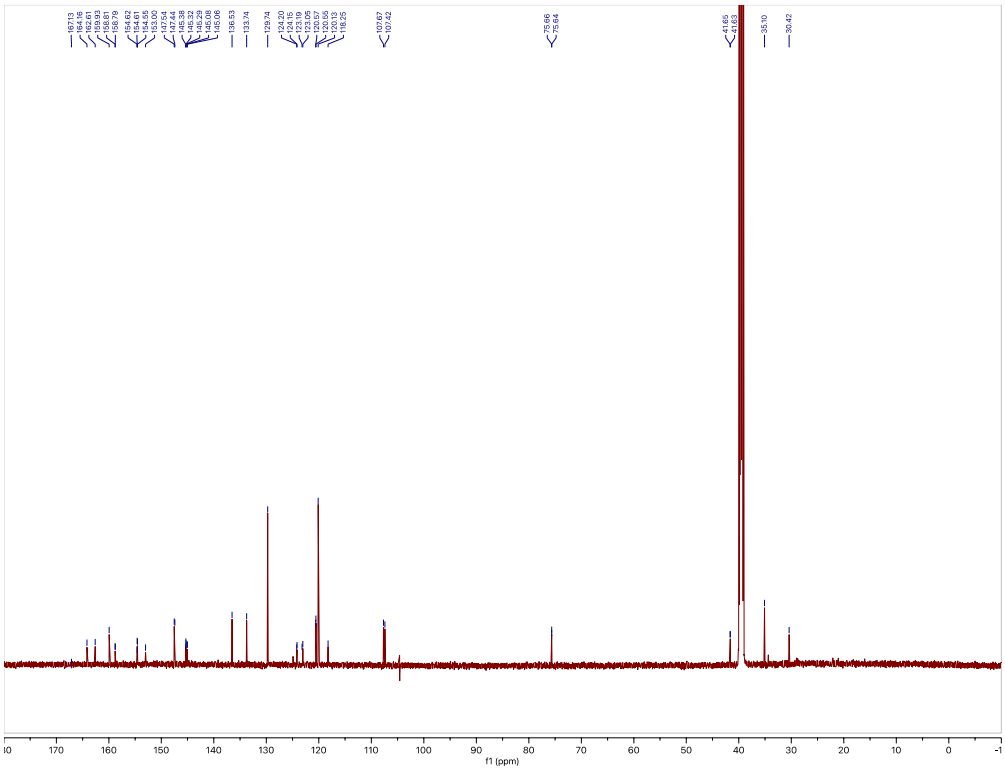

Compound 29f

^{1}H-NMR (600 MHz, $(CD_3)_2SO$)

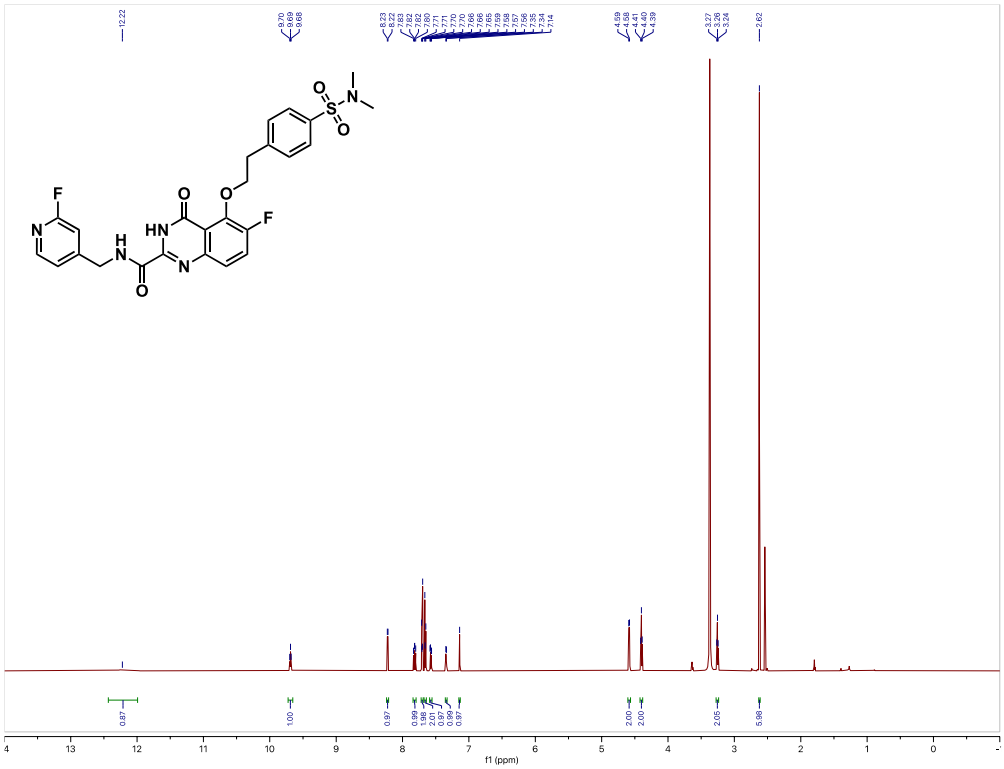

^{13}C-NMR (150 MHz, $(CD_3)_2SO$)

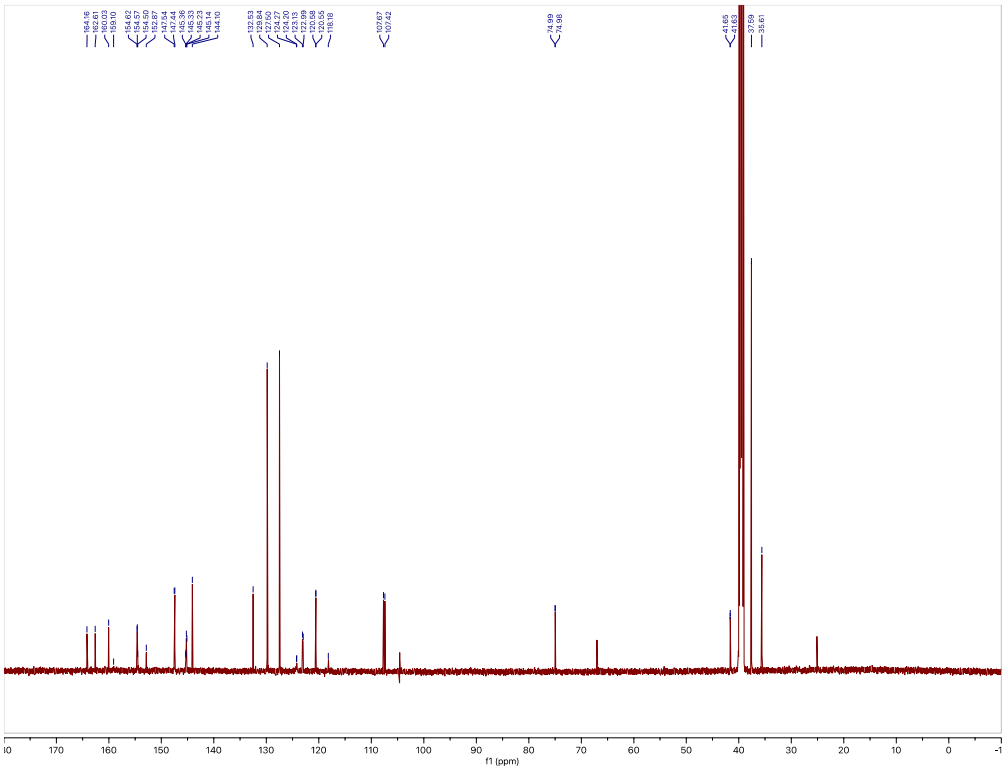

Compound 29g

^{1}H-NMR (600 MHz, $(CD_3)_2SO$)

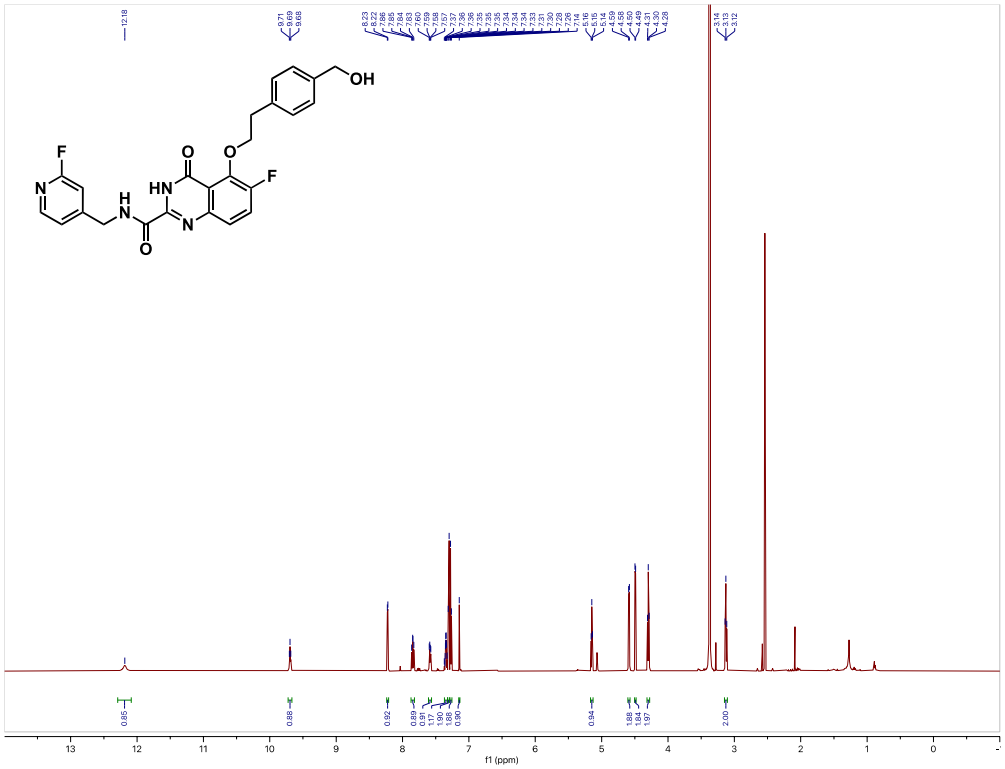

^{13}C-NMR (150 MHz, $(CD_3)_2SO$)

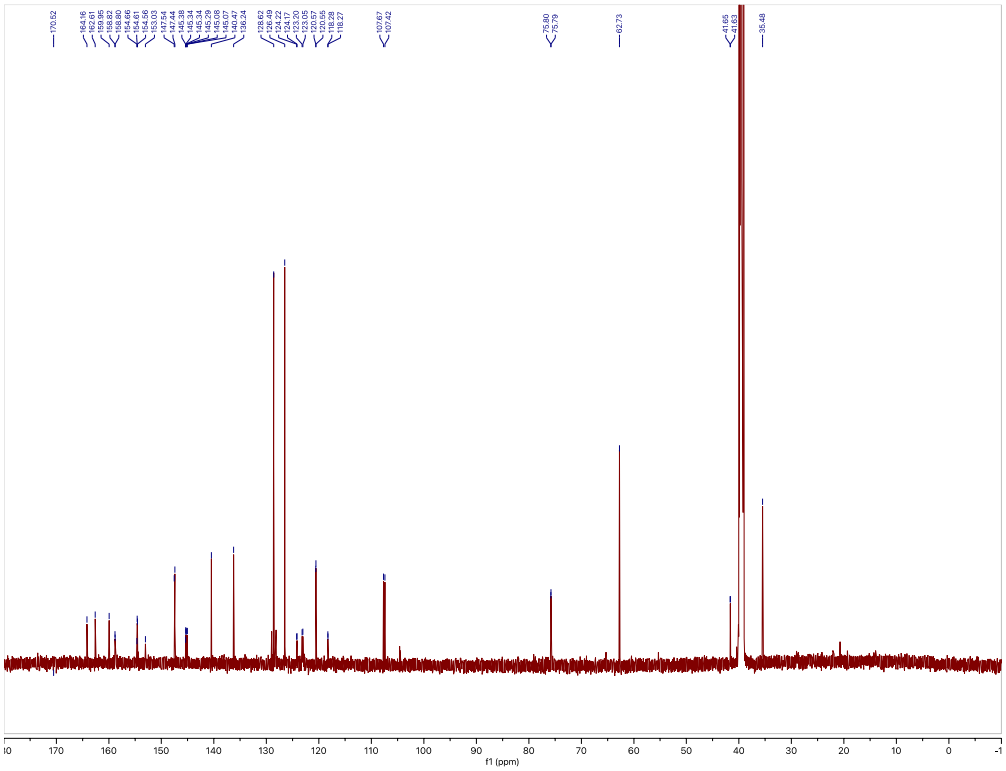

Compound 30

^{1}H-NMR (600 MHz, $(CD_3)_2SO$)

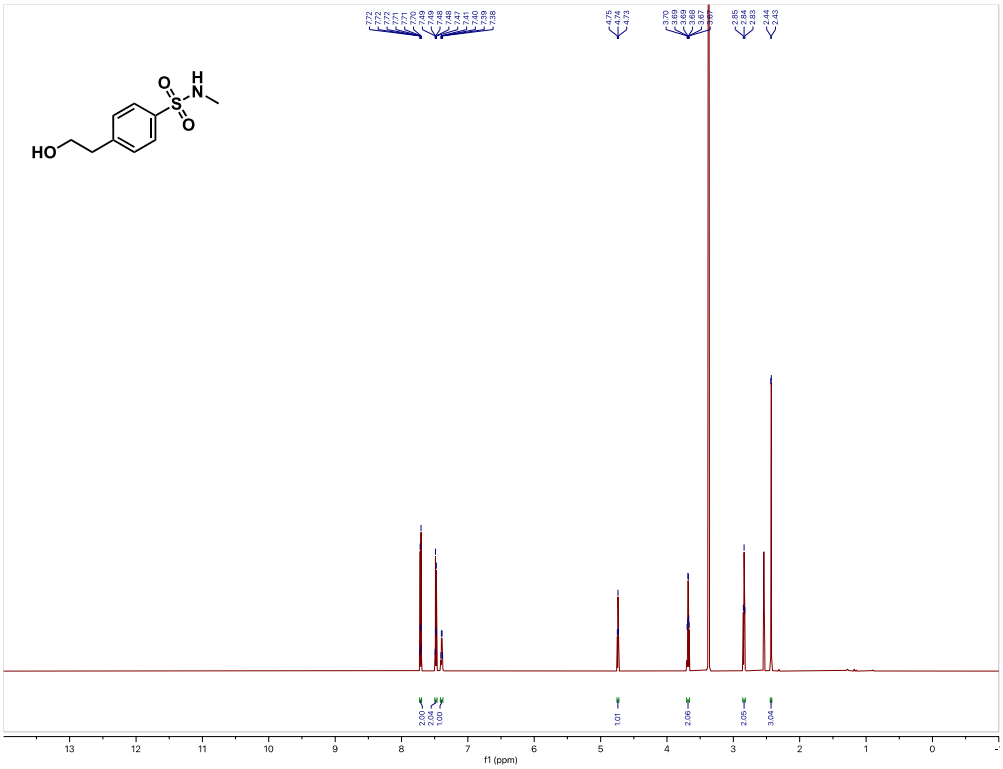

^{13}C-NMR (150 MHz, $(CD_3)_2SO$)

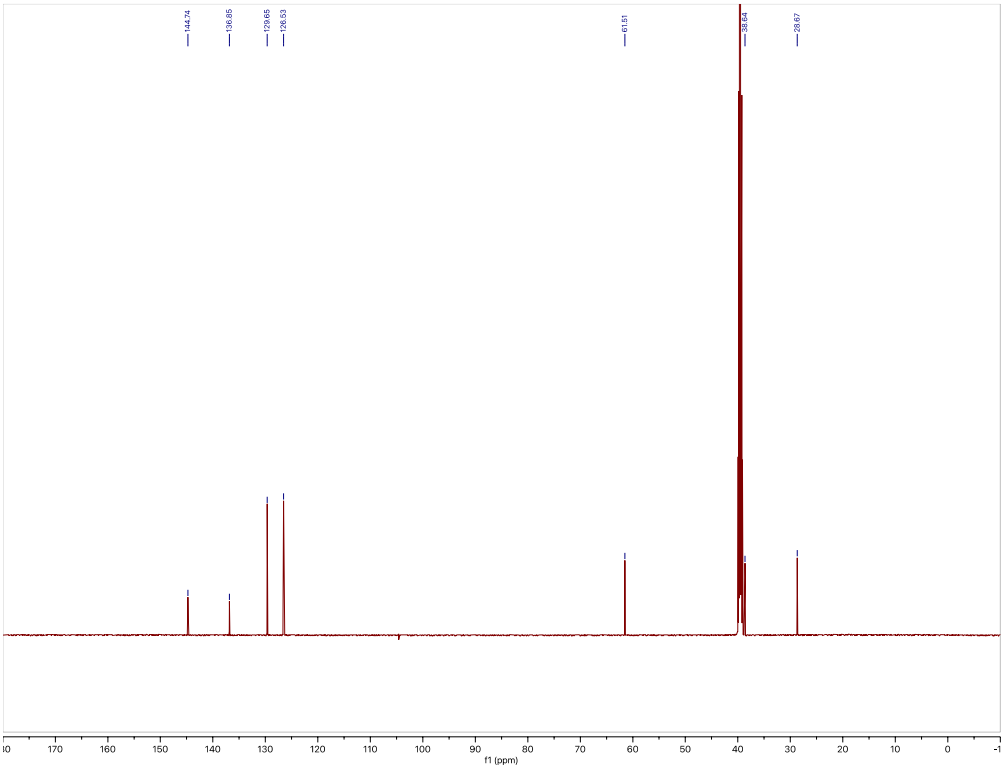

Compound 31

^{1}H-NMR (600 MHz, $(CD_3)_2SO$)

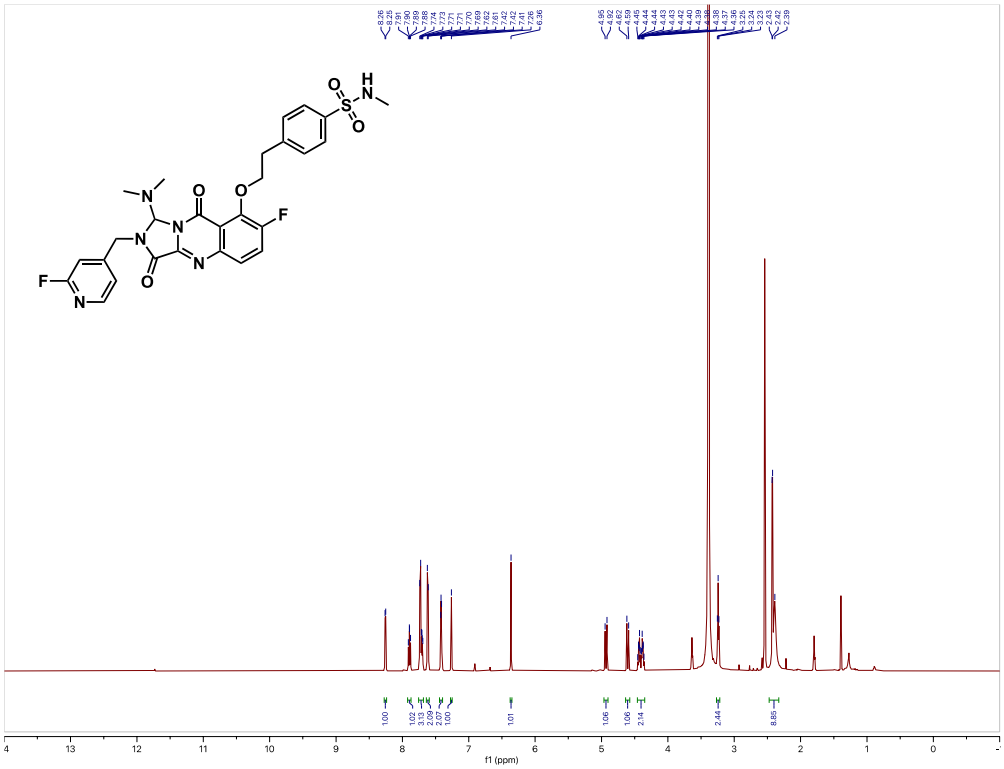

^{13}C-NMR (150 MHz, $(CD_3)_2SO$)

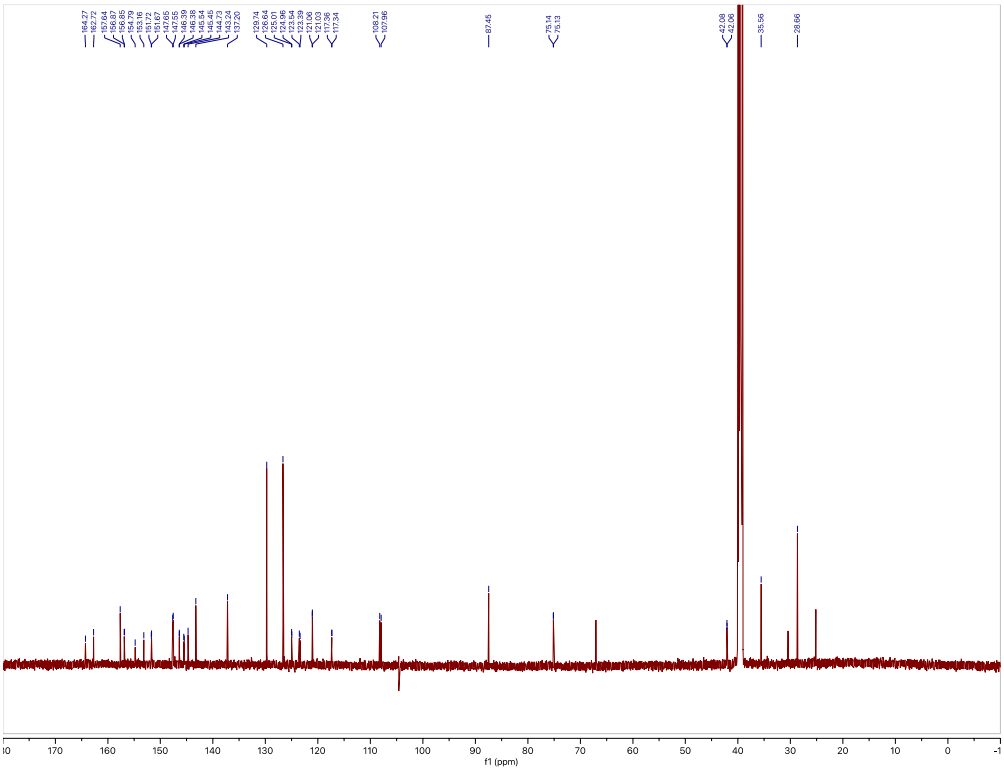

Compound 32

^{1}H-NMR (600 MHz, $(CD_3)_2SO$)

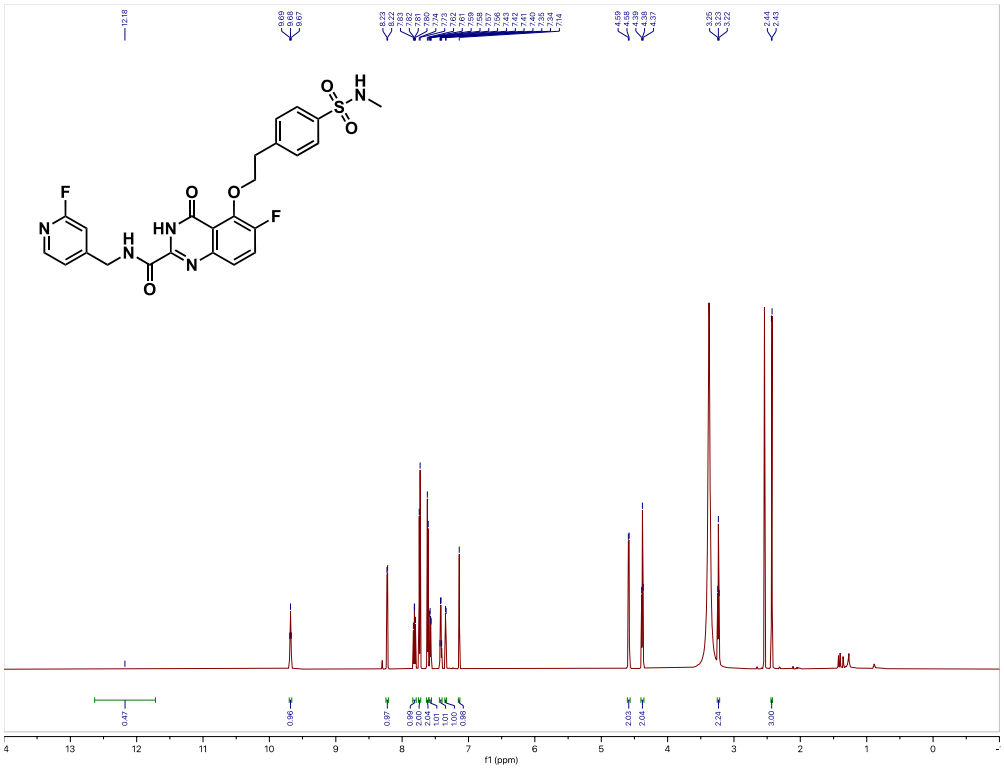

^{13}C-NMR (150 MHz, $(CD_3)_2SO$)

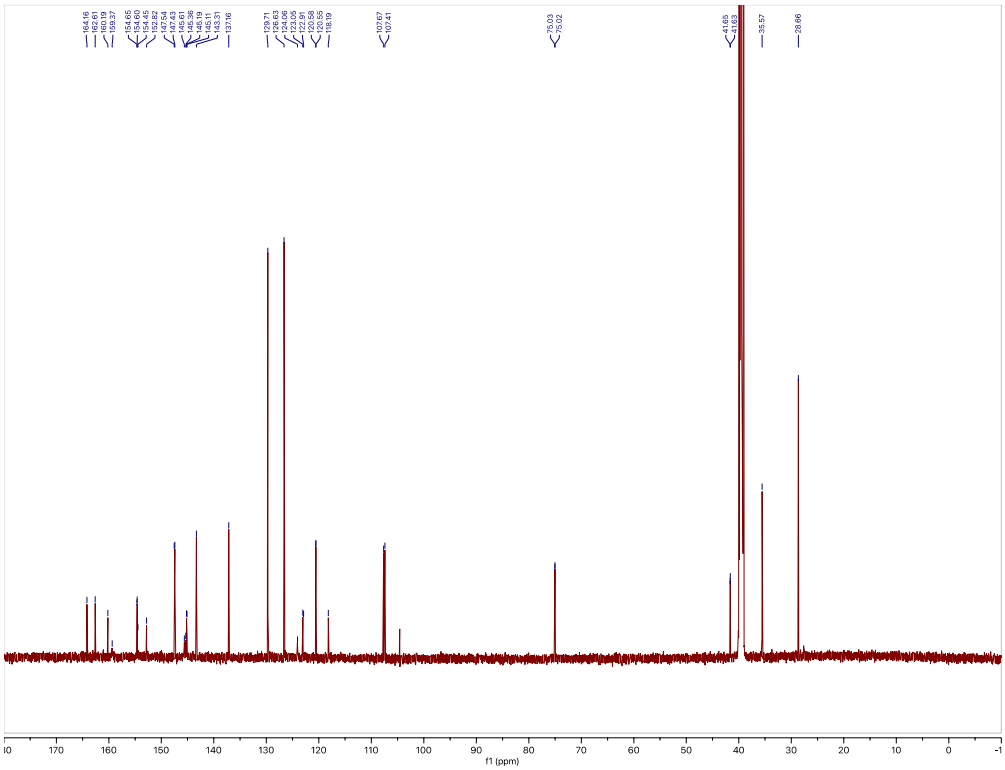

5.0 Chapter V: General Discussion

5.1 Context

CAD, characterized by atherosclerotic plaque formation within the coronary arteries, is the most common form of heart disease and a leading cause of death worldwide. While progressive atherosclerotic plaque formation can occlude the coronary arteries and limit blood flow to the heart, rupture of atherosclerotic plaques is considered causal in most fatal acute myocardial infarction events, strokes, and non-fatal acute coronary syndromes. Nevertheless, current diagnostic methods primarily focus on functional imaging by MPI or anatomical imaging by ICA/CCTA/CAC to assess total plaque burden and the extent of hemodynamic obstruction. These methods either rely on indirect measurements of myocardial ischemia caused by CAD, involve invasive procedures, or solely detect the presence of plaques and underestimate the risk of rupture.

PET imaging provides the opportunity for non-invasive molecular profiling of atherosclerotic plaque composition and direct assessments of plaque stability. Beyond measurements of microcalcification activity with [^{18}F]NaF, there is an unmet clinical need for specific and sensitive PET radiotracers capable of differentiating stable from unstable plaques and predicting risk of rupture. As central regulators of ECM remodeling, MMPs have been extensively implicated with atherosclerotic plaque destabilization. By degradation of the fibrous cap, MMPs contribute to formation of thin and collagen-poor atherosclerotic plaques that are most susceptible to rupture. Accordingly, MMPs represent promising biomarkers of atherosclerotic plaque vulnerability, suitable for the development of molecularly targeted PET radiotracers. As MMPs possess diverse and distinct (patho)physiological functions, current MMP-targeted radiotracers including [^{18}F]BR-351, [^{99m}Tc]RYM-1 or [^{64}Cu]RYM-2 which are based on broad-spectrum MMPIs are rather indiscriminate and have limited target tissue contrast. To this end, developing

selective PET radiotracers for MMP-13, the predominant interstitial collagenase found in atherosclerotic plaques, is poised to uniquely reflect destructive ECM remodeling and more accurately predict risk of rupture to prevent life-threatening outcomes.

5.2 Chapter II Discussion

5.2.1 Rationale and Objectives

Currently, very few MMP-13 selective radiotracers have been developed for *in vivo* PET imaging and none have been employed for atherosclerosis.[1,2] Outlined in chapter II of this thesis, we first sought to demonstrate the feasibility of utilizing an MMP-13 selective PET radiotracer for detecting ECM remodeling in atherosclerotic plaques and provided a head-to-head comparison of MMP-13 selective and broad-spectrum MMP imaging.[3] To accomplish this, [^{18}F]FMBP and [^{18}F]BR-351 were employed as previously developed MMP-13 selective and non-selective fluorine-18 labeled PET radiotracers and conducted their first *in vivo* evaluations in atherosclerotic mice. [^{18}F]FMBP (IC_{50}: ~55 nM) is derived from the pyrimidine-dicarboxamide inhibitor class and represented the most selective MMP-13 targeted radiotracer developed to date (>1800-fold).[2] Meanwhile, [^{18}F]BR-351 is based on an HA-containing broad-spectrum MMPI from the non-peptidic aryl sulfonamide class and selected for its excellent potency (IC_{50}'s: 4-50 nM), synthetically accessibility, and prior validation.[4–7]

5.2.2 Key Findings and Significance

This study validated the approach of using an MMP-13 selective PET radiotracer for molecular imaging of ECM remodeling in atherosclerotic mouse plaques.[3] While both [^{18}F]FMBP and [^{18}F]BR-351 could detect atherosclerotic plaques by *ex vivo* aortic autoradiography, [^{18}F]FMBP uptake was ~3-fold greater than [^{18}F]BR-351 or healthy controls. Blocking

experiments conducted by pre-treatment with non-radioactive FMBP completely reduced [^{18}F]FMBP uptake to levels indistinguishable from healthy controls. Analogous experiments with [^{18}F]BR-351 revealed no significant differences. These results demonstrate that MMP-13 selective imaging with [^{18}F]FMBP exhibits a greater extent of specific binding in atherosclerotic plaques. Immunofluorescent staining of lipid-rich atherosclerotic plaques identified by [^{18}F]FMBP autoradiography revealed elevated levels of macrophages (Mac-2) and MMP-13. Notably, MMP-13 expression was markedly increased within the outer curvature of the atherosclerotic plaque, consistent with its role in degrading collagen within the fibrous cap. No expression of Mac-2 or MMP-13 was observed in healthy control tissue. These findings provide evidence to suggest that [^{18}F]FMBP uptake is sensitive to markers of inflammation and destructive ECM remodeling.

5.2.3 Limitations

While this foundational study critically showed the *ex vivo* utility of [^{18}F]FMBP, we were unable to detect atherosclerotic mouse plaques non-invasively by PET imaging. Beyond the small physical size of the aorta and the lack of CT imaging for anatomical referencing, [^{18}F]FMBP possessed a suboptimal *in vivo* distribution. Biodistributions indicated a hepatobiliary excretion route with significant retention of radioactivity in the heart (~5 %ID·g^{-1}) and liver (~17 %ID·g^{-1}). These features pose challenges for quantification of nearby structures such as aortic plaques within the thoracic cavity. Moreover, accurate quantification of CAD would be difficult due to myocardial spillover, highlighting a need for new MMP-13 selective radiotracers with improved pharmacokinetics for cardiovascular imaging.[8–10]

5.3 Chapter III Discussion

5.3.1 Rationale and Objectives

The need for MMP-13 selective PET radiotracers with more desirable cardiovascular pharmacokinetics prompted an investigation of an alternative inhibitor scaffold, disclosed in chapter III.[11] Owing to their optimized structure, MMP-13 inhibitors based on the quinazoline-2-carboxamide core bind more tightly to the S1' pocket and are capable of deeply occupying the S1" side pocket.[12] This binding mode enables exploitation of additional interactions not observed among other pyrimidine dicarboxamide inhibitors, such as FMBP, and accounts for the greater MMP-13 potency and selectivity of this inhibitor class.[2,12] In particular, the previously identified lead quinazoline-2-carboxamide inhibitor (21k) features a carboxylic acid which forms additional hydrogen bonding and ionic interactions with Asn215 and Lys140 at the back of the S1" pocket, responsible for conferring best in class potency and selectivity.[12] Conveniently, compound 21k also possessed a reliable handle for ^{11}C-methylation, representing an excellent radiolabeling candidate for initial evaluations to assess its potential for atherosclerotic plaque imaging.

However, as some reports have indicated, the anionic nature of the carboxylic acid at physiological pH may render the molecule an OAT substrate.[13,14] To circumvent this potential liability and enhance structural diversity in pursuit of optimizing radiotracer pharmacokinetics, we sought expand upon the SAR of the quinazoline-2-carboxamide inhibitor class, focusing on non-carboxylate containing derivatives and incorporating functionality amenable to carbon-11 or fluorine-18 radiolabeling. This study details the first radiosynthesis and *in vivo* characterization of three MMP-13 selective PET radiotracers based on the quinazoline-2-carboxamide inhibitors and demonstrates their utility for atherosclerotic plaque imaging.[11]

5.3.2 Key Findings and Significance

Ex vivo experiments with [^{11}C]21k ([^{11}C]5b) revealed rapid excretion into the intestine (~53 %ID·g^{-1}) with elevated and sustained uptake in the kidneys (~31 %ID·g^{-1}), and no apparent atherosclerotic plaque uptake. This data confirmed that while the carboxylic acid significantly drives *in vitro* potency (MMP-13 IC_{50}: ~1 nM) and selectivity (~1800-fold), the molecule is likely susceptible to OAT transport and unsuitable for *in vivo* imaging.

Direct replacement or removal of the terminal arene bearing the carboxylic acid, as respectively performed for [^{11}C]5f and [^{18}F]5j, revealed a marked reduction in metabolic organs, highlighting the detrimental impact of this functional group on radiotracer pharmacokinetics. Importantly, the optimal candidate [^{18}F]5j, favourably exhibited renal clearance and was not significantly retained within the heart (~1 %ID·g^{-1}) or liver (~3 %ID·g^{-1}), addressing previous limitations of [^{18}F]FMBP. Importantly, *in vivo* functionality was restored as [^{18}F]5j could detect atherosclerotic plaques by *ex vivo* aortic autoradiography. Blocking experiments conducted by pre-treatment with either non-radioactive 5j or WAY170523 as a commercially available and structurally unrelated MMP-13 selective inhibitor displayed a significant reduction in atherosclerotic plaque uptake, demonstrating specificity to MMP-13 for the first time.

Altogether, these *in vivo* studies have greatly improved our understanding of quinazoline-2-carboxamide inhibitor SAR and demonstrated that it is an excellent scaffold for MMP-13 PET radiotracer development. We uncovered that non-carboxylate containing radioligands, such as [^{18}F]5j, offer superior pharmacokinetics for cardiovascular imaging compared to the pyrimidine dicarboxamide scaffold and can be utilized for *ex vivo* detection of atherosclerotic plaques. These

findings are expected to inform and expedite future development of MMP-13 targeted radiotracers and efficacious selective inhibitors for diagnosis and therapy.

5.3.3 Limitations

Irrespective of these improvements, non-invasive atherosclerotic plaque imaging by PET was not possible with [^{18}F]5j due insufficient clearance from the blood (~3 %ID·g^{-1}). Although late-time point imaging can be performed to provide adequate time for radiotracer circulation and clearance, [^{18}F]5j is rather lipophilic (LogD: ~3.1) and exhibits prolonged washout over time which increases background radioactivity and reduces atherosclerotic plaque imaging contrast.[15–19] Moreover, while removal of the carboxylic acid was imperative to maintain functionality, *in vitro* characterization revealed that all other derivatives including 5j were comparatively less potent (IC_{50}: ~16 nM) and selective (~75-fold) and may have contributed to the moderate extent of MMP-13 specific binding observed. As such, iterative optimization of MMP-13 selective PET radiotracers based on the quinazoline-2-carboxamide is needed to facilitate non-invasive imaging.

5.4 Chapter IV Discussion

5.4.1 Rationale and Objectives

To this end, second-generation MMP-13 selective PET radiotracers based on the quinazoline-2-carboxamide core were developed, as described in chapter IV. To simultaneously maintain the favourable characteristics of [^{18}F]5j and overcome its existing limitations, structural modifications were conducted to accelerate blood clearance by reducing lipophilicity and enhance potency and selectivity by restoring S1” interactions with Asn215/Lys140. To accomplish this, additional heteroatoms and polar functional groups were incorporated into the proximal and distal inhibitor arms which occupy the S1’ and S1” pockets, respectively.[18] Concurrently, inhibitors

bearing the para-substituted phenethyl linker found in 21k were designed with neutral and strong hydrogen bond acceptors that mimic the carboxylate, to enable deep S1" binding interactions without OAT-mediated transport.[13]

5.4.2 Key Findings and Significance

SAR of the proximal inhibitor arm revealed a striking preference for a 2-fluoropyridin-4-yl ring in the S1' pocket with equal MMP-13 potency to previously characterized intermediates (IC_{50}: ~100 nM). At the same time, the 2-fluoropyridine significantly lowered lipophilicity and provided a convenient method for eventual fluorine-18 labeling.[20] To explore the SAR of the distal inhibitor arm, several functionalized phenethyl alcohols were synthesized. As conventional S_NAr proved ineffective for conjugation of these fragments to the quinazoline core, Mitsunobu etherification was employed. To enable this transformation, a novel synthetic route for the corresponding 5-OH quinazoline-2-carboxamide core was developed and afforded the desired functionalized inhibitors, that were previously inaccessible with existing methods, in good yields.

SAR of the distal inhibitor arm revealed that restoring interactions with Asn215/Lys140 at the back of the S1" pocket using neutral hydrogen bond acceptors was an effective strategy to improve MMP-13 potency. A trend toward phenethyl linkers containing benzylic carbonyl or sulfonyl groups and a terminal dimethylamine moiety was uncovered. Molecular docking provided further support and indicated that the most potent derivative **29f** (IC_{50}: ~2.5 nM), containing a tertiary sulfonamide, utilizes its two oxygen atoms for simultaneous interaction with Asn215 and Lys140. Interestingly, the terminal dimethylamine is predicted to orient away from these residues and does not directly participate in hydrogen bonding interactions. Instead, its electron donating properties likely increase electron density at the sulfonyl oxygens, thereby strengthening their

hydrogen bonding capabilities and accounting for its remarkable potency, comparable to that of the carboxylic acid. Selectivity profiles of the most potent derivatives further revealed no appreciable inhibition of MMP-1,-2,-9 (IC_{50}'s > 10 μM) and only minimal inhibition of MMP-8 and -10 (IC_{50} > 6 μM). Molecular docking suggests that the 2-fluoropyridin-4-yl regioisomer is not well tolerated by other MMPs and that the larger S1" functional groups cannot be accommodated by these enzymes with shallower binding pockets.[21] Along with the increased potency, these inhibitors represent some of the most selective MMP-13 inhibitors reported to date. These discoveries mark significant advances that are anticipated to improve the synthetic availability and rationale design of highly potent and selective MMP-13 inhibitors from the quinazoline-2-carboxamide class.

A high-yielding automated radiosynthesis of **[^{11}C]29f** was developed using [^{11}C]CH_3OTf to expedite screenings of radiotracer performance in atherosclerotic mice. *Ex vivo* experiments with **[^{11}C]29f** revealed accelerated clearance from the blood (~1 %ID·g^{-1}) with minimal retention of radioactivity in the myocardium (~2 %ID·g^{-1}) and liver (~4 %ID·g^{-1}), maintaining superior pharmacokinetics over [^{18}F]FMBP. Overall, the distribution of **[^{11}C]29f** appears similar to [^{18}F]5j, albeit with a ~3-fold reduction in blood radioactivity, demonstrating that lowering lipophilicity (Log D: ~2.4) was an effective strategy to reduce background signal and enhance imaging contrast. While atherosclerotic plaques were detected with **[^{11}C]29f** by *ex vivo* aortic autoradiography, uptake was ~4-fold lower than [^{18}F]5j. Under WAY170523 blocking conditions, **[^{11}C]29f** uptake was not significantly reduced, suggesting that the observed uptake was likely non-specific. Considering that [^{18}F]5j exhibited greater atherosclerotic plaque uptake and demonstrated an extent of specific binding to MMP-13 in identical experiments, the higher blood radioactivity and prolonged systemic circulation of this radioligand may have been necessary to provide adequate

time for specific plaque accumulation. Nevertheless, this same pharmacokinetic property only permitted *ex vivo* detection and quantification of atherosclerotic plaque uptake. Rapid clearance of blood radioactivity is needed to achieve contrast for non-invasive vascular imaging but also requires a high affinity radioligand and a high-density molecular target to provide adequate plaque uptake. As **[^{11}C]29f** exhibits excellent MMP-13 potency and selectivity and possesses favourable pharmacokinetics, the expression of MMP-13 in atherosclerotic plaques of the *ApoE*$^{-/-}$ mouse model is likely insufficient for *in vivo* imaging.

Taken together, this study elucidated the essential structural features of the quinazoline-2-carbomaxide scaffold for the design of highly potent and selective MMP-13 inhibitors amenable to radiolabeling with fluorine-18 or carbon-11. The discovery of compound **29f**, bearing a tertiary sulfonamide, uncovered an optimized binding conformation that provides exceptional MMP-13 potency and selectivity, comparable to carboxylate-containing inhibitors, without risk of OAT liability. Translational PET studies with **[^{11}C]29f** demonstrated a favourable pharmacokinetic profile for vascular imaging, but atherosclerotic plaque uptake was found to be non-specific. Overall, while **[^{11}C]29f** is the most potent and selective MMP-13 PET radiotracer developed to date, it is unsuitable for atherosclerotic plaque imaging in *ApoE*$^{-/-}$ mice. Additional studies of **[^{11}C]29f** may uncover its utility for alternative applications in which MMP-13 is the primary target and greatly overexpressed.

5.4.3 Limitations

In the current study, ^{11}C-methylation of **29f** was performed as a robust and convenient method to take advantage of the dimethylamine on the tertiary sulfonamide and facilitate *in vivo* imaging without the need for significant optimization.[22] While this strategy proved efficient and

enabled characterization of radiotracer pharmacokinetics, the short half-life of carbon-11 is not well-suited for atherosclerotic plaque imaging and radiofluorination of the 2-fluoropyridine, together with its longer half-life and shorter positron range, may provide additional contrast and resolution at later imaging time points. As previously conducted for [^{18}F]5j, a time-course study up to 120 min with [^{18}F]29f would show if blood radioactivity continues to washout over time and better contrast can be expected with late imaging.[11]

5.4.4 Mouse Models of Atherosclerosis

5.4.4.1 ApoE$^{-/-}$ and LDLR$^{-/-}$ mice

Apoplipoprotein E deficient (*ApoE$^{-/-}$*) and low-density lipoprotein receptor deficient (*LDLR$^{-/-}$*) mice represent the two most widely utilized mouse models of atherosclerosis that operate through a related mechanism.[23] ApoE is a protein found on the surface of cholesterol-rich LDL particles that plays an important role in the transport and clearance of LDL from the bloodstream.[24] ApoE is a recognized ligand of LDLR, a cell-surface receptor primarily expressed in the liver that is responsible for LDL internalization and cholesterol usage or storage.[24] Deficiencies in either ApoE or LDLR lead to elevated levels of circulating LDL and initiation of atherosclerosis, either due to impaired uptake of LDL or the lack of the receptor needed for its clearance.[23] These genetic models exhibit significant atherosclerotic plaque formation in the aortic root aortic arch and carotid arteries. Differences in the lipid profiles and size of the developing atherosclerotic plaques exist, with ApoE$^{-/-}$ mice possessing higher levels of circulating cholesterol, triglyceride-rich VLDL particles, and larger plaques more characteristic of those observed in humans.[23,25,26] Moreover, unlike LDLR$^{-/-}$ mice which require a high-fat diet (HFD) to induce atherosclerotic plaque development, *ApoE$^{-/-}$* mice spontaneously develop plaques on standard diet, with plaque progression further accelerated on HFD.[25] Accordingly, *ApoE$^{-/-}$* mice were selected for preclinical

evaluations of radiotracer performance as the most reliable and well-established mouse model of atherosclerosis.

5.4.4.2 Limitations of the *ApoE*$^{-/-}$ model

While the availability of these mouse models has been instrumental in improving our understanding of the mechanisms of atherogenesis they differ from human atherosclerosis in terms of their plaque distribution and stability. Unlike in humans where CAD is most frequently detected and associated with future risk of myocardial infarction and heart failure, analyses of the coronary arteries in mice is precluded by their small size and the fact that neither model exhibits significant coronary artery atherosclerosis.[25] Additionally, these mouse models do not manifest unstable atherosclerotic plaques with evident rupture and overlying thrombosis that are considered causal in most life-threatening cardiovascular events.[25] This phenotype has only been observed sporadically in *ApoE*$^{-/-}$ mice after more than one year of HFD in the brachiocephalic artery and not considered a feasible or reproducible model of plaque rupture.[27] As such, studies to assess whether the developed MMP-13 selective PET radiotracer is capable of characterizing of high-risk atherosclerosis and differentiating stable from unstable plaques were not possible.

5.5 Future Directions

5.5.1 Correlative Imaging with MMP-13 and Collagen

While we initially conducted immunofluorescent staining to determine the percent positive areas of MMP-2, -9, and -13 in atherosclerotic plaques from ApoE$^{-/-}$ mice, absolute quantification of MMP activity and expression at the protein level by zymography and western blot at various stages in atherosclerotic plaque progression would be informative.[3,28] Considering that atherosclerotic plaque composition is highly dynamic and MMP-13 levels may evolve over time, correlations of *ex vivo* radiotracer plaque uptake with MMP-13 activity and collagen content would

demonstrate its sensitivity.[29,30] To accomplish this, ApoE$^{-/-}$ mice can be fed a high fat diet for 4-16 weeks to reproduce early, intermediate, and advances staged atherosclerosis and the ability of the radiotracer to track molecular changes in MMP-13 can be assessed.[31]

5.5.2 Larger Animal Models of Atherosclerosis

Notwithstanding the substantial achievements in radiotracer optimization, non-invasive detection of atherosclerotic mouse plaques with **[^{11}C]29f** is still unreliable. As such, it is believed that small anatomical size of the aortic vessel, which is at the limit in spatial resolution of PET/CT (~1 mm), is an inherent barrier for atherosclerotic plaque imaging in mice.[32–34] Outside [^{18}F]FDG and [^{18}F]NaF, few radiotracers have clearly shown non-invasive atherosclerotic plaque imaging in *ApoE*$^{-/-}$ mice and have largely relied on preclinical validation by *ex vivo* autoradiography or larger animals.[19,35–40] To this end, future imaging studies in larger animal models, such as atherosclerotic rabbits, may be warranted.[41]

5.5.3 Mouse Model of Plaque Rupture and MMP Activation

More recently, atherosclerotic *ApoE*$^{-/-}$ mice with a mutation (C1039G$^{+/-}$) in the fibrillin-1 (Fbn1) gene, which leads to elastin fragmentation, have been generated as a model of plaque instability and rupture, that more closely replicates human disease.[42,43] When fed a western atherogenic diet these *ApoE*$^{-/-}$*Fbn1*$^{C1039G+/-}$ hybrid mice develop atherosclerotic plaques with markedly increased necrotic core size, T-cell infiltration, decreased collagen content, extensive neovascularization, and intraplaque haemorrhage, compared with age matched ApoE$^{-/-}$ mice.[43] Most relevantly, these atherosclerotic plaques also possess significantly elevated levels of MMP-2,-9,-12 and -13 activity and rupture was frequently observed in the ascending aorta and brachiocephalic artery.[43] Therefore, this model appears suitable to differentiate radiotracer uptake

in stable and unstable atherosclerotic plaques and predict risk of rupture. As a significant proportion of these mice suddenly die between 15-30 weeks due to myocardial infarction (75%), treatment with the MMP-13 selective inhibitor **29f**, could also serve to demonstrate its efficacy as a plaque stabilizing therapy and ability to improve survival outcomes.

5.5.4 Alternative Application

As discussed, the initial discovery of selective MMP-13 inhibitors was motivated by its potential as an OA treatment. MMP-13 preferentially degrades type II collagen in chondrocytes, which represents the major structural component of joint cartilage, and plays a prominent role in growth plate development and bone remodeling.[44–46] Chondrocyte-selective MMP-13 knockout or inhibition has been shown to decelerate OA progression and increases articular cartilage area and thickness, accompanied by greater collagen content.[47,48] As briefly demonstrated for the carboxylate-containing quinazoline-2-carboxamide inhibitor, the rat model of monoiodoacetate (MIA)-induced OA can be employed to evaluate the efficacy of MMP-13 selective inhibition with **29f**.[12] Diagnostic **[^{11}C]29f** PET/CT imaging can be used to non-invasively monitor articular MMP-13 activity and **29f** treatment efficacy. Histological analyses of OA joint collagen content can be performed to support these findings. Sufficient *in vivo* OA imaging contrast is anticipated as **[^{11}C]29f** uptake in the primary structures surrounding the joint, including bone and muscle, remain low (~0.5 %ID·g^{-1}).

5.5.5 Working Hypothesis

Despite our efforts, non-invasive atherosclerotic mouse plaque imaging with an MMP-13 selective PET radiotracer has not yet been demonstrated. Given the destructive role of MMP-13 in collagen remodeling and the development of unstable atherosclerotic plaques, it remains an

imaging target of interest. As insufficient imaging contrast was achieved with **[^{11}C]29f** possessing excellent target affinity, selectivity, and pharmacokinetic properties for vascular imaging, it is conceivable that MMP-13 expression and activity in atherosclerotic mouse plaques is inadequate. MMP-13 may be differentially expressed in humans, but absolute quantification is necessary to confirm this possibility and remains an ongoing endeavor. Nevertheless, as MMPs can have distinct and opposing roles toward atherosclerotic plaque stabilization, selective MMP imaging is strategic and offers the potential for superior *in vivo* specificity, at the expense of sensitivity due to lower target density. To this end, it is hypothesized that targeting specific MMP subfamilies, rather than individual MMPs, with overlapping substrate specificity and pathophysiological functions may be advantageous. As each of the collagenases (MMP-1,-8, and -13) contribute to destructive collagen remodeling, perhaps to varying extents, and are known to colocalize together with cleaved collagen in unstable atherosclerotic plaques, their collectively greater target density may enhance sensitivity and ultimately facilitate non-invasive imaging of thin-capped and collagen poor atherosclerotic plaques most prone to rupture.[28,49,50]

5.6 References

(1) Kalinin, D. V.; Wagner, S.; Riemann, B.; Hermann, S.; Schmidt, F.; Becker-Pauly, C.; Rose-John, S.; Schäfers, M.; Holl, R. Novel Potent Proline-Based Metalloproteinase Inhibitors: Design, (Radio)Synthesis, and First in Vivo Evaluation as Radiotracers for Positron Emission Tomography. *J. Med. Chem.* **2016**, *59* (20), 9541–9559. https://doi.org/10.1021/acs.jmedchem.6b01291.

(2) Hugenberg, V.; Wagner, S.; Kopka, K.; Schäfers, M.; Schuit, R. C.; Windhorst, A. D.; Hermann, S. Radiolabeled Selective Matrix Metalloproteinase 13 (MMP-13) Inhibitors: (Radio)Syntheses and in Vitro and First in Vivo Evaluation. *J. Med. Chem.* **2017**, *60* (1), 307–321. https://doi.org/10.1021/acs.jmedchem.6b01284.

(3) Buchler, A.; Munch, M.; Farber, G.; Zhao, X.; Al-Haddad, R.; Farber, E.; Rotstein, B. H. Selective Imaging of Matrix Metalloproteinase-13 to Detect Extracellular Matrix Remodeling in Atherosclerotic Lesions. *Mol. Imaging Biol.* **2021**. https://doi.org/10.1007/s11307-021-01626-9.

(4) Wagner, S.; Breyholz, H.-J.; Law, M. P.; Faust, A.; Höltke, C.; Schröer, S.; Haufe, G.; Levkau, B.; Schober, O.; Schäfers, M.; Kopka, K. Novel Fluorinated Derivatives of the Broad-Spectrum MMP Inhibitors *N* -Hydroxy-2(*R*)-[[(4-Methoxyphenyl)Sulfonyl](Benzyl)- and (3-Picolyl)-Amino]-3-Methyl-Butanamide as Potential Tools for the Molecular Imaging of Activated MMPs with PET. *J. Med. Chem.* **2007**, *50* (23), 5752–5764. https://doi.org/10.1021/jm0708533.

(5) Zinnhardt, B.; Pigeon, H.; Thézé, B.; Viel, T.; Wachsmuth, L.; Fricke, I. B.; Schelhaas, S.; Honold, L.; Schwegmann, K.; Wagner, S.; Faust, A.; Faber, C.; Kuhlmann, M. T.; Hermann, S.; Schäfers, M.; Winkeler, A.; Jacobs, A. H. Combined PET Imaging of the

Inflammatory Tumor Microenvironment Identifies Margins of Unique Radiotracer Uptake. *Cancer Res.* **2017**, *77* (8), 1831–1841. https://doi.org/10.1158/0008-5472.CAN-16-2628.

(6) Vazquez, N.; Missault, S.; Vangestel, C.; Deleye, S.; Thomae, D.; Veken, P. V. der; Augustyns, K.; Staelens, S.; Dedeurwaerdere, S.; Wyffels, L. Evaluation of [18F]BR420 and [18F]BR351 as Radiotracers for MMP-9 Imaging in Colorectal Cancer. *J. Label. Compd. Radiopharm.* **2017**, *60* (1), 69–79. https://doi.org/10.1002/jlcr.3476.

(7) Zinnhardt, B.; Viel, T.; Wachsmuth, L.; Vrachimis, A.; Wagner, S.; Breyholz, H.-J.; Faust, A.; Hermann, S.; Kopka, K.; Faber, C.; Dollé, F.; Pappata, S.; Planas, A. M.; Tavitian, B.; Schäfers, M.; Sorokin, L. M.; Kuhlmann, M. T.; Jacobs, A. H. Multimodal Imaging Reveals Temporal and Spatial Microglia and Matrix Metalloproteinase Activity after Experimental Stroke. *J. Cereb. Blood Flow Metab.* **2015**, *35* (11), 1711–1721. https://doi.org/10.1038/jcbfm.2015.149.

(8) Joshi, N. V.; Vesey, A. T.; Williams, M. C.; Shah, A. S. V.; Calvert, P. A.; Craighead, F. H. M.; Yeoh, S. E.; Wallace, W.; Salter, D.; Fletcher, A. M.; van Beek, E. J. R.; Flapan, A. D.; Uren, N. G.; Behan, M. W. H.; Cruden, N. L. M.; Mills, N. L.; Fox, K. A. A.; Rudd, J. H. F.; Dweck, M. R.; Newby, D. E. 18F-Fluoride Positron Emission Tomography for Identification of Ruptured and High-Risk Coronary Atherosclerotic Plaques: A Prospective Clinical Trial. *The Lancet* **2014**, *383* (9918), 705–713. https://doi.org/10.1016/S0140-6736(13)61754-7.

(9) McKenney-Drake, M. L.; Moghbel, M. C.; Paydary, K.; Alloosh, M.; Houshmand, S.; Moe, S.; Salavati, A.; Sturek, J. M.; Territo, P. R.; Weaver, C.; Werner, T. J.; Høilund-Carlsen, P. F.; Sturek, M.; Alavi, A. 18F-NaF and 18F-FDG as Molecular Probes in the

Evaluation of Atherosclerosis. *Eur. J. Nucl. Med. Mol. Imaging* **2018**, *45* (12), 2190–2200. https://doi.org/10.1007/s00259-018-4078-0.

(10) Tawakol, A.; Migrino, R. Q.; Bashian, G. G.; Bedri, S.; Vermylen, D.; Cury, R. C.; Yates, D.; LaMuraglia, G. M.; Furie, K.; Houser, S.; Gewirtz, H.; Muller, J. E.; Brady, T. J.; Fischman, A. J. In Vivo 18F-Fluorodeoxyglucose Positron Emission Tomography Imaging Provides a Noninvasive Measure of Carotid Plaque Inflammation in Patients. *J. Am. Coll. Cardiol.* **2006**, *48* (9), 1818–1824. https://doi.org/10.1016/j.jacc.2006.05.076.

(11) Buchler, A.; Ismailani, U. S.; MacMullin, N.; Abdirahman, F.; Adi, M.; Bi, C.; Jany, C.; Keillor, J. W.; Rotstein, B. H. Quinazoline-2-Carboxamides as Selective PET Radiotracers for Matrix Metalloproteinase-13 Imaging in Atherosclerosis. *J. Med. Chem.* **2023**, *66* (10), 6682–6696. https://doi.org/10.1021/acs.jmedchem.2c02107.

(12) Nara, H.; Sato, K.; Naito, T.; Mototani, H.; Oki, H.; Yamamoto, Y.; Kuno, H.; Santou, T.; Kanzaki, N.; Terauchi, J.; Uchikawa, O.; Kori, M. Discovery of Novel, Highly Potent, and Selective Quinazoline-2-Carboxamide-Based Matrix Metalloproteinase (MMP)-13 Inhibitors without a Zinc Binding Group Using a Structure-Based Design Approach. *J. Med. Chem.* **2014**, *57* (21), 8886–8902. https://doi.org/10.1021/jm500981k.

(13) Ruminski, P. G.; Massa, M.; Strohbach, J.; Hanau, C. E.; Schmidt, M.; Scholten, J. A.; Fletcher, T. R.; Hamper, B. C.; Carroll, J. N.; Shieh, H. S.; Caspers, N.; Collins, B.; Grapperhaus, M.; Palmquist, K. E.; Collins, J.; Baldus, J. E.; Hitchcock, J.; Kleine, H. P.; Rogers, M. D.; McDonald, J.; Munie, G. E.; Messing, D. M.; Portolan, S.; Whiteley, L. O.; Sunyer, T.; Schnute, M. E. Discovery of N-(4-Fluoro-3-Methoxybenzyl)-6-(2-(((2S,5R)-5-(Hydroxymethyl)-1,4-Dioxan-2-Yl)Methyl)-2H-Tetrazol-5-Yl)-2-Methylpyrimidine-4-Carboxamide. A Highly Selective and Orally Bioavailable Matrix

Metalloproteinase-13 Inhibitor for the Potential Treatment of Osteoarthritis. *J. Med. Chem.* **2016**, *59* (1), 313–327. https://doi.org/10.1021/acs.jmedchem.5b01434.

(14) Cai, H.; Agrawal, A. K.; Putt, D. A.; Hashim, M.; Reddy, A.; Brodfuehrer, J.; Surendran, N.; Lash, L. H. Assessment of the Renal Toxicity of Novel Anti-Inflammatory Compounds Using Cynomolgus Monkey and Human Kidney Cells. *Toxicology* **2009**, *258* (1), 56–63. https://doi.org/10.1016/j.tox.2009.01.006.

(15) Rudd, J. H. F.; Myers, K. S.; Bansilal, S.; Machac, J.; Pinto, C. A.; Tong, C.; Rafique, A.; Hargeaves, R.; Farkouh, M.; Fuster, V.; Fayad, Z. A. Atherosclerosis Inflammation Imaging with ^{18} F-FDG PET: Carotid, Iliac, and Femoral Uptake Reproducibility, Quantification Methods, and Recommendations. *J. Nucl. Med.* **2008**, *49* (6), 871–878. https://doi.org/10.2967/jnumed.107.050294.

(16) Kubota, K.; Itoh, M.; Ozaki, K.; Ono, S.; Tashiro, M.; Yamaguchi, K.; Akaizawa, T.; Yamada, K.; Fukuda, H. Advantage of Delayed Whole-Body FDG-PET Imaging for Tumour Detection. *Eur. J. Nucl. Med.* **2001**, *28* (6), 696–703. https://doi.org/10.1007/s002590100537.

(17) Slart, R. H. J. A.; Glaudemans, A. W. J. M.; Gheysens, O.; Lubberink, M.; Kero, T.; Dweck, M. R.; Habib, G.; Gaemperli, O.; Saraste, A.; Gimelli, A.; Georgoulias, P.; Verberne, H. J.; Bucerius, J.; Rischpler, C.; Hyafil, F.; Erba, P. A. Procedural Recommendations of Cardiac PET/CT Imaging: Standardization in Inflammatory-, Infective-, Infiltrative-, and Innervation- (4Is) Related Cardiovascular Diseases: A Joint Collaboration of the EACVI and the EANM: Summary. *Eur. Heart J. Cardiovasc. Imaging* **2020**, *21* (12), 1320–1330. https://doi.org/10.1093/ehjci/jeaa299.

(18) Ye, Y.; Toczek, J.; Gona, K.; Kim, H.-Y.; Han, J.; Razavian, M.; Golestani, R.; Zhang, J.; Wu, T. L.; Ghosh, M.; Jung, J.-J.; Sadeghi, M. M. Novel Arginine-Containing Macrocyclic MMP Inhibitors: Synthesis, 99mTc-Labeling, and Evaluation. *Sci. Rep.* **2018**, *8*, 11647. https://doi.org/10.1038/s41598-018-29941-2.

(19) Toczek, J.; Ye, Y.; Gona, K.; Kim, H.-Y.; Han, J.; Razavian, M.; Golestani, R.; Zhang, J.; Wu, T. L.; Jung, J.-J.; Sadeghi, M. M. Preclinical Evaluation of RYM1, a Matrix Metalloproteinase-Targeted Tracer for Imaging Aneurysm. *J. Nucl. Med. Off. Publ. Soc. Nucl. Med.* **2017**, *58* (8), 1318–1323. https://doi.org/10.2967/jnumed.116.188656.

(20) Dollé, F. Fluorine-18-Labelled Fluoropyridines: Advances in Radiopharmaceutical Design. *Curr. Pharm. Des.* **2005**, *11* (25), 3221–3235. https://doi.org/10.2174/138161205774424645.

(21) Gimeno, A.; Beltrán-Debón, R.; Mulero, M.; Pujadas, G.; Garcia-Vallvé, S. Understanding the Variability of the S1′ Pocket to Improve Matrix Metalloproteinase Inhibitor Selectivity Profiles. *Drug Discov. Today* **2020**, *25* (1), 38–57. https://doi.org/10.1016/j.drudis.2019.07.013.

(22) Buchler, A.; Ismailani, U. S.; MacMullin, N.; Abdirahman, F.; Adi, M.; Bi, C.; Jany, C.; Keillor, J. W.; Rotstein, B. H. Quinazoline-2-Carboxamides as Selective PET Radiotracers for Matrix Metalloproteinase-13 Imaging in Atherosclerosis. *J. Med. Chem.* **2023**, *66* (10), 6682–6696. https://doi.org/10.1021/acs.jmedchem.2c02107.

(23) Getz, G. S.; Reardon, C. A. Do the Apoe−/− and Ldlr−/−mice Yield the Same Insight on Atherogenesis? *Arterioscler. Thromb. Vasc. Biol.* **2016**, *36* (9), 1734–1741. https://doi.org/10.1161/ATVBAHA.116.306874.

(24) Getz, G. S.; Reardon, C. A. Apoprotein E and Reverse Cholesterol Transport. *Int. J. Mol. Sci.* **2018**, *19* (11), 3479. https://doi.org/10.3390/ijms19113479.

(25) Getz, G. S.; Reardon, C. A. Animal Models of Atherosclerosis. *Arterioscler. Thromb. Vasc. Biol.* **2012**, *32* (5), 1104–1115. https://doi.org/10.1161/ATVBAHA.111.237693.

(26) Véniant, M. M.; Withycombe, S.; Young, S. G. Lipoprotein Size and Atherosclerosis Susceptibility in Apoe−/− and Ldlr−/− Mice. *Arterioscler. Thromb. Vasc. Biol.* **2001**, *21* (10), 1567–1570. https://doi.org/10.1161/hq1001.097780.

(27) Johnson, J. L.; Jackson, C. L. Atherosclerotic Plaque Rupture in the Apolipoprotein E Knockout Mouse. *Atherosclerosis* **2001**, *154* (2), 399–406. https://doi.org/10.1016/s0021-9150(00)00515-3.

(28) Sukhova, G. K.; Schönbeck, U.; Rabkin, E.; Schoen, F. J.; Poole, A. R.; Billinghurst, R. C.; Libby, P. Evidence for Increased Collagenolysis by Interstitial Collagenases-1 and -3 in Vulnerable Human Atheromatous Plaques. *Circulation* **1999**, *99* (19), 2503–2509. https://doi.org/10.1161/01.CIR.99.19.2503.

(29) Zhao, Y.; Ye, D.; Wang, J.; Calpe-Berdiel, L.; Azzis, S. B. R. N.; Van Berkel, T. J. C.; Van Eck, M. Stage-Specific Remodeling of Atherosclerotic Lesions upon Cholesterol Lowering in LDL Receptor Knockout Mice. *Am. J. Pathol.* **2011**, *179* (3), 1522–1532. https://doi.org/10.1016/j.ajpath.2011.05.020.

(30) Ohshima, S.; Petrov, A.; Fujimoto, S.; Zhou, J.; Azure, M.; Edwards, D. S.; Murohara, T.; Narula, N.; Tsimikas, S.; Narula, J. Molecular Imaging of Matrix Metalloproteinase Expression in Atherosclerotic Plaques of Mice Deficient in Apolipoprotein e or Low-Density-Lipoprotein Receptor. *J. Nucl. Med. Off. Publ. Soc. Nucl. Med.* **2009**, *50* (4), 612–617. https://doi.org/10.2967/jnumed.108.055889.

(31) Whitman, S. C. A Practical Approach to Using Mice in Atherosclerosis Research. *Clin. Biochem. Rev.* **2004**, *25* (1), 81–93.

(32) Alavi, A.; Werner, T. J.; Høilund-Carlsen, P. F. What Can Be and What Cannot Be Accomplished with PET to Detect and Characterize Atherosclerotic Plaques. *J. Nucl. Cardiol. Off. Publ. Am. Soc. Nucl. Cardiol.* **2018**, *25* (6), 2012–2015. https://doi.org/10.1007/s12350-017-0977-x.

(33) Alavi, A.; Werner, T. J.; Raynor, W.; Høilund-Carlsen, P. F.; Revheim, M.-E. Critical Review of PET Imaging for Detection and Characterization of the Atherosclerotic Plaques with Emphasis on Limitations of FDG-PET Compared to NaF-PET in This Setting. *Am. J. Nucl. Med. Mol. Imaging* **2021**, *11* (5), 337–351.

(34) Moses, W. W. Fundamental Limits of Spatial Resolution in PET. *Nucl. Instrum. Methods Phys. Res. Sect. Accel. Spectrometers Detect. Assoc. Equip.* **2011**, *648 Supplement 1*, S236–S240. https://doi.org/10.1016/j.nima.2010.11.092.

(35) Razavian, M.; Tavakoli, S.; Zhang, J.; Nie, L.; Dobrucki, L. W.; Sinusas, A. J.; Azure, M.; Robinson, S.; Sadeghi, M. M. Atherosclerosis Plaque Heterogeneity and Response to Therapy Detected by in Vivo Molecular Imaging of Matrix Metalloproteinase Activation. *J. Nucl. Med. Off. Publ. Soc. Nucl. Med.* **2011**, *52* (11), 1795–1802. https://doi.org/10.2967/jnumed.111.092379.

(36) Toczek, J.; Gona, K.; Liu, Y.; Ahmad, A.; Ghim, M.; Ojha, D.; Kukreja, G.; Salarian, M.; Luehmann, H.; Heo, G. S.; Guzman, R. J.; Ochoa Chaar, C. I.; Tellides, G.; Hassab, A. H. M.; Ye, Y.; Shoghi, K. I.; Zayed, M. A.; Gropler, R. J.; Sadeghi, M. M. Positron Emission Tomography Imaging of Vessel Wall Matrix Metalloproteinase Activity in Abdominal

Aortic Aneurysm. *Circ. Cardiovasc. Imaging* **2023**, *16* (1), e014615. https://doi.org/10.1161/CIRCIMAGING.122.014615.

(37) Fu, Z.; Lin, Q.; Xu, Z.; Zhao, Y.; Cheng, Y.; Shi, D.; Fu, W.; Yang, T.; Shi, H.; Cheng, D. P2X7 Receptor-Specific Radioligand 18F-FTTM for Atherosclerotic Plaque PET Imaging. *Eur. J. Nucl. Med. Mol. Imaging* **2022**, *49* (8), 2595–2604. https://doi.org/10.1007/s00259-022-05689-w.

(38) Li, X.; Bauer, W.; Kreissl, M. C.; Weirather, J.; Bauer, E.; Israel, I.; Richter, D.; Riehl, G.; Buck, A.; Samnick, S. Specific Somatostatin Receptor II Expression in Arterial Plaque: (68)Ga-DOTATATE Autoradiographic, Immunohistochemical and Flow Cytometric Studies in apoE-Deficient Mice. *Atherosclerosis* **2013**, *230* (1), 33–39. https://doi.org/10.1016/j.atherosclerosis.2013.06.018.

(39) Hyafil, F.; Pelisek, J.; Laitinen, I.; Schottelius, M.; Mohring, M.; Döring, Y.; Vorst, E. P. C. van der; Kallmayer, M.; Steiger, K.; Poschenrieder, A.; Notni, J.; Fischer, J.; Baumgartner, C.; Rischpler, C.; Nekolla, S. G.; Weber, C.; Eckstein, H.-H.; Wester, H.-J.; Schwaiger, M. Imaging the Cytokine Receptor CXCR4 in Atherosclerotic Plaques with the Radiotracer 68Ga-Pentixafor for PET. *J. Nucl. Med.* **2017**, *58* (3), 499–506. https://doi.org/10.2967/jnumed.116.179663.

(40) Blasi, F.; Oliveira, B. L.; Rietz, T. A.; Rotile, N. J.; Day, H.; Looby, R. J.; Ay, I.; Caravan, P. Effect of Chelate Type and Radioisotope on the Imaging Efficacy of 4 Fibrin-Specific PET Probes. *J. Nucl. Med.* **2014**, *55* (7), 1157–1163. https://doi.org/10.2967/jnumed.113.136275.

(41) Fan, J.; Kitajima, S.; Watanabe, T.; Xu, J.; Zhang, J.; Liu, E.; Chen, Y. E. Rabbit Models for the Study of Human Atherosclerosis: From Pathophysiological Mechanisms to

Translational Medicine. *Pharmacol. Ther.* **2015**, *0*, 104–119. https://doi.org/10.1016/j.pharmthera.2014.09.009.

(42) Van Herck, J. L.; De Meyer, G. R. Y.; Martinet, W.; Van Hove, C. E.; Foubert, K.; Theunis, M. H.; Apers, S.; Bult, H.; Vrints, C. J.; Herman, A. G. Impaired Fibrillin-1 Function Promotes Features of Plaque Instability in Apolipoprotein E-Deficient Mice. *Circulation* **2009**, *120* (24), 2478–2487. https://doi.org/10.1161/CIRCULATIONAHA.109.872663.

(43) Van der Donckt, C.; Van Herck, J. L.; Schrijvers, D. M.; Vanhoutte, G.; Verhoye, M.; Blockx, I.; Van Der Linden, A.; Bauters, D.; Lijnen, H. R.; Sluimer, J. C.; Roth, L.; Van Hove, C. E.; Fransen, P.; Knaapen, M. W.; Hervent, A.-S.; De Keulenaer, G. W.; Bult, H.; Martinet, W.; Herman, A. G.; De Meyer, G. R. Y. Elastin Fragmentation in Atherosclerotic Mice Leads to Intraplaque Neovascularization, Plaque Rupture, Myocardial Infarction, Stroke, and Sudden Death. *Eur. Heart J.* **2015**, *36* (17), 1049–1058. https://doi.org/10.1093/eurheartj/ehu041.

(44) Borden, P.; Solymar, D.; Sucharczuk, A.; Lindman, B.; Cannon, P.; Heller, R. A. Cytokine Control of Interstitial Collagenase and Collagenase-3 Gene Expression in Human Chondrocytes. *J. Biol. Chem.* **1996**, *271* (38), 23577–23581. https://doi.org/10.1074/jbc.271.38.23577.

(45) Inada, M.; Wang, Y.; Byrne, M. H.; Rahman, M. U.; Miyaura, C.; López-Otín, C.; Krane, S. M. Critical Roles for Collagenase-3 (Mmp13) in Development of Growth Plate Cartilage and in Endochondral Ossification. *Proc. Natl. Acad. Sci. U. S. A.* **2004**, *101* (49), 17192–17197. https://doi.org/10.1073/pnas.0407788101.

(46) Kamekura, S.; Hoshi, K.; Shimoaka, T.; Chung, U.; Chikuda, H.; Yamada, T.; Uchida, M.; Ogata, N.; Seichi, A.; Nakamura, K.; Kawaguchi, H. Osteoarthritis Development in Novel Experimental Mouse Models Induced by Knee Joint Instability. *Osteoarthritis Cartilage* **2005**, *13* (7), 632–641. https://doi.org/10.1016/j.joca.2005.03.004.

(47) Wang, M.; Sampson, E. R.; Jin, H.; Li, J.; Ke, Q. H.; Im, H.-J.; Chen, D. MMP13 Is a Critical Target Gene during the Progression of Osteoarthritis. *Arthritis Res. Ther.* **2013**, *15* (1), R5. https://doi.org/10.1186/ar4133.

(48) Little, C. B.; Barai, A.; Burkhardt, D.; Smith, S. M.; Fosang, A. J.; Werb, Z.; Shah, M.; Thompson, E. W. Matrix Metalloproteinase 13-Deficient Mice Are Resistant to Osteoarthritic Cartilage Erosion but Not Chondrocyte Hypertrophy or Osteophyte Development. *Arthritis Rheum.* **2009**, *60* (12), 3723–3733. https://doi.org/10.1002/art.25002.

(49) Molloy, K. J.; Thompson, M. M.; Jones, J. L.; Schwalbe, E. C.; Bell, P. R. F.; Naylor, A. R.; Loftus, I. M. Unstable Carotid Plaques Exhibit Raised Matrix Metalloproteinase-8 Activity. *Circulation* **2004**, *110* (3), 337–343. https://doi.org/10.1161/01.CIR.0000135588.65188.14.

(50) Nikkari, S. T.; O'Brien, K. D.; Ferguson, M.; Hatsukami, T.; Welgus, H. G.; Alpers, C. E.; Clowes, A. W. Interstitial Collagenase (MMP-1) Expression in Human Carotid Atherosclerosis. *Circulation* **1995**, *92* (6), 1393–1398. https://doi.org/10.1161/01.CIR.92.6.1393.